ASME
SETTING THE STANDARD

Transactions of the ASME, Journal of Applied Mechanics (ISSN 0021-8936) is published bimonthly (Jan., Mar., May, July, Sept., Nov.) by The American Society of Mechanical Engineers, Three Park Avenue, New York, NY 10016. Periodicals postage paid at New York, NY and additional mailing offices. POSTMASTER: Send address changes to Transactions of the ASME, Journal of Applied Mechanics, c/o THE AMERICAN SOCIETY OF MECHANICAL ENGINEERS, 22 Law Drive, Box 2300, Fairfield, NJ 07007-2300.
CHANGES OF ADDRESS must be received at Society headquarters seven weeks before they are to be effective. Please send old label and new address.
STATEMENT from By-Laws. The Society shall not be responsible for statements or opinions advanced in papers or printed in its publications (B7.1, Para. 3).

Journal of Applied Mechanics

Published Bimonthly by ASME

VOLUME 75 • NUMBER 6 • NOVEMBER 2008

RESEARCH PAPERS

(Contents continued on inside back cover)

This journal is printed on acid-free paper, which exceeds the ANSI Z39.48-1992 specification for permanence of paper and library materials. ♾™
♻ 85% recycled content, including 10% post-consumer fibers.

Journal of Applied Mechanics Volume 75, Number 6 NOVEMBER 2008

TECHNICAL BRIEFS

ERRATA

The ASME Journal of Applied Mechanics is abstracted and indexed in the following:

Alloys Index, Aluminum Industry Abstracts, Applied Science & Technology Index, Ceramic Abstracts, Chemical Abstracts, Civil Engineering Abstracts, Compendex (The electronic equivalent of Engineering Index), Computer & Information Systems Abstracts, Corrosion Abstracts, Current Contents, EEA (Earthquake Engineering Abstracts Database), Electronics & Communications Abstracts Journal, Engineered Materials Abstracts, Engineering Index, Environmental Engineering Abstracts, Environmental Science and Pollution Management, Fluidex, Fuel & Energy Abstracts, GeoRef, Geotechnical Abstracts, INSPEC, International Aerospace Abstracts, Journal of Ferrocement, Materials Science Citation Index, Mechanical Engineering Abstracts, METADEX (The electronic equivalent of Metals Abstracts and Alloys Index), Metals Abstracts, Nonferrous Metals Alert, Polymers Ceramics Composites Alert, Referativnyi Zhurnal, Science Citation Index, SciSearch (Electronic equivalent of Science Citation Index), Shock and Vibration Digest, Solid State and Superconductivity Abstracts, Steels Alert, Zentralblatt MATH

Stochastic Morphological Modeling of Random Multiphase Materials

Lori Graham-Brady
Department of Civil Engineering,
Johns Hopkins University,
3400 North Charles Street, Latrobe Hall,
Baltimore, MD 21218

X. Frank Xu
Department of Civil, Environmental,
and Ocean Engineering,
Stevens Institute of Technology,
Castle Point on Hudson,
Hoboken, NJ 07030

A short-range-correlation (SRC) model is introduced in the framework of Markov/Gibbs random field theory to characterize and simulate random media. The Metropolis spin-flip algorithm is applied to build a robust simulator for multiphase random materials. Through development of the SRC model, several crucial conceptual ambiguities are clarified, and higher-order statistical simulation of random materials becomes computationally feasible. In the numerical examples, second- and third-order statistical simulations are demonstrated for biphase random materials, which shed light on the relationship between nth-order correlation functions and morphological features. Based on the observations, further conjectures are made concerning some fundamental morphological questions, particularly for future investigation of physical behavior of random media. It is expected that the SRC model can also be extended to third- and higher-order simulations of non-Gaussian stochastic processes such as wind pressure, ocean waves, and earthquake accelerations, which is an important research direction for high fidelity simulation of physical processes. [DOI: 10.1115/1.2957598]

1 Introduction

Physical behavior of natural and synthetic complex heterogeneous materials has been a fundamental research topic in diverse disciplines of geophysics, material science, chemical physics, biomedical engineering, etc. [1–3]. Examples of research interests include transport, electromagnetic, and mechanical properties of cellular solids, colloids, tissue, bone, porous rocks, soils, and manufactured composites such as foamed solids and polymer blends. Modeling and design of complex materials across multiple length and time scales is currently becoming one of the most active engineering research topics; thanks to recent advances in nanotechnology, multiscale modeling, and high-performance computers. There are basically two essential issues in modeling of stochastic morphology for complex heterogeneous materials:

1. characterization: appropriate translation of morphological information, generally perceivable by human vision, into a mathematically tractable model
2. simulation: applicability of a morphological model, i.e., whether the model enables convenient Monte Carlo generation of samples with desired configurations

A satisfactory morphological model should address both issues successfully, and in this work such a model, namely, the short-range-correlation (SRC) model, is established explicitly in the framework of Markov/Gibbs random field theory and is formally introduced into random media applications. Cross-disciplinary expertise involved in this study includes stochastic processes and random field theory, mathematical morphology, statistical mechanics, perception, computer vision, signal processes, texture analysis, statistical geology, pattern recognition, and optics [4–8].

Through development of the SRC model, several crucial conceptual ambiguities are clarified, and higher-order statistical simulation of random materials becomes computationally feasible. The SRC model takes advantage of a Metropolis spin-flip algorithm with the aim of minimizing the SRC energy (a descriptor of the error) of the simulated morphology. A similar approach was applied by Yeong and Torquato [9] to morphological simulation, although that work differed from the current work in three ways. First, in this study, morphologies are characterized through short-range-correlation functions, instead of full-range ones, which captures essential morphological features and significantly improves computing efficiency. Second, the current algorithm allows more efficient sample generation, which is the direct result of using a spin-flip algorithm that allows the volume fraction to vary slightly from sample to sample. Such variations in volume fraction are realistic in light of the slight volume fraction variations that occur in many real materials. Third, the current SRC energy measure, or error measure, is based on the nth-order correlation functions. The advantage to measuring the morphological energy (error) in terms of the nth-order correlation functions is that the importance of various order statistics can be identified directly from the results. By applying the morphological energy optimization to other quantities (such as lineal path functions), the connection to the nth-order statistics of the random process is not clear. In other words, the most important order of statistics can be identified for a given microstructure with a given application. In the numerical examples, second- and third-order statistical simulations are demonstrated for biphase random materials, which shed light onto the relationship between nth-order correlation functions and morphological features. Based on the observations, further conjectures are made, particularly for future investigation of physical behavior of random media.

The basic premise of this work is that the morphology of a random microstructure can be described as a stochastic process that is completely defined by the multivariate distribution, or approximately characterized with partial statistical information such as a hierarchical order of statistical moments or correlation functions. Existing models on morphologies of random materials basically follow two directions: translation models and correlation models, which are described in the sections that follow.

1.1 Translation Model. Even if the multivariate distribution of a stochastic process is fully known, no direct methods are available for simulating such a process in general. Among the few that can be simulated, most are directly tied to Gaussian multivariate distribution, and the rest either present formidable computational problems or are too restrictive to be of general interest [8]. The translation model, pointwise transforming a Gaussian random

Contributed by the Applied Mechanics Division of ASME for publication in the JOURNAL OF APPLIED MECHANICS. Manuscript received September 28, 2005; final manuscript received January 9, 2007; published online August 15, 2008. Review conducted by Matthew R. Begley.

field into a non-Gaussian one, was first studied in Gaussian input nonlinear systems in the field of signal processing in the 1950s, and was mathematically developed in the bivariate translation system [10]. The model was applied to multivariate systems [11], porous media [7,12–14], random materials [15–18], and generalized to level-cut filtered Poisson fields [19]. The translation model has two limitations: the inflexible multivariate distribution structure, and the requirement of non-negative definiteness of the underlying Gaussian process, which limit the applicability of the model [20,21]. These restrictions have been further observed in Ref. [22], where for general real-life random media morphologies the translation model does not often meet the requirement of non-negative definiteness. This presents a major challenge in applying translation models to random media; in fact, for many random media, such models are inadequate to accurately represent the microstructural features such as shape or connectivity.

1.2 Correlation Models. Making use of correlation functions to approximate a target multivariate distribution alleviates many of the limitations described above. With correlation models, a morphological characterization problem involving randomness is effectively converted into a numerical optimization problem. The relationship between nth-order statistics and random images was investigated early in vision research [23], and afterwards the second-order statistics, i.e., gray-level co-occurrence models, were extensively applied to texture analysis and image processing (Ref. [5] and references therein). In random media research, correlation models and relevant simulation techniques were given attention only recently [9,24], and then were applied to simulation of particulate media [25] and microstructures [26].

With respect to the characterization issue, correlation models effectively translate morphological information into a hierarchical order of correlation functions. Meanwhile, estimation of correlation functions from a target configuration is also straightforward. In this regard, however, there accompany some interesting and challenging questions, i.e., how and which order of correlation functions connects with what characteristics of a specific morphology, and which is the lowest order of correlation functions that is sufficient for a certain level of engineering approximation, such as effective physical properties. These questions will be addressed with some conjectures in the numerical examples and conclusions of this paper. There is also a relevant uniqueness problem first posed as Julesz conjecture [23,27], i.e., whether the first two orders of statistics are adequate to visually determine a texture. Intricacy of this uniqueness problem is mainly due to ambiguous definition of texture and the conceptual confusion between ensemble statistical correlation functions and single sample deterministic correlation functions, as pointed out in Ref. [28]. In the field of material simulation, the same ambiguity could lead to unsuccessful applications of correlation models, as noted in Ref. [29].

The simulation issue, i.e., how to realize a configuration sample based on given lower-order correlation functions, is an interesting inverse problem and a global optimization problem. For the case of multiphase materials, the problem more specifically becomes that of combinatorial optimization. It is worth noting that the optimization algorithm based on the full range of the second-order correlation function from a single sample leads to deterministic image reconstruction, a problem intensively pursued in the field of optics [30]; however, they are of no interest for stochastic simulation and characterization of a random medium [31]. Short-range-correlation matching allows a morphology to vary randomly from sample to sample, by relaxing the requirement of a strict match between the correlation functions of the original sample and that of the simulated sample.

2 Short-Range-Correlation Model

The idea of short-range-correlation matching first appeared in texture synthesis [32] for the purpose of information reduction. A recent application of the idea is on random image simulation [33], where effectiveness of the method was not fully demonstrated due to utilization of incomplete windowed correlation functions. A crucial point of the SRC model is application of windowed correlation functions, assuming long-range independence of morphologies. Such an assumption is justified when considering the difference between the ensemble (or true) correlation function and the sample correlation function of a stochastic process. For instance, the ensemble covariance function (normalized second-order correlation function) will typically decay to zero as the lag vector becomes larger, while the sample covariance function may be significant even at long range. These apparent long-range dependencies are not true correlation values, but they are the result of numerical error arising from a finite sample. By windowing the correlation, only the important values of the estimated correlation function are retained, providing a more appropriate basis for establishing the energy (or error) of a simulated sample morphology. This concept of short-range dependence is tied to those of correlation length in stochastic process theory, neighborhood systems in Markov random field theory, textural resolution in texture analysis [32], local roving window in vision research [34], and stochastic representative volume element (SRVE) in random media study [35].

2.1 Markov and Gibbs Random Field Theory. To be consistent with the computer simulation scheme and the usual image processing modeling, the SRC morphological model in this study is built onto a two-dimensional discrete lattice. Let $\boldsymbol{S}=\{i \mid 1 \leqslant i \leqslant M_1 \cdot M_2\}$ index a discrete set of sites for a morphological set X on a rectangular lattice $M_1 \times M_2$. In Markov random field theory, a neighborhood system $\boldsymbol{N}$ means only neighboring sites or so-called cliques have direct interactions on each other. The conditional probability of the value x_i is therefore conditioned only on its neighborhood system $\boldsymbol{N} \subseteq \boldsymbol{S}$

$$P(x_i|x_{\boldsymbol{S}-\{i\}}) = P(x_i|x_{\boldsymbol{N}_i}) \tag{1}$$

where the subscript $\boldsymbol{S}-\{i\}$ indicates the full lattice excluding site i. The equivalence of Markov and Gibbs random field models, known as the Hammersley–Clifford theorem [36], makes statistical physics and spatial statistics closely linked. The set X becomes a Gibbs random field on $\boldsymbol{S}$ and has a Gibbs multivariate distribution

$$P(x) = \frac{e^{-U(x)/T}}{\sum_{x \in X} e^{-U(x)/T}} \tag{2}$$

where the energy $U(x)$ is defined as

$$U(x) = \sum_{n=1}^{N_c} V_n(x) \tag{3}$$

N_c is the number of order of statistics to be included in the energy. The nth-order potential $V_n(x)$ will be defined further in the next section. The "temperature" T in Eq. (2) is a parameter related to the desired configuration. For example, if $T \to \infty$, X tends to be equally distributed, assigning a large number of morphological configurations approximately equal probabilities, and if $T \to 0$, X tends to concentrate at a specific value, assigning significant probability only to the global energy minimum. With given T and $V_n(x)$, we can generate a specific morphological pattern by sampling the configuration space X according to the distribution (2).

Note that in the current work the nth-order potential is equivalent to an error norm that measures differences between the nth-order statistics in the original morphology and the simulated morphology. Staying consistent with the nomenclature used in the field of image analysis [4], however, this error norm will be referred to as energy in the current work.

2.2 Short-Range-Correlation Energy. In order to develop an expression for the energy norm $U(x)$, the n-point correlation function $S_n(\mathbf{r}_1,\ldots,\mathbf{r}_n)$ is used, which is defined as

$$S_n(\mathbf{r}_1,\ldots,\mathbf{r}_n) = \sum_{x\in X'} x_1 x_2 \cdots x_n P(x) \tag{4}$$

In Eq. (4) $\mathbf{r}_1,\ldots,\mathbf{r}_n$ denote the spatial coordinates of the points $1,\ldots,n$ in the configuration x, the set X' of which constitutes a finite window in the lattice. Application of such a window is equivalent to truncating to zero the value of the correlation function for all spatial coordinate pairs $\mathbf{r}_1,\ldots,\mathbf{r}_n$ that fall outside the finite window size. Applying such a finite window indicates that the correlation information within the window is not altered at all, but the correlation function outside of the window is set to zero. An advantage to applying this truncation as opposed to a moving-average filter to the correlation function is that the slope at the origin of the two-point correlation function is preserved to simulate the specific surface, an important morphological feature. Other common moving-window functions such as Bartlett, Hanning, Gaussian, etc., are not considered in this study since these windows can distort the short-range-correlation information.

For ergodic and homogeneous random fields up to the nth order, as assumed in this study, S_n can be estimated from a single configuration as

$$S_n(\mathbf{r}_2-\mathbf{r}_1,\ldots,\mathbf{r}_n-\mathbf{r}_1) = \frac{1}{M_1\cdot M_2}\sum_{\{\mathbf{s}\}\in S} x(\mathbf{s})x(\mathbf{r}_2-\mathbf{r}_1+\mathbf{s})x \times(\mathbf{r}_3-\mathbf{r}_1+\mathbf{s})\cdots x(\mathbf{r}_n-\mathbf{r}_1+\mathbf{s}) \tag{5}$$

In Eq. (5), when the sites at which x is evaluated fall outside of the rectangular lattice $M_1\times M_2$, either periodic conditions or other appropriate conditions can be applied. A closely related definition is the nth-order statistics $P_n(x_1,x_2,\ldots,x_n)$ or n-gram statistics, which is also termed as gray-level co-occurrence in textural analysis. Obviously the information contained in the n-point correlation function is a subset of that of the nth-order statistics.

The characteristics of a Gibbs random field are specified by appropriate formulation of the nth-order potential $V_n(x)$, while noting that sometimes different potential functions could lead to the same Gibbs distribution. In the SRC model, we define the potentials as metric norm of a distance between two windowed correlation functions, such as a simulated one $\tilde{S}_n$ and a target S_n. The first-order potential makes use of the first-order statistics, or the full histogram f, not simply the mean value. For multiphase materials, x takes values from a finite set D of gray levels, e.g., for two-phase materials $D=\{0,1\}$. The first-order potential is therefore defined as

$$V_1(x) = \alpha_1\left[\sum_{x_i\in D}|f(x_i)-\tilde{f}(x_i)|^p\right]^{1/p} \tag{6}$$

where D is the set of possible gray levels in the multiphase material. The second and third orders of the potentials are given below and the rest follow the trend.

$$V_2(x) = \alpha_2\left[\sum_{\{i,i'\}}^{N_2}|S_2(\mathbf{r}_{i'}-\mathbf{r}_i)-\tilde{S}_2(\mathbf{r}_{i'}-\mathbf{r}_i)|^p\right]^{1/p} \tag{7a}$$

$$V_3(x) = \alpha_3\left[\sum_{\{i,i',i''\}}^{N_3}|S_3(\mathbf{r}_{i'}-\mathbf{r}_i,\mathbf{r}_{i''}-\mathbf{r}_i)-\tilde{S}_3(\mathbf{r}_{i'}-\mathbf{r}_i,\mathbf{r}_{i''}-\mathbf{r}_i)|^p\right]^{1/p} \tag{7b}$$

In Eqs. (7*a*) and (7*b*), $1\leqslant p\leqslant\infty$, N_2 indicates the pair set of the SRC window, N_3 indicates the triple set of the SRC window, and α_1, α_2, and α_3 are coefficients used to manipulate the contributions of each order of statistics to the total energy. For example, α_3 may be set to zero if only the first- and second-order statistics are to be matched in the simulated morphology.

Let a function $d_p(\tilde{x},x)=U(\tilde{x})$ denote the distance between any two configurations $x,\tilde{x}\in X$, i.e., $d_p: X\times X\to\Re$ taking pairs of morphological configurations into real numbers. In order to make use of the SRC energy in subsequent simulations it is important to establish first that it is truly a metric.

THEOREM. *The short-range-correlation energy function* $d_p: X\times X\to\Re$, *as defined in* Eqs. (4), (7*a*), and (7*b*), *is a metric on the morphological set* X.

Proof. By the definition of metric, there are four sufficient and necessary conditions:

(i) $d_p(x,\tilde{x})\geqslant 0$ for every $x,\tilde{x}\in X$
(ii) $d_p(x,\tilde{x})=0$ if and only if $x=\tilde{x}$
(iii) $d_p(x,\tilde{x})=d_p(\tilde{x},x)$ for every $x,\tilde{x}\in X$
(iv) $d_p(x,\tilde{x})\leqslant d_p(x,\tilde{x}')+d_p(\tilde{x}',\tilde{x})$ for every $x,\tilde{x},\tilde{x}'\in X$

Conditions (i)–(iii) are directly obtained from Eqs. (7*a*) and (7*b*), and Condition (iv) is derived by using Minkowski's inequality [37]. □

Clearly for a finite set D a metric space (d_p,X) is the ℓ_p space, and as seen in Sec. 3 we confine algorithms to the ℓ_2 space that is convenient for numerical operations. Having established a metric for the SRC energy of a given morphology, an appropriate sampling process must be established for generating simulated morphologies.

2.3 Sampling Process. In Markov/Gibbs random field models, there are two well-established random sampling algorithms. The Metropolis sampler [38] uses a Monte Carlo procedure to generate a Markov chain of configurations, and acceptance of each configuration change is based on Eq. (2). The Gibbs sampler [39] generates the next configuration using conditional probability (1) instead of energy change. Both sampling algorithms have the Gibbs distribution as equilibrium, as illustrated from the perspective of the Bayesian paradigm of maximum a posteriori (MAP) estimation [40]. Based on an initial configuration $x^{(0)}$, usually being white noise, the maximum problem is written as

$$\max_X P(x|x^{(0)}) = \max_X \frac{P(x^{(0)}|x)P(x)}{P(x^{(0)})} \tag{8}$$

Since white noise $x^{(0)}$ can be generally treated as independent from the desired configuration, i.e.,

$$P(x^{(0)}|x)\approx P(x^{(0)}) \tag{9}$$

then Eq. (9) becomes

$$\max_X P(x|x^{(0)}) \approx \max_X P(x) = \max_X e^{-(1/T)U(x)} \tag{10}$$

Therefore, generation of a desired configuration corresponds to minimization of the energy $U(x)$ in Eq. (2) with a fixed temperature T.

The Metropolis algorithm for finding the maximum probability in Eq. (10) is the following:

(a) given target histogram f and correlation functions $S_n, n=2,3,\ldots$
(b) set SRC window size to be used for energy calculation
(c) initialize white noise $x^{(0)}$
(d) calculate the initial SRC energy $U(x^{(0)})$ using Eqs. (3), (7*a*), and (7*b*)
(e) iteration step for configuration m
  (i) generate $x^{(m)}$ based on perturbation of $x^{(m-1)}$
  (ii) calculate the SRC energy $U(x^{(m)})$ using Eqs. (3), (7*a*), and (7*b*)
  (iii) $\Delta U^{(m)}=U(x^{(m)})-U(x^{(m-1)})$
  (iv) $q=\min\{1,e^{-\Delta U^{(m)}/T}\}$

(v) if uniform $[0,1] > q$, then go to (i) to try another $x^{(m)}$; otherwise, $x^{(m)}$ is accepted and go to (e) for next iteration $m+1$

(f) until a prescribed criterion, i.e., equilibrium is reached.

Steps (iv) and (v) of (e) above allow the algorithm to escape from local minima in an attempt to reach the global minimum. When temperature is scheduled to cool down gradually to zero, the combined scheme is known as simulated annealing. This scheme requires significant computing time and is not necessary for the morphological simulations performed here. As mentioned earlier, the global minimum of the energy occurs when the morphology exactly matches the original morphology (i.e., deterministic reconstruction). Strict application of steps (a)-(f) with the full range of correlation functions would lead to such a deterministic reconstruction. For morphological simulation using the SRC model, the objective is to find many qualified local minima as desired configuration samples, and an absolute global minimum is not needed. In this work, we use short-range-correlation functions and a freezing temperature, resulting in a simple and fast algorithm, which modifies the Step (e) above as follows:

(e) iteration step for mth configuration

(i) generate $x^{(m)}$ based on perturbation of $x^{(m-1)}$
(ii) calculate the SRC energy $U(x^{(m)})$ using Eqs. (3), (7*a*), and (7*b*)
(iii) $\Delta U^{(m)} = U(x^{(m)}) - U(x^{(m-1)})$
(iv) if $\Delta U^{(m)} > 0$, then go to (i) to try another $x^{(m)}$; otherwise, $x^{(m)}$ is accepted and go to (e) for next iteration $m+1$

There are two important algorithmic issues remaining in Substep (i). The first issue is that of choosing from two possible branches in the Metropolis algorithm, spin-flip or spin-exchange. The spin-exchange approach, say in a two-phase medium, proceeds by exchanging two sites in different phases in each perturbation, which always keeps a fixed volume fraction. Alternatively, the spin-flip method flips the phase at a single site individually, allowing the volume fraction to vary from perturbation to perturbation. Spin-flip has been shown to be generally more efficient than spin-exchange in texture analysis [41]. Also, in real material samples, the first-order marginal distribution or histogram in Ref. [6] is not deterministically constrained. Therefore spin-flip naturally fits the SRC model. The second issue pertains to the procedure to select spin-flip sites, i.e., random scanning, periodic scanning, or raster scanning. In this study we choose random scanning that was demonstrated to be most effective in Ref. [32].

The most computationally demanding part of the algorithm described in Refs. [11,12] is the calculation of the second- and third-order correlations that are used to calculate the SRC energy (Substep (ii). Because of this, the most efficient updating schemes for the second- and third-order SRC models are needed. The pair and triple correlation functions can be computed for a morphological configuration x, using the fast Fourier transform [42]

$$S_2(\mathbf{r}) = \mathrm{IFFT2}\{|\hat{x}(\boldsymbol{\omega})|^2\} \tag{11a}$$

$$S_3(\mathbf{r}_1,\mathbf{r}_2) = \mathrm{IFFT3}\{\hat{x}(\boldsymbol{\omega}_1)\hat{x}(\boldsymbol{\omega}_2)\hat{x}^*(\boldsymbol{\omega}_1+\boldsymbol{\omega}_2)\} \tag{11b}$$

where superscript * denotes the conjugate complex, IFFT2 denotes the two-dimensional inverse fast Fourier transform, IFFT3 denotes the three-dimensional inverse fast Fourier transform, and $\hat{x}(\boldsymbol{\omega})$ is the fast Fourier transform of the sample $x(\mathbf{r})$

$$\hat{x}(\boldsymbol{\omega}) = \mathrm{FFT2}\{x(\mathbf{r})\} \tag{11c}$$

Equation (11*b*) requires a significant amount of computing memory, and direct calculation of the triple correlation function is computationally feasible only for small window sizes. During spin-flip iterations an alternative updating scheme for fast computing of the SRC energy at Substep (ii) is available, an idea which was also applied in Refs. [43,44]. When there is a spin-flip at site $x^{(m)}(\mathbf{r})$ in an image of resolution $M_1 \times M_2$, the covariance function (normalized second-order correlation function) can be updated as

$$C^{(m+1)}(\boldsymbol{\Delta}) = \frac{1}{\phi^{(m+1)} - \phi^{(m+1)^2}} \left\{ C^{(m)}(\boldsymbol{\Delta}) \cdot (\phi^{(m)} - \phi^{(m)^2}) + \phi^{(m)^2} + \frac{2x^m(\mathbf{r}) - 1}{M_1 \cdot M_2} \cdot [x^{(m)}(\mathbf{r}+\boldsymbol{\Delta}) + x^{(m)}(\mathbf{r}-\boldsymbol{\Delta})] - \phi^{(m+1)^2} \right\} \quad \forall\, \boldsymbol{\Delta} \neq \mathbf{0} \tag{12a}$$

$$C^{(m+1)}(\mathbf{0}) = \frac{1}{\phi^{(m+1)} - \phi^{(m+1)^2}} \left\{ C^{(m)}(\mathbf{0}) \cdot (\phi^{(m)} - \phi^{(m)^2}) + \phi^{(m)^2} + \frac{2x^m(\mathbf{r}) - 1}{M_1 \cdot M_2} - \phi^{(m+1)^2} \right\} \tag{12b}$$

where ϕ denotes volume fraction and $\boldsymbol{\Delta}$ denotes the correlation distance. Compared to the fast Fourier transform in Eqs. (11*a*)–(11*c*) taking $O(M_1 M_2 \log M_1 M_2)$ multiplication operations, the updating schemes (12*a*) and (12*b*) require only $O((2L_1+1) \times (L_2+1))$ operations, where L_1 and L_2 are the dimensions of a rectangular SRC window in the $M_1 \times M_2$ domain of the morphology. For a 256×256 image with SRC window size $L_1 = L_2 = 10$, the ratio of computing efficiency can be as large as 18,157.

The updating scheme for the third-order correlation function is given as follows:

$$S_3^{(m+1)}(\boldsymbol{\Delta}_1,\boldsymbol{\Delta}_2) = S_3^{(m)}(\boldsymbol{\Delta}_1,\boldsymbol{\Delta}_2) + (2x^m(\mathbf{r}) - 1) \cdot [x^{(m)}(\mathbf{r}+\boldsymbol{\Delta}_1)x^{(m)} \times (\mathbf{r}+\boldsymbol{\Delta}_2) + x^{(m)}(\mathbf{r}-\boldsymbol{\Delta}_1)x^{(m)}(\mathbf{r}-\boldsymbol{\Delta}_1+\boldsymbol{\Delta}_2) + x^{(m)} \times (\mathbf{r}-\boldsymbol{\Delta}_2)x^{(m)}(\mathbf{r}-\boldsymbol{\Delta}_2+\boldsymbol{\Delta}_1)] \quad \forall\, \boldsymbol{\Delta}_1 \neq \mathbf{0}\, \forall\, \boldsymbol{\Delta}_2 \neq \mathbf{0}\boldsymbol{\Delta}_1 \neq \boldsymbol{\Delta}_2 \tag{13a}$$

$$S_3^{(m+1)}(\boldsymbol{\Delta}_1,\mathbf{0}) = S_3^{(m)}(\boldsymbol{\Delta}_1,\mathbf{0}) + (2x^m(\mathbf{r}) - 1) \cdot [x^{(m)}(\mathbf{r}+\boldsymbol{\Delta}_1) + x^{(m)} \times (\mathbf{r}-\boldsymbol{\Delta}_1)] \quad \forall\, \boldsymbol{\Delta}_1 \neq \mathbf{0} \tag{13b}$$

$$S_3^{(m+1)}(\mathbf{0},\boldsymbol{\Delta}_2) = S_3^{(m)}(\mathbf{0},\boldsymbol{\Delta}_2) + (2x^m(\mathbf{r}) - 1) \cdot [x^{(m)}(\mathbf{r}+\boldsymbol{\Delta}_2) + x^{(m)} \times (\mathbf{r}-\boldsymbol{\Delta}_2)] \quad \forall\, \boldsymbol{\Delta}_2 \neq \mathbf{0} \tag{13c}$$

$$S_3^{(m+1)}(\boldsymbol{\Delta},\boldsymbol{\Delta}) = S_3^{(m)}(\boldsymbol{\Delta},\boldsymbol{\Delta}) + (2x^m(\mathbf{r}) - 1) \cdot [x^{(m)}(\mathbf{r}+\boldsymbol{\Delta}) + x^{(m)} \times (\mathbf{r}-\boldsymbol{\Delta})] \quad \forall\, \boldsymbol{\Delta} \neq \mathbf{0} \tag{13d}$$

$$S_3^{(m+1)}(\mathbf{0},\mathbf{0}) = S_3^{(m)}(\mathbf{0},\mathbf{0}) + (2x^{(m)}(\mathbf{r}) - 1) \tag{13e}$$

For each cycle of spin-flip throughout the whole domain of an image, the third-order simulations (13*a*)–(13*e*) require $O(M_1 M_2 (2L_1+1)^2 (L_2+1)^2)$ multiplication operations, $(2L_1+1) \times (L_2+1)$ times that required for the second-order model.

3 Numerical Simulation of Biphase Disordered Materials

For biphase disordered materials, specifically, the information of the nth-order correlation functions is equivalent to the nth-order statistics [45]. The first two order statistics are therefore simply the volume fraction ϕ and the autocorrelation function S_2. In this study, we choose volume fraction ϕ and the covariance function

$$C(l_1,l_2) = \frac{S_2(l_1,l_2) - \phi^2}{\phi - \phi^2} \tag{14}$$

as parameters for the second-order SRC metric function (following Eqs. (6), (7*a*), and (7*b*))

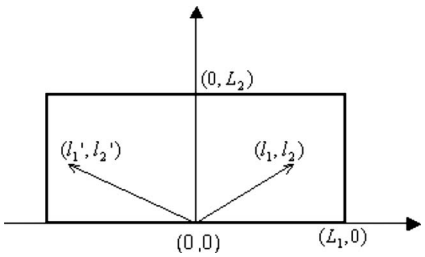

Fig. 1 Half window used in the calculation of energy (Eqs. (15) and (16)) in SRC formulation

$$U_2 = \alpha_1 \phi + \alpha_2 \sqrt{\sum_{l_1=-L_1}^{L_1} \sum_{l_2=0}^{L_2} |\tilde{C}(l_1,l_2) - C(l_1,l_2)|^2} \qquad (15)$$

Note in Eqs. (14) and (15) that l_1 and l_2 refer to coordinates, as shown in Fig. 1. The size of the short-range window $(2L_1 \times 2L_2)$ is a parameter that can be set in accordance with the target morphology. The effect of this window size will be discussed for specific examples later in this section. Results are complete using only half a window $(2L_1 \times L_2$ in Eq. (15)), due to the center-symmetry of covariance functions.

For the third-order SRC model, we simply let $\alpha_1 = \alpha_2 = 0$ and $\alpha_3 = 1$ in the simulation. Biphase processes represent a special case where the third-order correlation function contains all information about the first two orders of statistics. Therefore, there is no loss of information in discarding the first two orders in the energy expression. The energy U_3 becomes

$$U_3 = \sqrt{\sum_{l_1=-L_1}^{L_1} \sum_{l_2=0}^{L_2} \sum_{l_1'=-L_1}^{L_1} \sum_{l_2'=0}^{L_2} |\tilde{S}_3(l_1,l_2;l_1',l_2') - S_3(l_1,l_2;l_1',l_2')|^2} \qquad (16)$$

We will see that formulation (16) produces improved simulation quality over the energy norm U_2 contained in Eq. (15), as will be demonstrated by the examples in Sec. 3.2.

Six morphological patterns from P1 to P6 (Fig. 2) indicated with corresponding resolution are chosen as target configurations for numerical simulation. In the simulation process, periodic boundary conditions are prescribed. The criterion of iteration in Step (f) for the second-order SRC model is to run until there is no spin-flip allowed. For the computationally demanding third-order model, the iteration stops when the energy curve becomes close to flat, typically after five cycles of random scanning in our examples.

3.1 Effect of SRC Window Size. Pattern P2 shows a number of identical circles randomly distributed in a matrix, which corresponds to such random materials as fiber-reinforced composites. The lattice $M_1 \times M_2 = 128 \times 128$ and the radius of the circles is 4. To study the effect of window size in the second-order SRC model, we choose $L_1 = L_2 = L$ (Eq. (15)) being 1, 5, 10, 15, 20, 30, and 63, respectively. We set $\alpha_1 = 0.7$ and $\alpha_2 = 1.0$ for all the window sizes, in order to allow the volume fraction to deviate slightly from sample to sample. Resulting samples are shown in Fig. 3, which demonstrate that the volume fraction is close to the target value except for the SRC window size $L = 63$.

In Fig. 3 the best visual match (i.e., most circular shaped inclusions) appears when the SRC window size L is 10, 15, or 20, which is approximately two to three times the correlation length of the target configuration (Fig. 4). The interpretation is that too small a window size contains insufficient morphological information, while too large a window size beyond the correlation length

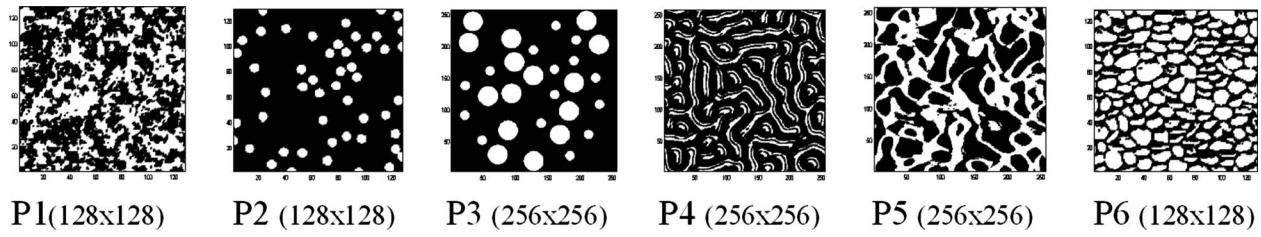

Fig. 2 Specific morphologies studied in this work

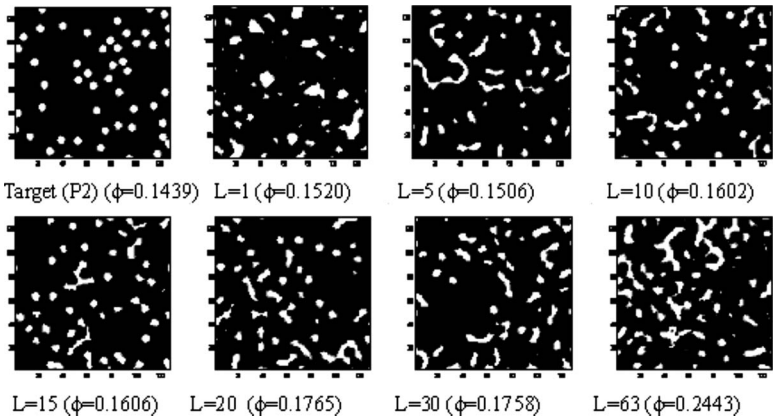

Fig. 3 The second-order SRC model for P2 with different SRC window sizes ($\alpha_1 = 0.7$, $\alpha_2 = 1.0$), with the respective volume fraction for each sample

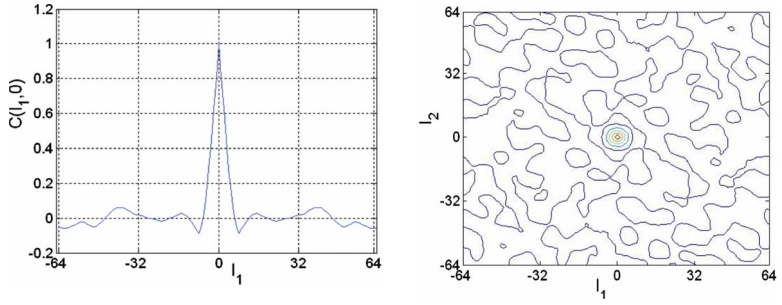

Fig. 4 Sample (target) covariance of P2: (left) profile; (right) contour

would include inaccurate information that pollutes the numerical optimization. Figure 5 shows the results of a simulation based on P5, which gives an even more striking representation of the window size effect. For the results in Fig. 5, it appears that none of the samples from the second-order simulations are a very good match. The window size of $L=10$ comes the closest in matching the pattern. Similar to the results from P2, this is approximately two times the correlation length of the original sample. These results show that for both patterns, a window size of approximately two to three times the correlation length of the original sample is needed to obtain good quality samples. The results from Pattern P5 show that for some microstructures second-order statistics are insufficient to represent key microstructural features. Therefore, extension to third-order statistics is addressed in the next section.

3.2 Third-Order SRC Model. Figures 6 and 7 show sample simulations based on Patterns P4 and P5, respectively, using the third-order SRC model (Eq. (16)). There is a window size effect similar to the second-order results in the third-order SRC model, as shown in Figs. 6 and 7. In other words, window sizes close to two to three times the correlation length of the original configuration still remain the optimal selection. Generated samples of P1–P6 are shown in Fig. 8 in order to provide a comparison between the second-order and the third-order results. The results corresponding to P1 show that second-order statistics are sufficient to represent the microstructural features. For the case of P2, the structural feature of separate circles becomes clearer in the third-order simulation. More obviously for the case of P3, the circular shape and distinct sizes of the inclusions are effectively reconstructed from the third-order simulation, where the second-order simulation fails. For P4 and P5, the third-order samples become much more improved and visually closer to the respective targets. P6 shows improvement in the samples when using a third-order rather than a second-order simulation; however, even the third-order simulation is insufficient to reflect such quantities as connectivity and percolation. In this simulation process, except for P2 (128×128) where $L=10$, the window size for the other five (256×256) is chosen as $L=15$.

As observable in Fig. 8, there is noise appearing in the third-order simulation samples. A denoising procedure is therefore developed by simply placing a third-order simulated sample as an initial configuration for a subsequent second-order simulation.

Fig. 5 Second-order simulation for P5 with different SRC window sizes ($\alpha_1=0.3$, $\alpha_2=1.0$)

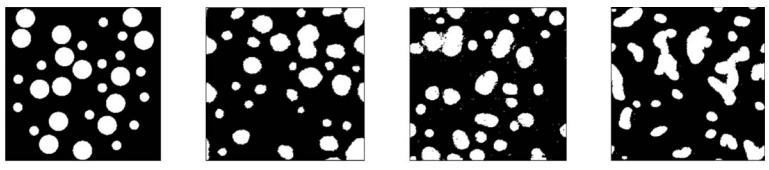

Fig. 6 Third-order simulation for P4 with different SRC window sizes

Fig. 7 Third-order simulation for P5 with different SRC window sizes

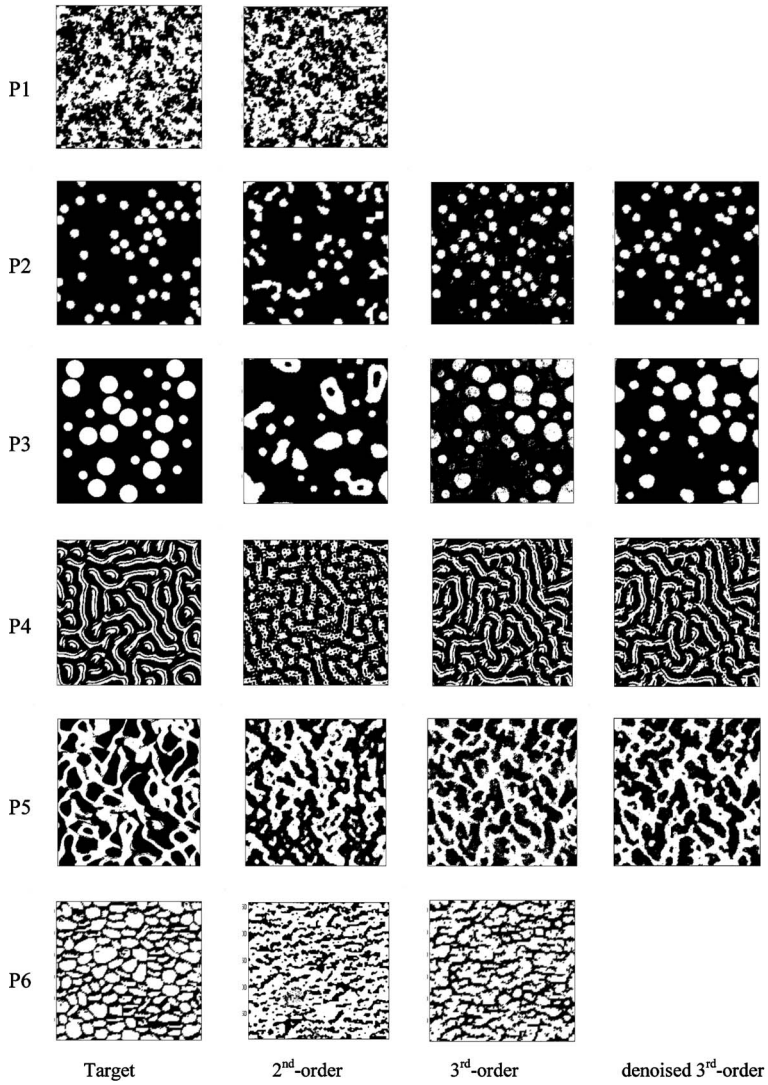

Fig. 8 Samples generated based on Patterns P1–P6, using the second-order SRC model (α_1=0.7, α_2=1.0, α_3=0), the third-order SRC model (α_1 =α_2=0, α_3=1.0), and the denoised third order SRC model

The effectiveness of the procedure is illustrated with the denoised samples shown in Fig. 8. To numerically interpret the procedure, the normalized energies E_2 and E_3 for samples before and after denoising are listed in Table 1, where E_2 and E_3 are defined by

$$E_2 = \frac{\sqrt{\sum_{l_1=-K_1}^{K_1}\sum_{l_2=0}^{K_2}|\tilde{C}(l_1,l_2)-C(l_1,l_2)|^2}}{\sqrt{\sum_{l_1=-K_1}^{K_1}\sum_{l_2=0}^{K_2}|C(l_1,l_2)|^2}} \tag{17}$$

$$E_3 = \frac{\sqrt{\sum_{l_1=-K_1}^{K_1}\sum_{l_2=0}^{K_2}\sum_{l_1'=-K_1}^{K_1}\sum_{l_2'=0}^{K_2}|\tilde{S}_3(l_1,l_2;l_1',l_2')-S_3(l_1,l_2;l_1',l_2')|^2}}{\sqrt{\sum_{l_1=-K_1}^{K_1}\sum_{l_2=0}^{K_2}\sum_{l_1'=-K_1}^{K_1}\sum_{l_2'=0}^{K_2}|S_3(l_1,l_2;l_1',l_2')|^2}} \tag{18}$$

It is observed from Table 1 that the noise is mostly due to the second-order energy E_2, which can be obviated by minimizing E_2

Table 1 Denoising

	P2		P4	
	Third-order simulation ((15a)–(15e))	Denoised procedure (3rd+2nd)	Third-order simulation ((15a)–(15e))	Denoised procedure (3rd+2nd)
E_2	0.1071	0.0078	0.1553	0.0041
E_3	0.0223	0.0555	0.0050	0.0195

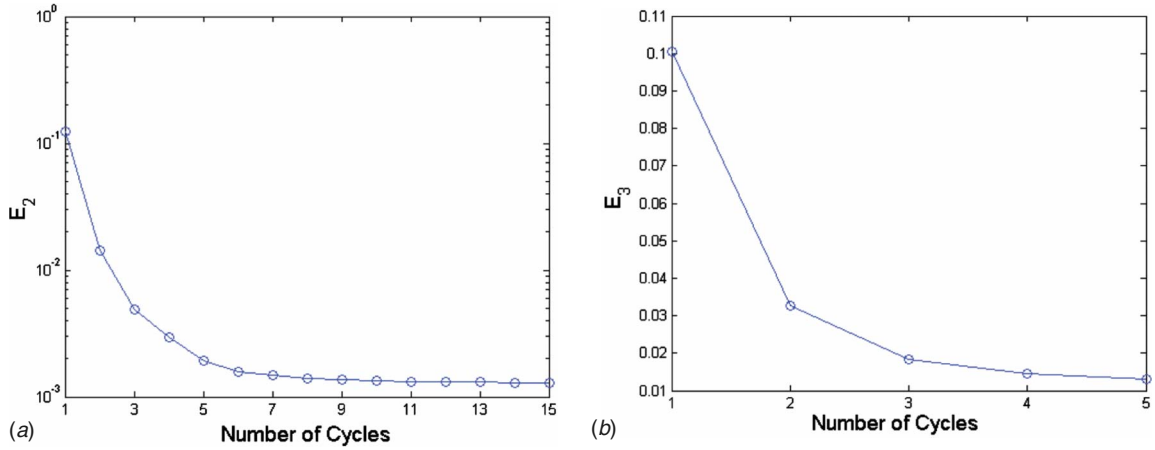

Fig. 9 Evolution of energy (error) in sample generation of P5: (*a*) second-order SRC model; (*b*) third-order SRC model

with the compromise of a slight increase in E_3.

The above examples reaffirm that there is morphological information that the second-order statistics miss and that can be retrieved from higher-order statistics.

The simulation process for P5 is graphed in terms of normalized energy in Fig. 9 for the second- and third-order SRC models, respectively, showing that the results converge rapidly. The computing time of a Pentium 4 CPU for different sample sizes and SRC window sizes is listed in Table 2. For a 256×256 image, the second- and third-order simulations would typically take about 30 s and 2 h per cycle, respectively, for window size $L_1 = L_2 = 10$. The magnitude of the time ratio is consistent with our estimate of operations in Sec. 3.1. Clearly, the third-order simulations come at a computational cost that must be balanced with the microstructural features that must be retained in the simulations.

4 Classification of Morphologies Based on the SRC Model

Many model-based techniques have been developed for pattern recognition of morphologies in texture analysis and image processing. This section is to initiate a generic method based on the SRC model for classification of morphologies, following the observation of Ref. [43] that second-order statistics can represent homogeneous textures such as P1, but have difficulty modeling structured textures (e.g., P2–P6). From the simulation examples graphed in Fig. 8, it is conjectured that the degree of structural complexity should be closely connected to a hierarchy order of statistics, i.e., the more complex the structural features are, the higher-order statistics that must be involved. For non-Gaussian translation processes, the first two orders of statistics are complete for representation (i.e., the process is completely defined by the probability density function and the two-point correlation function). As a result, non-Gaussian translation morphologies are not successful at retaining highly structured features of the morphology, such as shapes [22]. Morphologies that are predominantly controlled by the second-order statistics, and could therefore be appropriately described as translation morphologies, are referred to as nonstructured morphologies. P1 is a sample of such a morphology (Fig. 8).

Table 2 Computing time per cycle (Pentium 4 CPU 1400 MHz)

	256×256 resolution			128×128 resolution		
	$L=5$	$L=10$	$L=15$	$L=5$	$L=10$	$L=15$
Second order	26.0 s	29.6 s	35.2 s	6.9 s	7.4 s	8.7 s
Third order	32 min	122 min	276 min	14 min	29 min	84 min

For those morphologies mostly controlled by second-order statistics but still having observable structural features, we categorize them as lowly structured morphologies. One example is P2 in Fig. 8, where the second- and third-order simulation samples are similarly acceptable. For the cases of P3–P5 in Fig. 8, the third-order simulation samples are generally acceptable for visual similarity, while second-order statistics are inadequate to capture important morphological information. This class is referred to as medium structured morphologies, and it is thought that most real-life morphologies belong to this class. The class of highly structured morphologies refers to those morphologies that require an order of statistical modeling beyond third order. The example is P6 for which the third-order model has difficulty capturing connectivity and percolation [46]. Further statistical modeling efforts would be an important direction, since percolation and connectivity have wide applications in material and porous media fields, such as stochastic fibrous networks, membrane, porous rocks, etc.

5 Conclusions and Discussion

In this study, a short-range-correlation model is proposed in the framework of Markov and Gibbs random field theory to quantify random morphologies in metric space. A robust simulation procedure is established for morphologies of multiphase random media by using the Metropolis spin-flip algorithm. Through development of the SRC model, several issues of conceptual clarification are emphasized below.

- *Stochastic simulation versus deterministic reconstruction*. Stochastic simulation of random media using correlation models should be based on windowed correlation functions, i.e., focusing on spatially correlated information and assuming long-range independence. Utilization of full-range correlation functions would conceptually lead to deterministic reconstruction of the original configuration.
- *Statistical correlation functions versus sample (deterministic) correlation functions*. A uniqueness relationship exists between an image and its deterministic correlation functions. This issue is related to the first issue; in order to simulate samples that are close in the SRC metric space, the deterministic correlation functions describing the target configuration should be free to vary at long range.
- *n*th-*order statistics versus n*th-*order correlation function*. The latter is a subset of the former. Two-phase random media are a specific case where the two become equivalent.
- *Spin-flip versus spin-exchange*. The Metropolis spin-flip al-

gorithm greatly improves simulation efficiency by relaxing the first-order statistics. In other words, the volume fraction is not a rigidly fixed quantity, which might better reflect the nature of variability observed from one material morphology to the next.

From the simulation examples, we have the following observations.

- Morphological configurations close to each other in lower-order metric space tend to be visually similar, and the degree of similarity depends on the level of structural complexity in a morphological pattern;
- Second-order statistics give a global pattern, and are sufficient for unstructured and perhaps lowly structured morphologies (e.g., P1 and P2), but miss local structural features of structured morphologies that are important for many physical properties.
- Third-order statistics retrieve most local structural features and provide visual similarity for a large class of morphological patterns (e.g., P3–P5).
- For highly structured morphologies (e.g., P6), higher-order correlations than the third-order correlation function become necessary to capture connectivity and percolation properties.
- An interesting finding is that the SRC model can effectively simulate nonuniform patterns of inclusions such as P4 that has circles with two different diameters.

Based on the observations, we make the following conjectures concerning those intriguing morphological questions posed in various research fields (e.g., 1):

1. *Are there configurations close in n*th*-order statistics but different in* $(n+1)$th*-order statistics?* Yes, if generated in the context of windowed spatial statistics. One obvious example is the case of P3 in Fig. 8. The sample simulated with the second-order SRC model closely matches the target second-order statistics (Eq. (17)), but obviously it has failed to capture much of the third-(Eq. (18)) and higher-order statistics.
2. *Is morphology completely modeled by a hierarchical order of statistics?* Yes, the well-known statement is confirmed by the numerical analysis performed in this study; i.e., morphological information can be translated into a hierarchical order of statistics. The higher order of statistics that are known, the more detailed are the morphological features that are retrievable.
3. *Which is the lowest order of statistics for engineering interests?* Visual inspection of the results suggests that the third-order SRC model might be sufficient for many random media engineering problems (such as effective properties), except for those of percolation models. Future numerical evaluation of physical properties based on samples simulated by using the third-order SRC model is expected to verify this conjecture.
4. *What morphologies have the same lower-order statistics but widely different effective properties*? Lower-order statistics are insufficient to model highly structured morphologies that have small volume fractions and percolation properties. The example is P6 where the third-order simulation sample still lacks the appropriate connectivity properties.

As research interests of random media focus on physical properties, future work in the SRC modeling would continue in this direction by covering the following topics.

- Find a method to determining the optimal SRC window size for different types of morphologies and more detailed work of numerical analysis and relevant convergence study is expected on the topics of window sizes and correlation order.
- Optimize the third-order energy formulation of Eq. (16) in dealing with different classes of morphologies.
- Exploit applicability of the SRC model on highly structured morphologies such as stochastic fibrous networks.
- Investigate the relationship between resolution and simulation quality, and conduct multiresolution simulation to reduce computing time.
- Investigate the relationship among visual, morphological, and physical properties by numerically evaluating morphological features and physical properties of samples generated by the SRC model.
- Evaluate third-order bounds of effective properties by using the third-order SRC model for various morphologies classified in Sec. 4. Relevant work includes those on level-cut Gaussian random fields [18,47,48].
- Conduct a computationally demanding third-order three-dimensional simulation and develop a parallel computing algorithm.
- Conduct real materials statistical measurement and testing [49,50].

We also note that third- and higher-order statistical simulations of stochastic processes are an important direction. Simulation of non-Gaussian processes is generally limited to first two orders of statistics [51–56]. It is expected that the SRC model introduced in this study can be extended to simulation of general stochastic processes.

References

[1] Torquato, S., 2002, *Random Heterogeneous Materials, Microstructure and Macroscopic Properties*, Springer, New York.
[2] Sahimi, M., 2003, *Heterogeneous Materials I, Linear Transport and Optical Properties*, Springer, New York.
[3] Milton, G. W., 2002, *The Theory of Composites*, Cambridge University Press, Cambridge.
[4] Li, S. Z., 1995, *Markov Random Field Modeling in Computer Vision*, Springer, New York.
[5] Haralick, R. M., and Shapiro, L. G., 1992, *Computer and Robot Vision*, Vol. I, Addison-Wesley, Reading, MA.
[6] Torquato, S., 2002, "Statistical Description of Microstructures," Annu. Rev. Mater. Res., **32**, pp. 77–111.
[7] Adler, P. M., 1992, *Porous Media—Geometry and Transports*, Butterworth-Heinemann, New York.
[8] Johnson, M. E., 1987, *Multivariate Statistical Simulation*, Wiley, New York.
[9] Yeong, C. L. Y., and Torquato, S., 1998, "Reconstruction Random Media," Phys. Rev. E, **57**, pp. 495–506.
[10] Mardia, K. V., 1970, "Translation Family of Bivariate Distribution and Frechet's Bounds," Sankhya, Ser. A **32**, pp. 119–122.
[11] Grigoriu, M., 1984, "Crossings of Non-Gaussian Translation Processes," J. Eng. Mech., **110**(4), pp. 610–620.
[12] Joshi, M. Y., 1974, "A Class of Stochastic Models for Porous Media," Ph.D. thesis, University of Kansas, Lawrence, KS.
[13] Quiblier, J. A., 1984, "A New Three-Dimensional Modeling Technique for Studying Porous Media," J. Colloid Interface Sci., **98**, pp. 84–102.
[14] Giona, M., and Adrover, A., 1996, "Closed-Form Solution for the Reconstruction Problem in Porous Media," AIChE J., **42**, pp. 1407–1415.
[15] Cahn, J. W., 1965, "Phase Separation by Spinodal Decomposition in Isotropic Systems," J. Chem. Phys., **42**(1), pp. 93–99.
[16] Berk, N. F., 1991, "Scattering Properties of the Leveled-Wave Model of Random Morphologies," Phys. Rev. A, **44**(8), pp. 5069–5079.
[17] Roberts, A. P., and Teubner, M., 1995, "Transport Properties of Heterogeneous Materials Derived From Gaussian Random Fields: Bounds and Simulation," Phys. Rev. E, **51**(5), pp. 4141–4154.
[18] Roberts, A. P., and Knackstedt, M. A., 1996, "Structure-Property Correlations in Model Composite Materials," Phys. Rev. E, **54**(3), pp. 2313–2328.
[19] Grigoriu, M., 2003, "Random Field Models for Two-Phase Microstructures," J. Appl. Phys., **94**(6), pp. 3762–3770.
[20] Levitz, P., 1998, "Off-Lattice Reconstruction of Porous Media: Critical Evaluation, Geometrical Confinement and Molecular Transport," Adv. Colloid Interface Sci., **76–77**, pp. 71–106.
[21] Kainourgiakis, M. E., Kikkinides, E. S., Steriotis, T. A., Stubos, A. K., Tzevelekos, K. P., and Kanellopoulos, N. K., 2000, "Structural and Transport Properties of Alumina Porous Membranes From Process-Based and Statistical Reconstruction Techniques," J. Colloid Interface Sci., **231**, pp. 158–167.
[22] Xu, X. F., 2005, Ph.D. thesis, The Johns Hopkins University, Baltimore, MD.
[23] Julesz, B., 1962, "Visual Pattern Discrimination," IRE Trans. Inf. Theory, **IT-8**, pp. 84–92.
[24] Hazlett, R. D., 1997, "Statistical Characterization and Stochastic Modeling of Pore Networks in Relation to Fluid Flow," Math. Geol., **29**, pp. 801–822.
[25] Talukdar, M. S., Torsaeter, O., and Ioannidis, M. A., 2002, "Stochastic Reconstruction of Particulate Media From Two-Dimensional Images," J. Colloid

Interface Sci., **248**, pp. 419–428.
[26] Bochenek, B., and Pyrz, R., 2004, "Reconstruction of Random Microstructures—A Stochastic Optimization Problem," Comput. Mater. Sci., **31**, pp. 83–112.
[27] Julesz, B., Gilbert, E. N., Shepp, L. A., and Frisch, H. L., 1973, "Inability of Humans to Discriminate Between Visual Textures That Agree in Second-Order Statistics—Revisited," Perception, **2**, pp. 391–405.
[28] Chubb, C., and Yellot, J. I., 2000, "Every Discrete, Finite Image is Uniquely Determined by Its Dipole Histogram," Vision Res., **40**, pp. 485–492.
[29] Rozman, M. G., and Utz, M., 2002, "Uniqueness of Reconstruction of Multiphase Morphologies From Two-Point Correlation Functions," Phys. Rev. Lett., **89**(13), pp. 135501.
[30] Fienup, J. R., 1982, "Phase Retrieval Algorithms: A Comparison," Appl. Opt., **21**(15), pp. 2758–2769.
[31] Anguy, Y., Ehrlich, R., and Mercet, C., 2003, "Is It Possible to Characterize the Geometry of a Real Porous Medium by a Direct Measurement on a Finite Section? 1: The Phase-Retrieval Problem," Math. Geol., **35**(7), pp. 763–788.
[32] Gagalowicz, A., and Ma, S. D., 1985, "Sequential Synthesis of Natural Textures," Comput. Vis. Graph. Image Process., **30**, pp. 289–315.
[33] Aubert, A., and Jeulin, D., 2000, "Estimation of the Influence of Second- and Third-Order Moments on Random Sets Reconstructions," Pattern Recogn., **33**(6), pp. 1083–1104.
[34] Tyler, C. W., 2004, "Theory of Texture Discrimination of Based on Higher-Order Perturbations in Individual Texture Samples," Vision Res., **44**, pp. 2179–2186.
[35] Xu, X. F., and Graham-Brady, L., 2005, "A Stochastic Computation Method for Evaluation of Global and Local Behavior of Random Elastic Media," Comput. Methods Appl. Mech. Eng., **194**(42–44), pp. 4362–4385.
[36] Hammersley, J. M., and Clifford, P., 1971, "Markov Field on Finite Graphs and Lattices," unpublished.
[37] 1972, *Handbook of Mathematical Functions With Formulas, Graphs, and Mathematical Tables*, 9th ed., M. Abramowitz and I. A. Stegun, eds. Dover, New York, p. 11.
[38] Metropolis, N., Rosenbluth, A. W., Rosenbluth, M. N., Teller, A. H., and Teller, E., 1953, "Equations of State Calculations by Fast Computational Machine," J. Chem. Phys., **21**, pp. 1087–1091.
[39] Geman, S., and Geman, D., 1984, "Stochastic Relaxation, Gibbs Distribution and the Bayesian Restoration of Images," IEEE Trans. Pattern Anal. Mach. Intell., **6**(6), pp. 721–741.
[40] Elfadel, I. M., and Picard, R. W., 1994, "Gibbs Random Fields, Cooccurrences, and Texture Modeling," IEEE Trans. Pattern Anal. Mach. Intell., **16**(1), pp. 24–37.
[41] Copeland, A. C., Ravichandran, G., Trivedi, M. M., 2001, "Texture Synthesis Using Gray-Level Cooccurrence Models: Algorithms, Experimental Analysis, and Psychophysical Support," Opt. Eng. (Bellingham), **40**(11), pp. 2655–2673.
[42] Nikias, C. L., and Petropulu, A. P., 1993, *Higher-Order Spectra Analysis, A Nonlinear Signal Processing Framework*, Prentice-Hall, Englewood Cliffs, NJ.
[43] Gagalowicz, A., and Tournier-Lasserve, C., 1986, "Third Order Model for Non-Homogeneous Natural Textures," *Proceedings of the Eighth International Conference on Pattern Recognition*, pp. 409–411.
[44] Rozman, M. G., and Utz, M., 2001, "Efficient Reconstruction of Multiphase Morphologies From Correlation Functions," Phys. Rev. E, **63**(6), p. 066701.
[45] Frisch, H. L., 1965, "Statistics of Random Media," Trans. Soc. Rheol., **9**(1), pp. 293–312.
[46] Pikaz, A., and Averbuch, A., 1998, "On the Relation Between Second-Order Statistics, Connectivity Analysis, and Percolation Models in Digital Textures," Graph. Models Image Process., **60**(3), pp. 226–232.
[47] Hilfer, R., and Manwart, C., 2001, "Permeability and Conductivity for Reconstruction Models of Porous Media," Phys. Rev. E, **64**(2), p. 021304.
[48] Myroshnychenko, V., and Brosseau, C., 2005, "Finite-Element Method for Calculation of the Effective Permittivity of Random Inhomogeneous Media," Phys. Rev. E, **71**(1), p. 016701.
[49] Berryman, J. G., 1985, "Measurement of Spatial Correlation Function Using Image Processing Techniques," J. Appl. Phys., **57**(7), pp. 2374–2384.
[50] Tewari, A., Gokhale, A. M., Spowart, J. E., and Miracle, D. B., 2004, "Quantitative Characterization of Spatial Clustering in Three-Dimensional Microstructures Using Two-Point Correlation Functions," Acta Mater., **52**(2), pp. 307–319.
[51] Yamazaki, F., and Shinozuka, M., 1988, "Digital Generation of Non-Gaussian Stochastic Fields," J. Eng. Mech., **114**(7), pp. 1183–1197.
[52] Johnson, G. E., 1993, "Construction of Particular Random Processes," Proc. IEEE, **82**(2), pp. 270–285.
[53] Cai, G. Q., and Lin, Y. K., 1996, "Generation of Non-Gaussian Stationary Stochastic Processes," Phys. Rev. E, **54**(1), pp. 299–303.
[54] Gurley, K. R., Kareem, A., and Tognarelli, M. A., 1996, "Simulation of a Class of Non-Normal Random Processes," Int. J. Non-Linear Mech., **31**(5), pp. 601–617.
[55] Grigoriu, M., 1998, "Simulation of Stationary Non-Gaussian Translation Processes," J. Eng. Mech., **124**(2), pp. 121–126.
[56] Deodatis, G., and Micaletti, R. C., 2001, "Simulation of Highly Skewed Non-Gaussian Stochastic Processes," J. Eng. Mech., **127**(12), pp. 1284–1295.

Constructing Multilayer Feedforward Neural Networks to Approximate Nonlinear Functions in Engineering Mechanics Applications

Jin-Song Pei
Assistant Professor
School of Civil Engineering
and Environmental Science,
University of Oklahoma,
Norman, OK 73019-1024

Eric C. Mai
Honors Undergraduate Student
School of Civil Engineering
and Environmental Science,
Honors College,
University of Oklahoma,
Norman, OK 73019-1024

*This paper presents a major step in the development and validation of a systematic prototype-based methodology for designing multilayer feedforward neural networks to model nonlinearities common in engineering mechanics. The applications of this work include (but are not limited to) system identification of nonlinear dynamic systems and neural-network-based damage detection. In this and previous studies (Pei, J. S., 2001, "Parametric and Nonparametric Identification of Nonlinear Systems," Ph.D. thesis, Columbia University; Pei, J. S., and Smyth, A. W., 2006, "A New Approach to Design Multilayer Feedforward Neural Network Architecture in Modeling Nonlinear Restoring Forces. Part I: Formulation," J. Eng. Mech., **132**(12), pp. 1290–1300; Pei, J. S., and Smyth, A. W., 2006, "A New Approach to Design Multilayer Feedforward Neural Network Architecture in Modeling Nonlinear Restoring Forces. Part II: Applications," J. Eng. Mech., **132**(12), pp. 1301–1312; Pei, J. S., Wright, J. P., and Smyth, A. W., 2005, "Mapping Polynomial Fitting Into Feedforward Neural Networks for Modeling Nonlinear Dynamic Systems and Beyond," Comput. Methods Appl. Mech. Eng., **194**(42–44), pp. 4481–4505), the authors do not presume to provide a universal method to approximate any arbitrary function. Rather the focus is given to the development of a procedure which will consistently lead to successful approximations of nonlinear functions within the specified field. This is done by examining the dominant features of the function to be approximated and exploiting the strength of the sigmoidal basis function. As a result, a greater efficiency and understanding of both neural network architecture (e.g., the number of hidden nodes) as well as weight and bias values is achieved. Through the use of illuminating mathematical insights and a large number of training examples, this study demonstrates the simplicity, power, and versatility of the proposed prototype-based initialization methodology. A clear procedure for initializing neural networks to model various nonlinear functions commonly seen in engineering mechanics is provided. The proposed methodology is compared with the widely used Nguyen–Widrow initialization to demonstrate its robustness and efficiency in the specified applications. Future work is also identified.* [DOI: 10.1115/1.2957600]

1 Introduction

1.1 Motivation. The initialization of neural networks is the foremost step in training them to approximate functions. This critical step affects both the speed and precision of training convergence, as evidenced in previous studies (e.g., Ref. [1]). This challenge of initialization exists for both static and dynamic neural networks [2]. The universal approximator theorem [3,4] has proven the feasibility of function approximation but has not offered a constructive solution for neural network initialization. Other noteworthy existing efforts include methods built on a good understanding of the capabilities of sigmoidal functions [5–9], methods utilizing the features of the function to be approximated [1,8], constructive methods [5,10,11], and many more (e.g., those summarized in Refs. [12,13]. Reference [14] also provides a summary of existing initialization approaches that have inspired this study or are closely related to it.

Despite these previous efforts, it is the opinion of the neural network community that both analytic and heuristic approaches are still in need of ideas to guide practical applications of function approximation. With no exceptions, this is also the case in the use of neural networks in engineering mechanics to simulate and identify nonlinear functions, especially in the applications of structural health monitoring and damage detection [15,16]. According to previous studies [1,12], such a fundamental problem might be hard to overcome in a general sense and thus may only be addressed properly by looking into the features of the function to be approximated or, equivalently, the features of the error function surface. This philosophy lends itself to a direction of seeking effective domain-specific solutions for neural network initialization. Therefore, this study as well as the previous studies that it is built upon [15–18] do not aim for an initialization solution to any arbitrary nonlinear function. Rather the effort here is to rationally connect the understanding of the capabilities of sigmoidal functions and the domain knowledge of the function to be approximated to the inner workings of neural networks.

Throughout this study, the following expressions are adopted for multilayer feedforward neural networks with a logistic sigmoidal activation function S, as shown in Eq. (1) below. Furthermore, any given continuous scalar goal/target function $g(\mathbf{x})$ of vector $\mathbf{x}$

Contributed by the Applied Mechanics Division of ASME for publication in the JOURNAL OF APPLIED MECHANICS. Manuscript received May 26, 2006; final manuscript received August 26, 2007; published online August 15, 2008. Review conducted by Igor Mezic.

can be approximated by another scalar output function $y(\mathbf{x})$ using a linear summation [3,4] of sigmoidal functions as follows:

$$y(\mathbf{x}) = \sum_{j=1}^{n_h} w_{2,j} S(\mathbf{w_{1,j}}\mathbf{x} + b_j) = \sum_{j=1}^{n_h} \frac{w_{2,j}}{1 + e^{-(\mathbf{w_{1,j}}\mathbf{x}+b_j)}} \tag{1}$$

where $j=1, \ldots, n_h$, and n_h is the number of hidden nodes. Note that $\mathbf{w_{1,j}}$ corresponds to input layer weights, b_j to biases, and $w_{2,j}$ to layer weights (IW, b, and LW, respectively in the MATLAB Neural Network Toolbox [19]). Neural network initialization needs to address the following issues: (i) number of hidden layers, (ii) number of hidden nodes in each layer, i.e., the values of n_h appearing in Eq. (1), and (iii) values of the weights and biases, i.e., the values of IW, b, and LW.

1.2 Objectives and Scope. The ultimate goal of the authors is to develop a set of detailed guidelines with theoretical justifications for using data-driven techniques such as neural networks in engineering applications based on (i) the mathematical and physical insights of the problem to be modeled and (ii) the capabilities of neural networks in terms of a clear formulation of a linear sum of sigmoidal functions. The benefits of such an effort are many and include a more constructive approach for neural network initialization, more guaranteed training performance, and trained results with more meaningful interpretations than those obtained otherwise.

This study aims at substantiating the existing ideas and procedures proposed in a series of previous studies [15–18,20], with specific focus on applying neural networks to function approximation within engineering mechanics. The objectives are as follows: (i) to construct an explicit road map describing the proposed prototyped-based neural network initialization methodology; (ii) to develop a set of prototypes which can be used to approximate ten typical types of nonlinear functions commonly seen in engineering mechanics applications; (iii) to identify the interrelationships of these prototypes in order to streamline the proposed prototype-based methodology; (iv) to provide training examples to validate the training convergence and speed of the proposed initialization methodology, thus demonstrating its usefulness and power; (v) to analyze the similarities and differences between the proposed initialization methodology and the widely adopted Nguyen–Widrow initialization algorithm [6]; and (vi) to provide practical guidance on the remaining subjective design issues and shed light on the process of expanding this static neural network initialization methodology for dynamic neural networks.

Although not entirely arbitrary, the functions to be approximated in this study are not limited to nonlinear restoring forces, as previously done [15–18]. Here, the focus is given to approximating basic nonlinear functions that are widely encountered in engineering mechanics applications such as those seen in the stress-strain, moment-curvature, and load-displacement relationships, as well as time histories.

On one hand, this study is focused on memoryless and monotonic functions. Nonlinearities with memory are not treated in this study since they require different types of neural networks (e.g., recurrent neural networks, or multilayer feedforward neural networks with high dimensional inputs [2,21]). This study will lay a solid foundation for these other types of neural networks to build upon. On the other hand, monotonic nonlinearities are also the focus of this study. Several existing studies [8,10] have been carried out to analyze strategies for time-history-like nonlinearities with obvious peaks and valleys. However there is a gap in the literature on how to approximate ubiquitous monotonic nonlinearities using multilayer feedforward neural networks.

2 Proposed Initialization Methodology

2.1 Overview of the Proposed Three-Stage Initialization Methodology. The central drive of this domain-specific neural network initialization methodology is to transform an otherwise ambiguous and thus largely trial-and-error-based procedure into a clearly defined near-deterministic procedure that can be easily understood and executed. Before training takes place, this study proposes that three cohesive initialization stages—including Stage I (selecting prototypes), Stage II (selecting variants), and Stage III (deciding transformation), as outlined in Fig. 1—be implemented. This is recommended for a typical initialization procedure using a feedforward neural network with one hidden layer to approximate a nonlinear function.

The proposed initialization methodology for designing a multilayer feedforward neural network begins with selecting a proper prototype according to the main features of the function to be approximated. This is Stage I. In Stage II, some of the initial values of the weights and biases and their interrelationships can be further determined by considering various variants within the selected prototype. If non-normalized, the range of the input and output is further considered in Stage III by scaling and shifting the selected variant to complete initialization before batch mode training takes place.

In the flowchart shown in Fig. 1, both the accomplished work in this study and the tasks planned for future studies are presented. Multiple options for initialization exist throughout Stages I, II, and III, reflecting the highly adaptive nature of multilayer feedforward neural networks. However each decision can be made through a rational procedure, as presented in this study. In principle, all the options could be extensively examined to determine *the best* initialization strategy as depicted in the iterations of the three stages. It can be seen that these three cohesive stages explicitly address all aforementioned questions on initialization as mentioned in Sec. 1.1:

(i) Number of hidden layers: One hidden layer is recommended. This is based on the universal approximator theorem [3,4]. In certain situations, multiple hidden layers may be a better option than one hidden layer. The initialization methodology presented here can be generalized to work in the situations envisioned in Ref. [17].
(ii) Number of hidden nodes in each layer: Generally, a small number of hidden nodes is recommended, which is derived either through mathematical proofs/reasoning or numerical exercises of linear sums of sigmoidal functions. This is the outcome of Stage I.
(iii) Values of the weights and biases: Some predetermined weight and bias values are recommended to minimize or avoid using any randomization, such as that employed in the Nguyen–Widrow initialization [6]. Again, these values are determined through a progressive and iterative procedure consisting of Stages I–III.

2.2 Understanding Prototypes and Their Variants. The key elements in this proposed methodology, *prototypes* and their *variants*, are predetermined neural networks that are not obtained from an *inverse formulation* of training any data sets. Instead, they are constructed in advance from a *forward formulation* based on either the algebraic or geometric capabilities of linear sums of sigmoidal functions to capture some dominating features of the nonlinear function to be approximated in the specified applications. Preparing prototypes and variants takes time, but can be done in a *forward problem* fashion by following a clear procedure. The resulting prototypes and variants are generic; i.e., they can be used for numerous individual training tasks through proper transformations (as in Stage III), thus leading to a high overall efficiency in addition to the built-in rationality and transparency in this proposed initialization methodology.

A qualitative justification for applying a prototype-based approach for greater success in neural network training can be found in the balance between global and local search involved in training. Ideally, training neural networks in function approximation should belong to the "global search" category by finding global minima of error functions. However, currently employed training

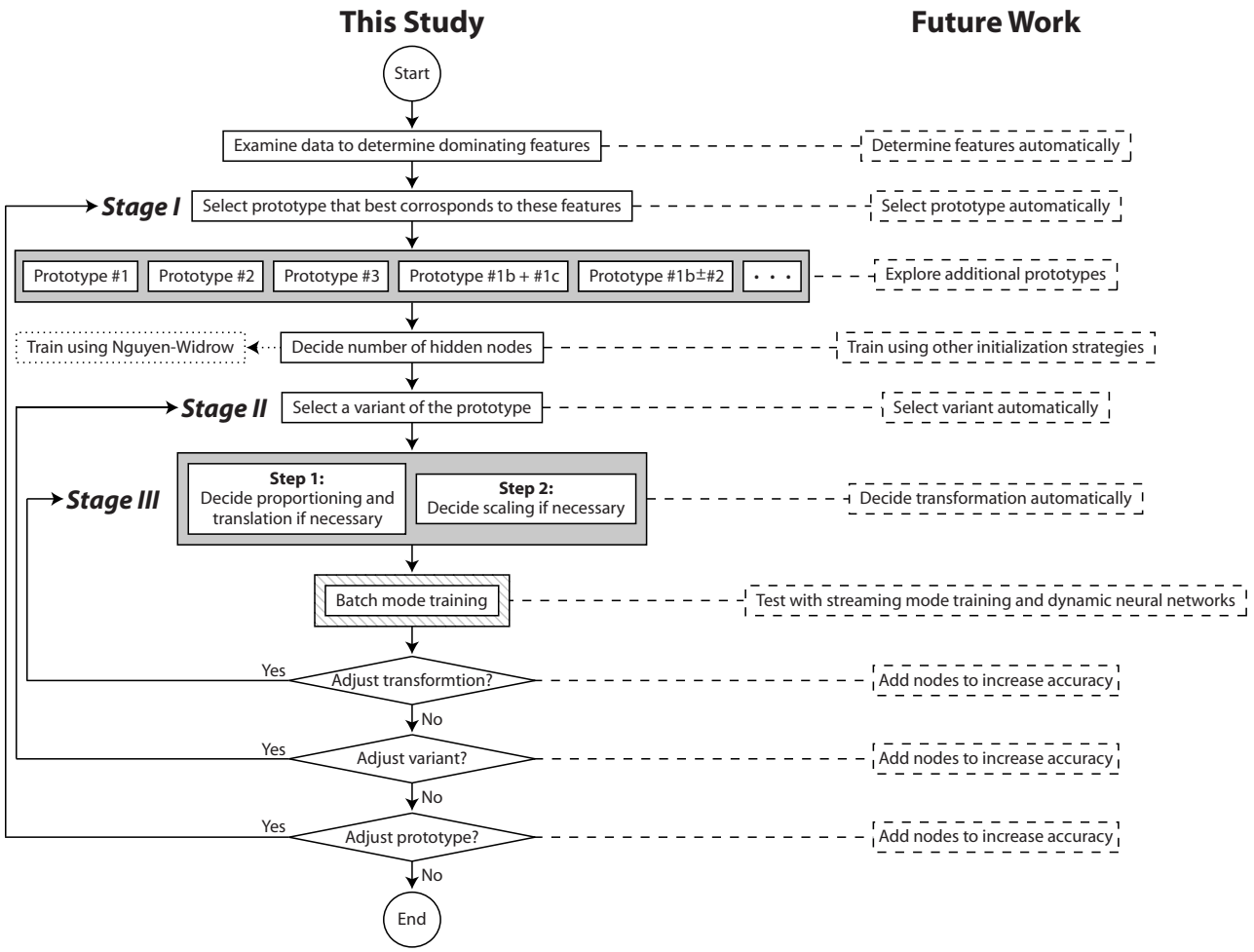

Fig. 1 Flowchart to illustrate the proposed prototype-based initialization and growing training technique

techniques are normally only "local search" tools [21]. Thus selecting a good initial point for neural network training is critical since the training process will normally result in trained values that are still in the neighborhood of their initial values. If domain knowledge or any other insight of the function to be approximated could be used to influence neural network initialization, then the training would more likely converge to the global minimum (instead of just a local minimum), making the trained neural network more accurate and meaningful. This is the guiding philosophy of the neural network initialization methodology proposed in this paper and in previous works related to it [15–18].

To validate and fully develop the proposed neural network initialization methodology, ten types of nonlinear functions appearing in Refs. [22,23] and presented in Fig. 2 are selected as target functions. These nonlinearities represent typical functions encountered in the applications of aerospace, mechanical, and structural engineering.

In this study, specific prototypes for training these nonlinearities are constructed. For the ten types of nonlinear functions specified in Fig. 2, it is recommended that only three prototypes be utilized either *individually* or *combinatorially* for neural network initialization. This finding reveals the versatility and efficiency of the proposed initialization. In other words, it does not always seem necessary to develop a brand new prototype for each non-

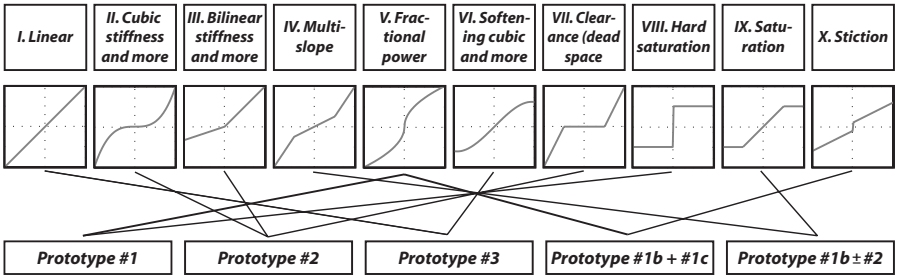

Fig. 2 Ten types of nonlinear functions commonly seen in engineering mechanics applications and the recommended multilayer feedforward neural network architectures (i.e., prototypes) used to train them. Note that the indicated relationships are not exhaustive.

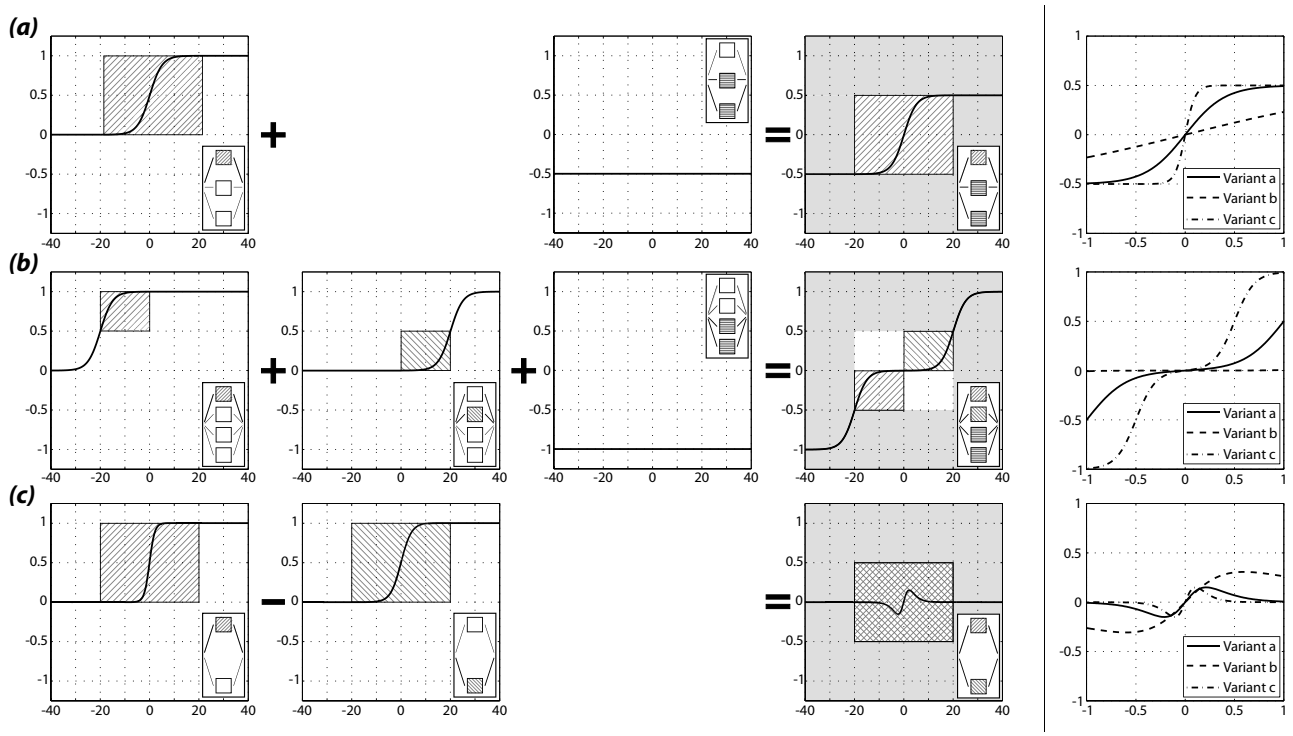

Fig. 3 A step-by-step procedure to illustrate the construction of the proposed (*a*) Prototype 1, variant *a*, (*b*) Prototype 2, variant *a*, and (*c*) Prototype 3, variant *a*. Three variants from each prototype are shown to the right of the procedure.

linearity since a prototype constructed for one nonlinearity might also work successfully in approximating another. This attractive feature is evidenced in this study (i) through a graphical "decomposition" of a complex nonlinearity into a combination of several simpler nonlinearities whose prototypes have already been identified and (ii) through numerous training examples. Further theoretical and numerical work is underway to reveal the inner workings of neural networks to more thoroughly verify, understand, and utilize this attractive feature of the proposed initialization [24].

2.3 Construction of Prototypes and Their Variants. For the three prototypes proposed in this study, a constructive step-by-step procedure is illustrated in Fig. 3. Bear in mind the following: (i) In constructing prototypes, one needs not strive for an exact approximation of any target function. Rather, one focuses on mimicking dominating features of nonlinearities while leaving fine tuning of the approximation to the training process of neural networks. (ii) The weights IW and biases b form the basis functions, and the weights LW correspond to the coefficients, as exercised in the previous works [15–18]. (iii) The input and output ranges in these three prototypes are normalized; handling non-normalized input and output will be elaborated further in Sec. 2.5.

The basic characteristics of nonlinearities, including softening, hardening, and oscillatory features, are sought in the construction of these three prototypes. Referring to Eq. (1), for each individual term (i.e., each hidden node) used, the built-in nonlinear features of the sigmoidal function are utilized to reproduce these characteristics by (i) adjusting the weight IW to "zoom" into or out of the sigmoidal function and (ii) changing the bias b to "slide" the sigmoidal function to select the right input range. These considerations are the driving force behind the determination of the values of the weight IW and bias b in an individual term/hidden node.

It can be seen that only three, four, and two terms/hidden nodes are utilized in the construction of Prototypes 1, 2, and 3, respectively. It can also be seen intuitively that these prototypes are essentially *one* sigmoidal term with a constant level of 0.5 removed, *a summation of two* symmetrical sigmoidal terms with a constant level of 1.0 removed, and *a subtraction of two* similar sigmoidal terms that share the same center.

Note that in each prototype there are (i) fixed values of weights and/or biases, (ii) weights and biases in one sigmoidal term/hidden node with a fixed relationship to those in other sigmoidal terms/hidden nodes (e.g., pairs of similar sigmoidal terms are often utilized to produce symmetrical features, which leads to certain constraints between the selected values for the weights IW's and LW's and/or the biases b's in different terms/hidden nodes), and (iii) some weights and biases with truly free values. It has been seen that combinations with very simple integer coefficients (such as ± 1 and ± 0.5) of just a few terms/hidden nodes are sufficient to form the nonlinear characteristics. The simplicity of producing linear sums of sigmoidal functions means that the construction of prototypes involves no tedious calculations. In principle, these simple integer values for the weights LW can be made free and should be fully exploited. However it has been decided in this study to leave this flexibility neither to the prototypes nor to their variants (to be discussed below). Rather it is entirely assigned to the proposed Stage III to allow for the largely fixed prototypes to adapt to various options.

Because of the flexibility of some of the weights and/or biases, there exists a theoretically infinite number of variants, which can be obtained by altering these values. The right side of Fig. 3 illustrates three possible variants for each proposed prototype for a normalized input. The values of the weights and biases used here can be found in Table 1. It can be seen that a single prototype can yield several variants with distinctive nonlinear characteristics through the adjustment of the flexible weights and biases. Thus selecting proper variants is critical and could be subjective. Once again, the authors do not use a random option when faced with such a challenge. Rather, a systematic procedure is proposed in Stage III to limit subjective decisions and make trial-and-error procedures as rational as possible.

2.4 Decomposition of More Complex Target Functions. The decomposition of a complex target function refers to the pro-

Table 1 Values of weights and biases used in Prototypes 1, 2, and 3. Note that in this table, normalized inputs and outputs are used. The quantities with * are fixed. The quantities with † are associated with the constant term [15,18] and are *not* scaled throughout this study. Also note the interrelationships between various IW, *b*, and LW values.

Prototype and variant	Weights in input layer, IW	Biases in input layer, *b*	Weights in output layer, LW
1*a*	$[5\ \ 1^{\dagger}\ -1^{\dagger}]^T$	$[0^*\ \ 0^*\ \ 0^*]^T$	$[1\ \ -0.5\ \ -0.5]$
1*b*	$[1\ \ 1^{\dagger}\ -1^{\dagger}]^T$	$[0^*\ \ 0^*\ \ 0^*]^T$	$[1\ \ -0.5\ \ -0.5]$
1*c*	$[20\ \ 1^{\dagger}\ -1^{\dagger}]^T$	$[0^*\ \ 0^*\ \ 0^*]^T$	$[1\ \ -0.5\ \ -0.5]$
2*a*	$[5\ \ 5\ \ 1^{\dagger}\ -1^{\dagger}]^T$	$[5\ \ -5\ \ 0^*\ \ 0^*]^T$	$[1\ \ 1\ \ -1\ \ -1]$
2*b*	$[5\ \ 5\ \ 1^{\dagger}\ -1^{\dagger}]^T$	$[10\ \ -10\ \ 0^*\ \ 0^*]^T$	$[1\ \ 1\ \ -1\ \ -1]$
2*c*	$[10\ \ 10\ \ 1^{\dagger}\ -1^{\dagger}]^T$	$[5\ \ -5\ \ 0^*\ \ 0^*]^T$	$[1\ \ 1\ \ -1\ \ -1]$
3*a*	$[10\ \ 5]^T$	$[0\ \ 0]^T$	$[1\ \ -1]$
3*b*	$[5\ \ 1]^T$	$[0\ \ 0]^T$	$[1\ \ -1]$
3*c*	$[20\ \ 10]^T$	$[0\ \ 0]^T$	$[1\ \ -1]$
1*b*+1*c*	$[1\ \ 20\ \ 1^{\dagger}\ -1^{\dagger}]^T$	$[0^*\ \ 0^*\ \ 0^*\ \ 0^*]^T$	$[1\ \ 1\ \ -1\ \ -1]$
1*b*+2*a*	$[1\ \ 5\ \ 5\ \ 1^{\dagger}\ -1^{\dagger}]^T$	$[0^*\ \ 5\ \ -5\ \ 0^*\ \ 0^*]^T$	$[1\ \ 1\ \ 1\ \ -1.5\ \ -1.5]$
1*b*−2*a*	$[1\ \ 5\ \ 5\ \ 1^{\dagger}\ -1^{\dagger}]^T$	$[0^*\ \ 5\ \ -5\ \ 0^*\ \ 0^*]^T$	$[1\ \ -1\ \ -1\ \ 0.5\ \ 0.5]$

cedure which converts the function into a summation of simpler functions that are conveniently related to the proposed prototypes and their variants. This procedure is required in (i) the selection of both prototypes and variants and (ii) the stage of transformation dealing with complex target functions. It is also envisioned that this technique will be necessary for the expansion of this work beyond the ten types of nonlinearities studied here.

The forward problem of the construction and exploration of the prototypes and their variants can be challenging. Furthermore, matching a target function with prototypes and selecting a proper variant are inverse problems and can thus be equally challenging, if not more so. An intuitive approach could be to develop every prototype or even a full spectrum of variants that could closely match any typical nonlinearity in engineering mechanics applications on a *one-to-one* basis. However, this approach would likely be neither feasible nor necessary. The number of types of nonlinearities can be enormous or even infinite in practice. Thus it might not be realistic to consider all of them when developing this prototype-based neural network initialization methodology. The adaptivity of neural networks, especially in the form of a universal approximator, should not be overlooked; it would be highly possible for a limited number of prototypes to suit a great number of nonlinearities. Section 4.1 further verifies the power of the adaptivity of neural networks paired with the proposed initialization methodology.

Even though the adaptivity of neural networks is fully utilized in the training process, this study focuses on a design of the initialization following a foolproof procedure. Here a key technique is offered to relate a limited number of prototypes to a large number of types of nonlinearities. This is done by seeking a means of utilizing the proposed prototypes as templates or basic building blocks in the initialization; accordingly, a target function with complex nonlinearities can be visualized as a linear sum of simple nonlinearities whose prototypes have already been constructed. Just like the construction of prototypes, this decomposition does not need to be exact. Delicate features are left to the adaptivity of the neural network during training.

Figure 4 illustrates the idea of decomposition. In Fig. 4(*a*), a wave form is spatially partitioned into several individual cycles, each of which can be approximated *independently* using Prototype 3 after some detailed treatment under Stage III transformation. The training results are presented in Refs. [25,26]. In Fig. 4(*b*), the summation of a straight line and a clearance (dead space) type nonlinearity over the same input range is exercised to produce a multislope nonlinearity. The training result is presented in Fig. 5. Using subtraction instead of summation, the saturation nonlinearity can be decomposed into the same two types of nonlinearities.

A good understanding of sigmoidal functions is necessary in the proposed decomposition. One unique advantage of Prototype 3 is that it offers a convenient local basis function since its neighboring areas are all zero. In contrast, Prototypes 1 and 2 have nonlocal basis functions since their neighboring areas are nonzero and can be highly nonlinear, as shown in Figs. 3(*a*) and 3(*b*). These features should be taken into account when decomposing complex target functions.

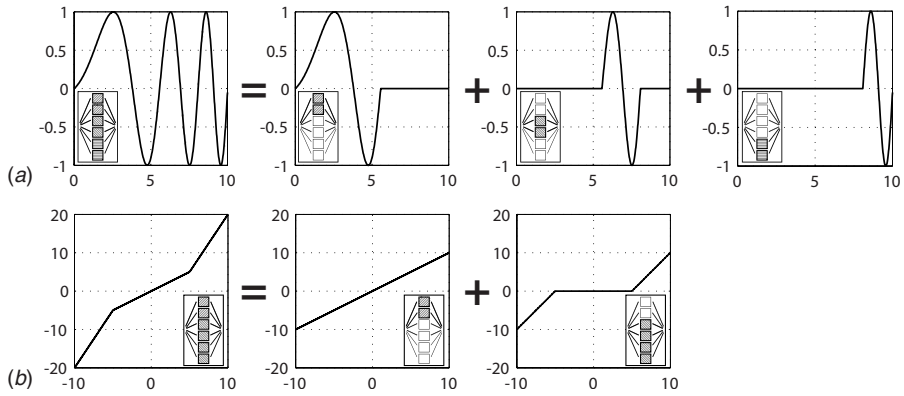

Fig. 4 Decomposing (*a*) swept sine and (*b*) multislope into a summation of some components that can be approximated directly using the proposed prototypes

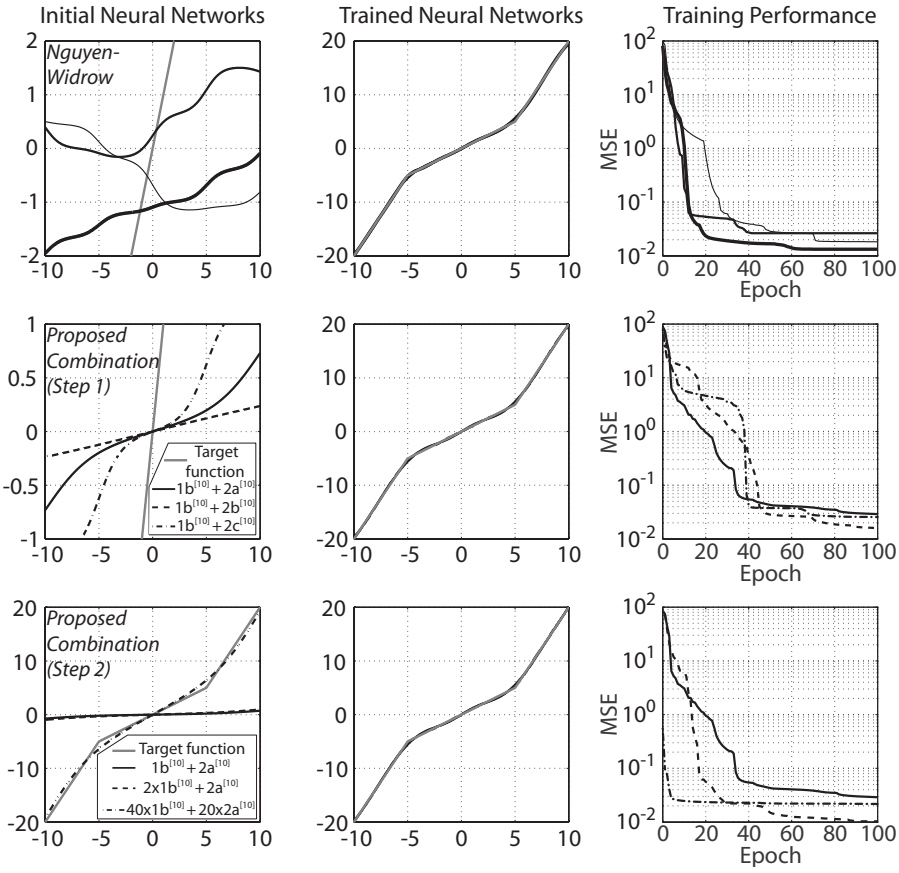

Fig. 5 An example of combining Prototypes 1 and 2 to train a multislope function. The idea of decomposition is presented in Fig. 4(*b*). The target function is in gray, while those black curves with different line thicknesses show four random options using the Nguyen–Widrow initialization [6]. Note that both Steps 1 and 2 were used to generate possible options for the initialization.

2.5 Transformation: Dealing With Non-Normalized Input and Output. The concept of prototypes and their variants is generic and thus should not be restricted to normalized input and output ranges. In principle, one could determine the values of IW, b, and LW based on arbitrary input and output ranges. This flexibility, however, could cause confusion and inconsistency, and needs to be handled with care for the sake of clarity in implementing the proposed methodology.

Having said this, it is adopted in this study to (i) define prototypes and their variants entirely based on normalized input (x) and output ($y(x)$) ranges and (ii) utilize a separate stage, Stage III, to further transform a selected prototype or its variant for a non-normalized input-output situation. Three scenarios involving non-normalized ranges can arise, and the corresponding strategies utilizing the derived prototypes and their variants for normalized ranges are given as follows:

(i) Non-normalized input, $\bar{x}=C_x x$: One can *proportion* the derived prototypes and their variants by "stretching" or "squeezing" the function approximated by the initial neural network along the x-direction in inverse relation to the non-normalized input. Quantitatively, the *transformed* value of IW, $\bar{w}$, is based on $wx+b=\bar{w}\bar{x}+b$, where $\bar{w}=(1/C_x)w$.

(ii) Offset of the target function along the input, $\bar{\bar{x}}=x+x_0$, or along the output, $\bar{y}=y+y_0$: To handle the offset, one can *translate* the derived prototypes and their variants by shifting the entire function to its new center while preserving its shape. When the input alone is offset, the transformed value of the basis, $\bar{b}$, is based on $wx+b=w\bar{\bar{x}}+\bar{b}$, where $\bar{b}=b-wx_0$. When the output is offset, one can utilize the two terms that are designated to approximate a constant [18].

(iii) Non-normalized output, $\bar{\bar{y}}=C_y y$: It is proposed that the LW values of the prototypes and their variants be *scaled* according to the non-normalized range of the output.

Since the values of IW and b determine the basis function in function approximation, the related transformations are referred to as *Step 1*. Similarly, the values of LW affect the coefficients, and their related transformations are referred to as *Step 2*. It is recommended that Steps 1 and 2 be carried out in this sequence. Both shorthand notations have been indicated in Fig. 1 and will be further utilized in the following training examples for clarity. In addition, the following notation will be used to denote a typical neural network generated from the proposed initialization methodology after the full procedure (including transformations) has been applied to the prototypes and their variants as introduced above:

$$\text{Initial neural network ID: } C_y \times n_{\langle x_0 \rangle}^{[C_x]} + y_0$$

where n denotes the prototype number and variant ID.

2.6 Comparison Between Proposed and Nguyen–Widrow Initialization. In addition to the comparisons throughout the training examples presented later, a couple of highlights are provided here to compare the proposed initialization with the Nguyen–Widrow initialization algorithm [6] as well as with some

Table 2 Initial values of the weights and biases used in Figs. 5, 6, 8, and 10. Note that in this table, normalized inputs and outputs are used. The quantities with * are fixed. The quantities with † are associated with the constant term [15,18] and are *not* scaled throughout this study. Also note the interrelationships between various IW, *b*, and LW values.

Prototype and variant	Weights in input layer, IW	Biases in input layer, b	Weights in output layer, LW
	Fig. 5 (multislope nonlinearity)		
$1b^{[10]}+2a^{[10]}$	$[0.1\ \ 0.5\ \ 0.5\ \ 1^{\dagger}\ \ -1^{\dagger}]^T$	$[0^*\ \ 5\ \ -5\ \ 0^*\ \ 0^*]^T$	$[1\ \ 1\ \ 1\ \ -1.5\ \ -1.5]$
$1b^{[10]}+2b^{[10]}$	$[0.1\ \ 0.5\ \ 0.5\ \ 1^{\dagger}\ \ -1^{\dagger}]^T$	$[0^*\ \ 10\ \ -10\ \ 0^*\ \ 0^*]^T$	$[1\ \ 1\ \ 1\ \ -1.5\ \ -1.5]$
$1b^{[10]}+2c^{[10]}$	$[0.1\ \ 1.0\ \ 1.0\ \ 1^{\dagger}\ \ -1^{\dagger}]^T$	$[0^*\ \ 5\ \ -5\ \ 0^*\ \ 0^*]^T$	$[1\ \ 1\ \ -1.5\ \ -1.5]$
$2\times 1b^{[10]}+2a^{[10]}$	$[0.1\ \ 0.5\ \ 0.5\ \ 1^{\dagger}\ \ -1^{\dagger}]^T$	$[0^*\ \ 5\ \ -5\ \ 0^*\ \ 0^*]^T$	$[2\ \ 1\ \ 1\ \ -2\ \ -2]$
$40\times 1b^{[10]}+20\times 2a^{[10]}$	$[0.1\ \ 0.5\ \ 0.5\ \ 1^{\dagger}\ \ -1^{\dagger}]^T$	$[0^*\ \ 5\ \ -5\ \ 0^*\ \ 0^*]^T$	$[40\ \ 20\ \ 20\ \ -40\ \ -40]$
	Fig. 6 (two-variable softening Duffing nonlinearity)		
$5\times 3a^{[10]}+1a^{[50]}$	$\begin{bmatrix}1.0 & 0.5 & 0 & 0 & 0\\ 0 & 0 & 0.1 & 1^{\dagger} & -1^{\dagger}\end{bmatrix}^T$	$[0\ \ 0\ \ 0^*\ \ 0^*\ \ 0^*]^T$	$[5\ \ -5\ \ 1\ \ -0.5\ \ -0.5]$
$4\times 3b^{[10]}+1a^{[50]}$	$\begin{bmatrix}0.5 & 0.1 & 0 & 0 & 0\\ 0 & 0 & 0.1 & 1^{\dagger} & -1^{\dagger}\end{bmatrix}^T$	$[0\ \ 0\ \ 0^*\ \ 0^*\ \ 0^*]^T$	$[4\ \ -4\ \ 1\ \ -0.5\ \ -0.5]$
	Fig. 8 (piecewise nonlinearity typical of concrete in compression)		
$100\times 2a^{[10]}$	$[0.5\ \ 0.5\ \ 1^{\dagger}\ \ -1^{\dagger}]^T$	$[5\ \ -5\ \ 0^*\ \ 0^*]^T$	$[100\ \ 100\ \ -100\ \ -100]$
$100\times 2a^{[10]}_{\langle 10\rangle}$	$[0.5\ \ 0.5\ \ 1^{\dagger}\ \ -1^{\dagger}]^T$	$[0\ \ -10\ \ 0^*\ \ 0^*]^T$	$[100\ \ 100\ \ -100\ \ -100]$
$100\times 2a^{[10]}_{\langle 10\rangle}+100$	$[0.5\ \ 0.5\ \ 1^{\dagger}\ \ -1^{\dagger}]^T$	$[0\ \ -10\ \ 0^*\ \ 0^*]^T$	$[100\ \ 100\ \ 0\ \ 0]$
	Fig. 10 (scaled output cubic nonlinearities)		
$1\times 2a$	$[5\ \ 5\ \ 1^{\dagger}\ \ -1^{\dagger}]^T$	$[5\ \ -5\ \ 0^*\ \ 0^*]^T$	$[1\ \ 1\ \ -1\ \ -1]$
$10\times 2a$	$[5\ \ 5\ \ 1^{\dagger}\ \ -1^{\dagger}]^T$	$[5\ \ -5\ \ 0^*\ \ 0^*]^T$	$[10\ \ 10\ \ -10\ \ -10]$
$100\times 2a$	$[5\ \ 5\ \ 1^{\dagger}\ \ -1^{\dagger}]^T$	$[5\ \ -5\ \ 0^*\ \ 0^*]^T$	$[100\ \ 100\ \ -100\ \ -100]$
$1000\times 2a$	$[5\ \ 5\ \ 1^{\dagger}\ \ -1^{\dagger}]^T$	$[5\ \ -5\ \ 0^*\ \ 0^*]^T$	$[1000\ \ 1000\ \ -1000\ \ -1000]$

previous work reviewed above in Sec. 1. Bear in mind that the proposed initialization is not aimed at approximating arbitrary functions. Rather it is a domain-specific application.

First of all, unlike the Nguyen–Widrow algorithm, the proposed initialization is constructive, i.e., it answers how many hidden nodes are needed. Similar to the Nguyen–Widrow algorithm, the proposed initialization (i) emphasizes understanding the function to be approximated (although the implementation is achieved in a different manner), (ii) utilizes the strength of sigmoidal functions (although the focus of these two approaches are different), and (iii) could still be subjective and involve some trial and error. Further details can be seen in Ref. [25].

3 Training Examples

All ten types of nonlinearities were successfully trained using the proposed methodology. While typical examples of directly adopting the proposed prototypes can be found in Refs. [25–27], the way to utilize the proposed decomposition technique is the focus of this section (see Table 2 for all values of the weights and biases). All trainings were carried out using the MATLAB Neural Network Toolbox [19] with the batch training mode and the Levenberg–Marquardt backpropagation algorithm [28]. Since the Nguyen–Widrow initialization algorithm does not specify the required number of hidden nodes, this critical piece of information is borrowed from the proposed initialization methodology whenever the Nguyen–Widrow initialization is used.

3.1 Approximating One-Variable Functions by Combining Prototypes. The decomposition approach presented in Sec. 2.4 can be applied to numerous types of nonlinearities that are more complex than those nonlinear functions that can be approximated directly by individual prototypes. As shown in Fig. 4(*a*), a swept sine can be approximated by applying Prototype 3 three times, yielding a neural network with six hidden nodes. In particular, the center of each cycle needs to be captured in the initialization through *translation* (i.e., adjusting the value of the bias, b), while the non-normalized input range needs to be taken into account through *proportioning* (i.e., scaling the value of the weights, IW). One feasible neural network initialization for a swept sine curve can be written: $-1\times 3a^{[2]}_{\langle 4\rangle}-1\times 3a^{[1,25]}_{\langle 7\rangle}-1\times 3a^{[1]}_{\langle 9\rangle}$. The results of a similar training can be found in Refs. [25,26].

One more example is shown in Fig. 5 for the multislope nonlinearity (type IV in Fig. 2) following the decomposition idea shown in Fig. 4(*b*). The option of $40\times 1b^{[10]}+20\times 2a^{[10]}$ seems to give the best performance when the epoch number is small, while that of $2\times 1b^{[10]}+2a^{[10]}$ tends to perform best in the long run. Note that multiple options exist for the training. The presented training results are not exhaustive; one can utilize the proposed Stage III to further generate and refine other options. The saturation and stiction nonlinearities (types IX and X in Fig. 2, respectively) have also been trained successfully as a further validation of the proposed decomposition approach. Additionally, the fractional power nonlinearity (type V in Fig. 2) can also be trained using a decomposition approach as presented in Ref. [26].

For the commonly seen functions in engineering mechanics presented thus far, the proposed initialization seems to be efficient. From these training examples, it can be seen that the proposed initialization starts with a neural network output that always mimics the target function to a certain extent and consequently leads to a successful training. In contrast, the Nguyen–Widrow initialization starts with a random realization that does not bear any similarity to the target function, and the corresponding training can have unpredictable success. As for convergence speed (as shown by the mean square error (MSE) versus epoch) in successful training cases, the proposed initialization is at least equivalent to that of Nguyen-Widrow's, if not faster. More predictable training success and faster convergence speed are the advantages of the proposed initialization, as well as (i) full knowledge of the required number of hidden nodes and (ii) a clear procedure at every stage of the initialization.

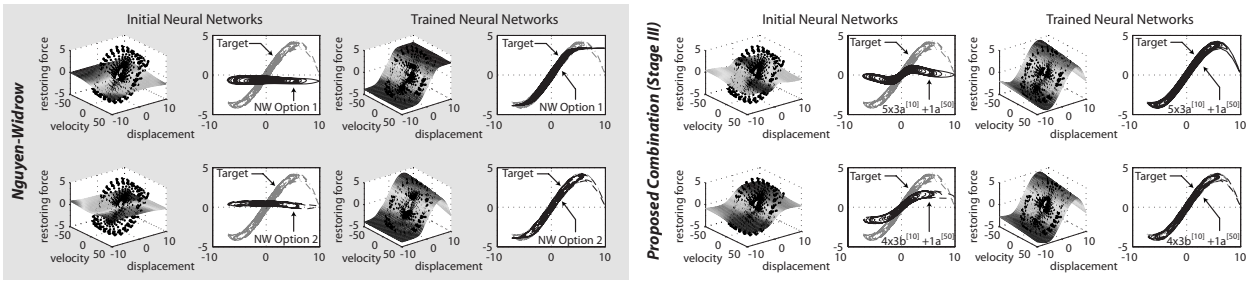

Fig. 6 Training results of a softening Duffing nonlinearity [30] based on two options using the Nguyen–Widrow algorithm and two other options using the proposed initialization methodology. All four trainings use neural network of five hidden nodes. The target function is in gray.

3.2 Approximating Two-Variable Functions by Combining Prototypes. Approximating a function of two (or more) variables is of great importance in engineering mechanics applications. For example, nonlinear hysteretic restoring force can be formulated as both displacement and velocity in a single-degree-of-freedom (SDOF) system, which is known as the force-state mapping formulation [29]. References [15–18] outline some of the strategies to map the force-state formulation into a feedforward neural network with one hidden layer. When the memory effect of nonlinear dynamics is considered, three state variables are needed in the formulation. When the degradation is further considered, four state variables are needed. All these point to the need of approximating functions with multiple variables.

To approximate a function of two variables, certain situations can be conveniently handled according to the proposed initialization for one-variable functions, as presented in Refs. [15–18]. The idea of decomposition is very useful in generalizing the solution from one-variable to two-variable functions, especially when dealing with two uncoupled variables. For example, a softening Duffing oscillator from Ref. [30] is described as $g(x,\dot{x})=x+0.0159\dot{x}-0.01x^3$, where x and $\dot{x}$ stand for displacement and velocity, respectively (i.e., the state variables). For x, Prototype 3 is utilized to capture the softening cubic nonlinearity (type VI in Fig. 2), while for $\dot{x}$, Prototype 1 is adopted to approximate either a linear viscous or a Coulomb damping term. Figure 6 presents the training results using both the Nguyen–Widrow and the proposed initialization, each with two options. It can be seen that the proposed initialization is more successful than the Nguyen–Widrow algorithm in approximating this function even when using only five nodes.

4 Versatility and Robustness of Proposed Prototypes

4.1 Understanding Versatility of Prototypes. This work would be trivial if the proposed forward-formulation-based prototypes and their variants could only successfully be trained to approximate the specific nonlinearities that they were derived for. In other words, a critical question is: "Can these prototypes and their variants be successfully trained to approximate nonlinearities of the same types but with different coefficients, or even nonlinearities beyond those types?" The answer to this critical question is positive. Indeed, the adaptivity of the proposed prototypes and their variants has proven to be superior.

For a normalized input and output, Prototype 1, variant *c*, can be used to train a range of fractional power nonlinearities (type V in Fig. 2), including $x=y$, $x=y^3$, etc., in addition to the hard limiting nonlinearity (type VIII) which it resembles most. Figure 7 further reveals the considerable adaptivity of Prototype 2, variant *a*, which can be trained to approximate (i) a wide range of polynomials, (ii) various combinations of piecewise polynomials, and (iii) clearance (dead space) nonlinearities. This variant with only four hidden nodes has demonstrated great flexibility to these popular nonlinearities, from which the merit of using sigmoidal functions as a unified basis in engineering mechanics applications

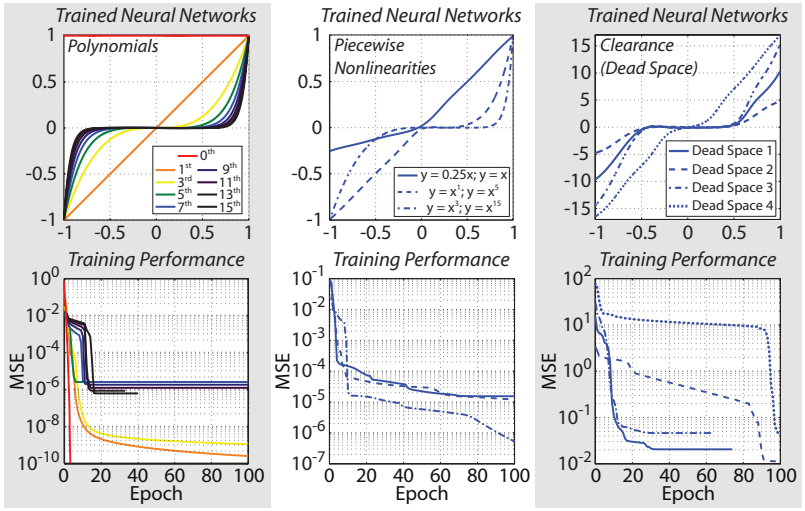

Fig. 7 Prototype 2, variant *a* (with four hidden nodes), is used to approximate various nonlinear functions. Note that some inputs and outputs are normalized. Also note that some of the trainings stopped prematurely.

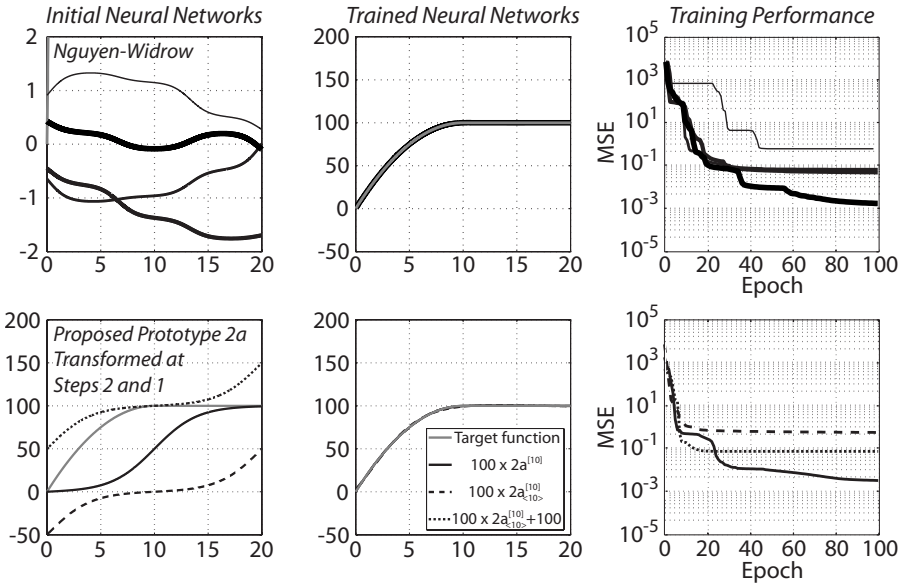

Fig. 8 An example of using Prototype 2, variant *a* (with four hidden nodes), to approximate an idealized piecewise unsymmetrical nonlinearity with an offset that is typical of concrete in compression. The target function is in gray, while those black curves with different line thicknesses show four random options using the Nguyen–Widrow initialization [6]. Note that both Steps 2 and 1 were gone through individually to generate three possible options for the initialization.

can be verified. The proposed initialization methodology demonstrates a constructive means to achieve this flexibility.

4.2 Approximating Piecewise Unsymmetrical Functions. Although the proposed prototypes are derived to approximate symmetrical and smooth nonlinearities, as demonstrated previously in Fig. 3, these prototypes have shown the ability to be trained and converged well to piecewise unsymmetrical nonlinearities over the specified input range, as revealed in the middle column of Fig. 7. Approximating these nonlinearities is of great practical significance. First, they represent experimental phenomena that can often be encountered in the practice of engineering mechanics such as concrete in compression, and clearance (dead space) joint behavior. Second, these situations involve the C^1 discontinuity where (i) polynomial fitting normally cannot perform as efficiently and (ii) the Fourier series causes nonuniform convergence (the so-called Gibbs phenomenon).

An idealized function typical of concrete in compression, a parabola joined by a horizontal line at its vertex, is approximated. Figure 8 shows the training results using both the Nguyen–Widrow algorithm and the proposed initialization methodology. It can be seen that the joint of the curves is offset both horizontally and vertically. Similar to Fig. 5, multiple options for the initialization exist, following the proposed methodology; those presented are merely some possibilities.

4.3 Handling Noise in Data. Multilayer feedforward neural networks are known to be robust to measurement noise in experimentally collected data [21]. A selection from each nonlinearity in Fig. 2 was contaminated with Gaussian noise to three different degrees and then trained with the proposed initialization methodology and compared with the Nguyen–Widrow initialization [6]. A typical example has been presented in Ref. [27]. When using the proposed initialization, a good selection of variants seems to make the training successful even with a high level of noise. Here a good selection appears to be guided by the similarity between the target function and initial neural network output, which will be further discussed in Sec. 5.2. When the Nguyen–Widrow algorithm is adopted, there are options leading to a successful training even when the noise level is high. However, the procedure of selecting the right Nguyen-Widrow option is uncertain due to the highly random nature of this scheme.

5 Subjective Issues

As outlined previously in Sec. 2, the proposed initialization methodology does contain subjective judgment, which originates from (i) matching a target function with a collection of preprepared prototypes and their variants as in Stages I and II and (ii) deciding the free values for some of the weights and biases as in Stage III. Since a matching process can be fundamentally considered a pattern classification problem, challenges arise when a pattern falls onto the boundary between two patterns or when a boundary itself is ambiguous. Varying the values of weights and biases within a prototype/variant will alter the degree of similarity between the target and the initial neural network output and will thus affect the decision associated with the initialization. The focus of the discussion hereafter is given to making the best decision for a successful training in terms of convergence and approximation accuracy.

5.1 Multiple Options in Selecting Prototypes and Variants. There are multiple options for initializing neural networks to approximate a given nonlinear function according to the proposed methodology. The prototypes introduced in Fig. 2 may not be exhaustive, nor are their combinations thought to be exhaustive. Furthermore, the correlations between the target functions and the prototypes or prototype combinations are not exhaustive. While one prototype/variant can be used to approximate multiple nonlinearities, as shown in Fig. 7, one type of nonlinearity may be successfully approximated by more than one prototype. The two options for prototypes shown in Fig. 2 for the approximation of a fractional power nonlinearity have been presented in Ref. [26]. There appears to be a many-to-many relationship between types of nonlinearities and prototypes, which should be confirmed in future studies.

5.2 Deciding Free Values in Weights and Biases. In this

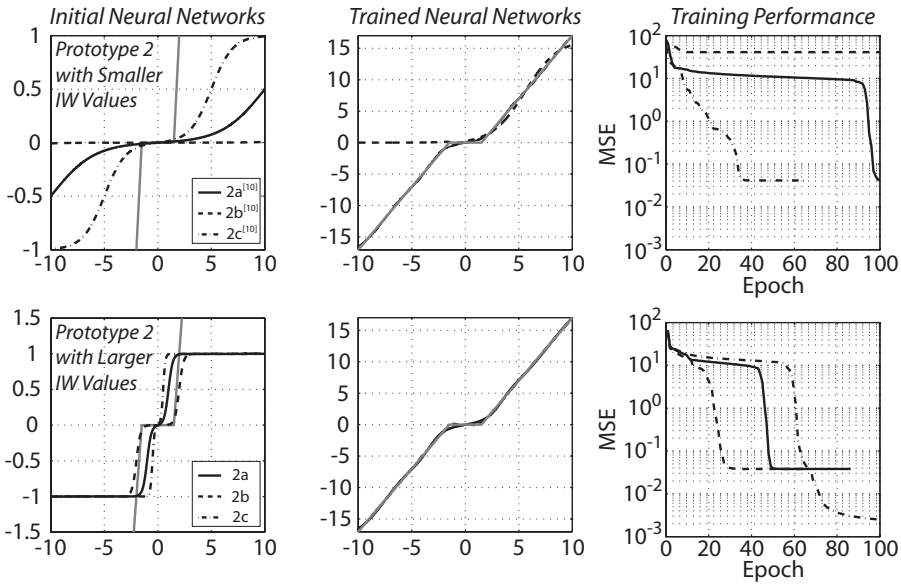

Fig. 9 An example of training performance as affected by the selection of the IW values. Here the target function (shown in gray) is a clearance (dead space) nonlinear function, while the three variants of Prototype 2 (with four hidden nodes) with and without proportioning during Step 1 of Stage III are selected for training. Note that some of the trainings stopped prematurely.

continuing development of previous efforts [15,17], one of the critical issues considered is how to decide the free values in the weights and biases. On one hand, all the options in each training example serve as case studies for the specified types of nonlinearities. On the other hand, the versatility explored in this study indicates that one does not need to make the output of the initial neural network match the target function exactly. Rather, one only needs to capture the dominating features. This might seem to relax the necessity of properly deciding the critical free values of the weights and biases. However, there are still nontrivial questions such as the following: (i) How should the major features of target functions that are required for this initialization methodology be defined? That is, what are the really "major" and "minor" features? To what extent should the neural network initialization capture them to lead to successful training? (ii) To what extent should one adjust the input layer weights IW, biases b, and layer weights LW during the initialization, and to what extent should these be left to training? Even though iterations are recommended, as shown in Fig. 1, and although there are also some general treatments on non-normalized inputs and outputs before and after training, as discussed elsewhere [15–17], there persists a practical need to decide whether and how to adjust these values especially for the purpose of real-time training.

The authors do not expect this paper to completely tackle all these challenging issues. However two typical examples, one for Step 1 and the other for Step 2 under Stage III, are presented to suggest solution strategies. Note that some of them are not entirely consistent with other studies on training neural networks.

To train a clearance (dead space) nonlinearity (type VII in Fig. 2), Fig. 7 has suggested the possibility of using Prototype 2, variant a. Figure 9 presents a parametric study involving proportioning and translation at Step 1, where different values for IW (between the two rows in the figure) and b (within each row) are used. The three variants of Prototype 2 (with four hidden nodes) with and without proportioning during Step 1 are selected for training. It seems that commonly recommended small values of IW [12,13] do not always lead to good training performance. Rather, a high value of IW, along with an initial neural network output that more closely resembles the target function, leads to better training performance in this case.

The other example presented in Fig. 10 focuses on the effect of *scaling* at Step 2 when the values of LW are adjusted according to the range of a non-normalized output. It demonstrates that selecting proper values for LW can affect training performance and thus requires careful consideration. This is not entirely consistent with the findings of previous studies [31]. Again, it appears that trying to find the closest "resemblance" could be a better strategy than selecting small values for LW when direct training of a non-normalized input and output data set is required.

6 Discussion

Admittedly, approximating functions by following this proposed initialization methodology involves more preliminary work than would be necessary if the Nguyen–Widrow initialization algorithm were used. However, it should be noted that this study's primary aim is to clarify the use of neural networks, not to decrease the emphasis on the initialization. As has been shown in this study, an additional consideration made when selecting a proper neural network initialization more often results in a more accurate approximation. Furthermore, it is envisioned that the desirability of a prototype-based methodology like this one will increase further once the prototype and variant selection process can be automated, an avenue which has been identified for future work.

Although analytical rather than experimental training data have been used exclusively throughout, this study is still relevant for general engineering mechanics applications. First, the work presents a set of specific tactics on how to approximate ten or even more typical nonlinearities using multilayer feedforward neural networks. Second, the results on the versatility of the proposed prototypes show great promise for the success of applying this initialization methodology to many other practical cases that are not included in this paper. Finally, the authors have trained data containing noise simulating real-world situations.

Mathematically, it is very important to note that throughout this study, the proposed initialization does *not* involve considering the orthogonality of the basis functions. Having orthogonal basis

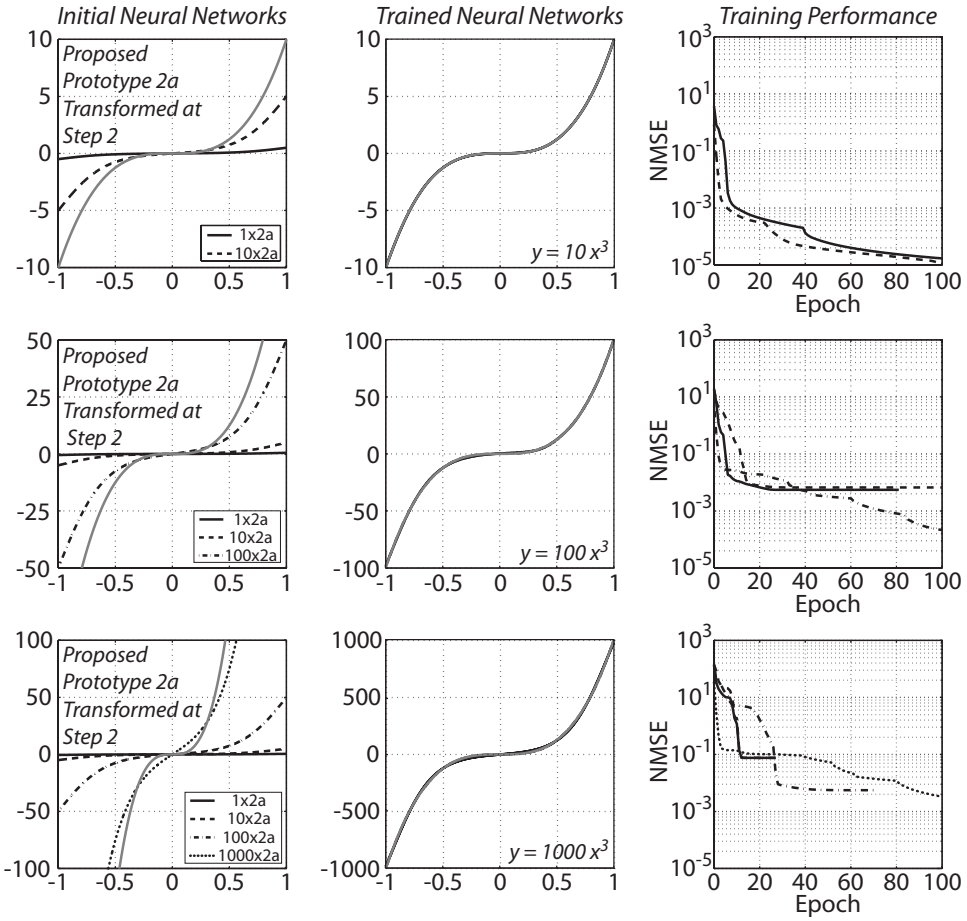

Fig. 10 An example of training performance as affected by the selection of the LW values. Note that the input is normalized while the output is not. The target functions are in gray, while those in black with different line types show various options created by scaling up the LW values of Prototype 2, variant *a* (with four hidden nodes). Note that some of the trainings stopped prematurely. Also note that normalized mean square error (NMSE) is used in the last panel for convenience of comparison.

functions is always preferred in functional expansion (e.g., Fourier expansion) and is also popular for data-driven techniques (e.g., wavelet decomposition). However, the goal and driving interest of this study is not to look for a set of orthogonal sigmoidal functions to start neural network training. Given the feasibility proven by the universal approximator theorem [3,4], this body of work focuses on the constructibility which can be achieved by injecting the domain knowledge and exercising clear engineering judgement rather than treating the initialization largely as a trial-and-error procedure.

Some topics are identified for future work in Fig. 1. For the commonly seen nonlinear functions in engineering mechanics studied here, the proposed initialization scheme seems to be effective (in terms of convergence of training) and efficient (in terms of utilizing a small number of hidden nodes). In regard to approximation accuracy, the training performance time histories of MSE versus epoch give a generally acceptable order of magnitude. For those examples where training stopped prematurely, one of the causes could be an insufficient number of hidden nodes. This indicates a need to study how to add extra sigmoidal terms (i.e., hidden nodes) to improve approximation accuracy. Another relevant topic to be addressed is the generalization of this study to a high dimensional input space so that the memory and degradation of nonlinear dynamic systems can be modeled. The guiding principle of exploiting mathematical reasoning and physical meaning should be continually practiced to reveal the inner workings of neural networks.

7 Conclusion

The core idea behind this study is the injection of mathematical reasoning and physical meaning into the neural network initialization for a successful training. Neural networks can be highly versatile and efficient in adapting to data when approximating nonlinear functions. However, these qualities can be achieved only if neural networks are initialized properly, as constructively verified in this study. A structured and detailed initialization methodology has been presented as a continuous development of the heuristic prototype-based initialization approach for multilayer feedforward neural networks proposed in previous studies [15–18]. A range of typical nonlinear functions used in engineering mechanics applications has been targeted, and training performance has been presented and compared with the Nguyen–Widrow initialization algorithm. Technical challenges have been identified, and solution strategies have been provided. The proposed initialization methodology has shown satisfactory versatility and robustness in addition to being a constructive method.

Acknowledgments

The Junior Faculty Research Program awarded to the first author by Dr. T. H. Lee Williams, the Vice President for Research at the University of Oklahoma, is greatly appreciated. Funding from the Undergraduate Research Opportunities Program (UROP) awarded to the second author is also greatly appreciated.

References

[1] Denoeux, T., and Lengellé, R., 1993, "Initializing Back Propagation Networks With Prototypes," Neural Networks, **6**, pp. 351–363.

[2] Sandberg, I. W., Lo, J. T., Fancourt, C. L., Principe, J. C., Katagiri, S., and Haykin, S., 2001, *Nonlinear Dynamical Systems: Feedforward Neural Network Perspectives*, Wiley, New York.

[3] Cybenko, G., 1989, "Approximation by Superpositions of Sigmoidal Function," Math. Control, Signals, Syst., **2**, pp. 303–314.

[4] Hornik, K., Stinchcombe, M., and White, H., 1989, "Multilayer Feedforward Networks are Universal Approximators," Neural Networks, **2**, 359–366.

[5] Jones, L. K., 1990, "Constructive Approximations for Neural Networks by Sigmoidal Functions," Proc. IEEE, **78**(10), pp. 1586–1589.

[6] Nguyen, D., and Widrow, B., 1990, "Improving the Learning Speed of Two-Layer Neural Networks by Choosing Initial Values of the Adaptive Weights," *Proceedings of the International Joint Conference on Neural Networks*, July, Vol. III, pp. 21–26.

[7] Burrows, T. L., and Niranjan, M., 1993, "Feed-Forward and Recurrent Neural Networks for System Identification," Cambridge University Engineering Department, Technical Report No. CUED/F-INFENG/TR158.

[8] Osowski, S., 1993, "New Approach to Selection of Initial Values of Weights in Neural Function Approximation," Electron. Lett., **29**(3), pp. 313–315.

[9] Costa, P., and Larzabal, P., 1999, "Initialization of Supervised Training for Parametric Estimation," *Neural Processing Letters*, Vol. 9, Kluwer, Netherlands, pp. 53–61.

[10] Lapedes, A., and Farber, R., 1988, "How Neural Nets Work," *Neural Information Processing Systems*, D. Anderson, ed., American Institute of Physics, New York, pp. 442–456.

[11] Ma, L., and Khorasani, K., 2004, "New Training Strategies for Constructive Neural Networks With Application to Regression Problems," Neural Networks, **17**, pp. 589–609.

[12] Lehtokangas, M., 1999, "Fast Initialization for Cascade-Corrolation Learning," IEEE Trans. Neural Netw., **10**(2), pp. 410–414.

[13] Yam, J. Y. F., and Chow, T. W. S., 2001, "Feedforward Networks Training Speed Enhancement by Optimal Initialization of the Synaptic Coefficients," IEEE Trans. Neural Netw., **12**(2), pp. 430–434.

[14] Pei, J. S., Wright, J. P., and Smyth, A. W., 2005, "Neural Network Initialization With Prototypes—A Case Study in Function Approximation," *Proceedings of the International Joint Conference on Neural Networks 2005 (IJCNN'05)*, Montreal, Canada, Jul. 31–Aug. 4, pp. 1377–1382.

[15] Pei, J. S., 2001, "Parametric and Nonparametric Identification of Nonlinear Systems," Ph.D. thesis, Columbia University, New York.

[16] Pei, J. S., and Smyth, A. W., 2006, "A New Approach to Design Multilayer Feedforward Neural Network Architecture in Modeling Nonlinear Restoring Forces. Part I: Formulation," J. Eng. Mech., **132**(12), pp. 1290–1300.

[17] Pei, J. S., and Smyth, A. W., 2006, "A New Approach to Design Multilayer Feedforward Neural Network Architecture in Modeling Nonlinear Restoring Forces. Part II: Applications," J. Eng. Mech., **132**(12), pp. 1301–1312.

[18] Pei, J. S., Wright, J. P., and Smyth, A. W., 2005, "Mapping Polynomial Fitting Into Feedforward Neural Networks for Modeling Nonlinear Dynamic Systems and Beyond," Comput. Methods Appl. Mech. Eng., **194**(42–44), pp. 4481–4505.

[19] Hagan, M. T., Demuth, H. B., and Beale, M., 1995, *Neural Network Design*, PWS, Boston.

[20] Pei, J. S., Smyth, A. W., and Kosmatopoulos, E. B., 2004, "Analysis and Modification of Volterra/Wiener Neural Networks for Identification of Nonlinear Hysteretic Dynamic Systems," J. Sound Vib., **275**(3–5), 693–718.

[21] Nelles, O., 2000, *Nonlinear System Identification: From Classical Approaches to Neural Networks and Fuzzy Models*, Springer-Verlag, Berlin.

[22] Adams, D. E., and Allemang, R. J., 2000, "Non-Linear Vibrations Classnotes," Course No. 20-263-781.

[23] Worden, K., and Tomlinson, G. R., 2001, *Nonlinearity in Structural Dynamics: Detection, Identification and Modelling*, Institute of Physics, New York, p. 680.

[24] Wright, J. P., Pei, J. S., and Mai, E. C., 2008, "A Growing Neural Network Approach in Engineering Mechanics Applications," Comput. Methods Appl. Mech. Eng., to be submitted.

[25] Pei, J. S., and Mai, E. C., 2006, "Neural Network Initialization for Modeling Nonlinear Functions in Engineering Mechanics," *Proceedings of the 24th International Modal Analysis Conference (IMAC XXIV)*.

[26] Pei, J. S., and Mai, E. C., 2006, "A Heuristic Neural Network Initialization Scheme for Modeling Nonlinear Functions in Engineering Mechanics," SPIE International Symposia Smart Structures, Materials/NDE.

[27] Pei, J. S., Mai, E. C., and Piyawat, K., 2006, "Multilayer Feedforward Neural Network Initialization Methodology for Modeling Nonlinear Restoring Forces and Beyond," Fourth World Conference on Structural Control and Monitoring.

[28] Haykin, S. S., 1998, *Neural Networks: A Comprehensive Foundation*, 2nd ed., Prentice-Hall, Englewood Cliffs, NJ, p. 842.

[29] Masri, S. F., and Caughey, T. K., 1979, "A Nonparametric Identification Technique for Nonlinear Dynamic Problems," J. Appl. Mech., **46**, pp. 433–447.

[30] Masri, S. F., Caffrey, J. P., Caughey, T. K., Smyth, A. W., and Chassiakos, A. G., 2004, "Identification of the State Equation in Complex Non-Linear Systems," Int. J. Non-Linear Mech., **39**, pp. 1111–1127.

[31] Wessels, L. F. A., and Barnard, E., 1992, "Avoiding False Local Minima by Proper Initialization of Connections," IEEE Trans. Neural Netw., **3**(6), pp. 899–905.

An Explicit Analytic Solution of Steady Three-Dimensional Stagnation Point Flow of Second Grade Fluid Toward a Heated Plate

Ahmer Mehmood[1]
e-mail: ahmerqau@yahoo.co.uk

Asif Ali

Department of Mathematics,
Quaid-I-Azam University,
Islamabad 44000, Pakistan

We present a purely analytic solution to the steady three-dimensional viscous stagnation point flow of second grade fluid over a heated flat plate moving with some constant speed. The analytic solution is obtained by a newly developed analytic technique, namely, homotopy analysis method. By giving a comparison with the existing results, it is shown that the obtained analytic solutions are highly accurate and are in good agreement with the results already present in literature. Also, the present analytic solution is uniformly valid for all values of the dimensionless second grade parameter α. The effects of α and the Prandtl number Pr on velocity and temperature profiles are discussed through graphs.
[DOI: 10.1115/1.2957597]

Keywords: stagnation point flow, heat transfer analysis, second grade fluid, analytic solution, homotopy analysis method

1 Introduction

Exact solutions of the Navier–Stokes equations with nonvanishing nonlinear terms can only be obtained in a small number of cases. Each such solution is of considerable methodological interest, even though not always of great physical importance. One tractable similarity solution is that corresponding to viscous incompressible flow in the neighborhood of a two-dimensional stagnation point. In the beginning of the 20th century, the orthogonal stagnation point flow was first studied by Blasius [1]. Heimenz [2] presented the numerical solution to Blasius's problem. Orthogonal stagnation flow on oscillating and translating plates has been studied by Glauert [3]. Two-dimensional oblique stagnation flow was solved by Stuart [4] and later by Davey [5] and Tamada [6]. The heat transfer due to a jet impinging orthogonally onto a horizontal moving surface has been solved by Dorepaal [7].

In recent years considerable amount of interest has been given to the stagnation point flows of viscous fluids (see, for instance, Refs. [8–15]). This is because of their great importance in both theoretical and practical points of views. From the theoretical point of view, such kind of flow is fundamental in fluid mechanics and forced convective heat transfer. From the practical point of view, these flows have applications in forced convection cooling processes where a coolant is impinged on a continuously moving plate. Due to their important applications in industry, the non-Newtonian fluids have received a lot of attention during the past few decades. Unlike Newtonian fluids, the non-Newtonian fluids could not be represented by a single flow model. There are many empirical and semiempirical flow models for these fluids. Amongst all these models, the second grade model has become very much popular. The constitutive assumption for the fluids of second grade or second order is in the following form:

$$\mathbf{T} = -p\mathbf{I} + \mu\mathbf{A}_1 + \alpha_1\mathbf{A}_2 + \alpha_2\mathbf{A}_1^2$$

where $\mathbf{T}$ is the Cauchy stress tensor, $-p\mathbf{I}$ is the spherical stress due to the constraint of incompressibility, μ is the coefficient of viscosity, α_1 and α_2 are the material moduli, and $\mathbf{A}_1$ and $\mathbf{A}_2$ are the first two Fosdick–Rajagopal tensors [16]. The Clausius–Duhem inequality and the assumption that the Helmholtz free energy is a minimum in equilibrium provides the following restrictions [17]:

$$\mu \geq 0, \quad \alpha_1 \geq 0, \quad \alpha_1 + \alpha_2 = 0$$

The third condition is the consequence of the Clausius–Duhem inequality, and the second follows the requirement that the Helmholtz free energy is a minimum in equilibrium. A comprehensive discussion on the restrictions for μ, α_1, and α_2 can be found in the work by Dunn and Rajagopal [18].

In this paper we consider the steady three-dimensional viscous stagnation point flow of a second grade fluid over a moving flat plate. The same problem has already been studied by Baris [15]. Baris applied the perturbation technique in order to reduce the order of the governing nonlinear equations. The obtained zero-order and first-order systems of nonlinear equations were then solved numerically. The results obtained by Baris [15] are valid only for $0 \leq \alpha \leq 0.2$. In order to investigate the flow phenomenon for $\alpha \geq 0.2$, we have solved the same problem analytically by the homotopy analysis method (HAM). The results obtained by HAM are purely analytic and uniformly valid for all values of α. The numerical results of Baris [15] can easily be determined from our present analytic solution by the suitable choice of the auxiliary parameter $\hbar$, which proves the accuracy of the present analytic results.

Although the nonlinear analytic techniques are fast developing, still they do not completely satisfy the mathematicians and engineers. It is however still very difficult to solve nonlinear problems by means of analytic techniques. The nonlinear analytic methods most widely applied by engineers are perturbation techniques [19]. Using the perturbation method, engineers have obtained many interesting and important results. However, like other nonlinear analytic techniques, perturbation methods have their own limitations. The application of perturbation techniques requires

[1]Corresponding author. Present address: Department of Mathematics (FBAS), International Islamic University Islamabad, Pakistan.

Contributed by the Applied Mechanics Division of ASME for publication in the JOURNAL OF APPLIED MECHANICS. Manuscript received June 12, 2006; final manuscript received January 25, 2007; published online August 15, 2008. Review conducted by Bassam A. Younis.

the presence of a small or large parameter in the equation, thus not applicable to the problems involving no small or large parameter. Even if such parameter is present, the obtained perturbation results are valid only for small or large values of that parameter. Currently, Liao [20] introduced an analytic technique for highly nonlinear differential equations arising in science and engineering. Unlike perturbation techniques, the homotopy analysis method is applicable to those nonlinear problems which do not involve any small or large parameter. Besides, it logically contains the other perturbative techniques, such as the Adomian's decomposition method [21], the δ-expansion method [22], and Lyapunov's small parameter method [23]. The method has been successfully applied to a large number of nonlinear problems by many researchers (see, for instance, Refs. [24–39]), which proves the validity of the method.

The paper is organized in four sections. Section 2 consists of flow analysis in which we present an analytic solution of the problem, its convergence, and the graphical representation of solution. Section 3 consists of heat transfer analysis. In Sec. 4 some concluding remarks are given, and at the end some constants appearing in the solution expressions are defined in the Appendix.

2 Flow Analysis

We consider an infinite plate adjacent to the xy-plane, and z-axis is taken perpendicular to it. The plate is moving with a constant velocity U in the x-direction. A non-Newtonian fluid of grade 2 flowing in the negative z-axis approaches the moving plate at $z=0$ and divides into streams proceeding away from the stagnation point at the origin. Far from the plate, the velocity components in x-, y-, and z-directions in the frictionless potential flow are given by

$$u_\infty = ax, \quad v_\infty = ay, \quad w_\infty = -2az \tag{1}$$

and the pressure distribution is given by the Euler equation

$$p - p_0 = -\frac{\rho}{2}(u_\infty{}^2 + v_\infty{}^2 + w_\infty{}^2) \tag{2}$$

where a is a physical constant, ρ is the density of the liquid, and p_0 is a constant corresponding to the pressure at the stagnation point. In order to get a solution which satisfies the no-slip boundary conditions and agrees with the outer solution far from the stagnation point, we shall seek a velocity field of the form

$$u = Uf(\eta) + axh'(\eta), \quad v = ayh'(\eta), \quad w = -2\sqrt{av}h(\eta) \tag{3}$$

where $\nu=\mu/\rho$ is the kinematic viscosity, $\eta=\sqrt{a/\nu}z$, and the primes denote the differentiation with respect to η. The equations governing such kind of flow of a second grade fluid in dimensionless form are given by [15]

$$h''' + 2hh'' - h'^2 + 1 + \alpha(2h'h''' - 2hh^{iv} - h''^2) = 0 \tag{4}$$

$$f'' + 2hf' - h'f + \alpha(-2hf''' + h'f'' - h''f' + h'''f) = 0 \tag{5}$$

subject to the boundary conditions

$$h = 0, \quad h' = 0, \quad f = 1 \quad \text{at } \eta = 0$$

$$h' \to 1, \quad f \to 0 \quad \text{as } \eta \to \infty \tag{6}$$

where $\alpha=a\alpha_1/\mu$ is the dimensionless second grade parameter.

2.1 Analytic Solution. We use the homotopy analysis method to solve systems (4)–(6) analytically. Due to the boundary conditions (Eq. (6)), the solution expressions for $h(\eta)$ and $f(\eta)$ can be expressed in the following form:

$$h(\eta) = A_{0,0} + \sum_{i=1}^{+\infty}\sum_{j=0}^{+\infty} A_{i;j}\eta^j e^{-i\eta} \tag{7}$$

$$f(\eta) = \sum_{i=1}^{+\infty}\sum_{j=0}^{+\infty} B_{i;j}\eta^j e^{-i\eta} \tag{8}$$

respectively, where $A_{i;j}$ and $B_{i;j}$ are coefficients. They provide us with the rule of solution expression, which plays an important role in the framework of the homotopy analysis method. According to the boundary conditions (Eq. (6)) and the foregoing rules of solution expressions defined by Eqs. (7) and (8), we choose the initial approximations

$$h_0(\eta) = -1 + \eta + e^{-\eta} \tag{9}$$

$$f_0(\eta) = e^{-\eta} \tag{10}$$

and the auxiliary linear operators are given by

$$L_h[H(\eta;p)] = \frac{\partial^3 H}{\partial \eta^3} - \frac{\partial H}{\partial \eta} \tag{11}$$

$$L_f[F(\eta;p)] = \frac{\partial^2 F}{\partial \eta^2} - F \tag{12}$$

From Eqs. (4) and (5) we define the nonlinear operators

$$N_h[H(\eta;p)] = \frac{\partial^3 H}{\partial \eta^3} + 2H\frac{\partial^2 H}{\partial \eta^2} - \left(\frac{\partial H}{\partial \eta}\right)^2 + 1 + \alpha\left[2\frac{\partial H}{\partial \eta}\frac{\partial^3 H}{\partial \eta^3} - 2H\frac{\partial^4 H}{\partial \eta^4} - \left(\frac{\partial^2 H}{\partial \eta^2}\right)^2\right] \tag{13}$$

$$N_f[F(\eta;p),H(\eta;p)] = \frac{\partial^2 F}{\partial \eta^2} + 2H\frac{\partial F}{\partial \eta} - \frac{\partial H}{\partial \eta}F + \alpha\begin{bmatrix} -2H\dfrac{\partial^3 F}{\partial \eta^3} + \dfrac{\partial H}{\partial \eta}\dfrac{\partial^2 F}{\partial \eta^2} \\ -\dfrac{\partial^2 H}{\partial \eta^2}\dfrac{\partial F}{\partial \eta} + \dfrac{\partial^3 H}{\partial \eta^3}F \end{bmatrix} \tag{14}$$

Let $\hbar$ denote the nonzero auxiliary parameter. We construct the so-called zero-order deformation equations

$$(1-p)L_h[H(\eta;p) - h_0(\eta)] = p\hbar N_h[H(\eta;p)] \tag{15}$$

$$(1-p)L_f[F(\eta;p) - f_0(\eta)] = p\hbar N_f[F(\eta;p),H(\eta;p)] \tag{16}$$

subject to the boundary conditions

$$H(0;p) = \left.\frac{\partial H(\eta;p)}{\partial \eta}\right|_{\eta=0} = 0, \quad F(0;p) = 1$$

$$\left.\frac{\partial H(\eta;p)}{\partial \eta}\right|_{\eta=+\infty} = 1, \quad F(+\infty;p) = 0 \tag{17}$$

where $p \in [0,1]$ is the embedding parameter. When $p=0$ and $p=1$, we have

$$H(\eta;0) = h_0(\eta), \quad F(\eta;0) = f_0(\eta) \tag{18}$$

and

$$H(\eta;1) = h(\eta), \quad F(\eta;1) = f(\eta) \tag{19}$$

respectively. Thus, as p increases from 0 to 1, $H(\eta)$ and $F(\eta)$ vary from the initial approximations $h_0(\eta)$ and $f_0(\eta)$ to the final solutions $h(\eta)$ and $f(\eta)$ of the original equations (Eqs. (4)–(6)). Assume that the auxiliary parameter $\hbar$ is so properly chosen that the Taylor series of $H(\eta;p)$ and $F(\eta;p)$ expanded with respect to the embedding parameters, i.e.,

$$H(\eta;p) = H(\eta;0) + \sum_{m=1}^{+\infty} h_m(\eta)p^m \tag{20}$$

$$F(\eta;p) = F(\eta;0) + \sum_{m=1}^{+\infty} f_m(\eta) p^m \tag{21}$$

where

$$h_m(\eta) = \frac{1}{m!} \left. \frac{\partial^m H(\eta;p)}{\partial p^m} \right|_{p=0} \tag{22}$$

$$f_m(\eta) = \frac{1}{m!} \left. \frac{\partial^m F(\eta;p)}{\partial p^m} \right|_{p=0} \tag{23}$$

converge at $p=1$. Then, from Eqs. (18) and (19),

$$h(\eta) = h_0(\eta) + \sum_{m=1}^{+\infty} h_m(\eta) \tag{24}$$

$$f(\eta) = f_0(\eta) + \sum_{m=1}^{+\infty} f_m(\eta) \tag{25}$$

Equations (24) and (25) provide us with a relationship between the initial guess solutions $h_0(\eta)$ and $f_0(\eta)$ and the unknown solutions $h(\eta)$ and $f(\eta)$, respectively. In order to get the governing equations for $h_m(\eta)$ and $f_m(\eta)$, $(m \geqslant 1)$, we first differentiate m times the two sides of equations (Eqs. (15)–(17)) about the embedding parameter p. Then set $p=0$, and finally divide them by $m!$. In this way we obtain the governing equations for $h_m(\eta)$ and $f_m(\eta)$, $(m \geqslant 1)$,

$$L_h[h_m(\eta) - \chi_m h_{m-1}(\eta)] = \hbar R_m(\eta) \tag{26}$$

$$L_f[f_m(\eta) - \chi_m f_{m-1}(\eta)] = \hbar Q_m(\eta) \tag{27}$$

subject to the boundary conditions

$$h_m(0) = h_m'(0) = h_m'(+\infty) = 0 \tag{28}$$

$$f_m(0) = f_m(+\infty) = 0 \tag{29}$$

where

$$R_m(\eta) = h_{m-1}''' + (1-\chi_m) + \sum_{k=0}^{m-1} [2h_{m-1-k}h_k'' - h_{m-1-k}'h_k' + \alpha(2h_{m-1-k}'h_k''' - 2h_{m-1-k}h_k^{iv} - h_{m-1-k}''h_k'')] \tag{30}$$

$$Q_m(\eta) = f_{m-1}'' + \sum_{k=0}^{m-1} [2h_{m-1-k}f_k' + h_{m-1-k}'f_k + \alpha(-2h_{m-1-k}f_k''' + h_{m-1-k}'f_k'' - h_{m-1-k}''f_k' + h_{m-1-k}'''f_k)] \tag{31}$$

and

$$\chi_m = \begin{cases} 0 & \text{for } m \leqslant 1 \\ 1 & \text{for } m \geqslant 2 \end{cases} \tag{32}$$

We emphasize here that Eqs. (26)–(29) are linear for all $m \geqslant 1$. Also, the left hand sides of Eqs. (26) and (27) are governed by the same linear operators L_h and L_f, respectively, for all $m \geqslant 1$. These linear operators can easily be solved especially by means of symbolic computation softwares MATHEMATICA, MATLAB, etc. By solving Eqs. (26)–(29) for the first few values of m, we find that the solution expressions can in general be expressed in the following forms:

$$h_m(\eta) = \sum_{n=0}^{2m+2} \sum_{q=0}^{2m+2-n} a_{m,n}{}^q \eta^q e^{-n\eta} \tag{33}$$

$$f_m(\eta) = \sum_{n=0}^{2m+2} \sum_{q=0}^{2m+2-n} b_{m,n}{}^q \eta^q e^{-n\eta} \tag{34}$$

where $a_{m,n}{}^q$ and $b_{m,n}{}^q$ are constant coefficients of the series, which can easily be determined through the following recurrence relations $(m \geqslant 1)$:

$$a_{m,0}{}^0 = \chi_m \chi_{2m+2} a_{m-1,0}{}^0 - \sum_{q=0}^{2m+2} \Gamma_{m,0}{}^q \mu_{0,1}{}^q - \sum_{q=0}^{2m+1} \Gamma_{m,1}{}^q \mu_{1,1}{}^q + \sum_{n=2}^{2m+2} \sum_{q=0}^{2m+2-n} (n-1)\Gamma_{m,n}{}^q \mu_{n,0}{}^q - \sum_{n=2}^{2m+2} \sum_{q=1}^{2m+2-n} \Gamma_{m,n}{}^q \mu_{n,1}{}^q \tag{35}$$

$$a_{m,0}{}^k = \chi_m \chi_{2m+2} \chi_{2m+2-k} a_{m-1,0}{}^k + \sum_{q=k-1}^{2m+1} \Gamma_{m,1}{}^q \mu_{1,k}{}^q, \quad 1 \leqslant k \leqslant 2m+2 \tag{36}$$

$$a_{m,1}{}^0 = \chi_m \chi_{2m+1} a_{m-1,1}{}^0 + \sum_{q=0}^{2m+2} \Gamma_{m,0}{}^q \mu_{0,1}{}^q + \sum_{q=0}^{2m+1} \Gamma_{m,1}{}^q \mu_{1,1}{}^q - \sum_{n=2}^{2m+2} \sum_{q=0}^{2m+2-n} n\Gamma_{m,n}{}^q \mu_{n,0}{}^q + \sum_{n=2}^{2m+2} \sum_{q=1}^{2m+2-n} \Gamma_{m,n}{}^q \mu_{n,1}{}^q \tag{37}$$

$$a_{m,1}{}^k = \chi_m \chi_{2m+1} \chi_{2m+1-k} a_{m-1,1}{}^k + \sum_{q=k-1}^{2m+1} \Gamma_{m,1}{}^q \mu_{1,k}{}^q, \quad 1 \leqslant k \leqslant 2m+1 \tag{38}$$

$$a_{m,n}{}^k = \chi_m \chi_{2m+2-n} \chi_{2m+2-n-k} a_{m-1,n}{}^k + \sum_{q=k}^{2m+2-n} \Gamma_{m,n}{}^q \mu_{n,k}{}^q$$

$$2 \leqslant n \leqslant 2m+2, \quad 0 \leqslant k \leqslant 2m+2-n \tag{39}$$

$$b_{m,1}{}^0 = \chi_m \chi_{2m+1} b_{m-1,1}{}^0 - \sum_{n=2}^{2m+2} \sum_{q=0}^{2m+2-n} \Delta_{m,n}{}^q \nu_{n,0}{}^q \tag{40}$$

$$b_{m,1}{}^k = \chi_m \chi_{2m+1} \chi_{2m+1-k} b_{m-1,1}{}^k + \sum_{q=k-1}^{2m+1} \Delta_{m,1}{}^q \nu_{1,k}{}^q, \quad 1 \leqslant k \leqslant 2m+1 \tag{41}$$

$$b_{m,n}{}^k = \chi_m \chi_{2m+2-n} \chi_{2m+2-n-k} b_{m-1,n}{}^k + \sum_{q=k}^{2m+2-n} \Delta_{m,n}{}^q \nu_{n,k}{}^q$$

$$2 \leqslant n \leqslant 2m+2, \quad 0 \leqslant k \leqslant 2m+2-n \tag{42}$$

where the different constants involved in the above recurrence relations are given in the Appendix.

Hence with the help of Eqs. (35)–(42), one can easily find all the constant coefficients of the solution series (Eqs. (33) and (34)) with the knowledge of the following:

$$a_{0,0}{}^0 = -1, \quad a_{0,0}{}^1 = 1, \quad a_{0,1}{}^0 = 1$$

$$a_{0,0}{}^2 = a_{0,1}{}^1 = a_{0,1}{}^2 = a_{0,2}{}^0 = a_{0,2}{}^1 = a_{0,2}{}^2 = 0 \tag{43}$$

and

$$b_{0,1}{}^0 = 1, \quad b_{0,1}{}^1 = b_{0,1}{}^2 = b_{0,2}{}^0 = b_{0,2}{}^1 = b_{0,2}{}^2 = 0 \tag{44}$$

Therefore, the complete analytic solution can be written as

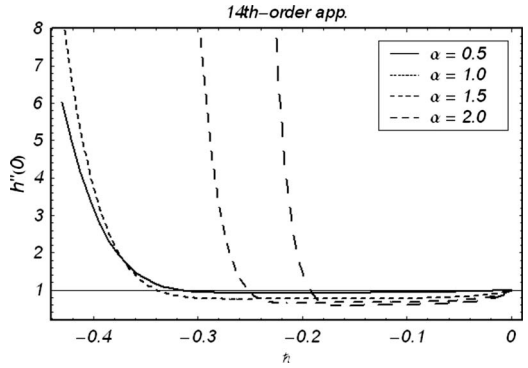

Fig. 1 $\hbar$**-curves of** $h(\eta)$ **plotted for different values of the parameter** α

$$h(\eta) = \sum_{M=0}^{+\infty} h_M(\eta) \tag{45}$$

$$f(\eta) = \sum_{M=0}^{+\infty} f_M(\eta) \tag{46}$$

2.2 Convergence of the Solution and Its Graphical Representation. Liao [20] showed that as long as a solution series given by the homotopy analysis method converges, it must be one of the solutions. So, it is important to ensure the convergence of the obtained solution series. As mentioned by Liao [20], the convergence of the solution series depends on the initial guess approximations, the auxiliary linear operators, and the nonzero auxiliary parameter $\hbar$. Once the initial guesses and the auxiliary linear operators are chosen, the convergence is then strongly dependent on the auxiliary parameter $\hbar$. The admissible values of $\hbar$ are determined by drawing the so-called $\hbar$-curves. For the problem under discussion, we have plotted the $\hbar$-curves (see Figs. 1 and 2) to determine the admissible values of $\hbar$ in order to make the solution series convergent. The intervals on $\hbar$-axis for which the $\hbar$-curve is parallel to the $\hbar$-axis represents the set of allowed values of $\hbar$.

From Figs. 1 and 2 it is clear that by increasing the values of α the interval of values of $\hbar$ shrinks down and shifts toward zero. This is due to the fact that large values of α correspond to strong nonlinearity, and when the nonlinearity becomes strong the choice of values of $\hbar$ becomes more restricted. To prove the validity of our HAM solution, we give a comparison between the present results and the results obtained by Baris [15] (see, for instance, Fig. 3).

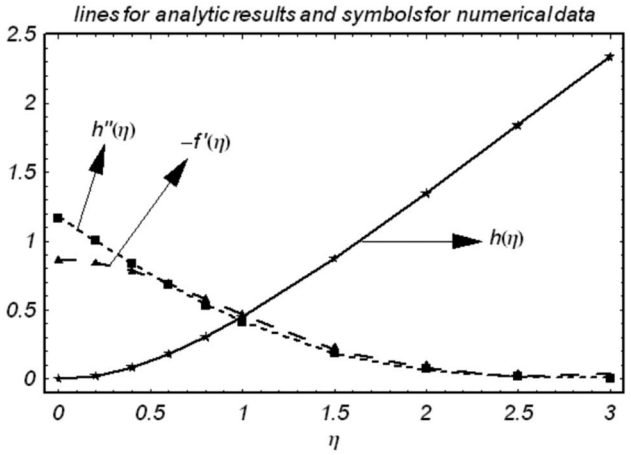

Fig. 3 Comparison between the analytic solution and the numerical data

Notice that the results plotted in Fig. 3 are obtained at $\alpha=0.1$ and $\hbar=-0.12$. From Fig. 3 it is clearly seen that the present analytic solution is in good agreement with the numerical results presented in Ref. [15]. Further, the present analytic solution is uniformly valid for all values of the second grade parameter α, as shown in Figs. 4–7.

3 Heat Transfer Analysis

The heat equation in dimensionless form is given by [15]

$$\theta'' + 2\mathrm{Pr}h\theta' = 0 \tag{47}$$

subject to the boundary conditions

$$\theta(0) = 1, \quad \theta(+\infty) = 0 \tag{48}$$

where $\mathrm{Pr}=\mu C_p/k$ is the Prandtl number, C_p is the specific heat, and k is the thermal conductivity of the fluid. Notice that the above Eq. (47) is modeled under the assumptions that the specific heat and thermal conductivity of the fluid are assumed to be constant. The heat flux vector is represented by Fourier's law, and the effects of the radiant heating and viscous dissipation are negligible.

In order to find an analytic solution of Eq. (47) subject to the boundary conditions (Eq. (48)), we follow the same procedure as performed in the previous section. To avoid the repetition we now

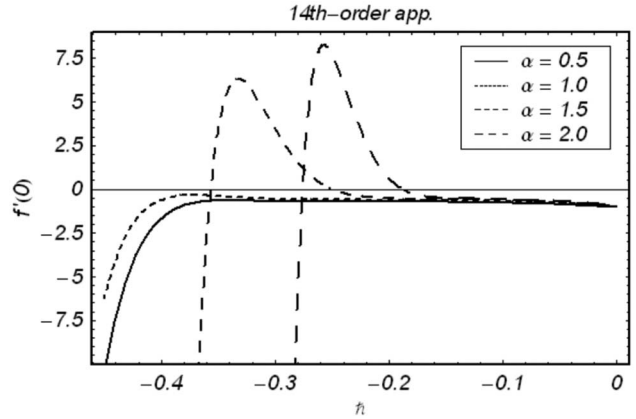

Fig. 2 $\hbar$**-curves of** $f(\eta)$ **plotted for different values of the parameter** α

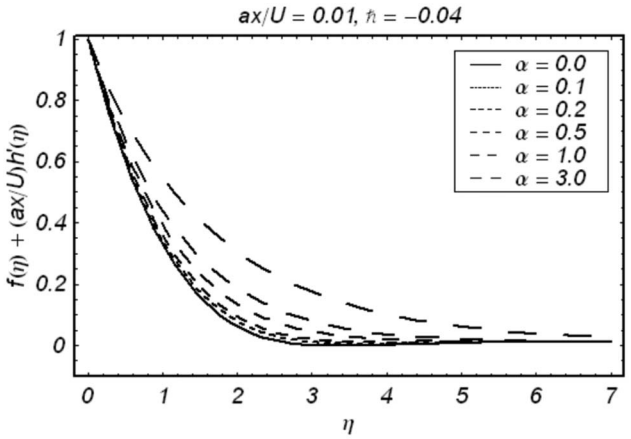

Fig. 4 Effect of the parameter α **on velocity distribution at** $aU/x=0.01$

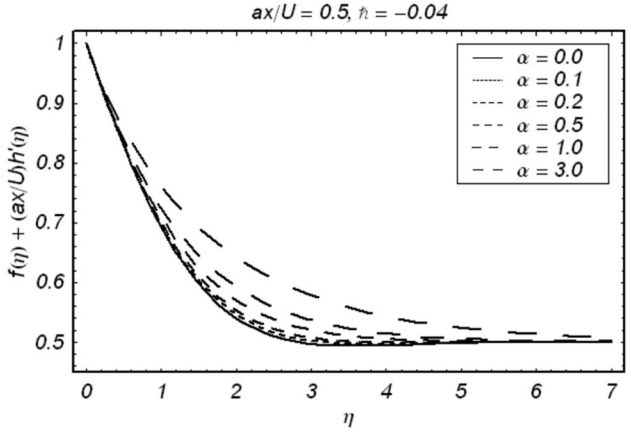

Fig. 5 Effect of the parameter α on velocity distribution at $aU/x=0.5$

omit the details. Due to the boundary conditions (Eq. (48)), we choose the initial guess approximation and the auxiliary linear operator of the form

$$\theta_0(\eta) = e^{-\eta} \tag{49}$$

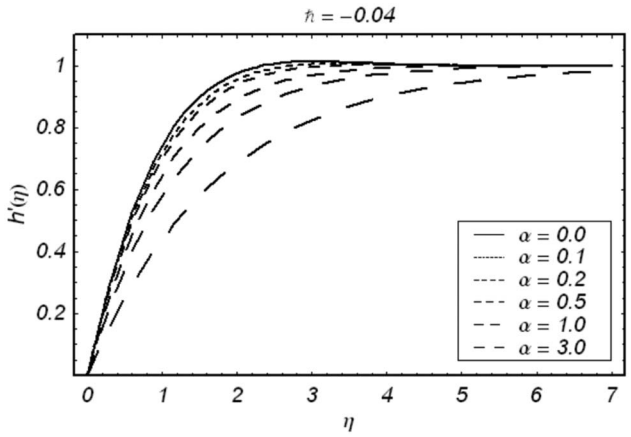

Fig. 6 Effect of the parameter α on nondimensional velocity $h'(\eta)$

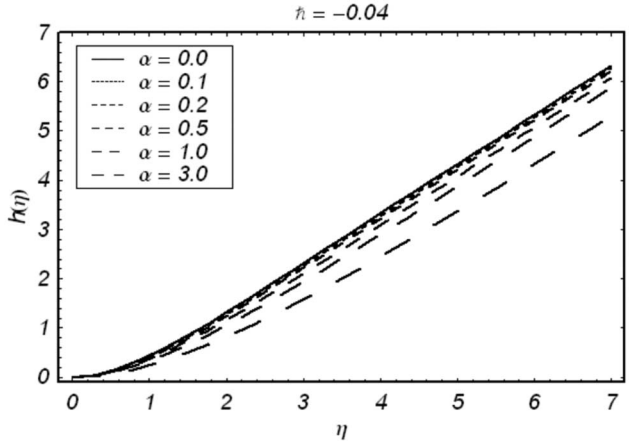

Fig. 7 Effect of the parameter α on nondimensional velocity $h(\eta)$

$$L_\theta[T(\eta;p)] = \frac{\partial^2 T}{\partial \eta^2} - T \tag{50}$$

We now construct the zero-order deformation equation

$$(1-p)L_\theta[T(\eta;p) - \theta_0(\eta)] = p\hbar N_\theta[T(\eta;p), H(\eta;p)] \tag{51}$$

subject to the boundary conditions

$$T(0;p) = 1, \quad T(+\infty;p) = 0 \tag{52}$$

where the nonlinear operator $N_\theta[T(\eta;p), H(\eta;p)]$ is defined through

$$N_\theta[T(\eta;p), H(\eta;p)] = \frac{\partial^2 T}{\partial \eta^2} + 2\mathrm{Pr}H\frac{\partial T}{\partial \eta} \tag{53}$$

and correspondingly the mth-order ($m \geqslant 1$) deformation equation is given by

$$L_\theta[\theta_m(\eta) - \chi_m \theta_{m-1}(\eta)] = \hbar W_m(\eta) \tag{54}$$

$$\theta_m(0) = 0, \quad \theta_m(+\infty) = 0 \tag{55}$$

where

$$W_m(\eta) = \theta_{m-1}'' + 2\mathrm{Pr}\sum_{k=0}^{+\infty} h_{m-1-k}\theta_k' \tag{56}$$

By solving Eqs. (54) and (55) for the first few values of m, we find that for a particular value of m the solution expression can generally be written as

$$\theta_m(\eta) = \sum_{n=1}^{2m+2}\sum_{q=0}^{2m+2-n} c_{m,n}{}^q \eta^q e^{-n\eta} \tag{57}$$

where $c_{m,n}{}^q$ are the constant coefficients, which can easily be determined by the following recurrence formulas ($m \geqslant 1$):

$$c_{m,1}{}^0 = \chi_m \chi_{2m+1} c_{m-1,1}{}^0 - \sum_{n=2}^{2m+2}\sum_{q=0}^{2m+2-n} \Omega_{m,n}{}^q \nu_{n,0}{}^q \tag{58}$$

$$c_{m,1}{}^k = \chi_m \chi_{2m+1}\chi_{2m+1-k} c_{m-1,1}{}^k + \sum_{q=k-1}^{2m+2} \Omega_{m,1}{}^q \nu_{1,k}{}^q, \quad 1 \leqslant k \leqslant 2m+1 \tag{59}$$

$$c_{m,n}{}^k = \chi_m \chi_{2m+2-n}\chi_{2m+2-n-k} c_{m-1,n}{}^k + \sum_{q=k}^{2m+2-n} \Omega_{m,n}{}^q \nu_{n,k}{}^q$$

$$2 \leqslant n \leqslant 2m+2, \quad 0 \leqslant k \leqslant 2m+2-n \tag{60}$$

where the constants appearing in the above relations are defined in the Appendix.

So, with the help of the above recurrence relations, one can easily determine all the unknown coefficients of the solution series (Eq. (57)) with the knowledge of the following:

$$c_{0,1}{}^0 = 1, \quad c_{0,1}{}^1 = c_{0,1}{}^2 = c_{0,2}{}^0 = c_{0,2}{}^1 = c_{0,2}{}^2 = 0 \tag{61}$$

Thus, the complete analytic solution in the form of an infinite series is then given by

$$\theta(\eta) = \sum_{M=0}^{+\infty} \theta_M(\eta) \tag{62}$$

3.1 Convergence of the Solution and Its Graphical Representation. To ensure the convergence of our HAM solution for temperature distribution, we have plotted the $\hbar$-curve in order to find the admissible values of $\hbar$ (see Fig. 8). It is also shown that the numerical results of Ref. [15] can easily be determined from our present analytic solution. For example, at $\alpha=0.2$ and $\mathrm{Pr}=0.2$, the value of the heat transfer parameter $\theta'(0)$ calculated in Ref.

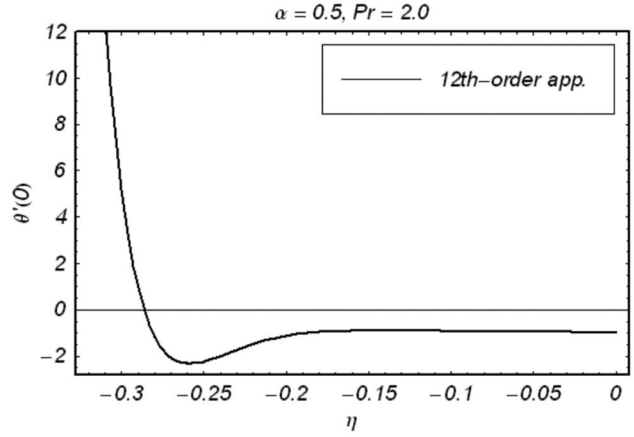

Fig. 8 $\hbar$-curves of $\theta(\eta)$ plotted at the 12th order of approximation

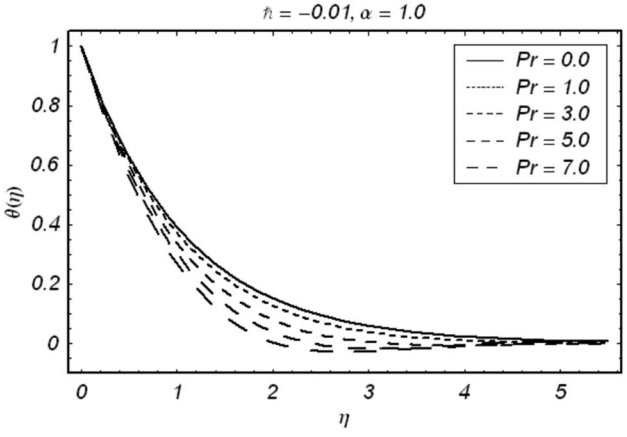

Fig. 10 Effect of the Prandtl number Pr on temperature distribution at a fixed value of the parameter α

[15] is −0.384962, whereas our HAM solution yields −0.38434; at $\alpha=0.2$ and Pr=10 the value of $\theta'(0)$ given in Ref. [15] is 1.618727 and the present analytic solution gives 1.61415. We mention here that the analytic approximations can further be refined by calculating the higher-order approximations. However, even at 12th-order approximation our analytic solution is in close agreement with numerical results, which proves the validity of our HAM solution.

In order to see the effects of the Prandtl number Pr and the second grade parameter α on temperature profile, we have plotted the graphs for different values of these parameters. In Fig. 9 the temperature profile $\theta(\eta)$ is plotted against the dimensionless independent variable η for different values of the second grade parameter α. Clearly, an increase in α causes the temperature to increase, but the effects of the Prandtl number Pr are quite opposite, as shown in Fig. 10. At high values of the Prandtl number, the temperature distribution is small. We mention here that the above graphs are plotted at the 12th order of approximation. As we have already mentioned in the previous section, the convergence of the HAM solution is strongly dependent on the auxiliary parameter $\hbar$. Our analysis shows that for large values of the parameters α and Pr, the solution series converges only for values of $\hbar$ close to zero. This fact has already been discussed in the previous section through Figs. 1 and 2.

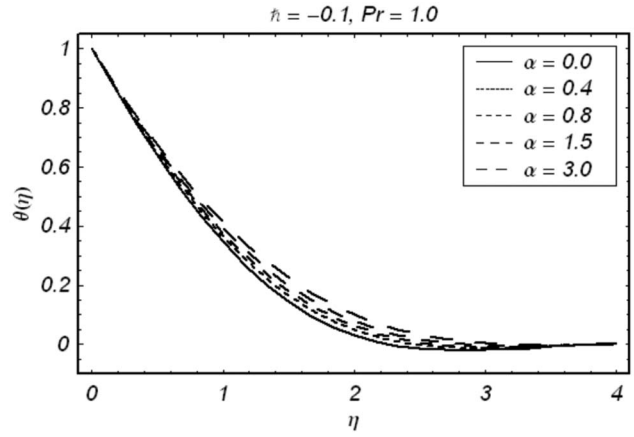

Fig. 9 Effect of the parameter α on temperature distribution at a fixed value of the Prandtl number Pr

4 Concluding Remarks

We have obtained the complete and purely analytic solution to the steady three-dimensional stagnation point flow of a second grade fluid with heat transfer analysis. It is shown that the solution is uniformly valid for all values of the dimensionless second grade parameter α and the Prandtl number Pr. The present analytic results (at suitably chosen values of $\hbar$) are in good agreement with the results obtained by Baris [15] for small values of α. Hence the present solution also contains the results of Baris [15]. It is observed that for large values of α and the Prandtl number, the series solutions converge for values of $\hbar$ close to zero. We emphasize here that the homotopy analysis method is a useful analytic technique for such kind of nonlinear problems.

Appendix

$$\Gamma_{m,n}^{\ q} = \hbar[\chi_{2m+2-n}\chi_{2m+2-n-q}C_{m-1,n}^{\ q} + (1-\chi_m)(1-\chi_{m+n+q}) + 2\alpha_{m,n}^{\ q} - \beta_{m,n}^{\ q} + \alpha(2\gamma_{m,n}^{\ q} - 2\delta_{m,n}^{\ q} - \omega_{m,n}^{\ q})] \quad \text{(A1)}$$

$$\Delta_{m,n}^{\ q} = \hbar[\chi_{2m+2-n}\chi_{2m+2-n-q}G_{m-1,n}^{\ q} + 2\varepsilon_{m,n}^{\ q} - \kappa_{m,n}^{\ q} + \alpha(-2\tau_{m,n}^{\ q} + \lambda_{m,n}^{\ q} - \sigma_{m,n}^{\ q} - \pi_{m,n}^{\ q})] \quad \text{(A2)}$$

$$\Omega_{m,n}^{\ q} = \hbar[\chi_{2m+2-n}\chi_{2m+2-n-q}K_{m-1,n}^{\ q} + 2\mathrm{Pr}\rho_{m-1,n}^{\ q}] \quad \text{(A3)}$$

in which

$$A_{m,n}^{\ q} = (q+1)a_{m,n}^{\ q+1} - na_{m,n}^{\ q} \quad \text{(A4)}$$

$$B_{m,n}^{\ q} = (q+1)A_{m,n}^{\ q+1} - nA_{m,n}^{\ q} \quad \text{(A5)}$$

$$C_{m,n}^{\ q} = (q+1)B_{m,n}^{\ q+1} - nB_{m,n}^{\ q} \quad \text{(A6)}$$

$$D_{m,n}^{\ q} = (q+1)C_{m,n}^{\ q+1} - nC_{m,n}^{\ q} \quad \text{(A7)}$$

$$E_{m,n}^{\ q} = (q+1)D_{m,n}^{\ q+1} - nD_{m,n}^{\ q} \quad \text{(A8)}$$

$$G_{m,n}^{\ q} = (q+1)E_{m,n}^{\ q+1} - nE_{m,n}^{\ q} \quad \text{(A9)}$$

$$I_{m,n}^{\ q} = (q+1)G_{m,n}^{\ q+1} - nG_{m,n}^{\ q} \quad \text{(A10)}$$

$$J_{m,n}^{\ q} = (q+1)I_{m,n}^{\ q+1} - nI_{m,n}^{\ q} \quad \text{(A11)}$$

$$K_{m,n}^{\ q} = (q+1)J_{m,n}^{\ q+1} - nJ_{m,n}^{\ q} \quad \text{(A12)}$$

$$\alpha_{m,n}{}^{q} = \sum_{k=0}^{m-1} \sum_{j=\max\{0,n-2m+2k\}}^{\min\{n,2k+2\}} \sum_{i=\max\{0,q-2m+2k+n-j\}}^{\min\{q,2k+2-j\}} B_{k,j}{}^{i} a_{m-1-k,n-j}{}^{q-1} \tag{A13}$$

$$\beta_{m,n}{}^{q} = \sum_{k=0}^{m-1} \sum_{j=\max\{0,n-2m+2k\}}^{\min\{n,2k+2\}} \sum_{i=\max\{0,q-2m+2k+n-j\}}^{\min\{q,2k+2-j\}} A_{k,j}{}^{i} A_{m-1-k,n-j}{}^{q-1} \tag{A14}$$

$$\gamma_{m,n}{}^{q} = \sum_{k=0}^{m-1} \sum_{j=\max\{0,n-2m+2k\}}^{\min\{n,2k+2\}} \sum_{i=\max\{0,q-2m+2k+n-j\}}^{\min\{q,2k+2-j\}} C_{k,j}{}^{i} A_{m-1-k,n-j}{}^{q-1} \tag{A15}$$

$$\delta_{m,n}{}^{q} = \sum_{k=0}^{m-1} \sum_{j=\max\{0,n-2m+2k\}}^{\min\{n,2k+2\}} \sum_{i=\max\{0,q-2m+2k+n-j\}}^{\min\{q,2k+2-j\}} D_{k,j}{}^{i} a_{m-1-k,n-j}{}^{q-1} \tag{A16}$$

$$\omega_{m,n}{}^{q} = \sum_{k=0}^{m-1} \sum_{j=\max\{0,n-2m+2k\}}^{\min\{n,2k+2\}} \sum_{i=\max\{0,q-2m+2k+n-j\}}^{\min\{q,2k+2-j\}} B_{k,j}{}^{i} B_{m-1-k,n-j}{}^{q-1} \tag{A17}$$

$$\varepsilon_{m,n}{}^{q} = \sum_{k=0}^{m-1} \sum_{j=\max\{1,n-2m+2k\}}^{\min\{n-1,2k+2\}} \sum_{i=\max\{0,q-2m+2k+n-j\}}^{\min\{q,2k+2-j\}} E_{k,j}{}^{i} a_{m-1-k,n-j}{}^{q-1} \tag{A18}$$

$$\kappa_{m,n}{}^{q} = \sum_{k=0}^{m-1} \sum_{j=\max\{1,n-2m+2k\}}^{\min\{n-1,2k+2\}} \sum_{i=\max\{0,q-2m+2k+n-j\}}^{\min\{q,2k+2-j\}} b_{k,j}{}^{i} A_{m-1-k,n-j}{}^{q-1} \tag{A19}$$

$$\tau_{m,n}{}^{q} = \sum_{k=0}^{m-1} \sum_{j=\max\{1,n-2m+2k\}}^{\min\{n-1,2k+2\}} \sum_{i=\max\{0,q-2m+2k+n-j\}}^{\min\{q,2k+2-j\}} I_{k,j}{}^{i} a_{m-1-k,n-j}{}^{q-1} \tag{A20}$$

$$\lambda_{m,n}{}^{q} = \sum_{k=0}^{m-1} \sum_{j=\max\{1,n-2m+2k\}}^{\min\{n-1,2k+2\}} \sum_{i=\max\{0,q-2m+2k+n-j\}}^{\min\{q,2k+2-j\}} G_{k,j}{}^{i} A_{m-1-k,n-j}{}^{q-1} \tag{A21}$$

$$\sigma_{m,n}{}^{q} = \sum_{k=0}^{m-1} \sum_{j=\max\{1,n-2m+2k\}}^{\min\{n-1,2k+2\}} \sum_{i=\max\{0,q-2m+2k+n-j\}}^{\min\{q,2k+2-j\}} E_{k,j}{}^{i} B_{m-1-k,n-j}{}^{q-1} \tag{A22}$$

$$\pi_{m,n}{}^{q} = \sum_{k=0}^{m-1} \sum_{j=\max\{1,n-2m+2k\}}^{\min\{n-1,2k+2\}} \sum_{i=\max\{0,q-2m+2k+n-j\}}^{\min\{q,2k+2-j\}} a_{k,j}{}^{i} C_{m-1-k,n-j}{}^{q-1} \tag{A23}$$

$$\rho_{m,n}{}^{q} = \sum_{k=0}^{m-1} \sum_{j=\max\{1,n-2m+2k\}}^{\min\{n-1,2k+2\}} \sum_{i=\max\{0,q-2m+2k+n-j\}}^{\min\{q,2k+2-j\}} J_{k,j}{}^{i} a_{m-1-k,n-j}{}^{q-1} \tag{A24}$$

and $\mu_{0,k}{}^{q}$, $\mu_{1,k}{}^{q}$, $\mu_{n,k}{}^{q}$, $\nu_{1,k}{}^{q}$, and $\nu_{n,k}{}^{q}$ are defined through

$$\mu_{0,k}{}^{q} = \sum_{p=0}^{q+1-k} \frac{q!(-1)^{p+1}}{k!}, \quad q \geqslant 0, \quad 1 \leqslant k \leqslant q+1 \tag{A25}$$

$$\mu_{1,k}{}^{q} = \sum_{p=0}^{q+1-k} \frac{q!}{k!2^{q+2-k-p}}, \quad q \geqslant 0, \quad 0 \leqslant k \leqslant q+1 \tag{A26}$$

$$\mu_{n,k}{}^{q} = \sum_{r=0}^{q-k} \sum_{p=0}^{q-k-r} \frac{-q!}{k!(n-1)^{q+1-k-r-p} n^{r+1} (n+1)^{p+1}}, \quad q \geqslant 0, \quad 0 \leqslant k \leqslant q, \quad n \geqslant 2 \tag{A27}$$

$$\nu_{1,k}{}^{q} = \frac{-q!}{k!2^{q+2-k}}, \quad q \geqslant 0, \quad 0 \leqslant k \leqslant q+1 \tag{A28}$$

$$\nu_{n,k}{}^{q} = \sum_{p=0}^{q-k} \frac{q!}{k!(n+1)^{q+1-k-p}(n-1)^{p+1}}, \quad n \geqslant 2, \quad 0 \leqslant k \leqslant q, \quad q \geqslant 0 \tag{A29}$$

respectively.

References

[1] Blasius, H., 1908, "Grenzschichten in Flussigkeiten mit Kleiner Reibung," Z. Math. Phys., **56**, pp. 1–17.
[2] Heimenz, K., 1911, "Die Grenzschicht an einem in den gleichformigen Flussigkeitsstrom eingetauchten geraden Kreiszylinder," Ph.D. thesis, Gottingen.
[3] Glauert, M. B., 1956, "The Laminar Boundary Layer on Oscillating Plates and Cylinders," J. Fluid Mech., **1**, pp. 97–110.
[4] Stuart, J. T., 1959, "The Viscous Flow Near a Stagnation Point When the External Flow Has Uniform Vorticity," J. Aerosp. Sci., **26**, pp. 124–125.
[5] Davey, A.,1961, "Boundary Layer Flow at a Saddle Point of Attachment," J. Fluid Mech., **10**, pp. 593–610.
[6] Tamada, K. J., 1979, "Two-Dimensional Stagnation Point Flow Impinging Obliquely on a Plane Wall," J. Phys. Soc. Jpn., **46**, pp. 310–311.
[7] Dorepaal, J. M., 1986, "An Exact Solution of the Navier-Stokes Equation Which Describes Non-Orthogonal Stagnation-Point Flow in two Dimensions," J. Fluid Mech., **163**, pp. 141–147.
[8] Zumbrunnen, D. A., 1991, "Convective Heat and Mass Transfer in The Stagnation Region of a Laminar Planar jet Impinging on a Moving Surface," ASME J. Heat Transfer, **113**, pp. 563–570.
[9] Wang, C. Y., 1985, "The Unsteady Oblique Stagnation Point Flow," Phys. Fluids, **28**, pp. 2046–2049.
[10] Ariel, P. D., 1994, "Three-Dimensional Stagnation Point Flow of a Viscoelastic Fluid," Mech. Res. Commun., **21**, pp. 389–396.
[11] Ariel, P. D., 1994, "Stagnation Point Flow With Suction: An Approximate Solution," ASME J. Appl. Mech., **61**, pp. 976–978.
[12] Ariel, P. D., 2001, "Axisymmetric Flow of a Second Grade Fluid Past a Stretching Sheet," Int. J. Eng. Sci., **39**, pp. 529–553.
[13] Bian, X., and Rangel, R. H., 1996, "The Viscous Stagnation Flow Solidification Problem," Int. J. Heat Mass Transfer, **39**, pp. 3581–3594.
[14] Mahapatra, T. R., and Gupta, A. S., 2002, "Heat Transfer in Stagnation Point Flow Towards a Stretching Sheet," Heat Mass Transfer, **38**, pp. 517–521.
[15] Baris, S., 2003, "Steady Three-Dimensional Flow of a Second Grade Fluid Towards a Stagnation Point at a Moving Flat Plate," Turk. J. Eng. Environ. Sci., **27**, pp. 21–29.
[16] Fosdick, R. L., and Rajagopal, K. R., 1978, "Uniqueness and Drag for Fluids of Second Grade in Steady Motion," Int. J. Non-Linear Mech., **13**, pp. 131–137.
[17] Dunn, J. E., and Fosdick, R. L., 1974, "Thermodynamics, Stability and Boundedness of Fluids of Complexity and Fluids of Second Grade," Arch. Ration. Mech. Anal., **56**, pp. 191–252).
[18] Dunn, J. E., and Rajagopal, K. R., 1995, "Fluids of Different Type—Critical Review and Thermodynamic Analysis," Int. J. Eng. Sci., **33**, pp. 689–729.
[19] Nayfeh, A. H., 2000, *Perturbation Methods*, Wiley, New York.
[20] Liao, S. J., 2003, *Beyond Perturbation: Introduction to Homotopy Analysis Method*, Chapman and Hall/CRC, Boca Raton, FL.
[21] Adomian, G., 1975, "Nonlinear Stochastic Differential Equations," J. Math. Anal. Appl., **55**, pp. 414–452.
[22] Karmishin, A. V., Zhukov, A. T., and Kolosov, V. G., 1990, *Methods of Dynamics Calculation and Testing for Thin-Walled Structures*, Mashiniostronie, Moscow, in Russian.
[23] Lyapunov, A. M., 1992, *General Problems on Stability of Motions*, Taylor and Francis, London, English translation.
[24] Liao, S. J., 2006, "An Analytic Solution of Unsteady Boundary-Layer Flows Caused by an Impulsively Stretching Plate," Commun. Nonlinear Sci. Numer. Simul., **11**, pp. 326–339.
[25] Xu, H., and Liao, S. J., 2005, "Series Solutions of Unsteady Magnetohydrodynamic Flows of Non-Newtonian Fluids Caused by an Impulsively Stretching Plate," J. Non-Newtonian Fluid Mech., **129**, pp. 46–55.
[26] Ali, A., and Mehmood, A., 2008, "Homotopy Analysis of Unsteady Boundary-Layer Flow Adjacent to Permeable Stretching Surface in a Porous Medium," Commun. Nonlinear Sci. Numer. Simul., **13**(2), pp. 340–349.

[27] Mehmood, A., and Ali, A., 2006, "Analytic Solution of Generalized Three-dimensional Flow and Heat Transfer Over a Stretching Plane Wall," Int. Commun. Heat Mass Transfer, **33**, pp. 1243–1252.
[28] Liao, S. J., 1999, "A Uniformly Valid Analytical Solution of 2D Viscous Flow Past a Semi Infinite Flat Plate," J. Fluid Mech., **385**, pp. 101–128.
[29] Liao, S. J., 1999, "An Explicit, Totally Analytic Approximate Solution for Blasius Viscous Flow Problems," Int. J. Non-Linear Mech., **34**, pp. 759–778.
[30] Liao, S. J., and Pop, I., 2004, "Explicit Analytic Solution for Similarity Boundary-Layer Equations," Int. J. Heat Mass Transfer, **47**(1), pp. 75–85.
[31] Liao, S. J., and Campo, A., 2002, "Analytic Solutions of the Temperature Distribution in Blasius Viscous Flow Problems," J. Fluid Mech., **453**, pp. 411–425.
[32] Liao, S. J., and Cheung, K. F., 2003, "Homotopy Analysis of Nonlinear Progressive Waves in Deep Water," J. Eng. Math., **45**(2), pp. 105–116.
[33] Xu, H., 2004, "An Explicit Analytic Solution for Free Convection About a Vertical Flat Plate Embedded in a Porous Media by Means of Homotopy Analysis Method," Appl. Math. Comput., **158**, pp. 433–443.
[34] Liao, S. J., 2004, "On the Homotopy Analysis Method for Nonlinear Problems," Appl. Math. Comput., **147**, pp. 499–513.
[35] Liao, S. J., 2003, "On the Analytic Solution of Magnetohydrodynamic Flows of Non-Newtonian Fluid Over a Stretching Sheet," J. Fluid Mech., **488**, pp. 189–212.
[36] Liao, S. J., 2005, "A New Branch of Solutions of Boundary-layer Flows Over an Impermeable Stretched Plate," Int. J. Heat Mass Transfer, **48**(12), pp. 2529–2539.
[37] Yang, C., and Liao, S. J., 2006, "On the Explicit, Purely Analytic Solution of Von Kármán Swirling Viscous Flow," Commun. Nonlinear Sci. Numer. Simul., **11**, pp. 83–93.
[38] Wang, C., Zhu, J. M., Liao, S. J., and Pop, I., 2003, "On the Explicit Analytic Solutions of Cheng-Chang Equations," Int. J. Heat Mass Transfer, **46**(10), pp. 1855–1860.
[39] Allan, F. M., and Syam, M. I., 2005, "On Analytic Solution of the Non-Homogeneous Blasius Problem," J. Comput. Appl. Math., **182**, pp. 355–365.

Modeling Helicopter Blade Sailing: Dynamic Formulation and Validation

A. S. Wall

F. F. Afagh

R. G. Langlois

Department of Mechanical and Aerospace Engineering,
Carleton University, 1125 Colonel By Drive,
Ottawa, ON, K1S 5B6, Canada

S. J. Zan

Aerodynamics Laboratory,
Institute for Aerospace Research,
National Research Council of Canada,
1200 Montreal Road,
Ottawa, ON, K1A 0R6, Canada

Rotor blade sailing, which is characterized by excessive deflection of rotor blades, can be experienced by shipboard helicopters during rotor start-up and shut-down. In an attempt to model the complete ship-helicopter-rotor system in a way that is geometrically representative and computationally efficient, the system was represented as a discrete-property rigid-body and flexible-element system capable of simulating many important dynamic effects that contribute to the motion of rotor blades. This paper describes the model in detail and discusses validation cases. While both dynamic effects and aerodynamic effects are believed to be important components of blade sailing, this paper focuses exclusively on the dynamics. The validation cases discussed herein suggest that the modeling approach presented offers excellent potential for efficiently modeling blade sailing and other blade motion phenomena. [DOI: 10.1115/1.2957599]

Keywords: blade sailing, tunnel strike, shipboard helicopter, multibody dynamics, Lagrangian dynamics, dynamic interface analysis, rotor engage/disengage, motion coupling

1 Background

Ensuring the safety of shipboard helicopters, during all phases of operation, is challenging and important. During start-up and shut-down operations on ship decks, helicopter rotor elastic response is of concern for flight and personnel safety reasons. While the rotors are engaged or disengaged, they turn at low speeds and therefore can be subjected to high wind-induced aerodynamic forces without the benefit of the centrifugal stiffening present at normal operating speeds. This excitation, combined with ship deck motion during all but the most benign sea and wind conditions, can cause excessive deflection of rotor blades, and as a result, the blades can come into contact with the fuselage or tailboom of the helicopter. This phenomenon, called "tunnel strike" or "tailboom strike," compromises the safety of flight crews, results in airframe damage, and may bring the airworthiness of the helicopter into question.

Over the past 20 years, the blade sailing phenomenon has been extensively studied [1]. Although blade sailing occurrences were documented much earlier, as with the H-46 Sea Knight, which came into operation in the shipboard environment in 1964, publicly available research on blade sailing began in the 1980's [2,3]. Hurst and Newman addressed the aerodynamic aspects of the issue by comparing airwakes measured in the wind tunnel with full scale data [4], by proposing simple airwake gust models that were intended to capture the important components of steady airwake [5], and by examining the effect of a more complex experimental airwake on blade sailing depending on the position of the helicopter on the flight deck [6]. Newman modeled the blade dynamics using the first four structural modes of semirigid rotors [4,5] and articulated rotors [6]. These results have been compared to validation data from wind tunnel experiments and full scale trials. Geyer, Smith, and Keller also made significant contributions to the body of work on blade sailing by using finite elements to model rotor dynamics [7] and by adding torsional flexibility, which influences the aerodynamic loads through blade twist. They have used Newman's simplified gust models [8] and a steady flow airwake model derived from computational fluid dynamics [9] to achieve aerodynamic loading. Parametric studies have been conducted on some of the factors that may contribute to the blade sailing phenomenon, including rotor collective setting [10]. The behavior of flap and droop stops has been studied independently using validation experiments on the subject [11,12]. Bottasso and Bauchau focused on the dynamics of the blade sailing problem, using a library of predefined and prevalidated finite elements to create a multibody formulation that simulates the rotor behavior with droop and flap stop impacts [13]. Kang and He used commercial software to develop a multibody formulation of a helicopter and ship, including realistic ship motion and contributions from the helicopter suspension to the dynamics of the problem [14].

Three effects have been identified as potential major contributors to the blade sailing phenomenon and are thus being considered in the current research program: helicopter dynamics, ship motion, and aerodynamics. The dynamics, including helicopter suspension and blade flexibility in all directions, characterize how the blade responds to a variety of inputs. Ship motion is transmitted through the landing gear of a helicopter and may significantly affect blade dynamic response. Aerodynamic effects are believed to contribute to the serious blade deflections that characterize blade sailing. Specifically, ship airwake turbulence and ship rolling motion induce unsteady loading, particularly at rotor-system resonant frequencies and thus must be modeled. Despite the existing body of knowledge on blade sailing, the relative contribution of dynamics, aerodynamics, and ship motion is not systematically understood and there is much room for research in the field of blade sailing phenomena. As part of an ongoing study in which the unsteady aerodynamic effects will be considered, this paper describes in detail the development and validation of the dynamic model, which includes the effect of realistic ship motion.

2 Modeling

The dynamic modeling of helicopter rotor blades is an active field. Kunz summarizes blade modeling methods developed during the first 40 years of the helicopter [15]. Detailed models have been developed for rotors with hinges and those without [16], using analytical methods and finite elements [17]. Results from

Contributed by the Applied Mechanics Division of ASME for publication in the JOURNAL OF APPLIED MECHANICS. Manuscript received September 21, 2006; final manuscript received May 2, 2008; published online August 15, 2008. Review conducted by Oliver M. O'Reilly.

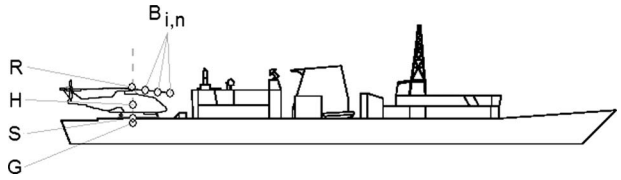

Fig. 1 The model coordinate systems

many of these have been used to validate the dynamic model described herein.

The current research uses a dynamic helicopter and blade model that is based on the philosophy that a flexible continuous system can be modeled with reasonable accuracy using a series of discrete rigid bodies and flexible elements, provided that the discrete properties are representative of the real system and that an adequate number of degrees of freedom is included [18,19]. The approach supports incorporation of geometric nonlinearities and modal coupling. Rigid-body models of systems are at an advantage over continuous models in that a closed-form set of dynamics equations can be easily derived. This characteristic leads to equations that are easily and quickly handled by numerical solvers. Some assumptions are required in the definition of a rigid segment model for a flexible system; the major one being that continuous deformation characteristics can be assumed to act at point locations. Once the model has been defined, the solution is exact for that model and no terms need be neglected to achieve solvability. As far as the authors are aware, this modeling approach has not previously been used in the blade sailing context.

The dynamic model was developed according to the modeling priorities summarized in the following.

- Blade flap is the motion of greatest concern, since it is the primary motion in blade sailing. Torsion, to the extent that it affects aerodynamic loads and thus flap, is also of concern. This includes flap-twist coupling. Lead/lag, while included in the model, is of lesser concern.
- The small angle assumption for blade flap deformation is invalid since blade sailing deflections can be severe. The rigid-segment model allows the analyst complete freedom in choosing the number of segments, thereby introducing the possibility of large angles through individual joints.
- Blade sailing occurs at low rotor speeds and exhibits mainly rigid body and first elastic mode oscillation of the rotor blades. Effects acting in the range of 0.1–3 Hz are carefully included; effects acting at greater than 10 Hz are of lesser concern.
- Blade extension flexibility was not modeled, as the extension is minimal at low rotor speeds.
- Model versatility, in the sense that all system properties can be easily modified by the analyst, is of utmost importance. Efforts were made to allow a wide range of options and operating conditions.
- Time domain results are desired.

The developed mathematical model represents the ship-helicopter-rotor system shown in Fig. 1. The helicopter, which has been approximately modeled as a midsize maritime helicopter (such as an Augusta-Westland EH101), operates from the flight deck of a typical frigate. The helicopter body is modeled as a single rigid body and the rotor blades are each divided into a series of rigid segments that are connected by three-dimensional rotational springs. These springs allow blade flexibility in the torsion, flap, and lead/lag directions. Ship motion excites the helicopter body through a suspension system model, and the ship airwake excites blade segments through an aerodynamic model. Other external forces are easily included in the system dynamics without affecting the modeling approach or changing the basics of the derived equations of motion.

It is worthwhile to briefly describe the system of body-fixed coordinate systems, and the related nomenclature, used to derive the equations of motion. The approximate locations of these can be seen in Fig. 1.

The global or inertial coordinate system, G, is a translating-earth reference frame. It exists at the center of the flight deck when all ship motions, except constant forward speed, are zero. All dynamic equations are ultimately expressed in the global frame of reference. The orientations of this and subsequent reference frames are defined by Bryan Euler angles.

The ship frame of reference, S, is defined relative to the global coordinate system and originates at the center of the flight deck. The position of the ship frame is given by the ship motion algorithm and is in the form (surge, sway, and heave). The orientation of the ship is given by (roll, pitch, and yaw), which are assumed equal to the frame Bryan angles. This assumption is inherent in linear ship motion theory, which is widely used [20], and is valid if only one rotation angle is expected to be large at a time.

The helicopter coordinate system, H, is also defined relative to the global system. The coordinate system has its origin at the helicopter center of mass.

The rotor frame of reference, R, is a coordinate system that defines the axis of the rotor and allows the blades to turn together. It is defined relative to the helicopter frame of reference, and the origin is located at the center of the rotor hub in line with the plane of the blades. The first two Bryan angles are defined by the helicopter geometry and set the axis of rotation for the rotor. The final Bryan angle varies with time in accordance with a representative rotor engage or disengage profile.

The flexible interfaces between the rigid blade segments are referred to as "joints." The first joint is the interface between the rotor hub and the first segment. This joint is referred to as the "root." If the helicopter rotor being modeled is of the articulated type, then the root joint is modeled as a hinge. Semirigid rotors have flexible root joints, but they do not have hinges.

The blade segment reference frames, $B_{(i,n)}$, are defined relative to the rotor reference frame, R, if $i=1$, or relative to the previous blade segment reference frame, $B_{i-1,n}$, where i represents the blade segment number starting with 1 at the inboard segment. Each segment is defined with properties $m_{(i,n)}$, the segment mass which is assumed concentrated at a point in space, $\{\mathbf{r}_{b_{(i,n)}}\}$, at the mass center of the segment, and $[J_{(i,n)}]$, the segment rotational inertia matrix about its center of mass. Each blade segment is connected to the last at point $\{\mathbf{r}_{B_{(i,n)}}\}$ in the coordinate system of the preceding segment. This location should be coincident with the local shear center of the blade cross section, which can change with radial position. These joints have a rotational element stiffness matrix, $[k_{(i,n)}]$, and viscous rotational damping coefficient matrix, $[c_{(i,n)}]$. The subscripts (i,n) indicate that the quantity is specified for the i^{th} segment on the n^{th} blade and that each $(i,n)^{\text{th}}$ quantity can be defined independently from the others. Thus, the blade need not be uniform, straight, or untwisted, the elastic axes and joints need not lie along a straight axial line, and the joints need not be equidistant. Since the properties can be individually assigned to each segment, they can be tuned to approximate closely any continuous and generally nonuniform rotor blade. As with variable finite element gridding, shorter segments can be used in areas of higher flexibility, while longer segments can be used in stiffer areas. The total number, size, and shape of the blade segments are completely definable.

The Bryan angles for each segment can be used to track blade torsion, bending, and lead-lag in time. If the local orientation angles of each blade segment are small, then a linear approximation of each local transformation matrix could be used while maintaining the overall ability of the model to capture large displacements. This approximation was not utilized in order to avoid

the modeling restriction that the number of rigid segments be sufficient to maintain each local angle in the linear range.

The rigid blade segment coordinate systems, $B_{\text{rigid}(i,n)}$, define the undeflected shape of the blade. They are based on the undeflected Bryan angles for the $(i,n)^{\text{th}}$ segment and allow any structural deviations from a straight blade to be assigned. These systems are used as a reference for the spring energy calculations at each joint and for calculating hinge friction. For an undeflected blade, the coordinate system $B_{(i,n)}$ is coincident with $B_{\text{rigid}(i,n)}$.

Model degrees of freedom are defined as the position and orientation of the helicopter coordinate system, and the relative orientations of the blade segments, with the exception torsion on the first segment of each blade. This is because the "torsion" at the first joint is defined by predefined time-varying collective and cyclic angles. Also defined by time-varying functions are ship motion and rotor rotation.

The axial extension is known to be a dynamic variable of important consideration for flexible bodies rotating at high velocities. In addition to small axial displacements which can affect the final blade tip location, the axial extension is known to change slightly the torsional rigidity of blades with structural twist. This coupling between axial extension and torsion can lead to changes in the aerodynamic angle of attack at high rotor speeds. Discrete axial flexibility and the related coupling effects could be included in a similar manner as the torsional and bending flexibilities, as shown in Ref. [21], without rendering the equations of motion unsolvable. Since the blade sailing phenomenon is believed to occur at low rotational speeds (less than 50% full speed), the axial extension effects are believed to be minor and have therefore not been included in the current version of the dynamic model.

2.1 Equations of Motion. The equations of motion for the ship-helicopter-rotor system were derived using Lagrange's equation, and distilled symbolically into the matrix form of Newton's second law [22]. The equations were then converted to first order and time-history solution was propagated using a conventional numerical integrator. A summary of the modeling of each system component in Lagrange's equation follows.

2.1.1 Kinetic and Gravitational Energy. The translational kinetic energy, rotational kinetic energy, and gravitational potential energy all depend on the absolute body positions and velocities, which have not been linearized. The expressions contain characteristic cascading sums and products that vary in size with blade and segment number. The derivation of the terms in Lagrange's equation has proven challenging owing to the variability of the equations; however, a procedure has now been defined for a similar planar problem [22]. Expanding these methods into the three-dimensional case is straightforward, yet interesting, and shall be discussed in the Appendix.

2.1.2 Blade Joint Spring Potential Energy. The flexibility in helicopter rotor blades is simulated at the joints that connect the rigid blade elements. Since the Euler angles that define the motion at each joint do not explicitly give the displacements of the individual joint springs, the projected rotation angles must be calculated to find the individual linear spring forces about each axis. Structural coupling can be preserved by employing a fully populated stiffness matrix, such that the potential energy of each joint is given by

$$U_{(i,n)} = \tfrac{1}{2}\{\theta_{(i,n)}\}^T[k_{(i,n)}]\{\theta_{(i,n)}\} \tag{1}$$

where

$$\{\theta_{(i,n)}\} = \begin{Bmatrix} \theta_{x(i,n)} \\ \theta_{y(i,n)} \\ \theta_{z(i,n)} \end{Bmatrix} \tag{2}$$

and the components of $\{\theta_{(i,n)}\}$ are projected angles.

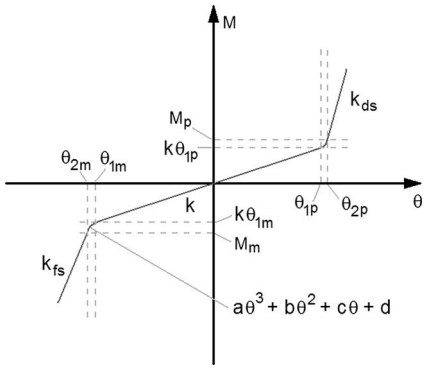

Fig. 2 General stiffness curve for blade root springs

2.1.3 Blade Root Potential Energy. Depending on whether the helicopter being modeled has semirigid or articulated rotor blades, the root modeling requirements change. If the blades are semirigid, they can be approximated by a cantilever beam-type model, and the joint is modeled similar to the outboard segment joints.

Articulated blades are hinged at the root. In this case, the joint itself has lesser or no stiffness to approximate a hinge and the blade must then be supported at low rotational speeds by droop stops. At operational speeds, the inertial moment lifts the rotor off the stops, and thus they are often retracted. Flap stops prevent the blade from excessive upward flapping during engage and disengage, and they also retract and extend at a given rotational speed. The lead/lag stops, often hydraulic or elastomeric dampers, similarly restrict blade motion outside a given acceptable range of motion; however, their modeling is simplified by the fact that they do not extend or retract during operation. These blade motion limits are modeled using additional rotational springs and dampers at the blade root when the angle of blade displacement at the root exceeds the acceptable deadband range.

The stiffness curve for these elements is shown in Fig. 2 where the subscript m refers to quantities in the range of negative θ values. The subscript p refers to quantities in the positive range of θ. The negative and positive properties can be defined separately. The quantities k, k_{fs}, and k_{ds} refer to the joint stiffness, flap stop stiffness, and droop stop stiffness, respectively. For the lead/lag stops, k_{fs} refers to the stiffness of the stop when the joint angle is negative, and so on. While the root hinge joint can be assigned a stiffness value as per the figure, it is usually set to zero since the hinges do not exhibit spring characteristics between the stop regions.

The discontinuity between the stopping element and the hinge stiffness is smoothed with a cubic function as shown in Fig. 2 where the coefficients of the smoothing function are a, b, c, and d. The values θ_{1m} and θ_{1p} are the stop contact angles in the negative and positive angular directions, respectively. The values θ_{2m}, θ_{2p}, M_m, and M_p are selected so that the curve fit occurs over a small angle and the shape of the curve does not include inflection points.

The extension and retraction of droop and flap stops presents some interesting modeling challenges. For instance, they retract and extend at a given rotational speed; however, they cannot extend or retract if the blade is in contact with the stop when the critical speed is reached. In addition, the extension and retraction must occur over some measurable time and the blade might come into contact with the stop during the process. The extra applied moment due to the stop is assumed to vary linearly between its fully engaged value and zero during the extension and retraction process. These operational cases are all modeled and handled using appropriate logic within the simulation.

For use in Lagrange's equation, the potential energy expression for the variable spring element shown in Fig. 2 is

$$U_{(1,n)} = \begin{cases} M_m\theta + \frac{1}{2}k_{\mathrm{fs}}\theta^2 - k_{\mathrm{fs}}\theta_{2m}\theta + C_1 & \text{if } -\infty < \theta \le \theta_{2m} \text{ and } \omega < \omega_{\mathrm{fs}} \\ \frac{1}{4}a_m\theta^4 + \frac{1}{3}b_m\theta^3 + \frac{1}{2}c_m\theta^2 + d_m\theta + C_2 & \text{if } \theta_{2m} < \theta \le \theta_{1m} \text{ and } \omega < \omega_{\mathrm{fs}} \\ \frac{1}{2}k\theta^2 + C_3 & \text{if } \theta_{1m} < \theta \le \theta_{1p} \text{ or } \omega > \omega_{\mathrm{ds}} \text{ or } \omega_{\mathrm{fs}} \\ \frac{1}{4}a_p\theta^4 + \frac{1}{3}b_p\theta^3 + \frac{1}{2}c_p\theta^2 + d_p\theta + C_4 & \text{if } \theta_{1p} < \theta \le \theta_{2p} \text{ and } \omega < \omega_{\mathrm{ds}} \\ M_p\theta + \frac{1}{2}k_{\mathrm{ds}}\theta^2 - k_{\mathrm{ds}}\theta_{2p}\theta + C_5 & \text{if } \theta_{2p} < \theta \le \infty \text{ and } \omega < \omega_{\mathrm{ds}} \end{cases} \tag{3}$$

where the constants C_1-C_5 do not appear in the equations of motion. The polynomial coefficients a_m, b_m, a_p, b_p, etc., are the negative and positive angle equivalents of the coefficients shown in Fig. 2. The quantities ω, ω_{ds}, and ω_{fs} refer to the rotor speed and the stop retraction speed for the droop and flap stops, respectively. In the case of the lead/lag stops, the conditions on ω do not apply since they do not retract and extend.

2.2 Nonconservative Contributions. Many system components contribute to the equations of motion as nonconservative effects. These include the suspension forces, including the effect of ship motion; the damping forces associated with the blade segment joints and the blade stopping elements; aerodynamic effects; and any other applied forces. The details of each contribution are briefly discussed.

2.2.1 Ship Motion and Suspension. When exposed to dynamic sea conditions, a ship will respond with motion in six degrees of freedom: three translational motions: surge, sway, and heave; and three angular motions: roll, pitch, and yaw. Ship motion is often obtained by multiplying the spectra of ship response, called response amplitude operators (RAOs) [20], by the incoming wave spectrum [23]. This yields a representation of the ship motion in the frequency domain, which can be used to generate a time-history of ship motion at the center of mass, or at some other point such as the center of the flight deck, using a Fourier series. Once the RAOs have been determined either computationally or experimentally [24], the displacement of each ship degree of freedom can be reconstructed, typically with 40 frequency components. The amplitudes and frequencies are found using simulated models of ship behavior, and the phase is generated randomly to enhance simulation fidelity [25].

Once the ship motion has been determined, the suspension forces on the helicopter body can be calculated. The number of suspension points is selected by the analyst, with definable geometry and characteristic properties. In the helicopter coordinate system, the vertical suspension stiffness can be largely attributed to the oleo, or other vertical suspension element, in addition to the tire. The horizontal stiffnesses can be attributed to the behavior of the tire. The current model assumes that the helicopter is secured such that the tires cannot slide, roll, or lift off the deck.

The suspension stiffness and damping forces are assumed to be quadratically related to suspension displacement and velocity, respectively, in each orthogonal force direction in the helicopter frame of reference. The location of application of the forces should be clarified. The true point of application is the deflected suspension contact point. However, since the suspension motions are not defined as system degrees of freedom, the force application points are approximated as the undeflected suspension contact points.

2.2.2 Articulated Hinge Friction. The friction that exists in an articulated blade root hinge, flap, or lead/lag is an important part of the model. The frictional moment due to hinge friction is considered to depend on the friction force acting between the sliding surfaces of the hinge and the radius of the hinge pin. A continuous approximation for the theoretical discontinuous friction function can be achieved using a modified friction function, which includes the Schiller friction model [26]. In this model, two quantities, ε and η, scale the smoothing components of the modified functions. The quantity ε is a small positive velocity, which represents the time constant of the smoothing exponential decay from the static peak of the friction function to the sliding friction component. The smaller the velocity, the more representative the continuous approximation. A value of $\eta = 1/0.02\varepsilon$ provides good smoothing through zero velocity without largely affecting the magnitude of the static friction peak.

Owing to the fact that the equations of motion are formulated using Lagrange, the reaction forces in each hinge joint are calculated separately using a method suggested by Kane and Levinson [27]. This method assumes an additional translational degree of freedom in the hinge joint, which is the direction of the reaction force desired, and then sums the inertial and active forces to zero. The unknown in this summation is the reaction force vector. The forces normal to each hinge are extracted from this reaction force vector and used in the Schiller friction model.

2.2.3 Blade Joint Damping. The blade segment damping consists of a number of possible components, depending on the blades being modeled. The following rotational viscous damping terms can be independently defined:

- the structural damping associated with the outboard blade joints;
- the root joint damping, having a damping value consistent with a semirigid joint or a hinge; and
- additional damping associated with the flap/droop and lead/lag stops, applied when the blade root angle is in the applicable range and the stops are extended.

In order that the damping of the motion stops be applied only in the angular range over which the stops act, the damping force is multiplied by the filter, f, which has a value of 1 in the angular range of the stop and zero otherwise. A smoothing function, with the same transitional angles as for the stop stiffness profile, is used to eliminate the discontinuity that occurs when the stops are impacted.

The damping moment about one hinge due to the corresponding motion stops is therefore calculated by applying the filter value using

$$M_{\mathrm{damping}} = \begin{cases} -fc_{\mathrm{fs}}\dot{\theta} & \text{if } \theta < 0 \text{ and } \omega \le \omega_{\mathrm{fs}} \\ -fc_{\mathrm{ds}}\dot{\theta} & \text{if } \theta > 0 \text{ and } \omega \le \omega_{\mathrm{ds}} \end{cases} \tag{4}$$

where c_{fs} and c_{ds} are the damping coefficients of the flap and droop stops, respectively. As with droop and flap stop stiffnesses, the extension and retraction of the flap and droop stops means that the extra damping is only applied if the rotor angular velocity is below the critical speed for flap and droop stop extension, ω_{fs} and ω_{ds}, respectively.

2.2.4 System Proportional Damping. The model also contains a proportional damping feature, which allows the user to employ a linearized proportional damping relationship

$$[\mathbf{C}_{\text{linear}}] = a[\mathbf{M}_{\text{linear}}] + b[\mathbf{K}_{\text{linear}}] \tag{5}$$

where the constants a and b are user defined. In the proportional damping model, the linear mass and stiffness matrices $[\mathbf{M}_{\text{linear}}]$ and $[\mathbf{K}_{\text{linear}}]$ are calculated about a specified operating point such that $[\mathbf{C}_{\text{linear}}]$ remains constant throughout the simulation.

In the model, the analyst has the option to toggle proportional damping on and off, or apply proportional damping to certain degrees of freedom and not to others. This is done by zeroing the unwanted columns and rows in the linearized proportional damping matrix. Proportional damping can be applied in addition to other forms of damping available in the model; if multiple damping sources exist, they are superimposed.

2.3 Blade Motion Coupling. There are several sources of blade motion coupling which should be included in any helicopter blade model in order to correctly capture blade response to a variety of conditions. The rigid-segment model captures all these coupling sources either through a fully populated stiffness matrix or because the equations of motion have not been linearized.

Dynamic Coupling. This arises from out-of-plane gyroscopic motion captured by the dynamics in the equations of motion.

Inertial Coupling. This occurs if the blade mass center axis is offset from the elastic axis. As the rotor turns, the centrifugal force that is generated will result in blade deflections. Similarly, flap and lead-lag can lead to coupled torsional motion about the elastic axis.

Structural Coupling. This results from a blade shear center that is offset from the elastic axis. It can occur on isotropic and composite blades.

Composite-Structural Coupling. This occurs as a result of the composite fibers in the lay-up of a composite rotor blade.

Twist Coupling. This can include effects from the other types of coupling but emphasizes the idea that the coupling properties of the blade will change with radius if a built-in twist angle is present.

2.4 Property Determination. A challenge of the rigid-segment model is property determination, especially the stiffness properties of the blade segments. Three determination methods are here proposed; the most appropriate one for a given situation depends on the information available.

2.4.1 Property Tuning. This method involves tuning the blade response by comparing the rigid-segment results with experimental (or some other known) results. Depending on the available information, the researcher may have to make some assumptions about the model, and combine these with the available data to arrive at a complete set of properties. The tuning method often requires iteration and more than one set of data such that the properties can be tuned to one set and then validated against another.

2.4.2 Deflection/Load Case Fit. If a certain deflection shape resulting from a known load case exists, then the individual joint stiffnesses can be calculated by matching the deflections at each joint to the known profile given the same load case. The Bernoulli–Euler beam equation gives a straightforward way to estimate a deflected shape for a simple load case such as a tip force or a uniformly distributed blade weight.

Linear cantilever beam theory also provides a convenient way of estimating the stiffness of a continuous uniform blade if the natural frequencies are known.

2.4.3 Direct Method. If detailed continuous stiffness distributions for the blade are available, then the discrete joint stiffnesses can be calculated directly. Much research is currently being conducted regarding the calculation of coupled stiffness matrices for helicopter rotor blades [28], especially in composite blade applications, where the coupled components are known to be significant. One typical formulation gives the blade energy per unit length, U_b/L stored in a deflected beam as

$$\frac{U_b}{L} = \frac{1}{2}\{\bar{\epsilon}\}^T[k_b]\{\bar{\epsilon}\} \tag{6}$$

where

$$\{\bar{\epsilon}\} = \begin{Bmatrix} \theta_1' \\ u_3'' \\ u_2'' \end{Bmatrix} \tag{7}$$

The quantity θ_1 is the twist about x, and u_2 and u_3 are deflections of the beam reference line in y and z, respectively.

Here, $\{\bar{\epsilon}\}$ contains the curvatures in torsion, flap, and lead/lag, respectively. These represent the rate of change of displacement angle. Equation (6) is compared to Eq. (1), where $\{\theta_{(i,n)}\}$ is a measure of the change in angle across a joint, an effective curvature. By considering a beam segment of length $L=l_{(i,n)}$ and the definition of a derivative, it can be justified that

$$\{\bar{\epsilon}\} \simeq \frac{\{\theta_{(i,n)}\}}{l_{(i,n)}} \tag{8}$$

By substitution, it can then be shown that the discrete stiffnesses are simply the continuous stiffnesses divided by the length of the segment over which they act.

$$[k_{(i,n)}] = \frac{[k_b]}{l_{(i,n)}} \tag{9}$$

The accuracy of the approximation is good, provided the curvature does not change significantly along the length of each individual blade segment. This can be managed by the user by careful selection of segment length based on the geometry, properties, and other model conditions. The direct method was validated using the tuning approach previously detailed.

2.4.4 Example. The time-history of blade tip deflection for an actual nonrotating blade on a typical maritime helicopter was captured on video. Based on the frequency exhibited in the video, an effective stiffness for an equivalent isotropic uniform beam can be estimated. If a model of this helicopter is desired, then one of the following blade models could be developed.

Case 1. If the blade resting on the droop stops is assumed a cantilever with no initial hinge angle, and the total blade mass is known, then the blade can be sectioned into segments of equal length, equal mass, and equal stiffness and damping properties then can be tuned to achieve similar tip response.

Case 2. If the blade resting on the droop stops is assumed a cantilever with no initial hinge angle, and the mass distribution as a function of radius is available, then the blade can be sectioned into segments with appropriate masses and the appropriate stiffness and damping properties can be found using the deflection/load fit for a cantilever beam subject to gravity and its own weight. Figure 3 shows the experimental data compared to the simulation results for a hingeless blade approximated by different numbers of blade segments.

Case 3. If the droop stops are modeled using the hinge and droop stop model described above and the mass distribution as a function of radius is available, then a different set of equivalent stiffnesses can be achieved using the deflection/load fit.

Table 1 shows first natural frequency and static deflection results for the test blade in flap modeled using Bernoulli–Euler beam theory and the three test cases. Case 1 and the Bernoulli–Euler beam theory frequencies are similar because both assume

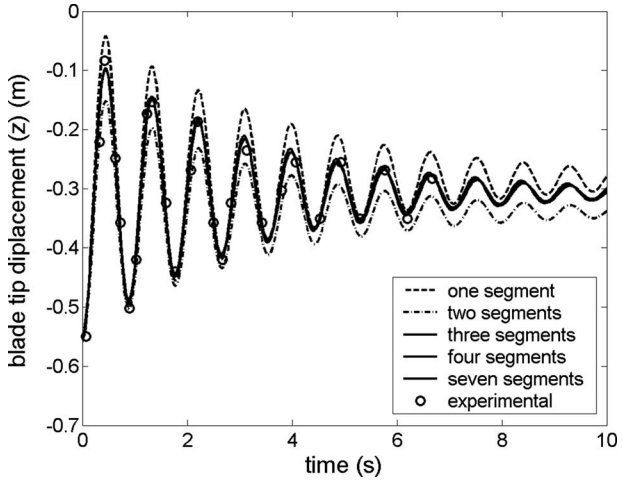

Fig. 3 Blade response in flap to a pull test (hingeless blade with varying number of segments)

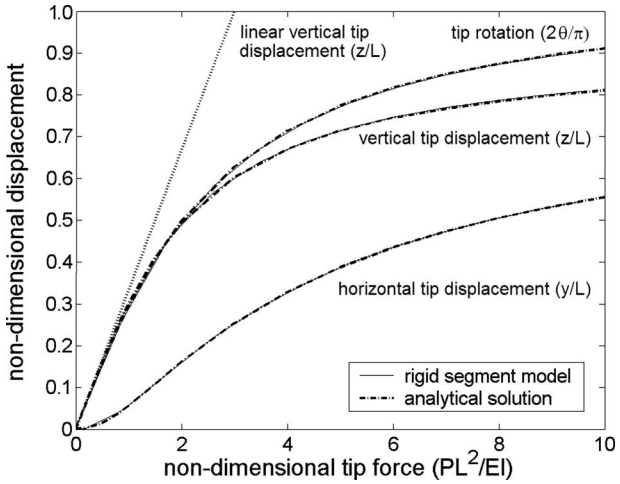

Fig. 4 Large bending tip deflections due to static tip force (ten segments)

uniform beam properties. Cases 2 and 3 allow variable mass and stiffness properties, and therefore agree with the experimental results, which also include variable mass and stiffness. This validation case begins to show the suitability of the discrete approach for modeling beams with variable properties.

3 Model Validation

The numerical simulation is undergoing a lengthy process of validation to explore the level of applicability of this model to the blade sailing phenomenon. The characteristic of most concern is the behavior of the segmented blade as a flexible body. This means consistency of natural frequencies, coupled and uncoupled, and consistency of deflected shapes, both static and dynamic. The vibration properties of helicopter blades are known to change with blade rotation speed, as the centrifugal and tensile forces in the blade change its effective stiffness. These effects and the ability of the simulation to deal with them have been explored. The final characteristic of concern is the coupling of blade motions due to structural considerations such as blade twist and elastic axis offset.

3.1 Blade Bending Behavior. In the blade sailing context, the behavior of the blade in bending, especially in flap, is of specific interest. A wide variety of continuous blade and beam bending models exist, and the performance of the rigid-segment model was validated against these and experimental data in order to show the appropriateness of the rigid-segment model for simulating blade behavior.

Table 1 Summary of results for bending vibration cases

	Stiffness	Mass	Freq (rad/s)	Static Δ (m)
Model case 1	Discrete, uniform[a]	Discrete, uniform	7.07	0.307
Bernoulli–Euler beam	Continuous, uniform	Continuous, uniform	7.06	0.305
Model case 2	Discrete, variable[b]	Discrete, variable[c]	7.11	0.305
Model case 3	Discrete, variable[b]	Discrete, variable[c]	7.11	0.305
Expt.	Continuous, variable	Continuous, variable	7.11	0.305

[a]Equal joint rotational spring stiffnesses approximate some variable continuous stiffness profile.
[b]Variable joint rotational spring stiffnesses properly tuned approximate uniform continuous stiffness.
[c]Discrete variable masses are chosen to be representative of the real blade, with the blade tip much lighter than the blade root.

3.1.1 Large Deflections. Since blade sailing can involve large deflections, a model that captures bending of a geometrically linear beam is insufficient. The static flap deflections of a uniform isotropic beam with a vertical load applied at the tip are shown in Fig. 4. Ten identical rigid segments were used to model the beam, and the results are compared to published results [29]. The rigid-segment results agree very well with the published values.

The large deflections in a dynamics sense were also validated using a uniform isotropic beam undergoing spin-up from rest to a constant rotational speed in the horizontal plane. The beam is extremely flexible in the lead-lag direction, and since the model applies no damping, it oscillates as a result of the initial rotational acceleration. The number of segments required to achieve numerical convergence was examined, and six segments were selected as a good compromise between solution accuracy and solution speed. The time-history of beam tip deflection for a six-segment beam shows a satisfactory agreement, within 4%, with the nonlinear finite element solutions [30,31] in Fig. 5.

3.1.2 Flapping Behavior With Rotational Speed. The bending frequencies of rotating blades are known to increase with rotational speed as a result of the centrifugal forces acting on the blade. An assumed mode solution to Lagrange's equation for a continuous uniform isotropic beam is used to validate this capability of the rigid-segment model [32]. Figure 6 shows a fan plot, which includes the rigid body and first elastic flapping modes of a blade with six rigid segments. Satisfactory agreement, within 1 rad/s, is shown between the rigid segment solution and the Lagrangian solution.

3.2 Blade Motion Coupling. The ability of the rigid-segment model to capture blade motion coupling has been validated using published cases.

3.2.1 Dynamic (Gyroscopic) Coupling. Classical helicopter theory textbooks discuss blade motion coupling that occurs between flap and lead/lag due to the Coriolis coupling when the blade is rotates at a constant speed. Articulated rotors allow this coupled motion since motions about the lead/lag hinge and the bending hinge are essentially unrestrained. A simplified set of equations of motion is solved to give the moment at the lead/lag hinge that would be required to restrain the motion of a rigid articulated blade in lead/lag [32]. This moment is

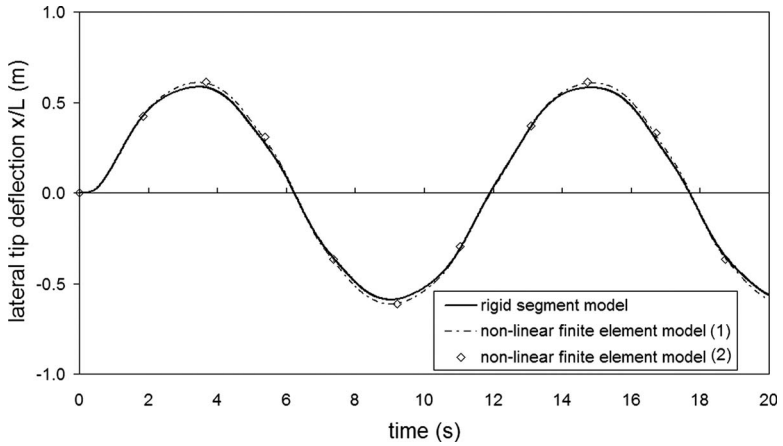

Fig. 5 Beam spin-up validation (finite element results from (1): Ref. [30] and (2): Ref. [31])

$$N = -2J_{yr}\Omega\dot{\beta}\sin\beta \tag{10}$$

where N is the moment about the lead-lag (z) axis, J_{yr} is the moment of inertia about the flap (y) axis through the joint instead of the center of gravity, Ω is the rotational speed of the hub (constant), and β is the flap angle. Figure 7 shows that the application of an equal and opposite moment N restrains the lead/lag motions to zero as soon as the initial transient response is removed with light damping.

3.2.2 Inertial Coupling. The definable properties of the model allow for the mass centers to be offset from the elastic axis, which is along the (x) axis of the blade segment in question. This causes a structural coupling of the natural frequencies of vibration such that most natural modes will contain both a bending and torsional component.

The inertial coupling between flap and torsion can be shown by solving for the coupled natural frequencies of an isotropic beam with a swept tip [17,33]. Lead-lag is also coupled in that the system is rotated at constant speed in the plane of the sweep angle and the beam achieves a steady-state deflection in the lead-lag sense for swept tip angles different from zero.

The first three bending-torsion coupled modes for a beam turning at 8.3 Hz are shown in Fig. 8. The rigid-segment model agrees with the published data to within 12% (1 Hz) for the fundamental mode and within 5% (2 Hz) for the second and third. This underprediction can likely be rectified by careful tuning of the root stiffnesses. In the figure, a rule-of-thumb approach was applied, in which the root stiffness is 2.15 times the calculated value for the other joints, provided the beam is uniform and the segment lengths are consistent. Still, the effects of tip sweep on the frequency trends are well captured.

3.3 Droop and Flap Stop Validation. The behavior of the droop and flap stops is important for the blade sailing of articulated blades. If the blades come into contact with the stops with significant kinetic energy, then it is transferred to potential energy, and the blades can undergo large deflections. The behavior of the blades when they come into contact with the stops has been validated against experimental results [11], where the details of the experimental blade can be found in Ref. [34].

Figures 9 and 10 show the tip deflection and the hinge angle, respectively, compared with the published experimental data. The rigid-segment model captures the general shape, magnitudes, and frequencies of the major blade response characteristics. Similar differences between numerical and experimental results are shown in Ref. [13].

4 Conclusions

The approach to helicopter modeling as discussed in this paper has been shown to attack the problem in a functional and versatile manner. The generality of the problem definition allows quick and easy parametric studies of a wide variety of situations. The individual components of the model have been validated, and the most important cases have been carefully discussed.

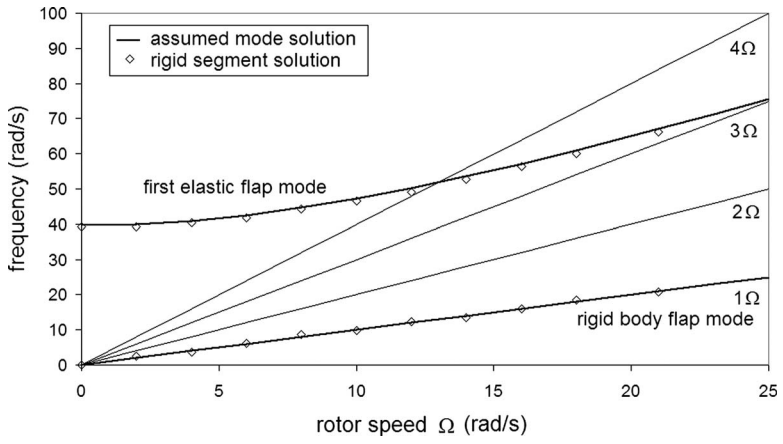

Fig. 6 Variation in flapping frequencies with rotor speed

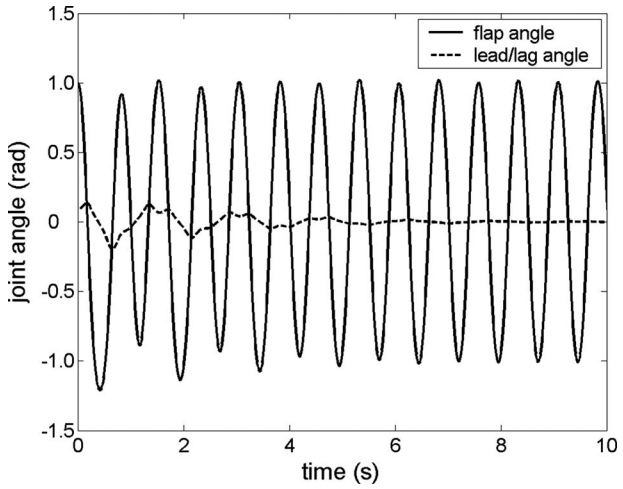

Fig. 7 Lead/lag motion restrained by Bramwell moment

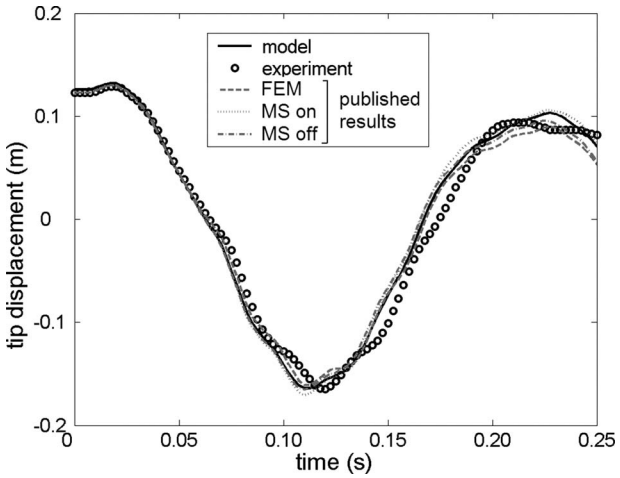

Fig. 9 Droop stop test blade tip deflection (experimental data and published results from Ref. [11])

The numerical model will be expanded to include an airwake turbulence model that contains spatially and temporally correlated turbulence based on statistical information gathered experimentally. The model will then be validated against experimental data from a series of tests on a scaled aeroelastic blade. The numerical model can then be used to study the blade sailing phenomenon.

Acknowledgment

For donations of time and information in support of this work, special thanks are due to Agusta-Westland Helicopters for providing helicopter property information; Maj. Chris Brown, from 424 Transport and Rescue Canadian Forces Squadron in Eight Wing from Trenton, ON, Canada, for facilitating field testing on a 424 Squadron helicopter; and Dr. E. Smith of Pennsylvania State University and Dr. J. Keller previously of Pennsylvania State University for providing experimental and numerical results. The project is supported both financially and actively by Carleton University and the Department of Mechanical and Aerospace Engineering, the Natural Sciences and Engineering Research Council of Canada (NSERC), the National Research Council Institute for Aerospace Research (NRC-IAR), and Defence Research and Development Canada (DRDC).

Appendix: Derivation of General Conservative Expressions

The extension of the general conservative energy expressions developed in Ref. [22] from the planar to the three-dimensional case is worth discussing. As an example to illustrate some important points, the kinetic energy arising from the horizontal (X) component of velocity associated with the masses of the blade segments of blade n shall be studied.

Before continuing with the description of the model, it is prudent to address some nomenclature. The quantity $\{\mathbf{r}_{a_b}\}$ is the position vector $\{\mathbf{r}_a\}$ defined in coordinate system b. If the subscript a refers to a coordinate system, then the position vector identifies the origin of coordinate system a in b. Transformation matrices are of the form $[\mathbf{R}_{ab}]$ and refer to a rotational transformation from the a coordinate system to the b coordinate system.

The kinetic energy expression for the three-dimensional case is given by

$$T_{X(n)} = \frac{1}{2}\sum_{i=1}^{n_s} m_{(i,n)}([1\ 0\ 0]\{\dot{\mathbf{r}}_{b_{(i,n)_G}}\})^2 \tag{A1}$$

where

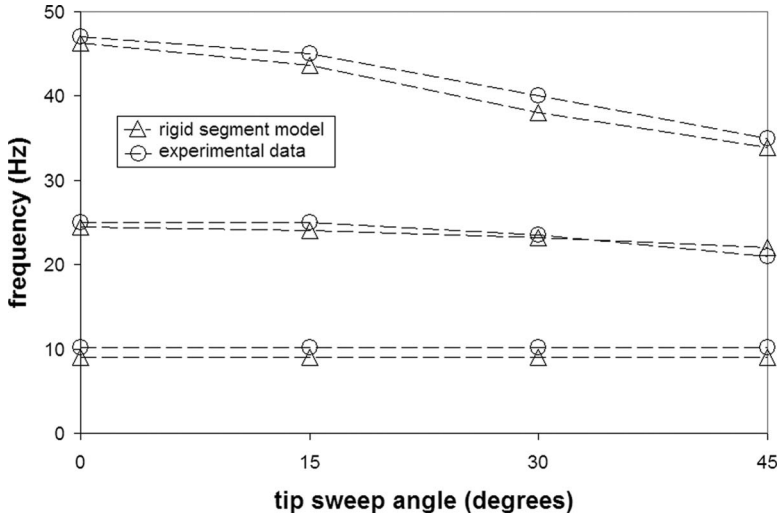

Fig. 8 First three flap-coupled frequencies for swept tip beam (experimental data from Ref. [33])

$$\{\dot{\mathbf{r}}_{b_{(i,n)_G}}\} = \{\dot{\mathbf{r}}_{H_G}\} + [\dot{\mathbf{R}}_{HG}]\{\mathbf{r}_{D_H}\} + \sum_{k=1}^{i-1}\left([\dot{\mathbf{R}}_{HG}][\mathbf{R}_{RH(n)}]\prod_{j=1}^{k}[\mathbf{R}_{B_{(j,n)}B_{(j-1,n)}}]\{\mathbf{r}_{B_{(k,n)}B_{(k-1,n)}}\} + [\mathbf{R}_{HG}][\dot{\mathbf{R}}_{RH(n)}]\prod_{j=1}^{k}[\mathbf{R}_{B_{(j,n)}B_{(j-1,n)}}]\{\mathbf{r}_{B_{(k,n)}B_{(k-1,n)}}\}\right.$$
$$+ \sum_{h=1}^{k}[\mathbf{R}_{HG}][\mathbf{R}_{RH(n)}]\left(\prod_{\alpha=1}^{h-1}[\mathbf{R}_{B_{(\alpha,n)}B_{(\alpha-1,n)}}]\right)[\dot{\mathbf{R}}_{B_{(h,n)}B_{(h-1,n)}}]\left(\prod_{\beta=h+1}^{k}[\mathbf{R}_{B_{(\beta,n)}B_{(\beta-1,n)}}]\right)\{\mathbf{r}_{B_{(k,n)}B_{(k-1,n)}}\}\Bigg)$$
$$+ [\dot{\mathbf{R}}_{HG}][\mathbf{R}_{RH(n)}]\prod_{j=1}^{i}[\mathbf{R}_{B_{(j,n)}B_{(j-1,n)}}]\{\mathbf{r}_{b_{(i,n)}B_{(i,n)}}\} + [\mathbf{R}_{HG}][\dot{\mathbf{R}}_{RH(n)}]\prod_{j=1}^{i}[\mathbf{R}_{B_{(j,n)}B_{(j-1,n)}}]\{\mathbf{r}_{b_{(i,n)}B_{(i,n)}}\}$$
$$+ \sum_{h=1}^{i}[\mathbf{R}_{HG}][\mathbf{R}_{RH(n)}]\left(\prod_{\alpha=1}^{h-1}[\mathbf{R}_{B_{(\alpha,n)}B_{(\alpha-1,n)}}]\right)[\dot{\mathbf{R}}_{B_{(h,n)}B_{(h-1,n)}}]\left(\prod_{\beta=h+1}^{k}[\mathbf{R}_{B_{(\beta,n)}B_{(\beta-1,n)}}]\right)\{\mathbf{r}_{b_{(i,n)}B_{(i,n)}}\}$$

where the distance vectors $\{\mathbf{r}_{H_G}\}$ and $\{\mathbf{r}_{D_H}\}$ refer to the globally defined position of the helicopter center of mass and the helicopter-defined position of the center of the rotor hub, respectively. The rotational matrix $[\mathbf{R}_{B_{(1,n)}B_{(0,n)}}]$ given inside the product operators is equivalent to $[\mathbf{R}_{B_{(1,n)R}}]$.

In comparison, the expression for the kinetic energy arising from the horizontal component of velocity of the port blade for the planar model is given by [22]

$$T_{X(1)} = \frac{1}{2}\sum_{i=1}^{n_s} m_{(i,1)}\left(\left(\dot{Y}_C - v\dot{\theta}\sin(\theta+a)\right.\right.$$
$$- \sum_{k=1}^{i}\left(\sin\left(\theta + \sum_{j=1}^{k}\phi_{(j,1)}\right)\right)\left(\dot{\theta} + \sum_{j=1}^{k}\dot{\phi}_{(j,1)}\right)d_{(k,1)}$$
$$\left.\left. + \frac{1}{2}\left(\sin\left(\theta + \sum_{j=1}^{i}\phi_{(j,1)}\right)\right)\left(\dot{\theta} + \sum_{j=1}^{i}\dot{\phi}_{(j,1)}\right)d_{(i,1)}\right)^2\right) \tag{A2}$$

where the planar orientation of the helicopter body is given by θ and the flap orientations of the blade segments are given by $\phi_{(i,1)}$. The length of each blade segment is given by $d_{(i,1)}$, and the center of mass is assumed to act halfway along the segment length. The quantity Y_C describes the horizontal position of the helicopter center of mass, and the quantity $(v\sin(\theta+a))$ gives the horizontal distance from the helicopter center of mass to the blade attachment point, and a and v are geometrical constants defined in Ref. [22].

The indices i and k represent the summation of equivalent phenomenon in both expressions and are subject to the index replacement rule described in Ref. [22]. The summation of cascading angles, given by index j in Eq. (A2), which is responsible for causing the index replacement rule, appears in a slightly different form in Eq. (A1). In the three-dimensional case, the expressions for blade position, velocity, and angular velocity are derived in vector form and are given in the global coordinate system through a series of cascading matrix transformations, which are given by the product operator, also in index j.

Two cases that result from the extension of the procedure into three dimensions are worth mentioning. First, when the energy expressions are differentiated with respect to time, an additional summation appears, shown in Eq. (A1) in index h. This results from the fact that the product rule must be applied to all the matrices in the cascading matrix product, since all depend on the variable time. When differentiating with respect to configuration coordinates or their derivatives as with Lagrange's equation, the differentiation quantity appears in only one matrix in each product and therefore the extra summation does not result. The product indices α and β result from the same phenomenon, and simply allow the cascading rotational matrix to which the time derivative is applied to be advanced from one to the next.

Second, a complete expression of the kinetic energy resulting from the horizontal component of velocity requires that this quantity be summed over the total number of blades present in the system (given as an index in n). The index replacement rule does not apply to this summation index since the degrees of freedom for each blade are independent and differentiation with respect to any one of them will result in zero components for all blades except the one of interest.

The derivation of all the required expressions for Lagrange's equation can be arrived at straightforwardly provided care is taken to ensure that the index replacement rule is applied only when necessary based on the logic given in Ref. [22].

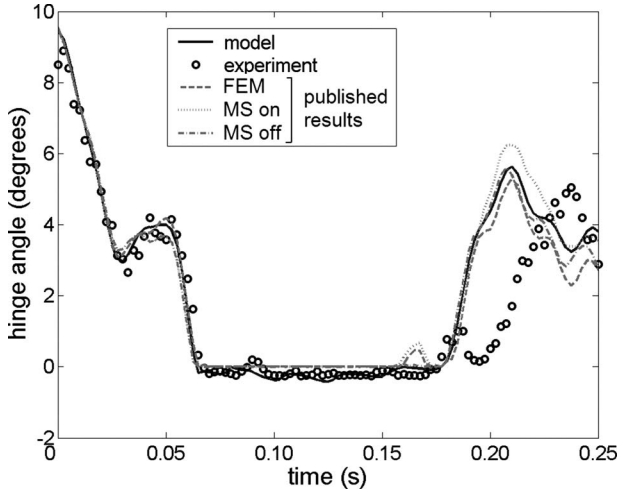

Fig. 10 Droop stop test flap hinge angle (experimental data and published results from Ref. [11])

References

[1] Newman, S. J., 1999, "The Phenomenon of Helicopter Rotor Blade Sailing," Proc. Inst. Mech. Eng., Part G: J. Aerospace Eng., **213**(G), pp. 347–363.

[2] Hurst, D. W., and Newman, S. J., 1985, "Wind Tunnel Measurements of a Ship Induced Turbulence and the Prediction of Helicopter Rotor Blade Response," *Eleventh European Rotorcraft Forum*, London, England, Sept. 10–13, Paper No. 99.

[3] Pavlov, V. A., Mikhailov, S. A., and Nikolaev, E. I., 1989, "Approach of Coaxial Main Rotor Blades During Startup on a Ship Deck," Izvestiya VUZ. Aviatsionnaya Tekhnika, **32**(1), pp. 25–28.

[4] Hurst, D. W., and Newman, S. J., 1988, "Wind Tunnel Measurements of a Ship Induced Turbulence and the Prediction of Helicopter Rotor Blade Response," Vertica, **12**(3), pp. 267–278.

[5] Newman, S. J., 1990, "A Theoretical Model for Predicting the Blade Sailing Behaviour of a Semi-Rigid Rotor Helicopter," Vertica, **14**(4), pp. 531–544.

[6] Newman, S. J., 1995, "The Verification of a Theoretical Helicopter Rotor

Blade Sailing Method by Means of Wind Tunnel Testing," Aeronaut. J., **99**, pp. 41–51.
[7] Geyer, W. P., Jr., and Smith, E. C., 1995, "Aeroelastic Analysis of Transient Blade Dynamics During Shipboard Engage/Disengage Operations," *Proceedings of the Second International AHS Aeromechanics Specialists Meeting*, Alexandria, VA, Oct., American Helicopter Society, pp. 8-91–8-114.
[8] Geyer, W. P., Smith, E. C., and Keller, J. A., 1996, "Validation and Application of a Transient Aeroelastic Analysis for Shipboard Engage/Disengage Operations," *Proceedings of American Helicopter Society 52nd Annual Forum*, Washington, DC, Jun., American Helicopter Society.
[9] Keller, J. A., and Smith, E. C., 1999, "Analysis and Control of the Transient Shipboard Engagement Behaviour of Rotor Systems," *Proceedings of American Helicopter Society 55th Annual Forum*, Montreal, QC, May, American Helicopter Society.
[10] Keller, J. A., 2001, "Analysis and Control of the Transient Aeroelastic Response of Rotors During Shipboard Engagement and Disengagement Operations," Ph.D. thesis, The Pennsylvania State University, University Park, PA.
[11] Keller, J. A., and Smith, E. C., 1999, "Experimental and Theoretical Correlation of Helicopter Rotor Blade-Droop Stop Impacts," J. Aircr., **36**(2), pp. 443–450.
[12] Smith, E. C., Keller, J. A., and Kang, H., 1998, "Recent Developments in the Analytical Investigation of Shipboard Rotorcraft Engage and Disengage Operations," *Proceedings of 15th NATO RTO Meeting on Fluid Dynamics Problems of Vehicles Operating Near or In the Air-Sea Interface*, Amsterdam, The Netherlands, Oct., Research and Technology Organization, Applied Vehicle Technology.
[13] Bottasso, C. L., and Bauchau, O. A., 2001, "Multibody Modeling of Engage and Disengage Operations of Helicopter Rotors," J. Am. Helicopter Soc., **46**(4), pp. 290–300.
[14] Kang, H., and He, C., 2004, "Modeling and Simulation of Rotor Engagement and Disengagement During Shipboard Operations," *Annual Forum Proceedings of the American Helicopter Society*, Vol. 1.
[15] Kunz, D. L., 1994, "Survey and Comparison of Engineering Beam Theories for Helicopter Rotor Blades," J. Aircr., **31**(3), pp. 473–479.
[16] Hodges, D. H., and Dowell, E. H., 1974, "Nonlinear Equations of Motion for the Elastic Bending and Torsion of Twisted Nonuniform Rotor Blades," NASA Technical Report No. TN D-7818.
[17] Hodges, D. H., Shang, X., and Cesnik, C. E. S., 1996, "Finite Element Solution of Nonlinear Intrinsic Equations for Curved Composite Beams," J. Am. Helicopter Soc., **41**(4), pp. 313–321.
[18] Langlois, R. G., and Anderson, R. J., 2005, "A Tutorial Presentation of Alternative Solutions to the Flexible Beam on a Rigid Cart Problem," Trans. Can. Soc. Mech. Eng., **29**(3), 357–374.
[19] Huston, R. L., 1991, "Computer Methods in Flexible Multibody Dynamics," Int. J. Numer. Methods Eng., **32**(8), pp. 1657–1668.
[20] McTaggart, K. A., 1997, "Shipmo7: An Updated Strip Theory Program for Predicting Ship Motions and Sea Loads in Waves," Defence Research Establishment Atlantic, DREA Technical Memorandum No. 96/243.
[21] Haering, W. J., 2004, "Simple Discrete Lumped Parameter Models: Insight Into Large Displacement Continuous Beam Models," 45th AIAA/ASME/ASCE/AHS/ASC Structures, Structural Dynamics and Materials Conference, Paper No. AIAA-1864.
[22] Wall, A. S., Langlois, R. G., and Afagh, F. F., 2007, "Modelling Helicopter Blade Sailing: Dynamic Formulation in the Planar Case," ASME J. Appl. Mech., **74**(6), pp. 1104–1113.
[23] Lloyd, A. R. J. M., 1998, *Seakeeping: Ship Behaviour in Rough Weather*, rev. ed., Gosport, UK.
[24] Lewis, E. V., ed., *Principles of Naval Architecture*, Vol. III, 2nd ed., The Society of Naval Architects and Marine Engineers, Jersey City, NJ.
[25] Phillion, R. H., and Langlois, R. G., 2004, "Avoiding Repetition in Ship Motion Simulation," *Proceedings of the 2004 CSME Forum*, Ontario, Canada, Jun. 1–4, Canadian Society for Mechanical Engineers.
[26] Schilling, R. J., 1990, *Fundamentals of Robotics: Analysis and Control*, Prentice-Hall, Englewood Cliffs, N.J.
[27] Kane, T. R., and Levinson, D. A., 1985, *Dynamics: Theory and Applications*, McGraw-Hill, New York.
[28] Khouli, F., Afagh, F. F., and Langlois, R. G., 2006, "Asymptotically-Correct Structural Modelling of Thin-Walled Anisotropic Closed Cross-Section Rotating Slender Beams," *International Conference on Advances in Engineering Structures, Mechanics and Construction*, Waterloo, Ontario, Canada, May 14–17.
[29] Gere, J. M., and Timoshenko, S. P., 1990, *Mechanics of Materials*, 3rd ed. PWS-Kent, Boston, MA.
[30] Langlois, R. G., and Anderson, R. J., 1999, "Multibody Dynamics of Very Flexible Damped Systems," Multibody Syst. Dyn., **3**(2), pp. 109–136.
[31] Christensen, E. R., and Lee, S. W., 1986, "Non-Linear Finite Element Modeling of the Dynamics of Unrestrained Flexible Structures," Comput. Struct., **23**(6), pp. 819–829.
[32] Bramwell, A. R. S., Done, G., and Balmford, D., 2001, *Bramwell's Helicopter Dynamics* (AAIA Education Series), 2nd ed., Butterworth-Heinemann, Oxford, UK.
[33] Epps, J. J., and Chandra, R., 1996, "The Natural Frequencies of Rotating Composite Beams With Tip Sweep," J. Am. Helicopter Soc., **41**(1), pp. 29–36.
[34] Keller, J. A., Smith, E. C., and Knarr, C. R., 1997, "Experimental/Theoretical Correlation of Analysis for Helicopter Rotor Blade/Droop Stop Impacts," 38th AIAA/ASME/ ASCE/AHS/ASC Structures, Structural Dynamics, and Materials Conference.

A. Srikantha Phani[1]
Department of Engineering,
University of Cambridge,
Trumpington Street,
Cambridge CB2 1PZ, UK
e-mail: skpa2@eng.cam.ac.uk

S. Adhikari
Department of Aerospace Engineering,
University of Bristol,
Queens Building, University Walk,
Bristol BS8 1TR, UK
e-mail: s.adhikari@bristol.ac.uk

Rayleigh Quotient and Dissipative Systems

Rayleigh quotients in the context of linear, nonconservative vibrating systems with viscous and nonviscous dissipative forces are studied in this paper. Of particular interest is the stationarity property of Rayleigh-like quotients for dissipative systems. Stationarity properties are examined based on the perturbation theory. It is shown that Rayleigh quotients with stationary properties exist for systems with proportional viscous and nonviscous damping forces. It is also shown that the stationarity property of Rayleigh quotients in the case of nonproportional damping (viscous and nonviscous) is conditional upon the diagonal dominance of the modal damping matrix. [DOI: 10.1115/1.2910898]

1 Introduction

In his classical treatise on the theory of sound [1], Rayleigh has introduced the notion of a quotient of two quadratics representing the potential and kinetic energies of a vibrating system. Since then, Rayleigh quotient has been widely applied in the analysis of many vibrating systems and their associated linear algebraic eigenvalue problems. Rayleigh quotient provides a variational approach to estimate the eigenvalues of an algebraic, generalized eigenvalue problem, as in the case of determining the natural frequencies of a vibrating system. Numerical methods to solve eigenvalue problems such as the shifted inverse power method rely on the properties of Rayleigh quotients for speedier convergence [2]. Thus, the practical utility of the Rayleigh quotient is wide ranging.

Traditionally, and in many textbooks on vibration analysis [3,4] and linear algebra [2,5], a Rayleigh quotient is defined as a ratio of two quadratics. In the case of a generalized eigenvalue problem involving two real and symmetric matrices $\boldsymbol{A}$ and $\boldsymbol{B}$, the Rayleigh quotient is defined as follows:

$$R(\boldsymbol{u}) = \frac{\boldsymbol{u}^T\boldsymbol{A}\boldsymbol{u}}{\boldsymbol{u}^T\boldsymbol{B}\boldsymbol{u}}, \quad \boldsymbol{A}\boldsymbol{v} = \lambda\boldsymbol{B}\boldsymbol{v} \quad \text{(EVP)} \tag{1}$$

where the eigenvalue problem is abbreviated as EVP.

The stationarity properties of this "classical" Rayleigh quotient are well established [2]. The objective of the present investigation is to explore whether similar Rayleigh-like quotients with stationary properties exist for a vibrating system with dissipation. Discrete vibrating systems are chosen here for the purpose of illustration; generalization of the results to continuous systems is straightforward.

This paper is presented as follows. Rayleigh quotients for discrete systems are defined in Sec. 2. Three quotients are introduced in the case of a viscously damped system and their stationary properties are investigated in Secs. 3 and 4. Rayleigh quotients in the context of nonviscously damped systems are studied in Sec. 5. The importance of Rayleigh quotients studied here is illustrated in Sec. 6, and main conclusions emerging from this study are summarized in Sec. 7. Throughout this study, the terms modes and eigenvectors are used interchangeably.

2 Rayleigh Quotients for Discrete Systems

Small oscillations of a discrete, linear vibrating system with viscous damping about its equilibrium position are governed by the following equations of motion:

$$\boldsymbol{M}\ddot{\boldsymbol{x}} + \boldsymbol{C}\dot{\boldsymbol{x}} + \boldsymbol{K}\boldsymbol{x} = \boldsymbol{f} \tag{2}$$

where the matrices $\boldsymbol{M}$, $\boldsymbol{K}$, and $\boldsymbol{C}$ are, respectively, the mass, stiffness, and damping matrices and the vectors $\boldsymbol{x}$ and $\boldsymbol{f}$ denote the displacement response and applied forces, respectively. In the absence of damping and applied forces, the above equation simplifies to

$$\boldsymbol{M}\ddot{\boldsymbol{x}} + \boldsymbol{K}\boldsymbol{x} = \boldsymbol{0} \tag{3}$$

The above equation leads to a linear, algebraic eigenvalue problem for the natural frequencies of free vibration, denoted by ω, given as follows:

$$\boldsymbol{K}\boldsymbol{u} = \lambda\boldsymbol{M}\boldsymbol{u} \tag{4}$$

where the eigenvalue λ is related to the frequency via $\omega = \sqrt{\lambda}$. Here, the positive branch of the square-root operation is assumed. $\boldsymbol{u}$ is the eigenvector (mode shape) associated with the eigenvalue λ (or vibration mode with natural frequency ω). For linear systems that obey Rayleigh's reciprocity principle, the matrices $\boldsymbol{M}$ and $\boldsymbol{K}$ are symmetric. This implies that the solutions of the eigenvalue problem in Eq. (4), λ and $\boldsymbol{u}$, are real.

In the context of vibration analysis of undamped systems, the two quadratic functions in the Rayleigh quotient assume the physical meaning of the kinetic and potential energies. Thus, associated with any admissible deformation vector ($\boldsymbol{\phi}$), one can define the following quantities:

$$\mathcal{U} = \boldsymbol{\phi}^T\boldsymbol{K}\boldsymbol{\phi}, \quad \mathcal{T} = \boldsymbol{\phi}^T\boldsymbol{M}\boldsymbol{\phi}$$

$$R(\boldsymbol{\phi}) = \frac{\mathcal{U}}{\mathcal{T}} = \frac{\boldsymbol{\phi}^T\boldsymbol{K}\boldsymbol{\phi}}{\boldsymbol{\phi}^T\boldsymbol{M}\boldsymbol{\phi}} \tag{5}$$

where $\mathcal{T}$ and $\mathcal{U}$ are the kinetic and potential energies of the system and R is the classical Rayleigh quotient.

However, when systems with dissipation are considered, one is faced with three quadratics. In this situation, one can define *three* quotients as follows:

$$\mathcal{U} = \boldsymbol{\phi}^T\boldsymbol{K}\boldsymbol{\phi}, \quad \mathcal{T} = \boldsymbol{\phi}^T\boldsymbol{M}\boldsymbol{\phi}, \quad \mathcal{D} = \boldsymbol{\phi}^T\boldsymbol{C}\boldsymbol{\phi}$$

$$R_1(\boldsymbol{\phi}) = \frac{\mathcal{U}}{\mathcal{T}} = \frac{\boldsymbol{\phi}^T\boldsymbol{K}\boldsymbol{\phi}}{\boldsymbol{\phi}^T\boldsymbol{M}\boldsymbol{\phi}}$$

$$R_2(\boldsymbol{\phi}) = \frac{\mathcal{D}}{\mathcal{T}} = \frac{\boldsymbol{\phi}^T\boldsymbol{C}\boldsymbol{\phi}}{\boldsymbol{\phi}^T\boldsymbol{M}\boldsymbol{\phi}}$$

[1]Corresponding author. Assistant Professor, Department of Mechanical Engineering, The University of British Columbia, 2054–6250 Applied Science Lane, Vancouver, B.C., V6T 1Z4, Canada.

Contributed by the Applied Mechanics Division of ASME for publication in the JOURNAL OF APPLIED MECHANICS. Manuscript received September 20, 2006; final manuscript received December 2, 2007; published online August 15, 2008. Review conducted by N. Sri Namachchivaya.

$$R_3(\boldsymbol{\phi}) = \frac{\mathcal{D}}{\mathcal{U}} = \frac{\boldsymbol{\phi}^T \boldsymbol{C} \boldsymbol{\phi}}{\boldsymbol{\phi}^T \boldsymbol{K} \boldsymbol{\phi}} \tag{6}$$

Note that for Rayleigh quotient to be finite, the denominator terms in the above equation should not be equal to zero. This requires that $\boldsymbol{M}$ be positive definite for R_1 and R_2 to be finite, and $\boldsymbol{K}$ be positive definite for R_3 to be finite. For majority of vibrating systems, $\boldsymbol{M}$ is positive definite while $\boldsymbol{K}$ need not be. Thus, the existence of R_3 is case specific.

It is the objective of this work to investigate the stationarity properties of the quotients defined in Eqs. (5) and (6). The proof of stationary property of the quotient defined in Eq. (5) is well known [2,5,6]. However, it is repeated here for the sake of completeness and also since the proof of stationarity for other quotients closely follows a similar procedure.

2.1 Stationarity of $R(\boldsymbol{\phi})$. Let a vector $\boldsymbol{\phi}$ be chosen such that it is close to one of the eigenvectors (modes) $\boldsymbol{u}_r$ of the system so that we can express $\boldsymbol{\phi}$ as

$$\boldsymbol{\phi} = \sum_i c_i \boldsymbol{u}_i = \boldsymbol{u}_r + \sum_{i \neq r} \epsilon_i \boldsymbol{u}_i, \quad \epsilon_i = \frac{c_i}{c_r} \ll 1 \tag{7}$$

where ϵ_i is a small real quantity. Now, the Rayleigh quotient reads

$$R(\boldsymbol{\phi}) = \frac{\boldsymbol{\phi}^T \boldsymbol{K} \boldsymbol{\phi}}{\boldsymbol{\phi}^T \boldsymbol{M} \boldsymbol{\phi}} = \frac{\boldsymbol{u}_r^T \boldsymbol{K} \boldsymbol{u}_r + 2\sum_{i \neq r} \epsilon_i \boldsymbol{u}_i^T \boldsymbol{K} \boldsymbol{u}_r + O(\epsilon^2)}{\boldsymbol{u}_r^T \boldsymbol{M} \boldsymbol{u}_r + 2\sum_{i \neq r} \epsilon_i \boldsymbol{u}_i^T \boldsymbol{M} \boldsymbol{u}_r + O(\epsilon^2)} \tag{8}$$

here, the symmetry of $\boldsymbol{M}$ and $\boldsymbol{K}$ is assumed. Due to the orthogonality properties of the eigenvectors [2,5],

$$\boldsymbol{u}_i^T \boldsymbol{M} \boldsymbol{u}_j = \delta_{ij}, \quad \boldsymbol{u}_i^T \boldsymbol{K} \boldsymbol{u}_j = 0, \quad \boldsymbol{u}_i^T \boldsymbol{K} \boldsymbol{u}_i = \lambda_i \tag{9}$$

Equation (8) simplifies to

$$R(\boldsymbol{\phi}) = \frac{\lambda_r + O(\epsilon^2)}{1 + O(\epsilon^2)} = \lambda_r (1 + O(\epsilon^2)) \tag{10}$$

The above result proves the stationarity of the Rayleigh quotient, i.e., first order changes in $\boldsymbol{\phi}$ lead to second order changes in $R(\boldsymbol{\phi})$. When $\boldsymbol{\phi}$ is close to one of the eigenvectors, the corresponding value of the quotient is stationary. Further choosing the first eigenvector as the trial vector $\boldsymbol{\phi}$ leads to a minimum value of $R(\boldsymbol{\phi})$. $R(\boldsymbol{\phi})$ is maximum when the trial vector is close to the eigenvector corresponding to the highest eigenvalue. For intermediate eigenvectors, $R(\boldsymbol{\phi})$ is neither a minimum nor a maximum, i.e., $R(\boldsymbol{\phi})$ is at a saddle point. A mini-max (or inf-sup) principle due to Courant and Fischer applies in this case [2,6].

3 Proportional Damping

We consider first the case of proportional damping. Here, proportional damping is defined in the sense that the same vector $\boldsymbol{\phi}$ simultaneously diagonalizes the three quadratics $\mathcal{T}$, $\mathcal{U}$, and $\mathcal{D}$. In other words, the three matrices $\boldsymbol{M}$, $\boldsymbol{K}$, and $\boldsymbol{C}$ can be simultaneously diagonalized. Although a viscous damping matrix of the form $\boldsymbol{C} = \alpha \boldsymbol{M} + \beta \boldsymbol{K}$ is the most widely understood model of a proportional damping model, it is only a subset of a wider class of models [7]. The necessary and sufficient conditions for proportional damping are established in Ref. [7] and revisited in Refs. [8–11]. Adhikari [10] showed that viscously damped linear systems will have classical normal modes if and only if the damping matrix can be represented by

(a) $\boldsymbol{C} = \boldsymbol{M}\beta_1(\boldsymbol{M}^{-1}\boldsymbol{K}) + \boldsymbol{K}\beta_2(\boldsymbol{K}^{-1}\boldsymbol{M})$
or
(b) $\boldsymbol{C} = \beta_3(\boldsymbol{K}\boldsymbol{M}^{-1})\boldsymbol{M} + \beta_4(\boldsymbol{M}\boldsymbol{K}^{-1})\boldsymbol{K}$

where $\beta_i(\bullet)$ are smooth analytic functions in the neighborhood of all the eigenvalues of their argument matrices. Rayleigh's result can be obtained directly from this "generalized proportional damping" as a special case by choosing each matrix function $\beta_i(\bullet)$ as a real scalar times an identity matrix, that is $\beta_i(\bullet) = \alpha_i \boldsymbol{I}$. In the case of proportionally damped systems, the eigenvectors are real but the eigenvalues are not, i.e., the undamped modes are also the modes of the proportionally damped system. Thus, the proof of stationarity of the first Rayleigh quotient $R_1(\boldsymbol{\phi})$ is the same as that given in Sec. 2.1.

We consider the second Rayleigh quotient associated with any admissible deformation vector $\boldsymbol{\phi}$ as defined in Eq. (7),

$$R_2(\boldsymbol{\phi}) = \frac{\boldsymbol{\phi}^T \boldsymbol{C} \boldsymbol{\phi}}{\boldsymbol{\phi}^T \boldsymbol{M} \boldsymbol{\phi}} = \frac{\boldsymbol{u}_r^T \boldsymbol{C} \boldsymbol{u}_r + 2\sum_{i \neq r} \epsilon_i \boldsymbol{u}_i^T \boldsymbol{C} \boldsymbol{u}_r + O(\epsilon^2)}{\boldsymbol{u}_r^T \boldsymbol{M} \boldsymbol{u}_r + 2\sum_{i \neq r} \epsilon_i \boldsymbol{u}_i^T \boldsymbol{M} \boldsymbol{u}_r + O(\epsilon^2)} \tag{11}$$

here, the symmetry of $\boldsymbol{M}$ and $\boldsymbol{C}$ is assumed. Due to the orthogonality properties of the eigenvectors,

$$\boldsymbol{u}_i^T \boldsymbol{M} \boldsymbol{u}_j = \delta_{ij} \tag{12}$$

We define

$$\boldsymbol{u}_i^T \boldsymbol{C} \boldsymbol{u}_j = C'_{ij}, \quad \boldsymbol{u}_i^T \boldsymbol{C} \boldsymbol{u}_i = C'_{ii} \tag{13}$$

With the above definition, Eq. (11) can be expressed as

$$R_2(\boldsymbol{\phi}) = \frac{C'_{rr} + 2\Sigma_{i \neq r} \epsilon_i C'_{ir} + O(\epsilon^2)}{1 + O(\epsilon^2)} \tag{14}$$

When damping is proportional, the matrix $\boldsymbol{C}'_{ir}$ is diagonal, i.e., $\boldsymbol{C}'_{ir} = 0$ for $i \neq r$. In this case, the above equation simplifies to

$$R_2(\boldsymbol{\phi}) = \frac{C'_{rr} + O(\epsilon^2)}{1 + O(\epsilon^2)} = C'_{rr}(1 + O(\epsilon^2)) \tag{15}$$

which proves the stationarity of Rayleigh quotient in the case of a proportionally damped system.

Similar proof can be constructed for $R_3(\boldsymbol{\phi})$. The equation corresponding to Eq. (15) in this case will read as

$$R_3(\boldsymbol{\phi}) = \frac{C'_{rr} + O(\epsilon^2)}{\omega_r^2 + O(\epsilon^2)} = \frac{C'_{rr}}{\omega_r^2}(1 + O(\epsilon^2)) \tag{16}$$

4 Nonproportional Damping

We consider the case of nonproportional damping wherein the damping matrix $\boldsymbol{C}$ cannot be diagonalized simultaneously with $\boldsymbol{M}$ and $\boldsymbol{K}$ matrices. Consequently, the vector $\boldsymbol{\phi}$ is not necessarily real. Vibrating systems with nonproportional damping are known to possess complex modes in general. Physically, the complex modes represent *nearly* standing waves. For systems with small dissipation, a perturbation theory originally due to Rayleigh [1] can be used to represent the complex modes in terms of the real modes of the undamped system.

According to the first order perturbation theory [12], the complex modes of a viscously damped system are related to the corresponding undamped modes by

$$z_n \approx \boldsymbol{u}_n + \imath \sum_{k \neq n} \alpha_{kn} \boldsymbol{u}_k \quad \text{where } \alpha_{kn} = \frac{\omega_n C'_{kn}}{\omega_n^2 - \omega_k^2} < 1 \tag{17}$$

The undamped modes are mass normalized i.e., $\boldsymbol{u}_n^T \boldsymbol{M} \boldsymbol{u}_n = 1$. In the above equation, $\boldsymbol{C}'$ is the damping matrix in modal coordinates, i.e., $C'_{kn} = \boldsymbol{u}_k^T \boldsymbol{C} \boldsymbol{u}_n$. The assumption in the perturbation theory is that the terms of the order α_{kn}^2 are very small and hence negligible.

When k and n refer to two adjacent modes, the coefficient α_{kn} can be related to the modal overlap factor defined as $\mu_{kn} \equiv \zeta_n \omega_n / (\omega_k - \omega_n)$ and the ratio $\gamma_{kn} = C'_{kn} / C'_{nn}$ by $\alpha_{kn} \approx (1/2)\mu_{kn}\gamma_{kn}$. Notice that γ_{kn} is a measure of the diagonal dominance of the $\boldsymbol{C}'$ matrix. μ_{kn} is a measure of the spacing of adjacent modes normalized with respect to the half power bandwidth of each mode. Thus, significantly complex modes are to be expected when the modal damping matrix is not diagonally domi-

nant and the modal overlap is not small. Unless the modal overlap factor is of the order of unity, the second and higher order powers of the α_{kn} can be safely ignored. If not, then the perturbation expansion has to be extended suitably until the imaginary part of the complex mode converges. Adequacy of the first order theory for systems with small damping has been shown in Ref. [12].

Since the complex eigenvectors z_i, $i=1\cdots n$ form the complete basis in an n dimensional complex vector space, any arbitrary complex vector $\boldsymbol{\psi}$ can be written as

$$\boldsymbol{\psi} = \sum_i c_i z_i \tag{18}$$

We select a vector close to z_r, which can be written as

$$\boldsymbol{\psi} = z_r + \sum_{i\neq r} \epsilon_i z_i, \quad |\epsilon_i| = \left|\frac{c_i}{c_r}\right| \ll 1. \tag{19}$$

We consider the first real valued Rayleigh quotient associated with the above trial vector,

$$R_1(\boldsymbol{\psi}) = \frac{\boldsymbol{\psi}^H \boldsymbol{K}\boldsymbol{\psi}}{\boldsymbol{\psi}^H \boldsymbol{M}\boldsymbol{\psi}} = \frac{z_r^H \boldsymbol{K} z_r + 2\sum_{i\neq r} \Re(\epsilon_i) z_i^H \boldsymbol{K} z_r + O(|\epsilon|^2)}{z_r^H \boldsymbol{M} z_r + 2\sum_{i\neq r} \Re(\epsilon_i) z_i^H \boldsymbol{M} z_r + O(|\epsilon|^2)} \tag{20}$$

Noting the orthogonality properties given in Eq. (9), one can deduce the following equations:

$$z_r^H \boldsymbol{M} z_r = 1 + O(\alpha^2) \tag{21}$$

and

$$z_i^H \boldsymbol{M} z_r = O(\alpha^2) \tag{22}$$

Similarly with $\boldsymbol{K}$, one can show

$$z_r^H \boldsymbol{K} z_r = \omega_r^2 + O(\alpha^2) \tag{23}$$

and

$$z_i^H \boldsymbol{K} z_r = O(\alpha^2) \tag{24}$$

Substituting Eqs. (21)–(24) in Eq. (20), one obtains

$$R_1(\boldsymbol{\psi}) = \frac{\omega_r^2 + O(\alpha^2) + O(\epsilon^2)}{1 + O(\alpha^2) + O(\epsilon^2)} \approx \omega_r^2 (1 - O(\epsilon^2)) \tag{25}$$

which proves the stationarity of $R_1(\boldsymbol{\psi})$.

We consider the second real valued Rayleigh quotient defined as follows:

$$R_2(\boldsymbol{\psi}) = \frac{z^H \boldsymbol{C} z}{z^H \boldsymbol{M} z} \tag{26}$$

Substituting Eq. (17) in the above equation leads to

$$R_2(\boldsymbol{\psi}) = \frac{\boldsymbol{\psi}^H \boldsymbol{C}\boldsymbol{\psi}}{\boldsymbol{\psi}^H \boldsymbol{M}\boldsymbol{\psi}} = \frac{z_r^H \boldsymbol{C} z_r + 2\sum_{i\neq r} \Re(\epsilon_i) z_i^H \boldsymbol{C} z_r + O(|\epsilon|^2)}{z_r^H \boldsymbol{M} z_r + 2\sum_{i\neq r} \Re(\epsilon_i) z_i^H \boldsymbol{M} z_r + O(|\epsilon|^2)} \tag{27}$$

Now $z_r^H \boldsymbol{C} z_r$ can be expanded as

$$\begin{aligned} z_r^H \boldsymbol{C} z_r &= \left[\boldsymbol{u}_r^T - \iota \sum_{k\neq r} \alpha_{kr} \boldsymbol{u}_k^T\right] \boldsymbol{C} \left[\boldsymbol{u}_r + \iota \sum_{k\neq r} \alpha_{kr} \boldsymbol{u}_k\right] \\ &= C'_{rr} - \iota \sum_{k\neq r} \alpha_{kr} [\boldsymbol{u}_k^T \boldsymbol{C} \boldsymbol{u}_r - \boldsymbol{u}_r^T \boldsymbol{C} \boldsymbol{u}_k] + O(\alpha^2) = C'_{rr} + O(\alpha^2) \end{aligned} \tag{28}$$

Note that $\boldsymbol{C}$ is assumed to be symmetric in simplifying the above equation. Similarly, one can write

$$\begin{aligned} z_i^H \boldsymbol{C} z_r &= \left[\boldsymbol{u}_i^T - \iota \sum_{k\neq i} \alpha_{ki} \boldsymbol{u}_k^T\right] \boldsymbol{C} \left[\boldsymbol{u}_r + \iota \sum_{k\neq r} \alpha_{kr} \boldsymbol{u}_k\right] \\ &= C'_{ir} - \iota \sum_{k\neq i} \alpha_{ki} C'_{kr} + \iota \sum_{k\neq r} \alpha_{kr} C'_{ik} + O(\alpha^2) \\ &= C'_{ir} + O(\alpha) + O(\alpha^2) \end{aligned} \tag{29}$$

Substituting Eqs. (21) and (22), and Eqs. (28) and (29) in Eq. (27), one obtains

$$R_2(\boldsymbol{\psi}) = \frac{C'_{rr} + 2\sum_{i\neq r} \Re(\epsilon_i) C'_{ir} + O(\epsilon) O(\alpha) + O(\epsilon^2) + O(\alpha^2)}{1 + O(\epsilon^2) + O(\alpha^2)} \tag{30}$$

It can be seen that first order changes in $\boldsymbol{\psi}$ lead to first order changes in $R_2(\boldsymbol{\psi})$. However, if the modal damping matrix is diagonally dominant, i.e.,

$$\frac{C'_{ir}}{C'_{rr}} \ll 1 \tag{31}$$

then first order changes in $\boldsymbol{\psi}$ lead to second order changes in $R_2(\boldsymbol{\psi})$. In this case, stationarity of the Rayleigh quotient is obtained.

Returning to the third quotient $R_3(\boldsymbol{\psi})$,

$$\begin{aligned} R_3(\boldsymbol{\psi}) &= \frac{\boldsymbol{\psi}^H \boldsymbol{C}\boldsymbol{\psi}}{\boldsymbol{\psi}^H \boldsymbol{K}\boldsymbol{\psi}} \\ &= \frac{C'_{rr} + 2\sum_{i\neq r} \Re(\epsilon_i) C'_{ir} + O(\epsilon) O(\alpha) + O(\epsilon^2) + O(\alpha^2)}{\omega_r^2 + O(\epsilon^2) + O(\alpha^2)} \end{aligned} \tag{32}$$

The above quotient is not stationary in general. However, when the modal damping matrix is diagonally dominant in accordance with Eq. (31), stationarity of $R_3(\boldsymbol{\psi})$ can be shown as earlier (see Sec. 3).

In the case of a complex vector $\boldsymbol{\psi}$, one is also tempted to define complex valued Rayleigh quotients by replacing the Hermitian transpose (complex conjugate transpose) with the ordinary transpose operator. The stationarity property of these complex valued quotients, however, cannot be shown. Hence, the discussion of these quotients will not be pursued any further.

5 Nonviscous Damping

In this section, we consider general linear damping models, described by convolution integrals of the generalized coordinates over appropriate kernel functions. The equation of motion of a N degrees-of-freedom nonviscously damped system is given by

$$\boldsymbol{M}\ddot{\boldsymbol{x}}(t) + \int_{-\infty}^{t} \boldsymbol{G}(t-\tau)\dot{\boldsymbol{x}}(\tau)\mathrm{d}\tau + \boldsymbol{K}\boldsymbol{x}(t) = \boldsymbol{f}(t) \tag{33}$$

Here, $\boldsymbol{G}(t)$ is a $N\times N$ matrix of kernel functions. It will be assumed that $\boldsymbol{G}(t)$ is a symmetric matrix so that reciprocity automatically holds. In the special case when $\boldsymbol{G}(t)=\boldsymbol{C}\delta(t)$, where $\delta(t)$ is the Dirac delta function and $\boldsymbol{C}$ is a $N\times N$ matrix, Eq. (33) reduces to the standard form for viscous damping.

Taking the Fourier transform of Eq. (33), the eigenvalue equation can be expressed as

$$-\lambda_n^2 \boldsymbol{M} z_n + \iota \lambda_n \boldsymbol{G}(\lambda_n) z_n + \boldsymbol{K} z_n = \boldsymbol{0} \tag{34}$$

where $\boldsymbol{G}(\lambda)$ is the Fourier transform of $\boldsymbol{G}(t)$. In general, $\boldsymbol{G}(\lambda)$ is a complex valued function of λ. For viscously damped system, $\boldsymbol{G}(\lambda)=\boldsymbol{C}$, $\forall\,\lambda$. Equation (34) is a nonlinear eigenvalue problem. In contrast with the viscously damped case, the number of eigenvalues will not necessarily be equal to $2N$, since additional eigenvalues may be introduced by the form of the functions $\boldsymbol{G}(\lambda_n)$. Wood-

house [12] and Adhikari [13] have treated this problem using a first order perturbation method assuming the damping to be small. We suppose the undamped problem has eigenvalues (natural frequencies) ω_n and eigenvectors (modes) $\boldsymbol{u}_n$. The complex eigenvalues can then be expressed as

$$\lambda_n \approx \pm \omega_n + \imath G'_{nn}(\pm \omega_n)/2 \tag{35}$$

where $G'_{kl}(\omega_n)=\boldsymbol{u}_k^T\boldsymbol{G}(\omega_n)\boldsymbol{u}_l$ is the frequency dependent damping matrix expressed in normal coordinates. Since the inverse Fourier transform of $\boldsymbol{G}(\omega)$ must be real, it must satisfy the condition $\boldsymbol{G}(-\omega)=\boldsymbol{G}(\omega)^*$, where $(\bullet)^*$ denotes complex conjugation. It follows that the eigenvalues of the generally damped system appear in pairs λ and $-\lambda^*$ (unless λ is purely imaginary). The first order approximate expression for the complex eigenvectors can be obtained in a way similar to that used for the viscously damped system (as was first given by Rayleigh [1]). The result is

$$\boldsymbol{z}_n \approx \boldsymbol{u}_n + \imath \sum_{k\neq n} \beta_{kn}\boldsymbol{u}_k \quad \text{where } \beta_{kn} = \frac{\omega_n G'_{kn}(\omega_n)}{(\omega_n^2 - \omega_k^2)} \tag{36}$$

Note that the eigenvectors also appear in complex conjugate pairs. Since, in general, $G'_{kn}(\omega_n)$ will be complex, in contrast to the viscously damped case, the real part of natural frequencies and mode shapes do not coincide with the undamped ones. Adequacy of the first order theory for systems with small damping has been investigated in Refs. [12,13].

Since the complex eigenvectors $\boldsymbol{z}_i, i=1\cdots N$ form the complete basis of an N-dimensional complex vector space, any arbitrary complex vector $\boldsymbol{\psi}$ can be expressed as

$$\boldsymbol{\psi} = \sum_i c_i \boldsymbol{z}_i \tag{37}$$

We consider a vector close to $\boldsymbol{z}_r$, which can be written as

$$\boldsymbol{\psi} = \boldsymbol{z}_r + \sum_{i\neq r} \epsilon_i \boldsymbol{z}_i, \quad |\epsilon_i| = \left|\frac{c_i}{c_r}\right| \ll 1 \tag{38}$$

Replacing the matrix $\boldsymbol{G}(\omega_r)$ with $\boldsymbol{M}$ and noting the orthogonality properties given in Eq. (9), one obtains

$$\boldsymbol{z}_r^H\boldsymbol{M}\boldsymbol{z}_r = 1 + O(|\beta|^2) \tag{39}$$

$$\boldsymbol{z}_i^H\boldsymbol{M}\boldsymbol{z}_r = O(|\beta|^2) \tag{40}$$

Similarly with $\boldsymbol{K}$, one obtains

$$\boldsymbol{z}_r^H\boldsymbol{K}\boldsymbol{z}_r = \omega_r^2 + O(|\beta|^2) \tag{41}$$

$$\boldsymbol{z}_i^H\boldsymbol{K}\boldsymbol{z}_r = O(|\beta|^2) \tag{42}$$

We consider the first Rayleigh quotient

$$R_1(\boldsymbol{\psi}) = \frac{\boldsymbol{\psi}^H\boldsymbol{K}\boldsymbol{\psi}}{\boldsymbol{\psi}^H\boldsymbol{M}\boldsymbol{\psi}} = \frac{\boldsymbol{z}_r^H\boldsymbol{K}\boldsymbol{z}_r + 2\sum_{i\neq r}\Re(\epsilon_i)\boldsymbol{z}_i^H\boldsymbol{K}\boldsymbol{z}_r + O(|\epsilon|^2)}{\boldsymbol{z}_r^H\boldsymbol{M}\boldsymbol{z}_r + 2\sum_{i\neq r}\Re(\epsilon_i)\boldsymbol{z}_i^H\boldsymbol{M}\boldsymbol{z}_r + O(|\epsilon|^2)} \tag{43}$$

Substituting Eqs. (39)–(42) in the above equation, one obtains

$$R_1(\boldsymbol{\psi}) = \frac{\omega_r^2 + O(|\beta|^2) + O(\epsilon^2)}{1 + O(|\beta|^2) + O(\epsilon^2)} \approx \omega_r^2(1 - O(\epsilon^2)) \tag{44}$$

which proves the stationarity of $R_1(\boldsymbol{\psi})$.

The second and third Rayleigh quotients involving the damping term need to be carefully defined. The difference between the viscous and the nonviscous case is that the (effective) damping matrix for the nonviscous case is complex valued and a function of frequency. Therefore, in order to define a meaningful Rayleigh quotient, we need to select a value of frequency. If we are interested in studying the stationary behavior of rth mode, then it is logical to select the frequency value as ω_r. We define the real valued Rayleigh quotient for a nonviscously damped system as

$$R_2(\boldsymbol{\psi}, \omega_r) = \frac{|\boldsymbol{\psi}^H\boldsymbol{G}(\omega_r)\boldsymbol{\psi}|}{\boldsymbol{\psi}^H\boldsymbol{M}\boldsymbol{\psi}} \tag{45}$$

For a viscously damped system $\boldsymbol{G}(\omega_r)=\boldsymbol{C}, \forall r$ and because $\boldsymbol{C}$ is a real matrix, Eq. (45) reduces to Eq. (26) as a special case. Therefore, Eq. (45) can be viewed as a generalization of the Rayleigh quotient defined in Eq. (26).

Substituting Eq. (36) in the above equation leads to

$$\begin{aligned} R_2(\boldsymbol{\psi}) &= \frac{\boldsymbol{\psi}^H\boldsymbol{G}(\omega_r)\boldsymbol{\psi}}{\boldsymbol{\psi}^H\boldsymbol{M}\boldsymbol{\psi}} \\ &= \frac{|\boldsymbol{z}_r^H\boldsymbol{G}(\omega_r)\boldsymbol{z}_r + 2\sum_{i\neq r}\Re(\epsilon_i)\boldsymbol{z}_i^H\boldsymbol{G}(\omega_r)\boldsymbol{z}_r + O(|\epsilon|^2)|}{\boldsymbol{z}_r^H\boldsymbol{M}\boldsymbol{z}_r + 2\sum_{i\neq r}\Re(\epsilon_i)\boldsymbol{z}_i^H\boldsymbol{M}\boldsymbol{z}_r + O(|\epsilon|^2)} \end{aligned} \tag{46}$$

The first term in numerator can be expressed as

$$\begin{aligned} \boldsymbol{z}_r^H\boldsymbol{G}(\omega_r)\boldsymbol{z}_r &= \left[\boldsymbol{u}_r^T - \imath\sum_{k\neq r}\beta_{kr}^*\boldsymbol{u}_k^T\right]\boldsymbol{G}(\omega_r)\left[\boldsymbol{u}_r + \imath\sum_{k\neq r}\beta_{kr}\boldsymbol{u}_k\right] \\ &= \boldsymbol{u}_r^T\boldsymbol{G}(\omega_r)\boldsymbol{u}_r - \imath\sum_{k\neq r}(\beta_{kr}^* - \beta_{kr})[\boldsymbol{u}_k^T\boldsymbol{G}(\omega_r)\boldsymbol{u}_r \\ &\quad - \boldsymbol{u}_r^T\boldsymbol{G}(\omega_r)\boldsymbol{u}_k] + O(|\beta|^2) \\ &= G'_{rr} + 2\imath\sum_{k\neq r}\Im(\beta_{kr})[\boldsymbol{u}_k^T\boldsymbol{G}(\omega_r)\boldsymbol{u}_r \\ &\quad - \boldsymbol{u}_r^T\boldsymbol{G}(\omega_r)\boldsymbol{u}_k] + O(|\beta|^2) \\ &= G'_{rr} + O(\Im(\beta)) + O(|\beta|^2) \end{aligned} \tag{47}$$

where $G'_{rr}=\boldsymbol{u}_r^T\boldsymbol{G}(\omega_r)\boldsymbol{u}_r$. Note that $\boldsymbol{G}(\omega_r)$ is assumed to be symmetric in simplifying the above equation. From the second term in the numerator of Eq. (46), one has

$$\begin{aligned} \boldsymbol{z}_i^H\boldsymbol{G}(\omega_r)\boldsymbol{z}_r &= \left[\boldsymbol{u}_i^T - \imath\sum_{k\neq i}\beta_{ki}^*\boldsymbol{u}_k^T\right]\boldsymbol{G}(\omega_r)\left[\boldsymbol{u}_r + \imath\sum_{k\neq r}\beta_{kr}\boldsymbol{u}_k\right] \\ &= \boldsymbol{u}_i^T\boldsymbol{G}(\omega_r)\boldsymbol{u}_r - \imath\sum_{k\neq i}\beta_{ki}^*\boldsymbol{u}_k^T\boldsymbol{G}(\omega_r)\boldsymbol{u}_r \\ &\quad + \imath\sum_{k\neq r}\beta_{kr}\boldsymbol{u}_i^T\boldsymbol{G}(\omega_r)\boldsymbol{u}_k + O(|\beta|^2) \\ &= G'_{ir} + O(\beta) + O(|\beta|^2) \end{aligned} \tag{48}$$

where $G'_{ir}=\boldsymbol{u}_i^T\boldsymbol{G}(\omega_r)\boldsymbol{u}_r$.

Substituting Eqs. (47), (46), (45), (44), (43), (42), (41), and (40) in Eq. (46), one obtains

$$R_2(\boldsymbol{\psi}) = \frac{|G'_{rr} + 2\sum_{i\neq r}\Re(\epsilon_i)G'_{ir} + O(\epsilon)O(\beta) + O(\epsilon^2) + O(\Im(\beta)) + O(|\beta|^2)|}{1 + O(\epsilon^2) + O(|\beta|^2)}$$
$$< \frac{|G'_{rr}| + 2\Sigma_{i\neq r}\Re(\epsilon_i)|G'_{ir}| + O(\epsilon)O(\beta) + O(\epsilon^2) + O(\Im(\beta)) + O(|\beta|^2)}{1 + O(\epsilon^2) + O(|\beta|^2)} \tag{49}$$

The last line in the above equation follows from the triangle inequality. The terms involving $O(\Im(\beta))$ are smaller than $O(|\beta|)$ terms. Moreover, for lightly nonviscous systems, the terms involving $O(\Im(\beta))$ are expected to be smaller than the $O(\Re(\beta))$ terms [14]. As a result, one expects to have the inequality

$$O(\Im(\beta)) < O(\Re(\beta)) < O(|\beta|) \tag{50}$$

From Eq. (49), it can be seen that first order changes in $\boldsymbol{\psi}$ lead to first order changes in $R_2(\boldsymbol{\psi})$. However, if the complex modal damping matrix is diagonally dominant, i.e.,

$$\frac{|G'_{ir}|}{|G'_{rr}|} \ll 1 \tag{51}$$

then first order changes in $\boldsymbol{\psi}$ lead to second order changes in $R_2(\boldsymbol{\psi})$. In this case, stationarity of the Rayleigh quotient is obtained.

Returning to the third quotient, the equation corresponding to Eq. (46) in the case of $R_3(\boldsymbol{\psi})$ is

$$R_3(\boldsymbol{\psi}) = \frac{|\boldsymbol{\psi}^H \mathbf{G}(\omega_r)\boldsymbol{\psi}|}{\boldsymbol{\psi}^H \mathbf{K}\boldsymbol{\psi}} < \frac{|G'_{rr}| + 2\sum_{i\neq r}\Re(\epsilon_i)|G'_{ir}| + O(\epsilon)O(\beta) + O(\epsilon^2) + O(\Im(\beta)) + O(|\beta|^2)}{\omega_r^2 + O(\epsilon^2) + O(|\beta|^2)} \tag{52}$$

The above quotient is not stationary. However, when the modal damping matrix is diagonally dominant in accordance with Eq. (31), stationarity of $R_3(\boldsymbol{\psi})$ holds.

6 Application of Rayleigh Quotients

In the case of a single degree of freedom system with viscous damping the three quotients simplify to $R_1=\omega^2$, $R_2=2\zeta\omega$, and $R_3=2\zeta/\omega$, where ω and ζ denote the natural frequency and the critical damping factor, respectively. The response of the system in the time domain is described by $\exp(-\zeta\omega t - \imath\omega\sqrt{1-\zeta^2}t)$. We note that R_2 governs the decay rate (or real part of the complex eigenvalue) of vibration in the time domain. The same will be true for a multidegree of freedom system, provided that its response can be decomposed into a single degree of freedom system using modal summation i.e., damping is proportional [3].

The Rayleigh quotient R_1 and its usefulness in solving the eigenvalue problem associated with the undamped system are well documented [2,3,5]. Consequent to the stationary property of R_1, a theorem originally due to Rayleigh, known as Rayleigh's principle or interlacing theorem, gives the influence of constraints. It states that the eigenvalues of the constrained system (ω') interlace with the eigenvalues of the unconstrained system (ω) such that $\omega_n \leq \omega'_n \leq \omega_{n+1}$.

Similar results follow from the stationarity of R_2 and R_3. In this context, we refer to Rayleigh's original statement in Sec. 88 of Ref. [1]: "… theorems, of importance in other branches of science, may be stated for systems such that only T and F, or only V and F, are sensible." We note that $T\equiv\mathcal{T}$, $V\equiv\mathcal{U}$, and $F\equiv\mathcal{D}$ in the notation of the present paper. Thus, stationarity of R_2 implies that the decay rates of each normal mode are stationary. The interlacing theorem would suggest that the decay rates of each normal mode also interlace when a constraint is applied. The interlacing property was discussed in Sec. 88 of Ref. [1] and a less known work of Rayleigh [15]. The present study extends these ideas to the general case of nonconservative systems with viscous or nonviscous dissipative processes.

In a viscoelastic system, one deals with elastic potentials and dissipative potentials. Stationarity of R_3 has important consequences for such problems, especially in conjunction with the interlacing theorem. A noteworthy work on applying the Rayleigh quotients to determine the elastic and material loss constants of orthotropic sheet materials was undertaken in Refs. [16,17].

Our primary aim in this work has been to show the range of applicability of stationarity principles in nonconservative viscous and nonviscous systems. Further application of these results remains to be explored in future studies.

7 Conclusions

Rayleigh quotients are revisited in the context of dissipative systems. The study of their stationarity properties leads to the following conclusions.

1. In the case of a proportionally damped viscous system, the three Rayleigh quotients associated with the damped system are stationary.
2. In the case of a nonproportionally damped system, the Rayleigh quotient involving mass and stiffness matrix is stationary while the remaining two involving damping matrix are not. Stationarity in this case is subject to the diagonal dominance of the modal damping matrix. For an arbitrarily chosen viscous damping matrix, the stationarity property does not hold true. However, this negative conclusion is to be balanced by the wide variety of practical engineering structures where the modal damping is diagonally dominant; consequently, Rayleigh quotients are stationary.
3. In the case of a nonviscously damped system, the Rayleigh quotient involving mass and stiffness matrix is still stationary while the remaining two involving the frequency dependent damping matrix are not. Stationarity in this case is subject to (a) the diagonal dominance of the absolute value of the frequency dependent complex modal damping matrix, and (b) light nonviscous damping. For an arbitrarily chosen nonviscous damping function, the stationarity property does not hold true.

Acknowledgment

A.S.P. acknowledges financial support from Cambridge Commonwealth Trust and Nehru Trust for Cambridge University through the award of Nehru Fellowship; ORS award from CVCP, UK; and Bursaries from St. John's college, Cambridge, UK. S.A. acknowledges the support of the UK Engineering and Physical Sciences Research Council (EPSRC) through the award of an Advanced Research Fellowship, Grant No. GR/T03369/01.

References

[1] Rayleigh, J. W., 1894, *The Theory of Sound*, Dover, New York, Vol. 1.
[2] Strang, G., 1988, *Linear Algebra and its Applications*, 3rd ed., Hardcourt Brace Jovanovich, Orlando, FL.
[3] Meirovitch, L., 1986, *Elements of Vibration Analysis*, 2nd ed., McGraw-Hill, New York.
[4] Newland, D. E., 1990, *Mechanical Vibration Analysis & Computation*, rep. ed., Longmans, Green, New York.
[5] Wilkinson, J. H., 1965, *The Algebraic Eigenvalue Problem*, 1st ed., Clarendon, Oxford.
[6] Courant, R., and Hilbert, D., 1989, *Methods of Mathematical Physics: Volume 1*, 1st ed., Wiley, New York.
[7] Caughey, T. K., and O'Kelly, M. E. J., 1965, "Classical Normal Modes in Damped Linear Dynamic Systems," J. Appl. Mech., **32**, pp. 583–588.
[8] Adhikari, S., 2001, "Classical Normal Modes in Non-Viscously Damped Linear Systems," AIAA J., **39**(5), pp. 978–980.
[9] Phani, A. S., 2003, "On the Necessary and Sufficient Conditions for the Existence of Classical Normal Modes in Damped Linear Dynamic Systems," J. Sound Vib., **264**(3), pp. 741–745.
[10] Adhikari, S., 2006, "Damping Modelling Using Generalized Proportional Damping," J. Sound Vib., **293**(1–2), pp. 156–170.
[11] Adhikari, S., and Phani, A., 2007, "Experimental Identification of Generalized Proportional Damping," ASME J. Vibr. Acoust., to be published.
[12] Woodhouse, J., 1998, "Linear Damping Models for Structural Vibration," J. Sound Vib., **215**(3), pp. 547–569.
[13] Adhikari, S., 2002, "Dynamics of Non-Viscously Damped Linear Systems," J. Eng. Mech., **128**(3), pp. 328–339.
[14] Adhikari, S., and Woodhouse, J., 2003, "Quantification of Non-Viscous Damping in Discrete Linear Systems," J. Sound Vib., **260**(3), pp. 499–518.
[15] Rayleigh, J. W., 1885, "A Theorem Relating to the Time-Moduli of Dissipative Systems," Report of the British Association, pp. 911–912.
[16] McIntyre, M. E., and Woodhouse, J., 1978, "The Influence of Geometry on Damping," Acustica, **39**(4), pp. 210–224.
[17] McIntyre, M. E., and Woodhouse, J., 1988, "On Measuring the Elastic and Damping Constants of Orthotropic Sheet Materials," Acta Metall., **36**(6), pp. 1397–1416.

J. Wu

K. C. Hwang

FML, Department of Engineering Mechanics,
Tsinghua University,
Beijing 100084, P. R. China

Y. Huang[1]
Department of Civil and Environmental Engineering,
and Department of Mechanical Engineering,
Northwestern University,
Evanston, IL 60208
e-mail: y-huang@northwestern.edu

J. Song
Department of Mechanical Science and Engineering,
University of Illinois,
Urbana, IL 61801

A Finite-Deformation Shell Theory for Carbon Nanotubes Based on the Interatomic Potential—Part I: Basic Theory

A finite-deformation shell theory for carbon nanotubes (CNTs) is established directly from the interatomic potential for carbon to account for the effect of bending and curvature. Its constitutive relation accounts for the nonlinear multibody atomistic interactions and therefore can model the important effect of CNT chirality and radius. The equilibrium equations and boundary conditions are obtained for the symmetric stresses and bending moments, which are different from many existing shell theories that involve asymmetric stress and bending moments. The theory is used in Part II of this paper to study the instability of carbon nanotubes subjected to different loadings.
[DOI: 10.1115/1.2965366]

Keywords: shell theory, carbon nanotube, interatomic potential, finite deformation

1 Introduction

A single-wall carbon nanotube (CNT) is a cylinder of a single layer of carbon atoms. Its diameter is on the order of 1 nm, and its length may reach 100 μm or longer. It displays superior mechanical properties [1–3], such as yield strain more than 4% [4] and Young's modulus on the order of 1 TPa reported in experiments [5–8] and atomistic studies [4,9–22].

There exist continuum theories for CNTs based on the interatomic potential for carbon. Arroyo and Belytschko [23], Zhang et al. [24,25], and Yang and E [26] used a modified Cauchy–Born rule [27,28] to incorporate the interatomic potential into a continuum framework. Arroyo and Belytschko [23] accounted for the effect of CNT curvature via an exponential mapping and studied CNTs under various loadings. Zhang et al. [24] obtained the CNT elastic modulus and tensile stress-strain curve and found good agreements with molecular dynamics simulations. Zhang et al. [25] studied the instability of CNT under tension and determined the critical strain for defect nucleation. Yang and E [26] studied the higher-order, local, and exponential Cauchy–Born rules for CNTs and used the local Cauchy–Born rule to account for some effects of CNT curvature via the Laplacian of displacement.

The continuum theory based on the interatomic potential [24,25], however, is a membrane theory that does not account for the effect of bending stiffness. It is therefore not applicable to CNTs subject to bending nor to the instability analysis of CNTs under compression or torsion because the critical buckling loads are governed by the bending stiffness.

The purpose of this paper is to establish a shell theory directly from the interatomic potential and the CNT atomic structure to account for the nonlinear multibody atomistic interactions. It is a finite-deformation shell theory for CNTs since CNTs may undergo large deformation and rotation. The paper consists of two parts: the basic theory in Part I and the instability analyses for CNT subject to tension, compression, external or internal pressure, and torsion in Part II. Part I of this paper is outlined as follows. Based on the Brenner potential for carbon [29] and its second-generation potential [30] summarized in the Appendix A, Wu et al. [31] established the constitutive model for CNTs to account for the effect of bending and curvature. The constitutive model is briefly summarized in Sec. 2. The equilibrium equations for this finite-deformation shell theory based on the interatomic potential are given in Sec. 3. They involve the symmetric stresses and bending moments only and are therefore different from the commonly used shell theories involving nonsymmetric quantities. Some examples illustrating the finite-deformation shell theory based on the interatomic potential are given in Sec. 4.

2 Constitutive Model for the Finite-Deformation Shell Theory Based on the Interatomic Potential

Wu et al. [31] established the constitutive model for CNTs based on the Brenner potential for carbon [29] or its second-generation potential [30]. The constitutive model accounts for the effect of bending and curvature and is summarized in this section.

2.1 Strains and Curvatures. Let $\boldsymbol{P}(\theta,Z)$ denote a point on the CNT of radius R prior to deformation (Fig. 1), where θ and Z are the cylindrical coordinates. A nearby point $\boldsymbol{P}+\Delta\boldsymbol{P}$ with the coordinates $\theta+\Delta\theta$ and $Z+\Delta Z$ can be expanded in the Taylor series with respect to $\boldsymbol{P}$ as

$$\Delta\boldsymbol{P}=\left[\Delta\theta-\frac{1}{6}(\Delta\theta)^3\right]R\boldsymbol{e}_\theta+\Delta Z\boldsymbol{e}_Z-\frac{R}{2}(\Delta\theta)^2\boldsymbol{e}_R \tag{2.1}$$

where the terms on the order of $(\Delta\theta)^4$ and $(\Delta Z)^4$ or higher are neglected, and $\boldsymbol{e}_R,\boldsymbol{e}_\theta$ and $\boldsymbol{e}_Z$ are the unit vectors in the cylindrical coordinates. The length of $\Delta\boldsymbol{P}$ is given by

$$|\Delta\boldsymbol{P}|^2=R^2(\Delta\theta)^2+(\Delta Z)^2-\frac{R^2}{12}(\Delta\theta)^4 \tag{2.2}$$

The angle φ between the two vectors $\Delta\boldsymbol{P}_{(1)}$ and $\Delta\boldsymbol{P}_{(2)}$ is obtained from $\cos\varphi=(\Delta\boldsymbol{P}_{(1)}\cdot\Delta\boldsymbol{P}_{(2)})/(|\Delta\boldsymbol{P}_{(1)}||\Delta\boldsymbol{P}_{(2)}|)$, where

$$\Delta\boldsymbol{P}_{(1)}\cdot\Delta\boldsymbol{P}_{(2)}=R^2\Delta\theta_{(1)}\Delta\theta_{(2)}+\Delta Z_{(1)}\Delta Z_{(2)}-\tfrac{1}{12}R^2\Delta\theta_{(1)}\Delta\theta_{(2)}\times[2(\Delta\theta_{(2)})^2+2(\Delta\theta_{(1)})^2-3\Delta\theta_{(1)}\Delta\theta_{(2)}] \tag{2.3}$$

[1]Corresponding author.

Contributed by the Applied Mechanics Division of ASME for publication in the JOURNAL OF APPLIED MECHANICS. Manuscript received June 16, 2007; final manuscript received May 10, 2008; published online August 20, 2008. Review conducted by Robert M. McMeeking.

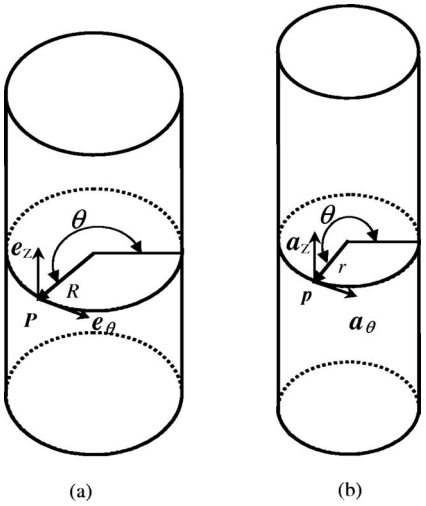

Fig. 1 A schematic of (*a*) initial undeformed configuration and (*b*) deformed configuration of carbon nanotubes

The point $\boldsymbol{P}(\theta,Z)$ moves to $\boldsymbol{p}(\theta,Z)=\boldsymbol{P}(\theta,Z)+\boldsymbol{U}(\theta,Z)$ after the deformation (Fig. 1), where $\boldsymbol{U}(\theta,Z)$ is the displacement vector. Similarly $\boldsymbol{P}+\Delta\boldsymbol{P}$ moves to $\boldsymbol{p}+\Delta\boldsymbol{p}$. The base vectors for the deformed CNT are

$$\boldsymbol{a}_\theta=\frac{1}{R}\frac{\partial\boldsymbol{p}}{\partial\theta}=\boldsymbol{e}_\theta+\frac{1}{R}\frac{\partial\boldsymbol{U}}{\partial\theta},\quad \boldsymbol{a}_Z=\frac{\partial\boldsymbol{p}}{\partial Z}=\boldsymbol{e}_Z+\frac{\partial\boldsymbol{U}}{\partial Z} \tag{2.4}$$

The unit normal of the deformed CNT is $\boldsymbol{n}=(\boldsymbol{a}_\theta\times\boldsymbol{a}_Z)/(|\boldsymbol{a}_\theta\times\boldsymbol{a}_Z|)$.

The deformed CNT has the coefficients of first fundamental form

$$a_{\alpha\beta}=\boldsymbol{a}_\alpha\cdot\boldsymbol{a}_\beta\quad(\alpha,\beta=\theta,Z) \tag{2.5}$$

and second fundamental form

$$b_{\theta\theta}=\boldsymbol{n}\cdot\frac{1}{R^2}\frac{\partial^2\boldsymbol{p}}{\partial\theta^2},\quad b_{ZZ}=\boldsymbol{n}\cdot\frac{\partial^2\boldsymbol{p}}{\partial Z^2},\quad b_{\theta Z}=\boldsymbol{n}\cdot\frac{1}{R}\frac{\partial^2\boldsymbol{p}}{\partial\theta\,\partial Z} \tag{2.6}$$

The length of $\Delta\boldsymbol{p}$, which is needed in the interatomic potential in Appendix A, is given by

$$|\Delta\boldsymbol{p}|^2=a_{\alpha\beta}\Delta\xi^\alpha\Delta\xi^\beta-\tfrac{1}{12}(b_{\alpha\beta}\Delta\xi^\alpha\Delta\xi^\beta)^2 \tag{2.7}$$

where $\Delta\xi^\theta=R\Delta\theta$ and $\Delta\xi^Z=\Delta Z$. The angle φ between vectors $\Delta\boldsymbol{p}_{(1)}$ and $\Delta\boldsymbol{p}_{(2)}$ becomes $\cos\varphi=(\Delta\boldsymbol{p}_{(1)}\cdot\Delta\boldsymbol{p}_{(2)})/(|\Delta\boldsymbol{p}_{(1)}||\Delta\boldsymbol{p}_{(2)}|)$, and

$$\Delta\boldsymbol{p}_{(1)}\cdot\Delta\boldsymbol{p}_{(2)}=a_{\alpha\beta}\Delta\xi^\alpha_{(1)}\Delta\xi^\beta_{(2)}-\frac{1}{12}b_{\alpha\beta}b_{\gamma\lambda}\Delta\xi^\alpha_{(1)}\Delta\xi^\lambda_{(2)}(2\Delta\xi^\beta_{(2)}\Delta\xi^\gamma_{(2)}+2\Delta\xi^\beta_{(1)}\Delta\xi^\gamma_{(1)}-3\Delta\xi^\beta_{(1)}\Delta\xi^\gamma_{(2)}) \tag{2.8}$$

The components of the Green strain tensor $\boldsymbol{E}$ are half of the difference between $a_{\alpha\beta}$ and their counterpart $\delta_{\alpha\beta}$ (Kronecker delta) for the underformed CNT, i.e.,

$$E_{\theta\theta}=\tfrac{1}{2}(a_{\theta\theta}-1),\quad E_{ZZ}=\tfrac{1}{2}(a_{ZZ}-1),\quad E_{\theta Z}=E_{Z\theta}=\tfrac{1}{2}a_{\theta Z} \tag{2.9}$$

The components of the curvature tensor $\boldsymbol{K}$ are the difference between $b_{\alpha\beta}$ and their counterpart for the undeformed CNT, i.e.,

$$K_{\theta\theta}=b_{\theta\theta}+\frac{1}{R},\quad K_{ZZ}=b_{ZZ},\quad K_{\theta Z}=K_{Z\theta}=b_{\theta Z} \tag{2.10}$$

2.2 Strain Energy Density. The Cauchy–Born rule [32] equates the continuum strain energy to the energy in atomic bonds and ensures the equilibrium of atoms for a simple Bravais lattice [27,28]. A CNT, however, is a Bravais multilattice whose hexagonal lattice structure can be decomposed to two triangular sublattices as marked by the open and solid circles in Fig. 2(*a*). Each sublattice is a simple Bravais lattice and follows the Cauchy–Born rule. The two sublattices, however, may undergo a shift defined by vector $\boldsymbol{\eta}$, as shown in Fig. 2(*b*). The shift vector $\boldsymbol{\eta}$ is the same for all atoms between the two sublattices and is to be determined in order to minimize energy and therefore reach equilibrium of atoms [23–25]. The vector $\Delta\boldsymbol{P}$ between the two atoms from different sublattices has the coordinates $R\Delta\theta$ and ΔZ on the underformed CNT. After deformation $\Delta\boldsymbol{P}$ becomes $\Delta\boldsymbol{p}$ on the deformed CNT and has the new coordinates

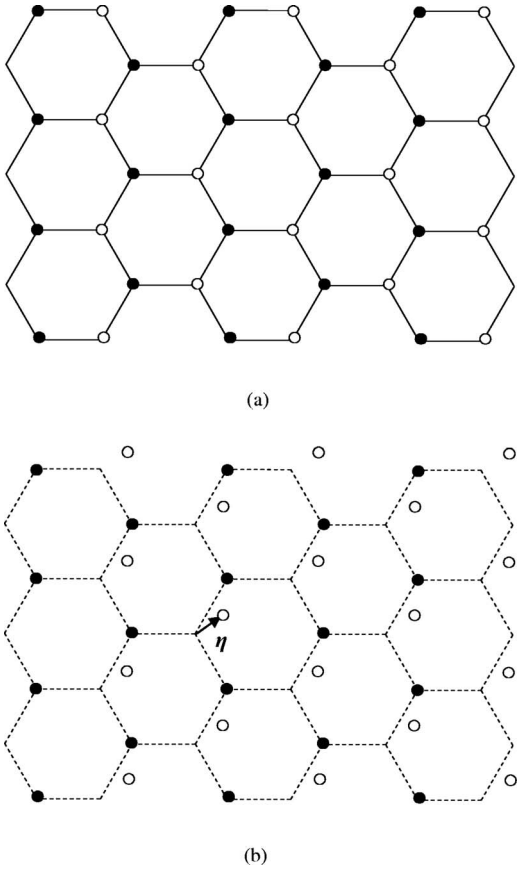

Fig. 2 (*a*) The decomposition of a hexagonal lattice to two triangular sublattices. (*b*) A shift vector η between the two sublattices to ensure the equilibrium of atoms.

$$R\Delta\bar{\theta}=R\Delta\theta+\eta_\theta,\quad \Delta\bar{Z}=\Delta Z+\eta_Z \tag{2.11}$$

The bond length and angle can then be obtained from Eqs. (2.7) and (2.8) by replacing $R\Delta\theta$ and ΔZ with $R\Delta\bar{\theta}$ and $\Delta\bar{Z}$, respectively, i.e.,

$$|\Delta\boldsymbol{p}|^2=a_{\alpha\beta}\Delta\bar{\xi}^\alpha\Delta\bar{\xi}^\beta-\tfrac{1}{12}(b_{\alpha\beta}\Delta\bar{\xi}^\alpha\Delta\bar{\xi}^\beta)^2 \tag{2.12}$$

$$\cos\varphi=\frac{\Delta\boldsymbol{p}_{(1)}\cdot\Delta\boldsymbol{p}_{(2)}}{|\Delta\boldsymbol{p}_{(1)}||\Delta\boldsymbol{p}_{(2)}|},\quad\text{and}$$

$$\Delta\boldsymbol{p}_{(1)}\cdot\Delta\boldsymbol{p}_{(2)}=a_{\alpha\beta}\Delta\bar{\xi}^\alpha_{(1)}\Delta\bar{\xi}^\beta_{(2)}-\tfrac{1}{12}b_{\alpha\beta}b_{\gamma\lambda}\Delta\bar{\xi}^\alpha_{(1)}\Delta\bar{\xi}^\lambda_{(2)}(2\Delta\bar{\xi}^\beta_{(2)}\Delta\bar{\xi}^\gamma_{(2)}+2\Delta\bar{\xi}^\beta_{(1)}\Delta\bar{\xi}^\gamma_{(1)}-3\Delta\bar{\xi}^\beta_{(1)}\Delta\bar{\xi}^\gamma_{(2)}) \tag{2.13}$$

where $\Delta\bar{\xi}^\theta=R\Delta\bar{\theta}$ and $\Delta\bar{\xi}^Z=\Delta\bar{Z}$.

The bond length and angle now depend on the Green strain, curvature, and shift vector,

$$r_{ij} = r_{ij}(\boldsymbol{E},\boldsymbol{K},\boldsymbol{\eta}), \quad \varphi_{ijk} = \varphi_{ijk}(\boldsymbol{E},\boldsymbol{K},\boldsymbol{\eta}) \tag{2.14}$$

and so does the bond energy $V=V(r_{ij};\ \varphi_{ijk}, k\neq i,j)$ in Appendix A. The strain energy density W is obtained from the sum of energy in three bonds for each atom via the modified Born rule [24,25]

$$W(\boldsymbol{E},\boldsymbol{K},\boldsymbol{\eta}) = \frac{1}{2}\frac{\sum_{1\le j\le 3} V(r_{ij};\varphi_{ijk}, k\neq i,j)}{S_0} \tag{2.15}$$

where the factor 1/2 results from the equal partition of bond energy between atoms, and $S_0=R\int\int d\theta dZ$ is the average area per atom. The shift vector $\boldsymbol{\eta}=\boldsymbol{\eta}(\boldsymbol{E},\boldsymbol{K})$ is determined in term of the Green strain $\boldsymbol{E}$ and curvature $\boldsymbol{K}$ by minimizing W,

$$\frac{\partial W}{\partial \eta_\theta} = \frac{\partial W}{\partial \eta_Z} = 0 \tag{2.16}$$

2.3 Stresses and Bending Moments. The second Piola–Kirchhoff stress $\boldsymbol{T}$ is the work conjugate of the Green strain $\boldsymbol{E}$,

$$\boldsymbol{T} = \frac{DW}{D\boldsymbol{E}} = \frac{\partial W}{\partial \boldsymbol{E}} + \frac{\partial W}{\partial \boldsymbol{\eta}}\cdot\frac{\partial \boldsymbol{\eta}}{\partial \boldsymbol{E}} = \frac{\partial W}{\partial \boldsymbol{E}} \tag{2.17}$$

where $\partial W/\partial\boldsymbol{\eta}=0$ in Eq. (2.16) has been used, and $\boldsymbol{T}$ has the contravariant components. However, for the cylindrical coordinates of the underformed CNT, the contravariant and covariant components become the same such that $\boldsymbol{T}$ can be written as $\boldsymbol{T}=T_{\theta\theta}\boldsymbol{e}_\theta\boldsymbol{e}_\theta + T_{ZZ}\boldsymbol{e}_Z\boldsymbol{e}_Z + T_{\theta Z}(\boldsymbol{e}_\theta\boldsymbol{e}_Z+\boldsymbol{e}_Z\boldsymbol{e}_\theta)$ and is symmetric. The bending moment tensor is the work conjugate of the curvature $\boldsymbol{K}$,

$$\boldsymbol{M} = \frac{DW}{D\boldsymbol{K}} = \frac{\partial W}{\partial \boldsymbol{K}} + \frac{\partial W}{\partial \boldsymbol{\eta}}\cdot\frac{\partial \boldsymbol{\eta}}{\partial \boldsymbol{K}} = \frac{\partial W}{\partial \boldsymbol{K}} \tag{2.18}$$

which can be expressed as $\boldsymbol{M}=M_{\theta\theta}\boldsymbol{e}_\theta\boldsymbol{e}_\theta + M_{ZZ}\boldsymbol{e}_Z\boldsymbol{e}_Z + M_{\theta Z}(\boldsymbol{e}_\theta\boldsymbol{e}_Z + \boldsymbol{e}_Z\boldsymbol{e}_\theta)$ and is also symmetric. The symmetric stresses and bending moments are different from those in many existing shell theories that involve asymmetric stress and bending moments and even assume the constitutive relations for the asymmetric parts. However, the symmetric stress and bending moment tensors are consistent with the finite-deformation shell theories of Sanders [33], Koiter [34], and Niordson [35].

The increments of stress $\dot{\boldsymbol{T}}$ and bending moment $\dot{\boldsymbol{M}}$ are related to the increments of strain $\dot{\boldsymbol{E}}$ and curvature $\dot{\boldsymbol{K}}$ by

$$\dot{\boldsymbol{T}} = \boldsymbol{L}:\dot{\boldsymbol{E}} + \boldsymbol{H}:\dot{\boldsymbol{K}}, \quad \dot{\boldsymbol{M}} = \boldsymbol{H}^{\mathrm{T}}:\dot{\boldsymbol{E}} + \boldsymbol{S}:\dot{\boldsymbol{K}} \tag{2.19}$$

where $\boldsymbol{L}=\boldsymbol{L}^{\mathrm{T}}$ and $\boldsymbol{S}=\boldsymbol{S}^{\mathrm{T}}$ are the symmetric tensile and bending rigidity tensors given by

$$\boldsymbol{L} = \frac{D}{D\boldsymbol{E}}\left(\frac{\partial W}{\partial \boldsymbol{E}}\right) = \frac{\partial^2 W}{\partial \boldsymbol{E}\,\partial \boldsymbol{E}} - \frac{\partial^2 W}{\partial \boldsymbol{E}\,\partial \boldsymbol{\eta}}\cdot\left(\frac{\partial^2 W}{\partial \boldsymbol{\eta}\,\partial \boldsymbol{\eta}}\right)^{-1}\cdot\frac{\partial^2 W}{\partial \boldsymbol{\eta}\,\partial \boldsymbol{E}}$$

$$\boldsymbol{S} = \frac{D}{D\boldsymbol{K}}\left(\frac{\partial W}{\partial \boldsymbol{K}}\right) = \frac{\partial^2 W}{\partial \boldsymbol{K}\,\partial \boldsymbol{K}} - \frac{\partial^2 W}{\partial \boldsymbol{K}\,\partial \boldsymbol{\eta}}\cdot\left(\frac{\partial^2 W}{\partial \boldsymbol{\eta}\,\partial \boldsymbol{\eta}}\right)^{-1}\cdot\frac{\partial^2 W}{\partial \boldsymbol{\eta}\,\partial \boldsymbol{K}} \tag{2.20}$$

and $\boldsymbol{H}$ and $\boldsymbol{H}^{\mathrm{T}}$ are the coupled tensile/bending rigidity tensors given by

$$\boldsymbol{H} = \frac{D}{D\boldsymbol{K}}\left(\frac{\partial W}{\partial \boldsymbol{E}}\right) = \frac{\partial^2 W}{\partial \boldsymbol{E}\,\partial \boldsymbol{K}} - \frac{\partial^2 W}{\partial \boldsymbol{E}\,\partial \boldsymbol{\eta}}\cdot\left(\frac{\partial^2 W}{\partial \boldsymbol{\eta}\,\partial \boldsymbol{\eta}}\right)^{-1}\cdot\frac{\partial^2 W}{\partial \boldsymbol{\eta}\,\partial \boldsymbol{K}}$$

$$\boldsymbol{H}^{\mathrm{T}} = \frac{D}{D\boldsymbol{E}}\left(\frac{\partial W}{\partial \boldsymbol{K}}\right) = \frac{\partial^2 W}{\partial \boldsymbol{K}\,\partial \boldsymbol{E}} - \frac{\partial^2 W}{\partial \boldsymbol{K}\,\partial \boldsymbol{\eta}}\cdot\left(\frac{\partial^2 W}{\partial \boldsymbol{\eta}\,\partial \boldsymbol{\eta}}\right)^{-1}\cdot\frac{\partial^2 W}{\partial \boldsymbol{\eta}\,\partial \boldsymbol{E}} \tag{2.21}$$

3 Equilibrium Equations for the Symmetric Stress and Bending Moment

The Cauchy stress tensor $\boldsymbol{t}$, defined for the deformed configuration, is related to the second Piola–Kirchhoff stress $\boldsymbol{T}$ by

$$\boldsymbol{t} = \frac{1}{J}\mathring{\boldsymbol{F}}\cdot\boldsymbol{T}\cdot\mathring{\boldsymbol{F}}^{\mathrm{T}} \tag{3.1}$$

where

$$\mathring{\boldsymbol{F}} = \boldsymbol{a}_\theta\boldsymbol{e}_\theta + \boldsymbol{a}_Z\boldsymbol{e}_Z \tag{3.2}$$

is the deformation gradient tensor, which maps an infinitesimal element $d\boldsymbol{P}=Rd\theta\boldsymbol{e}_\theta+dZ\boldsymbol{e}_Z$ of the undeformed CNT to $d\boldsymbol{p}=\mathring{\boldsymbol{F}}\cdot d\boldsymbol{P} = Rd\theta\boldsymbol{a}_\theta+dZ\boldsymbol{a}_Z$ of the deformed CNT, $\boldsymbol{a}_\theta$ and $\boldsymbol{a}_Z$ are the base vectors for the deformed CNT given in Eq. (2.4), $\mathring{\boldsymbol{F}}^{\mathrm{T}}=\boldsymbol{e}_\theta\boldsymbol{a}_\theta+\boldsymbol{e}_Z\boldsymbol{a}_Z$ and $J=\sqrt{a_{\theta\theta}a_{ZZ}-(a_{\theta Z})^2}$ in Eq. (3.1) are the transpose and Jacobian of $\mathring{\boldsymbol{F}}$, respectively. The Cauchy stress is then obtained from Eqs. (3.1) and (3.2) as $\boldsymbol{t}=1/J[T_{\theta\theta}\boldsymbol{a}_\theta\boldsymbol{a}_\theta+T_{ZZ}\boldsymbol{a}_Z\boldsymbol{a}_Z+T_{\theta Z}(\boldsymbol{a}_\theta\boldsymbol{a}_Z+\boldsymbol{a}_Z\boldsymbol{a}_\theta)]$, which has the same components $T_{\alpha\beta}$ as the second Piola–Kirchhoff stress (except the factor $1/J$) but different base vectors.

Similarly, the bending moment tensor $\boldsymbol{m}$ for the deformed configuration is

$$\boldsymbol{m} = \frac{1}{J}\mathring{\boldsymbol{F}}\cdot\boldsymbol{M}\cdot\mathring{\boldsymbol{F}}^{\mathrm{T}} \tag{3.3}$$

which gives $\boldsymbol{m}=1/J[M_{\theta\theta}\boldsymbol{a}_\theta\boldsymbol{a}_\theta+M_{ZZ}\boldsymbol{a}_Z\boldsymbol{a}_Z+M_{\theta Z}(\boldsymbol{a}_\theta\boldsymbol{a}_Z+\boldsymbol{a}_Z\boldsymbol{a}_\theta)]$, and has the same components as the bending moment tensor $\boldsymbol{M}$ (except the factor $1/J$) but different base vectors. The relations among $\boldsymbol{t}$, $\boldsymbol{m}$, and asymmetric stress and moment tensors in most shell theories are discussed in the Appendix B.

The equilibrium equations in the finite-deformation shell theory can be written in terms of $\boldsymbol{t}$ and $\boldsymbol{m}$ as [33–35]

$$t^{\alpha\beta}_{;\beta} + 2b^{\alpha}_{\cdot\beta}m^{\beta\lambda}_{;\lambda} + b^{\alpha}_{\cdot\lambda;\beta}m^{\lambda\beta} + \bar{\mathcal{X}}^{\alpha} = 0 \quad (\alpha=\theta,Z) \tag{3.4}$$

$$b_{\alpha\beta}t^{\alpha\beta} + b_{\alpha\beta}b^{\beta}_{\cdot\lambda}m^{\alpha\lambda} - m^{\beta\lambda}_{;\beta\lambda} + \bar{\mathcal{X}}^{n} = 0 \tag{3.5}$$

where ";" are the covariant derivatives given in Appendix B; $\bar{\mathcal{X}}^{\alpha}$ and $\bar{\mathcal{X}}^{n}$ are the effective in-surface and out-of-surface area forces (applied force per unit area), respectively, $\boldsymbol{n}$ is the unit normal of the deformed CNT surface; $t^{\alpha\beta}$ are the contravariant components of $\boldsymbol{t}$ and are proportional to the (contravariant) components of $\boldsymbol{T}$, $t^{\theta\theta}=T_{\theta\theta}/J$, $t^{ZZ}=T_{ZZ}/J$, and $t^{\theta Z}=t^{Z\theta}=T_{\theta Z}/J$; similarly the contravariant components of $\boldsymbol{m}$ are $m^{\theta\theta}=M_{\theta\theta}/J$, $m^{ZZ}=M_{ZZ}/J$, and $m^{\theta Z}=m^{Z\theta}=M_{\theta Z}/J$; $b_{\alpha\beta}$, defined in Eq. (2.6), are related to the curvatures via Eq. (2.10), $b^{\alpha}_{\cdot\beta}=(a^{-1})_{\alpha\lambda}b_{\lambda\beta}$, and $(a^{-1})_{\alpha\lambda}$ is the inverse of $a_{\alpha\lambda}$.

The traction boundary conditions are [35]

$$(t^{\alpha\beta} + 2b^{\alpha}_{\cdot\lambda}m^{\lambda\beta})\upsilon_\beta = \bar{t}^{\alpha} + b^{\alpha}_{\cdot\lambda}\bar{m}^{\lambda} \quad (\alpha=\theta,Z) \tag{3.6}$$

$$m^{\alpha\beta}_{;\alpha}\upsilon_\beta + \frac{\partial}{\partial s}(m^{\alpha\beta}\upsilon_\alpha s_\beta) = -\bar{t}^{n} + \frac{\partial \bar{m}_T}{\partial s} \tag{3.7}$$

$$m^{\alpha\beta}\upsilon_\alpha\upsilon_\beta = \bar{m}_B \tag{3.8}$$

where $\boldsymbol{s}$ is the unit vector along the boundary, $\boldsymbol{\upsilon}=\boldsymbol{s}\times\boldsymbol{n}$ is the in-surface unit normal, $\bar{t}^{\alpha}$ and $\bar{t}^{n}$ are the prescribed effective in-surface and out-of-surface tractions, and the prescribed moment on the boundary is $\bar{\boldsymbol{m}}=\bar{m}_T\boldsymbol{s}+\bar{m}_B\boldsymbol{\upsilon}$ with $\bar{m}_B$ and $\bar{m}_T$ being the prescribed bending moment and torque, respectively.

The incremental equilibrium equations, which are needed in the instability analysis in Part II of this paper, are

$$\frac{d}{dt}(t^{\alpha\beta}_{;\beta}) + 2\frac{d}{dt}(b^{\alpha}_{\cdot\beta}m^{\beta\lambda}_{;\lambda}) + \frac{d}{dt}(b^{\alpha}_{\cdot\lambda;\beta}m^{\lambda\beta}) + \frac{d\bar{\mathcal{X}}^{\alpha}}{dt} = 0 \quad (\alpha=\theta,Z) \tag{3.9}$$

$$\frac{d}{dt}(b_{\alpha\beta}t^{\alpha\beta}) + \frac{d}{dt}(b_{\alpha\beta}b^{\beta}_{\lambda}m^{\alpha\lambda}) - \frac{d}{dt}(m^{\beta\lambda}_{;\lambda\beta}) + \frac{d\bar{\mathcal{X}}^n}{dt} = 0 \quad (3.10)$$

4 Analytical Solutions

We present the analytical solutions for a CNT of radius R subject to axial strain $\varepsilon_{\text{axial}}$, lateral strain $\varepsilon_{\text{lateral}}$ (circumferential direction), and twist κ (rotation per unit length). Such solutions pave the way for the instability analysis in Part II of this paper.

The deformed CNT remains to have circular cross section under such loadings. A point $\boldsymbol{P}=R\boldsymbol{e}_R+Z\boldsymbol{e}_Z$ prior to deformation moves to $\boldsymbol{p}=R(1+\varepsilon_{\text{lateral}})(\boldsymbol{e}_R\cos\kappa Z+\boldsymbol{e}_\theta\sin\kappa Z)+Z(1+\varepsilon_{\text{axial}})\boldsymbol{e}_Z$. The base vectors for the deformed configuration are

$$\boldsymbol{a}_\theta = \frac{1}{R}\frac{\partial \boldsymbol{p}}{\partial\theta} = (1+\varepsilon_{\text{lateral}})(-\boldsymbol{e}_R\sin\kappa Z+\boldsymbol{e}_\theta\cos\kappa Z)$$

$$\boldsymbol{a}_Z = \frac{\partial \boldsymbol{p}}{\partial Z} = \kappa R(1+\varepsilon_{\text{lateral}})(-\boldsymbol{e}_R\sin\kappa Z+\boldsymbol{e}_\theta\cos\kappa Z)+(1+\varepsilon_{\text{axial}})\boldsymbol{e}_Z \quad (4.1)$$

The coefficients of first and second fundamental forms are

$$a_{\theta\theta}=(1+\varepsilon_{\text{lateral}})^2,\quad a_{ZZ}=\kappa^2R^2(1+\varepsilon_{\text{lateral}})^2+(1+\varepsilon_{\text{axial}})^2,$$

$$a_{\theta Z}=\kappa R(1+\varepsilon_{\text{lateral}})^2,\quad b_{\theta\theta}=-\frac{1+\varepsilon_{\text{lateral}}}{R},$$

$$b_{ZZ}=-\kappa^2R(1+\varepsilon_{\text{lateral}}),\quad b_{\theta Z}=-\kappa(1+\varepsilon_{\text{lateral}}) \quad (4.2)$$

The deformation gradient becomes

$$\mathring{\boldsymbol{F}} = (1+\varepsilon_{\text{lateral}})(-\boldsymbol{e}_R\boldsymbol{e}_\theta\sin\kappa Z+\boldsymbol{e}_\theta\boldsymbol{e}_\theta\cos\kappa Z)+\kappa R(1+\varepsilon_{\text{lateral}})\times(-\boldsymbol{e}_R\boldsymbol{e}_Z\sin\kappa Z+\boldsymbol{e}_\theta\boldsymbol{e}_Z\cos\kappa Z)+(1+\varepsilon_{\text{axial}})\boldsymbol{e}_Z\boldsymbol{e}_Z \quad (4.3)$$

which gives the Jacobian $J=(1+\varepsilon_{\text{lateral}})(1+\varepsilon_{\text{axial}})$. The components of the Green strain are

$$E_{\theta\theta}=\varepsilon_{\text{lateral}}+\frac{1}{2}\varepsilon^2_{\text{lateral}}$$

$$E_{ZZ}=\varepsilon_{\text{axial}}+\frac{1}{2}\varepsilon^2_{\text{axial}}+\frac{1}{2}\kappa^2R^2(1+\varepsilon_{\text{lateral}})^2$$

$$E_{\theta Z}=\frac{1}{2}\kappa R(1+\varepsilon_{\text{lateral}})^2 \quad (4.4)$$

The components of the curvature tensor are

$$K_{\theta\theta}=-\frac{\varepsilon_{\text{lateral}}}{R},\quad K_{ZZ}=-\kappa^2R(1+\varepsilon_{\text{lateral}}),\quad K_{\theta Z}=-\kappa(1+\varepsilon_{\text{lateral}}) \quad (4.5)$$

The second Piola–Kirchhoff stress $\boldsymbol{T}$ and bending moment $\boldsymbol{M}$ are obtained from Eqs. (2.17) and (2.18), respectively. The Cauchy stress $\boldsymbol{t}$ and bending moment $\boldsymbol{m}$ are then obtained from Eqs. (3.1) and (3.3). The in-surface equilibrium Eq. (3.4) are satisfied automatically, while the out-of-surface equilibrium Eq. (3.5) gives the lateral pressure (out-of-surface area force) $\bar{\mathcal{X}}^n=-b_{\alpha\beta}t^{\alpha\beta}-b_{\alpha\beta}b^{\beta}_{;\lambda}m^{\alpha\lambda}$. The boundary conditions in Eqs. (3.6)–(3.8) give the stress and bending moment tractions at the end of the CNT as

$$\bar{t}^\theta-\frac{\bar{m}^\theta}{(1+\varepsilon_{\text{lateral}})R}=\frac{T_{\theta Z}+\kappa RT_{ZZ}}{1+\varepsilon_{\text{lateral}}}-\frac{2M_{\theta Z}+2\kappa RM_{ZZ}}{(1+\varepsilon_{\text{lateral}})^2R} \quad (4.6)$$

$$\bar{t}^Z=\frac{T_{ZZ}}{1+\varepsilon_{\text{lateral}}} \quad (4.7)$$

$$\bar{t}^n=0 \quad (4.8)$$

$$\bar{m}_B=\frac{1}{(1+\varepsilon_{\text{lateral}})(1+\varepsilon_{\text{axial}})}M_{ZZ} \quad (4.9)$$

These give the net force and torque of the CNT as $2\pi R(1+\varepsilon_{\text{lateral}})(1+\varepsilon_{\text{axial}})\bar{t}^Z$ and $2\pi R^2(1+\varepsilon_{\text{lateral}})^3[\bar{t}^\theta-(1+\varepsilon_{\text{lateral}})^{-1}R^{-1}\times\bar{m}^\theta]$, respectively.

5 Concluding Remarks and Discussion

A finite-deformation shell theory for CNTs is established directly from the interatomic potential for carbon in this paper. Its constitutive relation accounts for the nonlinear multibody atomistic interactions and therefore can model the important effect of CNT chirality and radius. The equilibrium equations and boundary conditions are established for the symmetric stresses and bending moments, which are different from many existing shell theories that involve asymmetric stress and bending moments. An analytical solution is given for the CNT subjected to the axial strain, lateral strain, and twist.

The theory accounts for the effect of finite deformation for the following reasons:

(i) many CNTs undergo large rotation and deformation in their applications;
(ii) finite deformation is important in the instability analysis of CNTs, as to be studied in Part II of this paper.

The present shell theory is different from the prior shell theories for CNTs in that it is directly based on the interatomic potential and does not require any fitting of Young's modulus and CNT thickness. For a single-wall CNT subjected to small deformation, the moment of inertia I is πR^3h, and the area A is $2\pi Rh$, where R is the CNT radius and h is the wall thickness. The bending stiffness $E_{\text{CNT}}I$ and tension stiffness $E_{\text{CNT}}A$ become $E_{\text{CNT}}h\cdot\pi R^3$ and $E_{\text{CNT}}h\cdot 2\pi R$, respectively, where CNT Young's modulus E_{CNT} and thickness h appear together via their product $E_{\text{CNT}}h$. Huang et al. [36] showed that it is unnecessary to define CNT Young's modulus and thickness separately since all experimentally measurable or theoretically calculable properties involve $E_{\text{CNT}}h$, not E_{CNT} nor h separately. The prior studies of CNT Young's modulus and thickness can be grouped to two types: one takes the interlayer spacing of graphite 0.34 nm as the thickness, and the resulting Young modulus is around 1 TPa [13,37–39]; the other is based on bending stiffness of graphene and continuum shell modeling, which gives the thickness around 0.066 nm and Young's modulus of 5.5 TPa [4,40–44]. These two types give approximately the same $E_{\text{CNT}}h$, 0.34 TPa nm for the first group and 0.36 TPa nm for the second group. As shown in this paper for CNTS as well as by Wu et al. [31] for graphene, the bending stiffness and tension stiffness can be directly obtained from the interatomic potential. This avoids the ambiguous definition of CNT Young's modulus and thickness.

Acknowledgment

Y.H. acknowledges the supports from the NSF through Nano-CEMMS (Grant No. DMI03-28162) at the University of Illinois and ONR Composites for Marine Structures Program (Grant No. N00014-01-1-0205, Program Manager Dr. Y. D. S. Rajapakse). The authors also acknowledge the supports from the NSFC and Ministry of Education of China. K.C.H. also acknowledges the support from National Basic Research Program of China (973 Program) Grant No. 2007CB936803.

Appendix A: Interatomic Potentials for Carbon

Brenner [29] established an interatomic potential for carbon from the Tersoff [45] formalism as

$$V = V_R(r_{ij}) - B_{ij}V_A(r_{ij}) \tag{A1}$$

for atoms i and j, where r_{ij} is the distance between atoms i and j, V_R and V_A are the repulsive and attractive pair terms (i.e., depending only on r_{ij}) given by

$$V_R(r) = \frac{D^{(e)}}{S-1} e^{-\sqrt{2S}\beta(r-R^{(e)})} f_c(r) \tag{A2}$$

$$V_A(r) = \frac{D^{(e)}S}{S-1} e^{-\sqrt{2/S}\beta(r-R^{(e)})} f_c(r) \tag{A3}$$

where the constants $D^{(e)}$, S, β, and $R^{(e)}$ can be found in Brenner [29]; the function f_c is merely a smooth cutoff function given by

$$f_c(r) = \begin{cases} 1, & r < R^{(1)} \\ \frac{1}{2}\left\{1 + \cos\left[\frac{\pi(r-R^{(1)})}{R^{(2)}-R^{(1)}}\right]\right\}, & R^{(1)} \le r \le R^{(2)} \\ 0, & r > R^{(2)} \end{cases} \tag{A4}$$

where $R^{(2)}=0.2$ nm and $R^{(1)}=0.17$ nm to include only the first-neighbor atoms for carbon.

The bond order function B_{ij} in Eq. (A1) represents a multibody coupling of atoms i and j and the local environment and is given by

$$B_{ij} = \left[1 + \sum_{k(\neq i,j)} G(\varphi_{ijk}) f_c(r_{ik})\right]^{-\delta} \tag{A5}$$

where k represents the atoms other than i and j, r_{ik} is the distance between the atoms i and k, f_c is the cutoff function in Eq. (A4), φ_{ijk} is the angle between bonds i-j and i-k, the function G is given by

$$G(\varphi) = a_0\left[1 + \frac{c_0^2}{d_0^2} - \frac{c_0^2}{d_0^2 + (1+\cos\varphi)^2}\right] \tag{A6}$$

and a_0, c_0, and d_0 are the constants given in Brenner [29]. For atoms i and j having different local environments, the coefficient B_{ij} in Eq. (A5) is replaced by

$$\bar{B}_{ij} = 1/2(B_{ij} + B_{ji}) \tag{A7}$$

The second-generation potential for carbon [30] takes the same form of Eq. (A1) but the repulsive and attractive pair terms in Eqs. (A2) and (A3) become

$$V_R(r) = \left(1 + \frac{Q}{r}\right) A e^{-\alpha r} f_c(r) \tag{A8}$$

$$V_A(r) = \sum_{1\le n\le 3} B_n e^{-\beta_n r} f_c(r) \tag{A9}$$

where the constants Q, A, α, B_n, and $\beta_n (n=1,2,3)$ can be found in Brenner et al. [30]; the function f_c is the same cutoff function in Eq. (A4). The bond order function B_{ij} in Eq. (A1) becomes

$$B_{ij} = \frac{1}{2}(B_{ij}^{\sigma-\pi} + B_{ji}^{\sigma-\pi}) + \Pi_{ij}^{RC} + B_{ij}^{DH} \tag{A10}$$

where Π_{ij}^{RC} and B_{ij}^{DH} are the tricubic splines given in Brenner et al. [30].

$$B_{ij}^{\sigma-\pi} = \left[1 + \sum_{k(\neq i,j)} f_c(r_{ik}) G(\varphi_{ijk})\right]^{-1/2} \tag{A11}$$

and G is a six-order polynomial spline given in Brenner et al. [30].

Appendix B: The Symmetric Stress and Bending Moment, and Covariant Derivatives

B.1 Symmetric Versus Asymmetric Stresses and Bending Moments

The asymmetric stress tensor $\boldsymbol{t}_{\text{asym}}$ and bending moment $\boldsymbol{m}_{\text{asym}}$ in existing shell theories satisfy the three force equilibrium equations and the three moment equilibrium equations:

$$t^{\alpha\beta}_{\text{asym}\,;\beta} - b^{\alpha}_{\cdot\beta} t^{n\beta}_{\text{asym}} + X^{\alpha} = 0 \quad (\alpha = \theta, Z) \tag{B1}$$

$$t^{n\beta}_{\text{asym}\,;\beta} + b_{\lambda\beta} t^{\lambda\beta}_{\text{asym}} + X^{n} = 0 \tag{B2}$$

$$m^{\alpha\beta}_{\text{asym}\,;\beta} + t^{n\alpha}_{\text{asym}} + M^{\alpha} = 0 \quad (\alpha = \theta, Z) \tag{B3}$$

$$c_{\alpha\beta}(t^{\alpha\beta}_{\text{asym}} + b^{\beta}_{\cdot\gamma} m^{\alpha\gamma}_{\text{asym}}) = 0 \tag{B4}$$

where $c_{\alpha\beta}=Je_{\alpha\beta}$ and $e_{\alpha\beta}$ is the two-dimensional permutation tensor ($e_{11}=e_{22}=0$, $e_{12}=-e_{21}=1$). The substitution of out-of-surface shear stress $t^{n\beta}_{\text{asym}}$ in Eq. (B3) into Eqs. (B1) and (B2) yields three equilibrium equations (3.4) and (3.5). The symmetric bending moment $\boldsymbol{m}$ in Eqs. (3.4) and (3.5) is the symmetric part of the above asymmetric bending moment $\boldsymbol{m}_{\text{asym}}$,

$$\boldsymbol{m} = 1/2(\boldsymbol{m}_{\text{asym}} + \boldsymbol{m}^{\text{T}}_{\text{asym}}) \tag{B5}$$

The symmetric stress is given by

$$\boldsymbol{t} = \mathring{\boldsymbol{t}}_{\text{asym}} - \boldsymbol{b}\cdot\boldsymbol{m}^{\text{T}}_{\text{asym}} = \mathring{\boldsymbol{t}}^{\text{T}}_{\text{asym}} - \boldsymbol{m}_{\text{asym}}\cdot\boldsymbol{b} = \boldsymbol{t}^{\text{T}} \tag{B6}$$

which is symmetric due to Eq. (B4), where $\mathring{\boldsymbol{t}}_{\text{asym}}$ is the in-surface part of the $\boldsymbol{t}_{\text{asym}}$.

B.2 The Covariant Derivatives

The covariant derivatives of vector and tensor are

$$S^{\alpha}_{;\lambda} = \frac{\partial S^{\alpha}}{\partial \xi^{\lambda}} + S^{\mu}\gamma^{\alpha}_{\mu\lambda} \tag{B7}$$

$$S^{\alpha}_{\cdot\beta;\lambda} = \frac{\partial S^{\alpha}_{\cdot\beta}}{\partial \xi^{\lambda}} + S^{\mu}_{\cdot\beta}\gamma^{\alpha}_{\mu\lambda} - S^{\alpha}_{\cdot\mu}\gamma^{\mu}_{\beta\lambda} \tag{B8}$$

$$S^{\alpha\beta}_{;\lambda} = \frac{\partial S^{\alpha\beta}}{\partial \xi^{\lambda}} + S^{\mu\beta}\gamma^{\alpha}_{\mu\lambda} + S^{\alpha\mu}\gamma^{\beta}_{\mu\lambda} \tag{B9}$$

where $\gamma^{\alpha}_{\mu\lambda}$ is the Christoffel symbol for the deformed CNT.

References

[1] Srivastava, D., Menon, M., and Cho, K. J., 2001, "Computational Nanotechnology With Carbon Nanotubes and Fullerenes," Comput. Sci. Eng., **3**, pp. 42–55.

[2] Yakobson, B. I., and Avouris, P., 2001, "Mechanical Properties of Carbon Nanotubes," Top. Appl. Phys., **80**, pp. 287–329.

[3] Qian, D., Wagner, G. J., Liu, W. K., Yu, M.-F., and Ruoff, R. S., 2002, "Mechanics of Carbon Nanotubes," Appl. Mech. Rev., **55**, pp. 495–533.

[4] Yakobson, B. I., Brabec, C. J., and Bernholc, J., 1996, "Nanomechanics of Carbon Tubes: Instabilities Beyond Linear Response," Phys. Rev. Lett., **76**, pp. 2511–2514.

[5] Krishnan, A., Dujardin, E., Ebbesen, T. W., Yianilos, P. N., and Treacy, M. M. J., 1998, "Young's Modulus of Single-Walled Nanotubes," Phys. Rev. B, **58**, pp. 14013–14019.

[6] Muster, J., Burghard, M., Roth, S., Duesberg, G. S., HernMandez, E., and Rubio, A., 1998, "Scanning Force Microscopy Characterization of Individual Carbon Nanotubes on Electrode Arrays," J. Vac. Sci. Technol. B, **16**, pp. 2796–2801.

[7] Salvetat, J.-P., Briggs, G. A. D., Bonard, J.-M., Bacsa, R. R., and Kulik, A. J., 1999, "Elastic and Shear Moduli of Single-Walled Carbon Nanotube Ropes," Phys. Rev. Lett., **82**, pp. 944–947.

[8] Tombler, T. W., Zhou, C., Alexseyev, L., Kong, J., Dai, H., Liu, L., Jayanthi, C. S., Tang, M., and Wu, S.-Y., 2000, "Reversible Electromechanical Characteristics of Carbon Nanotubes Under Local-Probe Manipulation," Nature (London), **405**, pp. 769–772.

[9] Robertson, D. H., Brenner, D. W., and Mintmire, J. W., 1992, "Energetics of Nanoscale Graphitic Tubules," Phys. Rev. B, **45**, pp. 12592–12595.

[10] Overney, G., Zhong, W., and TomManek, D., 1993, "Structural Rigidity and

Low-Frequency Vibrational Modes of Long Carbon Tubules," Z. Phys. D: At., Mol. Clusters, **27**, pp. 93–96.
[11] Molina, J. M., Savinsky, S. S., and Khokhriakov, N. V., 1996, "A Tight-Binding Model for Calculations of Structures and Properties of Graphitic Nanotubes," J. Chem. Phys., **104**, pp. 4652–4656.
[12] Halicioglu, T., 1998, "Stress Calculations for Carbon Nanotubes," Thin Solid Films, **312**, pp. 11–14.
[13] Hernández, E., Goze, C., Bernier, P., and Rubio, A., 1998, "Elastic Properties of C and BxCyNz Composite Nanotubes," Phys. Rev. Lett., **80**, pp. 4502–4505.
[14] Goze, C., Vaccarini, L., Henrard, L., Bernier, P., Hernandez, E., and Rubio, A., 1999, "Elastic and Mechanical Properties of Carbon Nanotubes," Synth. Met., **103**, pp. 2500–2501.
[15] Sánchez-Portal, D., Artacho, E., Soler, J. M., Rubio, A., and Ordejón, P., 1999, "Ab Initio Structural, Elastic, and Vibrational Properties of Carbon Nanotubes," Phys. Rev. B, **59**, pp. 12678–12688.
[16] Van Lier, G., Van Alsenoy, C., Van Doran, V., and Geerlings, P., 2000, "Ab Initio Study of the Elastic Properties of Single-Walled Carbon Nanotubes and Graphene," Chem. Phys. Lett., **326**, pp. 181–185.
[17] Popov, V. N., van Doren, V. E., and Balkanski, M., 2000, "Elastic Properties of Single-Walled Carbon Nanotubes," Phys. Rev. B, **61**, pp. 3078–3084.
[18] Prylutskyy, Y. I., Durov, S. S., Ogloblya, O. V., Buzaneva, E. V., and Scharff, P., 2000, "Molecular Dynamics Simulations of Mechanical, Vibrational and Electronic Properties of Carbon Nanotubes," Comput. Mater. Sci., **17**, pp. 352–355.
[19] Vaccarini, L., Goze, C., Henrard, L., HernMandez, E., Bernier, P., and Rubio, A., 2000, "Mechanical and Electronic Properties of Carbon and Boron-Nitride Nanotubes," Carbon, **38**, pp. 1681–1690.
[20] Zhou, G., Duan, W., and Gu, B., 2001, "First-Principles Study on Morphology and Mechanical Properties of Single-Walled Carbon Nanotube," Chem. Phys. Lett., **333**, pp. 344–349.
[21] Liu, B., Huang, Y., Jiang, H., Qu, S., and Hwang, K. C., 2004, "The Atomic-Scale Finite Element Method," Comput. Methods Appl. Mech. Eng., **193**, pp. 1849–1864.
[22] Liu, B., Yu, M. F., and Huang, Y., 2004, "Role of Lattice Registry in the Full Collapse and Twist Formation of Carbon Nanotubes," Phys. Rev. B, **70**, p. 161402.
[23] Arroyo, M., and Belytschko, T., 2002, "An Atomistic-Based Finite Deformation Membrane for Single Layer Crystalline Films," J. Mech. Phys. Solids, **50**, pp. 1941–1977.
[24] Zhang, P., Huang, Y., Geubelle, P. H., Klein, P. A., and Hwang, K. C., 2002, "The Elastic Modulus of Single-Wall Carbon Nanotubes: A Continuum Analysis Incorporating Interatomic Potentials," Int. J. Solids Struct., **39**, pp. 3893–3906.
[25] Zhang, P., Jiang, H., Huang, Y., Geubelle, P. H., and Hwang, K. C., 2004, "An Atomistic-Based Continuum Theory for Carbonnanotubes: Analysis of Fracture Nucleation," J. Mech. Phys. Solids, **52**, pp. 977–998.
[26] Yang, J. Z., and E, W., 2006, "Generalized Cauchy–Born Rules for Elastic Deformation of Sheets, Plates, and Rods: Derivation of Continuum Models From Atomistic Models," Phys. Rev. B, **74**, p. 184110.
[27] Weiner, J. H., 1983, *Statistical Mechanics of Elasticity*, Wiley, New York.
[28] Tadmor, E. B., Smith, G. S., Bernstein, N., and Kaxiras, E., 1999, "Mixed Finite Element and Atomistic Formulation for Complex Crystals," Phys. Rev. B, **59**, pp. 235–245.
[29] Brenner, D. W., 1990, "Empirical Potential for Hydrocarbons for Use in Simulating the Chemical Vapor Deposition of Diamond Films," Phys. Rev. B, **42**, pp. 9458–9471.
[30] Brenner, D. W., Shenderova, O. A., Harrison, J. A., Stuart, S. J., Ni, B., and Sinnott, S. B., 2002, "A Second-Generation Reactive Empirical Bond Order (Rebo) Potential Energy Expression for Hydrocarbons," J. Phys.: Condens. Matter, **14**, pp. 783–802.
[31] Wu, J., Hwang, K. C., and Huang, Y., 2008, "An Atomistic-Based Finite-Deformation Shell Theory for Single-Wall Carbon Nanotubes," J. Mech. Phys. Solids, **56**, 279–292.
[32] Born, M., and Huang, K., 1959, *Dynamical Theory of Crystal Lattices*, Oxford University Press, New York.
[33] Sanders, J. L., 1963, "Nonlinear Theories for Thin Shells," Q. Appl. Math., **21**, pp. 21–36.
[34] Koiter, W. T., 1966, "On the Nonlinear Theory of Thin Elastic Shells, I, II, III," Proc. K. Ned. Akad. Wet., Ser. B: Phys. Sci., **69**, pp. 1–54.
[35] Niordson, F., 1985, *Shell Theory* (North-Holland Series in Applied Mathematics and Mechanics) Vol. 29, North-Holland, Amsterdam.
[36] Huang, Y., Wu, J., and Hwang, K. C., 2006, "Thickness of Graphene and Single-Wall Carbon Nanotubes," Phys. Rev. B, **74**, p. 245413.
[37] Lu, J. P., 1997, "Elastic Properties of Carbon Nanotubes and Nanoropes," Phys. Rev. Lett., **79**, pp. 1297–1300.
[38] Li, C. Y., and Chou, T. W., 2003, "A Structural Mechanics Approach for the Analysis of Carbon Nanotubes," Int. J. Solids Struct., **40**, pp. 2487–2499.
[39] Jin, Y., and Yuan, F. G., 2003, "Simulation of Elastic Properties of Single-Walled Carbon Nanotubes," Compos. Sci. Technol., **63**, pp. 1507–1515.
[40] Zhou, X., Zhou, J. J., and Ou-yang, Z. C., 2000, "Strain Energy and Young's Modulus of Single-Wall Carbon Nanotubes Calculated From Electronic Energy-Band Theory," Phys. Rev. B, **62**, pp. 13692–13696.
[41] Kudin, K. N., Scuseria, G. E., and Yakobson, B. I., 2001, "C2F, BN, and C Nanoshell Elasticity From Ab Initio Computations," Phys. Rev. B, **64**, p. 235406.
[42] Tu, Z. C., and Ou-yang, Z., 2002, "Single-Walled and Multi-Walled Carbon Nanotubes Viewed as Elastic Tubes With the Effective Young's Moduli Dependent on Layer Number," Phys. Rev. B, **65**, p. 233407.
[43] Pantano, A., Parks, D. M., and Boyce, C. M., 2004, "Mechanics of Deformation of Single- and Multi-Wall Carbon Nanotubes," J. Mech. Phys. Solids, **52**, pp. 789–821.
[44] Wang, L. F., Zheng, Q. S., Liu, J. Z., and Jiang, Q., 2005, "Size Dependence of the Thin-Shell Model for Carbon Nanotubes," Phys. Rev. Lett., **95**, p. 105501.
[45] Tersoff, J., 1988, "New Empirical Approach for the Structure and Energy of Covalent Systems," Phys. Rev. B, **37**, pp. 6991–7000.

J. Wu

K. C. Hwang

FML, Department of Engineering Mechanics,
Tsinghua University,
Beijing 100084, P.R. China

J. Song
Department of Mechanical Science and Engineering,
University of Illinois,
1206 W. Green Street,
Urbana, IL 61801

Y. Huang[1]
Department of Civil and Environmental Engineering,
and Department of Mechanical Engineering,
Northwestern University,
Evanston, IL 60208
e-mail: y-huang@northwestern.edu

A Finite-Deformation Shell Theory for Carbon Nanotubes Based on the Interatomic Potential—Part II: Instability Analysis

Based on the finite-deformation shell theory for carbon nanotubes established from the interatomic potential in Part I of this paper, we have studied the instability of carbon nanotubes subjected to different loadings (tension, compression, internal and external pressures, and torsion). Similar to the conventional shells, carbon nanotubes may undergo bifurcation under compression/torsion/external pressure. Our analysis, however, shows that carbon nanotubes may also undergo bifurcation in tension and internal pressure, though the bifurcation modes for tension and compression are very different, and so are the modes for the internal and external pressures. The critical load for instability and bifurcation depends on the interatomic potential used. [DOI: 10.1115/1.2965367]

Keywords: shell theory, carbon nanotube, interatomic potential, finite deformation, instability

1 Introduction

There exist many atomistic studies of carbon nanotubes (CNTs) subject to tension, compression, and torsion [1–5]. As a CNT deforms, instability in the form of bifurcation occurs such that there may exist multiple equilibrium configurations under the same loading. The instability usually triggers the defect nucleation in the CNT and the eventual failure of the CNT.

The atomistic studies show that the bifurcation mode of CNT under compression [1] may be different from the Euler beam buckling [6], particularly for relatively short CNTs. This suggests that, if a CNT is to be modeled as a continuum structure element, it should be considered as a shell rather than a beam. A finite-deformation shell theory for CNTs is established in Part I of this paper based on the interatomic potentials [7,8] to account for the nonlinear and multibody atomistic interactions, as well as the CNT atomic structure (e.g., chirality). The shell theory also accounts for the finite deformation of CNTs, which is important in the instability or bifurcation analyses. In Part II of this paper, we use the finite-deformation shell theory to study the instability of CNTs subjected to tension, compression, internal and external pressures, and torsion.

The initial configuration of the CNT prior to any deformation is determined via the energy minimization [9]. For the CNT subjected to tension/compression, internal and external pressures, and torsion, the deformation prior to instability is uniform and is obtained analytical in Part I of this paper. The effect of finite temperature is not accounted for in the present study.

2 Instability of Carbon Nanotubes in Tension

2.1 Prebifurcation: Uniform Deformation. For an armchair or zigzag CNT of radius R subjected to simple tension, the deformation is uniform and axisymmetric prior to bifurcation. A material point $\boldsymbol{P}=R\boldsymbol{e}_R+Z\boldsymbol{e}_Z$ on the CNT prior to deformation moves to $\boldsymbol{p}=R(1+\varepsilon_{\text{lateral}})\boldsymbol{e}_R+Z(1+\varepsilon_{\text{axial}})\boldsymbol{e}_Z$ after the deformation, where $\varepsilon_{\text{axial}}$ is the axial strain, and the strain in circumferential direction $\varepsilon_{\text{lateral}}$ is to be determined.

The base vectors on the deformed CNT are

$$\boldsymbol{a}_\theta=\frac{1}{R}\frac{\partial \boldsymbol{p}}{\partial \theta}=(1+\varepsilon_{\text{lateral}})\boldsymbol{e}_\theta,\quad \boldsymbol{a}_Z=\frac{\partial \boldsymbol{p}}{\partial Z}=(1+\varepsilon_{\text{axial}})\boldsymbol{e}_Z \tag{2.1}$$

which give the nonvanishing components of the Green strain and curvature tensors as

$$E_{\theta\theta}=\varepsilon_{\text{lateral}}+\frac{1}{2}\varepsilon_{\text{lateral}}^2,\quad E_{ZZ}=\varepsilon_{\text{axial}}+\frac{1}{2}\varepsilon_{\text{axial}}^2,\quad K_{\theta\theta}=-\frac{\varepsilon_{\text{lateral}}}{R} \tag{2.2}$$

The strain energy density $W=W(E_{\theta\theta},E_{ZZ},K_{\theta\theta})$ is obtained from the modified Born rule (Eq. (2.15) in Part I of this paper). It gives the nonvanishing components of second Piola–Kirchhoff stress and bending moment tensors:

$$T_{\theta\theta}=\frac{\partial W}{\partial E_{\theta\theta}},\quad T_{ZZ}=\frac{\partial W}{\partial E_{ZZ}},\quad M_{\theta\theta}=\frac{\partial W}{\partial K_{\theta\theta}},\quad M_{ZZ}=\frac{\partial W}{\partial K_{ZZ}} \tag{2.3}$$

The equilibrium equations become

$$T_{\theta\theta}-\frac{M_{\theta\theta}}{R(1+\varepsilon_{\text{lateral}})}=0 \tag{2.4}$$

which determines the strain $\varepsilon_{\text{lateral}}$ in the circumferential direction in terms of the axial strain $\varepsilon_{\text{axial}}$, i.e., $\varepsilon_{\text{lateral}}=\varepsilon_{\text{lateral}}(\varepsilon_{\text{axial}})$.

2.2 Onset of Bifurcation: Nonuniform Increment of Deformation. The deformation is still uniform at the onset of bifurcation, but its increment (rate) is not. Let $\boldsymbol{v}=\dot{\boldsymbol{U}}$ denote the velocity with the components v_R, v_θ, and v_Z. For a CNT of length L subjected to the axial force but no shear at two ends $Z=0$ and L, the velocity at the onset of bifurcation satisfies [3]

[1]Corresponding author.

Contributed by the Applied Mechanics Division and Sound of ASME for publication in the JOURNAL OF APPLIED MECHANICS. Manuscript received June 16, 2007; final manuscript received May 10, 2008; published online August 20, 2008. Review conducted by Robert M. McMeeking.

$$v_Z = \frac{\partial v_\theta}{\partial Z} = \frac{\partial v_R}{\partial Z} = 0 \quad \text{at} \quad Z = 0, L \tag{2.5}$$

We first consider the axisymmetric bifurcation. The axisymmetric velocity field in the CNT, satisfying the incremental equilibrium equations (Eqs. (3.9) and (3.10) in Part I of this paper) and boundary condition (Eq. (2.5)), is given by

$$v_\theta = 0, \quad v_Z = V_{Z0} \sin\frac{m\pi Z}{L}, \quad v_R = V_{R0} \cos\frac{m\pi Z}{L} \tag{2.6}$$

where $m = 1, 2, 3, \ldots$ is the eigenmode number, and (V_{Z0}, V_{R0}) is the corresponding eigenvector satisfying the following homogeneous algebraic equation:

$$\begin{pmatrix} Q_{ZZ} & Q_{ZR} \\ Q_{RZ} & Q_{RR} \end{pmatrix} \begin{pmatrix} V_{Z0} \\ V_{R0} \end{pmatrix} = 0 \tag{2.7}$$

Here the coefficients are given in terms of the incremental tensile, bending, and coupled tensile/bending rigidity tensors $\boldsymbol{L}$, $\boldsymbol{S}$, and $\boldsymbol{H}$ (Eqs. (2.20) and (2.21) in Part I of this paper) and the stress and bending moment tensors $\boldsymbol{T}$ and $\boldsymbol{M}$ by

$$Q_{ZZ} = -\left[L_{ZZZZ} + \frac{T_{ZZ}}{(1+\varepsilon_{\text{axial}})^2}\right]\left(\frac{m\pi}{L}\right)^2$$

$$Q_{ZR} = Q_{RZ} = -\frac{1+\varepsilon_{\text{lateral}}}{R}\left[L_{ZZ\theta\theta} - \frac{H_{ZZ\theta\theta}}{R(1+\varepsilon_{\text{lateral}})}\right]\frac{m\pi}{L} + \left[H_{ZZZZ} + \frac{M_{ZZ}}{(1+\varepsilon_{\text{axial}})^2}\right]\left(\frac{m\pi}{L}\right)^3$$

$$Q_{RR} = -\frac{(1+\varepsilon_{\text{lateral}})^2}{R^2}\left[L_{\theta\theta\theta\theta} - \frac{2H_{\theta\theta\theta\theta}}{R(1+\varepsilon_{\text{lateral}})} + \frac{S_{\theta\theta\theta\theta}}{R^2(1+\varepsilon_{\text{lateral}})^2} + \frac{M_{\theta\theta}}{R(1+\varepsilon_{\text{lateral}})^3}\right] + \left[\frac{2(1+\varepsilon_{\text{lateral}})}{R}H_{\theta\theta ZZ} - \frac{2}{R^2}S_{\theta\theta ZZ} - T_{ZZ} - \frac{1+\varepsilon_{\text{lateral}}}{R(1+\varepsilon_{\text{axial}})^2}M_{\theta\theta}\right]\left(\frac{m\pi}{L}\right)^2 - S_{ZZZZ}\left(\frac{m\pi}{L}\right)^4 \tag{2.8}$$

In order to have a nontrivial solution, the determinant of the 2×2 matrix in Eq. (2.7) must vanish, which gives the critical condition for the axisymmetric bifurcation as

$$\begin{vmatrix} Q_{ZZ} & Q_{ZR} \\ Q_{RZ} & Q_{RR} \end{vmatrix} = 0 \tag{2.9}$$

The first axial strain $\varepsilon_{\text{axial}}$ that satisfies the above equation is the critical strain for bifurcation in tension and is denoted by $\varepsilon_{\text{cr}}^{\text{tension}}$. Figure 1 shows $\varepsilon_{\text{cr}}^{\text{tension}}$ based on the Brenner potential [7] versus mR/L for an (8,8) armchair CNT, where $m(=1,2,3,...)$ is the eigenmode number, and R and L are the CNT radius and length, respectively. The critical strain for axisymmetric bifurcation is essentially a constant of 0.356, independent of the CNT length L. This critical strain is identical to the one given by the membrane theory of CNT [3] based on the same interatomic potential [7]. The same bifurcation strain given by the membrane theory [3] and present shell theory suggests that the CNT bending rigidity has essentially no effect on the bifurcation in tension.

For nonaxisymmetric bifurcation, the velocity field in the CNT, satisfying the incremental equilibrium equations (Eqs. (3.9) and (3.10) in Part I of this paper) and boundary condition (Eq. (2.5)), is given by

$$v_\theta = V_{\theta 0} \sin n\theta \cos\frac{m\pi Z}{L}, \quad v_Z = V_{Z0} \cos n\theta \sin\frac{m\pi Z}{L},$$

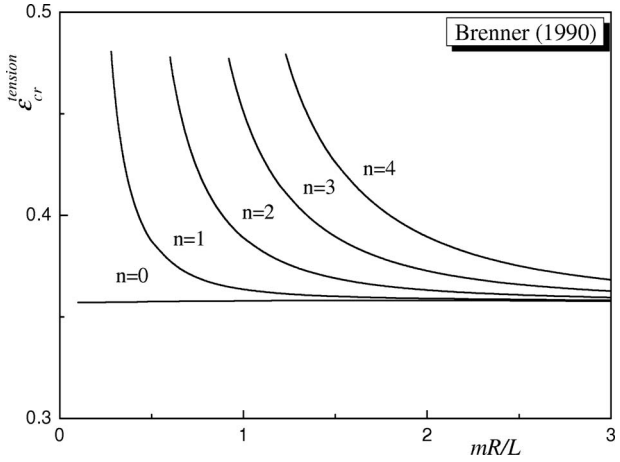

Fig. 1 The critical strain for bifurcation in tension based on the Brenner potential [7] versus mR/L for the (8,8) armchair carbon nanotube, where $m(=1,2,3,...)$ is the bifurcation mode number, R and L are the radius and length of the carbon nanotube, respectively, $n=0$ represents the axisymmetric bifurcation, and $n=1,2,3,...$ represents the nonaxisymmetric bifurcation

$$v_R = V_{R0} \cos n\theta \cos\frac{m\pi Z}{L} \tag{2.10}$$

where $n = 1, 2, 3, \ldots$, $n=0$ degenerates to the axisymmetric bifurcation (Eq. (2.6)), and the eigenvector $(V_{\theta 0}, V_{Z0}, V_{R0})$ satisfies a set of homogeneous algebraic equations. The vanishing of the determinant of the coefficient matrix gives the condition for nonaxisymmetric bifurcation. Figure 1 shows the critical strain $\varepsilon_{\text{cr}}^{\text{tension}}$ for nonaxisymmetric bifurcation $(n=1,2,3,...)$ of the (8,8) armchair CNT in tension. The critical strain is always larger than its axisymmetric counterpart $(n=0)$ such that only axisymmetric bifurcation occurs in the (8,8) armchair CNT (when the tensile axial strain reaches 0.356).

The above observation, however, depends on the interatomic potential. Figure 2 shows the critical strain $\varepsilon_{\text{cr}}^{\text{tension}}$ for bifurcation in tension based on the second-generation potential [8]. The critical strain for axisymmetric bifurcation $(n=0)$ is approximately a

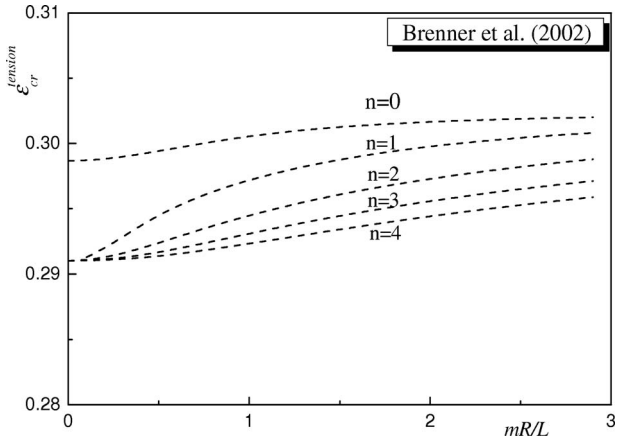

Fig. 2 The critical strain for bifurcation in tension based on the second-generation interatomic potential [8] versus mR/L for the (8,8) armchair carbon nanotube, where $m(=1,2,3,...)$ is the bifurcation mode number, R and L are the radius and length of the carbon nanotube, respectively, $n=0$ represents the axisymmetric bifurcation, and $n=1,2,3,...$ represents the nonaxisymmetric bifurcation

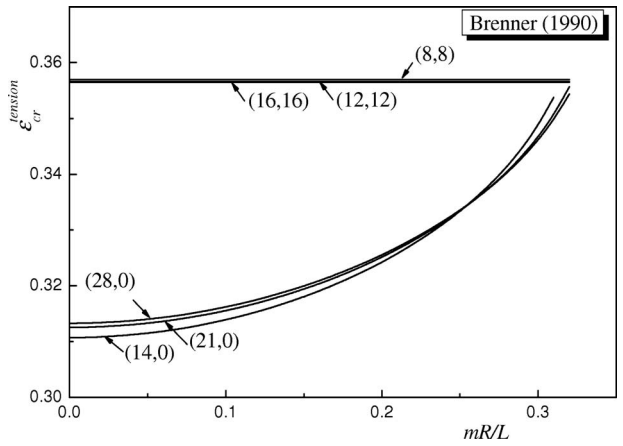

Fig. 3 The critical strain for bifurcation in tension based on the Brenner potential [7] versus *mR*/*L* for several armchair and zigzag carbon nanotubes, where *m*(=1,2,3,...) is the bifurcation mode number, and *R* and *L* are the radius and length of the carbon nanotube, respectively

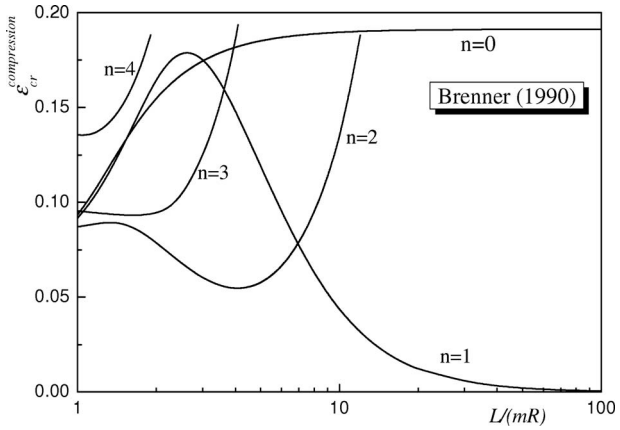

Fig. 4 The critical strain for bifurcation in compression based on the Brenner potential [7] versus *L*/(*mR*) for the (8,8) armchair carbon nanotube, where *m*(=1,2,3,...) is the bifurcation mode number, *R* and *L* are the radius and length of the carbon nanotube, respectively, *n*=0 represents the axisymmetric bifurcation, and *n*=1,2,3,... represents the nonaxisymmetric bifurcation

constant of 0.299 and is smaller than 0.356 in Fig. 1 based on the Brenner potential [7]. Furthermore, the critical strain for nonaxisymmetric bifurcation ($n=1,2,3,...$) is smaller than the axisymmetric bifurcation strain ($n=0$) such that the nonaxisymmetric bifurcation occurs, which is contrary to the results in Fig. 1 based on the Brenner potential [7]. This opposite behavior results from the different expressions and parameters used in the Brenner potential [7] and its second-generation potential [8]. This is partially because the parameters in interatomic potentials are determined by fitting the binding energy, lattice constants, elastic properties, and vacancy formation energy of diamond and graphite, which are mainly properties at the vanishing strain level and therefore not accounting for the behavior at the finite strain (e.g., around 30% strain).

Figure 3 shows the critical strain for bifurcation in tension based on the Brenner potential [7] for the (8,8), (12,12), and (16,16) armchair CNTs and the (14,0), (21,0), and (28,0) zigzag CNTs. The CNT radius has essentially no effect on the critical strain for bifurcation in tension since the curves for armchair CNTs are almost identical and so are the ones for zigzag CNTs. The CNT chirality, however, contributes to the bifurcation in tension. For example, the (8,8) armchair and (14,0) zigzag CNTs have approximately the same radius, but the critical strain for the (14,0) zigzag CNT is lower than that for the (8,8) armchair CNT.

3 Instability of Carbon Nanotubes in Compression

Even though the membrane theory and shell theory for CNTs give the same critical strain for bifurcation in tension in Sec. 2.2, the membrane theory is not applicable to instability of CNTs in compression since it does not have bending rigidity. We use the finite-deformation shell theory established in Part I of this paper to study the instability of CNTs in compression. The deformation is uniform prior to bifurcation and is the same as that in Sec. 2.1 except for the axial strain $\varepsilon_{\text{axial}}<0$. Once the compressive strain reaches a critical value, $-\varepsilon_{\text{cr}}^{\text{compression}}$, bifurcation occurs. In the following, $\varepsilon_{\text{cr}}^{\text{compression}}$ is called the buckling strain.

The onset of bifurcation is governed by the analysis in Sec. 2.2, except that $\varepsilon_{\text{axial}}<0$. Figure 4 shows the buckling strain $\varepsilon_{\text{cr}}^{\text{compression}}$ based on the Brenner potential [7] versus L/mR for the (8,8) armchair CNT in compression, where $m(=1,2,3,...)$ is the eigenmode number, and L and R are the CNT length and radius, respectively. Both the axisymmetric ($n=0$) and nonaxisymmetric bifurcations ($n=1,2,3,...$) are considered, where the velocity field for $n=1$ is identical to that for the Euler beam buckling. For long CNTs $L/(mR)>6.9$, $n=1$ (Euler beam buckling) gives the smallest buckling strain $\varepsilon_{\text{cr}}^{\text{compression}}$. For relatively short CNTs $L/(mR)<6.9$, $n=2$ gives the smallest $\varepsilon_{\text{cr}}^{\text{compression}}$. The axisymmetric bifurcation ($n=0$) never occurs in compression.

Figure 5 shows the buckling strain $\varepsilon_{\text{cr}}^{\text{compression}}$ based on the second-generation interatomic potential [8] for the (8,8) armchair CNT in compression. The curves look similar to those in Fig. 4, but they give smaller buckling strain. The difference once again results from the different functions and parameters in the second-generation interatomic potential [8] and the Brenner potential [7].

Figure 6 shows the buckling strain based on the Brenner potential [7] for the (8,8), (12,12), and (16,16) armchair CNTs in compression. For long CNTs (large $L/(mR)$), all curves coincide and give the same buckling strain $\varepsilon_{\text{cr}}^{\text{compression}}$ corresponding to the Euler beam buckling $n=1$. For relatively short CNTs, other buckling modes appear, such as $n=2$ for the (8,8) armchair CNT and n

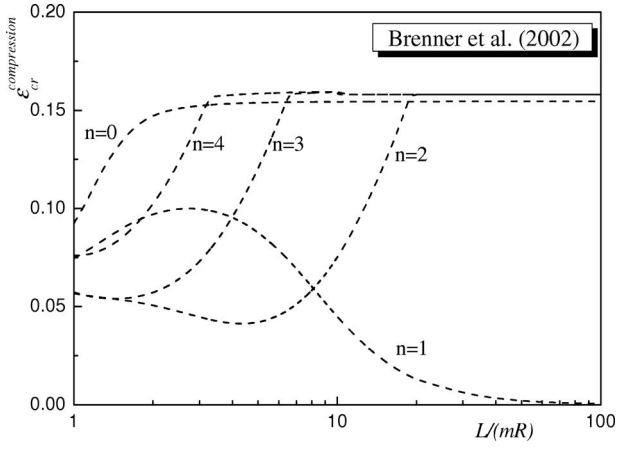

Fig. 5 The critical strain for bifurcation in compression based on the second-generation interatomic potential [8] versus *L*/(*mR*) for the (8,8) armchair carbon nanotube, where *m*(=1,2,3,...) is the bifurcation mode number, *R* and *L* are the radius and length of the carbon nanotube, respectively, *n*=0 represents the axisymmetric bifurcation, and *n*=1,2,3,... represents the nonaxisymmetric bifurcation

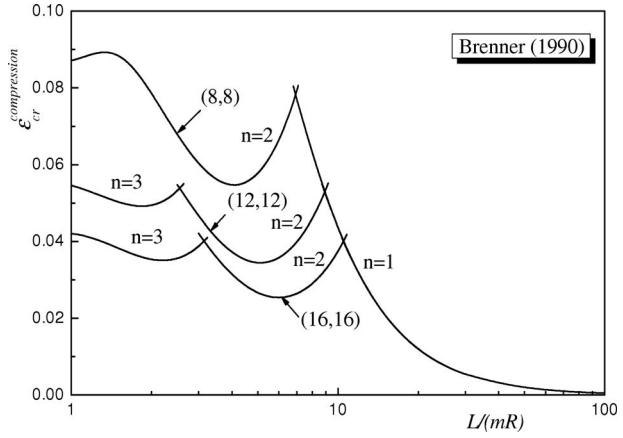

Fig. 6 The critical strain for bifurcation in compression based on the Brenner potential [7] versus $L/(mR)$ for the (8,8), (12,12), and (16,16) armchair carbon nanotubes, where $m(=1,2,3,...)$ is the bifurcation mode number, R and L are the radius and length of the carbon nanotube, respectively, and $n=1,2,3,...$ represents the nonaxisymmetric bifurcation

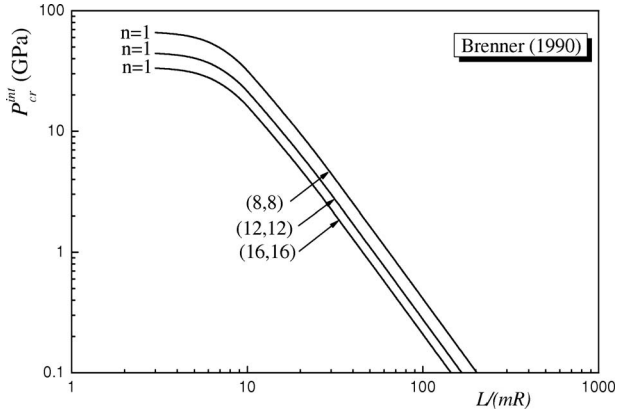

Fig. 7 The critical internal pressure for bifurcation based on the Brenner potential [7] versus $L/(mR)$ for the (8,8), (12,12), and (16,16) armchair carbon nanotubes, where $m(=1,2,3,...)$ is the bifurcation mode number, and R and L are the radius and length of the carbon nanotube, respectively. The bifurcation corresponds to $n=1$ (nonaxisymmetric bifurcation).

$=2$ and $n=3$ for the (12,12) and (16,16) armchair CNTs. This strong dependence on the CNT radius did not occur in tension bifurcation (Sec. 2).

Using the molecular dynamics simulations based on the Brenner potential [7], Yakobson et al. [1] studied the buckling of a 6-nm-long (7,7) armchair CNT under compression. They reported the buckling strain around 5% for $n=2$, while the present analysis gives 6% for the same n. The molecular dynamics simulations based on the second-generation interatomic potential [8] gave the buckling strain around 13% for a 4.3-nm-long (8,0) zigzag CNT under compression [10], while the present analysis gives 11%.

4 Instability of Carbon Nanotubes Subjected to Internal Pressure

4.1 Prebifurcation: Uniform Deformation. CNTs subjected to internal pressure have important applications such as hydrogen storage. For an armchair or zigzag CNT of radius R subjected to internal pressure P^{int}, the deformation is uniform and axisymmetric prior to bifurcation. The analysis in Sec. 2.1 still holds except that the equilibrium (Eq. (2.4)) becomes

$$T_{\theta\theta} - \frac{M_{\theta\theta}}{R(1+\varepsilon_{\text{lateral}})} = \frac{P^{\text{int}}R}{1+\varepsilon_{\text{lateral}}} \tag{4.1}$$

The traction-free condition at the end of CNT gives

$$T_{ZZ} = 0 \tag{4.2}$$

Equations (4.1) and (4.2) determine the axial strain $\varepsilon_{\text{axial}}$ and the strain $\varepsilon_{\text{lateral}}$ in the circumferential direction in terms of the internal pressure P^{int}.

4.2 Onset of Bifurcation: Nonuniform Increment of Deformation. Similar to Sec. 2.2, the deformation is still uniform at the onset of bifurcation, but its increment (rate) is not. The velocity field in the CNT is given by Eq. (2.10). The incremental equilibrium equations (Eqs. (3.9) and (3.10) in Part I of this paper) then give a homogeneous algebraic equation for $(V_{\theta 0}, V_{Z0}, V_{R0})$,

$$\begin{pmatrix} Q_{\theta\theta} & Q_{\theta Z} & Q_{\theta R} \\ Q_{Z\theta} & Q_{ZZ} & Q_{ZR} \\ Q_{R\theta} & Q_{RZ} & Q_{RR} \end{pmatrix} \begin{pmatrix} V_{\theta 0} \\ V_{Z0} \\ V_{R0} \end{pmatrix} = 0 \tag{4.3}$$

where, similar to Eq. (2.8), the coefficients Q_{IJ} are given analytically in terms of the incremental rigidity tensors $\boldsymbol{L}$, $\boldsymbol{S}$, and $\boldsymbol{H}$, and the stress and bending moment tensors $\boldsymbol{T}$ and $\boldsymbol{M}$. In order to have a nontrivial solution, the determinant of the 3×3 matrix in Eq. (4.3) must vanish, which gives the critical condition for bifurcation of CNTs subjected to internal pressure.

Figure 7 shows the critical internal pressure for bifurcation $P_{\text{cr}}^{\text{int}}$ based on the Brenner potential [7] versus L/mR for the (8,8), (12,12), and (16,16) armchair CNTs, where $m(=1,2,3,...)$ is the eigenmode number, and R and L are the CNT radius and length, respectively. The bifurcation mode always corresponds to $n=1$ (the same mode as the Euler beam buckling). The CNT radius has little effect on the critical internal pressure for bifurcation since the curves in Fig. 7 are close. This is similar to the bifurcation in tension (Sec. 2) since the stress state is also in tension for the CNT subjected to the internal pressure. The critical internal pressure for bifurcation $P_{\text{cr}}^{\text{int}}$ decreases monotonically with the increasing CNT length L. For the CNT length/radius ratio $L/R=200$, $P_{\text{cr}}^{\text{int}}$ is about 100 MPa.

Figure 8 shows the critical internal pressure for bifurcation $P_{\text{cr}}^{\text{int}}$ based on the second-generation interatomic potential [8] for the (8,8), (12,12), and (16,16) armchair CNTs. The bifurcation mode

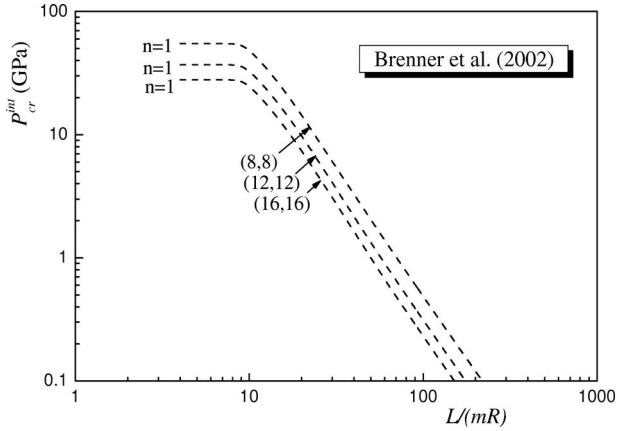

Fig. 8 The critical internal pressure for bifurcation based on the second-generation interatomic potential [8] versus $L/(mR)$ for the (8,8), (12,12), and (16,16) armchair carbon nanotubes, where $m(=1,2,3,...)$ is the bifurcation mode number, and R and L are the radius and length of the carbon nanotube, respectively. The bifurcation corresponds to $n=1$ (nonaxisymmetric bifurcation).

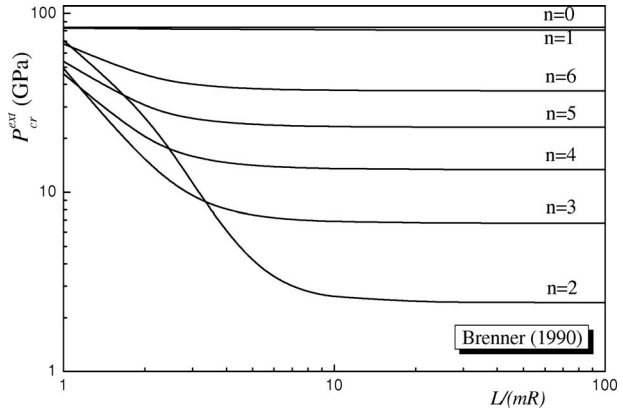

Fig. 9 The critical external pressure for bifurcation based on the Brenner potential [7] versus $L/(mR)$ for the (8,8) armchair carbon nanotube, where $m(=1,2,3,...)$ is the bifurcation mode number, R and L are the radius and length of the carbon nanotube, respectively, $n=0$ represents the axisymmetric bifurcation, and $n=1,2,3,...$ represents the nonaxisymmetric bifurcation

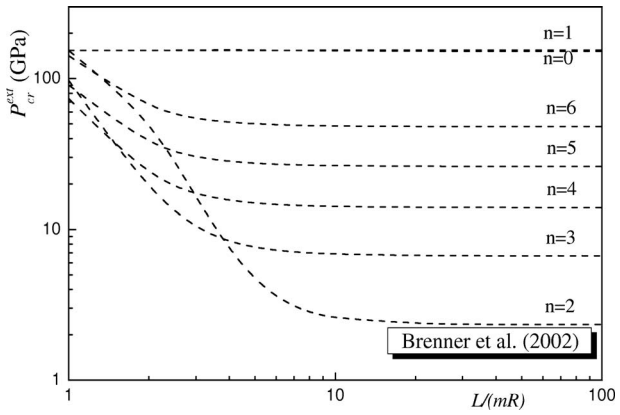

Fig. 10 The critical external pressure for bifurcation based on the second-generation interatomic potential [8] versus $L/(mR)$ for the (8,8) armchair carbon nanotube, where $m(=1,2,3,...)$ is the bifurcation mode number, R and L are the radius and length of the carbon nanotube, respectively, $n=0$ represents the axisymmetric bifurcation, and $n=1,2,3,...$ represents the nonaxisymmetric bifurcation

corresponds to $n=1$ (the same mode as Euler beam buckling). The curves in Fig. 8 are rather similar to those in Fig. 7.

5 Instability of Carbon Nanotubes Subjected to External Pressure

For an armchair or zigzag CNT of radius R subjected to external pressure P^{ext}, the deformation is uniform and axisymmetric prior to bifurcation. The analysis in Sec. 4 still holds except that the internal pressure P_{int} is replaced by $-P_{\text{ext}}$. Equation (4.3) also gives the critical condition for bifurcation of CNTs subjected to external pressure (if P_{int} is replaced by $-P_{\text{ext}}$).

Figure 9 shows the critical external pressure for bifurcation $P_{\text{cr}}^{\text{ext}}$ based on the Brenner potential [7] versus L/mR for the (8,8) armchair CNT, where $m(=1,2,3,...)$ is the eigenmode number, and R and L are the CNT radius and length, respectively. Both the axisymmetric ($n=0$) and nonaxisymmetric bifurcations ($n=1,2,3,...$) are considered. For CNT length $L/(mR)>3.3$, $n=2$ gives the lowest critical external pressure $P_{\text{cr}}^{\text{ext}}$. For very short CNTs $L/(mR)<3.3$, other bifurcation modes ($n=3,4,...$) appear, but the axisymmetric bifurcation ($n=0$) or nonaxisymmetric bifurcation with $n=1$ never occur. The bifurcation modes ($n=2,3,4,...$) for the external pressure are completely different from that for the internal pressure ($n=1$) in Sec. 4.

Figure 10 shows the critical external pressure for bifurcation $P_{\text{cr}}^{\text{ext}}$ based on the second-generation interatomic potential [8] for the (8,8) armchair CNT. The results are somewhat different from those in Fig. 9 for the Brenner potential [7], reflecting the difference between the two interatomic potentials [7,8].

Figure 11 shows the critical external pressure for bifurcation $P_{\text{cr}}^{\text{ext}}$ based on the Brenner potential [7] for the (8,8), (12,12), and (16,16) armchair CNTs. Similar to Fig. 9, the bifurcation mode corresponds to $n=2$ for long CNTs (large $L/(mR)$) and to $n=3,4,...$ for shorter CNTs, and never to $n=0$ (axisymmetric bifurcation) and $n=1$. The critical external pressure for bifurcation decreases rapidly as the CNT radius increases since $P_{\text{cr}}^{\text{ext}}$ for the (16,16) armchair CNT is much smaller than that for the (8,8) armchair CNT.

6 Instability of Carbon Nanotubes in Torsion

6.1 Prebifurcation: Uniform Deformation. For an armchair or zigzag CNT of radius R subjected to torsion, the deformation is uniform prior to bifurcation. Let κ denote the twist (rotation per unit length). The axial strain $\varepsilon_{\text{axial}}$ and the strain in circumferential direction $\varepsilon_{\text{lateral}}$ result from the finite twist and are to be determined. A material point $\boldsymbol{P}=R\boldsymbol{e}_R+Z\boldsymbol{e}_Z$ on the CNT prior to deformation moves to $\boldsymbol{p}=R(1+\varepsilon_{\text{lateral}})(\boldsymbol{e}_R\cos\kappa Z+\boldsymbol{e}_\theta\sin\kappa Z)+Z(1+\varepsilon_{\text{axial}})\boldsymbol{e}_Z$ after the deformation.

The base vectors on the deformed CNT are

$$\boldsymbol{a}_\theta=\frac{1}{R}\frac{\partial\boldsymbol{p}}{\partial\theta}=(1+\varepsilon_{\text{lateral}})(-\boldsymbol{e}_R\sin\kappa Z+\boldsymbol{e}_\theta\cos\kappa Z)$$

$$\boldsymbol{a}_Z=\frac{\partial\boldsymbol{p}}{\partial Z}=\kappa R(1+\varepsilon_{\text{lateral}})(-\boldsymbol{e}_R\sin\kappa Z+\boldsymbol{e}_\theta\cos\kappa Z)+(1+\varepsilon_{\text{axial}})\boldsymbol{e}_Z \tag{6.1}$$

They give the components of the Green strain and curvature as

$$E_{\theta\theta}=\varepsilon_{\text{lateral}}+\frac{1}{2}\varepsilon_{\text{lateral}}^2$$

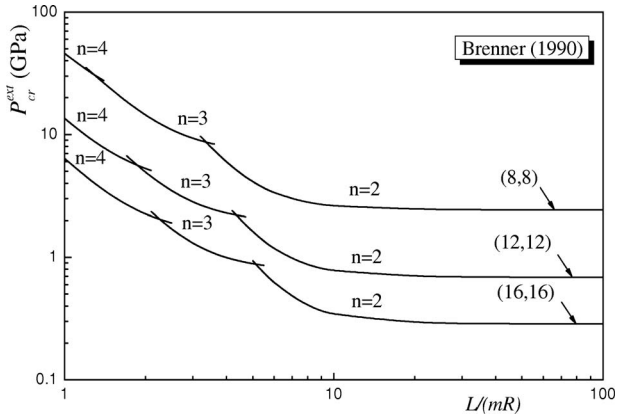

Fig. 11 The critical external pressure for bifurcation based on the Brenner potential [7] versus $L/(mR)$ for the (8,8), (12,12), and (16,16) armchair carbon nanotubes, where $m(=1,2,3,...)$ is the bifurcation mode number, R and L are the radius and length of the carbon nanotube, respectively, and $n=1,2,3,...$ represents the nonaxisymmetric bifurcation

$$E_{ZZ} = \varepsilon_{\text{axial}} + \frac{1}{2}\varepsilon_{\text{axial}}^2 + \frac{1}{2}\kappa^2 R^2 (1 + \varepsilon_{\text{lateral}})^2$$

$$E_{\theta Z} = \frac{1}{2}\kappa R (1 + \varepsilon_{\text{lateral}})^2 \tag{6.2}$$

$$K_{\theta\theta} = -\frac{\varepsilon_{\text{lateral}}}{R}, \quad K_{ZZ} = -\kappa^2 R (1 + \varepsilon_{\text{lateral}}), \quad K_{\theta Z} = -\kappa (1 + \varepsilon_{\text{lateral}}) \tag{6.3}$$

The strain energy density $W = W(E_{\alpha\beta}, K_{\alpha\beta})$ is obtained from the modified Born rule (Eq. (2.15) in Part I of this paper). It gives the components of second Piola–Kirchhoff stress and bending moment,

$$T_{\alpha\beta} = \frac{\partial W}{\partial E_{\alpha\beta}}, \quad M_{\alpha\beta} = \frac{\partial W}{\partial K_{\alpha\beta}} \tag{6.4}$$

The equilibrium equations become

$$T_{\theta\theta} + 2\kappa R T_{\theta Z} - \frac{M_{\theta\theta} + 2\kappa R M_{\theta Z} + \kappa^2 R^2 M_{ZZ}}{R(1 + \varepsilon_{\text{lateral}})} = 0 \tag{6.5}$$

The boundary conditions for pure torsion give

$$T_{ZZ} = 0 \tag{6.6}$$

Equations (6.5) and (6.6) determine the axial strain $\varepsilon_{\text{axial}}$ and the strain $\varepsilon_{\text{lateral}}$ in the circumferential direction in terms of the twist κ.

6.2 Onset of Bifurcation: Nonuniform Increment of Deformation. The deformation is still uniform at the onset of bifurcation, but its increment (rate) is not. Let $\boldsymbol{v} = \dot{\boldsymbol{U}}$ denote the velocity with the components v_R, v_θ, and v_Z. The velocity field in the CNT can be expressed as[1]

$$v_\theta = V_{\theta 0} \cos\left(\frac{m\pi Z}{L} - n\theta\right), \quad v_Z = V_{Z0} \cos\left(\frac{m\pi Z}{L} - n\theta\right),$$

$$v_R = V_{R0} \sin\left(\frac{m\pi Z}{L} - n\theta\right) \tag{6.7}$$

where $n = 0, 1, 2, 3, \ldots$, $m(=1, 2, 3, \ldots)$ is the eigenmode number, R and L are the radius and length of the CNT, respectively, and $(V_{\theta 0}, V_{Z0}, V_{R0})$ is the corresponding eigenvector. The substitution of Eq. (6.7) into the incremental equilibrium equations (Eqs. (3.9) and (3.10) in Part I of this paper) yields the homogeneous algebraic equations for $(V_{\theta 0}, V_{Z0}, V_{R0})$. The vanishing of determinant of the coefficient matrix gives the condition for bifurcation in torsion.

Figure 12 shows $\kappa_{\text{cr}} R$ based on the Brenner potential [7] versus L/mR for the (8,8), (12,12), and (16,16) armchair CNTs, where κ_{cr} is the critical twist for bifurcation, $m(=1, 2, 3, \ldots)$ is the eigenmode number, and R and L are the CNT radius and length, respectively. For long CNTs (large $L/(mR)$), the bifurcation mode is always $n = 2$. The corresponding critical twist for bifurcation κ_{cr} becomes a constant for each CNT, and this constant decreases rapidly with the increasing CNT radius. For relatively short CNTs, other bifurcation modes $n = 3, 4, \ldots$ appear, but $n = 0$ and $n = 1$ never occur.

Figure 13 shows the critical twist for bifurcation $\kappa_{\text{cr}} R$ based on the second-generation interatomic potential [8]. The curves are similar to those in Fig. 12. Therefore, the Brenner potential [7] and its second-generation interatomic potential [8] give noticeable different critical twists for bifurcation in torsion.

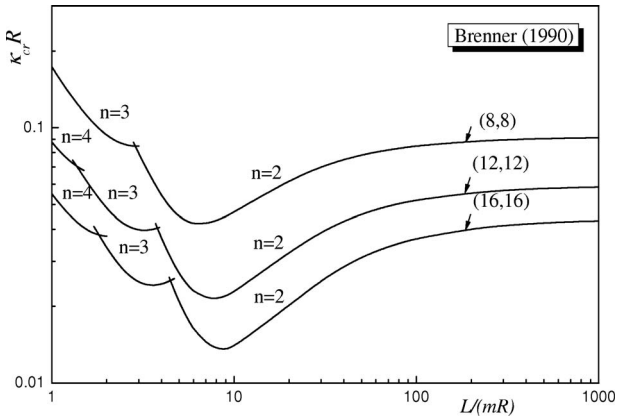

Fig. 12 The critical twist k_{cr} for bifurcation based on the Brenner potential [7] versus $L/(mR)$ for the (8,8), (12,12), and (16,16) armchair carbon nanotubes, where $m(=1,2,3,\ldots)$ is the bifurcation mode number, R and L are the radius and length of the carbon nanotube, respectively, and $n=1,2,3,\ldots$ represents the nonaxisymmetric bifurcation

Using the molecular dynamics simulations based on the Brenner potential [7], Yakobson et al. [1] studied the buckling of a 23-nm-long (13,0) zigzag CNT under torsion. They reported the critical twist $\kappa_{\text{cr}} R$ for bifurcation around 0.061 for $n = 2$, while the present analysis gives 0.048 for the same n.

7 Concluding Remarks

Based on the finite-deformation shell theory for CNTs established from the interatomic potential in Part I of this paper, we have studied the instability of CNTs subjected to different loadings (tension, compression, internal and external pressures, and torsion). Similar to the conventional shells, CNTs may undergo bifurcation under compression/torsion/external pressure. Our analysis, however, shows that CNTs may also undergo bifurcation in tension and internal pressure, though the bifurcation modes for tension and compression are very different, and so are the modes for internal and external pressures.

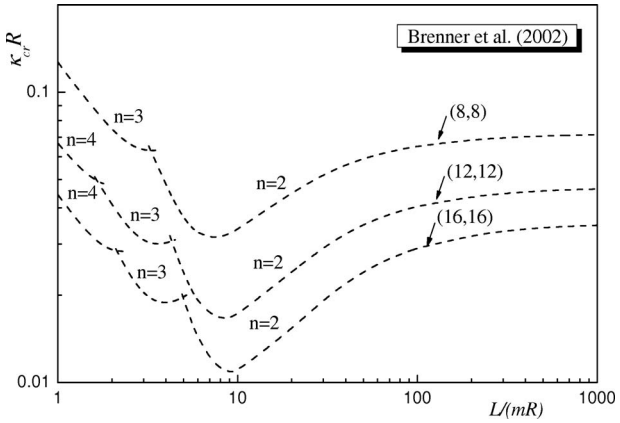

Fig. 13 The critical twist k_{cr} for bifurcation based on the second-generation interatomic potential [8] versus $L/(mR)$ for the (8,8), (12,12), and (16,16) armchair carbon nanotubes, where $m(=1,2,3,\ldots)$ is the bifurcation mode number, R and L are the radius and length of the carbon nanotube, respectively, and $n=1,2,3,\ldots$ represents the nonaxisymmetric bifurcation

[1]The complete expansion of the velocity v_θ includes the terms $\sin n\theta \sin m\pi Z/L$, $\sin n\theta \cos m\pi Z/L$, $\cos n\theta \sin m\pi Z/L$, and $\cos n\theta \cos m\pi Z/L$ $(n = 0, 1, 2, \ldots, m = 1, 2, 3, \ldots)$, which are equivalent to $\cos(m\pi Z/L - n\theta)$, $\cos(m\pi Z/L + n\theta)$, $\sin(m\pi Z/L - n\theta)$, and $\sin(m\pi Z/L + n\theta)$. It can be shown that these four terms lead to the same bifurcation condition as the first one $\cos(m\pi Z/L - n\theta)$ in v_θ in Eq. (6.7).

The critical load for instability and bifurcation depends on the interatomic potential used. The Brenner potential [7] and its second-generation potential [8] may give quite different critical loads. This is partially because the parameters in interatomic potentials are determined by fitting the binding energy, lattice constants, elastic properties, and vacancy formation energy of diamond and graphite, which are properties at the vanishing strain level, i.e., not accounting for the behavior at the finite strain.

Acknowledgment

Y.H. acknowledges the support from the NSF through NanoCEMMS (Grant No. DMI03-28162) at the University of Illinois and ONR Composites for Marine Structures Program (Grant No. N00014-01-1-0205, Program Manager Dr. Y. D. S. Rajapakse). The authors also acknowledge the support from the NSFC and Ministry of Education of China. K.C.H. also acknowledges the support from National Basic Research Program of China (973 Program) Grant No. 2007CB936803.

References

[1] Yakobson, B. I., Brabec, C. J., and Bernholc, J., 1996, "Nanomechanics of Carbon Tubes: Instabilities Beyond Linear Response," Phys. Rev. Lett., **76**, pp. 2511–2514.

[2] Buehler, M. J., Kong, Y., and Gao, H. J., 2004, "Deformation Mechanism of Very Long Single-Wall Carbon Nanotubes Subject to Compressive Loading," ASME J. Eng. Mater. Technol., **126**, pp. 245–249.

[3] Zhang, P., Jiang, H., Huang, Y., Geubelle, P. H., and Hwang, K. C., 2004, "An Atomistic-Based Continuum Theory for Carbonnanotubes: Analysis of Fracture Nucleation," J. Mech. Phys. Solids, **52**, pp. 977–998.

[4] Cao, G. X., and Chen, X., 2006, "Buckling of Single-Walled Carbon Nanotubes Upon Bending: Molecular Dynamics Simulations and Finite Element Method," Phys. Rev. B, **73**, p. 155435.

[5] Duan, X. J., Tang, C., Zhang, J., Guo, W., and Liu, Z., 2007, "Two Distinct Buckling Modes in Carbon Nanotube Bending," Nano Lett., **7**, pp. 143–148.

[6] Timoshenko, S., and Gere, J., 1961, *Theory of Elastic Stability*, McGraw-Hill, New York.

[7] Brenner, D. W., 1990, "Empirical Potential for Hydrocarbons for Use in Simulating the Chemical Vapor Deposition of Diamond Dilms," Phys. Rev. B, **42**, pp. 9458–9471.

[8] Brenner, D. W., Shenderova, O. A., Harrison, J. A., Stuart, S. J., Ni, B., and Sinnott, S. B., 2002, "A Second-Generation Reactive Empirical Bond Order (Rebo) Potential Energy Expression for Hydrocarbons," J. Phys.: Condens. Matter, **14**, pp. 783–802.

[9] Wu, J., Hwang, K. C., and Huang, Y., 2008, "An Atomistic-Based Finite-Deformation Shell Theory for Single-Wall Carbon Nanotubes," J. Mech. Phys. Solids, **56**, pp. 279–292.

[10] Liew, K. M., Wong, C. H., He, X. Q., Tan, M. J., and Meguid, S. A., 2004, "Nanomechanics of Single and Multiwalled Carbon Nanotubes," Phys. Rev. B, **69**, p. 115429.

Surface Effect and Size Dependence on the Energy Release Due to a Nanosized Hole Expansion in Plane Elastic Materials

Q. Li

Y. H. Chen

School of Aerospace, SVL,
Xian Jiao-Tong University,
Xian, 710049, P.R.C.
e-mail: liqun@mailst.xjtu.edu.cn

This paper deals with the surface effect and size dependence on the M-integral representing the energy release due to a nanodefect expansion in plane elasticity. Due to the high surface-to-volume ratio for reinforcing particles in the nanometer scale, the surface effect along the nanosized hole may be induced from the residual surface stress and the surface Lamé constants. The invariant integrals such as the J_k-integral vector and the M-integral customarily used in macrofracture mechanics are extended to treat plane elastic materials containing a nanosized hole. It is concluded that both components of the J_k-integral vanish when the contour selected to calculate the integral encloses the whole nanosized hole. This leads to the independence of the M-integral from the global coordinate shift. It is concluded that the surface effect and the size dependence on the energy release due to the nanohole expansion are significant especially when the hole size is less than 40 nm. This present study reveals that the discrepancies of the M-integral value with the surface effect from the referenced value M_0 without the surface effect are mainly induced from the residual surface stress τ^0 rather than from the surface Lamé constants μ^s and λ^s. [DOI: 10.1115/1.2965368]

Keywords: invariant integral, nanosized hole, surface effect size dependence

1 Introduction

The microelectromechanical system (MEMS) and advanced materials in the nanometer scale become increasingly popular owing to their wide potential applications in constructing new microinstruments and highly effective memory materials. These motivate a new interest in nanomechanics. A detailed review has been given by Ortiz [1]. On the other hand, the well-known invariant integrals derived from Noether's theorem in macroelasticity such as the J_k-integral vector and M-integral have been proved to be extremely attractive over the past three decades [2–5]. Physically, the J_k-integral vector ($k=1,2$) and M-integral can be interpreted as the energy release for defect movements and uniform defect expansion, respectively [6]. More recently, Chen [7,8] concluded that the physical meaning of the M-integral can be interpreted as the energy release in many macrodefect cases. However, to the present authors' knowledge, the above mentioned integrals were always limited to the macroelasticity and no one in open literature had accounted for the role of the invariant integrals played in nanomaterials. As well known, due to the high surface-to-volume ratio for reinforcing particles in the nanometer scale, the surface effect and the size dependence should be considered in detail, which may yield an un-negligible traction on the surface of a nanosized hole. This is quite different from those in macroelasticity, where the traction-free condition is always assumed along the surface of the macrosized hole. Hence, some basic properties of the invariant integrals are needed to be re-analyzed in nanomaterials when considering the surface effect on the nanosized hole. Only after doing so could the extensive application of the invariant integrals in the nanomaterials be developed.

The goal of this paper is to supply the lack of the invariant integrals (e.g., J_k-integral vector and M-integral) in nanomechanics with defects. Attention is focused on the surface effect and its influence on the size dependence of the invariant integrals in nanomaterials with defects. As an initial attempt, an infinite elastic plane containing a nanosized circular hole is considered, as shown in Fig. 1. The analytical solution of the full fields can be obtained by using the classical complex potential method [9] together with the surface effect or the non-traction-free condition along the rim of the nanosized hole. It is concluded that a conservation law of the J_k-integral vector still exists in this case. That is, both components of the J_k-integral vector defined in a global coordinate system vanish when the integration contour chosen to calculate the two components of the vector encloses the whole nanosized hole. It is also concluded that the M-integral in nanomaterials possesses the independence from the coordinate system shift or rotation even though the surface effect or the non-traction-free condition is considered. Numerical results reveal that the influence of the surface effect on the M-integral is size dependent on both the surface constants and the residual surface stress. However, we find that the large discrepancies of the M-integral value from the referenced value M_0 without the surface effect are mainly induced from the residual surface stress λ^0 rather than from the surface Lamé constants μ^s and λ^s. That is, in the absence of the residual surface stress τ^0, the surface Lamé constants μ^s and λ^s only yield some very small effect on the M-integral. In most cases, the relative errors, i.e., $(M_0-M)/M_0$, are less than 5% except for the case when the hole is extremely small (say, less than 2 nm). Whereas, in the absence of the surface Lamé constants μ^s and λ^s, the residual surface stress τ^0 yields a significant effect on the

Contributed by the Applied Mechanics Division of ASME for publication in the JOURNAL OF APPLIED MECHANICS. Manuscript received November 11, 2007; final manuscript received March 18, 2008; published online August 20, 2008. Review conducted by Horacio D. Espinosa.

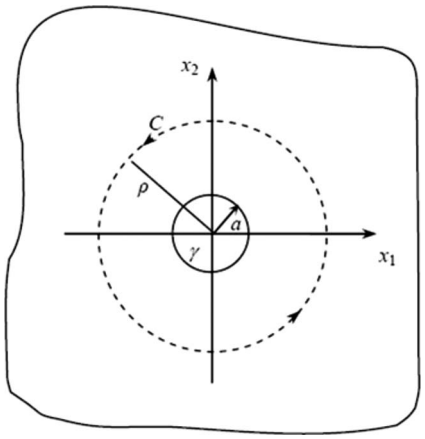

Fig. 1 Plane elasticity containing a nanosized hole with the surface effect

M-integral. In most cases, the discrepancies may be larger than 100%. Even when the hole is large enough, say, 40 nm, the discrepancy is still over 10%. This provides a possible way to study the coalescence or interaction among many nanosized holes.

2 Analytical Solutions for Plane Elasticity Containing a Nanosized Circular Hole

We consider an infinite elastic plane containing a nanosized circular hole with radius a, as shown in Fig. 1. The remote loadings are denoted by σ_{11}^{∞}, σ_{12}^{∞}, and σ_{22}^{∞}, respectively. Here, the hole surface is no longer traction-free, rather, the surface stress that originated from the intrinsic surface/interface energy should be taken into account, which may play a significant role in controlling the deformation of the nanoscale structure. In plane isotropic elasticity in the absence of body forces with the assumption that the surface adheres to the bulk without slipping, the equilibrium and constitutive equations can be expressed as follows:

$$\sigma_{ij,j} = 0 \tag{1}$$

$$\sigma_{ij} = \lambda \varepsilon_{kk} \delta_{ij} + 2\mu \varepsilon_{ij} \tag{2}$$

where λ and μ are the Lamé constants, δ_{ij} is the Kronecker delta, and σ_{ij} and ε_{ij} are the stress and strain components, respectively; the implicit summation convention by the repeated index has been adopted.

Due to the high surface-to-volume ratio for reinforcing particles at nanoscale, the role of surface effect along the nanosized hole becomes important. This yields an un-negligible traction on the surface of the nanosized hole. Assume that the surface adheres perfectly to the bulk material without slipping. The equilibrium equation and the constitutive relations on the surface are expressed as [10–13]

$$\sigma_{ij} n_i n_j = \frac{\sigma_{\alpha\beta}^s}{a} \tag{3}$$

$$\sigma_{\alpha\beta}^s = \tau^0 \delta_{\alpha\beta} + 2(\mu^s - \tau^0)\varepsilon_{\alpha\beta} + (\lambda^s + \tau^0)\varepsilon_{\gamma\gamma}\delta_{\alpha\beta} \tag{4}$$

where n_i is the normal vector of the surface, σ_{ab}^s is the surface stress tensor, a is the radius of the nanohole, τ^0 is the residual surface stress under an unstrained condition, and μ^s and λ^s are the surface Lamé constants, which depend on the material type and the surface crystal orientation. As seen in Eq. (3), when the size of hole is in macroscale, the surface effect can be neglected. However, when the size of hole is in nanoscale, the surface effect would be significant and has to be considered in analysis.

In the classical complex potential method in plane elasticity, the stress components ($\sigma_{\rho\rho}$, $\sigma_{\theta\theta}$, $\sigma_{\rho\theta}$) and the displacement components (u_ρ, u_θ) in the polar coordinate system (ρ, θ) can be expressed by two functions $\phi(z)$ and $\psi(z)$:

$$\sigma_{\rho\rho} + \sigma_{\theta\theta} = 4\,\mathrm{Re}\,\phi'(z)$$

$$\sigma_{\rho\rho} - i\sigma_{\rho\theta} = \phi'(z) + \overline{\phi'(z)} - e^{2i\theta}[\bar{z}\phi''(z) + \psi'(z)]$$

$$2\mu(u_\rho + iu_\theta) = e^{-i\theta}[\kappa\phi(z) - z\overline{\phi'(z)} - \overline{\psi(z)}] \tag{5}$$

where $k=(3-n)/(1+n)$ is for the plane stress problem, $k=(3-4n)$ is for the plane strain problem, and υ is the Poisson ratio.

Generally speaking, the complex potentials $\phi(z)$ and $\psi(z)$ can be expanded into the following Laurent series form [9,13]:

$$\phi(z) = Az + \sum_{n=1}^{\infty} A_n z^{-n}, \quad \psi(z) = Bz + \sum_{n=1}^{\infty} B_n z^{-n} \tag{6}$$

Substituting Eq. (6) into Eq. (5) and using Eqs. (3) and (4) at the surface of the nanosized hole as well as the loading condition at infinity, we can obtain

$$A = \frac{\sigma_{11}^{\infty} + \sigma_{22}^{\infty}}{4}, \quad B = \frac{\sigma_{22}^{\infty} - \sigma_{11}^{\infty} + 2i\sigma_{12}^{\infty}}{2}$$

$$A_1 = \frac{-(1+2\Lambda_1)B}{1+4\Lambda_1+\Lambda_2(\Lambda_1+\Lambda_3)}, \quad A_n = 0 \quad (n \geq 2)$$

$$B_1 = \frac{\tau^0 + 2A\Lambda_2(\Lambda_1+\Lambda_3) - 2A}{1+2\Lambda_1}, \quad B_2 = 0$$

$$B_3 = \frac{B\Lambda_2(\Lambda_1+\Lambda_3) - B}{1+4\Lambda_1+\Lambda_2(\Lambda_1+\Lambda_3)}, \quad B_n = 0 \quad (n \geq 4) \tag{7}$$

where

$$\Lambda_1 = \frac{2\mu^s + \lambda^s - \tau^0}{4a\mu} \tag{8}$$

for plane strain

$$\Lambda_2 = \frac{2\mu}{\lambda+\mu}, \quad \Lambda_3 = 0 \tag{9}$$

and for plane stress

$$\Lambda_2 = \frac{2(\lambda+2\mu)}{(3\lambda+2\mu)}, \quad \Lambda_3 = \frac{(\lambda^s+\tau^0)\nu}{4a\mu(\nu-1)} \tag{10}$$

The complete expressions of the stresses and the displacements can be given by substituting Eqs. (6)–(10) into Eq. (5). After lengthy but straightforward manipulations, we have

$$\sigma_{\rho\rho} = \frac{1}{a}\left[2A + \frac{B_1 a^2}{\rho^2} + \left(-\frac{4A_1 a^2}{\rho^2} + \frac{3B_3 a^4}{\rho^4} - B\right)\cos(2\theta)\right]$$

$$\sigma_{\rho\theta} = \frac{1}{a}\left(-\frac{2A_1 a^2}{\rho^2} + \frac{3B_3 a^4}{\rho^4} + B\right)\sin(2\theta)$$

$$\sigma_{\theta\theta} = \frac{1}{a}\left[2A - \frac{B_1 a^2}{\rho^2} - \left(\frac{3B_3 a^4}{\rho^4} - B\right)\cos(2\theta)\right] \tag{11}$$

$$u_\rho = \frac{1}{2\mu}\left[\frac{\kappa A\rho}{a} - \frac{\overline{B}_1 a}{\rho} - \frac{A\rho}{a} + \left(\frac{\kappa A_1 a}{\rho} - \frac{\overline{B}\rho}{a} - \frac{\overline{B}_3 a^3}{\rho^3} + \frac{\overline{A}_1 a}{\rho}\right)\cos(2\theta)\right]$$

$$u_\theta = \frac{1}{2\mu}\left(-\frac{\kappa A_1 a}{\rho} + \frac{\overline{B}\rho}{a} - \frac{\overline{B}_3 a^3}{\rho^3} + \frac{\overline{A}_1 a}{\rho}\right)\sin(2\theta) \tag{12}$$

3 Some Basic Properties of the Invariant Integrals as Influenced by the Surface Effect

The M-integral and J_k-integral vectors [3,4] in macroplane elasticity can be extended to treat nanomaterials with defects, which are formulated as follows:

$$M = \oint_C (wx_i n_i - T_k u_{k,i} x_i) ds \tag{13}$$

$$J_k = \oint_C (wn_k - u_{i,k} T)_i ds \quad (k = 1,2) \tag{14}$$

where C is a counterclockwise contour enclosing the whole nanosized hole, as shown in Fig. 1, $w = \sigma_{ij}\varepsilon_{ij}/2$ is the strain energy density, T_k is the principle traction acting on the outside of a closed contour C, x_j with $j = 1,2$ representing a rectangular plane coordinate system, and n_i is the outside normal component of Contour C.

For convenience, we prefer to obtain the expressions of such invariant integrals from the polar coordinate system (ρ, θ), which are cited below:

$$J_1 = \oint_C \left\{ w \cos\theta - \left(\varepsilon_{\rho\rho} \cos\theta - \frac{\sin\theta}{\rho} \frac{\partial u_\rho}{\partial \theta} \right) T_\rho - \left(\frac{\partial u_\theta}{\partial \rho} \cos\theta - \frac{\sin\theta}{\rho} \frac{\partial u_\theta}{\partial \theta} \right) T_\theta \right\} ds \tag{15}$$

$$J_2 = \oint_C \left\{ w \sin\theta - \left(\varepsilon_{\rho\rho} \sin\theta + \frac{\cos\theta}{\rho} \frac{\partial u_\rho}{\partial \theta} \right) T_\rho - \left(\frac{\partial u_\theta}{\partial \rho} \sin\theta + \frac{\cos\theta}{\rho} \frac{\partial u_\theta}{\partial \theta} \right) T_\theta \right\} ds \tag{16}$$

$$M = \oint_C \left[w - T_\rho \varepsilon_{\rho\rho} - T_\theta \left(2\varepsilon_{\rho\theta} + \frac{u_\theta}{\rho} - \frac{1}{\rho} \frac{\partial u_\theta}{\partial \theta} \right) \right] \rho ds \tag{17}$$

According to the intrinsic path-independence of the invariant integrals, we select a special circular contour as the integral path (see Contour C in Fig. 1), along which we have

$$T_\rho = \sigma_{\rho\rho}, \quad T_\theta = \sigma_{\rho\theta}, \quad ds = \rho d\theta \tag{18}$$

Substituting Eqs. (11), (12), and (18) into Eqs. (15) and (16), we can prove that the following relations are always valid:

$$J_1 \equiv 0, \quad J_2 \equiv 0 \tag{19}$$

In deriving Eq. (19), we have used the following identities:

$$\int_0^{2\pi} \cos(n\theta) d\theta = 0, \quad \int_0^{2\pi} \sin(n\theta) d\theta = 0, \quad (n \neq 0) \tag{20}$$

Equation (19) shows that both the remote loadings and the surface effect have no contribution to the value of the J_k-integral. In other words, both the J_1-integral and the J_2-integral always vanish, provided that the closed contour encloses the whole nanohole. This means that a conservation law of the J_k-integral vector exists in nanomaterials with defects even though some unknown stresses are attached on the nanosized hole surfaces.

On the other hand, the independence of the M-integral from the coordinate system shift or rotation should also be clarified in detail. When the coordinate axes (x_1, x_2) are rotated through an angle $-\varphi^*$, a new coordinate system (x_1^*, x_2^*) is proposed. Since the M-integral is an inner product of the J_k-integral vector and the vector $x_k = (x_1, x_2)$, as defined in Eq. (13), it is scalar and hence invariant after the rotation

$$M^*(x_1^*, x_2^*) = M(x_1, x_2) \tag{21}$$

where the integrals $M^*(x_1^*, x_2^*)$ and $M(x_1, x_2)$ are defined in (x_1^*, x_2^*) and (x_1, x_2), respectively.

Now, we consider whether the M-integral varies when one system of rectangular coordinates (x_1, x_2) shifts to another (x_{01}, x_{02}) with the following relations:

$$x_1 = x_{01} - \eta_1$$

$$x_2 = x_{02} - \eta_2 \tag{22}$$

The value of the M-integral in the new system (x_{01}, x_{02}) denoted by M' should be given by substituting Eq. (22) into Eq. (13),

$$M'(x_{01}, x_{02}) = \oint_C (wx_{0i} n_i - T_k u_{k,i} x_{0i}) ds = M(x_1, x_2) + \eta_1 J_1(x_1, x_2) + \eta_2 J_2(x_1, x_2) \tag{23}$$

Obviously, the first term in the right hand of Eq. (23) is just the same as the M-integral in the original system (x_1, x_2), whereas, according to the conservation laws of the J_k-integral in Eq. (19), the last two terms in Eq. (23) should vanish. Thus, the value of the M-integral in nanomaterials does not depend on the shift and rotation of the global coordinate system even though the surface of the nanohole is no longer traction-free.

Subsequently, attention is paid to the influence of the surface effect on the M-integral value. Substituting Eqs. (11) and (12) into Eq. (17) yields

$$M = \frac{-8AB_1\pi(1-\upsilon^2)}{E} \tag{24}$$

where E is Young's modulus; the coefficients A and B_1 have been given by Eq. (7), which is determined by the remote loadings, the size of the hole, the surface effect, and the material constants. For the plane stress condition, E in Eq. (24) should be replaced by $E(1-\upsilon^2)$.

In order to clearly understand the influence of the surface effect or the size dependence on the energy release represented by the M-integral, we take a typical polycrystalline aluminum ($E = 70.3$ GPa, $\upsilon = 0.345$)) as an example and calculate numerical results of the M-integral by Eq. (24) under plane strain deformation. The surface effect along the nanosized hole is represented by the surface Lamé constants μ^s and λ^s and the residual surface stress τ^0. Two different cases of surface effect are considered in the present investigation, respectively, i.e., (i) $\mu^s = -5.4251$ N/m, $\lambda^s = 3.4939$ N/m, and $\tau^0 = 0.5689$ N/m for the Al [1 0 0] surface and (ii) $\mu^s = -0.3760$ N/m, $\lambda^s = 6.8511$ N/m, and $\tau^0 = 0.9108$ N/m for the Al [1 1 1] surface [13].

First, the effect of the surface Lamé constants μ^s and λ^s on the M-integral is plotted in Fig. 2 for the case $\tau^0 = 0$, where M_0 denotes the referenced value obtained in the classical elasticity without the surface effect, i.e., $\mu^s = 0$, $\lambda^s = 0$, and $\tau^0 = 0$. Figure 2 shows that different surface constants yield some different values of the M-integral as compared to the referenced value. However, the differences are not significant due to the relative errors, i.e., $(M_0 - M)/M_0$, which are less than 5% in most cases. Only when the hole radius is extremely small as less than 2 nm would the errors be larger than 5%. This indicates that the surface constants without the residual surface stress τ^0 do not significantly influence the M-integral and in turn the size dependence on the M-integral is very small except the hole size being extremely small (less than 2 nm). Indeed, as shown in Fig. 2, the effect of the surface constants without the residual surface stress τ^0 is negligible when the hole radius is over 5 nm with the values of the M-integral being nearly equal to the referenced value M_0.

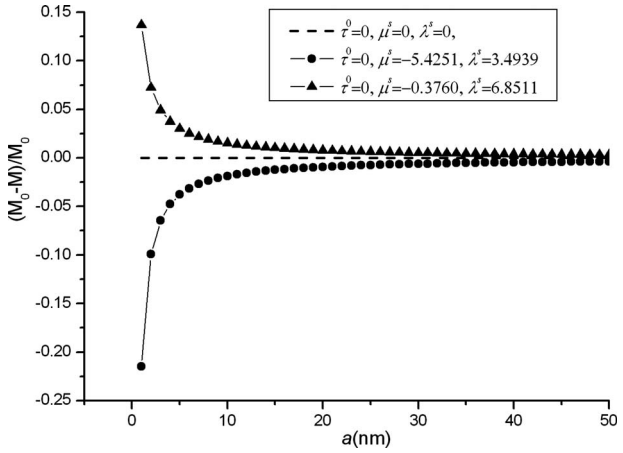

Fig. 2 The effect of the surface constants on the *M*-integral against the size of the hole without a residual surface stress ($\tau^0=0$)

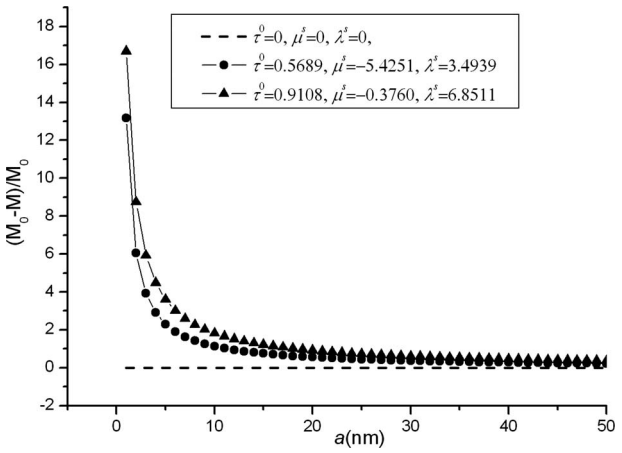

Fig. 4 The effect of both the residual stress and the surface constants on the *M*-integral against the size of the hole

Second, Fig. 3 shows the effect of the residual surface stress τ^0 on the M-integral for the case without the surface constants ($\mu^s=0$, $\lambda^s=0$). Large discrepancies can be found between the values of the M-integral and the referenced value M_0 without the surface effect. As seen in Fig. 3, these discrepancies increase very rapidly when the radius of the hole decreases. For example, the relative errors become 100% or more when the hole size is 5 nm. Even when the hole size is large enough, say, 40 nm, these errors are still larger than 10%, which could not be neglected. It is concluded that the surface effect is mainly due to the residual stress τ^0 rather than the surface Lamé constants μ^s and λ^s, whereas the existence of the residual stress along the nanohole always decreases the energy release as represented by the M-integral.

Third, Fig. 4 shows the discrepancies between the M-integral for two different combinations of the residual surface stress τ^0 and the surface constants μ^s and λ^s. Similar to the above discussions, the surface effect or size dependence is significant mainly due to the existence of the residual surface stress τ^0. The larger the residual surface stress is, the larger the discrepancy is. For example, the residual surface stress τ^0 being 0.9108 N/m yields much larger discrepancies of the M-integral from the referenced value than those for τ^0 being 0.5689 N/m. Even when the hole size is large enough, say, 40 nm, these discrepancies are still larger than 10%, which could not be neglected.

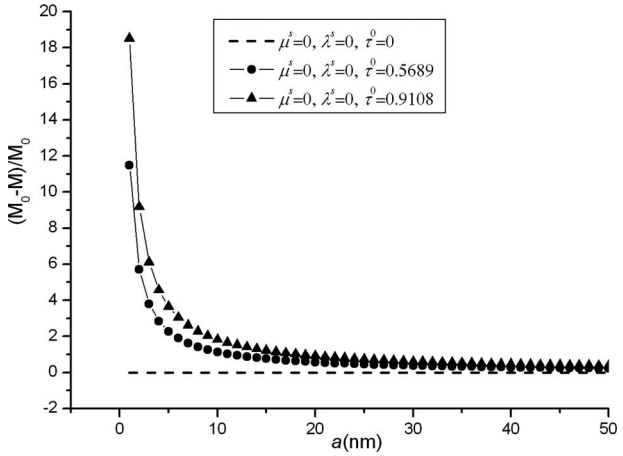

Fig. 3 The effect of the surface residual stress on the *M*-integral against the size of the hole without surface constants ($\mu^s=0$, $\lambda^s=0$)

4 Conclusions and Remarks

Although the surface effect of the nanosized hole induced from the residual stress τ^0 and the surface Lamé constants μ^s and λ^s exists and the hole surfaces are no longer traction-free, this study clarifies that the M-integral is still independent from the coordinate shift or rotation and both components of the J_k-integral vector vanish in plane elastic materials with a single nanosized hole. It is concluded that the surface effect or the size dependence on the energy release due to the hole expansion, i.e., the M-integral, is significant. However, this is mainly due to the residual stress τ^0 rather than from the surface Lamé constants μ^s and λ^s. This study is consistent with those obtained in previous investigations, where the surface effect has been proved to yield significant influence on some other mechanical properties in nanomaterials, e.g., the deformation state [14], the effective modulus [15], the plane waves [16], etc. The present investigation provides some fundamental understanding on the J_k-integral and the M-integral in nanodefect mechanics. As the M-integral represents the energy release due to defect expansion, it could be used to describe the surface effect induced from other nanodefects. For example, the surface effect on the coalescence or interaction between two nanoholes is of physical importance, which will be presented in our consequent work. It should be emphasized that Jiang et al. [17] developed a cohesive law for interfaces between a carbon nanotube (CNT) and polymer to estimate the surface effect from the atomistic model. However, we pay more attention to the continuum model in our present study and the atomistic model established by Jiang et al. [17] would be perhaps involved in our consequent work.

Acknowledgment

This work was supported by the National Natural Science Foundation of China (Grant No. 10572110) and Doctoral Funds of Chinese Education Ministry.

References

[1] Ortiz, M., 1999, "Nanomechanics of Defects in Solids," Adv. Appl. Mech., **36**, pp. 2–79.
[2] Rice, J. R., 1968, "A Path-Independent Integral and the Approximation Analysis of Strain Concentration by Notches and Cracks," ASME J. Appl. Mech., **35**, pp. 297–320.
[3] Knowles, J. K., and Stermberg, E., 1972, "On a Class of Conservation Laws in Linearized and Finite Elastostatics," Arch. Ration. Mech. Anal., **44**, pp. 187–211.
[4] Budiansky, B., and Rice, J. R., 1973, "Conservation Laws and Energy Release Rates," ASME J. Appl. Mech., **40**, pp. 201–203.
[5] Kanninen, M. F., and Popelar, C. F., 1985, *Advanced Fracture Mechanics*, Oxford University Press, New York.
[6] Herrmann, A. G., and Herrmann, G., 1981, "On Energy Release Rate for a Plane Crack," ASME J. Appl. Mech., **48**, pp. 525–528.

[7] Chen, Y. H., 2001, "*M*-Integral Analysis for Two-Dimensional Solids With Strongly Interacting Cracks, Part I: In an Infinite Brittle Solid," Int. J. Solids Struct., **38**, pp. 3193–3212.
[8] Chen, Y. H., 2001, "*M*-Integral Analysis for Two-Dimensional Solids With Strongly Interacting Cracks, Part II: In the Brittle Phase of an Infinite Metal/Ceramic Bimaterial," Int. J. Solids Struct., **38**, pp. 3213–3232.
[9] Muskhelishvili, N. I., 1953, *Some Basic Problems of the Mathematical Theory of Elasticity*, Noordhoff, Leyden.
[10] Huang, Z. P., and Wang, J., 2006, "A Theory of Hyperelasticity of Multi-Phase Media With Surface/Interface Energy Effect," Acta Mech., **182**, pp. 195–210.
[11] Chen, T., Dvorak, G. J., and Yu, C. C., 2007, "Size-Dependent Elastic Properties of Unidirectional Nano-Composites With Interface Stresses," Acta Mech., **188**, pp. 39–54.
[12] Huang, Z. P., and Sun, L., 2007, "Size-Dependent Effective Properties of a Heterogeneous Material With Interface Energy Effect: From Finite Deformation Theory to Infinitesimal Strain Analysis," Acta Mech., **190**, pp. 151–163.
[13] Tian, L., and Rajapakse, R. K. N. D., 2007, "Analytical Solution for Size-Dependent Elastic Field of a Nanoscale Circular Inhomogeneity," ASME J. Appl. Mech., **74**, pp. 568–574.
[14] Wang, G. F., and Wang, T. J., 2006, "Deformation Around a Nanosized Elliptical Hole With Surface Effect," Appl. Phys. Lett., **89**, p. 161901.
[15] Yang, F. Q., 2004, "Size-Dependent Effective Modulus of Elastic Composite Materials: Spherical Nanocavities at Dilute Concentrations," J. Appl. Phys., **95**, pp. 3516–3521.
[16] Wang, G. F., Wang, T. J., and Feng, X. Q., 2006, "Surface Effects on the Diffraction of Plane Compressional Waves by a Nanosized Circular Hole," Appl. Phys. Lett., **89**, p. 231923.
[17] Jiang, L. Y., Huang, Y., Jiang, H., Ravichandran, G., Gao, H., Hwang, K. C., and Liu, B., 2006, "A Cohesive Law for Carbon Nanotube/Polymer Interfaces Based on the Van Der Waals Force," J. Mech. Phys. Solids, **54**, pp. 2436–2452.

Structure Design of a Piezoelectric Composite Disk for Control of Thermal Stress

Fumihiro Ashida
e-mail: ashida@ecs.shimane-u.ac.jp

Sei-ichiro Sakata
e-mail: sakata@ecs.shimane-u.ac.jp

Department of Electronic and Control Systems Engineering,
Shimane University,
1060 Nishikawatsu-cho,
Matsue-shi, Shimane 690-8504, Japan

Kouhei Matsumoto
Vehicle Engineering Department,
Mazda Engineering and Technology Co., Ltd.,
2-1-26 Niho, Minami-ku,
Hiroshima-shi, Hiroshima 734-0026, Japan
e-mail: matsumoto.koh@mspr.co.jp

In order to realize a plan for a hypersonic aircraft, development of a smart heat-resisting plate possible to control a thermal stress has been required because the safety of structural members must be secured even if they are exposed to a severe thermal loading beyond an estimated load. In view of such a background, this paper deals with a control problem of a thermal stress in a multilayer composite circular disk consisting of a structural layer and piezoceramic layers with concentrically arranged electrodes. When a heating temperature distribution acts on the structural layer surface, the maximum thermal stress in the structural layer can be suppressed by applying appropriate voltages to the electrodes. This thermo-elastic problem has been theoretically analyzed by employing the potential function techniques. Utilizing the analytical results, the nonlinear optimization problem for determining the applied voltages is transformed into a linear programming problem and then the optimum solution is successfully obtained. Based on the obtained solutions, the structure of a composite disk has been designed in order to demonstrate the function of stress control to the fullest extent possible. Finally, numerical results for the stresses before and after applying the determined voltages as well as for the structure design of the composite disk and the suppression ratio of the maximum thermal stress are shown in graphical and tabular forms. It is seen from the numerical results that the maximum thermal stress can be reduced by about 34% when the structure of the composite disk is designed optimally. [DOI: 10.1115/1.2965369]

Keywords: thermo-elasticity, stress control, piezoelectric actuation, multilayer composite disk, structure design, linear programming

1 Introduction

Researches on smart structures have attracted considerable attention in recent two decades. Since piezoelectric materials perform both functions called "self-monitoring" and "self-control," which are essential for smart structures, various electro-elastic problems of piezoelectric-based structures have been analyzed. Saravanos and Heyliger [1] as well as Wang and Yang [2] delivered review papers on mechanics and high-order theories for laminated piezoelectric plates. Rao and Sunar [3,4] and Irschik [5] reviewed important articles on smart structures mainly operated under isothermal conditions, while Tauchert et al. [6–8] reviewed papers concerning smart structures adaptable to the change in thermal environments.

As regards recent papers discussing the control of a thermal displacement, steady [9] and transient [10] thermo-elastic problems of functionally graded material (FGM) plates with a piezoelectric layer were analyzed and the distributions of applied voltages for suppressing the deflection at the center of the plates were numerically determined. Other related investigations include Ootao and Tanigawa [11], Ishihara and Noda [12,13], Yang et al. [14], and Oh [15]]. Focused on the control of a thermal displacement distribution, steady [16,17] and transient [18–20] thermo-elastic problems in piezoelectric composite plates were analyzed and the distributions of applied voltages were theoretically obtained so that the bottom surface of the plate had a desired displacement distribution. For a more realistic model, the work [17] was extended to the problems of controlling a thermal displacement distribution through application of stepwise voltages [21,22], in which case the applied voltages were determined by optimization.

Now, concerning the control of a thermal stress, it seems that there is only a paper [23] within the authors' knowledge. The paper demonstrated the possibility of controlling a thermal stress in a composite disk consisting of a structural layer and piezoceramic layers when the structural layer surface was exposed to a heating temperature distribution. It was then assumed that a number of electrodes of the same width were arranged at equal intervals on each piezoceramic layer. Applied voltages were determined by solving a nonlinear optimization problem in order to minimize the maximum thermal stress in the structural layer. For successful and efficient utilization of smart structures for control of a thermal stress, further research is needed.

The present paper extends the previous work [23] to a structure design problem of the composite disk in order to demonstrate the function of stress control to the fullest extent possible. The nonlinear optimization problem of determining the applied voltages is transformed to a linear programming problem by introducing new optimization variables. The applied voltages can be successfully determined so that the maximum thermal stress in the structural layer is minimized subject to constraints on stresses in piezoceramic layers. It is seen from numerical results that the maximum thermal stress can be reduced by about 34% when the structure of the composite disk is designed optimally. This reduction is about twice as high as that obtained under similar conditions in the previous work [23].

2 Basic Equations

For an axisymmetric problem of thermo-elasticity in transversely isotropic solids, it is convenient to represent the temperature change T as the sum of two functions:

Contributed by the Applied Mechanics Division of ASME for publication in the JOURNAL OF APPLIED MECHANICS. Manuscript received November 12, 2007; final manuscript received March 14, 2008; published online August 20, 2008. Review conducted by Martin Ostoja-Starzewski.

$$T(r,z) = T_z(z) + T_{rz}(r,z) \tag{1}$$

The temperature field is governed by Fourier's heat conduction equation:

$$T_{z,zz} = 0, \quad \lambda_r \Delta_1 T_{rz} + \lambda_z T_{rz,zz} = 0 \tag{2}$$

where λ_i are coefficients of thermal conductivity, $T_{z,z} = \partial T_z / \partial z$, and $\Delta_1 = \partial^2 / \partial r^2 + r^{-1} \partial / \partial r$.

In the following analysis, material constants of nonpiezoelectric solids will be denoted by symbols with a tilde such as $\tilde{\lambda}_i$, whereas those of piezoelectric solids will be represented by symbols without a tilde such as λ_i.

2.1 Response of Transversely Isotropic Solids. Constitutive equations for the thermo-elastic field of transversely isotropic solids without the piezoelectric effect are expressed as

$$\sigma_{rr} = \tilde{c}_{11} u_{r,r} + \tilde{c}_{12} r^{-1} u_r + \tilde{c}_{13} u_{z,z} - \tilde{\beta}_1 T$$

$$\sigma_{\theta\theta} = \tilde{c}_{12} u_{r,r} + \tilde{c}_{11} r^{-1} u_r + \tilde{c}_{13} u_{z,z} - \tilde{\beta}_1 T$$

$$\sigma_{zz} = \tilde{c}_{13} u_{r,r} + \tilde{c}_{13} r^{-1} u_r + \tilde{c}_{33} u_{z,z} - \tilde{\beta}_3 T$$

$$\sigma_{zr} = \tilde{c}_{44} (u_{z,r} + u_{r,z}) \tag{3}$$

where σ_{ij} are stresses, u_i are displacements, $\tilde{c}_{ij}$ are elastic stiffnesses, and $\tilde{\beta}_i$ are stress-temperature coefficients.

The displacements are expressed in terms of six potential functions ϕ_i and ψ_i $(i=0-2)$ as [19,24]

$$u_r = (\phi_1 + \phi_2 + \psi_1 + \psi_2)_{,r}$$

$$u_z = (\phi_0 + \tilde{k}_1 \phi_1 + \tilde{k}_2 \phi_2 + \psi_0 + \tilde{k}_1 \psi_1 + \tilde{k}_2 \psi_2)_{,z} \tag{4}$$

The governing equations of the potential functions are

$$\phi_{0,zz} = \frac{\tilde{\beta}_3}{\tilde{c}_{33}} T_z, \quad \Delta_1 \phi_i + \tilde{\mu}_i \phi_{i,zz} = \tilde{\xi}_i T_{rz} \quad (i = 1,2) \tag{5}$$

$$\psi_{0,zz} = 0, \quad \Delta_1 \psi_i + \tilde{\mu}_i \psi_{i,zz} = 0 \quad (i = 1,2) \tag{6}$$

where $\tilde{k}_i$, $\tilde{\mu}_i$, and $\tilde{\xi}_i$ are known coefficients related to the material constants [19,24].

2.2 Response of Piezoelectric Solids. For the thermo-elastic field in piezoelectric solids exhibiting the symmetry properties of crystal class 6 mm, constitutive equations are

$$\sigma_{rr} = c_{11} u_{r,r} + c_{12} r^{-1} u_r + c_{13} u_{z,z} + e_1 \Phi_{,z} - \beta_1 T$$

$$\sigma_{\theta\theta} = c_{12} u_{r,r} + c_{11} r^{-1} u_r + c_{13} u_{z,z} + e_1 \Phi_{,z} - \beta_1 T$$

$$\sigma_{zz} = c_{13} u_{r,r} + c_{13} r^{-1} u_r + c_{33} u_{z,z} + e_3 \Phi_{,z} - \beta_3 T$$

$$\sigma_{zr} = c_{44} (u_{z,r} + u_{r,z}) + e_4 \Phi_{,r} \tag{7}$$

whereas constitutive equations for the electric field are

$$D_r = e_4 (u_{z,r} + u_{r,z}) - \eta_1 \Phi_{,r}$$

$$D_z = e_1 u_{r,r} + e_1 r^{-1} u_r + e_3 u_{z,z} - \eta_3 \Phi_{,z} + p_3 T \tag{8}$$

in which Φ is the electric potential, D_i are dielectric flux densities, e_i are piezoelectric constants, η_i are dielectric permittivities, and p_3 is the pyroelectric constant.

The displacements and electric potential are expressed as [19,25]

$$u_r = (\phi_1 + \phi_2 + \sum_{i=1}^{3} \ell_i \psi_i)_{,r}$$

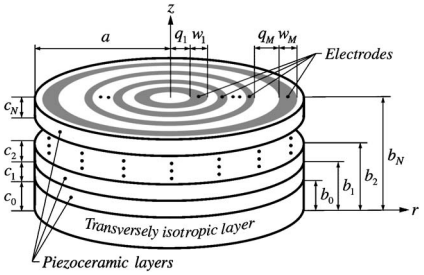

Fig. 1 Geometry of a multilayer composite disk

$$u_z = (\phi_0 + k_1 \phi_1 + j_1 \phi_2 + \psi_0 + \sum_{i=1}^{3} m_i \psi_i)_{,z} \tag{9}$$

$$\Phi = \chi_0 + \chi_1 + \varphi_0 + \sum_{i=1}^{3} n_i \psi_{i,z} \tag{10}$$

where ϕ_i $(i=0-2)$, χ_i $(i=0,1)$, φ_0, and ψ_i $(i=0-3)$ are potential functions governed by

$$\phi_{0,zz} = \gamma_1 T_z$$

$$\left(\Delta_1 + \mu_1 \frac{\partial^2}{\partial z^2}\right)\left(\Delta_1 + \mu_2 \frac{\partial^2}{\partial z^2}\right)\left(\Delta_1 + \mu_3 \frac{\partial^2}{\partial z^2}\right)\phi_1$$

$$= d_2 \Delta_1 \Delta_1 T_{rz} + d_1 \Delta_1 T_{rz,zz} + d_0 T_{rz,zzzz}$$

$$\phi_{2,zz} = \frac{1}{\xi_1}(\Delta_1 \phi_1 + \nu_1 \phi_{1,zz} - \delta_1 T_{rz}) \tag{11}$$

$$\chi_{0,z} = \gamma_2 T_z, \quad \chi_{1,z} = \frac{1}{\xi_2}(\Delta_1 \phi_2 + \nu_2 \phi_{2,zz} - \delta_2 T_{rz}) \tag{12}$$

$$\varphi_{0,z} = C, \quad \psi_{0,zz} = -\frac{e_3}{c_{33}} C, \quad \Delta_1 \psi_i + \mu_i \psi_{i,zz} = 0 \quad (i = 1-3) \tag{13}$$

in which C is an unknown coefficient to be determined from boundary conditions and ℓ_i, m_i, n_i, k_1, j_1, γ_i, μ_i, d_i, ν_i, ξ_i, and δ_i are known coefficients related to the material constants [19,25].

3 Presentation of Problem and Analysis

Let us consider a composite disk consisting of a transversely isotropic structural layer and piezoceramic layers of crystal class 6mm, as shown in Fig. 1. A number of electrodes are arranged concentrically on the upper surface of each piezoceramic layer. The layers are numbered $0-N$ from the bottom and the electrodes are numbered $1-M$ from the center. The thickness of the ith layer is denoted by c_i, the width of the kth electrode is represented by w_k, and the interval between the $(k-1)$th and kth electrodes is designated by q_k. The existence of folia such as electrodes and glue lines between the adjoining layers can be disregarded and perfect contact between the adjoining layers is assumed in the analysis.

3.1 Thermo-Elastic Response. Let us consider a thermo-elastic problem of the composite disk, when a heating temperature distribution $T_c f(r)$ acts on the bottom surface, heat convection occurs over the top surface, and the cylindrical surface is thermally insulated. The thermal boundary and interface conditions are then expressed as

$$T_{0,z} - h_0 T_0 = -h_0 T_c f(r) \quad \text{on} \quad z = 0 \tag{14}$$

$$T_0 = T_1, \quad -\tilde{\lambda}_z T_{0,z} = -\lambda_z T_{1,z} \quad \text{on} z = b_0$$

$$T_i = T_{i+1}, \quad -\lambda_z T_{i,z} = -\lambda_z T_{i+1,z} \quad \text{on } z = b_i \quad (i = 1-(N-1)) \tag{15}$$

$$T_{N,z} + h_N T_N = 0 \quad \text{on } z = b_N \tag{16}$$

$$T_{i,r} = 0 \quad \text{on } r = a \quad (i = 0-N) \tag{17}$$

where response quantities in the ith layer are represented by corresponding symbols with the subscript i, T_c is a constant temperature, and h_i are coefficients of relative heat transfer.

It is considered that the bottom and top surfaces of the composite disk are taken to be traction free, the cylindrical surface is smoothly constrained against radial deformation, and the cylindrical edge of the bottom surface is simply supported. In this case the elastic boundary and interface conditions are given by

$$u_{ir}^T = 0, \quad \sigma_{irz}^T = 0 \quad \text{on } r = a \quad (i = 0-N) \tag{18}$$

$$\sigma_{0zz}^T = \sigma_{0rz}^T = 0 \quad \text{on } z = 0 \tag{19}$$

$$u_{ir}^T = u_{(i+1)r}^T, \quad u_{iz}^T = u_{(i+1)z}^T, \quad \sigma_{izz}^T = \sigma_{(i+1)zz}^T, \quad \sigma_{irz}^T = \sigma_{(i+1)rz}^T$$
$$\text{on } z = b_i \quad (i = 0-(N-1)) \tag{20}$$

$$\sigma_{Nzz}^T = \sigma_{Nrz}^T = 0 \quad \text{on } z = b_N \tag{21}$$

$$u_{0z}^T = 0 \quad \text{at } r = a, z = 0 \tag{22}$$

where symbols with the superscript T denote response quantities induced by the thermal load.

Assuming that the upper and cylindrical surfaces of all piezoceramic layers are free of electric charge and the lower surface of every piezoceramic layer is electrically grounded, the electric boundary conditions are given by

$$D_{ir}^T = 0 \quad \text{on } r = a \quad (i = 1-N) \tag{23}$$

$$\Phi_i^T = 0 \quad \text{on } z = b_{i-1} \quad (i = 1-N) \tag{24}$$

$$D_{iz}^T = 0 \quad \text{on } z = b_i \quad (i = 1-N) \tag{25}$$

Let us analyze the thermo-elastic problem described above. The solutions to Eq. (2) are expressed as

$$T_{iz} = A_{i0}^T + B_{i0}^T z$$

$$T_{irz} = \sum_{l=1}^{\infty} J_0(\alpha_l r)\left(A_{il}^T \cosh\frac{\alpha_l z}{\lambda_i} + B_{il}^T \sinh\frac{\alpha_l z}{\lambda_i}\right) \quad (i = 0-N) \tag{26}$$

where $\lambda_0^2 = \tilde{\lambda}^2 = \tilde{\lambda}_z/\tilde{\lambda}_r$ and $\lambda_i^2 = \lambda^2 = \lambda_z/\lambda_r$ $(i = 1-N)$. Equation (26) is found to satisfy the boundary conditions (17), providing α_l are the roots of the equation

$$J_1(\alpha_l a) = 0 \tag{27}$$

Utilizing the boundary conditions (14)–(16), the coefficients A_{i0}^T, B_{i0}^T, A_{il}^T, and B_{il}^T can be determined.

For a thermo-elastic field of the structural layer, potential functions which satisfy their governing equations given in Eqs. (5) and (6) are given by

$$\phi_{00}^T = \frac{\tilde{\beta}_3}{\tilde{c}_{33}}\left(A_{00}^T \frac{z^2}{2} + B_{00}^T \frac{z^3}{6}\right)$$

$$\phi_{0j}^T = \tilde{F}_j \sum_{l=1}^{\infty} \frac{J_0(\alpha_l r)}{\alpha_l^2}\left\{A_{0l}^T \cosh\frac{\alpha_l z}{\tilde{\lambda}} + B_{0l}^T \sinh\frac{\alpha_l z}{\tilde{\lambda}}\right\} \quad (j = 1,2) \tag{28}$$

$$\psi_{00}^T = C_{00}^T z$$

$$\psi_{0j}^T = \sum_{l=1}^{\infty} \frac{J_0(\alpha_l r)}{\alpha_l^2}\left\{D_{0jl}^T \cosh\frac{\alpha_l z}{\sqrt{\tilde{\mu}_j}} + E_{0jl}^T \sinh\frac{\alpha_l z}{\sqrt{\tilde{\mu}_j}}\right\} \quad (j = 1,2) \tag{29}$$

where $\tilde{F}_j$ are known coefficients, while C_{00}^T, D_{0jl}^T, and E_{0jl}^T are unknown coefficients to be determined from the boundary conditions. Substituting Eqs. (26), (28), and (29) into Eqs. (4) and (3), the displacements and stresses in the structural layer can be obtained. For example, the radial stress is expressed by

$$\begin{aligned}\sigma_{0rr}^T = {} & \left(\frac{\tilde{c}_{13}}{\tilde{c}_{33}}\tilde{\beta}_3 - \tilde{\beta}_1\right)(A_{00}^T + B_{00}^T z) \\ & + \sum_{l=1}^{\infty}\left[\left\{\left\langle -\tilde{c}_{11}(\tilde{F}_1 + \tilde{F}_2) + \frac{\tilde{c}_{13}(\tilde{k}_1\tilde{F}_1 + \tilde{k}_2\tilde{F}_2)}{\tilde{\lambda}^2} - \tilde{\beta}_1\right\rangle J_0(\alpha_l r)\right.\right. \\ & \left.\left. + (\tilde{c}_{11} - \tilde{c}_{12})(\tilde{F}_1 + \tilde{F}_2)\frac{J_1(\alpha_l r)}{\alpha_l r}\right\} \right. \\ & \times\left\{A_{0l}^T \cosh\frac{\alpha_l z}{\tilde{\lambda}} + B_{0l}^T \sinh\frac{\alpha_l z}{\tilde{\lambda}}\right\} \\ & - \sum_{j=1}^{2}\left\{\left(\tilde{c}_{11} - \frac{\tilde{c}_{13}\tilde{k}_j}{\tilde{\mu}_j}\right)J_0(\alpha_l r) - (\tilde{c}_{11} - \tilde{c}_{12})\frac{J_1(\alpha_l r)}{\alpha_l r}\right\} \\ & \left. \times\left\{D_{0jl}^T \cosh\frac{\alpha_l z}{\sqrt{\tilde{\mu}_j}} + E_{0jl}^T \sinh\frac{\alpha_l z}{\sqrt{\tilde{\mu}_j}}\right\}\right]\end{aligned} \tag{30}$$

For thermo-electro-elastic fields of the piezoceramic layers, the potential functions which satisfy their governing equations given in Eqs. (11)–(13) are taken to be

$$\left.\begin{aligned}\phi_{i0}^T &= \gamma_1\left(A_{i0}^T \frac{z^2}{2} + B_{i0}^T \frac{z^3}{6}\right) \\ \phi_{ij}^T &= F_j \sum_{l=1}^{\infty} \frac{J_0(\alpha_l r)}{\alpha_l^2}\left\{A_{il}^T \cosh\frac{\alpha_l z}{\lambda} + B_{il}^T \sinh\frac{\alpha_l z}{\lambda}\right\} \quad (j = 1,2)\end{aligned}\right\} \quad (i = 1-N) \tag{31}$$

$$\left.\begin{aligned}\chi_{i0}^T &= \gamma_2\left(A_{i0}^T z + B_{i0}^T \frac{z^2}{2}\right) \\ \chi_{i1}^T &= F_3 \sum_{n=1}^{\infty} \frac{J_0(\alpha_l r)}{\alpha_l}\left\{A_{il}^T \sinh\frac{\alpha_l z}{\lambda} + B_{il}^T \cosh\frac{\alpha_l z}{\lambda}\right\}\end{aligned}\right\} \quad (i = 1-N) \tag{32}$$

$$\left.\begin{aligned}\varphi_{i0}^T &= C_{i0}^T z + G_{i0}^T, \quad \psi_{i0}^T = -\frac{e_3}{c_{33}} C_{i0}^T \frac{z^2}{2} + C_{i1}^T z \\ \psi_{ij}^T &= \sum_{l=1}^{\infty} \frac{J_0(\alpha_l r)}{\alpha_l^2}\left\{D_{ijl}^T \cosh\frac{\alpha_l z}{\sqrt{\mu_j}} + E_{ijl}^T \sinh\frac{\alpha_l z}{\sqrt{\mu_j}}\right\} \quad (j = 1-3)\end{aligned}\right\} \quad (i = 1-N) \tag{33}$$

where F_j are known coefficients, while C_{ij}^T, G_{i0}^T, D_{ijl}^T, and E_{ijl}^T are unknown coefficients to be determined from the boundary conditions. Substituting Eqs. (26) and (31)–(33) into Eqs. (9), (10), (7), and (8), the displacements, electric potential, stresses and dielectric flux densities in every piezoceramic layer can be obtained. For example, the electric potentials and radial stresses are expressed by

$$\Phi_i^T = \gamma_2\left(A_{i0}^T z + B_{i0}^T \frac{z^2}{2}\right) + C_{i0}^T z + G_{i0}^T + \sum_{l=1}^{\infty} \frac{J_0(\alpha_l r)}{\alpha_l}\left[F_3\left\{A_{il}^T \sinh\frac{\alpha_l z}{\lambda} + B_{il}^T \cosh\frac{\alpha_l z}{\lambda}\right\} + \sum_{j=1}^{3} \frac{n_j}{\sqrt{\mu_j}}\left\{D_{ijl}^T \sinh\frac{\alpha_l z}{\sqrt{\mu_j}} + E_{ijl}^T \cosh\frac{\alpha_l z}{\sqrt{\mu_j}}\right\}\right] \quad (i = 1-N) \tag{34}$$

$$\sigma_{irr}^T = (c_{13}\gamma_1 + e_1\gamma_2 - \beta_1)(A_{i0}^T + B_{i0}^T z) + \left(e_1 - \frac{c_{13}e_3}{c_{33}}\right)C_{i0}^T + \sum_{l=1}^{\infty}\left[\left\{\left\langle -c_{11}(F_1+F_2) + \frac{c_{13}(k_1F_1 + j_1F_2)}{\lambda^2} + \frac{e_1F_3}{\lambda} - \beta_1\right\rangle J_0(\alpha_l r) + (c_{11}-c_{12})(F_1+F_2)\frac{J_1(\alpha_l r)}{\alpha_l r}\right\} \times\left\{A_{il}^T \cosh\frac{\alpha_l z}{\lambda} + B_{il}^T \sinh\frac{\alpha_l z}{\lambda}\right\} - \sum_{j=1}^{3}\left\{\left(c_{11}\ell_j - \frac{c_{13}m_j + e_1 n_j}{\mu_j}\right)J_0(\alpha_l r) - (c_{11}-c_{12})\ell_j\frac{J_1(\alpha_l r)}{\alpha_l r}\right\} \times\left\{D_{ijl}^E \cosh\frac{\alpha_l z}{\sqrt{\mu_j}} + E_{ijl}^T \sinh\frac{\alpha_l z}{\sqrt{\mu_j}}\right\}\right] \quad (i = 1-N) \tag{35}$$

Utilizing the boundary conditions given in Eqs. (19)–(22), (24), and (25), all unknown coefficients C_{ij}^T, G_{i0}^T, D_{ijl}^T, and E_{ijl}^T can be determined, where Eqs. (18) and (23) are satisfied identically because of Eq. (27).

3.2 Electro-Elastic Response. Let us consider an electro-elastic problem of the composite disk when stepwise voltages are applied to electrodes on every piezoceramic layer:

$$\Phi_i^E = \sum_{k=1}^{M} V_{ik}\{H(r - r_k + w_k) - H(r - r_k)\} \quad \text{on} \quad z = b_i \quad (i = 1-N) \tag{36}$$

where V_{ik} is the voltage applied to the kth electrode on the ith piezoceramic layer (i.e., $(i-k)$th electrode), $H(r)$ is Heaviside's unit step function, r_k is the outer radius of the kth electrode, and symbols with the superscript E denote response quantities induced by the electric load. The boundary conditions given in Eqs. (18)–(24) are still applicable in this situation, but the superscript must be changed from T to E.

In order to analyze this problem efficiently, we consider a case where the unit voltage V_u is applied to the $(n-m)$th electrode only. Let the discrete response quantities in the ith layer induced by the unit voltage be $(\Delta u_{ij}^E)_{nm}$, $(\Delta\sigma_{ijk}^E)_{nm}$, $(\Delta\Phi_i^E)_{nm}$, and $(\Delta D_{ij}^E)_{nm}$, they can be obtained by employing the potential function techniques. As a result, eliminating the terms of the temperature change from the expressions for the thermo-elastic response, namely, substituting $A_{i0}^T = B_{i0}^T = A_{il}^T = B_{il}^T = 0$ into Eqs. (30), (34), and (35), the discrete electro-elastic response quantities can be obtained:

$$(\Delta\sigma_{0rr}^E)_{nm} = -\sum_{l=1}^{\infty}\sum_{j=1}^{2}\left\{\left(\tilde{c}_{11} - \frac{\tilde{c}_{13}\tilde{k}_j}{\tilde{\mu}_j}\right)J_0(\alpha_l r) - (\tilde{c}_{11} - \tilde{c}_{12})\frac{J_1(\alpha_l r)}{\alpha_l r}\right\} \times\left\{(\Delta D_{0jl}^E)_{nm}\cosh\frac{\alpha_l z}{\sqrt{\tilde{\mu}_j}} + (\Delta E_{0jl}^E)_{nm}\sinh\frac{\alpha_l z}{\sqrt{\tilde{\mu}_j}}\right\} \tag{37}$$

$$(\Delta\Phi_i^E)_{nm} = (\Delta C_{i0}^E)_{nm} z + (\Delta G_{i0}^E)_{nm} + \sum_{l=1}^{\infty}\frac{J_0(\alpha_l r)}{\alpha_l}\sum_{j=1}^{3}\frac{n_j}{\sqrt{\mu_j}}\left\{(\Delta D_{ijl}^E)_{nm}\sinh\frac{\alpha_l z}{\sqrt{\mu_j}} + (\Delta E_{ijl}^E)_{nm}\cosh\frac{\alpha_l z}{\sqrt{\mu_j}}\right\} \quad (i = 1-N) \tag{38}$$

$$(\Delta\sigma_{irr}^E)_{nm} = \left(e_1 - \frac{c_{13}e_3}{c_{33}}\right)(\Delta C_{i0}^E)_{nm} - \sum_{l=1}^{\infty}\sum_{j=1}^{3}\left\{\left(c_{11}\ell_j - \frac{c_{13}m_j + e_1 n_j}{\mu_j}\right)J_0(\alpha_l r) - (c_{11}-c_{12})\ell_j\frac{J_1(\alpha_l r)}{\alpha_l r}\right\} \times\left\{(\Delta D_{ijl}^E)_{nm}\cosh\frac{\alpha_l z}{\sqrt{\mu_j}} + (\Delta E_{ijl}^E)_{nm}\sinh\frac{\alpha_l z}{\sqrt{\mu_j}}\right\} \quad (i = 1-N) \tag{39}$$

where $(\Delta C_{ij}^E)_{nm}$, $(\Delta G_{i0}^E)_{nm}$, $(\Delta D_{ijl}^E)_{nm}$, and $(\Delta E_{ijl}^E)_{nm}$ are unknown coefficients and determined by utilizing the boundary conditions corresponding to Eqs. (19)–(22) and (24) as well as the boundary conditions (36) when $V_{ik} = V_u (i = n, k = m)$ and $V_{ik} = 0 (i \neq n, k \neq m)$. The boundary conditions corresponding to Eqs. (18) and (23) are identically satisfied because of Eq. (27). The discrete response quantities resulting from the unit voltage applied to each electrode can be calculated in advance and recorded in a database.

When a voltage of arbitrary magnitude V_{nm} is applied to the $(n-m)$th electrode, it is expressed as

$$V_{nm} = P_{nm} V_u \tag{40}$$

in which P_{nm} is the magnification factor. In the case where an arbitrary voltage is applied to every electrode, the response quantities are given by

$$\{u_{ij}^E, \sigma_{ijk}^E, \Phi_i^E, D_{ij}^E\} = \sum_{n=1}^{N}\sum_{m=1}^{M} P_{nm}\{(\Delta u_{ij}^E)_{nm}, (\Delta\sigma_{ijk}^E)_{nm}, (\Delta\Phi_i^E)_{nm}, (\Delta D_{ij}^E)_{nm}\} \tag{41}$$

3.3 Thermo-Electro-Elastic Response. When the composite disk is subjected to both thermal and electric loads, the resultant response is obtained by superimposing the responses due to each load:

$$\{u_{ij}, \sigma_{ijk}, \Phi_i, D_{ij}\} = \{u_{ij}^T, \sigma_{ijk}^T, \Phi_i^T, D_{ij}^T\} + \{u_{ij}^E, \sigma_{ijk}^E, \Phi_i^E, D_{ij}^E\} \tag{42}$$

4 Determination of Applied Voltages

Let us determine the applied voltages V_{ik} so that the maximum thermal stress in the structural layer is minimized subject to constraints on the stresses in the piezoceramic layers. This optimization problem is defined by

$$\text{find} \quad \mathbf{V} = (V_{11}, V_{12}, \ldots, V_{NM})^{\mathrm{T}}$$

$$\text{to minimize} \quad f_{\text{obj}}(\mathbf{V}) = \max_{r,z}(\sigma_{st}, |\sigma_{sc}|, |\sigma_{ss}|)$$

$$\text{subject to} \quad \sigma_{pt} \leq \sigma_{pt}^A, \quad |\sigma_{pc}| \leq |\sigma_{pc}^A|, \quad |\sigma_{ps}| \leq \sigma_{ps}^A \tag{43}$$

where $(\,)^{\mathrm{T}}$ denotes a transposed matrix; σ_{st}, σ_{sc}, and σ_{ss} are the maximum tensile, compressive, and shear stresses in the structural layer; σ_{pt}, σ_{pc}, and σ_{ps} are the maximum stresses in the piezoceramic layers; and σ_{pt}^A, σ_{pc}^A, and σ_{ps}^A are the corresponding allowable stresses. In order to assess a performance of the stress control, the ratio R evaluating the suppression of the maximum thermal stress in the structural layer is introduced:

$$R = (1 - R_s) \times 100\,[\%], \quad R_s = \frac{\sigma_{0\,\max}}{\sigma^T_{0\,\max}} \tag{44}$$

where

$$\sigma^T_{0\,\max} = \max_{r,z}(|\sigma^T_{0rr}|, |\sigma^T_{0\theta\theta}|, |\sigma^T_{0zz}|, |\sigma^T_{0rz}|)$$

$$\sigma_{0\,\max} = \max_{r,z}(|\sigma_{0rr}|, |\sigma_{0\theta\theta}|, |\sigma_{0zz}|, |\sigma_{0rz}|) \tag{45}$$

In the previous work [23], the quasi-Newton method was employed for solving a nonlinear optimization problem similar to Eq. (43), but the solution strongly depended on the choice of initial optimization variables and easily got stuck in a local minimum. Therefore, it is very difficult to obtain numerous optimum solutions necessary for a structure design of the composite disk by solving Eq. (43) repeatedly under different conditions for the thousandth time.

Now, let us consider a linearization of the nonlinear optimization problem (43). For that purpose, a new variable $s_{\max}$ is introduced:

$$\max_{r,z}(|\sigma_{0rr}|, |\sigma_{0\theta\theta}|, |\sigma_{0zz}|, |\sigma_{0rz}|) \le s_{\max} \tag{46}$$

Here, Eqs. (44)–(46) lead to $s_{\max} = R_s \sigma^T_{0\,\max}$. The response quantities induced by the heating temperature and the discrete response quantities caused by each unit voltage have been obtained, respectively. Therefore, utilizing Eqs. (40)–(42) and (46), the nonlinear optimization problem (43) is transformed into the linear programming problem as follows:

$$\begin{aligned}
&\text{find} \quad \mathbf{X} = \{P_{11}, P_{12}, \ldots, P_{nm}, R_s\}^{\mathrm{T}} \\
&\text{to minimize} \quad f_{\mathrm{obj}}(\mathbf{X}) = R_s \sigma^T_{0\,\max} \\
&\text{subject to} \quad \{|\sigma_{0rr}|, |\sigma_{0\theta\theta}|, |\sigma_{0zz}|, |\sigma_{0rz}|\} \le R_s \sigma^T_{0\,\max} \\
&\sigma^A_{pc} \le \{\sigma_{irr}, \sigma_{i\theta\theta}, \sigma_{izz}\} \le \sigma^A_{pt} \\
&-\sigma^A_{ps} \le \sigma_{irz} \le \sigma^A_{ps}
\end{aligned} \tag{47}$$

This linearization brings the advantage that the optimum solution can be certainly obtained.

5 Numerical Results

The structural layer is considered to be carbon fiber reinforced plastic (CFRP) with the properties [19],

$$(\tilde{\lambda}_r, \tilde{\lambda}_z) = (1, 0.5)\ \ \mathrm{W\ m^{-1}\ K^{-1}}$$

$$(\tilde{\beta}_1, \tilde{\beta}_3) = (1.84, 0.40) \times 10^6\ \ \mathrm{N\ K^{-1}\ m^{-2}}$$

$$(\tilde{c}_{11}, \tilde{c}_{12}, \tilde{c}_{13}, \tilde{c}_{33}, \tilde{c}_{44}) = (100.2, 49.8, 6.86, 10.9, 2.87) \times 10^9\ \ \mathrm{N\ m^{-2}}$$

$$\tilde{Y}_r = 74.3 \times 10^9\ \ \mathrm{N\ m^{-2}}, \quad \tilde{\alpha}_r = 11.3 \times 10^{-6}\ \ \mathrm{K^{-1}}$$

whereas the piezoceramic layers are taken to be cadmium selenide having the properties [19]:

$$\lambda_r = \lambda_z = 9\ \ \mathrm{W\ m^{-1}\ K^{-1}}$$

$$(\beta_1, \beta_3) = (0.621, 0.551) \times 10^6\ \ \mathrm{N\ K^{-1}\ m^{-2}}$$

$$(c_{11}, c_{12}, c_{13}, c_{33}, c_{44}) = (74.1, 45.2, 39.3, 83.6, 13.2) \times 10^9\ \ \mathrm{N\ m^{-2}}$$

$$(e_1, e_3, e_4) = (-0.160, 0.347, -0.138)\ \ \mathrm{C\ m^{-2}}$$

$$(\eta_1, \eta_3) = (82.6, 90.3) \times 10^{-12}\ \ \mathrm{C^2\ N^{-1}\ m^{-2}}$$

$$p_3 = -2.94 \times 10^{-6}\ \ \mathrm{C\ K^{-1}\ m^{-2}}, \quad d_1 = -3.92 \times 10^{-12}\ \ \mathrm{C\ N^{-1}}$$

in which $\tilde{Y}_r$ is Young's modulus, $\tilde{\alpha}_r$ is the coefficient of linear thermal expansion, and d_1 is the piezoelectric coefficient.

For convenience in presentation of numerical results, the following dimensionless quantities are introduced:

$$(\bar{r}, \bar{z}, \bar{c}_i, \bar{b}_i, \bar{w}_k, \bar{q}_k) = \frac{(r, z, c_i, b_i, w_k, q_k)}{a}, \quad B_i = a h_i$$

$$\bar{V}_{ik} = \frac{|d_1| V_{ik}}{a \tilde{\alpha}_r T_c}, \quad \bar{\sigma}_{ijk} = \frac{\sigma_{ijk}}{\tilde{\alpha}_r \tilde{Y}_r T_c}$$

where the unit voltage is given by $V_u = a \tilde{\alpha}_r T_c / |d_1|$. The heating temperature acting on the bottom surface of the composite disk is considered to have a distribution of the form

$$f(\bar{r}) = H(\bar{r}_o - \bar{r})\left(1 - 2\frac{\bar{r}^2}{\bar{r}_o^2} + \frac{\bar{r}^4}{\bar{r}_o^4}\right)$$

where $\bar{r}_o$ is the radius of the heating region and taken to be $\bar{r}_o = 0.5$. It is assumed that the thicknesses of the layers are $\bar{c}_0 = 0.002$ and $\bar{c}_i = 0.02/N (i = 1-N)$, and Biot's numbers are $B_0 = 1.0$ and $B_N = 0.1$. In order to improve the convergence of infinite series contained in the analytical solution, the step function is approximated as

$$\begin{aligned}
&H(\bar{r} - \bar{r}_k + \bar{w}_k) - H(\bar{r} - \bar{r}_k) \\
&\quad = [\{1 + \exp\langle -s(\bar{r} - \bar{r}_k + \bar{w}_k)\rangle\}\{1 + \exp\langle s(\bar{r} - \bar{r}_k)\rangle\}]^{-1}
\end{aligned}$$

where s is a parameter that governs the accuracy of the approximation and is taken to be $s = 200$. The allowable stresses in the piezoceramic layers are assumed to be $\bar{\sigma}^A_{pt} = 0.004$, $\bar{\sigma}^A_{pc} = -0.04$, and $\bar{\sigma}^A_{ps} = 0.002$.

Figure 2 illustrates the distributions of radial and hoop thermal stresses on the upper surface of each layer induced by the heating temperature in the case of four piezoceramic layers ($N = 4$). Since the axial and shear stresses are much smaller than the radial and hoop stresses, they are omitted here. Values of the maximum tensile, compressive, and shear thermal stresses in the structural layer and those in piezoceramic layers are, respectively,

$$\begin{aligned}
&\bar{\sigma}^T_{st} = 2.6412 \times 10^{-6}, \quad \bar{\sigma}^T_{sc} = -0.1298, \quad \bar{\sigma}^T_{ss} = -0.2513 \times 10^{-3} \\
&\bar{\sigma}^T_{pt} = 7.9532 \times 10^{-6}, \quad \bar{\sigma}^T_{pc} = -0.0291, \quad \bar{\sigma}^T_{ps} = -0.2513 \times 10^{-3}
\end{aligned} \tag{48}$$

5.1 Optimization Problem Without Stress Constraints. The linear programming problem when the stress constraints are eliminated from Eq. (47) has been solved for various widths and numbers of electrodes as well as for various numbers of piezoceramic layers, assuming that the electrodes of the same width ($\bar{w}_k = \bar{w}$) are arranged at equal intervals ($\bar{q}_1 = 0$, $\bar{q}_k = \bar{q} = 1/M - \bar{w} \ge 0.05$ ($k \ge 2$)). Figure 3 illustrates how the number M and width $\bar{w}$ of electrodes exert influence on the suppression ratio of the maximum thermal stress R in the case of four piezoceramic layers ($N = 4$). It is seen from Fig. 3 that the suppression ratio is strongly influenced not only by the number of electrodes but also by the width of electrodes and its maximum value $R_{\max}$ is obtained when the number and width of electrodes are $M = 4$ and $\bar{w} = 0.2$. Similar results have been obtained for a composite disk with one to three piezoceramic layers ($N = 1-3$). Table 1 summarizes numerical results obtained for the electrode arrangement when the suppression ratio reaches a maximum for the case of $N = 1-4$. This table shows that the maximum suppression ratio $R_{\max}$ slightly increases with increasing number of piezoceramic layers and is 33.6% in the case of $N = 4$. Figure 4 illustrates the distributions of radial and hoop stresses on the upper surface of each layer after applying the determined voltages in the case of $N = 4$. Compared with the stresses

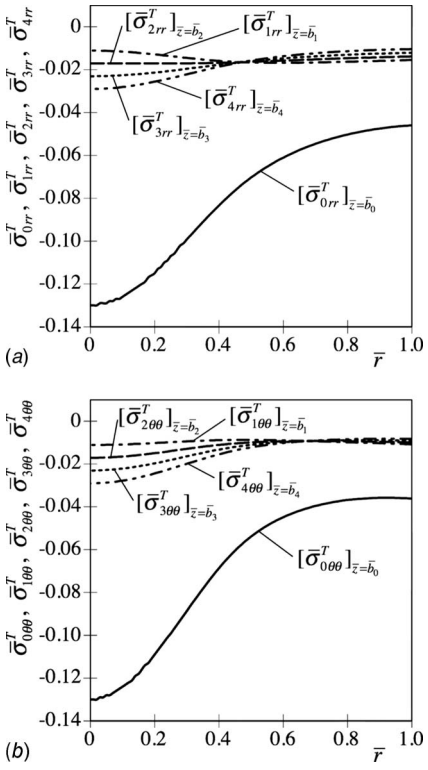

Fig. 2 Distributions of radial and hoop thermal stresses on the upper surface of each layer (N=4)

illustrated in Fig. 2, it is seen from Fig. 4 that by applying the determined voltages, the maximum compressive thermal stress at the center of the structural layer is suppressed effectively, but the compressive and tensile stresses in the piezoceramic layers, respectively, increase in the regions of the first and third electrodes in particular. It follows from these results that constraints should be imposed on the stresses in the piezoceramic layers.

5.2 Optimization Problem With Stress Constraints. The linear programming problem with stress constraints given in Eq. (47) has been solved for various widths and numbers of electrodes as well as for various numbers of piezoceramic layers when the electrodes of the same width are arranged at equal intervals. Figure 5 illustrates effects of the number M and width $\bar{w}$ of electrodes on the suppression ratio of the maximum thermal stress R in the case of N=4. This figure shows that the suppression ratio strongly

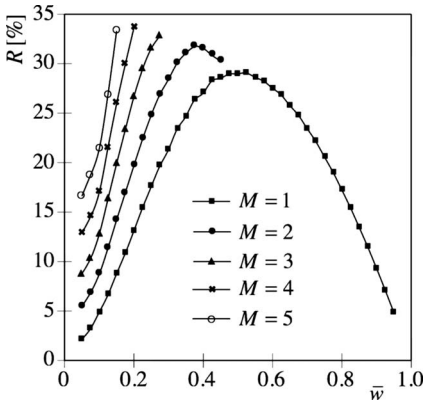

Fig. 3 Effects of the number and width of electrodes on the suppression ratio of the maximum thermal stress derived under no stress constraints (N=4)

Table 1 Numerical results for the maximum suppression ratio derived under no stress constraints in the case of the same electrode width and interval

N	1	2	3	4
M	4	4	4	4
$\bar{w}$	0.200	0.200	0.200	0.200
$\bar{q}$	0.050	0.050	0.050	0.050
$\bar{V}_{11}\times10^3$	0.4709	0.1224	−0.2466	−2.3238
$\bar{V}_{12}\times10^3$	−0.0031	−0.1263	−0.1494	−1.6188
$\bar{V}_{13}\times10^3$	−0.8752	−0.1660	0.9875	4.8586
$\bar{V}_{14}\times10^3$	−1.2524	−0.3064	1.5168	3.9975
$\bar{V}_{21}\times10^3$	–	0.1670	0.7342	5.2926
$\bar{V}_{22}\times10^3$	–	−0.0893	0.0004	3.9375
$\bar{V}_{23}\times10^3$	–	−0.4016	−2.3893	−9.7061
$\bar{V}_{24}\times10^3$	–	−0.5832	−3.7546	−7.3589
$\bar{V}_{31}\times10^3$	–	–	−0.1910	−2.6305
$\bar{V}_{32}\times10^3$	–	–	−0.0744	−2.0438
$\bar{V}_{33}\times10^3$	–	–	0.8264	4.5749
$\bar{V}_{34}\times10^3$	–	–	1.3323	2.0922
$\bar{V}_{41}\times10^3$	–	–	–	0.2901
$\bar{V}_{42}\times10^3$	–	–	–	0.2291
$\bar{V}_{43}\times10^3$	–	–	–	−0.0832
$\bar{V}_{44}\times10^3$	–	–	–	0.6263
$\bar{\sigma}_{st}\times10^3$	0.2421	0.1731	0.7879	0.5334
$\bar{\sigma}_{sc}$	−0.0885	−0.0880	−0.0872	−0.0862
$\bar{\sigma}_{ss}\times10^3$	−2.6041	−3.0688	−6.2592	−4.4431
$\bar{\sigma}_{pt}$	0.0663	0.0486	0.6106	2.1534
$\bar{\sigma}_{pc}$	−0.0105	−0.0149	−0.2893	−1.1702
$\bar{\sigma}_{ps}$	−0.0026	0.0032	−0.0646	0.2098
$R_{\max}$ [%]	31.8	32.2	32.9	33.6

depends on both width and number of electrodes and its maximum value $R_{\max}$ is found to be obtained in the case of M=2 and $\bar{w}$ =0.375. Table 2 summarizes numerical results obtained for the electrode arrangement when the suppression ratio reaches a maximum for the case of N=1–4. Compared with the results given in Table 1, it is seen from Table 2 that the introduction of the stress constraints leads to a deterioration in the effectiveness of the stress control, but the maximum suppression ratio is still about 30% in the case of N=3 and 4. Figure 6 illustrates the distributions of radial and hoop stresses on the upper surface of each layer after applying the determined voltages in the case of N=4. Compared with the stresses illustrated in Fig. 4, the distributions of radial and hoop stresses shown in Fig. 6 are found to be considerably changed so that the maximum tensile and compressive stresses in the piezoceramic layers do not exceed the stress constraints.

5.3 Structure Design of a Composite Disk. The linear programming problem with stress constraints given in Eq. (47) has been solved for various numbers, widths, and intervals of electrodes as well as for various numbers of piezoceramic layers. The ranges of design variables are $1\leq N\leq4$, $1\leq M\leq5$, $0\leq\bar{w}_k\leq0.5$, and $0\leq\bar{q}_k\leq0.5$, and the increments of $\bar{w}_k$ and $\bar{q}_k$ are taken to be 0.025. Based on the obtained numerical results, the structure of the composite disk is designed in order to maximize the suppression ratio of the maximum thermal stress in the structural layer. The determined numbers, widths, and intervals of electrodes as well as the corresponding numerical results are summarized in Table 3. It is seen from Table 3 that the maximum suppression ratio, which is obtained for the case of M=3, increases with increasing number of piezoceramic layers. Compared with the results given in Table 2, the suppression ratio in the case of the

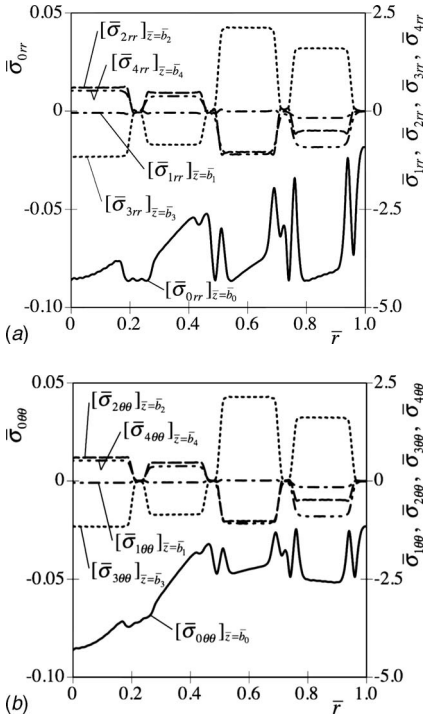

Fig. 4 Distributions of radial and hoop stresses on the upper surface of each layer after applying the determined voltages derived under no stress constraints (*N*=4, *M*=4, $\bar{w}$=0.20, and $\bar{q}$=0.05)

different electrode widths and intervals is higher than that in the case of the same electrode width and interval. The maximum suppression ratio reaches 33.7%, in which case the design variables are determined as $N=4$, $M=3$, $\bar{q}_1=0$, $\bar{w}_1=0.4$, $\bar{q}_2=0.125$, $\bar{w}_2=0.1$, $\bar{q}_3=0.025$, and $\bar{w}_3=0.35$.

6 Concluding Remarks

In a composite disk consisting of a transversely isotropic structural layer and piezoceramic layers with concentrically arranged electrodes, a problem of controlling the maximum thermal stress through piezoelectric actuation is studied. By solving the linear programming problem, which is transformed from the nonlinear optimization problem, the applied voltages have been determined so that the maximum thermal stress in the structural layer is minimized subject to constraints on the stresses in piezoceramic layers.

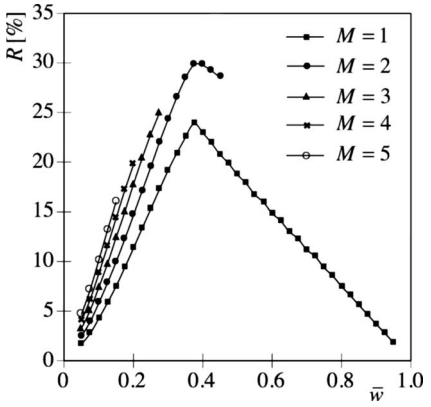

Fig. 5 Effects of the number and width of electrodes on the suppression ratio of the maximum thermal stress derived under stress constraints (*N*=4)

Table 2 Numerical results for the maximum suppression ratio derived under stress constraints in the case of the same electrode width and interval

N	1	2	3	4
M	2	2	2	2
$\bar{w}$	0.300	0.375	0.400	0.375
$\bar{q}$	0.200	0.125	0.100	0.125
$\bar{V}_{11}\times10^3$	0.6222	0.3083	0.1896	0.1438
$\bar{V}_{12}\times10^3$	−0.2379	−0.1111	0.0197	0.0682
$\bar{V}_{21}\times10^3$	–	0.4244	0.2649	0.1927
$\bar{V}_{22}\times10^3$	–	−0.1064	−0.0769	−0.0600
$\bar{V}_{31}\times10^3$	–	–	0.2882	0.2145
$\bar{V}_{32}\times10^3$	–	–	−0.0678	−0.0586
$\bar{V}_{41}\times10^3$	–	–	–	0.1965
$\bar{V}_{42}\times10^3$	–	–	–	−0.0533
$\bar{\sigma}_{st}\times10^3$	0.1218	0.1113	0.1140	0.0788
$\bar{\sigma}_{sc}$	−0.1045	−0.0947	−0.0910	−0.0912
$\bar{\sigma}_{ss}\times10^3$	1.0723	1.8492	2.0000	1.8814
$\bar{\sigma}_{pt}\times10^3$	4.0000	4.0000	4.0000	4.0000
$\bar{\sigma}_{pc}$	−0.0400	−0.0400	−0.0400	−0.0400
$\bar{\sigma}_{ps}\times10^3$	1.0723	−1.8495	2.0000	−1.9968
$R_{\max}$ (%)	19.5	27.1	29.9	29.8

Based on the obtained solutions, the structure design of the composite disk has been prepared in order to maximize the suppression ratio of the maximum thermal stress. It is seen from the design results that the maximum thermal stress can be reduced by about 34%, even in the case where constraints are imposed on the stresses in the piezoceramic layers.

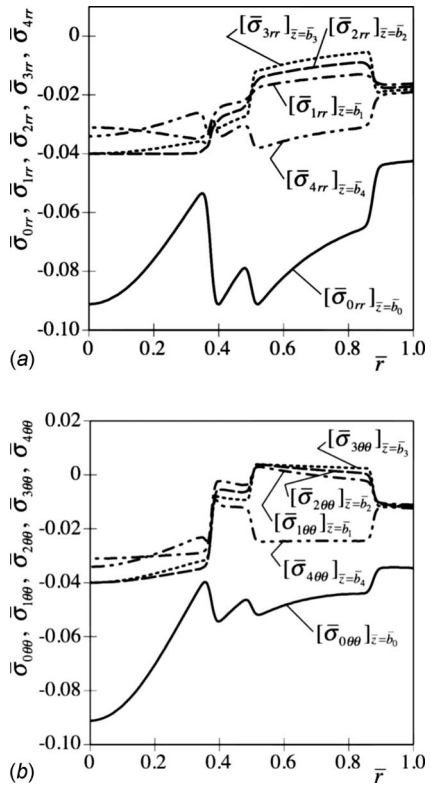

Fig. 6 Distributions of radial and hoop stresses on the upper surface of each layer after applying the determined voltages derived under stress constraints (*N*=4, *M*=2, $\bar{w}$=0.375, and $\bar{q}$=0.125)

Table 3 Numerical results for the maximum suppression ratio derived under stress constraints in the case of different electrode widths and intervals

N	1	2	3	4
M	3	3	3	3
$\bar{w}_1$	0.300	0.400	0.400	0.400
$\bar{w}_2$	0.250	0.175	0.125	0.100
$\bar{w}_3$	0.225	0.300	0.350	0.350
$\bar{q}_1$	0	0	0	0
$\bar{q}_2$	0.100	0.100	0.100	0.125
$\bar{q}_3$	0.025	0.025	0.025	0.025
$\bar{V}_{11}\times 10^3$	0.6394	0.2965	0.2320	0.1894
$\bar{V}_{12}\times 10^3$	−0.1811	−0.0578	0.0656	0.0539
$\bar{V}_{13}\times 10^3$	−0.1651	−0.1300	0.0595	0.0736
$\bar{V}_{21}\times 10^3$	–	0.4363	0.2762	0.2100
$\bar{V}_{22}\times 10^3$	–	−0.0850	−0.0638	−0.0567
$\bar{V}_{23}\times 10^3$	–	−0.1392	−0.0872	−0.0654
$\bar{V}_{31}\times 10^3$	–	–	0.3026	0.2314
$\bar{V}_{32}\times 10^3$	–	–	−0.0528	−0.0504
$\bar{V}_{33}\times 10^3$	–	–	−0.0893	−0.0669
$\bar{V}_{41}\times 10^3$	–	–	–	0.2228
$\bar{V}_{42}\times 10^3$	–	–	–	−0.0423
$\bar{V}_{43}\times 10^3$	–	–	–	−0.0670
$\bar{\sigma}_{st}\times 10^3$	0.1256	0.1141	0.1172	0.1137
$\bar{\sigma}_{sc}$	−0.1035	−0.0911	−0.0862	−0.0861
$\bar{\sigma}_{ss}\times 10^3$	1.1104	1.9550	1.9830	2.0000
$\bar{\sigma}_{pt}\times 10^3$	4.0000	4.0000	4.0000	4.0000
$\bar{\sigma}_{pc}$	−0.0400	−0.0400	−0.0400	−0.0400
$\bar{\sigma}_{ps}\times 10^3$	1.1104	−1.9982	1.9830	2.0000
$R_{\max}$ [%]	20.3	29.8	33.6	33.7

Acknowledgment

The authors are pleased to acknowledge support in part by a Grant-in-Aid for Scientific Research (No. 15560074) from the Japan Society for the Promotion of Science.

References

[1] Saravanos, D. A., and Heyliger, P. R., 1999, "Mechanics and Computational Models for Laminated Piezoelectric Beams, Plates, and Shells," Appl. Mech. Rev., **52**(10), pp. 305–320.
[2] Wang, J., and Yang, J., 2000, "Higher-Order Theories of Piezoelectric Plates and Applications," Appl. Mech. Rev., **53**(4), pp. 87–99.
[3] Rao, S. S., and Sunar, M., 1994, "Piezoelectricity and Its Use in Disturbance Sensing and Control of Flexible Structures: A Survey," Appl. Mech. Rev., **47**(4), pp. 113–123.
[4] Sunar, M., and Rao, S. S., 1999, "Recent Advances in Sensing and Control of Flexible Structures Via Piezoelectric Materials Technology," Appl. Mech. Rev., **52**(1), pp. 1–16.
[5] Irschik, H., 2002, "A Review on Static and Dynamic Shape Control of Structures by Piezoelectric Actuation," Appl. Mech. Rev., **24**(1), pp. 5–11.
[6] Tauchert, T. R., Ashida, F., and Noda, N., 1999, "Recent Developments in Piezothermo-Elasticity: Inverse Problems Relevant to Smart Structures," JSME Int. J., Ser. A, **42**(4), pp. 452–458.
[7] Tauchert, T. R., Ashida, F., Noda, N., Adali, S., and Verijenko, V., 2000, "Developments in Thermopiezoelasticity With Relevance to Smart Composite Structures," Compos. Struct., **48**(1–3), pp. 31–38.
[8] Tauchert, T. R., and Ashida, F., 2003, "Control of Transient Response in Intelligent Piezothermoelastic Structures," J. Therm. Stresses, **26**(6), pp. 559–582.
[9] Reddy, J. N., and Cheng, Z.-Q., 2001, "Three-Dimensional Solutions of Smart Functionally Graded Plates," ASME J. Appl. Mech., **68**(2), pp. 234–241.
[10] Ootao, Y., and Tanigawa, Y., 2001, "Control of the Transient Thermoelastic Displacement of a Functionally Graded Rectangular Plate Bonded to a Piezoelectric Plate Due to Nonuniform Heating," Acta Mech., **148**(1–4), pp. 17–33.
[11] Ootao, Y., and Tanigawa, Y., 2001, "Control of Transient Thermoelastic Displacement of a Two-Layered Composite Plate Constructed of Isotropic Elastic and Piezoelectric Layers Due to Nonuniform Heating," Arch. Appl. Mech., **71**(4-5), pp. 207–220.
[12] Ishihara, M., and Noda, N., 2002, "Dynamic Behavior of a Piezothermoelastic Laminate Considering the Effect of Transverse Shear," Smart Mater. Struct., **11**(2), pp. 202–208.
[13] Ishihara, M., and Noda, N., 2003, "Nonlinear Dynamic Behavior of a Piezothermoelastic Laminate Considering the Effect of Transverse Shear," J. Therm. Stresses, **26**(11–12), pp. 1093–1112.
[14] Yang, J., Kitipornchai, S., and Liew, K. M., 2004, "Non-Linear Analysis of the Thermo-Electro-Mechanical Behaviour of Shear Deformable FGM Plates With Piezoelectric Actuators," Int. J. Numer. Methods Eng., **59**(12), pp. 1605–1632.
[15] Oh, I.-K., 2005, "Thermopiezoelastic Nonlinear Dynamics of Active Piezolaminated Plates," Smart Mater. Struct., **14**(4), pp. 823–834.
[16] Choi, J.-S., Ashida, F., and Noda, N., 1997, "Control of Thermally Induced Elastic Displacement of an Isotropic Structural Plate Bonded to a Piezoelectric Ceramic Plate," Acta Mech., **122**(1–4), pp. 49–63.
[17] Tauchert, T. R., and Ashida, F., 1999, "Application of the Potential Function Method in Piezothermoelasticity: Solutions for Composite Circular Plates," J. Therm. Stresses, **22**(4-5), pp. 387–419.
[18] Ashida, F., and Noda, N., 1997, "Control of Transient Thermoelastic Displacement of an Isotropic Plate Associated With a Piezoelectric Ceramic Plate," J. Therm. Stresses, **20**(3-4), pp. 407–427.
[19] Ashida, F., and Tauchert, T. R., 2002, "Control of Transient Thermoelastic Displacement in a Composite Disk," J. Therm. Stresses, **25**(2), pp. 99–121.
[20] Ashida, F., Tauchert, T. R., Sakata, S., and Yamashita, Y., 2003, "Control of Transient Deformation in a Heated Intelligent Composite Disk," Smart Mater. Struct., **12**(5), pp. 825–835.
[21] Ashida, F., Sakata, S., Tauchert, T. R., and Yoshida, S., 2007, "Optimum Design of a Piezo-Composite Disk for Control of Thermoelastic Displacement Distribution," J. Therm. Stresses, **30**(6), pp. 559–586.
[22] Ashida, F., Tauchert, T. R., Sakata, S., and Yoshida, S., 2008, "Control of Thermoelastic Deformation in a Smart Composite Disk by a Stepwise Applied Electric Potential Distribution," Acta Mech., **195**(1–4), pp. 13–26.
[23] Ashida, F., Sakata, S., and Matsumoto, K., 2007, "Control of Thermal Stress in a Piezo-Composite Disk," J. Therm. Stresses, **30**(9-10), pp. 1025–1040.
[24] Ashida, F., Noda, N., and Okumura, I. A., 1993, "General Solution Technique for Transient Thermoelasticity of Transversely Isotropic Solids in Cylindrical Coordinates," Acta Mech., **101**(1–4), pp. 215–230.
[25] Ashida, F., Tauchert, T. R., and Noda, N., 1994, "Potential Function Method for Piezothermoelastic Problems of Solids of Crystal Class 6 mm in Cylindrical Coordinates," J. Therm. Stresses, **17**(3), pp. 361–375.

Wall Thickness and Radial Breathing Modes of Single-Walled Carbon Nanotubes

R. C. Batra
Fellow ASME
e-mail: rbatra@vt.edu

S. S. Gupta
e-mail: ssgupta@vt.edu

Department of Engineering Science and Mechanics,
M/C 0219 Virginia Polytechnic Institute and State University,
Blacksburg, VA 24061

We postulate that an equivalent continuum structure (ECS) of a single-walled carbon nanotube (SWCNT) is a hollow cylinder with mean radius and length equal to that of the SWCNT, and find the thickness of the ECS so that its mechanical response in free vibrations is the same as that of the SWCNT. That is, for mechanical deformations, the ECS is energetically equivalent to the SWCNT. We use MM3 potential to study axial, torsional, radial breathing and bending vibrations of several traction free–traction free SWCNTs of different helicities and diameters and compare them with the corresponding vibrational modes and frequencies of traction free–traction free ECSs obtained by using the three-dimensional linear elasticity theory and the finite element analysis (3D-FEA). The consideration of free ends eliminates the effects of boundary conditions and avoids resolving equivalence between boundary conditions in the analyses of SWCNTs and their ECSs. It is found that the wall thickness of the ECS (and hence of a SWCNT) is ~1 Å and Young's modulus of the material of the ECS (and hence of the SWCNT) is ~3.3 TPa. Both quantities are independent of the helicity and the diameter of the SWCNT. We also study radial breathing mode (RBM) vibrations with the molecular dynamics and the 3D-FEA simulations, and compare them with experimental findings. Accuracy in the assignment of spectral lines for RBMs in the Raman spectroscopy is discussed.
[DOI: 10.1115/1.2965370]

1 Introduction

Since their discovery by Iijima [1] there has been significant interest in characterizing the mechanical properties of both single-walled and multiwalled carbon nanotubes (SWCNTs and MWCNTs, respectively). An inherent difficulty in completing this task is assigning a thickness to the nanotube. Nearly all studies to date have assumed that a SWCNT can be obtained by rolling a graphene sheet into a cylindrical tube about a vector with components (m,n), and the response of a SWCNT is equivalent to that of a continuum structure (see Fig. 1) undergoing the same deformations as the SWCNT. In these studies the thickness of a SWCNT varies from 0.66 Å to 6.8 Å. While most studies have assumed the wall thickness to be 3.4 Å (the interlayer separation distance of graphene sheets in the bulk graphite) some works have taken it to be less than 3.4 Å [2–12] and a few have taken it to be 6.8 Å [12,13]. This large variation in thickness gives values of Young's modulus ranging from 0.27 TPa for MWCNTs [14] to 5.5 TPa for SWCNTs [2].

The mechanical properties of ECSs can be used to deduce the effective elastic moduli of SWCNTs-reinforced composites from those of their constituents and their volume fractions by using a homogenization technique; see, e.g., Ref. [15]. Good agreement between the computed effective moduli of the composite and the measured ones will validate the mechanical properties of ECSs and hence of SWCNTs. This is not pursued here.

Raman spectroscopy is a reliable technique to *identify* SWCNTs experimentally. A peak corresponding to a radial breathing mode (RBM) is a significant spectral line observed during experiments. The identification of SWCNTs and the determination of their RBM frequencies using quantum mechanical simulations and spectroscopy are described in Refs. [16–19].

Here we analyze the normal mode vibrations of traction free–traction free SWCNTs of various helicities and diameters using MM3 potential and compare their vibrational modes and frequencies with the corresponding ones for an ECS derived by using the three-dimensional theory of elasticity and the finite element analysis (3D-FEA) to ascertain values of the thickness and the elastic moduli of the ECS and hence of the SWCNT. An advantage of the 3D-FEA is that it incorporates both in-plane and out-of-plane deformations, and provides more realistic deformations of the continuum tube than those obtained by using either a beam or a shell theory.

Whereas the MM3 (and other) potential includes the effect of van der Waals forces, which describe the long range interactions between unbonded atoms, the classical elasticity theory is local. A good agreement between predictions from molecular dynamics (MD) simulations and 3D-FEA using linear elasticity theory will imply that van der Waals forces play a less significant role than that played by forces between bonded atoms. One can use such comparisons between the results of the MD and the 3D-FE simulations to delimit the class of deformations for which the effects of van der Waals forces are negligible.

We describe below the details of the MD and 3D-FE simulations, and the conclusions of our work.

2 Molecular Dynamics, Three-Dimensional Elasticity, and Finite Element Simulations

The MM3 [20] Class II pairwise potential with both higher-order expansions and cross-terms and Type 2 (alkene) carbon atoms with a bond length of ~1.42 Å is used to model SWCNTs in the computer code TINKER [21]. This potential is appropriate for carbon nanotubes due to the similarity between graphitic bonds in the nanotube and the aromatic protein structures for which the potential is constructed. The MM3 potential is given as Eq. (1) in which U_s, U_θ, and U_ϕ are the primary bond deformation terms accounting, respectively, for the change in the bond length, the change in the angle between adjoining bonds, and the twisting of bonds with respect to the one to which it is bonded. The potential U_s has terms that are quadratic, cubic, and quartic in the change of

Contributed by the Applied Mechanics Division of ASME for publication in the JOURNAL OF APPLIED MECHANICS. Manuscript received November 15, 2007; final manuscript received March 11, 2008; published online August 20, 2008. Review conducted by Yonggang Huang.

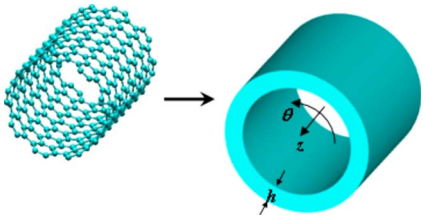

Fig. 1 Cylindrical tube equivalent in mechanical response to a SWCNT

bond lengths, and hence is asymmetric with respect to the decrease and increase in the bond length. U_{vdW} is the potential of nonbonded van der Waals forces, and its expression involving terms $(r_v/r)^6$ and $\exp(-12r/r_v)$ is different from that in the Lennard–Jones potential; U_{vdW} is negligible for r_v/r greater than 2 where r_v is a material parameter and r is the bond length. $U_{s\theta}$ and $U_{\phi s}$ are potentials due to interactions among stretching and bending deformations, and between stretching and twisting deformations. $U_{\theta\theta'}$ represents the interactions between different bending modes. Parameters r, θ, and ϕ used in Eq. (1) are shown in Fig. 2. A subscript, e, on a variable signifies its value in the configuration of minimum potential energy. The total energy of a body equals the sum of the potentials of all atoms in the body (the indices i and j in Eq. (1) range over bonded atoms, and the index k over all atoms).

$$U = \sum_i \sum_j (U_s + U_\theta + U_\phi + U_{s\theta} + U_{\phi s} + U_{\theta\theta'}) + \sum_i \sum_k U_{\mathrm{vdW}}$$

$$U_s = 71.94K_s(r-r_e)^2\left[1 - 2.55(r-r_e) + \left(\tfrac{7}{12}\right)2.55(r-r_e)^2\right]$$

$$U_\theta = 0.021914K_\theta(\theta-\theta_e)^2[1 - 0.014(\theta-\theta_e) + 5.6(10)^{-5}(\theta-\theta_e)^2 - 7.0(10)^{-7}(\theta-\theta_e)^3 + 9.0(10)^{-10}(\theta-\theta_e)^4]$$

$$U_\phi = (V_1/2)(1+\cos\phi) + (V_2/2)(1-\cos 2\phi) + (V_3/2)(1+\cos 3\phi)$$

$$U_{s\theta} = 2.51118K_{s\theta}[(r-r_e) + (r'-r'_e)](\theta-\theta_e)$$

$$U_{\phi s} = 11.995(K_{\phi s}/2)(r-r_e)(1+\cos 3\phi)$$

$$U_{\theta\theta'} = -0.021914K_{\theta\theta'}(\theta-\theta_e)(\theta'-\theta'_e) \quad \text{and}$$

$$U_{\mathrm{vdW}} = \varepsilon_e\{-2.25(r_v/r)^6 + 1.84(10)^5\exp[-12.0(r/r_v)]\} \qquad (1)$$

The values of constants K_s, K_θ, V_1, V_2, V_3, ε_e, r_v, $K_{s\theta}$, $K_{\phi s}$, and $K_{\theta\theta'}$ are given in Ref. [20]. The potential includes contributions from bond stretching, bending deformations that change angles between adjoining bonds, torsion, and van der Waals forces. Moreover, it also accounts for interactions between stretching and bending, and stretching and twisting. Contributions from different terms in Eq. (1) for axial tensile and compressive deformations plotted in Fig. 9 of Ref. [22] reveal that in axial deformations of a (16,0) SWCNT the angle bend mode of deformation makes a significant contribution to the total energy of deformation. Also, deformations due to van der Waals forces contribute more to the total energy of deformation during compressive deformations than that during tensile deformations. The stretching mode of deformation contributes most to the energy of deformation during axial tensile deformations. However, during axial compressive deformations, contributions from angle mode and bond stretching terms are nearly equal to each other.

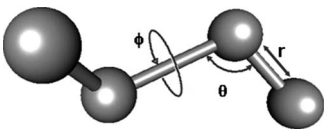

Fig. 2 Depictions of variables r, θ, and ϕ used in the MM3 potential

The following procedure is adopted to analyze the vibrations of free-free SWCNTs; here free-free implies that the end surfaces of a SWCNT and its ECS are traction free. These boundary conditions can be achieved in a laboratory more readily than those of either simply supported or clamped edges. A SWCNT is first relaxed to find the minimum energy configuration at room temperature to within 0.001 kcal/mol/Å rms without using any cut-off distance. Thus each atom of the SWCNT can potentially influence the deformations of other atoms in the tube. However, depending on the value of r_v in Eq. (1) for the van der Walls force potential, the van der Walls force between two atoms separated by three or four times the distance between two bonded atoms is negligible as compared with other forces acting on an atom. It is ensured that each tube in the relaxed configuration has an aspect ratio (length/diameter) of about 15, so that when studying vibrations of its ECS the transverse inertia effects, which couple the thickness, Young's modulus, Poisson's ratio, and the frequency of axial oscillations, are minimized. Furthermore, a high aspect ratio satisfies the criterion [23] $l_e/j \gg r_e$ for identifying the frequency of a RBM equivalent to that of an infinitely long tube (e.g., periodic boundary conditions on the unit cell), where j is the number of half-wavelengths along the longitudinal direction, and l_e and r_e are, respectively, the length and the mean radius of the relaxed SWCNT. The length l_e is the Euclidean distance between planes of atoms at the two end faces of the relaxed tube, and the radius r_e of an (m,n) SWCNT is given by $r_e = 1.1026\ a_e(m^2+n^2+mn)^{1/2}$ where a_e is the bond length in its relaxed configuration. Tubes with $m=n$ are called armchair, those with either $n=0$ or $m=0$ are called zigzag, and others are called chiral.

The VIBRATE module in computer code TINKER is used to find frequencies of axial, torsional, radial breathing, and bending modes of vibrations of free-free SWCNTs of different diameters and helicities. This module computes the Hessian of the system by finding second-order derivatives of the MM3 potential with respect to variables appearing in the expression for the potential, and then diagonalizes the mass weighted Hessian to compute the eigenvalues and eigenvectors of normal modes. Frequencies computed using TINKER are equated to those of the corresponding modes of vibration of the ECS using the three-dimensional linear elasticity theory for isotropic materials and the FE computer code ABAQUS [24] with 20-node solid elements and one element through the thickness. The mean diameter and the length of the continuum cylindrical tube are taken to equal to those of the corresponding relaxed SWCNT.

Young's modulus (E) and the shear modulus (G) for a SWCNT are obtained by equating the frequencies of axial (ω_{iA}) and torsional modes (ω_{iT}) of vibration of a SWCNT computed with MD simulations and the 3D-FEA of the ECS. Frequencies, in rad/s, of free-free tubes from the elasticity theory [23] are given by

$$\omega_{iA} = i\pi(l_e)^{-1}(E/\rho)^{1/2} \quad \text{and} \quad \omega_{iT} = i\pi(l_e)^{-1}(G/\rho)^{1/2} \quad \text{for} \quad i = 1,2,3,\ldots \qquad (2)$$

where ω_{iA} and ω_{iT} are, respectively, the frequency of the ith axial and torsional modes of vibration of the ECS. The mass density (ρ) is obtained by dividing the total mass of carbon atoms in the SWCNT by the volume of corresponding ECS with thickness as a variable. Poisson's ratio (ν) of the material of the ECS is expressed in terms of values of the ith frequencies of the axial and the torsional vibrations obtained with the MD simulations as

$$\nu = 0.5(\omega_{iA}/\omega_{iT})^2 - 1 \qquad (3)$$

which holds because $E=2G(1+\nu)$ for an isotropic linear elastic material.

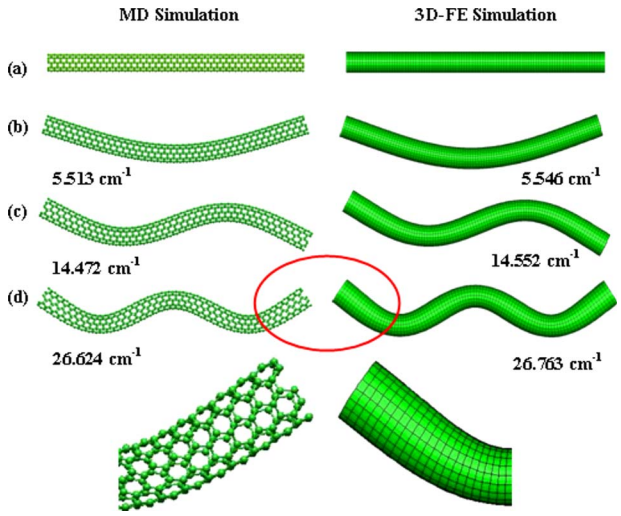

Fig. 3 Vibrational modes of free-free (5,5) SWCNT: (*a*) relaxed tube, (*b*) first bending mode, (*c*) second bending mode, and (*d*) third bending mode with zoomed ends indicating the presence of out-of-plane deformations

We note that a necessary condition for the existence of an ECS is that the frequency of the *i*th axial (or torsional) mode of vibration of a SWCNT derived from the MD simulations equals *i* times that of the first mode.

The thickness of the ECS is varied until the frequencies of the first three modes of axial, torsional, and bending modes from the MD simulations and the 3D-FEA match with each other within the prescribed tolerance of 1.0%. It should be noted that the variation in thickness does *not* alter the ratio (E/G); therefore, the bending mode frequency determines the termination of the iteration process for finding the thickness of the ECS. A good match between frequencies of the RBMs validates the thickness of the ECS.

3 Results and Discussion

Simulations for several SWCNTs have been carried out to delineate the dependence of material moduli and the wall thickness on their diameters and helicities. The afore-stated procedure gave a wall thickness of ~1 Å. For this value of the wall thickness, frequencies of vibrational modes from MD and 3D-FE simulations differed from each other by less than 1.0%. Figures 3(*b*)–3(*d*) illustrate the mode shapes and the corresponding frequencies from MD and 3D-FE simulations for bending modes for the (5,5) SWCNT. It can be observed that the flaring (i.e., out-of-plane deformations) at the end faces of the SWCNT marked in red circles in Fig. 3(*d*) is captured in the 3D-FEA but not in a beam or in a shell model of a SWCNT. For a SWCNT of small aspect ratio, the energy of deformation associated with end flaring may be significant. Tables 1 and 2 list the number of carbon atoms in a

Table 1 SWCNT parameters, frequencies (Hz/speed of light in cm/s) from molecular dynamics (MD) and finite element (FE) simulations, and values of elastic moduli

Tube	Geometry/atoms/ finite elements (r_0, l_0) (Å) [a] (r_e, l_e) (Å) [a] n_C, N [e]	No.[f]	MD (MM3 potential) T [b] (cm^{-1})	MD (MM3 potential) A [c] (cm^{-1})	MD (MM3 potential) B [d] (cm^{-1})	$\langle E\rangle$ (TPa) $\langle\nu\rangle$ $\langle G\rangle$ (TPa)	3D-FEA |% error| with respect to MD results T [b]	3D-FEA |% error| with respect to MD results A [c]	3D-FEA |% error| with respect to MD results B [d]
(5,0)	(1.957,59.640)	1	37.546	58.006	9.823	3.182	0.165	0.207	0.657
	(1.869,55.425)	2	74.994	115.842	25.855	0.193	0.043	0.131	0.181
	280, 660	3	112.243	173.311	47.694	1.330	0.178	0.001	0.288
(5,5)	(3.390, 103.299)	1	22.270	33.730	5.513	3.271	0.009	0.151	0.595
	(3.222, 97.043)	2	44.541	67.384	14.472	0.144	0.011	0.076	0.550
	840, 2037	3	66.818	100.878	26.624	1.430	0.022	0.054	0.519
(10,0)	(3.915, 119.280)	1	18.732	29.633	4.802	3.401	0.053	0.135	0.249
	(3.716, 112.969)	2	37.464	59.218	12.589	0.251	0.053	0.162	0.269
	1120, 2712	3	56.161	88.698	23.123	1.361	0.011	0.210	0.302
(9,6)	(5.119, 167.120)	1	13.622	20.893	3.167	3.317	0.044	0.115	0.095
	(4.856, 158.100)	2	27.244	41.753	8.355	0.175	0.048	0.079	0.143
	2052, 5056	3	40.866	62.542	15.462	1.422	0.047	0.021	0.187
(8,8)	(5.425, 164.787)	1	13.833	21.161	3.433	3.294	0.014	0.132	0.464
	(5.146, 155.261)	2	27.667	42.284	9.006	0.167	0.011	0.090	0.464
	2144, 5115	3	41.503	63.321	16.557	1.411	0.007	0.011	0.451
(14,2)	(5.911, 182.253)	1	12.282	19.276	3.075	3.367	0.008	0.119	0.033
	(5.606, 172.808)	2	24.561	38.522	8.071	0.229	0.024	0.130	0.074
	2584, 6228	3	36.840	57.710	14.846	1.369	0.027	0.160	0.114
(9,9)	(6.103, 184.463)	1	12.319	18.902	3.076	3.296	0.016	0.132	0.453
	(5.787, 173.879)	2	24.637	37.769	8.069	0.174	0.024	0.093	0.407
	2700, 6612	3	36.956	56.562	14.825	1.403	0.022	0.027	0.396
(16,0)	(6.264, 191.700)	1	11.633	18.329	2.943	3.360	0.000	0.126	0.271
	(5.939, 181.303)	2	23.263	36.631	7.719	0.239	0.009	0.148	0.271
	2880, 6878	3	34.891	54.871	14.185	1.356	0.020	0.184	0.288
(10,10)	(6.780, 204.139)	1	11.101	17.077	2.788	3.297	0.027	0.129	0.393
	(6.429, 192.503)	2	22.202	34.124	7.309	0.180	0.023	0.100	0.368
	3320, 8106	3	33.304	51.104	13.422	1.396	0.021	0.041	0.356

[a] r and l are the radius and the length of a SWCNT, and subscripts 0 and e refer to the initial and the relaxed configurations, respectively.
[b] Torsional mode.
[c] Axial mode.
[d] Bending mode.
[e] n_C and N are, respectively, the number of carbon atoms in the SWCNT, and the number of 20-node hexahedral elements into which the equivalent continuum tube is discretized.
[f] Mode number.

Table 2 SWCNT parameters, frequencies (Hz/speed of light in cm/s) from molecular dynamics (MD) and finite element (FE) simulations, and values of elastic moduli

Tube	Geometry/atoms/ finite elements (r_0,l_0) (Å) [a] (r_e,l_e) (Å) [a] n_C,N [e]	No.[f]	MD (MM3 potential) T [b] (cm^{-1})	MD (MM3 potential) A [c] (cm^{-1})	MD (MM3 potential) B [d] (cm^{-1})	$\langle E\rangle$ (TPa) $\langle\nu\rangle$ $\langle G\rangle$ (TPa)	3D-FEA |% error| with respect to MD results T [b]	3D-FEA |% error| with respect to MD results A [c]	3D-FEA |% error| with respect to MD results B [d]
(15,5)	(7.058, 215.035)	1	10.443	16.270	2.624	3.337	0.010	0.123	0.000
	(6.691, 203.737)	2	20.886	32.515	6.883	0.211	0.010	0.123	0.015
	3640, 8976	3	31.328	48.701	12.648	1.378	0.013	0.111	0.055
(11,11)	(7.459, 223.816)	1	10.103	15.574	2.549	3.303	0.020	0.045	0.430
	(7.071, 211.130)	2	20.206	31.122	6.680	0.187	0.020	0.026	0.403
	4004, 9706	3	30.309	46.722	12.263	1.391	0.020	0.221	0.390
(20,0)	(7.830, 238.560)	1	9.346	14.691	2.367	3.304	0.000	0.129	0.713
	(7.422, 222.966)	2	18.691	29.359	6.207	0.233	0.005	0.143	0.672
	4480, 10704	3	28.034	43.977	11.402	1.356	0.014	0.175	0.645
(19,3)	(8.090, 264.085)	1	8.464	13.258	2.001	3.349	0.738	0.829	0.908
	(7.666, 250.557)	2	16.928	26.498	5.277	0.225	0.732	0.837	0.841
	5124, 12299	3	25.390	39.697	9.760	1.367	0.726	9.163	0.795
(13,13)	(8.815, 265.627)	1	8.484	13.120	2.137	3.299	0.000	0.130	0.280
	(8.355, 250.718)	2	16.969	26.217	5.602	0.193	0.000	0.107	0.267
	5616, 13554	3	25.453	39.265	10.288	1.383	0.000	0.071	0.242
(17,9)	(8.953, 292.268)	1	7.689	11.938	1.802	3.329	0.000	0.109	0.167
	(8.485, 277.197)	2	15.379	23.858	4.754	0.203	0.000	0.096	0.147
	6276, 14958	3	23.069	35.742	8.796	1.384	0.004	0.078	0.102
(23,0)	(9.004, 272.640)	1	8.177	12.837	2.080	3.301	0.000	0.125	0.288
	(8.534, 255.246)	2	16.354	25.655	5.451	0.230	0.006	0.144	0.147
	5888, 14025	3	24.530	38.428	10.009	1.370	0.000	0.172	0.150
(15,15)	(10.171, 309.898)	1	7.255	11.244	1.811	3.302	0.041	0.098	0.275
	(9.640, 292.642)	2	14.511	22.488	4.753	0.198	0.041	0.165	0.063
	7560, 18166	3	21.768	33.654	8.738	1.377	0.032	0.054	0.240
(26,0)	(10.179, 315.240)	1	7.073	11.092	1.758	3.301	0.028	0.117	0.114
	(9.646, 295.587)	2	14.145	22.168	4.618	0.228	0.021	0.136	0.108
	7696, 18352	3	21.217	33.207	8.500	1.369	0.019	0.151	0.118

[a] r and l are the radius and the length of a SWCNT, and subscripts 0 and e refer to the initial and the relaxed configurations, respectively.
[b] Torsional mode.
[c] Axial mode.
[d] Bending mode.
[e] n_C and N are, respectively, the number of carbon atoms in the SWCNT, and the number of 20-node hexahedral elements into which the equivalent continuum tube is discretized.
[f] Mode number.

SWCNT and 20-node brick elements in its ECS, frequencies of first three axial, torsional, and bending modes of vibration from the two approaches, and computed values of Young's modulus, Poisson's ratio, and the shear modulus with the wall thickness of 1 Å. It can be concluded that the value of Young's modulus of a SWCNT varies from 3.182 TPa to 3.401 TPa, has mean and median values of 3.312 TPa and 3.303 TPa, and has standard deviation of 0.046 TPa. The largest and the smallest values of E are for the (10,0) and (5,0) SWCNTs, respectively. Young's modulus is independent of the tube diameter and its helicity within an error of 6.4%. With an increase in the diameter of the SWCNT, Poisson's ratio converges to 0.20 for armchair tubes, to 0.23 for zigzag tubes, and to 0.21 for chiral tubes. It varies from the lowest value of 0.144 for the (5,5) SWCNT to the highest value of 0.251 for the (10,0) SWCNT, and the mean, the median, and the standard deviations are, respectively, 0.203, 0.201, and 0.029.

For the SWCNTs studied herein, the frequencies of the first bending mode from MD simulations, Euler's beam theory (EBT) [23], and FE simulations are compared in Table 3 for wall thickness of 1 Å. It is observed that the frequencies from the EBT have on average 3% error as compared with those from MD simulations. If one extracts the thickness by equating the frequencies given by the MD simulations and the EBT then one gets an imaginary value of the wall thickness. However, this is not the case for the thickness computed using the frequencies obtained from the 3D elasticity theory. It suggests that the EBT theory may not be adequate to model the vibrations of SWCNTs. Consequently val-

Table 3 Comparison of frequencies of the first bending mode from 3D-FEA and EBT with those from MD simulations

Tube	Molecular dynamics (cm^{-1})	3D-FEA |% error|	EBT |% error|
(5,0)	9.823	0.657	3.763
(5,5)	5.513	0.595	3.373
(10,0)	4.802	0.249	3.034
(9,6)	3.167	0.095	2.475
(8,8)	3.433	0.464	3.245
(14,2)	3.075	0.033	2.715
(9,9)	3.076	0.453	3.252
(16,0)	2.943	0.271	3.000
(10,10)	2.788	0.393	3.207
(15,5)	2.624	0.000	2.726
(11,11)	2.549	0.430	3.272
(20,0)	2.367	0.713	4.172
(19,3)	2.001	0.908	1.480
(13,13)	2.137	0.280	3.098
(17,9)	1.802	0.167	2.200
(23,0)	2.080	0.288	3.987
(15,15)	1.811	0.275	3.051
(26,0)	1.758	0.114	3.727
Mean % Error		0.355	3.099
Maximum % Error		0.908	4.172

Table 4 Frequencies of radial breathing modes for SWCNTs (N.A.=not available) from MD and 3D-FE simulations, and values reported in literature

Tube	Molecular dynamics (cm^{-1})	Present 3D-FEA (cm^{-1})	|% error| with respect to MD results	Rao et al. [16] (cm^{-1})	Lawler et al. [17] (cm^{-1})	Kurti et al. [18] (cm^{-1})	Kuzmany et al. [19] (cm^{-1}) (Expt.)
(5,0)	568.847	569.857	0.178	N.A.	602	N.A.	N.A.
(5,5)	332.881	328.515	1.312	N.A.	341	N.A.	N.A.
(10,0)	290.463	298.025	2.603	N.A.	294	298	N.A.
(8,8)	209.008	206.493	1.203	206	210	219	211
(14,2)	192.508	194.731	1.155	N.A.	191	N.A.	N.A.
(9,9)	185.896	183.816	1.119	183	187	195	195
(16,0)	181.747	183.790	1.124	N.A.	177	188 (fitted)	185
(10,10)	167.377	165.621	1.049	165	169	175	177
(11,11)	152.207	150.904	0.856	150	N.A.	159	162
(20,0)	145.363	144.598	0.526	N.A.	N.A.	150	N.A.
Maximum % error			2.6				

ues of Young's modulus predicted [25] using experimental frequencies of oscillations coupled with the EBT may not be very reliable.

Frequencies (Hz/speed of light in cm/s) of RBMs computed from the MD and the 3D-FE simulations are listed in Table 4 for $j=1$ along with those reported in literature using theoretical and spectroscopic analyses. It is observed that the frequencies of RBMs for SWCNTs from MD and of ECSs from FE simulations agree well with each other, and are in good agreement with those obtained by other investigators thus validating our computed value of the wall thickness of the ECS. In the absence of geometric details of SWCNTs used in experimental studies one cannot discuss the sources of discrepancy between the simulation and the experimental results. Simulations can incorporate periodic boundary conditions on a unit cell thus mimicking an infinitely long tube, while experiments are conducted with the *finite length* tubes. Therefore it is appropriate in experimental studies that the criterion, $l_e/j \gg r_e$, be met for identifying the frequencies of RBMs. Furthermore, it is observed that *axisymmetric* modes for $j \geq 1$ are closely packed in the phonon spectrum (from both MD and 3D-FE simulations). Therefore the assignment of spectral lines in experiments for RBMs may be difficult and have an error due to not satisfying $l_e/j \gg r_e$. Figure 4 shows *axisymmetric* modes for the (8,8) tube for $j=1$ and 2 from MD and 3D-FE simulations. We note that the experimental value, 211 cm^{-1}, of the frequency of the RBM listed in Table 4 for the (8,8) SWCNT corresponds to the one from simulations with $j>1$.

Based on the results of compression of a bundle of SWCNTs by external hydrostatic pressure, it has been proposed [7] that the wall thickness of a SWCNT must be less than the theoretical diameter of a carbon atom (1.42 Å). Our work based on dynamical quantities predicts the wall thickness to be ~1 Å.

4 Remarks

The values of Young's modulus, the shear modulus, and Poisson's ratio computed herein from MD simulations of vibrations differ from those reported by other investigators mainly due to the different value of the wall thickness. Whereas we have deduced the value of the thickness of the ECS by equating the frequencies of bending modes of vibration, most other studies have assumed it a priori. Using MM simulations with the MM3 potential, Sears and Batra [22] found that for the (16,0) SWCNT

$$E = \frac{1.18 \times 10^{-6}}{2\pi r_e h} \text{Pa}$$

where h is the wall thickness of the ECS. Substitution for $r_e = 5.939$ Å and $h=1$ Å gives $E=3.162$ TPa, which compares well with the 3.36 TPa obtained herein. Thus simulations of static deformations and vibrations give values of E with a difference of 6%. The values of G for the (16,0) SWCNT computed from Sears and Batra's [22] MM simulations and our present work are 1.298 TPa and 1.356 TPa, respectively, and have a difference of about 4.3%.

Whereas we have derived the elastic moduli of the ECS by comparing the results of MD simulations with those of FEA using the 3D elasticity theory for isotropic materials, Huang et al. [26], Wu et al. [27], and Peng et al. [28] have used the Brenner potential to derive elastic properties of a nonlinear elastic shell and found its stiffness in tension, bending, and torsion. They have also studied deformations of the shell due to radial loads applied on the inner and on the outer surfaces of the shell, and its buckling due to axial loads. The Brenner potential includes energies due to bond stretching, and bending induced by changes in angles between adjacent bonds. They [26–28] have shown that the material of the shell should be modeled as orthotropic. For atomic spacing, Δ, tube radius, R, and characteristic length of the continuum structure, L, they [26–28] have estimated errors in the results from shell theories as a function of Δ/R and Δ/L. For the SWCNTs studied herein, $\Delta/L = \sim 15$ and the error in the ECS is only a function of Δ/R. For the error to be of $O[(\Delta/R)^3]$, a SWCNT cannot be represented by a conventional shell theory because constitutive relations involve coupling between tension and curvature, and between bending and axial strain. For the error to be $O[(\Delta/R)^2]$, the tension and bending rigidities of SWCNTs can be represented by an elastic orthotropic thin shell, but not by the thickness and the elastic modulus. Only for the error of $O[(\Delta/R)]$, a universal constant shell thickness can be defined and a SWCNT can be modeled as a thin shell of uniform thickness and made of an isotropic elastic material. In the present work, we have used FEA results from the 3D linear elasticity theory of isotropic materials to deduce the elastic moduli and the uniform thickness of the ECS. Also, the MM3 potential includes energies due to torsion, and coupling between twisting and stretching, bending and stretching, and van der Waals forces. Thus, it is not easy to estimate errors in the linear elastic cylindrical tube comprised of an isotropic elastic material that is equivalent to the SWCNT.

Batra and Sears [29] proposed that the ECS of a SWCNT be a cylindrical tube of mean radius equal to that of the SWCNT, and

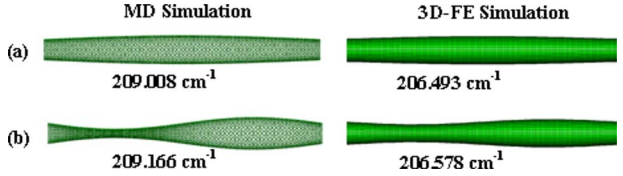

Fig. 4 Radial breathing modes of free-free (8,8) SWCNT corresponding to (*a*) $j=1$ and (*b*) $j=2$

be made of a transversely isotropic material with the axis of transverse isotropy along the radial direction. They studied the radial deformations of the ECS and of the SWCNT due to pressures applied on the inner and on the outer surfaces, and found that Young's modulus in the radial direction is nearly one-fourth of that in the axial direction. If a similar assumption were made here, then the presently computed value of E is for Young's modulus in the axial and circumferential directions, and the values of Poisson's ratio and the shear modulus in the θz-plane have been found. Here z-axis is along the axis of the tube and θ denotes the angular position of a point. In the vibration modes studied, displacements only in one direction are dominant. However, we cannot find the remaining two elastic moduli of the transversely isotropic linear elastic material from the vibration modes studied here.

We note that Wang and Zhang [30] have recently summarized the values of wall thickness of a SWCNT obtained by different research groups. Also, Sears and Batra [31] have used the MM3 potential to study buckling, due to axial compression, of single- and mult-walled CNTs.

5 Conclusions

We conclude that SWCNTs of different chiralities can be regarded as ~ 1 Å thick with the axial Young's modulus of between 3.2 TPa and 3.4 TPa with a standard deviation of 0.046. The values of Poisson's ratio range between 0.144 and 0.251, and their mean and standard deviations are 0.203 and 0.029, respectively. The frequencies of radial breathing modes of tubes of different helicities from MD and 3D-FEA simulations are found to agree well with each other with a maximum difference of 2.6%. These are close to those derived by other researchers either from quantum mechanical simulations or experimental studies. The results presented herein have important consequences in designing SWCNT based nanodevices.

Acknowledgment

This work was supported by the Office of Naval Research Grant No. N00014-98-06-0567 to Virginia Polytechnic Institute and State University with Dr. Y.D.S. Rajapakse as the program manager. Financial support from Virginia Tech's Institute of Critical Technologies and Sciences is gratefully acknowledged.

References

[1] Ijima, S., 1991, "Helical Microtubules of Graphitic Carbon," Nature (London), **354**, pp. 56–58.
[2] Yakobson, B. I., Brabec, C. J., and Bernholc, J., 1996, "Nanomechanics of Carbon Tubes: Instabilities Beyond Linear Response," Phys. Rev. Lett., **76**, pp. 2511–2514.
[3] Zhou, X., Zhou, J., and Ou-Yang, Z., 2000, "Strain Energy and Young's Modulus of Single-Walled Carbon Nanotubes Calculated From Electronic Energy-Band Theory," Phys. Rev. B, **62**, pp. 13692–13696.
[4] Kudin, K. N., Scuseria, G. E., and Yakobson, B. I., 2001, "C_2F, BN, and C Nanoshell Elasticity From *Ab Initio* Computations," Phys. Rev. B, **64**, p. 235406.
[5] Tu, Z. C., and Ou-Yang, Z., 2002, "Single-Walled and Multiwalled Carbon Nanotubes Viewed as Elastic Tubes With the Effective Young's Moduli Dependent on Layer Number," Phys. Rev. B, **65**, p. 233407.
[6] Reich, S., Thomsen, C., and Ordejon, P., 2002, "Elastic Properties of Carbon Nanotubes Under Hydrostatic Pressure," Phys. Rev. B, **65**, p. 153407.
[7] Vodenitcharova, T., and Zhang, L. C., 2003, "Effective Wall Thickness of a Single-Walled Carbon Nanotube," Phys. Rev. B, **68**, p. 165401.
[8] Pantano, A., Parks, D. M., and Boyce, M. C., 2004, "Mechanics of Deformation of Single- and Multi-Wall Carbon Nanotubes," J. Mech. Phys. Solids, **52**, pp. 789–821.
[9] Wang, L., Zheng, Q., Liu, J. Z., and Jiang, Q., 2005, "Size Dependence of the Thin-Shell Model for Carbon Nanotubes," Phys. Rev. Lett., **95**, p. 105501.
[10] Chen, X., and Cao, G., 2006, "A Structural Mechanics Study of Single-Walled Carbon Nanotubes Generalized From Atomistic Simulation," Nanotechnology, **17**, pp. 1004–1015.
[11] Wu, Y., Xhang, X., Leung, A. Y. T., and Zhong, W., 2006, "An Energy-Equivalent Model on Studying the Mechanical Properties of Single-Walled Carbon Nanotubes," Thin-Walled Struct., **44**, pp. 667–676.
[12] Kalamkarov, A. L., Georgiades, A. V., Rokkam, S. K., Veedu, V. P., and Ghasemi-Nejhad, M. N., 2006, "Analytical and Numerical Techniques to Predict Carbon Nanotubes Properties," Int. J. Solids Struct., **43**, pp. 6832–6854.
[13] Halicioglu, T., 1998, "Stress Calculations for Carbon Nanotubes," Thin Solid Films, **312**, pp. 11–14.
[14] Yu, M.-F., Lourie, O., Dyer, M. J., Moloni, K., Kelly, T. F., and Rodney, S. R., 2000, "Strength and Breaking Mechanisms of Multiwalled Carbon Nanotubes Under Tensile Load," Science, **287**, pp. 637–640.
[15] Ray, M. C., and Batra, R. C., 2007, "A Single-Walled Carbon Nanotube Reinforced 1-3 Piezoelectric Composite for Active Control of Smart Structures," Smart Mater. Struct., **16**, pp. 1936–1947.
[16] Rao, A. M., Richter, E., Bandow, S., Chase, B., Eklund, P. C., Williams, K. A., Fang, S., Subbaswamy, K. R., Menon, M., Thess, A., Smalley, R. E., Dresselhaus, G., and Dresselhaus, M. S., 1997, "Diameter-Selective Raman Scattering From Vibrational Modes in Carbon Nanotubes," Science, **275**, pp. 187–191.
[17] Lawler, H. M., Areshkin, D., Mintmire, J. W., and White, C. T., 2005, "Radial-Breathing Mode Frequencies for Single-Walled Carbon Nanotubes of Arbitrary Chirality: First-Principle Calculations," Phys. Rev. B, **72**, p. 233403.
[18] Kurti, J., Kresse, G., and Kuzmany, H., 1998, "First-Principles Calculations of the Radial Breathing Mode of Single-Wall Carbon Nanotubes," Phys. Rev. B, **58**, pp. R8869–8872.
[19] Kuzmany, H., Burger, B., Hulman, M., Kurti, J., Rinzler, A. G., and Smalley, R. E., 1998, "Spectroscopic Analysis of Different Types of Single-Wall Carbon Nanotubes," Europhys. Lett., **44**, pp. 518–524.
[20] Allinger, N. L., Yuh, Y. H., and Lii, J. H., 1998, "Molecular Mechanics. The MM3 Force Field for Hydrocarbons," J. Am. Chem. Soc., **111**, pp. 8551–8566.
[21] Ponder, J. W., 2004, User's Guide TINKER Molecular Modelling Package 4.2.
[22] Sears, A., and Batra, R. C., 2004, "Macroscopic Properties of Carbon Nanotubes From Molecular-Mechanics Simulations," Phys. Rev. B, **69**, pp. 235406.
[23] Blevins, R. D., 1979, *Formulas For Natural Frequencies and Mode Shapes*, Van Nostrand Reinhold, New York.
[24] User's Manual Finite Element Computer Code ABAQUS 6.6.
[25] Krishnan, A., Dujardin, E., Ebbesen, T. W., Yianilos, P. N., and Treacy, M. M. J., 1998, "Young's Modulus of Single-Walled Nanotubes," Phys. Rev. B, **58**, pp. 14013–14019.
[26] Huang, Y., Wu, J., and Hwang, K. C., 2006, "Thickness of Graphene and Single-Wall Carbon Nanotubes," Phys. Rev. B, **74**, pp. 245413.
[27] Wu, J., Hwang, K. C., and Huang, Y., 2008, "An Atomistic-Based Finite-Deformation Shell Theory for Single-Wall Carbon Nanotubes," J. Mech. Phys. Solids, **56**, pp. 279–292.
[28] Peng, J., Wu, J., Hwang, K. C., Song, J., and Huang, Y., 2008, "Can a Single-Wall Carbon Nanotube be Modelled as a Thin Shell?," J. Mech. Phys. Solids, to be published.
[29] Batra, R. C., and Sears, A., 2007, "Uniform Radial Expansion/Contraction of Carbon Nanotubes and Their Transverse Elastic Moduli," Modell. Simul. Mater. Sci. Eng., **15**, pp. 835–844.
[30] Wang, C. Y., and Zhang, L. C., 2008, "A Critical Assessment of the Elastic Properties and Effective Wall Thickness of Single-Walled Carbon Nanotubes," Nanotechnology, **19**, p. 075705.
[31] Sears, A., and Batra, R. C., 2006, "Buckling of Multi-Walled Carbon Nanotubes Under Axial Compression," Phys. Rev. B, **73**, p. 085410.

Impact of Viscoplastic Bodies: Dissipation and Restitution

K. A. Ismail

W. J. Stronge
e-mail: wjs@eng.cam.ac.uk

Department of Engineering,
University of Cambridge,
Cambridge, CB2 1PZ, UK

A viscoplastic coefficient of restitution (COR) that accounts for nonfrictional sources of energy dissipation is determined for direct collision between hard compliant bodies. This COR incorporates effects of both irreversible elastic-plastic material (rate-independent) and viscoelastic (rate-dependent) behaviors. The COR is calculated based on a modified Maxwell model for compliance of the bodies in the small deforming region around the initial contact point. Modifications to the Maxwell model incorporate the effects of plasticity and viscoelasticity, so the calculated COR gives a value that considers both hysteresis due to the plastic deformation and viscoelastic (rate-dependent) sources of energy dissipation during collision. [DOI: 10.1115/1.2965371]

Keywords: impact, coefficient restitution, viscoplastic dissipation, bilinear Maxwell model

1 Introduction

The coefficient of restitution (COR) is an important impact parameter characterizing nonfrictional energy dissipation during the collision. The concept of a COR was first expressed as the Newtonian (kinematic) COR, then as the Poisson (kinetic) COR, and finally as an *energetic* COR [1]. These definitions of COR are equivalent unless there is friction and the direction of sliding changes during the collision; in this case, only the energetic COR correctly accounts for all sources of energy dissipation.

Coaplen et al. [2] introduced the *composite* COR to represent the energy dissipated during a collision between two hard bodies with dissimilar material properties. Their development assumed rate-independent behavior of the compliance. The energy losses during collision that are associated with the normal component of relative motion were related to internal dissipation (elastic-plastic deformation). They calculated the composite COR based on (a) an elastic compliance of the contact region and (b) an energetic coefficient of restitution for each body COR_i, where $i=1,2$ as measured in a self-similar collision.

The effect of viscoelasticity or rate-dependence in the compliance of colliding bodies is another source of dissipation during collision. This effect can be significant in understanding the dynamic behavior of many types of colliding bodies. Butcher and Segalman [3] characterized impact using elementary vibration concepts, which assume that the compliance can be represented by a linear elastic spring and a linear dashpot that dissipates energy. Their studies also included higher-order viscoelastic models. Other research regarding impact between bodies with viscoelastic compliance have been presented by Hunt and Crossley [4] and Atanackovic and Spasic [5].

Previous analyses of a COR for collision of compliant bodies have investigated either inelastic or rate-dependent behaviors. The present paper combines these effects to obtain a viscoplastic COR e_*. The basis of the analysis is a nonlinear Maxwell model. In contrast with the Kelvin–Voight viscoelastic model [4], this modified Maxwell model eliminates any problem of discontinuity of the contact force at incidence ($t=0$).

2 Viscoplastic (Modified Maxwell) Compliance

This analysis for velocity changes that occur during direct collision between two relatively hard bodies of masses M_1 and M_2, respectively, employs a lumped-parameter representation for the compliance of a small contact region around the initial contact point C (Fig. 1). This representation assumes that all deformation occurs in a negligibly small region around C. The remainder of the bodies are assumed to be rigid. The collision is composed of a period of compression wherein the bodies are approaching each other followed by a period of restitution wherein they separate. The compression period starts at incidence and ends when the normal relative velocity of the colliding bodies vanishes. The subsequent period of restitution terminates at separation.

The compliance of the small deforming region around C is represented by a bilinear spring (elastic-plastic element) in series with a linear dashpot (viscous element) with *damping constant* c. Rather than a linear elastic spring (as in viscoelastic compliance), a bilinear elastic-plastic spring is used to represent energy loss due to plastic deformation (Fig. 2). The ratio of spring stiffness during restitution to stiffness during compression is γ^{-2} such that the ratio of work done by the elastic-plastic element during restitution to that done during compression is $-\gamma^2$. Hence γ is termed the *plastic loss factor*. This represents rate-independent internal energy dissipation [1] and is in addition to energy dissipated by the viscous element.[1] The total work done on the deforming region during compression equals the work done to transform kinetic energy into internal energy, while during restitution, the total work equals the work recovered from the deformable region as it transforms internal energy into kinetic energy of relative motion.

The normal component of the relative displacement of the bodies u gives rise to the normal contact force F. This nonlinear Maxwell model gives a normal contact force between the bodies that is equal to the force acting on either the spring or the dashpot. Relative displacement of the dashpot is defined as y relative to the contact surface. The formulation of the equation of normal motion for this system with viscoplastic compliance is formulated for successive phases of compression and restitution.

3 Equation of Motion During Compression

The contact force acting on the colliding bodies during compression is

$$F = -\kappa z = -c\dot{y} \tag{1a}$$

where the extension of the spring z is given as

Contributed by the Applied Mechanics Division of ASME for publication in the JOURNAL OF APPLIED MECHANICS. Manuscript received November 22, 2007; final manuscript received March 11, 2008; published online August 20, 2008. Review conducted by Robert M. McMeeking.

[1]For rate-independent compliance where $c\to\infty$ (i.e., the dashpot behaves as a rigid link), the plastic loss factor γ equals the COR e_*.

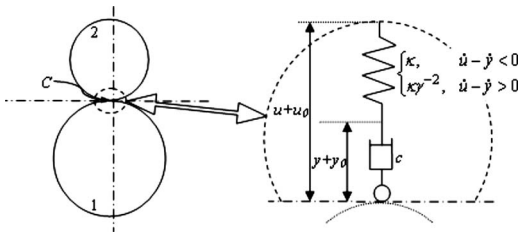

Fig. 1 Viscoplastic compliance for impact between hard bodies with local compliance

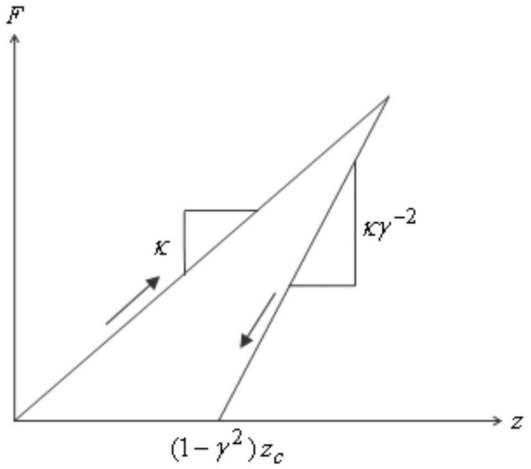

Fig. 2 Force-deflection relations for bilinear elastic-plastic element representing viscoplastic compliance of the contact region. Stiffness of the elastic-plastic element increases from κ to $\kappa\gamma^{-2}$ at the instant of maximum compression giving a ratio of energy dissipation from hysteresis to maximum energy stored in elastic-plastic element γ^2.

$$z = (u - y) \tag{1b}$$

Applying Newton's law of motion on the body gives

$$m\ddot{u} = -\kappa z \tag{1c}$$

where an effective mass $m=(M_1^{-1}+M_2^{-1})^{-1}$. Differentiating Eq. (1*a*) once and Eq. (1*b*) twice, then substituting these into Eq. (1*c*) gives an equation of motion in terms of the spring extension.

$$\ddot{z} + 2\zeta\omega_0\dot{z} + \omega_0^2 z = 0 \tag{2a}$$

where the *damping factor* ζ and the undamped natural frequency ω_0 are defined as follows:[2]

$$\zeta = \frac{m\omega_0}{2c} \tag{2b}$$

$$\omega_0^2 = \frac{\kappa}{m} \tag{2c}$$

The initial conditions for a direct collision between bodies colliding at an initial normal relative velocity of v_0 are

$$u(0) = z(0) = y(0) = 0$$

$$\dot{u}(0) = \dot{z}(0) = -v_0, \quad \dot{y}(0) = 0$$

For cases where the damping factor $\zeta < 1$, the equation of motion (Eq. (2*a*)) has a solution,

$$z(t) = -\frac{v_0}{\omega_d} e^{-\zeta\omega_0 t} \sin(\omega_d t) \tag{3}$$

where the damped resonant frequency $\omega_d=\omega_0\sqrt{1-\zeta^2}$. Expressing the contact force (using Eqs. (1*a*) and (3)) as a nondimensional quantity gives

$$\frac{F}{m\omega_0 v_0} = \frac{1}{\sqrt{1-\zeta^2}} e^{-\zeta\omega_0 t} \sin(\omega_d t) \tag{4}$$

Having solved for the displacement of the spring, the normal relative velocity of the bodies is then

$$\dot{u}(t) = -\frac{v_0}{\omega_d} e^{-\zeta\omega_0 t}[\zeta\omega_0 \sin(\omega_d t) + \omega_d \cos(\omega_d t)] \tag{5}$$

The impulse acting on the colliding bodies at any time t during an initial period of compression is obtained as the change in linear relative momentum of the bodies.

$$p(t) = m[\dot{u}(t) - \dot{u}(0)] \tag{6}$$

At any time during compression ($0 \le t \le t_c$), the impulse acting on the system is

$$p(t) = mv_0\left\{1 - e^{-\zeta\omega_0 t}\left[\frac{\zeta}{\sqrt{1-\zeta^2}}\sin(\omega_d t) + \cos(\omega_d t)\right]\right\} \tag{7}$$

The transition from compression to restitution occurs at time t_c when the normal relative velocity vanishes, i.e., when the normal impulse has eliminated the initial normal relative momentum.

$$p_c = p(t_c) = mv_0 \tag{8}$$

This gives the nondimensional time of transition from compression to restitution as

$$\omega_0 t_c = \frac{1}{\sqrt{1-\zeta^2}}\left[\pi - \tan^{-1}\left(\frac{\sqrt{1-\zeta^2}}{\zeta}\right)\right] \tag{9}$$

At the time of transition, the relative displacement z_c and the relative velocity $\dot{z}_c$ of the spring are given by

$$z_c = z(t_c) = -\frac{v_0}{\omega_0} e^{-\zeta\omega_0 t_c} \tag{10a}$$

$$\dot{z}_c = \dot{z}(t_c) = 2v_0\zeta e^{-\zeta\omega_0 t_c} \tag{10b}$$

4 Equation of Motion During Restitution

The normal force acting between the bodies during the restitution is given by

$$F(t) = -\frac{\kappa}{\gamma^2} z - \kappa\left(1 - \frac{1}{\gamma^2}\right) z_c = -c\dot{y} \tag{11}$$

The equation of motion for the spring element during the restitution is expressed as

$$\ddot{z} + \frac{\kappa}{\gamma^2 c}\dot{z} + \frac{\kappa}{\gamma^2 m} z = -\frac{\kappa}{m}\left(1 - \frac{1}{\gamma^2}\right) z_c \tag{12}$$

4.1 Case I: $\zeta < \gamma$. For $\zeta < \gamma$, Eq. (12) gives a superposition of complementary and particular solutions for the displacement of the spring as

[2]Although the equation of motion (Eq. (2*a*)) is conveniently written in a form similar to that of the Kelvin–Voight model [3], the physics are completely different (Eq. (2*b*)) since the damping factor ζ is inversely proportional to the damping constant c.

$$z(t) = \psi e^{-(\zeta/\gamma^2)\omega_0 t} \sin\left(\frac{1}{\gamma}\sqrt{1-\frac{\zeta^2}{\gamma^2}}\omega_0 t + \phi\right) + (1-\gamma^2)z_c \tag{13a}$$

where the coefficient $\psi(\omega_0, \gamma, \zeta, v_0)$ and the phase angle ϕ are defined as follows:

$$\psi = \frac{v_0 \gamma^2 e^{(\zeta/\gamma^2)(1-\gamma^2)\omega_0 t_c}}{\omega_0 \sqrt{1-\frac{\zeta^2}{\gamma^2}}} \tag{13b}$$

$$\phi = \tan^{-1}\left(-\frac{\gamma}{\zeta}\sqrt{1-\frac{\zeta^2}{\gamma^2}}\right) - \frac{1}{\gamma}\sqrt{1-\frac{\zeta^2}{\gamma^2}}\omega_0 t_c \tag{13c}$$

The end of restitution is determined by the condition that the normal contact force vanishes.

$$F(t_f) = -\frac{\kappa}{\gamma^2}\psi e^{-(\zeta/\gamma^2)\omega_0 t_f} \sin\left(\frac{1}{\gamma}\sqrt{1-\frac{\zeta^2}{\gamma^2}}\omega_0 t_f + \phi\right) = 0 \tag{14}$$

Equation (14) gives the nondimensional time for the end of the restitution period $\omega_0 t_f$ as

$$\omega_0 t_f = -\frac{\gamma\phi}{\sqrt{1-\frac{\zeta^2}{\gamma^2}}} \tag{15}$$

The normal impulse that drives the colliding bodies apart during restitution ($t_c < t \le t_f$) is given as

$$p(t) = \psi m \omega_0 e^{-(\zeta/\gamma^2)\omega_0 t}\left[\frac{\zeta}{\gamma^2}\sin\left(\frac{1}{\gamma}\sqrt{1-\frac{\zeta^2}{\gamma^2}}\omega_0 t + \phi\right) + \frac{1}{\gamma}\sqrt{1-\frac{\zeta^2}{\gamma^2}}\cos\left(\frac{1}{\gamma}\sqrt{1-\frac{\zeta^2}{\gamma^2}}\omega_0 t + \phi\right)\right] + mv_0 \tag{16}$$

4.2 Case II: $\gamma < \zeta < 1$. For $\gamma < \zeta < 1$, Eq. (12) gives a superposition of complementary and particular solutions for the displacement of the spring as

$$z(t) = -\frac{v_0\gamma^2}{2\omega_0\sqrt{1-\frac{\gamma^2}{\zeta^2}}} e^{-\zeta\omega_0 t_c}\left\{\left(1+\sqrt{1-\frac{\gamma^2}{\zeta^2}}\right) \times e^{-(\zeta/\gamma^2)\omega_0\left(1+\sqrt{1-(\gamma^2/\zeta^2)}\right)\omega_0(t-t_c)} - \left(1-\sqrt{1-\frac{\gamma^2}{\zeta^2}}\right) \times e^{-(\zeta/\gamma^2)\left(1-\sqrt{1-(\gamma^2/\zeta^2)}\right)\omega_0(t-t_c)}\right\} + (1-\gamma^2)z_c \tag{17}$$

The end of restitution is determined by the condition that the normal contact force vanishes, which gives the nondimensional time of separation as

$$\omega_0 t_f = -\frac{\gamma^2}{2\zeta\sqrt{1-\frac{\gamma^2}{\zeta^2}}} \ln\left[\frac{\left(1-\sqrt{1-\frac{\gamma^2}{\zeta^2}}\right)}{\left(1+\sqrt{1-\frac{\gamma^2}{\zeta^2}}\right)} e^{-2(\zeta/\gamma^2)\sqrt{1-(\gamma^2/\zeta^2)}\omega_0 t_c}\right] \tag{18}$$

The normal impulse that drives the colliding bodies apart during restitution is given as

$$p(t) = -\frac{mv_0\gamma^2}{2\zeta\sqrt{1-\frac{\gamma^2}{\zeta^2}}} e^{-\zeta\omega_0 t_c}\left\{e^{-(\zeta/\gamma^2)\left(1+\sqrt{1-(\gamma^2/\zeta^2)}\right)\omega_0(t-t_c)} - e^{-(\zeta/\gamma^2)\left(1-\sqrt{1-(\gamma^2/\zeta^2)}\right)\omega_0(t-t_c)}\right\} + mv_0 \tag{19}$$

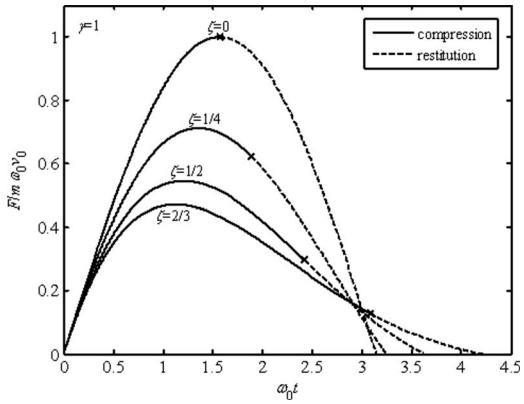

Fig. 3 Contact force for impact with viscoelastic compliance $\gamma=1$ for different values of the damping factor ζ. Note that $\gamma=1$, $\zeta=0$ (i.e., damping constant $c\to\infty$) represents a perfectly elastic collision with no energy dissipation.

During collision between bodies with rate-dependent material properties, the transition from compression to restitution occurs after the time of maximum compressive force (Fig. 3). The period between the maximum force and the transition time t_c increases as the damping factor ζ increases. Furthermore, the maximum contact force decreases and the contact period increases with increasing damping factor.

For bilinear modeling of internal plastic deformation, the force versus the time profiles for viscoplastic compliance differs from those for viscoelastic compliance only during the restitution phase (Fig. 4). With this modeling, the duration of the restitution phase decreases as the plastic loss factor γ decreases, i.e., as energy dissipated by plastic deformation increases.

5 Work of Contact Force

The work done by the normal contact force during the compression and the restitution phases can be calculated separately for elastic-plastic and viscous elements. The work done by the viscous element during compression W_{VC} is defined as follows:

$$W_{VC} = \int_0^{t_c} F\dot{y}dt, \quad \frac{W_{VC}}{\frac{1}{2}mv_0^2} = e^{-2\zeta\omega_0 t_c} - 1 \tag{20a}$$

and likewise the work done by the bilinear elastic-plastic element during compression W_{SC} is obtained as follows:

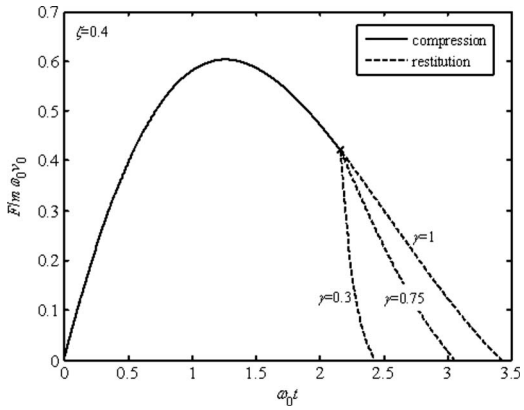

Fig. 4 Contact force profile for viscoplastic compliance with a damping factor $\zeta=1/4$

$$W_{SC} = \int_0^{t_c} F\dot{z}dt$$

$$\frac{W_{SC}}{\frac{1}{2}mv_0^2} = -\frac{1}{1-\zeta^2}e^{-2\zeta\omega_0 t_c}\sin^2(\omega_d t_c) \tag{20b}$$

The total work W_{TC} by the system during compression is the sum of the work done by the viscous and elastic-plastic elements,

$$W_{TC} = \int_0^{t_c} F\dot{u}dt = \int_0^{t_c} F(\dot{z}+\dot{y})dt$$

$$\frac{W_{TC}}{\frac{1}{2}mv_0^2} = e^{-2\zeta\omega_0 t_c}\left\{1 - \frac{1}{1-\zeta^2}\sin^2(\omega_d t_c)\right\} - 1 = -1 \tag{20c}$$

During compression, both elastic-plastic and viscous elements do negative partial work on these colliding bodies. This reduces the kinetic energy of the system (Fig. 5). The contact force does work on the elastic-plastic element by transforming part of the initial kinetic energy of the relative motion into internal energy. The viscous force always opposes the relative motion of the colliding bodies and thus dissipates energy during collision. The energy dissipated by the viscous element during compression is an increasing part of the total dissipation as the damping factor ζ increases. At the end of compression, the total work equals the initial kinetic energy of the normal relative motion, i.e., the normal relative velocity has been brought to a halt. As $\zeta \to 1$, the total work in the system is governed by the work done on the viscous element. All the kinetic energy of the normal relative motion is dissipated during compression.

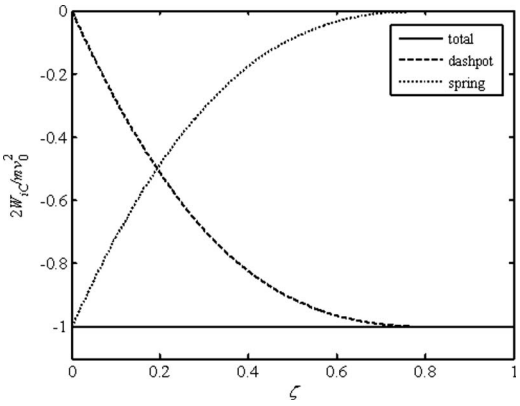

Fig. 5 Distribution of the work done during compression by viscous and elastic-plastic elements as a function of damping factor ζ. The total work equals the initial kinetic energy of normal relative motion.

The work done by the viscous element during restitution W_{VR} in Case I ($\zeta < \gamma$) is expressed as follows:

$$\frac{W_{VR}}{\frac{1}{2}mv_0^2} = -\left|\frac{\psi^2\omega_0^2}{v_0^2}\frac{e^{-2(\zeta/\gamma^2)\omega_0 t}}{\gamma^4}\zeta \times \left\{\cos^2\phi\left[-2\zeta\sin^2\left(\frac{1}{\gamma}\sqrt{1-\frac{\zeta^2}{\gamma^2}}\omega_0 t\right) - \gamma\sqrt{1-\frac{\zeta^2}{\gamma^2}}\sin\left(\frac{2}{\gamma}\sqrt{1-\frac{\zeta^2}{\gamma^2}}\omega_0 t\right) - \frac{(\gamma^2-\zeta^2)}{\zeta}\right]\right.\right.$$
$$-\sin 2\phi\left[\zeta\sin\left(\frac{2}{\gamma}\sqrt{1-\frac{\zeta^2}{\gamma^2}}\omega_0 t\right) + \gamma\sqrt{1-\frac{\zeta^2}{\gamma^2}}\cos\left(\frac{2}{\gamma}\sqrt{1-\frac{\zeta^2}{\gamma^2}}\omega_0 t\right)\right] + \sin^2\phi\left[-2\zeta\cos^2\left(\frac{1}{\gamma}\sqrt{1-\frac{\zeta^2}{\gamma^2}}\omega_0 t\right)\right.$$
$$\left.\left.\left.+\gamma\sqrt{1-\frac{\zeta^2}{\gamma^2}}\sin\left(\frac{2}{\gamma}\sqrt{1-\frac{\zeta^2}{\gamma^2}}\omega_0 t\right) - \frac{(\gamma^2-\zeta^2)}{\zeta}\right]\right\}\right|_{t_c}^{t_f} \tag{21a}$$

and likewise, the work done by the bilinear elastic-plastic element during restitution W_{SR} is expressed as follows:

$$\frac{W_{SR}}{\frac{1}{2}mv_0^2} = -\frac{W_{VR}}{mv_0^2} - \left|\frac{\psi^2\omega_0^2}{v_0^2}\frac{e^{-2(\zeta/\gamma^2)\omega_0 t}}{2\gamma^3}\sqrt{1-\frac{\zeta^2}{\gamma^2}}\right.$$
$$\times\left\{\sin 2\phi\left[\gamma\sqrt{1-\frac{\zeta^2}{\gamma^2}}\sin\left(\frac{2}{\gamma}\sqrt{1-\frac{\zeta^2}{\gamma^2}}\omega_0 t\right)\right.\right.$$
$$\left.-\zeta\cos\left(\frac{2}{\gamma}\sqrt{1-\frac{\zeta^2}{\gamma^2}}\omega_0 t\right)\right]$$
$$-\cos 2\phi\left[\zeta\sin\left(\frac{2}{\gamma}\sqrt{1-\frac{\zeta^2}{\gamma^2}}\omega_0 t\right)\right.$$
$$\left.\left.\left.+\gamma\sqrt{1-\frac{\zeta^2}{\gamma^2}}\cos\left(\frac{2}{\gamma}\sqrt{1-\frac{\zeta^2}{\gamma^2}}\omega_0 t\right)\right]\right\}\right|_{t_c}^{t_f} \tag{21b}$$

During restitution, the normal contact force does negative work on the elastic-plastic element and positive work on the viscous element (Fig. 6), i.e., the spring extends while the dashpot continues to compress. The total work on the colliding bodies during restitution has the opposite sign of work done on the compliant elements and is given by the sum of the work on the elements. Thus,

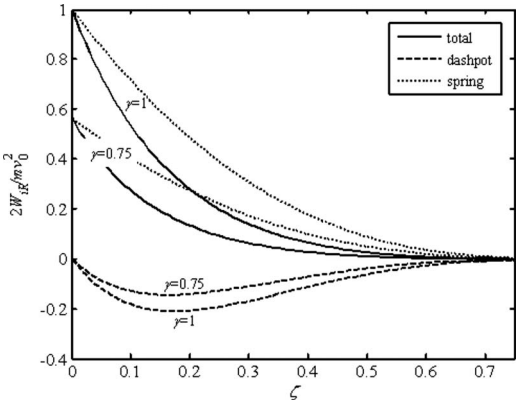

Fig. 6 Distribution of the work done during restitution by viscous and elastic-plastic elements as a function of damping factor ζ for the viscoplastic compliance (Case I: $\zeta < \gamma$). Also shown are curves for the total work by the system.

during restitution there is positive work done on the colliding bodies and a net increase in kinetic energy of the relative motion for the system. The total work on the colliding bodies during restitution decreases as the damping factor ζ increases. It also decreases with decreasing value of plastic loss factor γ.

5.1 Kinetic COR e_* . For collinear collision, the idea of a viscoplastic COR e_* for energy losses during collision between bodies whose contact compliance can be represented as inelastic and rate-dependent can be expressed using the kinetic definition of COR. The kinetic COR is defined as the ratio of normal impulse during restitution to the normal impulse during compression. Thus, an expression for the viscoplastic COR e_* is as follows.

In Case I: $\zeta < \gamma$,

$$e_* = \frac{p_f - p_c}{p_c} = \gamma e^{(\zeta/\gamma^2)[(1-\gamma^2)\omega_0 t_c - \omega_0 t_f]} \tag{22a}$$

In Case II: $\gamma < \zeta < 1$,

$$e_* = -\frac{\gamma^2}{2\zeta\sqrt{1-\frac{\gamma^2}{\zeta^2}}} e^{-\zeta\omega_0 t_c}\{e^{-(\zeta/\gamma^2)(1+\sqrt{1-(\gamma^2/\zeta^2)})\omega_0(t_f-t_c)} - e^{-(\zeta/\gamma^2)(1-\sqrt{1-(\gamma^2/\zeta^2)})\omega_0(t_f-t_c)}\} \tag{22b}$$

For a direct collision, this analytical expression for kinetic COR is equivalent to the energetic COR.

In the absence of viscous damping (i.e., when $\zeta=0$), the viscoplastic COR e_* equals the plastic loss factor γ (Fig. 7). Furthermore, the viscoplastic COR e_* decreases with increasing value of the damping factor ζ (i.e., decreasing c). Irrespective of internal plastic deformation, the viscoplastic COR e_* asymptotically approaches zero at large values of the damping factor ($\zeta > 0.8$).

6 Discussion

Throughout this analysis we considered only $\zeta < 1$ ($c > m\omega_0/2$), a limit that is necessary for contact force to provide sufficient impulse to bring the initial normal relative velocity at the contact point to a halt during compression. For $\zeta < 1$, as the damping factor $\zeta \to 1$, the period of compression increases without bound (see Eq. (9)). Also, as $\zeta \to 1$ the elastic stored energy decreases toward zero at the end of compression (see Fig. 5), i.e., as $\zeta \to 1$, at the end of compression there is negligibly small stored energy that remains to drive the bodies apart during restitution. Hence, the present model represents the dynamics of impact only if $c > m\omega_0/2$, i.e., $\zeta < 1$.

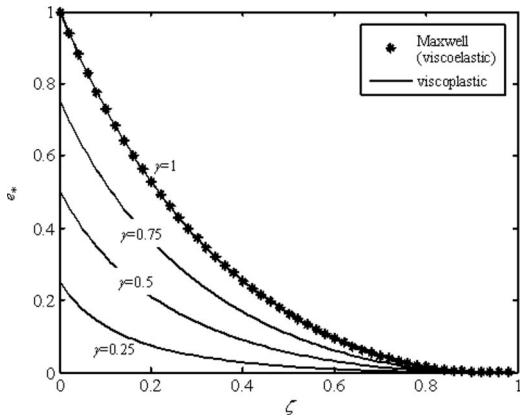

Fig. 7 COR for bilinear Maxwell model with both plastic deformation and rate-dependent energy losses (viscoplastic compliance). Also plotted is the result of COR for viscoelastic compliance [6], which is identical to the viscoplastic compliance if internal dissipation is negligible ($\gamma=1$).

The concept of an energetic COR has been extended to model dissipative collision for bodies with both rate-independent plastic and rate-dependent viscous energy dissipation. An expression for the viscoplastic COR e_* has been presented for direct collision of collinear bodies with local contact regions that exhibit both plastic deformation and rate-dependence. This COR is not a simple sum of the parameters associated with internal inelastic behavior and rate-dependent effects but rather is represented by an equation that depends on the undamped natural frequency ω_0, the plastic loss factor γ, and the damping factor ζ (Eq. (22)). This model, like the linear viscoelastic Maxwell model, gives a COR that is independent of impact speed. The value of the viscoplastic COR e_* is bounded between zero and the plastic loss factor ($0 \le e_* \le \gamma$).

References

[1] Stronge, W. J., 1990, "Rigid Body Collisions With Friction," Proc. R. Soc. London, Ser. A, **431**, pp. 169–181.

[2] Coaplen, J., Stronge, W. J., and Ravani, B., 2004, "Work Equivalent Composite Coefficient of Restitution," Int. J. Impact Eng., **30**, pp. 581–591.

[3] Butcher, E. A., and Segalman, D. J., 2000, "Characterizing Damping and Restitution in Compliant Impacts Via Modified K-V and Higher-Order Linear Viscoelastic Models," ASME J. Appl. Mech., **67**(4), pp. 831–834.

[4] Hunt, K. H., and Crossley, F. R. E., 1975, "Coefficient of Restitution Interpreted as Damping in Vibroimpact," ASME J. Appl. Mech., **42**, pp. 440–445.

[5] Atanackovic, T. M., and Spasic, D. T., 2004, "On Viscoelastic Compliant Contact-Impact Models," ASME J. Appl. Mech., **71**(1), pp. 134–138.

[6] Stronge, W. J., 2000, *Impact Mechanics*, Cambridge University Press, Cambridge, Chap. 5.

Dynamics of Mechanical Systems and the Generalized Free-Body Diagram—Part I: General Formulation

József Kövecses
Department of Mechanical Engineering and
Centre for Intelligent Machines,
McGill University,
817 Sherbrooke St. West,
Montréal, Québec, H3A 2K6, Canada
e-mail: jozsef.kovecses@mcgill.ca

In this paper, we generalize the idea of the free-body diagram for analytical mechanics for representations of mechanical systems in configuration space. The configuration space is characterized locally by an Euclidean tangent space. A key element in this work relies on the relaxation of constraint conditions. A new set of steps is proposed to treat constrained systems. According to this, the analysis should be broken down to two levels: (1) the specification of a transformation via the relaxation of the constraints; this defines a subspace, the space of constrained motion; and (2) specification of conditions on the motion in the space of constrained motion. The formulation and analysis associated with the first step can be seen as the generalization of the idea of the free-body diagram. This formulation is worked out in detail in this paper. The complement of the space of constrained motion is the space of admissible motion. The parametrization of this second subspace is generally the task of the analyst. If the two subspaces are orthogonal then useful decoupling can be achieved in the dynamics formulation. Conditions are developed for this orthogonality. Based on this, the dynamic equations are developed for constrained and admissible motions. These are the dynamic equilibrium equations associated with the generalized free-body diagram. They are valid for a broad range of constrained systems, which can include, for example, bilaterally constrained systems, redundantly constrained systems, unilaterally constrained systems, and nonideal constraint realization. [DOI: 10.1115/1.2965372]

Keywords: analytical mechanics, principle of relaxation of constraints, constrained and admissible motions, generalized force, geometric representation, global and local parametrizations

1 Introduction

The free-body diagram is a fundamental idea for the analysis of bodies and systems in static or dynamic equilibrium. The general recipe can be given as follows: free the body/system from its surroundings, represent all the external and inertial forces/moments acting on this new "freed" body/system, and write the equations representing the static or dynamic equilibrium. For a rigid body model, these equations are the Newton–Euler equations describing force and moment balances.

In this paper we describe a framework generalizing this idea to mechanical systems, which can be represented in a finite dimensional configuration space. Our approach is essentially based on the full development of the *principle of relaxation of constraints*. This principle is probably best described by Papastavridis [1] as a general principle of mechanics. However, it can be traced back to other earlier works, e.g., Hamel [2,3] also gave a detailed discussion on this topic. To a limited extent, it is implicitly present in several methods of analytical mechanics. For example, the method of Lagrangian multipliers can be seen as an application of the principle of relaxation of constraints. Another later appearance of the principle is in the work of Kane and Levinson [4] where they used ideas of constraint relaxation, which were also described by Hamel [2], together with Kane's efficient algorithmic approach to "bring noncontributing forces into evidence." This was also used by Djerassi and Bamberger [5], Lesser [6], and Blajer [7] to further develop the approach. These are specific applications of the principle of relaxation of constraints to determine generalized constraint forces without the explicit introduction of Lagrange multipliers.

Geometric considerations are quite fundamental in analytical mechanics to understand the global and local structures of the configuration space of a mechanical system. One very important contribution for such description was made by Synge [8] and Synge and Schild [9]. Brauchli [10] further extended this formulation introducing the idea of mass-orthogonal projection. Blajer [11,12] provided geometric interpretations for some of the techniques used in multibody dynamics. Papastavridis [13] gave recently a detailed description of the application of tensor calculus in analytical mechanics.

Decomposition of kinematic and kinetic quantities along admissible and constrained directions of motion is central in this paper. Ideas of such decompositions to some extent have already appeared. Both Blajer [11] and Papastavridis [1] used a simple planar diagram to illustrate this geometric idea. Papastavridis [1,13] called the dynamic equations associated with the constrained directions *kinetostatic equations*, which can be used for bilateral constraints. Lesser [6] also developed such kinetostatic equations for constrained directions for ideal bilateral constraints. Blajer [14] expressed kinetic and kinetostatic equations using a minimum set of generalized velocities and the associated projectors. He decomposed the configuration space locally to orthogonal and tangent subspaces, which is similar to our concepts of constrained and admissible motions. Brauchli [10] also considered ideal bilateral constraints, and decomposed the generalized velocity vector and called this decomposition the spaces of admissible and inadmissible velocities. He derived dynamic equations using the decomposition performed at the velocity and momentum levels only.

Contributed by the Applied Mechanics Division of ASME for publication in the JOURNAL OF APPLIED MECHANICS. Manuscript received November 25, 2007; final manuscript received May 21, 2008; published online August 20, 2008. Review conducted by Martin Ostoja-Starzewski.

For multi-rigid-body systems and perfect bilateral holonomic constraints, Glocker [15] decomposed the virtual displacements into two arrays that are compatible and incompatible with the constraints. These are then used to state the dynamic equations in minimum coordinates with respect to the bilateral constraints. Kövecses et al. [16,17] also developed a similar decomposition of the virtual displacements, and via that the decomposition of the d'Alembert–Lagrange principle, for general bilaterally constrained mechanical systems, which decomposition is also applicable for redundant constraints. This was used to establish simulation algorithms for constrained systems.

We will further expand these cited works and results in this present paper to fully interpret the dynamics associated with constrained and admissible motions, and develop the concept of the generalized free-body diagram. Besides the description of the idea of the generalized free-body diagram, the target of this paper is to derive a unified formulation based on this concept to address a broad range of constrained motion problems in one single framework. These constrained motion problems can include bilateral and unilateral conditions, nonideal phenomena stemming from the realization of constraints, and redundantly constrained systems. Such applications will be addressed in detail in Part II of this work [18].

2 Generalized Free-Body Diagram

Let us consider that the $n\times 1$ dimensional array of generalized coordinates $\mathbf{q}=[q^1\ q^2\ \dots\ q^n]^T$ defines the configuration and the time derivatives of these generalized coordinates $\dot{\mathbf{q}}=[\dot{q}^1\ \dot{q}^2\ \dots\ \dot{q}^n]^T$ give a possible set of generalized velocities of the system. We will here use a more general description for the velocities employing components $\mathbf{v}=[v^1\ v^2\ \dots\ v^n]^T$, which can be interpreted as general linear combinations of the time derivatives of the generalized coordinates as $\mathbf{v}=\mathbf{N}\dot{\mathbf{q}}$ and $\dot{\mathbf{q}}=\mathbf{N}^{-1}\mathbf{v}$, where $\mathbf{N}$ is an $n\times n$ transformation matrix that can depend on the generalized coordinates and time. The elements of $\mathbf{v}$ are not necessarily time derivatives (i.e., can be nonholonomic coordinates). For a given configuration, the configuration space can be represented locally by an Euclidean tangent space.

One of the main differences between the so-called Newton–Euler approach and the Lagrangian approach to Dynamics lies in the way how forces acting on an element of a mechanical system are decomposed. In the Newton–Euler approach forces are normally decomposed to external and internal forces; and in the Lagrangian approach they are decomposed to constraint and impressed forces. In general such a classification is associated with the presence of bilateral or unilateral constraints. These, for a particular configuration $\mathbf{q}$, can be given at the velocity level as

$$\mathbf{A}\mathbf{v}=\mathbf{b}(\mathbf{q},t)\ \text{ or }\ \mathbf{A}\mathbf{v}\geq\mathbf{b}(\mathbf{q},t) \tag{1}$$

where $\mathbf{A}=\mathbf{A}(\mathbf{q},t)$ is usually an $r\times n$ constraint Jacobian matrix that is generally a function of configuration and time, and $\mathbf{b}$ is a given function of $\mathbf{q}$ and t. The simplest, and perhaps most frequent, case is $\mathbf{b}=\mathbf{0}$.

These constraint equations and inequalities can, however, also be seen from another perspective:

(1) Equation

$$\mathbf{A}\mathbf{v}=\mathbf{u}_c \tag{2}$$

gives a partial linear transformation of kinematic quantities in the tangent space, and defines an r-dimensional subspace: the *space of constrained motion* (SCM). In this, $\mathbf{u}_c$ is an $r\times 1$ array giving velocity components in the SCM with respect to a local basis of that subspace.

(2) Constraint conditions, equalities/inequalities are specified for $\mathbf{u}_c$, i.e., for motion in the SCM (e.g., given by $\mathbf{b}$). Other conditions can also be given for some of the associated generalized forces in that subspace.

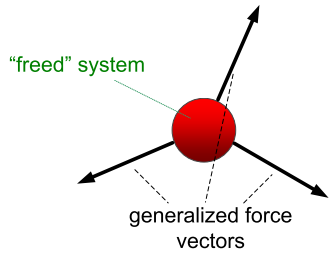

Fig. 1 Generalized force balance

No matter what the conditions imposed in Step (2) are, Step (1), the definition of the transformation to the SCM, is always necessary. A great deal of insight can be gained by relaxing the conditions of Step (2) first and by studying the decompositions of the dynamics of the system under the transformation of Step (1). This concept can be seen as the generalization of the idea of the free-body diagram. The constraint conditions can later be reinstated at the appropriate stage.

Figure 1 illustrates the force balances for a generalized free-body diagram. For a static or dynamic equilibrium the generalized force balance can be written in a coordinate-free form as

$$\sum\vec{F}=\vec{0} \tag{3}$$

where $\Sigma\vec{F}$ represents the sum of the generalized force vectors, i.e., their resultant, which for the dynamics case includes the generalized inertial force vector as well. The generalized force vectors are interpreted in the tangent space and can be decomposed, and represented with components, with respect to any valid parametrization and basis of that space. This is essentially the generalized form of the ordinary way employed for force and moment balances related to free-body diagrams of a simple particle or a rigid body. We will further elaborate on the decomposition of Eq. (3) in later sections.

The subspace that complements the space of constrained motion to the tangent space will be called the *space of admissible motion* (SAM). In general, we can consider that local (or minimal) generalized velocity components given in the $(n-r)\times 1$ array $\mathbf{u}_a$ parametrize the motion in that subspace. Unlike $\mathbf{u}_c$, the definition of $\mathbf{u}_a$ is usually not given, and it is up to the analyst to select the minimum set of generalized velocities characterizing admissible motion. Transformation of Eq. (2) applies to the general, possibly nonholonomic case. A subset of this is the case of holonomic systems (Appendix).

Besides $\mathbf{v}$, components given in $\mathbf{u}=[\mathbf{u}_c^T\mathbf{u}_a^T]^T$ can also be seen to give an alternative complete parametrization for the dynamics of the system. We will call representations associated with $\mathbf{v}$ a *global* parametrization and $\mathbf{u}$ a *local* parametrization (Fig. 2). Let us consider that generalized force components associated with parametrizations $\mathbf{v}$ and $\mathbf{u}$ are represented by $n\times 1$ dimensional arrays $\mathbf{f}$ and $\mathbf{s}$, respectively. Then, the dynamic equilibrium conditions of Eq. (3) can be further expanded as

$$\sum\vec{F}=\sum[\vec{g}^*]^T\mathbf{f}=\sum[\vec{h}^*]^T\mathbf{s}=\vec{0} \tag{4}$$

where $[\vec{g}^*]=[\vec{g}^1\ \vec{g}^2\ \dots\ \vec{g}^n]^T$ and $[\vec{h}^*]=[\vec{h}^1\ \vec{h}^2\ \dots\ \vec{h}^n]^T$ are $n\times 1$ dimensional arrays that contain linearly independent contravariant base vectors of the tangent space for parametrizations $\mathbf{v}$ and $\mathbf{u}$, respectively. The notation used is different for these two arrays to indicate that each element is a geometric (coordinate-free) vector, not a scalar.

3 Parametrizations

The coordinate transformation for kinematic quantities for the

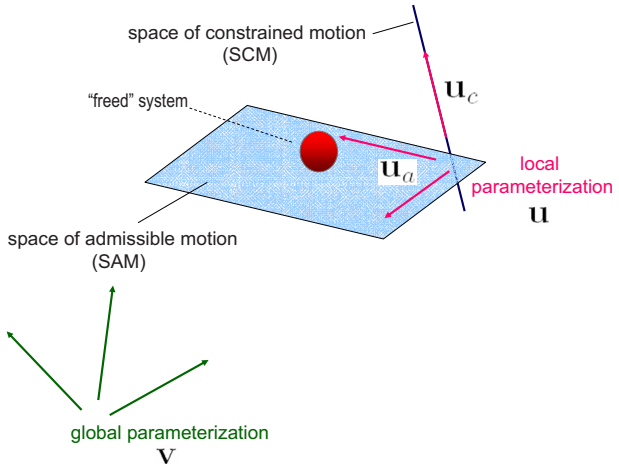

Fig. 2 Subspaces, global and local parametrizations

entire tangent space can be given with[1]

$$\mathbf{R}\mathbf{v} = \mathbf{u} \tag{5}$$

where

$$\mathbf{R} = \begin{bmatrix} \mathbf{A} \\ \mathbf{B} \end{bmatrix} \quad \text{and} \quad \mathbf{u} = \begin{bmatrix} \mathbf{u}_c \\ \mathbf{u}_a \end{bmatrix} \tag{6}$$

$\mathbf{R}$ is the $n \times n$ transformation matrix, $\mathbf{u}$ is an $n \times 1$ array, and $\mathbf{u}_c$ and $\mathbf{u}_a$ are $r \times 1$ and $(n-r) \times 1$ arrays, respectively. Matrix $\mathbf{A}$ is defined by the specification of the transformation to the SCM, and $\mathbf{B}$ is an $(n-r) \times n$ matrix that depends on the selection of the local parametrization for the SAM. The dual of transformation (5) can be interpreted for kinetic quantities, and given for generalized forces as

$$\mathbf{R}^T\mathbf{s} = \mathbf{f} \tag{7}$$

where

$$\mathbf{s} = \begin{bmatrix} \mathbf{s}_c \\ \mathbf{s}_a \end{bmatrix} \quad \text{and} \quad \mathbf{f} = \mathbf{f}_c + \mathbf{f}_a \tag{8}$$

As shown in Eq. (8), these generalized forces can also be decomposed to parts associated with the two subspaces: $\mathbf{f}_c$ and $\mathbf{f}_a$, and $\mathbf{s}_c$ and $\mathbf{s}_a$. These decompositions will be studied in detail. Equation (7) can simply be derived considering that based on the power of forces, $\mathbf{v}^T\mathbf{f} = \mathbf{u}^T\mathbf{s} = \mathbf{v}^T\mathbf{R}^T\mathbf{s}$.

Let us consider that $\mathbf{M}$ and $\mathbf{W}$ represent the mass matrices associated with parametrizations $\mathbf{v}$ and $\mathbf{u}$, respectively. Then the kinetic energy of the "freed" system can be written as

$$T = \tfrac{1}{2}\mathbf{v}^T\mathbf{M}\mathbf{v} = \tfrac{1}{2}\mathbf{u}^T\mathbf{W}\mathbf{u} \tag{9}$$

These mass matrices give two valid representations of the covariant components of the metric tensor of the tangent space, and their inverses represent the contravariant components of the same tensor. The components of the generalized acceleration vector, [8], associated with parametrizations $\mathbf{v}$ and $\mathbf{u}$, can be written in arrays $\mathbf{a}_v$ and $\mathbf{a}_u$ as

$$\mathbf{a}_v = \dot{\mathbf{v}} + \mathbf{M}^{-1}\mathbf{c} \tag{10}$$

$$\mathbf{a}_u = \dot{\mathbf{u}} + \mathbf{W}^{-1}\mathbf{z} \tag{11}$$

where arrays $\mathbf{c}$ and $\mathbf{z}$ contain Coriolis and centrifugal terms, and

$$-\mathbf{M}\mathbf{a}_v = -(\mathbf{M}\dot{\mathbf{v}} + \mathbf{c}) = \mathbf{f}_I \quad \text{and} \quad -\mathbf{W}\mathbf{a}_u = -(\mathbf{W}\dot{\mathbf{u}} + \mathbf{z}) = \mathbf{s}_I \tag{12}$$

give the generalized inertial forces in terms of the global and local parametrizations, respectively. These can also be established from the Gibbs–Appell function of the system, S, as $\mathbf{f}_I = -\partial S/\partial \dot{\mathbf{v}}$ and $\mathbf{s}_I = -\partial S/\partial \dot{\mathbf{u}}$.[2]

Based on the transformation of kinematic components, which are contravariant components of generalized vectors, the generalized accelerations also transform, using Eq. (5), as

$$\mathbf{R}\mathbf{a}_v = \mathbf{a}_u \tag{13}$$

and for the generalized inertial forces (kinetic quantities), according to Eq. (7), as

$$\mathbf{R}^T\mathbf{s}_I = \mathbf{f}_I \tag{14}$$

and also, based on Eqs. (5) and (10)–(13), we can obtain

$$\mathbf{z} = \mathbf{W}\mathbf{R}\mathbf{M}^{-1}\mathbf{c} - \mathbf{W}\dot{\mathbf{R}}\mathbf{v} = \mathbf{W}\mathbf{R}\mathbf{M}^{-1}\mathbf{c} - \mathbf{W}\dot{\mathbf{R}}\mathbf{R}^{-1}\mathbf{u} \tag{15}$$

For the transformation between kinematic and kinetic components we also have

$$\mathbf{M}\mathbf{v} = \mathbf{p} \quad \text{and} \quad \mathbf{M}\mathbf{a}_v = \mathbf{f} \tag{16}$$

$$\mathbf{W}\mathbf{u} = \boldsymbol{\eta} \quad \text{and} \quad \mathbf{W}\mathbf{a}_u = \mathbf{s} \tag{17}$$

where $\mathbf{f}$ and $\mathbf{s}$ can simply represent in this particular case kinetic components at the force-acceleration level; furthermore, $\mathbf{p}$ and $\boldsymbol{\eta}$ are generalized momenta associated with parametrizations $\mathbf{v}$ and $\mathbf{u}$, respectively. Transformation relationships similar to Eqs. (7) and (8) can also be interpreted for these momentum components.

Using the above expressions, we can establish for the transformation of the mass matrices that

$$\mathbf{M} = \mathbf{R}^T\mathbf{W}\mathbf{R} \quad \text{and} \quad \mathbf{W}^{-1} = \mathbf{R}\mathbf{M}^{-1}\mathbf{R}^T \tag{18}$$

Generalized mass matrix $\mathbf{M}$ can be decomposed as

$$\mathbf{M} = \mathbf{G}^T\mathbf{G} \tag{19}$$

where $\mathbf{G}$ represents an $n \times n$ nonsingular matrix. Such a decomposition can be achieved in several different ways via the Cholesky or the square-root factorizations, for example.[3] Given that $\mathbf{M}$ is a representation of the metric tensor in covariant components, the columns of $\mathbf{G}$ can also be seen as giving the components of the covariant base vectors, associated with parametrization $\mathbf{v}$, with respect to a unitless, orthonormal n-dimensional Cartesian basis. The components of the contravariant base vectors, elements of $[\tilde{g}^*]$ in Eq. (4), with respect to this Cartesian basis are in the columns of $\mathbf{G}^{-T}$. This decomposition of $\mathbf{M}$ can be used to introduce *physical components* [19,20] at the velocity-momentum level as

$$\boldsymbol{\pi} = \mathbf{G}\mathbf{v} = \mathbf{G}^{-T}\mathbf{p} \tag{20}$$

which are homogeneous in physical units (as can be seen based on the expression of the kinetic energy (9)). They can also be considered as a special set of nonholonomic quasivelocities. The physical components are interpreted relative to the unitless orthonormal Cartesian basis of the tangent space, and as such they are the same for parametrization $\mathbf{u}$ as well. This can also be seen from the two expressions of the kinetic energy in Eq. (9). The unit of the physical components at the velocity-momentum level is $\sqrt{kg}\, m/s$. At the acceleration-force level the physical components can be introduced as

[1]The transformation here is illustrated for velocity components. However, it can also be defined for other kinematic quantities (e.g., acceleration components) in the same form as long as the elements of the arrays can be interpreted as components of a generalized geometric vector in the tangent space.

[2]Inertial forces can of course also be established in many other ways (e.g., using the kinetic energy function). However, the most compact and general form may be given with the Gibbs–Appell function.

[3]For the Cholesky factorization, in particular, it can be shown that the algorithm contains operations that are consistent with the possibly different physical units of the elements of $\mathbf{M}$.

$$\boldsymbol{\gamma} = \mathbf{G}\mathbf{a}_v = \mathbf{G}^{-T}\mathbf{f} \tag{21}$$

with units of $\sqrt{kg}\, m/s^2$ where $\mathbf{f}$ represents kinetic components.

Performing some of the derivations using physical components will be advantageous since this makes the use of matrix computation algorithms possible and consistent with physical units. Using physical components, transformation equations (5) and (7) can be written as

$$\mathbf{R}\mathbf{G}^{-1}\boldsymbol{\pi} = \mathbf{u} \tag{22}$$

and

$$\mathbf{G}^{-T}\mathbf{R}^T\mathbf{s} = \boldsymbol{\gamma} \tag{23}$$

Breaking these relationships down to the subspaces, the transformations related to the SCM and SAM can be given in terms of physical components as

$$\mathbf{A}\mathbf{G}^{-1}\boldsymbol{\pi} = \mathbf{u}_c \quad \mathbf{G}^{-T}\mathbf{A}^T\mathbf{s}_c = \boldsymbol{\gamma}_c \tag{24}$$

and

$$\mathbf{B}\mathbf{G}^{-1}\boldsymbol{\pi} = \mathbf{u}_a \quad \mathbf{G}^{-T}\mathbf{B}^T\mathbf{s}_a = \boldsymbol{\gamma}_a \tag{25}$$

Based on Eqs. (5), (6), and (18), $\mathbf{W}^{-1}$ and $\mathbf{W}$ can be expanded as

$$\mathbf{W}^{-1} = \begin{bmatrix} \mathbf{A}\mathbf{M}^{-1}\mathbf{A}^T & \mathbf{A}\mathbf{M}^{-1}\mathbf{B}^T \\ \mathbf{B}\mathbf{M}^{-1}\mathbf{A}^T & \mathbf{B}\mathbf{M}^{-1}\mathbf{B}^T \end{bmatrix} \quad \text{and} \quad \mathbf{M} = \mathbf{A}^T\mathbf{W}\mathbf{A} + \mathbf{B}^T\mathbf{W}\mathbf{B} \tag{26}$$

Using the block matrix inversion formula [21]

$$\mathbf{W} = \begin{bmatrix} \mathbf{W}_{cc} & \mathbf{W}_{ca} \\ \mathbf{W}_{ac} & \mathbf{W}_{aa} \end{bmatrix} \tag{27}$$

where

$$\mathbf{W}_{cc} = (\mathbf{A}\mathbf{M}^{-1}\mathbf{A}^T)^{-1} + (\mathbf{A}\mathbf{M}^{-1}\mathbf{A}^T)^{-1}\mathbf{A}\mathbf{M}^{-1}\mathbf{B}^T\mathbf{W}_{aa}\mathbf{B}\mathbf{M}^{-1}\mathbf{A}^T(\mathbf{A}\mathbf{M}^{-1}\mathbf{A}^T)^{-1} \tag{28}$$

$$\mathbf{W}_{ca} = \mathbf{W}_{ac}^T = -(\mathbf{A}\mathbf{M}^{-1}\mathbf{A}^T)^{-1}\mathbf{A}\mathbf{M}^{-1}\mathbf{B}^T\mathbf{W}_{aa} \tag{29}$$

$$\mathbf{W}_{aa} = \left(\mathbf{B}\mathbf{M}^{-1}\mathbf{B}^T - \mathbf{B}\mathbf{M}^{-1}\mathbf{A}^T(\mathbf{A}\mathbf{M}^{-1}\mathbf{A}^T)^{-1}\mathbf{A}\mathbf{M}^{-1}\mathbf{B}^T\right)^{-1} \tag{30}$$

If $\mathbf{A}\mathbf{M}^{-1}\mathbf{B}^T = \mathbf{0}$ (and $\mathbf{B}\mathbf{M}^{-1}\mathbf{A}^T = \mathbf{0}$) then the two subspaces are *orthogonal* to each other, and the expressions of $\mathbf{W}^{-1}$ and $\mathbf{W}$ are greatly simplified since the coupling terms $\mathbf{W}_{ca}$ and $\mathbf{W}_{ac}$ vanish. This case will play an important role in our later investigations. However, for a little while, let us still consider the general case. $\mathbf{W}$ and $\mathbf{W}^{-1}$ also represent the covariant and contravariant components of the metric tensor in local parametrization. The decomposition of $\mathbf{W} = \mathbf{H}^T\mathbf{H}$ (similar to $\mathbf{M}$) can then give the physical components of the covariant and contravariant base vectors associated with the local parametrization (e.g., these contravariant base vectors are the elements of $[\vec{h}^*]$ in Eq. (4)).

3.1 Singular Transformation to the Space of Constrained Motion. One aspect we also have to address is the possibility to define the transformations in a way that components in the SCM are interpreted by giving a redundant set of transformation equations (e.g., the case of redundant constraints). This is often neglected in deriving formulations in analytical dynamics, but has great practical importance in several problems. In this case $\mathbf{A}$ is an $m \times n$ matrix ($m > r$) and does not have a full row rank; its rank equals r. This can also be interpreted as if $\mathbf{A}^T\mathbf{s}_c = \mathbf{f}_c$ (or $\mathbf{R}^T\mathbf{s} = \mathbf{f}$) were given at the first place as opposed to $\mathbf{A}\mathbf{v} = \mathbf{u}_c$ (or $\mathbf{R}\mathbf{v} = \mathbf{u}$).[4] Therefore, those transformation relationships that do not require the formation of $\mathbf{R}^{-1}$ will hold.

Let us now consider for this general case of transformation how components belonging to various subspaces can be determined. First, we will look at the transformations relating to the physical components, since they are homogeneous in physical units. For the case of redundant rows in $\mathbf{A}\mathbf{G}^{-1}$ there are several procedures available to select an independent set of r rows, hence, base vectors for the SCM. Examples of such techniques can be the ones that are based on forming the physically meaningful, but singular, inverse mass matrix $\mathbf{A}\mathbf{G}^{-1}\mathbf{G}^{-T}\mathbf{A}^T = \mathbf{A}\mathbf{M}^{-1}\mathbf{A}^T$, and analyzing its eigenvalue problem (e.g., via the singular value decomposition (SVD) of $\mathbf{A}\mathbf{G}^{-1}$); or another technique can be based on the use of Gram–Schmidt orthogonalization. It can also be possible by simply detecting and removing the redundant rows by elementary techniques, hence determining new, now nonredundant $\mathbf{A}\mathbf{G}^{-1}$ and $\mathbf{A}$.

Once we determined such an independent set from the rows of $\mathbf{A}\mathbf{G}^{-1}$ then it can be used to construct the rows of an $r \times n$ matrix $\boldsymbol{\Gamma}$ and rewrite relations in terms of components interpreted relative to independent base vectors. Then, the expression for $\mathbf{W}^{-1}$ in Eq. (26) can be written as

$$\mathbf{W}^{-1} = \begin{bmatrix} \boldsymbol{\Gamma}\boldsymbol{\Gamma}^T & \boldsymbol{\Gamma}\mathbf{G}^{-T}\mathbf{B}^T \\ \mathbf{B}\mathbf{G}^{-1}\boldsymbol{\Gamma}^T & \mathbf{B}\mathbf{M}^{-1}\mathbf{B}^T \end{bmatrix} \tag{31}$$

We have to note, however, that in such a case the independent base vectors may no longer be associated with the originally redundantly given $\mathbf{u}_c$-based local parametrization of the SCM. However, this does not present a problem, particularly, if global parametrization is employed to represent the dynamics formulation. For local parametrization we would need to identify a new nonredundant $\mathbf{A}$ from $\boldsymbol{\Gamma}$, which may be done as $\mathbf{A} = \boldsymbol{\Gamma}\mathbf{G}$. In the case of a nonredundant set of transformation equations ($m = r$), or when $\mathbf{A}$ was redefined by identifying and removing the redundant rows, $\boldsymbol{\Gamma} = \mathbf{A}\mathbf{G}^{-1}$ is, of course, a valid selection.

With these more general considerations the condition for orthogonality of the two subspaces can be given as $\boldsymbol{\Gamma}\mathbf{G}^{-T}\mathbf{B}^T = \mathbf{0}$ or $\mathbf{B}\mathbf{G}^{-1}\boldsymbol{\Gamma}^T = \mathbf{0}$. If the two subspaces are orthogonal to each other then Eq. (31) is simplified as

$$\mathbf{W}^{-1} = \begin{bmatrix} \boldsymbol{\Gamma}\boldsymbol{\Gamma}^T & 0 \\ 0 & \mathbf{B}\mathbf{M}^{-1}\mathbf{B}^T \end{bmatrix} \tag{32}$$

and $\boldsymbol{\Gamma}\boldsymbol{\Gamma}^T$ and $(\boldsymbol{\Gamma}\boldsymbol{\Gamma}^T)^{-1}$ can play the role of the inner product matrices for the SCM in place of $\mathbf{A}\mathbf{M}^{-1}\mathbf{A}^T$ and $(\mathbf{A}\mathbf{M}^{-1}\mathbf{A}^T)^{-1}$, respectively.

4 Orthogonal Decompositions

4.1 Physical Components and Global Parametrization. Let us consider here the general case and, based on Sec. 3, replace $\mathbf{A}\mathbf{G}^{-1}$ with $\boldsymbol{\Gamma}$ in the appropriate expressions

$$\mathbf{A}\mathbf{G}^{-1} \quad \rightarrow \quad \boldsymbol{\Gamma} \tag{33}$$

We will derive formulas of general validity for the decomposition of physical, kinematic, and kinetic components. To present these in a compact form, a condensed notation will be used in this section. The three representations of a generalized geometric vector, $\vec{r}$, will be denoted by $\hat{\mathbf{r}}$, $\mathbf{r}$, and $\bar{\mathbf{r}}$, respectively, for this section only. Array $\hat{\mathbf{r}} = \hat{\mathbf{r}}_c + \hat{\mathbf{r}}_a$ will represent the physical components ($\boldsymbol{\pi}$ or $\boldsymbol{\gamma}$); $\mathbf{r}_u = [\mathbf{r}_{u_c}^T \mathbf{r}_{u_a}^T]^T$ and $\mathbf{r}_v = \mathbf{r}_{v_c} + \mathbf{r}_{v_a}$ will be used for the kinematic components ($\mathbf{v}, \mathbf{u}$ or $\mathbf{a}_v, \mathbf{a}_u$); and $\bar{\mathbf{r}}_u = [\bar{\mathbf{r}}_{u_c}^T \bar{\mathbf{r}}_{u_a}^T]^T$ and $\bar{\mathbf{r}}_v = \bar{\mathbf{r}}_{v_c} + \bar{\mathbf{r}}_{v_a}$ will represent the kinetic components ($\mathbf{p}, \boldsymbol{\eta}$ or $\mathbf{f}, \mathbf{s}$).

If the two subspaces are orthogonal to each other then for the physical components the following transformation relationships hold based on Eqs. (22)–(25) and (32):

$$\boldsymbol{\Gamma}\hat{\mathbf{r}} = \mathbf{r}_{u_c} \tag{34}$$

and

[4] In this case, $\mathbf{s}_c$ and $\mathbf{u}_c$ are $m \times 1$ arrays, $\mathbf{s}_a$ and $\mathbf{u}_a$ are $(n-r) \times 1$ arrays, $\mathbf{s}$ is an $(n-r+m) \times 1$ array, and $\mathbf{R}$ is an $(n-r+m) \times n$ matrix.

$$\boldsymbol{\Gamma}^T\bar{\mathbf{r}}_{u_c} = \hat{\mathbf{r}}_c \tag{35}$$

where $\hat{\mathbf{r}}_c$ is an $n \times 1$ array representing the physical components of the part of the vector which belongs to the SCM.

Based on Eq. (32), a general representation for the inverse mass matrix and the mass matrix in the SCM can be formed as $\boldsymbol{\Gamma}\boldsymbol{\Gamma}^T$ and $(\boldsymbol{\Gamma}\boldsymbol{\Gamma}^T)^{-1}$, respectively. Then, according to Eqs. (17) and (32), the kinematic and kinetic components in this subspace can be transformed into each other as

$$\boldsymbol{\Gamma}\boldsymbol{\Gamma}^T\bar{\mathbf{r}}_{u_c} = \mathbf{r}_{u_c} \quad \text{and} \quad (\boldsymbol{\Gamma}\boldsymbol{\Gamma}^T)^{-1}\mathbf{r}_{u_c} = \bar{\mathbf{r}}_{u_c} \tag{36}$$

Based on these and using Eqs. (34) and (35) we can develop that

$$\boldsymbol{\Gamma}^T(\boldsymbol{\Gamma}\boldsymbol{\Gamma}^T)^{-1}\mathbf{r}_{u_c} = \hat{\mathbf{r}}_c \tag{37}$$

and then

$$\boldsymbol{\Gamma}^T(\boldsymbol{\Gamma}\boldsymbol{\Gamma}^T)^{-1}\boldsymbol{\Gamma}\hat{\mathbf{r}} = \hat{\mathbf{r}}_c \tag{38}$$

and

$$\hat{\mathbf{r}} - \hat{\mathbf{r}}_c = \hat{\mathbf{r}}_a = (\mathbf{I}_{n\times n} - \boldsymbol{\Gamma}^T(\boldsymbol{\Gamma}\boldsymbol{\Gamma}^T)^{-1}\boldsymbol{\Gamma})\hat{\mathbf{r}} \tag{39}$$

where $\hat{\mathbf{r}}_a$ is an $n \times 1$ array representing the physical components of the part of the vector which belongs to the SAM, and $\mathbf{I}_{n\times n}$ is an $n \times n$ identity matrix. Equations (38) and (39) are two central formulas to determine the decomposition of the physical components. It is important to note again that these physical components are interpreted relative to the global n-dimensional unitless Cartesian basis.

Matrices

$$\hat{\mathbf{P}}_c = \boldsymbol{\Gamma}^T(\boldsymbol{\Gamma}\boldsymbol{\Gamma}^T)^{-1}\boldsymbol{\Gamma} \quad \text{and} \quad \hat{\mathbf{P}}_a = (\mathbf{I}_{n\times n} - \hat{\mathbf{P}}_c) \tag{40}$$

can also be called projector operators or projector matrices. They are dimensionless. It can be seen from Eqs. (38) and (39) that they are symmetric and idempotent. It can also be readily shown from the above equations that $\hat{\mathbf{P}}_c\hat{\mathbf{P}}_a = \hat{\mathbf{P}}_a\hat{\mathbf{P}}_c = \mathbf{0}_{n\times n}$. Therefore, as was already mentioned, the two subspaces can be considered as orthogonal complements of each other. If the rows of $\boldsymbol{\Gamma}$ contain components of orthonormal base vectors, i.e., $\boldsymbol{\Gamma}\boldsymbol{\Gamma}^T = \mathbf{I}_{r\times r}$, then the expression of the projector reduces to $\boldsymbol{\Gamma}^T\boldsymbol{\Gamma}$.

Such orthonormal vectors can result from the application of various techniques such as the singular value decomposition of $\mathbf{A}\mathbf{G}^{-1}$ that can be written as $\mathbf{A}\mathbf{G}^{-1} = \mathbf{Y}\mathbf{Z}\mathbf{V}^T$ [22]. This is also closely related to the right pseudo-inverse of $\mathbf{A}\mathbf{G}^{-1}$: $(\mathbf{A}\mathbf{G}^{-1})^\dagger = \mathbf{V}\mathbf{Z}^{-1}\mathbf{Y}^T$. In this case, $\mathbf{V}$ is an $n \times r$ matrix and its columns contain the physical components of r orthonormal vectors. Therefore, $\boldsymbol{\Gamma} = \mathbf{V}^T$ can be a possible selection for the physical components of orthonormal base vectors. Using this interpretation and the pseudo-inverse, the projector matrix can also be written as

$$\hat{\mathbf{P}}_c = (\mathbf{A}\mathbf{G}^{-1})^\dagger\mathbf{A}\mathbf{G}^{-1} \tag{41}$$

The use of a pseudo-inverse is of course just one possibility, and it is not a universal way, to express the projectors. We also have to note that the pseudo-inverse can also be established in various different ways, not only by using singular value decomposition.

Based on these considerations regarding the decomposition of the physical components, let us now consider how kinematic and kinetic components can be determined in the two subspaces in terms of a global parametrization. Using the interpretation of the physical components in Eqs. (20) and (21), the decomposition of kinematic components can be given as

$$\mathbf{G}^{-1}\boldsymbol{\Gamma}^T(\boldsymbol{\Gamma}\boldsymbol{\Gamma}^T)^{-1}\boldsymbol{\Gamma}\mathbf{G}\mathbf{r}_v = \mathbf{G}^{-1}\hat{\mathbf{P}}_c\mathbf{G}\mathbf{r}_v = \mathbf{P}_c\mathbf{r}_v = \mathbf{r}_{v_c} \tag{42}$$

and

$$\mathbf{G}^{-1}(\mathbf{I}_{n\times n} - \boldsymbol{\Gamma}^T(\boldsymbol{\Gamma}\boldsymbol{\Gamma}^T)^{-1}\boldsymbol{\Gamma})\mathbf{G}\mathbf{r}_v = \mathbf{G}^{-1}\hat{\mathbf{P}}_a\mathbf{G}\mathbf{r}_v = \mathbf{P}_a\mathbf{r}_v = \mathbf{r}_{v_a} \tag{43}$$

where

$$\mathbf{P}_c = \mathbf{G}^{-1}\hat{\mathbf{P}}_c\mathbf{G} \quad \text{and} \quad \mathbf{P}_a = \mathbf{G}^{-1}\hat{\mathbf{P}}_a\mathbf{G} \tag{44}$$

further, kinetic components can be decomposed as

$$\mathbf{G}^T\boldsymbol{\Gamma}^T(\boldsymbol{\Gamma}\boldsymbol{\Gamma}^T)^{-1}\boldsymbol{\Gamma}\mathbf{G}^{-T}\bar{\mathbf{r}}_v = \mathbf{G}^T\hat{\mathbf{P}}_c\mathbf{G}^{-T}\bar{\mathbf{r}}_v = \mathbf{P}_c^T\bar{\mathbf{r}}_v = \bar{\mathbf{r}}_{v_c} \tag{45}$$

and

$$\mathbf{G}^T(\mathbf{I}_{n\times n} - \boldsymbol{\Gamma}^T(\boldsymbol{\Gamma}\boldsymbol{\Gamma}^T)^{-1}\boldsymbol{\Gamma})\mathbf{G}^{-T}\bar{\mathbf{r}}_v = \mathbf{P}_a^T\bar{\mathbf{r}}_v = \bar{\mathbf{r}}_{v_a} \tag{46}$$

Projector matrices $\mathbf{P}_c$ and $\mathbf{P}_a$ are also idempotent, and $\mathbf{P}_c\mathbf{P}_a = \mathbf{P}_a\mathbf{P}_c = \mathbf{0}_{n\times n}$. This can be readily shown based on their definition above. However, we can also see that *they are not symmetric*. This is an interesting consequence, which is important to note and summarize: For the physical components the projector matrices are symmetric. However, for kinematic and kinetic components, the resulting projector matrices are generally not symmetric. Therefore, in general, $\mathbf{P}_c \neq \mathbf{P}_c^T$ and $\mathbf{P}_a \neq \mathbf{P}_a^T$. This property does not depend on the way how the $\mathbf{M} = \mathbf{G}^T\mathbf{G}$ factorization is performed. It holds even for the case where $\mathbf{G}$ is symmetric, $\mathbf{G}^T = \mathbf{G}$, e.g., when square-root factorization is employed to compute a set of base vectors.

From Eqs. (42)–(46) it can also be seen that

$$\mathbf{P}_a^T\mathbf{M}\mathbf{P}_c = \mathbf{0}_{n\times n} \quad \mathbf{P}_c^T\mathbf{M}\mathbf{P}_a = \mathbf{0}_{n\times n} \tag{47}$$

$$\mathbf{P}_c^T\mathbf{M}\mathbf{P}_c = \mathbf{P}_c^T\mathbf{M} = \mathbf{M}\mathbf{P}_c = \mathbf{G}^T\hat{\mathbf{P}}_c\mathbf{G} \tag{48}$$

and

$$\mathbf{P}_a^T\mathbf{M}\mathbf{P}_a = \mathbf{P}_a^T\mathbf{M} = \mathbf{M}\mathbf{P}_a = \mathbf{G}^T\hat{\mathbf{P}}_a\mathbf{G} \tag{49}$$

For the case where the $\boldsymbol{\Gamma} = \mathbf{A}\mathbf{G}^{-1}$ selection is possible and made, e.g., in the case of nonredundant $\mathbf{A}$, it can be seen that the projector matrices reduce to

$$\hat{\mathbf{P}}_c = \mathbf{G}^{-T}\mathbf{A}^T(\mathbf{A}\mathbf{M}^{-1}\mathbf{A}^T)^{-1}\mathbf{A}\mathbf{G}^{-1} \tag{50}$$

$$\mathbf{P}_c = \mathbf{M}^{-1}\mathbf{A}^T(\mathbf{A}\mathbf{M}^{-1}\mathbf{A}^T)^{-1}\mathbf{A} \tag{51}$$

and

$$\hat{\mathbf{P}}_a = \mathbf{I}_{n\times n} - \mathbf{G}^{-T}\mathbf{A}^T(\mathbf{A}\mathbf{M}^{-1}\mathbf{A}^T)^{-1}\mathbf{A}\mathbf{G}^{-1} \tag{52}$$

$$\mathbf{P}_a = \mathbf{I}_{n\times n} - \mathbf{M}^{-1}\mathbf{A}^T(\mathbf{A}\mathbf{M}^{-1}\mathbf{A}^T)^{-1}\mathbf{A} \tag{53}$$

also

$$\mathbf{G}^T\hat{\mathbf{P}}_c\mathbf{G} = \mathbf{A}^T(\mathbf{A}\mathbf{M}^{-1}\mathbf{A}^T)^{-1}\mathbf{A} \quad \mathbf{G}^T\hat{\mathbf{P}}_a\mathbf{G} = \mathbf{M} - \mathbf{A}^T(\mathbf{A}\mathbf{M}^{-1}\mathbf{A}^T)^{-1}\mathbf{A} \tag{54}$$

Let us again state separately an important property of the above decompositions of the various components. Here the decompositions were performed based on the knowledge of the transformation to the SCM only (matrix $\mathbf{A}$). However, the derivations also made sure that the other subspace, the SAM, is an orthogonal complement of the SCM.

The above orthogonal decomposition to the spaces of constrained and admissible motions was performed based on the global parametrization of the tangent space. The only condition that was used is that a transformation matrix $\mathbf{A}$ is known, which can also represent a singular transformation in our formulation. We were able to define the SAM and establish expressions for vector components there without explicitly specifying a local parametrization for that subspace. Such a local parametrization can be given by matrix $\mathbf{B}$. However, this matrix is usually not specified explicitly, and it is the task of the analyst to determine the local parametrization for the SAM. In the following we will reiterate the condition that is necessary to be satisfied by the selection of $\mathbf{B}$ in order for the two subspaces be orthogonal to each other. For this, based on Eq. (31), $\mathbf{B}$ needs to satisfy the condition

$$\boldsymbol{\Gamma}\mathbf{G}^{-T}\mathbf{B}^T = \mathbf{0} \tag{55}$$

and for the case where $\boldsymbol{\Gamma} = \mathbf{A}\mathbf{G}^{-1}$

$$\mathbf{A}\mathbf{M}^{-1}\mathbf{B}^T = \mathbf{0} \tag{56}$$

The satisfaction of this condition makes it possible to separate the dynamics of constrained and admissible motions using local parametrizations too. For the analysis of systems with bilateral constrains, the definition of matrix **B** is also equivalent to selecting a minimum set of independent generalized velocities. However, we have to note that there is a significant difference between the proper "orthogonal" specification of **B** and the way how the selection of independent generalized velocities is usually done. Instead of using the order of transformation given in Eqs. (5) and (13), usually order

$$[\mathbf{J} \quad \mathbf{D}]\begin{bmatrix}\mathbf{r}_{u_c}\\ \mathbf{r}_{u_a}\end{bmatrix} = \mathbf{r}_v \quad \leftrightarrow \quad \mathbf{R}^{-1}\mathbf{r}_u = \mathbf{r}_v \tag{57}$$

is given, where $\mathbf{R}^{-1}=[\mathbf{J} \quad \mathbf{D}]$, $\mathbf{r}_u=[\mathbf{r}_{u_c}^T \mathbf{r}_{u_a}^T]^T$, and very often only the form $\mathbf{D}\mathbf{r}_{u_a}=\mathbf{r}_v-\mathbf{J}\mathbf{r}_{u_c}$ is specified where term $\mathbf{J}\mathbf{r}_{u_c}$ is given for bilateral constraints. However, the use of matrix **D** is generally not equivalent to that of **B**. Considering Eqs. (6) and (57) it can be seen that **D** will be an orthogonal complement matrix to **A**, i.e., $\mathbf{AD}=\mathbf{0}$. This property of **D** was also shown by Blajer [14,12] using a different line of reasoning, with the assumption of orthogonal subspaces. It has also been widely applied in literature to find **D** and introduce a minimum set of independent generalized velocities for bilaterally constrained systems. In fact, $\mathbf{AD}=\mathbf{0}$ also holds when the SCM and the SAM are not orthogonal to each other (can be seen based on Eqs. (5), (6), and (57)). This is an important point that was missed in Refs. [14,12].

In general, the use of **D** does not lead to the decoupling of the dynamics. The way how **D** is defined cannot usually be used to find **B**. To determine a **B** suitable to decouple the two subspaces, according to Eq. (55) (or Eq. (56)), we need to find an orthogonal complement matrix to $\mathbf{\Gamma}\mathbf{G}^{-T}$, or to $\mathbf{A}\mathbf{M}^{-1}$. In turn, this will often lead to the definition of nonholonomic velocity components, $\mathbf{u}_a=\mathbf{B}\mathbf{v}$, for the local description of the SAM.

4.2 Local Parametrization of the Subspaces. In this subsection, we develop the transformation relationships that make it possible to determine the decompositions with respect to the local parametrizations of the subspaces. Given $\mathbf{r}_v$ and $\bar{\mathbf{r}}_v$, we want to determine $\mathbf{r}_{u_c}$, $\mathbf{r}_{u_a}$, $\bar{\mathbf{r}}_{u_c}$, and $\bar{\mathbf{r}}_{u_a}$. These expressions for $\mathbf{r}_{u_c}$ and $\mathbf{r}_{u_a}$ have already been given by Eqs. (5), (6), and (13). Here we aim for kinetic components. To give local representations for the SAM, it is assumed that **B** is already identified satisfying condition (55). Considering Eqs. (34) and (36) we can write that

$$(\mathbf{\Gamma}\mathbf{\Gamma}^T)^{-1}\mathbf{\Gamma}\hat{\mathbf{r}} = (\mathbf{\Gamma}\mathbf{\Gamma}^T)^{-1}\mathbf{\Gamma}\mathbf{G}^{-T}\bar{\mathbf{r}}_v = \bar{\mathbf{r}}_{u_c} \tag{58}$$

which gives the relations to determine local kinetic components in the SCM. If a nonredundant transformation matrix **A** is identified[5] then these equations are simplified to the form

$$(\mathbf{A}\mathbf{M}^{-1}\mathbf{A}^T)^{-1}\mathbf{A}\mathbf{G}^{-1}\hat{\mathbf{r}} = (\mathbf{A}\mathbf{M}^{-1}\mathbf{A}^T)^{-1}\mathbf{A}\mathbf{M}^{-1}\bar{\mathbf{r}}_v = \bar{\mathbf{r}}_{u_c} \tag{59}$$

Specifying matrix **B** also gives the transformation relationships between kinematic and kinetic components in the SAM via $\mathbf{B}\mathbf{M}^{-1}\mathbf{B}^T$ and $(\mathbf{B}\mathbf{M}^{-1}\mathbf{B}^T)^{-1}$. Considering this and based on Eqs. (17), (20), (21), and (32)

$$(\mathbf{B}\mathbf{M}^{-1}\mathbf{B}^T)^{-1}\mathbf{B}\mathbf{G}^{-1}\hat{\mathbf{r}} = (\mathbf{B}\mathbf{M}^{-1}\mathbf{B}^T)^{-1}\mathbf{B}\mathbf{M}^{-1}\bar{\mathbf{r}}_v = \bar{\mathbf{r}}_{u_a} \tag{60}$$

gives the transformation equations to determine local kinetic components in the SAM.

5 Kinetic Energy Decoupling

Based on Eqs. (42) and (43)

$$\mathbf{v} = \mathbf{v}_c + \mathbf{v}_a, \quad \mathbf{v}_c = \mathbf{P}_c\mathbf{v}, \quad \mathbf{v}_a = \mathbf{P}_a\mathbf{v} \tag{61}$$

also

$$\mathbf{u} = \begin{bmatrix}\mathbf{u}_c\\ \mathbf{u}_a\end{bmatrix}, \quad \mathbf{u}_c = \mathbf{A}\mathbf{v}, \quad \mathbf{u}_a = \mathbf{B}\mathbf{v} \tag{62}$$

Using these, Eqs. (9) and (32), and the properties of the projectors the kinetic energy can be decoupled as

$$T = T_c + T_a \tag{63}$$

where in global parametrization

$$T_c = \tfrac{1}{2}\mathbf{v}^T\mathbf{P}_c^T\mathbf{M}\mathbf{P}_c\mathbf{v} = \tfrac{1}{2}\mathbf{p}^T\mathbf{P}_c\mathbf{M}^{-1}\mathbf{P}_c^T\mathbf{p} \tag{64}$$

$$T_a = \tfrac{1}{2}\mathbf{v}^T\mathbf{P}_a^T\mathbf{M}\mathbf{P}_a\mathbf{v} = \tfrac{1}{2}\mathbf{p}^T\mathbf{P}_a\mathbf{M}^{-1}\mathbf{P}_a^T\mathbf{p} \tag{65}$$

and in local parametrization

$$T_c = \tfrac{1}{2}\mathbf{u}_c^T(\mathbf{A}\mathbf{M}^{-1}\mathbf{A}^T)^{-1}\mathbf{u}_c = \tfrac{1}{2}\boldsymbol{\eta}_c^T(\mathbf{A}\mathbf{M}^{-1}\mathbf{A}^T)\boldsymbol{\eta}_c \tag{66}$$

$$T_a = \tfrac{1}{2}\mathbf{u}_a^T(\mathbf{B}\mathbf{M}^{-1}\mathbf{B}^T)^{-1}\mathbf{u}_a = \tfrac{1}{2}\boldsymbol{\eta}_a^T(\mathbf{B}\mathbf{M}^{-1}\mathbf{B}^T)\boldsymbol{\eta}_a \tag{67}$$

This represents a complete decoupling of the kinetic energy. T_c is the kinetic energy contained in the SCM, and T_a is the kinetic energy associated with the SAM only.

6 Generalized Forces

A detailed partitioning of the resultant generalized force vector in Eq. (3) can be given as

$$\sum \vec{F} = \vec{F}_I + \vec{F}_A + \vec{F}_N + \vec{F}_R \tag{68}$$

where $\vec{F}_I$ represents the generalized inertial force vector, $\vec{F}_A$ is the generalized impressed force vector, $\vec{F}_N$ is the generalized nonideal force vector, and $\vec{F}_R$ gives the generalized constraint force vector. Both the generalized constraint and nonideal forces are associated with the specification and realization of constraint conditions in the SCM. However, their nature can be different, as will be discussed in Secs. 6.1 and 6.2. These are also the parts of the generalized forces that can be the subject of certain conditions as a result of constraint specifications in the SCM. As was already mentioned, this kind of partitioning of the forces is one of the fundamental characteristics of Lagrangian dynamics as opposed to the Newton–Euler description. A similar decomposition of constraint-related generalized forces was also described by O'Reilly and Srinivasa [23].

Based on Eq. (4), the partitioning of the generalized forces (68) in global parametrization can be given as

$$\sum \vec{F} \rightarrow \sum \mathbf{f} = \mathbf{f_I} + \mathbf{f_A} + \mathbf{f_N} + \mathbf{f_R} \tag{69}$$

and with respect to the local parametrization it can be written as

$$\sum \vec{F} \rightarrow \sum \mathbf{s} = \mathbf{s_I} + \mathbf{s_A} + \mathbf{s_N} + \mathbf{s_R} \tag{70}$$

Any of the above elements of the generalized forces can be decomposed into two parts: one in the SCM and the other in the SAM.

6.1 Generalized Constraint Forces. The definition of constraint forces in analytical dynamics is usually done for ideal bilateral constraints. Here, we will use a more general interpretation: Generalized constraint forces are embedded in the SCM and developed as a result of specifying certain conditions or restraints on the motion in that subspace. Constraint forces cannot directly influence the SAM. However, they can have indirect effects, for example, if the constraints are realized via nonideal interfaces that lead to the development of nonideal forces that can also depend on the constraint forces. Also, the generalized constraint forces can usually be different for ideal or nonideal realizations of the

[5]For local parametrizations, in the following, we will assume that such a selection of **A** is already done. For singular transformations this can be achieved as $\mathbf{A}=\mathbf{\Gamma}\mathbf{G}$.

same constraint specifications (examples are shown in Ref. [18]).

In local parametrization the generalized constraint forces can be given as

$$\mathbf{s_R} = \begin{bmatrix} \mathbf{s}_{\mathbf{R}_c} \\ \mathbf{s}_{\mathbf{R}_a} \end{bmatrix} = \begin{bmatrix} \boldsymbol{\lambda} \\ \mathbf{0} \end{bmatrix} \tag{71}$$

and

$$\mathbf{f_R} = \mathbf{f}_{\mathbf{R}_c} \tag{72}$$

where

$$\mathbf{A}^T\boldsymbol{\lambda} = \mathbf{f}_{\mathbf{R}_c} = \mathbf{P}_c^T\mathbf{f_R} \tag{73}$$

To simplify the notation, $\boldsymbol{\lambda}$ is used in place of $\mathbf{s}_{\mathbf{R}_c}$ to represent the local components of the generalized constraint forces in the SCM. Due to the physical nature of the constraint forces, $\mathbf{s}_{\mathbf{R}_a}=\mathbf{0}$ and $\mathbf{P}_a^T\mathbf{f_R}=\mathbf{f}_{\mathbf{R}_a}=\mathbf{0}$. In the analysis of systems subject to bilateral constraints, the elements of $\boldsymbol{\lambda}$ can correspond to the Lagrangian multipliers.

6.2 Generalized Nonideal Forces. In the case of nonideal realization of constraints, a special type of forces can arise. We will term these *generalized nonideal forces*. They enter only due to the realization of constraints. This is an important difference between such nonideal forces and the constraint forces discussed in Sec. 6.1. Generalized constraint forces are developed purely to satisfy specifications imposed on the motion in the SCM. On the other hand, generalized nonideal forces can arise due to the way how the constraint specifications (given for the SCM) are realized for the physical system. We can consider, for example, an ordinary particle moving on a surface. The constraint specification here is that no motion exists normal to the surface. The force component necessary to satisfy this specification is the normal force acting on the particle. This is the constraint force for that case. It is there, no matter how the constraint is physically realized. On the other hand, due to the nature of the physical realization of the constraint (e.g., the material properties of the surface), a tangential force component can also arise. This represents the nonideal force. If the surface is rough, then its value is different from zero; if the surface is smooth, then this tangential force vanishes.

Generalized nonideal forces can also depend on the generalized constraint forces (e.g., nonideal contacts with kinetic friction). They can have components in both the spaces of constrained and admissible motions (examples are detailed in Ref. [18]). In the dynamics literature, such nonideal forces are also often classified merely as components of the generalized constraint forces. However, this is not really the case as was pointed out in Refs. [1,24,15], and also explained here, for example. Such forces can have actually more the nature of impressed forces (e.g., kinetic friction). Thus, if we want to be precise then these could also be classified as impressed forces.

These nonideal forces are normally specified by force laws as functions of the constraint forces, the state of motion, and possibly time as

$$\mathbf{f_N} = \mathbf{f_N}(\boldsymbol{\lambda}, \mathbf{v}, \mathbf{q}, t) \quad \text{or} \quad \mathbf{f_N} = \mathbf{f_N}(\mathbf{f_R}, \mathbf{v}, \mathbf{q}, t) \tag{74}$$

The components in the subspaces can be determined in terms of global parametrization as

$$\mathbf{f}_{\mathbf{N}_c} = \mathbf{P}_c^T\mathbf{f_N} \quad \mathbf{f}_{\mathbf{N}_a} = \mathbf{P}_a^T\mathbf{f_N} \tag{75}$$

or in local parametrization as

$$\mathbf{s}_{\mathbf{N}_c} = \boldsymbol{\Lambda} = (\mathbf{A}\mathbf{M}^{-1}\mathbf{A}^T)^{-1}\mathbf{A}\mathbf{M}^{-1}\mathbf{f_N} \tag{76}$$

and

$$\mathbf{s}_{\mathbf{N}_a} = \boldsymbol{\beta} = (\mathbf{B}\mathbf{M}^{-1}\mathbf{B}^T)^{-1}\mathbf{B}\mathbf{M}^{-1}\mathbf{f_N} \tag{77}$$

where $\boldsymbol{\Lambda}$ and $\boldsymbol{\beta}$ are introduced to simplify the notation for the local components in the subspaces.

7 Dynamics Formulation: Constrained and Admissible Motions

7.1 Global Parametrization. Based on Eqs. (4) and (69), the dynamic equilibrium of the generalized free-body diagram of the system can be represented as

$$\sum \mathbf{f} = \mathbf{f_I} + \mathbf{f_A} + \mathbf{f_N} + \mathbf{f_R} = \mathbf{0} \tag{78}$$

Then, via the decomposition of this equation to the SCM and SAM, based on Eqs. (45) and (46), the dynamic equilibrium can be obtained for constrained motion as

$$\mathbf{P}_c^T(\mathbf{f_I} + \mathbf{f_A} + \mathbf{f_N} + \mathbf{f_R}) = \mathbf{0} \tag{79}$$

and for admissible motion as

$$\mathbf{P}_a^T(\mathbf{f_I} + \mathbf{f_A} + \mathbf{f_N} + \mathbf{f_R}) = \mathbf{0} \tag{80}$$

These equations represent the dynamic equilibrium of the system for one particular point in time regardless of what the specifications are on the motion.

Considering the expression of the generalized inertial forces given in Sec. 3 and Eq. (12), the partitioning of the generalized forces in Sec. 6, and the properties of the projectors in Sec. 4, the above equations can be expanded. The *dynamic equations for constrained motion in global parametrization* can be written as

$$-\mathbf{G}^T\hat{\mathbf{P}}_c\mathbf{G}\dot{\mathbf{v}} - \mathbf{P}_c^T\mathbf{c} + \mathbf{P}_c^T\mathbf{f_A} + \mathbf{P}_c^T\mathbf{f_N} + \mathbf{f_R} = \mathbf{0} \tag{81}$$

and the *dynamic equations for admissible motion in global parametrization* can be given as

$$-\mathbf{M}\dot{\mathbf{v}} + \mathbf{G}^T\hat{\mathbf{P}}_c\mathbf{G}\dot{\mathbf{v}} - \mathbf{P}_a^T\mathbf{c} + \mathbf{P}_a^T\mathbf{f_A} + \mathbf{P}_a^T\mathbf{f_N} = \mathbf{0} \tag{82}$$

These can be seen as a general form of dynamic equations for constrained and admissible motions.

The term $\mathbf{G}^T\hat{\mathbf{P}}_c\mathbf{G}\dot{\mathbf{v}}$ is an element in both equations. In the general case, this term can be expanded as

$$\mathbf{G}^T\hat{\mathbf{P}}_c\mathbf{G}\dot{\mathbf{v}} = \mathbf{G}^T\boldsymbol{\Gamma}^T(\boldsymbol{\Gamma}\boldsymbol{\Gamma}^T)^{-1}\boldsymbol{\Gamma}\mathbf{G}\dot{\mathbf{v}} \tag{83}$$

We also note that $\mathbf{A}\dot{\mathbf{v}}+\dot{\mathbf{A}}\mathbf{v}=\dot{\mathbf{u}}_c$. If $\boldsymbol{\Gamma}=\mathbf{A}\mathbf{G}^{-1}$ is used then the expression in Eq. (83) reduces to

$$\mathbf{G}^T\hat{\mathbf{P}}_c\mathbf{G}\dot{\mathbf{v}} = \mathbf{A}^T(\mathbf{A}\mathbf{M}^{-1}\mathbf{A}^T)^{-1}\mathbf{A}\dot{\mathbf{v}} = \mathbf{A}^T(\mathbf{A}\mathbf{M}^{-1}\mathbf{A}^T)^{-1}(\dot{\mathbf{u}}_c - \dot{\mathbf{A}}\mathbf{v}) \tag{84}$$

If the projector operator for the physical components $\hat{\mathbf{P}}_c$ is expressed using the pseudo-inverse as $\hat{\mathbf{P}}_c=(\mathbf{A}\mathbf{G}^{-1})^{\dagger}\mathbf{A}\mathbf{G}^{-1}$ then

$$\mathbf{G}^T\hat{\mathbf{P}}_c\mathbf{G}\dot{\mathbf{v}} = \mathbf{G}^T(\mathbf{A}\mathbf{G}^{-1})^{\dagger}\mathbf{A}\dot{\mathbf{v}} = \mathbf{G}^T(\mathbf{A}\mathbf{G}^{-1})^{\dagger}(\dot{\mathbf{u}}_c - \dot{\mathbf{A}}\mathbf{v}) \tag{85}$$

Depending on the way how $\boldsymbol{\Gamma}$ is selected other simplified expressions can also be possible for $\mathbf{G}^T\hat{\mathbf{P}}_c\mathbf{G}$. If $\boldsymbol{\Gamma}$ is determined based on purely numerical procedures then simplified expressions may not be possible. These above expressions hold for both singular and nonsingular cases of the specification of the transformation to the SCM.

7.2 Local Parametrization. Using Eqs. (4) and (70), the dynamic equilibrium of the generalized free-body diagram of the system can be written in local parametrization as

$$\mathbf{s_I} + \mathbf{s_A} + \mathbf{s_N} + \mathbf{s_R} = \mathbf{0} \tag{86}$$

where considering orthogonal subspaces

$$\mathbf{s}_I = -\mathbf{W}\dot{\mathbf{u}} - \mathbf{z} = -\mathbf{W}\mathbf{a}_u = -\underbrace{\begin{bmatrix} (\mathbf{A}\mathbf{M}^{-1}\mathbf{A}^T)^{-1} & 0 \\ 0 & (\mathbf{B}\mathbf{M}^{-1}\mathbf{B}^T)^{-1} \end{bmatrix}}_{\mathbf{W}}\underbrace{\begin{bmatrix} \dot{\mathbf{u}}_c \\ \dot{\mathbf{u}}_a \end{bmatrix}}_{\dot{\mathbf{u}}} - \underbrace{\begin{bmatrix} \mathbf{z}_c \\ \mathbf{z}_a \end{bmatrix}}_{\mathbf{z}} \tag{87}$$

and using Eq. (15)

$$\mathbf{z}_c = (\mathbf{A}\mathbf{M}^{-1}\mathbf{A}^T)^{-1}\mathbf{A}\mathbf{M}^{-1}\mathbf{c} - (\mathbf{A}\mathbf{M}^{-1}\mathbf{A}^T)^{-1}\dot{\mathbf{A}}\mathbf{v}$$
$$= (\mathbf{A}\mathbf{M}^{-1}\mathbf{A}^T)^{-1}\left(\mathbf{A}\mathbf{M}^{-1}\mathbf{c} - \dot{\mathbf{A}}\mathbf{R}^{-1}\mathbf{u}\right) \quad (88)$$

$$\mathbf{z}_a = (\mathbf{B}\mathbf{M}^{-1}\mathbf{B}^T)^{-1}\mathbf{B}\mathbf{M}^{-1}\mathbf{c} - (\mathbf{B}\mathbf{M}^{-1}\mathbf{B}^T)^{-1}\dot{\mathbf{B}}\mathbf{v}$$
$$= (\mathbf{B}\mathbf{M}^{-1}\mathbf{B}^T)^{-1}\left(\mathbf{B}\mathbf{M}^{-1}\mathbf{c} - \dot{\mathbf{B}}\mathbf{R}^{-1}\mathbf{u}\right) \quad (89)$$

Then, based on Eqs. (59) and (60) and the partitioning of the generalized forces in Sec. 6, we obtain the *dynamic equations of constrained motion in terms of local parametrization* as

$$-(\mathbf{A}\mathbf{M}^{-1}\mathbf{A}^T)^{-1}\dot{\mathbf{u}}_c - \mathbf{z}_c + (\mathbf{A}\mathbf{M}^{-1}\mathbf{A}^T)^{-1}\mathbf{A}\mathbf{M}^{-1}\mathbf{f}_\mathbf{A} + \boldsymbol{\Lambda} + \boldsymbol{\lambda} = \mathbf{0} \quad (90)$$

and the *dynamic equations of admissible motion in terms of local parametrization* as

$$-(\mathbf{B}\mathbf{M}^{-1}\mathbf{B}^T)^{-1}\dot{\mathbf{u}}_a - \mathbf{z}_a + (\mathbf{B}\mathbf{M}^{-1}\mathbf{B}^T)^{-1}\mathbf{B}\mathbf{M}^{-1}\mathbf{f}_\mathbf{A} + \boldsymbol{\beta} = \mathbf{0} \quad (91)$$

Equations (90) and (91) can also be called the minimum form of the dynamic equations, where the SAM is defined to be orthogonal to the SCM based on the mass metric. The generalized forces are decomposed and expressed in terms of the local, minimum parametrization of the two subspaces.

We have derived dynamics equations for both constrained and admissible motions in two parametrizations. These equations hold for the general case of a mechanical system. These can also be used in a mixed way in any of the following four possible combinations:

- Global parametrization is used for both constrained and admissible motions.
- Local parametrization is used for both constrained and admissible motions.
- Local parametrization is used for constrained motion and the global one for admissible motion.
- Global parametrization is used for constrained motion and local for admissible motion.

8 Examples

Let us consider here two examples to illustrate some of the potential of the material. The first one is a relatively simple but nontrivial example that makes it possible to establish the formulation in closed form. The second one involves a more complex engineering system, where some experimental results are used for demonstration.

8.1 Generalized Particle. This example is illustrated in Fig. 3. This is a modified version of the example of the ordinary particle [12]. The system is modeled using a generalized particle. It exhibits different inertia for motions in various directions: m_1 in the x_0 and m_2 in the y_0 directions, respectively. This generalized particle represents a more complex physically meaningful system. For example, this can be the task space model for a planar robotic arm having two prismatic joints where the joint axes are orthogonal to each other in the plane of motion [25]. The x_0y_0 coordinate system represents an inertial frame, and the block is stationary in this frame.

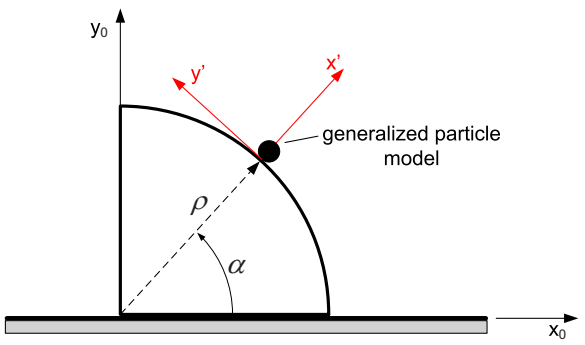

Fig. 3 A generalized particle on a circular block

The generalized coordinates of this system can be given as $\mathbf{q} = [x\ y]^T$, where these coordinates measure the location of the generalized particle relative to the origin of the x_0y_0 frame. The global parametrization of the tangent space can be represented with generalized velocities $\mathbf{v} = \dot{\mathbf{q}} = [\dot{x}\ \dot{y}]^T$.

The possible constraint we would like to characterize is related to the motion of the generalized particle on the surface of the block. To develop the dynamics associated with the generalized free-body diagram, the necessary transformation equations to define constrained and admissible motions can also be introduced at the coordinate level for this problem. This means that it is essentially possible to decompose the whole non-Euclidean configuration space to constrained and admissible configuration spaces. This configuration-level transformation can be given as

$$\sqrt{x^2 + y^2} = \varrho = d_c \quad (92)$$

where $d_c = \varrho$ gives a local parametrization of the constrained configuration space; and the local parametrization for the SCM can be given as $\mathbf{u}_c = \dot{d}_c = \dot{\varrho}$, which is a scalar quantity in this case. The SCM is a one-dimensional subspace.

Then the velocity and acceleration level transformations representing the relaxed constraints can be written as

$$\frac{x\dot{x} + y\dot{y}}{\sqrt{x^2 + y^2}} = \dot{\varrho} = u_c \quad (93)$$

$$\frac{x\ddot{x} + \dot{x}^2 + y\ddot{y} + \dot{y}^2}{\sqrt{x^2 + y^2}} - \frac{[x\dot{x} + y\dot{y}]^2}{[x^2 + y^2]^{\frac{3}{2}}} = \ddot{\varrho} = \dot{u}_c \quad (94)$$

and factoring out the transformation matrix we obtain

$$\begin{bmatrix} \frac{x}{\sqrt{x^2+y^2}} & \frac{y}{\sqrt{x^2+y^2}} \end{bmatrix}\begin{bmatrix} \dot{x} \\ \dot{y} \end{bmatrix} = \dot{\varrho} \quad \rightarrow$$
$$\rightarrow \quad \mathbf{A}\mathbf{v} = u_c \quad \mathbf{A} = \begin{bmatrix} \frac{x}{\sqrt{x^2+y^2}} & \frac{y}{\sqrt{x^2+y^2}} \end{bmatrix} \quad (95)$$

and

$$\mathbf{A}\dot{\mathbf{v}} + \underbrace{\left[\frac{\dot{x}^2 + \dot{y}^2}{\sqrt{x^2+y^2}} - \frac{[x\dot{x} + y\dot{y}]^2}{[x^2+y^2]^{\frac{3}{2}}}\right]}_{\dot{\mathbf{A}}\mathbf{v}} = \dot{u}_c \quad (96)$$

The elements of the generalized inertial and impressed forces in the global parametrization can be expressed as

$$\mathbf{f}_\mathbf{I} = -\mathbf{M}\dot{\mathbf{v}} - \mathbf{c} = -\begin{bmatrix} m_1 & 0 \\ 0 & m_2 \end{bmatrix}\begin{bmatrix} \ddot{x} \\ \ddot{y} \end{bmatrix} - \begin{bmatrix} 0 \\ 0 \end{bmatrix} \quad (97)$$

$$\mathbf{f}_\mathbf{A} = \begin{bmatrix} F_x \\ F_y \end{bmatrix} \quad (98)$$

where F_x and F_y are given applied forces acting on the generalized particle. For the components of the generalized constraint forces we can have

$$\mathbf{f}_\mathbf{R} = \begin{bmatrix} f_{R_1} \\ f_{R_2} \end{bmatrix} = \mathbf{A}^T\boldsymbol{\lambda} \quad (99)$$

and the nonideal forces (if they are present) need to be specified in the form

$$\mathbf{f}_\mathbf{N} = \mathbf{f}_\mathbf{N}(\boldsymbol{\lambda}, \mathbf{v}, \mathbf{q}, t) = \begin{bmatrix} f_{N_1} \\ f_{N_2} \end{bmatrix} \quad (100)$$

where $\boldsymbol{\lambda}$ in this example reduces to a single scalar λ.

Let us consider now the dynamics decomposition described in this work to establish the dynamic equations associated with admissible and constrained motions. The decomposition of the mass matrix $\mathbf{M}$ can be established as

$$\mathbf{M} = \mathbf{G}^T\mathbf{G}, \quad \mathbf{G} = \begin{bmatrix} \sqrt{m_1} & 0 \\ 0 & \sqrt{m_2} \end{bmatrix} \tag{101}$$

Since, in this example, we deal with one independent constraint the projector operators can be evaluated according to Eqs. (50)–(53) as

$$\mathbf{P}_c = \mathbf{M}^{-1}\mathbf{A}^T(\mathbf{A}\mathbf{M}^{-1}\mathbf{A}^T)^{-1}\mathbf{A} = \begin{bmatrix} \dfrac{m_2x^2}{m_2x^2+m_1y^2} & \dfrac{m_2xy}{m_2x^2+m_1y^2} \\ \dfrac{m_1xy}{m_2x^2+m_1y^2} & \dfrac{m_1y^2}{m_2x^2+m_1y^2} \end{bmatrix} \tag{102}$$

$$\mathbf{P}_a = \begin{bmatrix} 1 & 0 \\ 0 & 1 \end{bmatrix} - \begin{bmatrix} \dfrac{m_2x^2}{m_2x^2+m_1y^2} & \dfrac{m_2xy}{m_2x^2+m_1y^2} \\ \dfrac{m_1xy}{m_2x^2+m_1y^2} & \dfrac{m_1y^2}{m_2x^2+m_1y^2} \end{bmatrix} = \begin{bmatrix} \dfrac{m_1y^2}{m_2x^2+m_1y^2} & -\dfrac{m_2xy}{m_2x^2+m_1y^2} \\ -\dfrac{m_1xy}{m_2x^2+m_1y^2} & \dfrac{m_2x^2}{m_2x^2+m_1y^2} \end{bmatrix} \tag{103}$$

which are asymmetric (as we already discussed in Sec. 4.1). This also shows the reason why we called this example a simple but nontrivial one. Had we considered an ordinary particle model with $m_1=m_2$, then the projectors would have been symmetric. However, as we can see, for a more complex system these matrices are generally asymmetric.

Based on the above and Eq. (81) the dynamic equations of constrained motion can be obtained in terms of global parametrization as

$$-\begin{bmatrix} \dfrac{m_1m_2x\sqrt{x^2+y^2}}{m_2x^2+m_1y^2} \\ \dfrac{m_1m_2y\sqrt{x^2+y^2}}{m_2x^2+m_1y^2} \end{bmatrix}\left[\ddot{Q} - \left(\frac{\dot{x}^2+\dot{y}^2}{\sqrt{x^2+y^2}} - \frac{[x\dot{x}+y\dot{y}]^2}{[x^2+y^2]^{\frac{3}{2}}}\right)\right] + \begin{bmatrix} \dfrac{F_xm_2x^2+F_ym_1xy}{m_2x^2+m_1y^2} \\ \dfrac{F_xm_2xy+F_ym_1y^2}{m_2x^2+m_1y^2} \end{bmatrix} + \begin{bmatrix} \dfrac{f_{N_1}m_2x^2+f_{N_2}m_1xy}{m_2x^2+m_1y^2} \\ \dfrac{f_{N_1}m_2xy+f_{N_2}m_1y^2}{m_2x^2+m_1y^2} \end{bmatrix} + \begin{bmatrix} f_{R_1} \\ f_{R_2} \end{bmatrix} = \begin{bmatrix} 0 \\ 0 \end{bmatrix} \tag{104}$$

According to Eq. (82) the dynamic equations of admissible motion for this system can be written in terms of global parametrization as

$$-\begin{bmatrix} m_1 & 0 \\ 0 & m_2 \end{bmatrix}\begin{bmatrix} \ddot{x} \\ \ddot{y} \end{bmatrix} + \begin{bmatrix} \dfrac{m_1m_2x\sqrt{x^2+y^2}}{m_2x^2+m_1y^2} \\ \dfrac{m_1m_2y\sqrt{x^2+y^2}}{m_2x^2+m_1y^2} \end{bmatrix} \times \left[\ddot{Q} - \left(\frac{\dot{x}^2+\dot{y}^2}{\sqrt{x^2+y^2}} - \frac{[x\dot{x}+y\dot{y}]^2}{[x^2+y^2]^{\frac{3}{2}}}\right)\right] + \begin{bmatrix} \dfrac{F_xm_1y^2-F_ym_1xy}{m_2x^2+m_1y^2} \\ \dfrac{-F_xm_2xy+F_ym_2x^2}{m_2x^2+m_1y^2} \end{bmatrix} + \begin{bmatrix} \dfrac{f_{N_1}m_1y^2-f_{N_2}m_1xy}{m_2x^2+m_1y^2} \\ \dfrac{-f_{N_1}m_2xy+f_{N_2}m_2x^2}{m_2x^2+m_1y^2} \end{bmatrix} = \begin{bmatrix} 0 \\ 0 \end{bmatrix} \tag{105}$$

We already have a local parametrization for the SCM based on $u_c=\dot{Q}$. The dimension of the SAM in this example is also one. In order to introduce a local parametrization for the SAM, in a way that decoupling is achieved, a 1×2 matrix $\mathbf{B}=[B_1B_2]$ has to be selected, which satisfies Eq. (56). Based on that equation we can derive the following conditions for the elements of matrix $\mathbf{B}$:

$$\frac{B_1}{B_2} = -\frac{m_1y}{m_2x} \tag{106}$$

Therefore, the following selection:

$$\mathbf{B} = \begin{bmatrix} -\dfrac{m_1y}{m_2x} & 1 \end{bmatrix} \tag{107}$$

satisfies Eq. (56), and the generalized velocity for the local parametrization of the SAM can be determined as

$$u_a = \mathbf{B}\mathbf{v} = -\frac{m_1y}{m_2x}\dot{x} + \dot{y} \tag{108}$$

which is a nonholonomic quantity. It has a singularity at $x=0$. The potential problems associated with this can be avoided by redefining u_a and $\mathbf{B}$ in the neighborhood of $x=0$. For example, based on Eq. (106) the selection $\mathbf{B}=[1 \quad -(m_2x)/(m_1y)]$ is also possible, which results in an alternative $u_a=\dot{x}-\dot{y}(m_2x)/(m_1y)$ parametrization for the SAM, which is appropriate for the vicinity of $x=0$. In the following, here we will develop the details only for the case represented by Eqs. (107) and (108). The expressions for any other selection for the local parametrization can be developed in a similar way.

With the selection of $\mathbf{B}$, transformation matrix $\mathbf{R}$ in Eq. (5) between the two parametrizations of the tangent space is fully specified and can be written as

$$\mathbf{R} = \begin{bmatrix} \mathbf{A} \\ \mathbf{B} \end{bmatrix} = \begin{bmatrix} \dfrac{x}{\sqrt{x^2+y^2}} & \dfrac{y}{\sqrt{x^2+y^2}} \\ -\dfrac{m_1y}{m_2x} & 1 \end{bmatrix} \tag{109}$$

Its inverse and time derivative can also be determined as

$$\mathbf{R}^{-1} = \begin{bmatrix} \dfrac{m_2x\sqrt{x^2+y^2}}{m_2x^2+m_1y^2} & -\dfrac{m_2xy}{m_2x^2+m_1y^2} \\ \dfrac{m_1y\sqrt{x^2+y^2}}{m_2x^2+m_1y^2} & \dfrac{m_2x^2}{m_2x^2+m_1y^2} \end{bmatrix} \tag{110}$$

and

$$\dot{\mathbf{R}} = \begin{bmatrix} \dot{\mathbf{A}} \\ \dot{\mathbf{B}} \end{bmatrix} = \begin{bmatrix} \dfrac{\dot{x}}{\sqrt{x^2+y^2}} - \dfrac{x(x\dot{x}+y\dot{y})}{(x^2+y^2)^{3/2}} & \dfrac{\dot{y}}{\sqrt{x^2+y^2}} - \dfrac{y(x\dot{x}+y\dot{y})}{(x^2+y^2)^{3/2}} \\ -\dfrac{m_1}{m_2}\left(\dfrac{\dot{y}}{x} - \dfrac{y\dot{x}}{x^2}\right) & 0 \end{bmatrix} \tag{111}$$

Using $\mathbf{R}^{-1}$ the original parametrization $\mathbf{v}$ can be expressed in terms of the new local parametrization of $\mathbf{u}=[\dot{\varrho}\ u_a]^T$ as

$$\mathbf{v} = \begin{bmatrix} \dot{x} \\ \dot{y} \end{bmatrix} = \mathbf{R}^{-1}\mathbf{u} = \begin{bmatrix} \dfrac{m_2 x\sqrt{x^2+y^2}}{m_2x^2+m_1y^2}\dot{\varrho} - \dfrac{m_2xy}{m_2x^2+m_1y^2}u_a \\ \dfrac{m_1 y\sqrt{x^2+y^2}}{m_2x^2+m_1y^2}\dot{\varrho} + \dfrac{m_2x^2}{m_2x^2+m_1y^2}u_a \end{bmatrix} \tag{112}$$

Based on the expressions of $\mathbf{A}$ and $\mathbf{B}$

$$(\mathbf{A}\mathbf{M}^{-1}\mathbf{A}^T)^{-1}\mathbf{A}\mathbf{M}^{-1} = \begin{bmatrix} \dfrac{m_2x\sqrt{x^2+y^2}}{m_2x^2+m_1y^2} & \dfrac{m_1y\sqrt{x^2+y^2}}{m_2x^2+m_1y^2} \end{bmatrix} \tag{113}$$

and

$$(\mathbf{B}\mathbf{M}^{-1}\mathbf{B}^T)^{-1}\mathbf{B}\mathbf{M}^{-1} = \begin{bmatrix} -\dfrac{m_2xy}{m_2x^2+m_1y^2} & \dfrac{m_2x^2}{m_2x^2+m_1y^2} \end{bmatrix} \tag{114}$$

Using these and Eqs. (90) and (91) the dynamic equation of constrained motion in terms the local parametrization can be written as

$$-\left[\frac{m_1m_2(x^2+y^2)}{m_2x^2+m_1y^2}\right]\ddot{\varrho} + \left[\frac{m_1m_2(x^2+y^2)}{m_2x^2+m_1y^2}\left(\frac{\dot{x}^2+\dot{y}^2}{\sqrt{x^2+y^2}} - \frac{(x\dot{x}+y\dot{y})^2}{(x^2+y^2)^{\frac{3}{2}}}\right)\right] + \left[\frac{(m_2xF_x+m_1yF_y)\sqrt{x^2+y^2}}{m_2x^2+m_1y^2}\right] + \left[\frac{(m_2xf_{N_1}+m_1yf_{N_2})\sqrt{x^2+y^2}}{m_2x^2+m_1y^2}\right] + \lambda = 0 \tag{115}$$

and the dynamic equation of admissible motion in terms of the local parametrization can be obtained as

$$-\frac{m_2^2x^2}{m_2x^2+m_1y^2}\dot{u}_a - \frac{m_1m_2x^2}{m_2x^2+m_1y^2}\left(\frac{\dot{y}\dot{x}}{x} - \frac{y\dot{x}^2}{x^2}\right) + \frac{m_2x^2F_y - m_2xyF_x}{m_2x^2+m_1y^2} + \frac{m_2x^2f_{N_2} - m_2xyf_{N_1}}{m_2x^2+m_1y^2} = 0 \tag{116}$$

which can also be further simplified by multiplying it with $m_2x^2+m_1y^2$ and also by dividing it with m_2. In these equations, Eqs. (115) and (116), the generalized forces are decomposed with respect to the local base vectors of the two subspaces. However, in the detailed expansion of the formulas, elements of $\mathbf{v}$ still enter. These can be eliminated by using Eq. (112). On the other hand, since we generally deal with nonholonomic velocities, the original (global) generalized coordinates remain.

8.2 Dual-Pantograph Device. The second example includes a recently developed experimental system shown in Fig. 4. This is a six degree-of-freedom dual-pantograph mechanism.[6] It is a fully instrumented open-architecture system that uses the WINCON real-time control software with MATLAB/SIMULINK interface.

The global parametrization for the tangent space of this system can be defined with the time rates of six actuated joint angles. These joints are all instrumented. Therefore, the global parametrization here is based on directly measurable quantities. The dynamics formulation described in this paper has been implemented

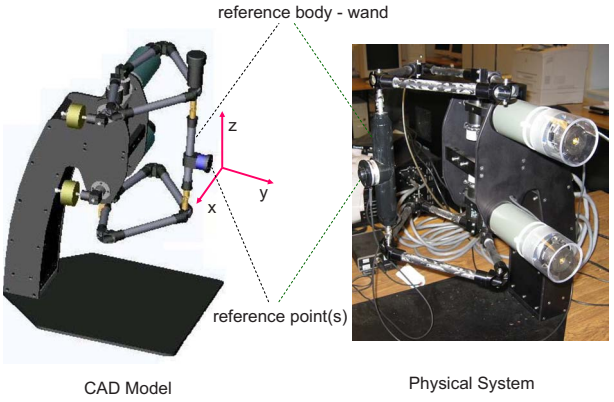

Fig. 4 Dual-pantograph device

on this experimental system in real-time using the global parametrization. We are able to compute and interpret everything online, which can also open up the possibility to explore the potential of the approach for control and design applications.

The reference body of this system can also be called a *wand*. The definition of the SCM and the related local parametrization here will be given associated with the motion of one or two reference points of the wand. We will consider a relatively simple motion of the system. The point at the center of the wand follows a circular trajectory in the xy plane, as shown in Fig. 5, with a constant speed. At the same time the wand rotates about one of its principal axes of inertia that is parallel to axis z and goes through the center point (Fig. 4).

We will investigate the system for each point of this trajectory for the possibility of imposing constraints on the motion of (1) one and (2) two points of the wand along the y direction. The approximate location of these reference points is shown in Fig. 4. For both cases, the points are in the xy plane. For the second case the two points are separated from each other by 25.4 mm (1 in). In Case (1) the SCM has one dimension, and in Case (2) it is a two-dimensional subspace. Defining the SCM with these specifications, and based on that, establishing the dynamics formulation of the generalized free-body diagram for the device can provide insight for several practical situations. For example, this can give useful information on what can be expected if the motion of the given reference point(s) of the wand are suddenly restrained by some bilateral or unilateral contacts along the y direction. The kinetic energy decoupling described in Sec. 5 can provide an important tool for this. The kinetic energy contents of the two subspaces can be representative to characterize what would happen if

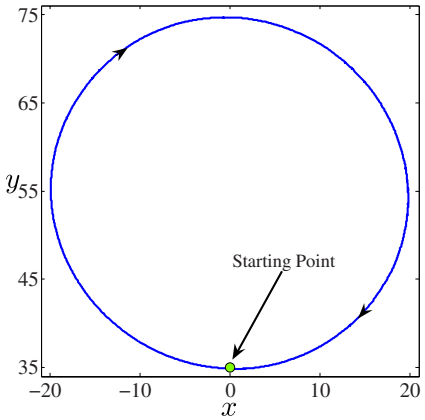

Fig. 5 Trajectory of the center point of the wand (units are in mm)

[6]This experimental test-bed was built by QUANSER.

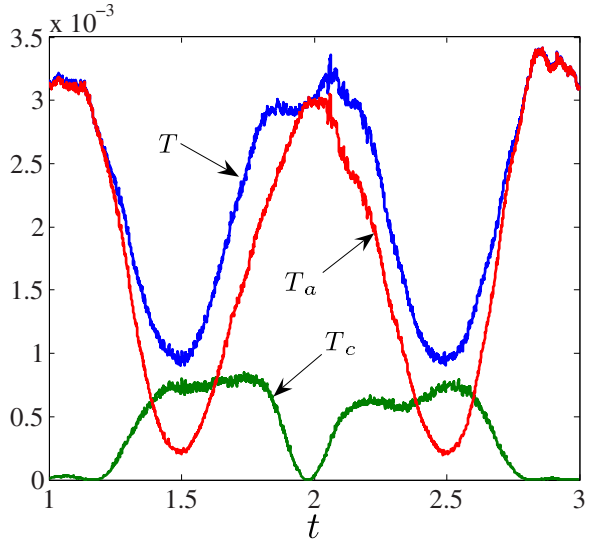

Fig. 6 Kinetic energy decomposition for one-dimensional SCM based on experimental data (units: time in s and energy in J)

constraints were imposed on the SCM. The results for the kinetic energy decomposition for the two cases are shown in Figs. 6 and 7, respectively. The starting point of Fig. 5 corresponds to $t=1$ s. These results are obtained based on the online implementation and processing of the dynamics formulation and the measured data for the investigated trajectory.

Depending on the objectives of the investigation several pieces of information can be gained from these results. For example, configurations along the trajectory associated with low kinetic energy content in the SCM (T_c) means that the sudden imposition of restraints on the motion of the representative point(s) along the y direction may be achieved in a relatively smooth way without inducing high constraint-related forces in the system. For the first case when the SCM is one dimensional and it concerns only the motion of one reference point of the wand, the results could probably be also concluded and confirmed based on the intuition of the analyst (e.g., the best situation can be close to when the point has low velocity along the possibly constrained direction, e.g., at configurations where $x=0$ in Fig. 5, and $t=1$ s and 2 s in Fig. 6).

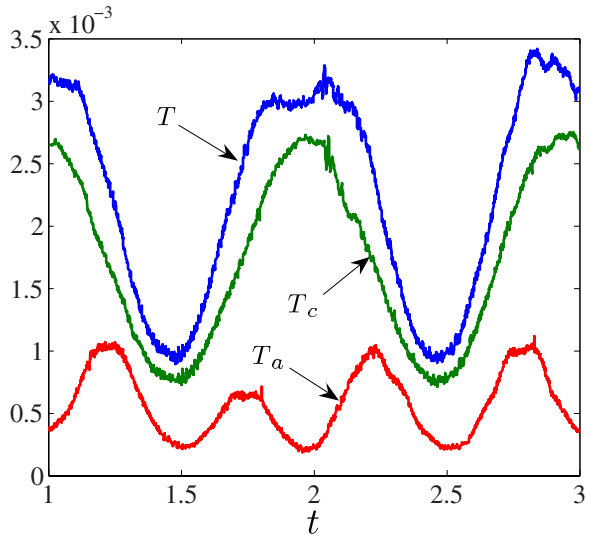

Fig. 7 Kinetic energy decomposition for two-dimensional SCM based on experimental data (units: time in s and energy in J)

However, even for this case, we have to emphasize that the decomposition is done here using a global parametrization, which is based on directly measurable and controllable quantities. For the second case (Fig. 7), when the SCM is two dimensional, the results are far from being that intuitively understandable even for such a simple trajectory. The structure of the SCM is much more complex for that case. It cannot be simply interpreted from the one-dimensional (one point is constrained) case. Imposing constraints on the motion of two points of the wand would also mean restricting its rotation about its principal axis of inertia parallel to z. This can greatly change the overall system behavior.

9 Conclusions

In this paper we generalized the idea of the free-body diagram for use in the analysis of mechanical systems represented in configuration space. The results presented give a direct extension of classical analytical mechanics based on a simple mathematical formulation. They provide a single unified framework that can be used, for example, for the analysis of bilaterally constrained systems with ideal interfaces, nonideal phenomena, redundant constraints, and some aspects of unilateral problems.

A key point is the replacement of the direct consideration of the constraint specifications with a two-level analysis: (1) The first level includes the definition of a transformation that interprets the space of constrained motion (SCM). Based on this, the interpretation of the space of admissible motion (SAM) is possible. This level also includes the full development of dynamic equations for these two subspaces. (2) The specification of conditions on the motion/forces in the SCM. This second step will be further analyzed in Part II of this work [18].

The dynamics formulation associated with the two subspaces have been derived in global and local parametrizations. They hold for the above-mentioned general group of mechanical systems. The constraint dynamics formulation represents a particular new contribution as such equations have not been derived before for the general case. The admissible dynamics equations are also interpreted in a novel way. The parametrization of the SAM is defined in this paper so that the two subspaces are orthogonal to each other. This property enables us to decouple the dynamics, which can be useful in many applications. The formulation derived also fully accounts for the possibly differing physical units of the various quantities.

Acknowledgment

This research was supported by the Natural Sciences and Engineering Research Council of Canada and the Canada Foundation for Innovation. The support is gratefully acknowledged.

Appendix: Holonomic Systems

An important case is when equation $\mathbf{Av}=\mathbf{u}_c$ can be transformed into an integrable form and can be represented by an equivalent nonlinear transformation relationship

$$\mathbf{\Phi}_c(\mathbf{q}) = \mathbf{d}_c \tag{A1}$$

at the configuration level, and $\dot{\mathbf{d}}_c=\mathbf{u}_c$. At the velocity level, from Eq. (A1),

$$\frac{\partial \mathbf{\Phi}_c}{\partial \mathbf{q}}\dot{\mathbf{q}} = \dot{\mathbf{d}}_c = \mathbf{u}_c \tag{A2}$$

and $\mathbf{Av}=\mathbf{u}_c$ can be recovered as

$$\underbrace{\frac{\partial \mathbf{\Phi}_c}{\partial \mathbf{q}}\mathbf{N}^{-1}}_{\mathbf{A}}\mathbf{v} = \dot{\mathbf{d}}_c = \mathbf{u}_c \tag{A3}$$

In this case, in addition to partitioning the tangent space, the nonlinear transformation of Eq. (A1) also defines a generally non-Euclidean subspace of the entire configuration space, which can

be termed the *constrained configuration space*. This is the case of holonomically constrained systems, for example. If $\mathbf{d}_c=0$ then the point representing the system in the configuration space is not part of this constrained subspace.

As for the tangent space via $\mathbf{Av}=\mathbf{u}_c$, transformation (A1) also gives the possibility to interpret the *admissible configuration space* that complements the constrained configuration space to the entire configuration space. An equivalent, configuration-level representation to $\mathbf{Bv}=\mathbf{u}_a$ may also be interpreted as

$$\mathbf{\Phi}_a(\mathbf{q}) = \mathbf{d}_a \tag{A4}$$

References

[1] Papastavridis, J. G., 2002, *Analytical Mechanics*, Oxford University Press, New York.
[2] Hamel, G., 1949, *Theoretische Mechanik*, Springer, Berlin.
[3] Leipholz, H. H. E., 1978, *Six Lectures on Variational Principles in Structural Engineering*, Solid Mechanics Division, University of Waterloo, Waterloo.
[4] Kane, T. R., and Levinson, D. A., 1985, *Dynamics, Theory and Applications*, McGraw-Hill, New York.
[5] Djerassi, S., and Bamberger, H., 2003, "Constraint Forces and the Method of Auxiliary Generalized Speeds," ASME J. Appl. Mech., **70**, pp. 568–574.
[6] Lesser, M., 1992, "A Geometrical Interpretation of Kane's Equations," Proc. R. Soc. London, **436**, pp. 69–87.
[7] Blajer, W., 2004, "On the Determination of Joint Reactions in Multibody Mechanisms," ASME J. Mech. Des., **126**, pp. 341–350.
[8] Synge, J. L., 1927, "On the Geometry of Dynamics," Philos. Trans. R. Soc. London, Ser. A, **226**, pp. 31–106.
[9] Synge, J. L., and Schild, A., 1969, *Tensor Calculus*, University of Toronto, Toronto.
[10] Brauchli, H., 1991, "Mass-Orthogonal Formulation of Equations of Motion for Multibody Systems," Z. Angew. Math. Phys., **42**, pp. 169–182.
[11] Blajer, W., 1997, "A Geometric Unification of Constrained System Dynamics," Multibody Syst. Dyn., **1**, pp. 3–21.
[12] Blajer, W., 2001, "A Geometrical Interpretation and Uniform Matrix Formulation of Multibody System Dynamics," Z. Angew. Math. Mech., **81**(4), pp. 247–259.
[13] Papastavridis, J. G., 1998, *Tensor Calculus and Analytical Dynamics*, CRC, Boca Raton, FL.
[14] Blajer, W., 1992, "A Projection Method Approach to Constrained Dynamic Analysis," ASME J. Appl. Mech., **59**, pp. 643–649.
[15] Glocker, Ch., 2001, *Set-Valued Force Laws: Dynamics of Non-Smooth Systems*, Springer-Verlag, Berlin.
[16] Kövecses, J., Piedbœuf, J.-C., and Lange, C., 2003, "Dynamics Modeling and Simulation of Constrained Robotic Systems," IEEE/ASME Trans. Mechatron., **8**(2), pp. 165–177.
[17] Kövecses, J., and Piedboeuf, J.-C., 2003, "A Novel Approach for the Dynamic Analysis and Simulation of Constrained Mechanical Systems," ASME Paper No. DETC2003-VIB-48318.
[18] Kövecses, J., 2008, "Dynamics of Mechanical Systems and the Generalized Free-Body Diagram, Part II: Imposition of Constraints," ASME J. Appl. Mech., **75**(6), p. 061013.
[19] Béda, Gy., Kozák, I., and Verhás, J., 1989, *Continuum Mechanics*, Academic Press, Budapest.
[20] Truesdell, C., 1953, "The Physical Components of Vectors and Tensors," Z. Angew. Math. Mech., **33**(10/11), pp. 345–356.
[21] Campbell, S. L., and Meyer, C. D., 1979, *Generalized Inverses of Linear Transformations*, Pitman, London.
[22] Golub, G. H., and van Loan, C. F., 1996, *Matrix Computations*, 3rd ed., The Johns Hopkins University Press, Baltimore.
[23] O'Reilly, O. M., and Srinivasa, A. R., 2001, "On a Decomposition of Generalized Constraint Forces," Proc. R. Soc. London, Ser. A, **457**, pp. 1307–1313.
[24] Rosenberg, R. M., 1977, *Analytical Dynamics of Discrete Systems*, Plenum Press, New York.
[25] Chen, K., Beale, D. G., and Wang, D., 2002, "A New Method to Determine the Base Inertial Parameters of Planar Mechanisms," Mech. Mach. Theory, **37**, pp. 971–984.

Dynamics of Mechanical Systems and the Generalized Free-Body Diagram—Part II: Imposition of Constraints

József Kövecses
Department of Mechanical Engineering
and Centre for Intelligent Machines,
McGill University,
817 Sherbrooke St. West,
Montréal, Québec, H3A 2K6, Canada
e-mail: jozsef.kovecses@mcgill.ca

*In this part of the work we present some applications of the formulation developed in Part I (Kövecses, 2008, "Dynamics of Mechanical Systems and the Generalized Free-Body Diagram—Part I: General Formulation," ASME J. Appl. Mech., **75**(6), p. 061012) for the generalized free-body diagram in configuration space. This involves the specification and imposition of constraint conditions, which were identified as Step 2 of the analysis of a mechanical system in Part I. We will particularly consider bilaterally and unilaterally constrained systems, where constraints are realized via ideal or nonideal interfaces. We also look at the general case where the constraint configuration is possibly redundant. The results represent novel forms of dynamics models for mechanical systems, and can offer the possibility to gain more insight for simulation, design, and control.*
[DOI: 10.1115/1.2965373]

Keywords: analytical mechanics, constraints, dynamics formulation, bilateral, unilateral, nonideal, parametrizations

1 Introduction

In this paper, we use the general formulation developed in Part I of this work [1] to study bilaterally or unilaterally constrained systems for the cases of ideal and nonideal realizations of constraints. This essentially includes the consideration of certain conditions given in the space of constrained motion (SCM).

Bilateral ideal constraints play a primary role in analytical mechanics. Fundamental works include, for example, that of Hamel [2], Rosenberg [3], Pars [4], Lure [5], Papastavridis [6], Kane and Levinson [7], and Greenwood [8]. Works of Schiehlen [9], Eberhard and Schiehlen [10], and Shabana [11] gave overviews of the applications of analytical mechanics for multibody systems with special attention to the computational aspects. Recent contributions can be cited from Udwadia and Kabala [12–18] who made significant steps toward extensions of the analytical formulation for systems with redundant constraints and nonideal constraints. Their formulation is derived based on Gauss' principle of least constraint, and the Moore–Penrose generalized inverse (pseudoinverse) plays a pivotal role in the equations. However, the applicability of their approach for systems where the "nonideal constraint force components" depend on the "normal constraint forces" is questionable (e.g., the case of Coulomb friction). This will be discussed later in this paper. Pfeiffer and Glocker [19] also studied the nonideal realization of bilateral constraints and redundant constraint configurations. They reported and summarized important observations regarding the solvability of problems with Coulomb friction.

For the modeling of unilaterally constrained systems and impulsive motion, significant contributions have been reported by Moreau [20], Pfeiffer [21], Pfeiffer and Glocker [19], Glocker [22], and Brogliato [23]. In the derivation of the underlying dynamics models, particularly the work of Pfeiffer and Glocker [19] can be seen as a primary reference. Glocker [22] further developed these concepts for nonsmooth systems and established a framework of force laws for the characterization of discontinuous interactions. We have to note that the problems of unilateral constraints are much more involved than that of bilateral conditions. The complete analysis of unilaterally constrained systems is not the topic of this present work. We address only some aspects of unilaterally constrained motion here. However, our development of various model formulations in this paper may also offer some additional insight into the modeling and analysis of unilateral problems.

For practical applications, it is not always straightforward to decide on what type of model can be the most representative. For example, the same physical system can be modeled in many different ways (e.g., using bilateral or unilateral constraints and ideal or nonideal interfaces) depending on the type of information the analyst needs. The formulations in this paper are derived from a unified framework provided by the generalized free-body diagram and can make it possible to easily switch between models and investigate the suitability of a particular model or parametrization. We will use the example of the generalized particle described in Part I to illustrate the development of the possible models for the same physical system. The terminology and nomenclature defined in Part I will be used in this paper also.

2 Imposition of Constraints

In this case, kinematic specifications are given for the motion in the SCM, i.e., the right-hand side of equation

$$\mathbf{A}\mathbf{v} = \mathbf{u}_c \tag{1}$$

is subject to conditions given either in the form of equalities (bilateral constraints) or inequalities (unilateral constraints). For the case of bilateral constraints no other conditions are necessary. However, for the case of unilateral constraints, kinetic specifications may also be necessary for the generalized constraint forces that are developed.

We have to note that the term "admissible" stems from the terminology of bilaterally constrained systems. For a general system the space of admissible motion (SAM) does not necessarily mean all *possible motions* of the system. As we will see for bilateral constraints, all possible motions are associated with the gen-

Contributed by the Applied Mechanics Division of ASME for publication in the JOURNAL OF APPLIED MECHANICS. Manuscript received November 25, 2007; final manuscript received May 21, 2008; published online August 20, 2008. Review conducted by Martin Ostoja-Starzewski.

eralized directions of the SAM. However, for unilateral constraints the range of possible motions is much broader, and besides the SAM, the SCM can also contain them. The refined geometric description of the tangent space becomes much more involved for unilateral constraints [20,22]. However, the kinematic constraint conditions imposed on the motion concern the SCM only. The formulation developed here is valid since the idea of the generalized free-body diagram and the associated decompositions hold for any of such cases.

For the case of bilateral constraints the dynamic equations of admissible motion are the so-called *equations of motion*.

2.1 Bilateral Constraints. In this case, $\mathbf{u}_c$ is fully specified, which can be represented as

$$\mathbf{u}_c = \mathbf{b} \quad \text{and} \quad \dot{\mathbf{u}}_c = \dot{\mathbf{b}} \tag{2}$$

where $\mathbf{b}$ is a given function. Typical examples are (1) when $\mathbf{b} = \mathbf{0}$ and (2) when $\mathbf{b}$ depends on the time and/or the generalized coordinates.

Such bilateral constraints can be holonomic, nonholonomic, scleronomic, or rheonomic depending on the nature of $\mathbf{b}$ and Eq. (1). Since $\mathbf{u}_c$ is fully given, the variations of generalized velocities in the SCM must be uniformly zero, i.e.,

$$\mathbf{A}\,\delta\mathbf{v} = \delta\mathbf{u}_c = \mathbf{0} \tag{3}$$

2.1.1 Ideal Realization: Ideal Physical Interfaces. The simplest case of the class of bilateral constraints is the group of ideal constraints that is the most studied problem in analytical mechanics. The definition of ideal constraints in analytical mechanics is that the totality of the virtual power (or virtual work) of the generalized constraint forces is equal to zero.

In our framework this corresponds to the case when no nonideal forces are developed as a result of the realization of the constraints, i.e.,

$$\mathbf{f_N} = \mathbf{0}, \quad \boldsymbol{\Lambda} = \mathbf{0}, \quad \boldsymbol{\beta} = \mathbf{0} \tag{4}$$

The components of the constraint forces $\boldsymbol{\lambda}$ and $\mathbf{f_R}$ can assume negative, zero, and positive values (they are free to vary). The vanishing of the totality of the virtual power is made sure by the bilateral specifications for the SCM, which implies Eq. (3).

Then the substitution of Eqs. (2) and (4) into Eqs. (81), (82), (90), and (91) in Part I results in the dynamic equations of constrained and admissible motions.

In *global parametrization*, the dynamic equations of constrained motion can be written as

$$-\mathbf{G}^T\hat{\mathbf{P}}_c\mathbf{G}\dot{\mathbf{v}} - \mathbf{P}_c^T\mathbf{c} + \mathbf{P}_c^T\mathbf{f_A} + \mathbf{f_R} = \mathbf{0} \tag{5}$$

and the dynamic equations of admissible motion are

$$-\mathbf{M}\dot{\mathbf{v}} + \mathbf{G}^T\hat{\mathbf{P}}_c\mathbf{G}\dot{\mathbf{v}} - \mathbf{P}_a^T\mathbf{c} + \mathbf{P}_a^T\mathbf{f_A} = \mathbf{0} \tag{6}$$

where

$$\mathbf{G}^T\hat{\mathbf{P}}_c\mathbf{G}\dot{\mathbf{v}} = \mathbf{A}^T(\mathbf{A}\mathbf{M}^{-1}\mathbf{A}^T)^{-1}\mathbf{A}\dot{\mathbf{v}} = \mathbf{A}^T(\mathbf{A}\mathbf{M}^{-1}\mathbf{A}^T)^{-1}(\dot{\mathbf{b}} - \dot{\mathbf{A}}\mathbf{v}) \tag{7}$$

for nonredundant constraints and, for example,

$$\mathbf{G}^T\hat{\mathbf{P}}_c\mathbf{G}\dot{\mathbf{v}} = \mathbf{G}^T(\mathbf{A}\mathbf{G}^{-1})^{\dagger}\mathbf{A}\dot{\mathbf{v}} = \mathbf{G}^T(\mathbf{A}\mathbf{G}^{-1})^{\dagger}(\dot{\mathbf{b}} - \dot{\mathbf{A}}\mathbf{v}) \tag{8}$$

can be used more generally, which also holds for redundantly constrained systems.

In *local parametrization*, the dynamic equations of constrained motion can be written as

$$-(\mathbf{A}\mathbf{M}^{-1}\mathbf{A}^T)^{-1}\dot{\mathbf{b}} - \mathbf{z}_c + (\mathbf{A}\mathbf{M}^{-1}\mathbf{A}^T)^{-1}\mathbf{A}\mathbf{M}^{-1}\mathbf{f_A} + \boldsymbol{\lambda} = \mathbf{0} \tag{9}$$

and the dynamic equations of admissible motion can be given as

$$-(\mathbf{B}\mathbf{M}^{-1}\mathbf{B}^T)^{-1}\dot{\mathbf{u}}_a - \mathbf{z}_a + (\mathbf{B}\mathbf{M}^{-1}\mathbf{B}^T)^{-1}\mathbf{B}\mathbf{M}^{-1}\mathbf{f_A} = \mathbf{0} \tag{10}$$

For this case, the dynamic equations of constrained motion expressed in either global or local parametrization, Eqs. (5) and (9), simply become a set of equations that can be used for the definition and interpretation of the generalized constraint forces. These generalized forces are necessary to be developed to satisfy the conditions imposed on $\mathbf{u}_c$ and on its time derivative. Generalized constraint force components in $\boldsymbol{\lambda}$ are often actual physical forces developed via contacts. On the other hand, in the global parametrization, generalized constraint forces in $\mathbf{f_R}$ may represent a resultant effect of the physical constraint forces. Therefore, the global parametrization works for both redundantly and nonredundantly constrained systems. The local parametrization can also be defined for both. However, all of the actual physical constraint forces may not be directly determined for redundantly constrained systems because in that case the local, minimum parametrization may not contain all information about the kinetics of the constraints.

For ideal constraints, as we can see based on Eqs. (6) and (10), the admissible dynamics equations can generally be solved independently of the constraint dynamics for either the accelerations (forward dynamics) or for some of the generalized impressed forces (inverse dynamics).

Even for this simplest case of constraints, the above equations contain several novel features. For example, Eq. (10) developed for admissible motion in the local parametrization is new. This is developed based on the orthogonal decomposition described in Part I, and can be useful in several applications to gain insight into the behavior of a system. It can also have application for high fidelity simulation algorithms to avoid constraint violations. Based on the definition of $\mathbf{B}$ in Part I, Eq. (10) can actually also be interpreted for redundantly constrained systems without the introduction of a minimum local parametrization for constrained motion.

Furthermore, for example, if a generalized inverse is used according to Eq. (8), then the dynamic equations of admissible motion in terms of global parametrization (Eq. (6)) can be written as

$$\mathbf{M}\dot{\mathbf{v}} + \mathbf{G}^T(\mathbf{A}\mathbf{G}^{-1})^{\dagger}(\dot{\mathbf{A}}\mathbf{v} - \dot{\mathbf{b}}) + \mathbf{P}_a^T\mathbf{c} - \mathbf{P}_a^T\mathbf{f_A} = \mathbf{0} \tag{11}$$

This, on its own, is a new general form of the equations of admissible motion for ideally constrained systems that can be used for both forward and inverse dynamics investigations. It applies to both redundantly ($\mathbf{A}$ does not have a full row rank) and nonredundantly ($\mathbf{A}$ has a full row rank) constrained systems, where the constraints can be holonomic and/or nonholonomic. As Eq. (11) uses a generalized inverse, it may also be seen as similar to the formulation of Udwadia and Kalaba [12,13]. However, the approach applied here and the form of the equations obtained are different. First, Eq. (11) is presented in the general form of nonholonomic velocity components, and the decomposition of the mass matrix to $\mathbf{M}=\mathbf{G}^T\mathbf{G}$ is not limited to the square-root factorization only. However, these are relatively minor differences. The Udwadia–Kalaba formulation can also be modified to include these. The main difference lies in the way constraint forces are handled. Generalized constraint forces are explicitly determined and *included* in the dynamic equations of Udwadia and Kalaba [12,13]. On the other hand, generalized constraint forces are *eliminated* in our formulation. This is a principal difference, which leads to two different forms to give the equations of motion. Since constraint forces are eliminated via projections, our formulation may also be better suited for the development of numerical integration algorithms, as was illustrated in Refs. [24,25], for example, with some simulation results.

2.1.2 Nonideal Realization. The realization of constraints often involves the application of nonideal contacts or other features, where, as a result of the imposition of the constraints, forces are induced in the SAM as well (e.g., due to friction). In this case, the relations of Eq. (4) do not hold and nonideal forces enter into the formulation. These can depend on the constraint forces and can generally be expressed by equations like Eqs. (74)–(77) of Part I.

A direct analogy can be drawn here with a particle moving on a flat surface where the contact force normal to the surface repre-

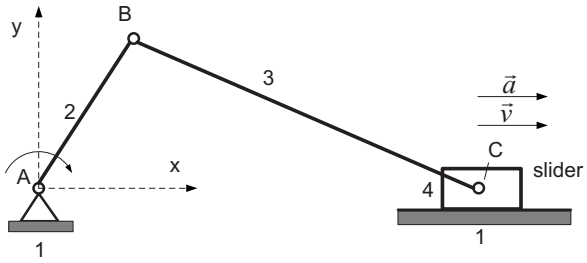

force balances for the free body diagram of the slider

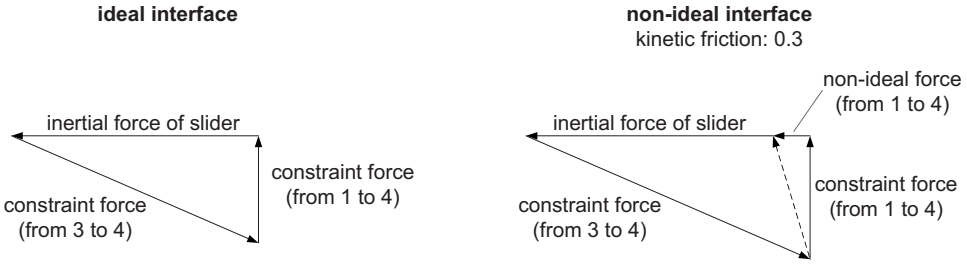

Fig. 1 Illustration of the effects of nonideal interfaces

sents the constraint force component and the friction force induced along the tangent plane of the surface is the nonideal force that depends explicitly on the normal contact force. For this simple example, the nonideal force acts along the tangential direction, which represents the SAM. However, in general, for more complex systems, such nonideal forces can also have components in the SCM. A typical example for this is the closed-loop slider-crank mechanism where the presence of friction between the slider and the base link changes not only the tangential force component (nonideal force) but also the normal force component (constraint force) (Fig. 1). Therefore, the physical tangential direction of the slider is not fully contained in the SAM (that is defined to be orthogonal to the SCM [1]). For the interpretation of Fig. 1, we note that the acceleration of the slider is considered the same for both cases; hence, the inertial force is also the same. The mass and the moment of inertia of Body 3 are assumed to be negligible; hence, that element is considered as a "two-force" member for this example.

The substitution of Eq. (2) into Eqs. (81), (82), (90), and (91) of Part I results in the dynamic equations of constrained and admissible motions for the case of nonideal realization. These can be written as follows.

In *global parametrization* the dynamic equations of constrained motion are

$$-\mathbf{G}^T\hat{\mathbf{P}}_c\mathbf{G}\dot{\mathbf{v}} - \mathbf{P}_c^T\mathbf{c} + \mathbf{P}_c^T\mathbf{f}_\mathbf{A} + \mathbf{P}_c^T\mathbf{f}_\mathbf{N} + \mathbf{f}_\mathbf{R} = \mathbf{0} \tag{12}$$

and the equations of admissible motion can be written as

$$-\mathbf{M}\dot{\mathbf{v}} + \mathbf{G}^T\hat{\mathbf{P}}_c\mathbf{G}\dot{\mathbf{v}} - \mathbf{P}_a^T\mathbf{c} + \mathbf{P}_a^T\mathbf{f}_\mathbf{A} + \mathbf{P}_a^T\mathbf{f}_\mathbf{N} = \mathbf{0} \tag{13}$$

where $\mathbf{G}^T\hat{\mathbf{P}}_c\mathbf{G}\dot{\mathbf{v}}$ can be interpreted according to Eqs. (7) and (8), for example.

In *local parametrization* the dynamics of constrained motion can be expressed as

$$-(\mathbf{A}\mathbf{M}^{-1}\mathbf{A}^T)^{-1}\dot{\mathbf{b}} - \mathbf{z}_c + (\mathbf{A}\mathbf{M}^{-1}\mathbf{A}^T)^{-1}\mathbf{A}\mathbf{M}^{-1}\mathbf{f}_\mathbf{A} + \mathbf{\Lambda} + \boldsymbol{\lambda} = \mathbf{0} \tag{14}$$

and the dynamic equations of admissible motion are written as

$$-(\mathbf{B}\mathbf{M}^{-1}\mathbf{B}^T)^{-1}\dot{\mathbf{u}}_a - \mathbf{z}_a + (\mathbf{B}\mathbf{M}^{-1}\mathbf{B}^T)^{-1}\mathbf{B}\mathbf{M}^{-1}\mathbf{f}_\mathbf{A} + \boldsymbol{\beta} = \mathbf{0} \tag{15}$$

These are also novel forms of dynamic equations for nonideal constraint realization.

In this case the equations of admissible motion cannot be solved independently of the dynamic equations of constrained motion (unlike in the case of ideal constraint realization). The constraint dynamics equations are still used to determine the expressions of the components of the generalized constraint forces in the SCM. However, new terms can enter via $\mathbf{\Lambda}$ and $\mathbf{f}_\mathbf{N}$. The constraint forces have to be computed first in a known state of motion and then they can be used to fully express and solve the equations of admissible motion either for the accelerations (forward dynamics) or for some of the generalized impressed forces (inverse dynamics). Again, just like in the case of ideal constraints, for redundant constraint configurations not all individual constraint forces may be determined using local parametrization. This can also cause problems with the solvability of such problems in general, since the nonideal forces may explicitly depend on all of the individual "local" constraint forces. This will also be discussed later.

As we already noted, Udwadia and Kabala [14–18] also developed a formulation to consider nonideal constraints. However, it is not clear how their formulation would work for the case of Coulomb friction, where the nonideal forces induced by friction depend on the "normal" constraint forces. As seen in the example in Fig. 1, for such cases it is generally not true that the "ideal" constraint force (determined with the assumption of ideal contact) could be used to evaluate the nonideal force. The "normal" constraint force itself is influenced by the presence of the nonideal contact. Therefore, some of the primary conclusions drawn in Refs. [14–18] do not hold for many mechanical systems. The examples shown in those papers for Coulomb friction are too simplistic to shed light on this shortcoming of their formulation. On the other hand, the formulation proposed in this present work can deal with such nonideal realizations.

2.2 Unilaterally Constrained Motion. In this case, $\mathbf{u}_c$ is only partially specified via the definition of inequalities that can be represented most typically[1] as

[1]We have to note that these conditions are valid in particular configurations only, e.g., when the unilateral contacts are closed. These velocity and acceleration level conditions cannot just simply be derived from configuration level inequalities via time differentiation.

$$\mathbf{u}_c \geq \mathbf{0} \quad \text{and} \quad \dot{\mathbf{u}}_c \geq \mathbf{0} \tag{16}$$

In this case, besides the SAM; motion is also possible in the SCM, hence, the associated virtual velocities will not vanish uniformly. This prevents performing the simplifications that are possible for the bilateral case. Also, for this unilateral case the developed constraint forces, elements of $\boldsymbol{\lambda}$, cannot take arbitrary values. They have to obey certain physical conditions, which can usually be represented as

$$\boldsymbol{\lambda} \geq \mathbf{0} \tag{17}$$

However, generally not all the combinations of the kinematic (Eq. (16)) and kinetic (Eq. (17)) conditions are possible. We can consider that based on the physics of the problem, the generalized constraint forces developed due to the constraint conditions of Eq. (16) cannot have power. Therefore, in Eq. (16) if the equality sign is valid (the constraint is active) then the associated generalized constraint force is not zero, and if the inequality is valid (the constraint is passive) then motion exists for those generalized directions of the SCM and the associated generalized constraint force is zero. These further conditions on the generalized constraint forces can be represented as

$$u_c^i \lambda_i = 0 \quad \text{and} \quad \dot{u}_c^i \lambda_i = 0, \quad i = 1, \ldots, r \tag{18}$$

at the velocity and acceleration levels, where λ_i represents the elements of $\boldsymbol{\lambda}$. These give r equations for each level of kinematics (velocity and acceleration). Pfeiffer and Glocker [19,21] called this set of conditions *the corner law of unilateral contacts*. Papastavridis [6] proved the necessity for the existence of the second set of Eq. (18). It is important to note that Eq. (18) is equivalent to $\mathbf{u}_c^T \boldsymbol{\lambda} = \mathbf{0}$ and $\dot{\mathbf{u}}_c^T \boldsymbol{\lambda} = \mathbf{0}$ under the conditions of Eqs. (16) and (17).

For this case the dynamic equations of constrained motion can be first written in the same forms as given by Eq. (81) or Eq. (90) of Part I. In this case, particularly the representation in terms of the local parametrization of the SCM can play an important role together with conditions of Eqs. (16)–(18). These dynamic equations of constrained motion in local parametrization can be written based on Eq. (90) of Part I as

$$-(\mathbf{A}\mathbf{M}^{-1}\mathbf{A}^T)^{-1}\dot{\mathbf{u}}_c - \mathbf{z}_c + (\mathbf{A}\mathbf{M}^{-1}\mathbf{A}^T)^{-1}\mathbf{A}\mathbf{M}^{-1}\mathbf{f}_\mathbf{A} + \boldsymbol{\lambda} + \boldsymbol{\Lambda}(\boldsymbol{\lambda}) = \mathbf{0} \tag{19}$$

For a given state of motion, both $\dot{\mathbf{u}}_c$ and $\boldsymbol{\lambda}$ represent unknowns. Therefore, we generally have r equations for $2r$ unknowns.

Equations (19) and (18) (taken at the acceleration level) represent a set of $2r$ algebraic equations for the $2r$ unknowns $\dot{\mathbf{u}}_c$ and $\boldsymbol{\lambda}$. They can be solved together with the constraint conditions of Eqs. (16) and (17). The set of equations and inequalities (Eqs. (16)–(19)) characterizes the constraint dynamics of the system, which is expressed in terms of the local, minimum parametrization for the SCM. This mathematically represents a *complementarity problem* expressed in minimum coordinates with respect to the unilateral constraints.

The above set of equations and inequalities for constrained motion is valid no matter whether the constraints are realized via ideal or nonideal interfaces. It is interesting to note a major difference between the solutions of the constraint dynamics equations for the case of bilateral and unilateral constraints. For bilateral constraints, $\dot{\mathbf{u}}_c$ is fully specified. The constraint dynamics equations are linear in the generalized constraint forces (provided that $\boldsymbol{\Lambda}$ is a linear function of $\boldsymbol{\lambda}$), and the solution for them can simply be obtained via substitution (ideal realization) or the solution of linear equations (nonideal realization). On the other hand, for unilateral constraints, $\dot{\mathbf{u}}_c$ is only partially specified, the constraint dynamics equations need to be handled together with the constraints and the conditions rising out from the nature of the constraint forces. In that case the formulation becomes nonlinear even for ideal realization, and the solution for the generalized constraint forces and for $\dot{\mathbf{u}}_c$ can only be obtained via iterative methods in general. We also have to note that for the case of models with redundant constraints and Coulomb friction, solution nonuniqueness and/or nonexistence problems can occur for both bilateral and unilateral constraints. Local parametrization is possible even for the case of redundant constraints via the appropriate determination of $\boldsymbol{\Gamma}$ (Part I), and based on this, via the redefinition of the originally redundantly given $\mathbf{A}$. However, for this case, the determination of each individual constraint force component associated with the original redundant constraint configuration may not be possible. Therefore, the actual "distribution" of the nonideal forces caused by Coulomb friction may not be determined, which can cause problems with the solution. This was also pointed out in Ref. [19]. One possibility to remedy this problem is to examine the model employed, and possibly introduce more degrees of freedom to include additional information about the physical system (e.g., flexibility of certain elements). This can then remove constraint redundancy.

2.2.1 Ideal Realization. Similar to bilateral constraints, in this case, the imposition of the constraints does not induce nonideal forces, which can be represented as

$$\mathbf{f}_\mathbf{N} = \mathbf{0}, \quad \boldsymbol{\Lambda} = \mathbf{0}, \quad \boldsymbol{\beta} = \mathbf{0} \tag{20}$$

Therefore, the constraint dynamics given by Eqs. (16)–(19) may take the form of a *linear complementarity problem*, which can be solved for $\boldsymbol{\lambda}$ and $\dot{\mathbf{u}}_c$.

Based on Eq. (82) of Part I, the dynamic equations for admissible motion can be written in global parametrization as

$$-\mathbf{M}\dot{\mathbf{v}} + \mathbf{G}^T\hat{\mathbf{P}}_c\mathbf{G}\dot{\mathbf{v}} - \mathbf{P}_a^T\mathbf{c} + \mathbf{P}_a^T\mathbf{f}_\mathbf{A} = \mathbf{0} \tag{21}$$

where based on Eqs. (84) and (85) of Part I

$$\mathbf{G}^T\hat{\mathbf{P}}_c\mathbf{G}\dot{\mathbf{v}} = \mathbf{A}^T(\mathbf{A}\mathbf{M}^{-1}\mathbf{A}^T)^{-1}\mathbf{A}\dot{\mathbf{v}} = \mathbf{A}^T(\mathbf{A}\mathbf{M}^{-1}\mathbf{A}^T)^{-1}(\dot{\mathbf{u}}_c - \dot{\mathbf{A}}\mathbf{v}) \tag{22}$$

for nonredundant constraints and, for example,

$$\mathbf{G}^T\hat{\mathbf{P}}_c\mathbf{G}\dot{\mathbf{v}} = \mathbf{G}^T(\mathbf{A}\mathbf{G}^{-1})^\dagger\mathbf{A}\dot{\mathbf{v}} = \mathbf{G}^T(\mathbf{A}\mathbf{G}^{-1})^\dagger(\dot{\mathbf{u}}_c - \dot{\mathbf{A}}\mathbf{v}) \tag{23}$$

can be used more generally (which also holds for redundantly constrained systems). In this case, the solution obtained for $\dot{\mathbf{u}}_c$ from the dynamic equations of constrained motion enters into the equations of admissible motion. Therefore, if global parametrization is used for the admissible motion, then even in the case of ideal constraint realization the solution is tied to the constraint dynamics equations.

In terms of local parametrization, based on Eq. (91) of Part I, the admissible dynamics equations can be given as

$$-(\mathbf{B}\mathbf{M}^{-1}\mathbf{B}^T)^{-1}\dot{\mathbf{u}}_a - \mathbf{z}_a + (\mathbf{B}\mathbf{M}^{-1}\mathbf{B}^T)^{-1}\mathbf{B}\mathbf{M}^{-1}\mathbf{f}_\mathbf{A} = \mathbf{0} \tag{24}$$

If local parametrization is used in the form of Eq. (24), then the admissible dynamics equations can be solved for $\dot{\mathbf{u}}_a$ independently of the constraint dynamics equations. However, here we emphasize again that the local parametrization has to be done properly, as discussed in Sec. 3, and matrix $\mathbf{B}$ must satisfy Eq. (56) of Part I.

2.2.2 Nonideal Realization. For this case the realization of the constraints induces nonideal forces that can have an effect on both constrained and admissible motions. These components are represented by equations such as Eqs. (74)–(77) given in Part I of this work. In general,

$$\mathbf{f}_\mathbf{N} \neq \mathbf{0}, \quad \boldsymbol{\Lambda} \neq \mathbf{0}, \quad \boldsymbol{\beta} \neq \mathbf{0} \tag{25}$$

Because of this, the model of the constraint dynamics (Eqs. (16)–(19)) takes generally the form of a *nonlinear complementarity problem* expressed in minimum coordinates. In some cases, a nonlinear complementarity problem can be transformed back into the form of linear complementarity problems as was illustrated in

Refs. [19,22], for example.

Based on Eqs. (82) and (91) of Part I, the dynamic equations for admissible motion can be written either in global parametrization as

$$-\mathbf{M}\dot{\mathbf{v}} + \mathbf{G}^T\hat{\mathbf{P}}_c\mathbf{G}\dot{\mathbf{v}} - \mathbf{P}_a^T\mathbf{c} + \mathbf{P}_a^T\mathbf{f}_\mathbf{A} + \mathbf{P}_a^T\mathbf{f}_\mathbf{N} = \mathbf{0} \tag{26}$$

where $\mathbf{G}^T\hat{\mathbf{P}}_c\mathbf{G}\dot{\mathbf{v}}$ can be interpreted according to Eq. (22) or Eq. (23); or in terms of local parametrization as

$$-(\mathbf{B}\mathbf{M}^{-1}\mathbf{B}^T)^{-1}\dot{\mathbf{u}}_a - \mathbf{z}_a + (\mathbf{B}\mathbf{M}^{-1}\mathbf{B}^T)^{-1}\mathbf{B}\mathbf{M}^{-1}\mathbf{f}_\mathbf{A} + \boldsymbol{\beta} = \mathbf{0} \tag{27}$$

The solution of the admissible dynamics equations in both global and local parametrizations is tied to the constraint dynamics formulation. If Eq. (26) is used, then both $\dot{\mathbf{u}}_c$ and $\boldsymbol{\lambda}$ are needed from the solution of the constraint dynamics to express the $\mathbf{G}^T\hat{\mathbf{P}}_c\mathbf{G}\dot{\mathbf{v}}$ and $\mathbf{f}_\mathbf{N}$ terms. If the local parametrization, Eq. (27), is employed then only $\boldsymbol{\lambda}$ is necessary to express $\boldsymbol{\beta}(\boldsymbol{\lambda})$.

In general, we can conclude here that the solution of the dynamic equations of admissible motion has a nature similar to that of the case of bilateral constraints once the quantities from the solution of the constraint dynamics formulation are known. The real complication caused by the unilateral nature of the constraints is that the structure and the solution of the constraint dynamics formulation can be much more complex. Instead of the relatively simple structure of bilateral problems, which can be expressed for the constraint forces, unilateral constraints add additional conditions and make the constraint dynamics nonlinear for all cases and result in complementarity problems. These problems can further be transformed, if necessary, to facilitate the numerical evaluation (e.g., based on the Augmented Lagrangian method [26]).

Pfeiffer and Glocker [19] derived complementarity problems in terms of a minimum parametrization using coordinates corresponding to the tangential directions of the contact pairs to represent admissible motion. This gives a powerful formulation. However, such parametrization of admissible motion does not correspond to an orthogonal decomposition and does not decouple the dynamics. Therefore, in their formulation, constrained and admissible motions (characterized by normal and tangential coordinates) are handled together. Also, they assumed that admissible motion can be fully parametrized by tangential directions of contact pairs, which is not always the case. The formulation presented in this paper may also offer some additional insight into some aspects of unilateral problems particularly in terms of the orthogonal decomposition of constrained and admissible dynamics in local parametrization. Also, the global parametrization of admissible motion is a novelty that can have useful features and potential in unilateral dynamics. These model formulations can also be taken further to the impulse-momentum level to study impulsive motion.

3 Example of the Generalized Particle

We will use the example of the generalized particle from Part I of this work (Fig. 2). It is described there in detail.

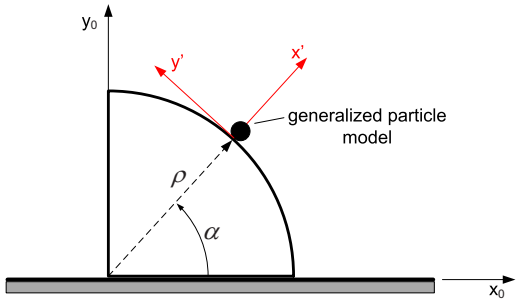

Fig. 2 A generalized particle moving on a circular block

The dynamic equilibrium equations associated with the generalized free-body diagram of this system have been derived in Part I. These will be used here to develop the formulations for the constraint specifications.

3.1 Bilateral Constraint. These can be expressed by the following holonomic constraint equation:

$$\varrho = L \tag{28}$$

where L is the radius of the sliding block. From this the velocity and acceleration level expressions can be established for the SCM as

$$\dot{\varrho} = 0, \quad \ddot{\varrho} = 0 \tag{29}$$

3.1.1 Ideal Realization. In this case there are no nonideal forces; hence, $f_{N_1}=0$ and $f_{N_2}=0$. These expressions together with the above constraint equations (Eqs. (28) and (29)) can be substituted into Eqs. (104), (105), (115), and (116) of Part I to yield the dynamic equations for constrained and admissible motions in both global and local parametrizations. For this case these can be written as follows.

The dynamic equations of constrained motion in global parametrization are

$$\begin{bmatrix} \dfrac{m_1m_2x\sqrt{x^2+y^2}}{m_2x^2+m_1y^2} \\ \dfrac{m_1m_2y\sqrt{x^2+y^2}}{m_2x^2+m_1y^2} \end{bmatrix} \left(\frac{\dot{x}^2+\dot{y}^2}{\sqrt{x^2+y^2}} - \frac{[x\dot{x}+y\dot{y}]^2}{[x^2+y^2]^{3/2}} \right) + \begin{bmatrix} \dfrac{F_xm_2x^2+F_ym_1xy}{m_2x^2+m_1y^2} \\ \dfrac{F_xm_2xy+F_ym_1y^2}{m_2x^2+m_1y^2} \end{bmatrix} + \begin{bmatrix} f_{R_1} \\ f_{R_2} \end{bmatrix} = \begin{bmatrix} 0 \\ 0 \end{bmatrix} \tag{30}$$

The dynamic equations of admissible motion in global parametrization can be written as

$$-\begin{bmatrix} m_1 & 0 \\ 0 & m_2 \end{bmatrix}\begin{bmatrix} \ddot{x} \\ \ddot{y} \end{bmatrix} - \begin{bmatrix} \dfrac{m_1m_2x\sqrt{x^2+y^2}}{m_2x^2+m_1y^2} \\ \dfrac{m_1m_2y\sqrt{x^2+y^2}}{m_2x^2+m_1y^2} \end{bmatrix} \left(\frac{\dot{x}^2+\dot{y}^2}{\sqrt{x^2+y^2}} - \frac{[x\dot{x}+y\dot{y}]^2}{[x^2+y^2]^{3/2}} \right) + \begin{bmatrix} \dfrac{F_xm_1y^2-F_ym_1xy}{m_2x^2+m_1y^2} \\ \dfrac{-F_xm_2xy+F_ym_2x^2}{m_2x^2+m_1y^2} \end{bmatrix} = \begin{bmatrix} 0 \\ 0 \end{bmatrix} \tag{31}$$

In this case based on Eq. (115) of Part I, the dynamic equation of constrained motion in local parametrization can be written as

$$\frac{m_1m_2(x^2+y^2)}{m_2x^2+m_1y^2}\left(\frac{\dot{x}^2+\dot{y}^2}{\sqrt{x^2+y^2}} - \frac{(x\dot{x}+y\dot{y})^2}{(x^2+y^2)^{3/2}} \right) + \frac{(m_2xF_x+m_1yF_y)\sqrt{x^2+y^2}}{m_2x^2+m_1y^2} + \lambda = 0 \tag{32}$$

The dynamic equation of admissible motion in local parametrization is obtained based on Eq. (116) of Part I as

$$-m_2x^2\dot{u}_a - m_1x^2\left(\frac{\dot{y}\dot{x}}{x} - \frac{y\dot{x}^2}{x^2} \right) + x^2F_y - xyF_x = 0 \tag{33}$$

For this case any possible constrained-admissible dynamics pairings of the four sets of dynamic equations can be used for the analysis (both forward and inverse dynamics). The generalized constraint forces can be determined based on Eqs. (30) and (32) in both global, $\mathbf{f}_\mathbf{R}$, and local, λ, parametrizations. We also note that based on Eq. (108) of Part I, the definition of u_a has a singularity

at $x=0$, which needs to be considered when the analysis of admissible motion dynamics is performed using local parametrization. This can be handled, for example, by redefining u_a for the vicinity of $x=0$, as was discussed in Part I [1] in more detail.

3.1.2 Nonideal Realization. Let us now consider the case where the constraint $\varrho=L$ is realized via nonideal contact between the block and the generalized particle. The constraint force associated with this constraint is λ. This defines the normal force component in terms of the local surface geometry of the circular block. This gives rise to a nonideal force component due to frictional interactions. The direction of this component is also governed by the local contact geometry (Fig. 2) and acts along the y' direction. We will use Coulomb's kinetic friction law to determine this nonideal force F_f as a function of the constraint force. This results in

$$F_f = -\operatorname{sgn}(\dot{\alpha})\mu\lambda \tag{34}$$

where μ is the kinetic friction coefficient of the contact and $\dot{\alpha}$ is used to specify the direction of the relative tangential velocity of the generalized particle. Figure 2 also shows the interpretations of the positive direction of F_f and the necessary coordinate systems to characterize the contact. From identities $\cos\alpha = x/\sqrt{x^2+y^2}$ and $\sin\alpha = y/\sqrt{x^2+y^2}$, it is straightforward to show that

$$\dot{\alpha} = \frac{x\dot{y} - y\dot{x}}{x^2+y^2} \tag{35}$$

which can now be used with the generalized coordinates and the global generalized velocities to determine the sign of the nonideal force component. Based on Eq. (112) of Part I and Eq. (29) above, $\dot{x}$ and $\dot{y}$ can also be expressed with generalized velocity u_a introduced to parametrize the SAM (so that orthogonal decoupling is possible in the local representation as well). Force F_f is associated with the relative motion between the block and the particle and is along the direction of Cartesian unit vector $\vec{e}_{y'} = -\sin\alpha\vec{e}_{x_0} + \cos\alpha\vec{e}_{y_0}$. Therefore, the generalized nonideal force components associated with generalized velocities $\dot{x}$ (f_{N_1}) and $\dot{y}$ (f_{N_2}) can be written as

$$f_{N_1} = -\frac{F_f y}{\sqrt{x^2+y^2}} = \frac{\operatorname{sgn}(\dot{\alpha})\mu\lambda y}{\sqrt{x^2+y^2}}, \quad f_{N_2} = \frac{F_f x}{\sqrt{x^2+y^2}} = -\frac{\operatorname{sgn}(\dot{\alpha})\mu\lambda x}{\sqrt{x^2+y^2}} \tag{36}$$

Equation (36) gives the relationships of Eq. (74) of Part I for this particular example.

With the expressions of Eqs. (34)–(36), the nonideal force components are completely defined and can be used together with Eqs. (28) and (29) in the dynamic equilibrium equations of Part I (Eqs. (104), (105), (115), and (116)). Based on these, the dynamic equations of constrained motion in global parametrization can be written as

$$\begin{bmatrix} \dfrac{m_1 m_2 x\sqrt{x^2+y^2}}{m_2x^2+m_1y^2} \\ \dfrac{m_1 m_2 y\sqrt{x^2+y^2}}{m_2x^2+m_1y^2} \end{bmatrix} \left(\frac{\dot{x}^2+\dot{y}^2}{\sqrt{x^2+y^2}} - \frac{[x\dot{x}+y\dot{y}]^2}{[x^2+y^2]^{3/2}} \right) + \begin{bmatrix} \dfrac{F_x m_2 x^2 + F_y m_1 xy}{m_2x^2+m_1y^2} \\ \dfrac{F_x m_2 xy + F_y m_1 y^2}{m_2x^2+m_1y^2} \end{bmatrix} + \begin{bmatrix} \dfrac{f_{N_1} m_2 x^2 + f_{N_2} m_1 xy}{m_2x^2+m_1y^2} \\ \dfrac{f_{N_1} m_2 xy + f_{N_2} m_1 y^2}{m_2x^2+m_1y^2} \end{bmatrix} + \begin{bmatrix} f_{R_1} \\ f_{R_2} \end{bmatrix} = \begin{bmatrix} 0 \\ 0 \end{bmatrix} \tag{37}$$

and the dynamic equations of admissible motion in global parametrization are

$$-\begin{bmatrix} m_1 & 0 \\ 0 & m_2 \end{bmatrix} \begin{bmatrix} \ddot{x} \\ \ddot{y} \end{bmatrix} - \begin{bmatrix} \dfrac{m_1 m_2 x\sqrt{x^2+y^2}}{m_2x^2+m_1y^2} \\ \dfrac{m_1 m_2 y\sqrt{x^2+y^2}}{m_2x^2+m_1y^2} \end{bmatrix} \left(\frac{\dot{x}^2+\dot{y}^2}{\sqrt{x^2+y^2}} - \frac{[x\dot{x}+y\dot{y}]^2}{[x^2+y^2]^{3/2}} \right) + \begin{bmatrix} \dfrac{F_x m_1 y^2 - F_y m_1 xy}{m_2x^2+m_1y^2} \\ \dfrac{-F_x m_2 xy + F_y m_2 x^2}{m_2x^2+m_1y^2} \end{bmatrix} + \begin{bmatrix} \dfrac{f_{N_1} m_1 y^2 - f_{N_2} m_1 xy}{m_2x^2+m_1y^2} \\ \dfrac{-f_{N_1} m_2 xy + f_{N_2} m_2 x^2}{m_2x^2+m_1y^2} \end{bmatrix} = \begin{bmatrix} 0 \\ 0 \end{bmatrix} \tag{38}$$

The constraint dynamics equation in local parametrization for the constraint on ϱ can be written, based on Eq. (115) of Part I, as

$$\frac{m_1 m_2 (x^2+y^2)}{m_2x^2+m_1y^2} \left(\frac{\dot{x}^2+\dot{y}^2}{\sqrt{x^2+y^2}} - \frac{(x\dot{x}+y\dot{y})^2}{(x^2+y^2)^{3/2}} \right) + \frac{(m_2 x F_x + m_1 y F_y)\sqrt{x^2+y^2}}{m_2x^2+m_1y^2} + \frac{(m_2 x f_{N_1} + m_1 y f_{N_2})\sqrt{x^2+y^2}}{m_2x^2+m_1y^2} + \lambda = 0 \tag{39}$$

The dynamic equation of admissible motion in local parametrization is obtained, based on Eq. (116) of Part I, as

$$-m_2x^2\dot{u}_a - m_1x^2\left(\frac{\dot{y}\dot{x}}{x} - \frac{y\dot{x}^2}{x^2}\right) + x^2F_y - xyF_x + x^2f_{N_2} - xyf_{N_1} = 0 \tag{40}$$

Using Eq. (36), in Eq. (39)

$$\frac{(m_2 x f_{N_1} + m_1 y f_{N_2})\sqrt{x^2+y^2}}{m_2x^2+m_1y^2} = \frac{(m_2-m_1)xy\,\operatorname{sgn}(\dot{\alpha})\mu\lambda}{m_2x^2+m_1y^2} \tag{41}$$

and in Eq. (40)

$$x^2 f_{N_2} - xy f_{N_1} = \frac{-\operatorname{sgn}(\dot{\alpha})\mu\lambda(x^3+xy^2)}{\sqrt{x^2+y^2}} \tag{42}$$

Equation (41) also shows that this is a simple, but nontrivial example[2] that is much more complex than an ordinary particle model. For example, in the case of an ordinary particle, expression (41) would vanish, and for the constraint dynamics equation (39) we would get back the same expression we had for the ideally constrained case, Eq. (32). On the other hand, for this generalized particle, the term of Eq. (41) will not vanish, since $m_1 \neq m_2$ in general, and this makes possible a closed-form illustration of how nonideal interfaces can affect the constraint forces. For the ideal case from Eq. (32)

$$\lambda^{(\text{ideal})} = -\frac{m_1 m_2 (x^2+y^2)}{m_2x^2+m_1y^2}\left(\frac{\dot{x}^2+\dot{y}^2}{\sqrt{x^2+y^2}} - \frac{(x\dot{x}+y\dot{y})^2}{(x^2+y^2)^{3/2}}\right) - \frac{(m_2 x F_x + m_1 y F_y)\sqrt{x^2+y^2}}{m_2x^2+m_1y^2} \tag{43}$$

and for the nonideal case from Eqs. (39) and (41)

[2] As we discussed in Part I, this example represents a meaningful physical system, e.g., a robot arm with two prismatic joints.

$$\lambda^{(\text{nonideal})} = -\frac{\dfrac{m_1 m_2 (x^2+y^2)}{m_2 x^2 + m_1 y^2}\left(\dfrac{\dot{x}^2+\dot{y}^2}{\sqrt{x^2+y^2}} - \dfrac{(x\dot{x}+y\dot{y})^2}{(x^2+y^2)^{3/2}}\right) + \dfrac{(m_2 x F_x + m_1 y F_y)\sqrt{x^2+y^2}}{m_2 x^2 + m_1 y^2}}{1 + \dfrac{(m_2 - m_1)xy\ \text{sgn}(\dot{\alpha})\mu}{m_2 x^2 + m_1 y^2}} \tag{44}$$

Comparing these two expressions we can see that $\lambda^{(\text{nonideal})}$ cannot be established from $\lambda^{(\text{ideal})}$ via adding a term of a predefined expression. In the admissible motion dynamics, Eq. (38) or Eq. (40), also $\lambda^{(\text{nonideal})}$ needs to be used. This shows that the effect of the nonideal interface (and the developed nonideal force) on the admissible motion of the system cannot be expressed explicitly as a function of the constraint force obtained for the ideally constrained case.

For this nonideally constrained situation, in principle, all possible constrained-admissible pairings of the four sets of dynamics equations could be used too. However, it can be seen that the global parametrization of the constraint dynamics (Eq. (37)) may not be the most advantageous in this case (nonideal interface with Coulomb friction), since f_{N_1} and f_{N_2} explicitly depend on the physical contact force λ determined in Eq. (44). This makes the determination of $\mathbf{f_R}$ difficult from Eq. (37) alone.

3.2 Unilateral Constraint. Let us consider here the case where the particle is unilaterally constrained to the block. Then, the constraint can be expressed at the configuration level by

$$\varrho \geq L \tag{45}$$

From this the velocity and acceleration level expressions can be established for the SCM for the configuration $\varrho = L$ as

$$\dot{\varrho} \geq 0, \quad \ddot{\varrho} \geq 0 \tag{46}$$

3.2.1 Constraint Dynamics. As was discussed in Sec. 2.2, in the case of the presence of unilateral constraints, the dynamic equations of constrained motion expressed in local coordinates can play an important role. For this system Eq. (115) of Part I represents this equation, which is associated with the constrained direction. The constraint dynamics equation for the unilateral constraint can be written as

$$-\frac{m_1 m_2 (x^2+y^2)}{m_2 x^2 + m_1 y^2}\ddot{\varrho} + \frac{m_1 m_2 (x^2+y^2)}{m_2 x^2 + m_1 y^2}\left(\frac{\dot{x}^2+\dot{y}^2}{\sqrt{x^2+y^2}} - \frac{(x\dot{x}+y\dot{y})^2}{(x^2+y^2)^{3/2}}\right) + \frac{(m_2 x F_x + m_1 y F_y)\sqrt{x^2+y^2}}{m_2 x^2 + m_1 y^2} + \frac{(m_2 x f_{N_1} + m_1 y f_{N_2})\sqrt{x^2+y^2}}{m_2 x^2 + m_1 y^2} + \lambda = 0 \tag{47}$$

The nonideal forces can also be expressed for this case according to Sec. 3.1.2. According to Sec. 2.2, besides Eq. (46), we can also write for the unilateral constraint

$$\lambda \geqslant 0 \tag{48}$$

and

$$\ddot{\varrho}\lambda = 0 \tag{49}$$

Then, Eq. (47), the inequality for $\ddot{\varrho}$ in Eq. (46), and Eqs. (48) and (49) give a complementarity problem that can be solved for $\ddot{\varrho}$ and λ. If the unilateral contact is ideal, then $f_{N_1} = f_{N_2} = 0$; if it is nonideal, then Eqs. (36) and (41) have to be employed.

3.2.2 Ideal Realization of the Unilateral Constraint. As was discussed, first the constraint dynamics formulation described above need to be solved. In this particular case, $f_{N_1} = f_{N_2} = 0$. For admissible motion one possibility is to use the global parametrization represented by Eq. (105) of Part I. In that case, the dynamics of admissible motion can be written as

$$-\begin{bmatrix} m_1 & 0 \\ 0 & m_2 \end{bmatrix}\begin{bmatrix} \ddot{x} \\ \ddot{y} \end{bmatrix} + \begin{bmatrix} \dfrac{m_1 m_2 x\sqrt{x^2+y^2}}{m_2 x^2 + m_1 y^2} \\ \dfrac{m_1 m_2 y\sqrt{x^2+y^2}}{m_2 x^2 + m_1 y^2} \end{bmatrix}\left(\ddot{\varrho} - \left[\frac{\dot{x}^2+\dot{y}^2}{\sqrt{x^2+y^2}} - \frac{[x\dot{x}+y\dot{y}]^2}{[x^2+y^2]^{3/2}}\right]\right) + \begin{bmatrix} \dfrac{F_x m_1 y^2 - F_y m_1 xy}{m_2 x^2 + m_1 y^2} \\ \dfrac{-F_x m_2 xy + F_y m_2 x^2}{m_2 x^2 + m_1 y^2} \end{bmatrix} = \begin{bmatrix} 0 \\ 0 \end{bmatrix} \tag{50}$$

This equation needs $\ddot{\varrho}$ from the solution of the constraint dynamics formulation. If local parametrization (Eq. (116) of Part I) is employed for admissible motion then the admissible dynamics equation can be written as

$$-m_2 x^2 \dot{u}_a - m_1 x^2\left(\frac{\dot{y}\dot{x}}{x} - \frac{y\dot{x}^2}{x^2}\right) + x^2 F_y - xyF_x = 0 \tag{51}$$

This can be solved for the acceleration $\dot{u}_a$ independently of the constraint dynamics formulation.

3.2.3 Nonideal Realization of the Unilateral Constraint. The nonideal forces f_{N_1} and f_{N_2} can be formulated based on Eqs. (36) and (41). Again, the constraint dynamics formulation given in Sec. 3.2.1 needs to be considered first. Then, for admissible motion, the dynamics in global parametrization can be expressed, according to Eq. (105) of Part I, as

$$-\begin{bmatrix} m_1 & 0 \\ 0 & m_2 \end{bmatrix}\begin{bmatrix} \ddot{x} \\ \ddot{y} \end{bmatrix} + \begin{bmatrix} \dfrac{m_1 m_2 x\sqrt{x^2+y^2}}{m_2 x^2 + m_1 y^2} \\ \dfrac{m_1 m_2 y\sqrt{x^2+y^2}}{m_2 x^2 + m_1 y^2} \end{bmatrix}\left(\ddot{\varrho} - \left[\frac{\dot{x}^2+\dot{y}^2}{\sqrt{x^2+y^2}} - \frac{[x\dot{x}+y\dot{y}]^2}{[x^2+y^2]^{3/2}}\right]\right) + \begin{bmatrix} \dfrac{F_x m_1 y^2 - F_y m_1 xy}{m_2 x^2 + m_1 y^2} \\ \dfrac{-F_x m_2 xy + F_y m_2 x^2}{m_2 x^2 + m_1 y^2} \end{bmatrix} + \begin{bmatrix} \dfrac{f_{N_1} m_1 y^2 - f_{N_2} m_1 xy}{m_2 x^2 + m_1 y^2} \\ \dfrac{-f_{N_1} m_2 xy + f_{N_2} m_2 x^2}{m_2 x^2 + m_1 y^2} \end{bmatrix} = \begin{bmatrix} 0 \\ 0 \end{bmatrix} \tag{52}$$

In local parametrization, the dynamic equation of admissible motion, according to Eq. (116) of Part I, can be given as

$$-m_2 x^2 \dot{u}_a - m_1 x^2\left(\frac{\dot{y}\dot{x}}{x} - \frac{y\dot{x}^2}{x^2}\right) + x^2 F_y - xyF_x + x^2 f_{N_2} - xy f_{N_1} = 0 \tag{53}$$

where Eq. (42) can also be employed to simplify the expression.

In this case both global and local parametrizations require the solution of the constraint dynamics formulation first. For the glo-

bal parametrization, $\ddot{q}$ and λ are needed. For the local description of admissible motion, only λ is necessary from the dynamics of constrained motion. The local parametrization of admissible motion defined based on the orthogonal decomposition using nonholonomic variable u_a is definitely a novel feature of this formulation. However, there are several other possible ways to employ the developed framework for analysis. Another possible formulation involves the use of local parametrization for the dynamics of constrained motion (Eq. (47)) and global parametrization for the admissible motion dynamics (Eq. (52)). This can also have considerable potential in both forward and inverse dynamics applications.

4 Conclusions

In this paper, bilaterally and unilaterally constrained mechanical systems were investigated using the generalized free-body diagram. The general case of possibly redundant constraints was considered. Both ideal and nonideal constraint realizations were addressed. Novel forms of dynamic equations and representations were obtained. Only a few particular notes are made here.

For bilateral constraints our equations based on global parametrization can be seen as a counterpart of the equations developed by Udwadia and Kalaba. In their formulation the explicit expressions of the constraint forces is included, while in our equations they are eliminated. Our equations are also interpreted for the general case of nonholonomic generalized velocities. The formulation developed in this paper is also better suited for nonideal interfaces.

In the case of nonideal constraint realization with Coulomb friction, local parametrization can be the best option for the constraint dynamics; and for admissible motion dynamics, both global and local parametrizations can be well suited.

For unilateral constraints the local parametrization based on orthogonal decomposition can be seen as one of the novelties. Another interesting novel unilateral formulation also appears in this work. This is based on local parametrization for the constraint dynamics (leading to a complementarity problem, which needs to be solved first) and global parametrization for admissible dynamics (that can lead to a set of linear equations for the accelerations). These may offer some alternatives and additional insight compared to the known unilateral models presented by Pfeiffer and Glocker [19], for example. Further potential of these formulations in practical applications will be investigated in upcoming works.

The methodology presented also makes it easy to switch between various models the analyst may want to try for a physical system (e.g., bilaterally or unilaterally constrained models).

Acknowledgment

This research was supported by the Natural Sciences and Engineering Research Council of Canada and the Canada Foundation for Innovation. The support is gratefully acknowledged.

References

[1] Kövecses, J., 2008, "Dynamics of Mechanical Systems and the Generalized Free-Body Diagram—Part I: General Formulation," ASME J. Appl. Mech., **75**(6), p. 061012.
[2] Hamel, G., 1949, *Theoretische Mechanik*, Springer, Berlin.
[3] Rosenberg, R. M., 1977, *Analytical Dynamics of Discrete Systems*, Plenum Press, New York.
[4] Pars, L. A., 1964, *A Treatise on Analytical Dynamics*, Heinemann, London.
[5] Lure, A., 2002, *Analytical Mechanics*, Springer, Berlin.
[6] Papastavridis, J. G., 2002, *Analytical Mechanics*, Oxford University Press, New York.
[7] Kane, T. R., and Levinson, D. A., 1985, *Dynamics, Theory and Applications*, McGraw-Hill, New York.
[8] Greenwood, D. T., 2003, *Advanced Dynamics*, Cambridge University Press, Cambridge.
[9] Schiehlen, W., 1997, "Multibody System Dynamics: Roots and Perspectives," Multibody Syst. Dyn., **1**(2), pp. 149–188.
[10] Eberhard, P., and Schiehlen, W., 2006, "Computational Dynamics of Multibody Systems: History, Formalisms, and Applications," ASME J. Comput. Nonlinear Dyn., **1**, pp. 3–12.
[11] Shabana, A. A., 2001, *Computational Dynamics*, Wiley, New York.
[12] Udwadia, F. E., and Kalaba, R. E., 1992, "A New Perspective on Constrained Motion," Proc. R. Soc. London, Ser. A, **439**(1906), pp. 407–410.
[13] Udwadia, F. E., and Kalaba, R. E., 1996, *Analytical Dynamics—A New Approach*, Cambridge University Press, Cambridge.
[14] Udwadia, F. E., and Kalaba, R. E., 2002, "What Is the General Form of the Explicit Equations of Motion for Constrained Mechanical Systems?," ASME J. Appl. Mech., **69**, pp. 335–339.
[15] Udwadia, F. E., and Kalaba, R. E., 2001, "Explicit Equations of Motion for Mechanical Systems with Nonideal Constraints," ASME J. Appl. Mech., **68**, pp. 462–467.
[16] Udwadia, F. E., Kalaba, R. E., and Phohomsiri, P., 2004, "Mechanical Systems With Nonideal Constraints: Explicit Equations Without the Use of Generalized Inverses," ASME J. Appl. Mech., **71**, pp. 615–621.
[17] Udwadia, F. E., and Kalaba, R. E., 2002, "On the Foundations of Analytical Dynamics," Int. J. Non-Linear Mech., **37**, pp. 1079–1090.
[18] Udwadia, F. E., and Kalaba, R. E., 2000, "Nonideal Constraints and Lagrangian Dynamics," J. Aerosp. Eng., **13**(1), pp. 17–22.
[19] Pfeiffer, F., and Glocker, Ch., 1996, *Multibody Dynamics With Unilateral Contacts*, Wiley, New York.
[20] Moreau, J. J., 1988, "Unilateral Contact and Dry Friction in Finite Freedom Dynamics," *Non-Smooth Mechanics and Applications* (CISM courses and Lectures Vol. 302), J. J. Moreau and P. D. Panagiotopoulos, eds., Springer, Wien, pp. 1–82.
[21] Pfeiffer, F., 1999, "Unilateral Problems of Dynamics," Arch. Appl. Mech., **69**, pp. 502–527.
[22] Glocker, Ch., 2001, *Set-Valued Force Laws: Dynamics of Non-Smooth Systems*, Springer-Verlag, Berlin.
[23] Brogliato, B., 1999, *Nonsmooth Mechanics*, Springer, London.
[24] Kövecses, J., Piedboeuf, J.-C., and Lange, C., 2003, "Dynamics Modeling and Simulation of Constrained Robotic Systems," IEEE/ASME Trans. Mechatron., **8**(2), pp. 165–177.
[25] Kövecses, J., and Piedboeuf, J.-C., 2003, "A Novel Approach for the Dynamic Analysis and Simulation of Constrained Mechanical Systems," ASME Paper No. DETC2003-VIB-48318.
[26] Pfeiffer, F., Foerg, M., and Ulbrich, H., 2006, "Numerical Aspects of Non-Smooth Multibody Dynamics," Comput. Methods Appl. Mech. Eng., **195**, pp. 6891–6908.

Surface Green Function With Surface Stresses and Surface Elasticity Using Stroh's Formalism

Hideo Koguchi
Department of Mechanical Engineering,
Nagaoka University of Technology,
1603-1 Kamitomioka, Nagaoka,
Niigata 940-2188, Japan
e-mail: koguchi@mech.nagaokaut.ac.jp

In the present paper, surface Green functions in an anisotropic elastic half-domain subjected to a concentrated force and a line force are derived using Stroh's formalism considering surface stress and surface elasticity. Formulation of the boundary condition based on Stroh's formalism is presented and is used to derive the surface Green functions. The displacement field far from the surface is affected only slightly by the surface stress and elasticity. However, the stress field is influenced to a somewhat greater degree by the surface stress and elasticity. The influence of the mechanical properties of the surface on the distributions of displacement and stress near the surface is investigated for various values of surface elastic modulus and surface stress. The surface stress and surface elasticity affect the displacements and stresses, respectively, in different manners. Displacement fields in molecular dynamics are compared with those in the Green function, and it is shown that the results are in fair agreement. [DOI: 10.1115/1.2967893]

1 Introduction

As the size of materials is reduced, the ratio of surface to volume of structures increases and the surface effect on the mechanical behavior of bulk in materials becomes noticeable. Ibach [1] reviewed previous research related to surface stress and reported the importance of surface stress on the deformation in a small cantilever and on the stabilization of mesoscopic pattern formation. The energy of atoms near a free surface is different from that of atoms in bulk. Furthermore, surface stress originated from surface energy affects the mechanical response in the nanoscaled domain. Recently, Muller and Saul [2] reviewed the effects of surface stress and surface elasticity on surface phenomena and surface physics. They reported that the surface Green function can be used to evaluate the interaction energy of surface steps, adatoms, and vacancies produced during a growing process in thin films. For instance, in a nanoscaled pattern formation on a free surface, any steps formed will be affected by the reconstruction of surface atoms due to the interaction between the surface and steps. Gao and Suo [3] analyzed many patterns formed on a crystalline substrate absorbing adatoms based on the minimization of free energy in a system. In their analysis, surface stress was reported to depend on the concentration, which is the fraction of surface sites covered by one or two atomic species, and does not depend on surface strain. A number of studies have investigated pattern formation and the modeling of surface steps using force dipoles and distributed forces [4–9]. Shenoy and Ciobanu [10] examined the stiffness of steps on [100], [110], and [111] surfaces of cubic crystals considering surface stresses and showed that surface stress tractions acting at a relaxed surface step edge can be described using an expression using the curvature of the step profile.

As a general approach, Gurtin and Murdoch [11,12] presented a mathematical framework for the mechanical behavior of material surfaces, including surface elasticity. They modeled the surface as a two-dimensional membrane adhering to an underlying bulk material. Later, Gurtin et al. [13] discussed deformation of a curved interface between solid phases and derived local equilibrium conditions that relate these interface stresses to stresses in the bulk. Thomson et al. [14] derived a static boundary condition taking into account surface stress and analyzed the stress field around a crack tip. Koguchi [15] independently derived a dynamic boundary condition considering interfacial stress and the density at an interface based on the membrane surface model. He analyzed the contact problem in which an elastic half-region coated with a thin film was penetrated by an axisymmetric elastic indenter in the boundary condition (Koguchi [16]) and deduced a new adhesion formulation, including the Johnson–Kendall–Roberts theory considering surface stress. In other studies [17–21], the curvature of a deformed surface under an external force was taken into consideration in the analyses. Surface elasticity also influences the mechanical response in the nanoscaled structures. Duan et al. [22,23] introduced the surface elasticity effect at nanoscaled inhomogeneities into the fundamental framework of micromechanics and showed the dependence of the elastic moduli on their sizes.

In several studies on the effect of surface stress on the elastic response of structures, stress analyses for isotropic materials have been carried out (He and Li [24,25], Mi and Kouris [26,27]). However, the mechanical behavior in nanoscaled structures generally depends on the anisotropy of the crystal. Stroh's formalism is an elegant and powerful tool for deriving a surface Green function in anisotropic elastic bodies. Wu [28] derived three-dimensional Green functions for anisotropic materials in Stroh's formalism using Radon transform. Ting [29–31] and Yang [32] derived Green functions for general anisotropic elastic materials. He and Lim [24] derived a surface Green function for isotropic materials considering surface stress. The surface Green function can be used for isotropic materials with positive surface elastic moduli. In previous studies, the surface Green function in anisotropic half-domains when ignoring the surface stress and surface elasticity was used. In the present paper, the surface Green function in Stroh's formalism using the boundary condition considering the dependency of surface stress on surface strain is deduced for three-dimensional half-regions. In addition, an explicit solution will be shown for the two-dimensional case. The effects of the surface stress and surface elasticity on displacement and stress fields will then be discussed. Furthermore, displacement fields near a surface calculated using this formulation are compared with

Contributed by the Applied Mechanics Division for publication in the JOURNAL OF APPLIED MECHANICS. Manuscript received May 3, 2007; final manuscript received June 2, 2008; published online August 21, 2008. Review conducted by Zhigang Suo.

those derived from molecular dynamics (MD) calculation, and the validity of surface Green function will be shown.

2 Boundary Condition Including Surface Stresses and Surface Elasticity

A semi-infinite anisotropic elastic solid is considered and a rectangular Cartesian coordinate system is used in the analysis. It will be assumed that the elastic medium $x_3 \leq 0$ is bounded by a plane of infinite extent, which we shall take to be $x_3=0$. The x_3 axis is taken normal to this plane to point into the medium. The stress-strain relationship in anisotropic materials can then be expressed as follows:

$$\sigma_{ij} = C_{ijkl}\varepsilon_{kl} \tag{1}$$

where σ_{ij} is the bulk stress and ε_{kl} is the bulk strain.

Now, a boundary condition considering surface stress and surface elasticity is formulated in Stroh's formalism. Dingreville et al. [33] presented a framework incorporating surface free energy into continuum mechanics and discussed the size effect of mechanical properties in elastic nanosized structural elements. The surface energy density function $\Gamma = S\gamma_s$ depends on the surface strain ε^s_{ij} and may be expressed as a series expansion of surface strain,

$$\Gamma(\varepsilon^s_{\alpha\beta}) = \Gamma_0 + \left.\frac{\partial\Gamma}{\partial\varepsilon^s_{\alpha\beta}}\right|_{\varepsilon^s_{\alpha\beta}=0}\varepsilon^s_{\alpha\beta} + \left.\frac{1}{2}\frac{\partial^2\Gamma}{\partial\varepsilon^s_{\alpha\beta}\partial\varepsilon^s_{\gamma\lambda}}\right|_{\substack{\varepsilon^s_{\alpha\beta}=0\\ \varepsilon^s_{\gamma\lambda}=0}}\varepsilon^s_{\alpha\beta}\varepsilon^s_{\gamma\lambda}$$

$$+ \ = \Gamma_0 + \tau^0_{\alpha\beta}\varepsilon^s_{\alpha\beta} + \frac{1}{2}d_{\alpha\beta\gamma\lambda}\varepsilon^s_{\alpha\beta}\varepsilon^s_{\gamma\lambda} + \tag{2}$$

where Γ_0 $(=S_0\gamma_{s0})$, $\tau^0_{\alpha\beta}$, and $d_{\alpha\beta\gamma\delta}$ are the surface energy density function, the surface stress tensor, and the surface elasticity for zero surface strain induced by an external load, respectively. In addition, S is the surface area and γ_s is the surface energy.

Surface stress is deduced by differentiating Eq. (2) with respect to surface strain, $\varepsilon^s_{\alpha\beta}$, as follows:

$$\tau_{\alpha\beta} = \tau^0_{\alpha\beta} + d_{\alpha\beta\gamma\lambda}\varepsilon^s_{\gamma\lambda} \tag{3}$$

Surface stress depends linearly on surface strain. The boundary condition is written using an equilibrium relationship of surface stress, bulk stress, and a traction vector $\mathbf{t}_i$, as follows [15]:

On the tangential plane of the surface:

$$\sigma_{i\alpha}\boldsymbol{\nu}_i - \tau_{\alpha\beta,\beta} = t_\alpha \tag{4}$$

In the normal direction of the surface,

$$\sigma_{i3}\boldsymbol{\nu}_i - \tau_{\mu\beta}\kappa_{\mu\beta}\boldsymbol{\nu}_3 = t_3 \tag{5}$$

where α, β, and $\mu=1,2$ correspond to the rectangular coordinate system on the surface, $i=1,2,3$ corresponds to the rectangular coordinate systems, the subscript "," denotes the derivative, $\kappa_{\alpha\beta}$ is the curvature tensor, $\boldsymbol{\nu}_1$ and $\boldsymbol{\nu}_2$ are the unit vectors in the tangential direction of the surface, and $\boldsymbol{\nu}_3$ is the unit normal vector of the surface.

Substituting Eq. (3) into Eq. (4) yields the following equilibrium equation for the tangential direction of the surface:

$$\sigma_{i\alpha}\boldsymbol{\nu}_i - \tau^0_{\alpha\beta,\beta} - d_{\alpha\beta\gamma\lambda}\varepsilon^s_{\gamma\lambda,\beta} = t_\alpha \tag{6}$$

The second term of the left-hand side is the contribution of surface stress to the bulk, when the surface stress varies with the location on a surface. Gao and Suo [3] analyzed the pattern formation considering the surface stress effect due to the concentration field of the monolayer. In their analysis, the second term in Eq. (6) contributes mainly to the free energy in the system. When the surface stress is uniform on the surface, the second term vanishes. The third term of the left-hand side is the contribution of surface elasticity to the bulk.

Substituting Eq. (3) into Eq. (5) yields the following equilibrium equation in the normal direction to the surface:

$$\sigma_{i3}\boldsymbol{\nu}_i - \tau_{\mu\beta}\kappa_{\mu\beta}\boldsymbol{\nu}_3 = \sigma_{i3}\boldsymbol{\nu}_i - (\tau^0_{\mu\beta} + d_{\mu\beta\gamma\lambda}\varepsilon^s_{\gamma\lambda})\kappa_{\mu\beta}\boldsymbol{\nu}_3 \tag{7}$$

where $\kappa_{\mu\beta}$ is the curvature of the deformed surface.

It is assumed that a deformed surface may be expressed by superposing an initial surface profile $h(x_1,x_2)$ and the displacement w_0 in the normal direction of the x_1-x_2 plane. Here, let the profile of the surface, g, describes as $g(x_1,x_2)=h(x_1,x_2)+w_0(x_1,x_2)$. The curvature of the surface is then expressed as

$$\kappa_{ij} = \frac{1}{H}\frac{\partial^2 g}{\partial x_i\partial x_j} \tag{8}$$

where $H=\sqrt{1+(\partial g/\partial x_1)^2+(\partial g/\partial x_2)^2}$.

Assuming $w_0 \ll h$ and neglecting the second-order infinitesimal quantity in H yields the following equations:

$$\kappa_{ij} = \frac{1}{\sqrt{1+(\partial(h+w_0)/\partial x_1)^2+(\partial(h+w_0)/\partial x_2)^2}}\frac{\partial^2(h+w_0)}{\partial x_i\partial x_j} \cong \frac{1}{\sqrt{1+(\partial h/\partial x_1)^2+(\partial h/\partial x_2)^2}}$$
$$\times\left\{1-\frac{1}{2}\left(\frac{2(\partial h/\partial x_1)(\partial w_0/\partial x_1)+(\partial w_0/\partial x_1)^2+2(\partial h/\partial x_2)(\partial w_0/\partial x_2)+(\partial w_0/\partial x_2)^2}{1+(\partial h/\partial x_1)^2+(\partial h/\partial x_2)^2}\right)+\cdots\right\}$$
$$\times\left(\frac{\partial^2 h}{\partial x_i\partial x_j}+\frac{\partial^2 w_0}{\partial x_i\partial x_j}\right) \cong \frac{1}{\sqrt{1+(\partial h/\partial x_1)^2+(\partial h/\partial x_2)^2}}\left(\frac{\partial^2 h}{\partial x_i\partial x_j}+\frac{\partial^2 w_0}{\partial x_i\partial x_j}\right) = \kappa^0_{ij}+\frac{1}{H_0}\frac{\partial^2 w_0}{\partial x_i\partial x_j} \tag{9}$$

where $H_0=\sqrt{1+(\partial h/\partial x_1)^2+(\partial h/\partial x_2)^2}$ and $\kappa^0_{ij}=(1/H_0)\times(\partial^2 h/\partial x_i\partial x_j)$.

Substituting Eq. (9) into Eq. (7) yields the following equation:

$$\sigma_{i3}\boldsymbol{\nu}_i - \tau_{\mu\beta}\kappa_{\mu\beta}\boldsymbol{\nu}_3 = \sigma_{i3}\boldsymbol{\nu}_i - \boldsymbol{\nu}_3(\tau^0_{ij}+d_{ij\gamma\lambda}\varepsilon^s_{\gamma\lambda})\left(\kappa^0_{ij}+\frac{1}{H_0}\frac{\partial^2 w_0}{\partial x_i\partial x_j}\right) \tag{10}$$

and neglecting the second-order infinitesimal quantity yields

$$= \sigma_{i3}\boldsymbol{\nu}_i - \boldsymbol{\nu}_3\frac{\tau^0_{\alpha\beta}}{H_0}\frac{\partial^2 w_0}{\partial x_\alpha\partial x_\beta} - \boldsymbol{\nu}_3\kappa^0_{\alpha\beta}d_{\alpha\beta\gamma\lambda}\varepsilon^s_{\gamma\lambda} - \boldsymbol{\nu}_3\tau^0_{\alpha\beta}\kappa^0_{\alpha\beta} \tag{11}$$

The second and the last terms on the right-hand side are the normal traction to the surface due to the Laplace pressure, which arises from surface stress. In particular, the last term acts as residual stresses due to the initial profile of the surface. Hence, this term might be neglected when the effect of surface stress on the mechanical response for external forces is investigated. The third term is the contribution to the normal traction due to the increment of in-plane stress. When a stress analysis for a material with

a curved surface is conducted, the effect of the third term depending on the initial curvature on bulk stress becomes large. In the present paper, a surface Green function for a flat surface is derived, i.e., $\kappa^0_{\alpha\beta}=0$.

3 Stroh's Formulation for a Half-Domain With a Flat Surface

The equilibrium equation for anisotropic materials can be expressed using the displacement, u_i:

$$C_{ijkl}u_{k,lj}=0 \tag{12}$$

Now, we introduce the two-dimensional spatial Fourier transforms applied to the in-plane coordinates (x_1,x_2) of the displacement and the stress components defined by the pair:

$$\tilde{f}(\eta_1,\eta_2,x_3)=\int_{-\infty}^{+\infty}\int_{-\infty}^{+\infty}f(x_1,x_2,x_3)e^{i(\eta_1x_1+\eta_2x_2)}dx_1dx_2$$

$$f(x_1,x_2,x_3)=\frac{1}{(2\pi)^2}\int_{-\infty}^{+\infty}\int_{-\infty}^{+\infty}f(\eta_1,\eta_2,x_3)e^{-i(\eta_1x_1+\eta_2x_2)}d\eta_1d\eta_2 \tag{13}$$

Applying the 2D Fourier transform to the governing equation (12), it becomes an ordinary differential equation as (Ting [31]; Yang and Pan [32]; Willis [34])

$$C_{i\alpha k\beta}\eta_\alpha\eta_\beta\tilde{u}_k+i(C_{i\alpha k3}+C_{i3k\alpha})\eta_\alpha\tilde{u}_{k,3}-C_{i3k3}\tilde{u}_{k,33}=0 \tag{14}$$

Here, a general solution for Eq. (14) can be expressed as follows:

$$\tilde{\mathbf{u}}(\eta_1,\eta_2,x_3)=\mathbf{a}e^{-ip\rho x_3} \tag{15}$$

where p and $\mathbf{a}$ satisfy the following eigenrelation:

$$\{\mathbf{Q}+p(\mathbf{R}+\mathbf{R}^T)+p^2\mathbf{T}\}\mathbf{a}=0 \tag{16}$$

where $Q_{ik}=C_{ijks}n_jn_s$, $R_{ik}=C_{ijks}n_jm_s$, and $T_{ik}=C_{ijks}m_jm_s$ with $\mathbf{n}=[n_1,\ n_2,\ 0]=[\cos\theta,\ \sin\theta,\ 0]^T$ and $\mathbf{m}=[0,0,1]^T$.

Matrix forms of the boundary condition are deduced using Eqs. (6) and (10). Boundary conditions in the tangential and normal directions to the surface, respectively, can be expressed as

$$t_\alpha=C_{\alpha3k\beta}u_{k,\beta}+C_{\alpha3k3}u_{k,3}-d_{\alpha\beta\gamma\lambda}u_{\gamma,\lambda\beta}$$

$$t_3=\left(C_{33k\alpha}u_{k,\alpha}+C_{33k3}u_{k,3}-\tau^0_{\alpha\beta}\frac{\partial^2w_0}{\partial x_\alpha\partial x_\beta}\right)\boldsymbol{\nu}_3 \tag{17}$$

where $(\boldsymbol{\nu}_1,\boldsymbol{\nu}_2,\boldsymbol{\nu}_3)\cong(0,0,1)$.

Taking w_0 to be u_3 at the surface and applying Fourier transforms with x_1 and x_2 to Eq. (17) yields

$$\tilde{t}_\alpha=-i\eta_\beta C_{\alpha3k\beta}\tilde{u}_k+C_{\alpha3\beta3}\tilde{u}_{k,3}+d_{\alpha\beta\gamma\lambda}\eta_\lambda\eta_\beta\tilde{u}_\gamma$$

$$\tilde{t}_3=-i\eta_\alpha C_{33k\alpha}\tilde{u}_k+C_{33k3}\tilde{u}_{k,3}+\tau^0_{\alpha\beta}\eta_\alpha\eta_\beta\tilde{u}_3 \tag{18}$$

and the use of Eq. (15) then yields

$$\tilde{t}_\alpha=-i\rho\{(C_{\alpha jks}m_jn_s+pC_{\alpha jks}m_jm_s)a_k+i\rho d_{\alpha\beta\gamma\lambda}n_\beta n_\lambda a_\gamma\}e^{-ip\rho x_3}$$

$$\tilde{t}_3=-i\rho(C_{3jks}n_sm_j+pC_{3jks}m_sm_j+i\rho\tau^0_{\alpha\beta}n_\alpha n_\beta m_k)a_ke^{-ip\rho x_3} \tag{19}$$

where $(\eta_1,\eta_2)=(\rho n_1,\rho n_2)$. Hence,

$$\tilde{\mathbf{t}}=-i\rho(\mathbf{b}+i\rho\mathbf{F})e^{-ip\rho x_3} \tag{20}$$

where

$$\mathbf{b}=(\mathbf{R}^T+p\mathbf{T})\mathbf{a}=-\frac{1}{p}(\mathbf{Q}+p\mathbf{R})\mathbf{a} \tag{21}$$

and

$$\mathbf{F}=\begin{bmatrix}d_{1\beta1\lambda}n_\beta n_\lambda & d_{1\beta2\lambda}n_\beta n_\lambda & 0\\ d_{2\beta1\lambda}n_\beta n_\lambda & d_{2\beta2\lambda}n_\beta n_\lambda & 0\\ 0 & 0 & \tau^0_{\alpha\beta}n_\alpha n_\beta\end{bmatrix}\mathbf{a} \tag{22}$$

The general solutions are obtained by superposing three solutions of Eqs. (15) and (20) associated with p_j and $\mathbf{a}_j$, $j=1,2,3$, which are eigenvalues and the corresponding eigenvectors, respectively:

$$\tilde{\mathbf{u}}(\eta_1,\eta_2,x_3)=\mathbf{A}\langle e^{-ip_*\rho x_3}\rangle\mathbf{q}$$

$$\tilde{\mathbf{t}}(\eta_1,\eta_2,x_3)=-i\rho(\mathbf{B}+i\rho\mathbf{F})\langle e^{-ip_*\rho x_3}\rangle\mathbf{q} \tag{23}$$

where $\mathbf{F}$ is a real matrix, $\mathbf{A}=[\mathbf{a}_1,\ \mathbf{a}_2,\ \mathbf{a}_3]$, $\mathbf{B}=[\mathbf{b}_1,\ \mathbf{b}_2,\ \mathbf{b}_3]$, and $\langle e^{-ip_*\rho x_3}\rangle=\mathrm{diag}[e^{-ip_1\rho x_3},\ e^{-ip_2\rho x_3},\ e^{-ip_3\rho x_3}]$, and $\mathbf{q}$ is a complex vector to be determined.

4 Three-Dimensional Surface Green Function for Anisotropic Materials

Now, let us consider the case in which a uniform force $\mathbf{p}$ is distributed on a surface, $x_3=0$. The applied force can then be expressed as

$$\mathbf{t}(x_1,x_2)=\mathbf{p}H(|a|-x_1)(|b|-x_2) \tag{24}$$

where $H(x)$ is the Heaviside step function: $H(x)=1(x>0)$, $1/2(x=0)$, $0(x<0)$.

Fourier transform is applied to Eq. (24), and the following equation is derived:

$$\tilde{\mathbf{t}}(\eta_1,\eta_2)=4\mathbf{p}\frac{\sin\eta_1a}{\eta_1}\frac{\sin\eta_2b}{\eta_2} \tag{25}$$

Equating Eq. (25) to Eq. (20) for $x_3=0$ yields

$$-i\rho(\mathbf{B}+i\rho\mathbf{F})\mathbf{q}=4\mathbf{p}\frac{\sin\eta_1a}{\eta_1}\frac{\sin\eta_2b}{\eta_2} \tag{26}$$

Solving Eq. (26) with respect to $\mathbf{q}$ yields

$$\mathbf{q}=4\frac{i}{\rho}(\mathbf{B}+i\rho\mathbf{F})^{-1}\mathbf{p}\frac{\sin\eta_1a}{\eta_1}\frac{\sin\eta_2b}{\eta_2} \tag{27}$$

and substituting this $\mathbf{q}$ into Eq. (23) yields

$$\tilde{\mathbf{u}}(\eta_1,\eta_2,x_3)=4\frac{i}{\rho}\mathbf{A}\langle e^{-ip_*\rho x_3}\rangle(\mathbf{B}+i\rho\mathbf{F})^{-1}\mathbf{p}\frac{\sin\eta_1a}{\eta_1}\frac{\sin\eta_2b}{\eta_2}$$

$$\tilde{\mathbf{t}}(\eta_1,\eta_2,x_3)=4(\mathbf{B}+i\rho\mathbf{F})\langle e^{-ip_*\rho x_3}\rangle(\mathbf{B}+i\rho\mathbf{F})^{-1}\mathbf{p}\frac{\sin\eta_1a}{\eta_1}\frac{\sin\eta_2b}{\eta_2} \tag{28}$$

Here, p_j of the positive imaginary part is used, because when x_3 goes to $-\infty$, the displacement is finite. The corresponding physical-domain solutions can be derived by the inverse Fourier transform for the transformed-domain solutions, Eq. (28).

$$\mathbf{u}(x_1,x_2,x_3)=\frac{i}{\pi^2}\int_{-\infty}^{\infty}\int_{-\infty}^{\infty}\frac{1}{\rho}\mathbf{A}\langle e^{-ip_*\rho x_3}\rangle(\mathbf{B}+i\rho\mathbf{F})^{-1}\mathbf{p}$$
$$\times\frac{\sin\eta_1a}{\eta_1}\frac{\sin\eta_2b}{\eta_2}e^{-i(\eta_1x_1+\eta_2x_2)}d\eta_1d\eta_2 \tag{29}$$

$$\mathbf{t}(x_1,x_2,x_3)=\frac{1}{\pi^2}\int_{-\infty}^{\infty}\int_{-\infty}^{\infty}(\mathbf{B}+i\rho\mathbf{F})\langle e^{-ip_*\rho x_3}\rangle(\mathbf{B}+i\rho\mathbf{F})^{-1}\mathbf{p}$$
$$\times\frac{\sin\eta_1a}{\eta_1}\frac{\sin\eta_2b}{\eta_2}e^{-i(\eta_1x_1+\eta_2x_2)}d\eta_1d\eta_2 \tag{30}$$

Here, a solution for a surface concentrated force vector $\mathbf{f}$ can be derived using the formula of $\lim_{\xi\to0}(\sin\xi/\xi)=1$. Thus,

$$\mathbf{p}\lim_{\substack{a\to 0\\ b\to 0}}\frac{a\sin\eta_1 a}{\eta_1 a}\frac{b\sin\eta_2 b}{\eta_2 b}=ab\mathbf{p} \tag{31}$$

and since $\mathbf{f}$ is the total force applied to the area $4ab$, $\mathbf{f}$ is equal to $4ab\mathbf{p}$.

Next, let us integrate the equations and replace $\mathbf{p}$ with $\mathbf{f}$ in Eqs. (29) and (30). The same equations can be derived using $\mathbf{t}=\mathbf{f}\delta(x_1)\delta(x_2)$. Here, $\delta(x)$ is Kronecker's delta. Before proceeding, the inverse matrix of $(\mathbf{B}+i\rho\mathbf{F})$ is expanded and arranged with respect to ρ. Here, $(\mathbf{B}+i\rho\mathbf{F})^{-1}$ is expressed as $\mathbf{W}(\rho)$, which yields

$$W_{lm}=w_{lm}\sum_{j=1}^{3}\frac{g_{jlm}}{\rho-h_{jlm}} \tag{32}$$

Now, let us introduce polar coordinate systems related to (x_1,x_2) by $x_1=r\cos\theta_0$ and $x_2=r\sin\theta_0$, and (η_1,η_2) by $\eta_1=\rho\cos\theta$ and $\eta_2=\rho\sin\theta$. Then, the displacement and traction vectors can be expressed using $d\eta_1 d\eta_2=\rho d\theta d\rho$ as follows:

$$\mathbf{u}(r,\theta_0,x_3)=\frac{i}{4\pi^2}\int_0^{2\pi}\left[\int_0^{\infty}\mathbf{A}\langle e^{-ip_*\rho x_3}\rangle\mathbf{W}(\rho)e^{-ir\rho\cos(\theta-\theta_0)}d\rho\right]\mathbf{f}d\theta$$

$$\mathbf{t}(r,\theta_0,x_3)=\frac{1}{4\pi^2}\int_0^{2\pi}\left[\int_0^{\infty}\rho(\mathbf{B}+i\rho\mathbf{F})\times\langle e^{-ip_*\rho x_3}\rangle\mathbf{W}(\rho)e^{-ir\rho\cos(\theta-\theta_0)}d\rho\right]\mathbf{f}d\theta \tag{33}$$

Here, matrices $\mathbf{A}$, $\mathbf{B}$, $\mathbf{F}$, and $\mathbf{W}$ and eigenvalue p have the following angular dependences:

$$p(\theta)=-\bar{p}(\theta+\pi),\quad \mathbf{A}(\theta)=\bar{\mathbf{A}}(\theta+\pi),$$

$$\mathbf{B}(\theta)=-\bar{\mathbf{B}}(\theta+\pi),\quad \mathbf{F}(\theta)=\bar{\mathbf{F}}(\theta+\pi)$$

$$\mathbf{W}(\theta)=-\bar{\mathbf{W}}(\theta+\pi) \tag{34}$$

The overbar symbol indicates a conjugate complex variable. Using Eq. (34) and integrating the first term in Eq. (33) with respect to ρ yield

$$\mathbf{u}(r,\theta_0,x_3)=\frac{i}{4\pi^2}\int_0^{\pi}\left[\left\{\mathbf{A}\int_0^{\infty}\langle e^{-i\rho(p_*x_3+r\cos(\theta-\theta_0))}\rangle\mathbf{W}(\rho)-\bar{\mathbf{A}}\int_0^{\infty}\langle e^{i\rho(\bar{p}_*x_3+r\cos(\theta-\theta_0))}\rangle\bar{\mathbf{W}}(\rho)\right\}d\rho\right]\mathbf{f}d\theta$$

$$=\frac{-1}{2\pi^2}\,\mathrm{Im}\int_0^{\pi}\mathbf{A}\Phi\mathbf{f}d\theta \tag{35}$$

where

$$\Phi_{rk}=w_{rk}\sum_{j=1}^{3}\int_0^{\infty}\frac{g_{jrk}}{\rho-h_{jrk}}e^{-i\rho\varsigma_k}d\rho=w_{rk}\sum_{j=1}^{3}g_{jrk}e^{-ih_{jrk}\varsigma_k}\Gamma(0,-ih_{jrk}\varsigma_k) \tag{36}$$

Here, $\varsigma_r=p_r x_3+r\cos(\theta-\theta_0)$ and $\Gamma(a,z)=\int_z^{\infty}t^{a-1}e^{-t}dt$ is the incomplete Gamma function. Traction vector $\mathbf{t}$ can be arranged as

$$\mathbf{t}(r,\theta_0,x_3)=\frac{1}{4\pi^2}\int_0^{2\pi}\left[\int_0^{\infty}\rho(\mathbf{B}+i\rho\mathbf{F})\langle e^{-i\rho\varsigma_*}\rangle\mathbf{W}(\rho)d\rho\right]\mathbf{f}d\theta$$

$$=\frac{1}{2\pi^2}\,\mathrm{Re}\int_0^{\pi}\Psi\mathbf{f}d\theta \tag{37}$$

where

$$\Psi_{rk}=\sum_{n=1}^{3}\sum_{j=1}^{3}\int_0^{\infty}\rho(b_{rn}+i\rho F_{rn})w_{kn}\frac{g_{jkn}}{\rho-h_{jkn}}e^{-i\rho\varsigma_n}d\rho$$

$$=\sum_{n=1}^{3}\sum_{j=1}^{3}w_{kn}g_{jkn}\int_0^{\infty}\left[(b_{rn}+iF_{rn}h_{kn})+iF_{rn}\rho+\frac{iF_{rn}h_{jkn}+b_{rn}}{\rho-h_{jkn}}h_{jkn}\right]e^{-i\rho\varsigma_n}d\rho$$

$$=\sum_{n=1}^{3}\sum_{j=1}^{3}w_{kn}g_{jkn}\left[\frac{-i(b_{rn}+iF_{rn}h_{kn})}{\varsigma_n}-\frac{iF_{rn}}{\varsigma_n^2}+(iF_{rn}h_{jkn}+b_{rn})h_{jkn}e^{-ih_{jkn}\varsigma_n}\Gamma(0,-ih_{jkn}\varsigma_n)\right] \tag{38}$$

where b_{rn} represents the component at the rth row and nth column in matrix $\mathbf{B}$.

5 Surface Green Function for a Surface Concentrated Line Force

When a concentrated line force is applied at $x_1=0$ in a surface of anisotropic half-domain ($x_3\le 0$), the surface Green function is easily obtained following the above analysis:

$$\mathbf{t}(x_1,x_2,0)=\mathbf{f}_2\delta(x_1) \tag{39}$$

where $\mathbf{f}_2=(f_1,f_2,f_3)$. Applying Fourier transform to Eq. (39) yields

$$\tilde{\mathbf{t}}(\eta_1,\eta_2,0)=\int_{-\infty}^{\infty}\int_{-\infty}^{\infty}\mathbf{f}_2\delta(x_1)e^{i(\eta_1x_1+\eta_2x_2)}dx_1dx_2=\mathbf{f}_2\delta(\eta_2) \tag{40}$$

Using Eq. (23) and solving this equation with respect to $\mathbf{q}$ yields

$$\mathbf{q}=\frac{i}{\rho}(\mathbf{B}+i\rho\mathbf{F})^{-1}\mathbf{f}_2\delta(\eta_2) \tag{41}$$

Substituting Eq. (41) into Eq. (23) yields

$$\tilde{\mathbf{u}}(\eta_1,\eta_2,x_3)=\frac{i}{\rho}\mathbf{A}\langle e^{-ip_*\rho x_3}\rangle(\mathbf{B}+i\rho\mathbf{F})^{-1}\mathbf{f}_2\delta(\eta_2)$$

$$\tilde{\mathbf{t}}(\eta_1,\eta_2,x_3)=(\mathbf{B}+i\rho\mathbf{F})\langle e^{-ip_*\rho x_3}\rangle(\mathbf{B}+i\rho\mathbf{F})^{-1}\mathbf{f}_2\delta(\eta_2) \tag{42}$$

Applying inverse Fourier transform to Eq. (42) yields

$$\mathbf{u}(x_1,x_3)=\frac{i}{4\pi^2}\int_{-\infty}^{\infty}\int_{-\infty}^{\infty}\frac{1}{\rho}\mathbf{A}\langle e^{-ip_*\rho x_3}\rangle(\mathbf{B}+i\rho\mathbf{F})^{-1}\mathbf{f}_2\delta(\eta_2)\times e^{-i(\eta_1x_1+\eta_2x_2)}d\eta_1d\eta_2$$

$$=\frac{i}{2\pi}\int_{-\infty}^{\infty}\frac{1}{\rho}\mathbf{A}\langle e^{-ip_*\rho x_3}\rangle(\mathbf{B}+i\rho\mathbf{F})^{-1}\mathbf{f}_2e^{-i\eta_1x_1}d\eta_1$$

$$=\frac{-1}{\pi}\,\mathrm{Im}\int_0^{\infty}\frac{1}{\eta_1}\mathbf{A}\langle e^{-ip_*\eta_1x_3}\rangle(\mathbf{B}+i\eta_1\mathbf{F})^{-1}\mathbf{f}_2e^{-i\eta_1x_1}d\eta_1$$

$$\mathbf{t}(x_1,x_3)=\frac{1}{\pi}\,\mathrm{Re}\int_0^{\infty}(\mathbf{B}+i\eta_1\mathbf{F})\langle e^{-ip_*\eta_1x_3}\rangle(\mathbf{B}+i\eta_1\mathbf{F})^{-1}\mathbf{f}_2e^{-i\eta_1x_1}d\eta_1 \tag{43}$$

The inverse matrix is then expanded and arranged with respect to ρ, which yields

$$\mathbf{u}(x_1,x_3)=\frac{-1}{\pi}\,\mathrm{Im}\int_0^{\infty}\mathbf{A}\langle e^{-i\eta_1(p_*x_3+x_1)}\rangle\mathbf{K}(\eta_1)\mathbf{f}_2d\eta_1$$

$$\mathbf{t}(x_1,x_3)=\frac{1}{\pi}\,\mathrm{Re}\int_0^{\infty}(\mathbf{B}+i\eta_1\mathbf{F})\langle e^{-i\eta_1(p_*x_3+x_1)}\rangle\mathbf{W}(\eta_1)\mathbf{f}_2 d\eta_1 \tag{44}$$

where $\mathbf{K}(\eta_1)=(\mathbf{B}+i\eta_1\mathbf{F})^{-1}/\eta_1$. Here, the element of matrix $\mathbf{K}$ can be expressed as

$$K_{lm}=\frac{k_{1lm}}{\eta_1}+k_{2lm}\sum_{j=1}^{3}\frac{v_{jlm}}{\eta_1-r_{jlm}} \tag{45}$$

The displacement and traction vectors are then deduced by integrating the first equation in Eq. (44).

$$u_j(x_1,x_3)=\frac{-1}{\pi}\,\mathrm{Im}\left[a_{jl}\left\{k_{1lm}\left\{\gamma_E-\ln(-(x_1+p_mx_3))+\frac{\pi}{2}i\right\}+k_{2lm}\sum_{j=1}^{3}v_{jlm}e^{-ir_{jlm}(x_1+p_mx_3)}\Gamma(0,-ir_{jlm}(x_1+p_mx_3))\right\}\right]f_m \tag{46}$$

$$\begin{aligned}t_r(x_1,x_3)&=\frac{1}{\pi}\,\mathrm{Re}\sum_{n=1}^{3}\sum_{j=1}^{3}\sum_{k=1}^{3}f_k\int_0^{\infty}(b_{rn}+i\eta_1F_{rn})\\&\quad\times\frac{w_{kn}g_{jkn}}{\eta_1-h_{jkn}}e^{-i\eta_1(p_kx_3+x_1)}d\eta_1\\&=\frac{1}{\pi}\,\mathrm{Re}\sum_{n=1}^{3}\sum_{j=1}^{3}\sum_{k=1}^{3}f_kw_{kn}g_{jkn}\left[\frac{F_{rn}}{x_1+p_kx_3}-(b_{rn}+iF_{rn}h_{jkn})\right.\\&\quad\left.\times e^{-ih_{jkn}(x_1+p_kx_3)}\Gamma(0,-ih_{jkn}(x_1+p_kx_3))\right]\end{aligned} \tag{47}$$

where γ_E represents Euler's constant, and w_{kn}, g_{jlm}, and h_{jlm} are the constants in Eq. (47).

6 Displacements and Stress Fields for a Half-Domain of [111] Surfaces

6.1 Mechanical Property of [111] Surface. First, surface stress and surface elastic moduli are calculated using MD. Here, the material used in the analysis is Fe. The Finnis–Sinclair (FS) potential function [35] is used to calculate the interatomic force. The FS potential function for Fe is expressed as follows:

$$E_{\mathrm{tot}}=\frac{1}{2}\sum_{\gamma\neq\eta}V(r^{\gamma\eta})-A\sum_{\gamma}F(\rho^{\gamma}) \tag{48}$$

where $r^{\gamma\eta}$ is the distance between atoms γ and η, $F(\rho)$ is an embedded atom function and is expressed as $F(\rho^{\gamma})=\sqrt{\rho^{\gamma}}$, and ρ^{γ} is the electron density and is given by $\rho^{\gamma}=\Sigma_{\eta}\phi(r^{\gamma\eta})$. Furthermore, $V(r)$ and $F(r)$ are the contributions of repulsion force between an atom and the electron density. Here, $V(r)$ and $\phi(r)$ are expressed by the following equations:

$$\phi(r)=\sum_{k=1}^{2}A_k(R_k-r)^3H(R_k-r) \tag{49}$$

$$V(r)=\sum_{k=1}^{6}a_k(r_k-r)^3H(r_k-r) \tag{50}$$

where $H(r)$ is the Heaviside step function, $a_1=-36.559853$ eV, $a_2=62.416005$ eV, $a_3=-13.155649$ eV, $a_4=-2.721376$ eV, $a_5=8.761986$ eV, $a_6=100.0$ eV, $A_1=1.08$ eV, $A_2=0.99$ eV, $R_1=1.18a_0$, $R_2=1.15a_0$, $r_1=0.93a_0$, $r_2=0.866025a_0$, $r_3=72.868366a_0$, $r_4=-100.944815a_0$, $r_5=1.3a_0$, $r_6=1.2a_0$, and a_0(=0.28665 nm) is the lattice constant of Fe.

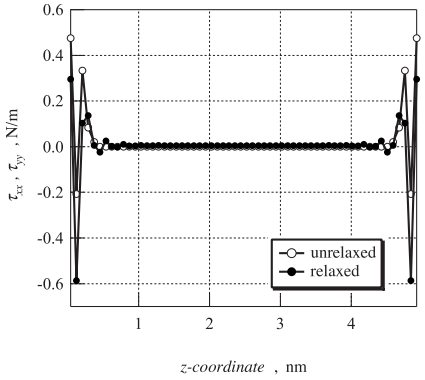

Fig. 1 Layer decomposition of the two components of the surface stress tensor

Surface stress can be calculated using interpotential energy, u_i, for one atom in a unit cell, as follows:

$$\tau_{\alpha\beta}=\frac{1}{A_c}\sum_i\frac{\partial u_i}{\partial\varepsilon_{\alpha\beta}} \tag{51}$$

where $U_c=\Sigma u_i$, U_c is the surface energy per cell, i is an atom, α and β are the directions of the coordinates, and A_c is the surface area of a unit cell.

The model for analysis is consisted of 60 atomic layers in the z-direction for calculating the surface stress tensor and surface elastic moduli. The sizes of the unit cell are 2.809 nm in the x-direction, 1.622 nm in the y-direction, and 4.965 nm in the z-direction. Here, (x_1,x_2,x_3) corresponds to (x,y,z). In the relaxation procedure of MD, the temperature in the system increases from 0 K at the initial state, to 1.0 K at 1000 steps, and remains at 1.0 K until 3000 steps. The temperature then decreases to 0 K at 8000 steps and remains at 0 K until 10000 steps. After the relaxation, the surface stress is calculated using Eq. (51) following Ackaland et al. [36].

Figure 1 shows the variation of surface stress with the distance from the surface. The surface stress is not localized only at the surface, and, as is often the case, the stress profile is oscillating within 1 nm from the surface, i.e., tension, compression, tension, and so on. By algebraic sum, the surface stress tensors for Fe are obtained as $\tau_{xx}=\tau_{yy}=-0.357$ N/m and $\tau_{xy}=0$. Furthermore, surface elastic moduli, $d_{\alpha\beta\gamma\lambda}$, are determined following Izumi et al. [37] and the values of elastic moduli used in the analysis are shown in Tables 1 and 2, respectively. Here, transformation between C_{ijks} and $C_{\alpha\beta}$ is accomplished by replacing the subscripts ij (or ks) by α (or β) using the following rules: ij (or ks) 11 to α (or β) 1, 22 to 2, 33 to 3, 23 or 32 to 4, 31 or 13 to 5, and 12 or 21 to 6.

6.2 Elastic Fields for a Normal Force f_z in a Half-Domain With the Surface [111]. First, the distributions of the displacement and the stress component for $f_z=1$ nN acting at the origin are calculated using Eqs. (35) and (37), as shown in Figs. 2(*a*)–2(*d*). The mapped area is $-10\ \mathrm{nm}\leq x\leq 10$ nm and -10 nm $\leq z\leq -0.1$ nm at $y=0$. Figures 2(*a*) and 2(*b*) show the distributions of displacements u_x and u_z. The results considering and ignoring the surface stress and surface elasticity are represented by

Table 1 Surface elastic moduli (N/m)

d_{1111}	d_{2222}	d_{1122}	d_{1212}
−14.27	−14.27	−4.39	−4.94

Table 2 Material properties used in analysis (GPa)

C_{11}	C_{12}	C_{13}	C_{15}	C_{22}	C_{23}	C_{25}	C_{33}	C_{44}	C_{46}	C_{55}	C_{66}
300.09	111.583	97.257	20.261	300.09	97.257	−20.261	314.417	79.927	−20.261	79.927	94.253

a solid line and a dashed line, respectively. Both distributions in the mapped area are in good agreement. The displacement u_x is asymmetric with respect to the y-axis due to the crystal anisotropy of the surface [111]. The maximum values of u_x are 2.54×10^{-3} nm and 2.70×10^{-3} nm, respectively, when considering and ignoring the surface stress and surface elasticity. The maximum values of u_z are 2.22×10^{-2} nm and 2.46×10^{-2} nm, respectively, when considering and ignoring the surface stress and surface elasticity. The maximum difference in u_x between these results occurs near the surface around the acting position of the force. Figures 2(c) and 2(d) show the distributions of stresses σ_{xz} and σ_{zz}, respectively The distributions of stress, σ_{zz}, when considering and ignoring the surface stress and surface elasticity are slightly different but those of σ_{xz} are approximately the same at the location far from the surface. The maximum values of σ_{zz} are 53.0 Pa and 64.4 Pa, respectively, when considering and ignoring surface stress and surface elasticity. The maximum value when considering the surface stress and surface elasticity is lower than that when ignoring the surface stress and surface elasticity. The maximum stress occurs at the location at which f_z acts.

Next, the elastic fields near the surface [111] are investigated for various values of surface stress and surface elasticity. The elastic fields are calculated using the surface elastic moduli shown in Table 1 for various values of surface stress, i.e., $m\tau_{\alpha\beta}$. Figures 3(a)–3(d) show the distributions of the displacement and stress at $y=0$ and $z=-0.05$ nm for several values of m. In this analysis, a force of 1.0 nN is applied at the origin in the z-direction. Figures 3(a) and 3(b) show the influence of m for surface stress on u_x and u_z, respectively. The influence of surface stress on the displacement, u_x, is less than that on the displacement u_z. In particular, when m increases, surface stress has a significant effect on u_z near the loading point. The displacements when ignoring the surface stress and surface elasticity are larger than those when considering the surface stress and surface elasticity. However, even if m varies greatly, u_x does not vary greatly. Surface stress affects the bulk stress, σ_{zz}, through the curvature of the surface and so suppresses deformation in the normal direction more than in the tangential direction.

Figures 3(c) and 3(d) show the distributions of σ_{xz} and σ_{zz} along the x-axis. In contrast to the effect of m on the displacements, σ_{xz} is affected greatly by the variation of m for surface stress. Figure 3(a) shows that the strain, ε_{xx}, deduced from the derivative of u_x with respect to x becomes large with decreasing m. Hence, when m decreases, $d_{ijkl}\varepsilon_{kl}$ in Eq. (17) increases significantly, and the bulk stress, σ_{xz}, then becomes large. The variation of stress, σ_{zz}, for m is small. Since the curvature of the surface, $\partial^2 u_z / \partial x^2$, becomes small with increasing surface stress multiplied by m, the product of the curvature and surface stress becomes approximately constant. Here, the difference between the result for small m and that for no surface stress or surface elasticity is attributed to the surface elasticity.

Figures 4(a)–4(d) show the distributions of displacement and stress at $y=0$ and $z=-0.05$ nm for several values of m. Here, the elastic fields are calculated while maintaining the surface stress as $\tau_{xx}=\tau_{yy}=-0.357$ N/m, $\tau_{xy}=0$ for various values of surface elasticity, i.e., md_{ijkl}. The influence of m on u_x is shown in Fig. 4(a), and u_x becomes small with increasing m in the same manner, as shown in Fig. 3(a). However, u_x is affected by the variation of m for surface elasticity more than that for surface stress. Figure 4(b) shows a semilog plot of u_z with respect to the x-coordinate. Displacement u_z is suppressed by the surface stress and surface elas-

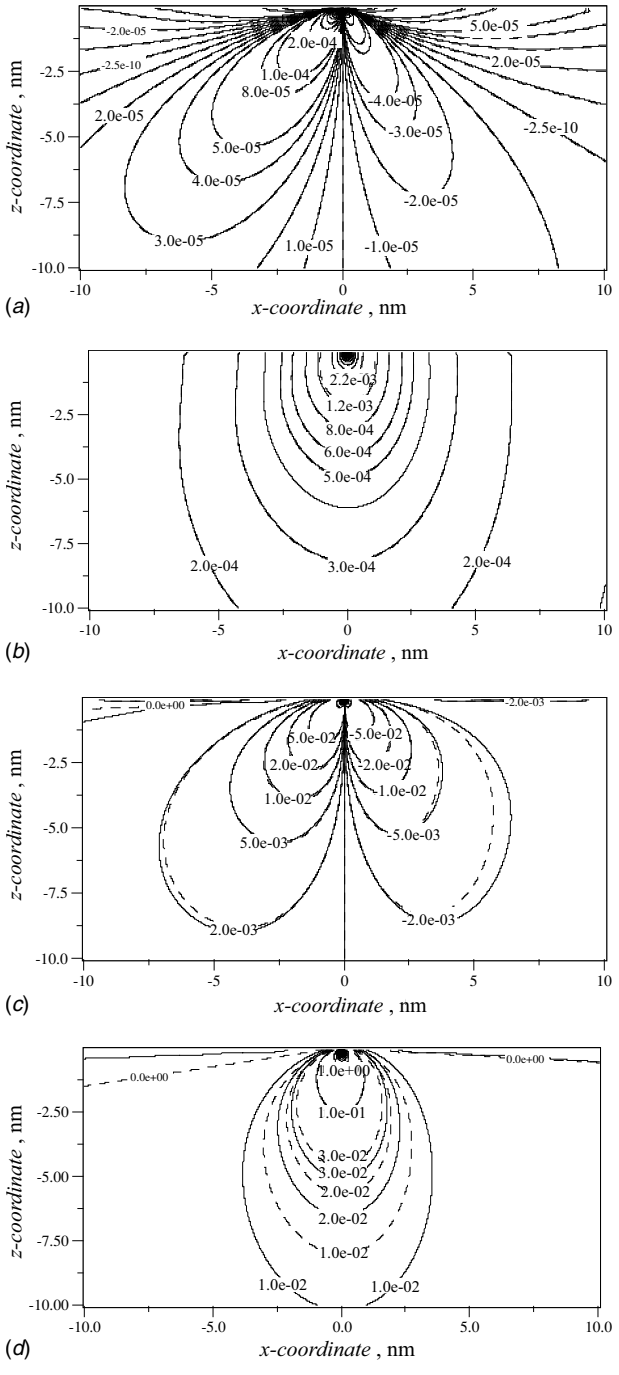

Fig. 2 Distributions of displacement and stress at $y=0$ for $f_z=1.0$ nN. (*a*) Displacement u_x (surface stress and elasticity: solid line, Min: -1.37×10^{-3} nm, Max: 2.54×10^{-3} nm, no surface stress or elasticity: dashed line, Min: -1.50×10^{-3} nm, Max: 2.70×10^{-3} nm). (*b*) Displacement u_z (surface stress and elasticity: solid line, Max: 2.22×10^{-2} nm, no surface stress or elasticity: dashed line, Max: 2.46×10^{-2} nm). (*c*) Stress σ_{xz} (surface stress and elasticity: solid line, Min: −13.9 Pa, Max: 15.5 Pa, no surface stress or elasticity: dashed line, Min: −12.4 Pa, Max: 14.1 Pa). (*d*) Stress σ_{zz} (surface stress and elasticity: solid line, Min: −0.03 Pa, Max: 53 Pa, no surface stress or elasticity: dashed line, Min: −0.04 Pa, Max: 64.4 Pa).

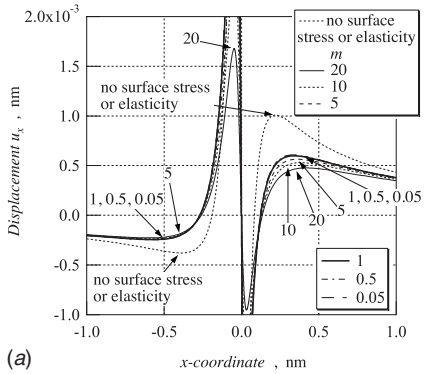

(*a*)

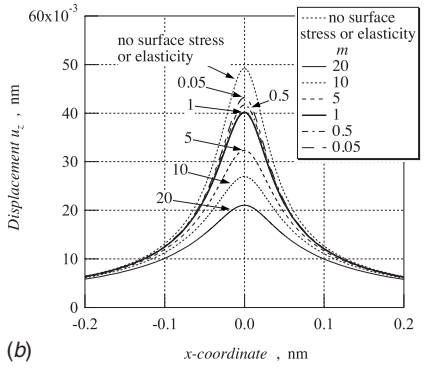

(*b*)

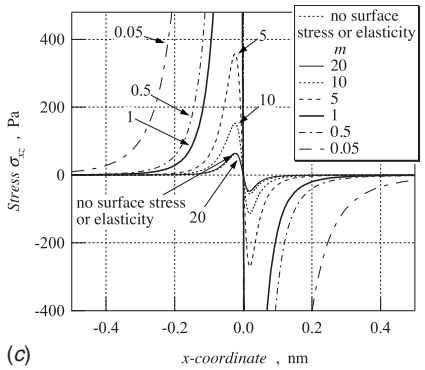

(*c*)

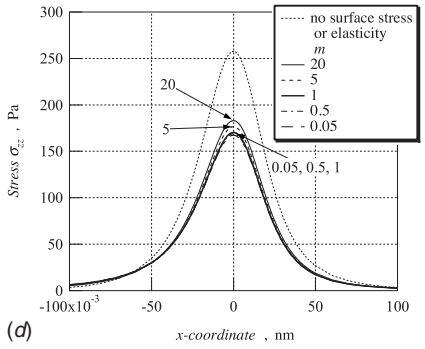

(*d*)

Fig. 3 Distribution of displacements and stresses for various *m* values of surface stress along the *x*-axis at *y*=0 and *z* =−0.05 nm for f_z=1.0 nN. (*a*) displacement u_x; (*b*) displacement u_z; (*c*) stress σ_{xz}; (*d*) stress σ_{zz}.

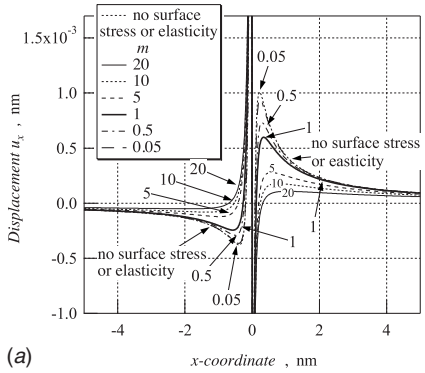

(*a*)

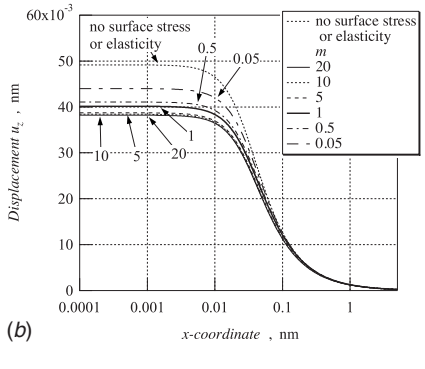

(*b*)

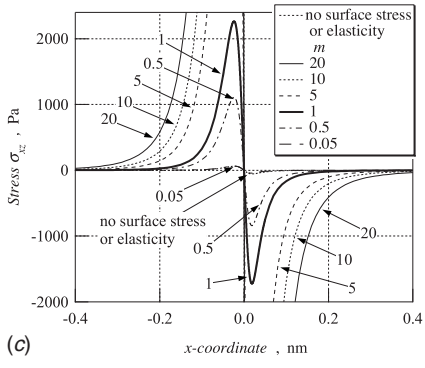

(*c*)

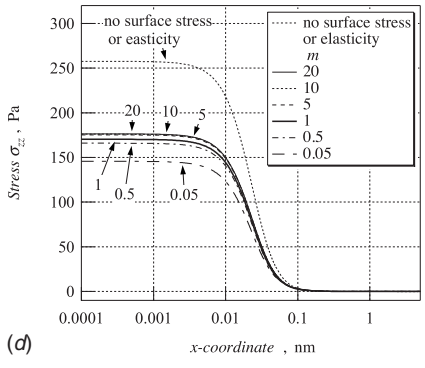

(*d*)

Fig. 4 Distribution of displacements and stresses for various *m* values of surface elasticity along the *x*-axis at *y*=0 and *z* =−0.05 nm for f_z=1.0 nN. (*a*) Displacement u_x; (*b*) displacement u_z; (*c*) stress σ_{xz}; (*d*) stress σ_{zz}.

ticity and is approximately constant within 0.01 nm of the *x*-coordinate. The effect of *m* for surface elasticity on u_z is less than that for surface stress. The distribution of bulk stress, σ_{xz}, is shown in Fig. 4(*c*). In contrast with the results shown in Fig. 3(*c*), σ_{xz} increases with increasing *m* and approaches the stress distribution considering surface stress only as *m* decreases. This is due to the amplification of *m* of the surface elasticity, i.e., $md_{ijkl}\varepsilon_{kl}$ in Eq. (17). Figure 4(*d*) shows a semilog plot of the bulk stress, σ_{zz}, with respect to the *x*-coordinate. Stress, σ_{zz}, reduces slightly with decreasing *m*. This is due to the increase of curvature, $\partial^2 u_z/\partial x^2$, with decreasing *m*, as shown in Fig. 4(*b*). When the curvature

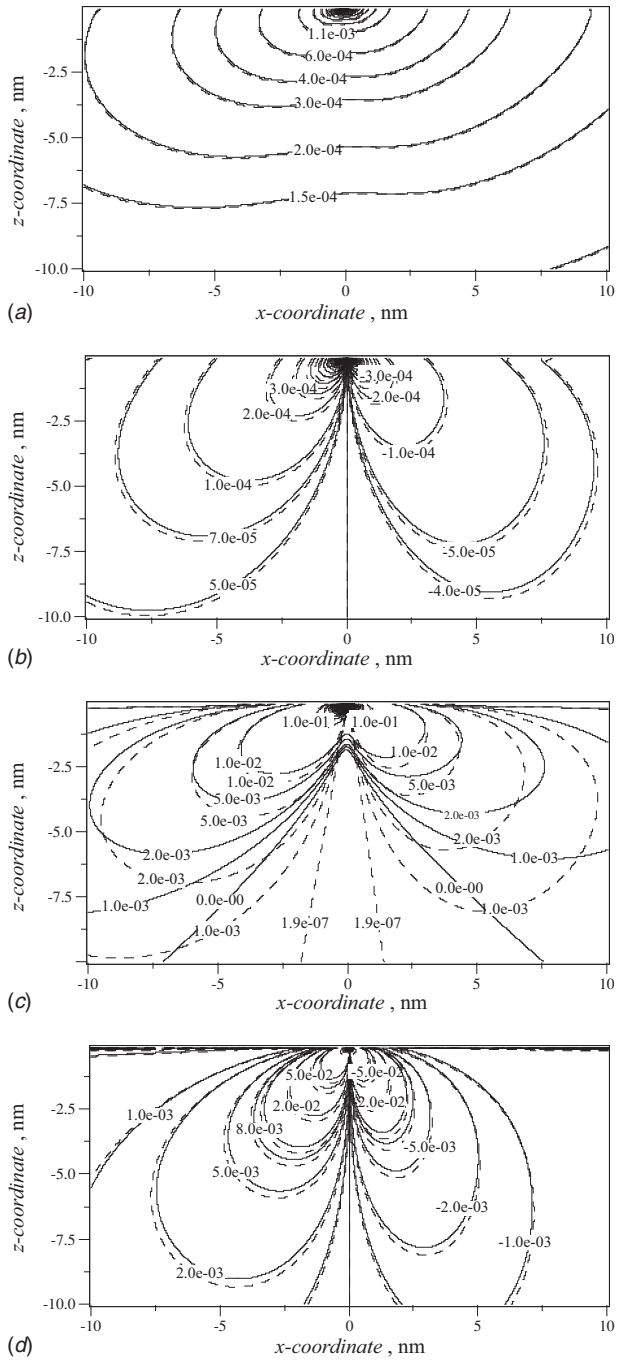

Fig. 5 Distributions of displacement and stress at $y=0$ for $f_x=1.0$ nN. (*a*) displacement u_x (surface stress and elasticity: solid line, Max: 8.27×10^{-3} nm, no surface stress or elasticity: dashed line, Max: 1.16×10^{-2} nm). (*b*) Displacement u_z (surface stress and elasticity: solid line, Min: -1.34×10^{-3} nm, Max: 1.97×10^{-3} nm, no surface stress or elasticity: dashed line, Min: -3.72×10^{-3} nm, Max: 4.98×10^{-3} nm). (*c*) Stress σ_{xz} (surface stress and elasticity: solid line, Min: −0.0053 Pa, Max: 9.30 Pa, no surface stress or elasticity: dashed line, Min: −1.60 Pa, Max: 9.60 Pa). (*d*) Stress σ_{zz} (surface stress and elasticity: solid line, Min: −4.0 Pa, Max: 6.38 Pa, no surface stress or elasticity: dashed line, Min: −31.0 Pa, Max: 40.0 Pa).

becomes large, σ_{zz} is suppressed because the product of the curvature and the surface stress becomes large. Here, the surface stress does not vary.

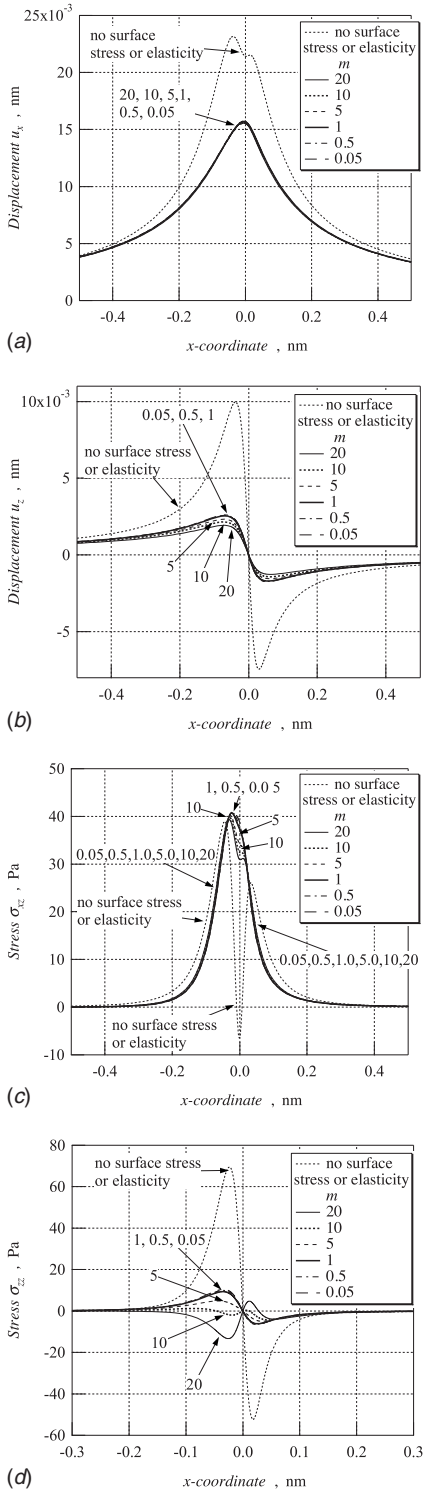

Fig. 6 Distribution of displacements and stresses for various *m* values of surface stress along the *x*-axis at $y=0$ and $z=-0.05$ nm for $f_x=1.0$ nN. (*a*) Displacement u_x; (*b*); displacement u_z; (*c*); stress σ_{xz}; (*d*) Stress σ_{zz}.

6.3 Elastic Fields for a Tangential Force f_x in a Half-Domain With the Surface [111]. The distributions of displacements and stress components for $f_x=1$ nN acting at the origin are shown in Figs. 5(*a*)–5(*d*). Figures 5(*a*) and 5(*b*) show the distributions of displacements u_x and u_z. Both distributions in the mapped area are in fairly good agreement. The maximum values of u_x are 8.27×10^{-3} nm and 1.16×10^{-2} nm, respectively, when

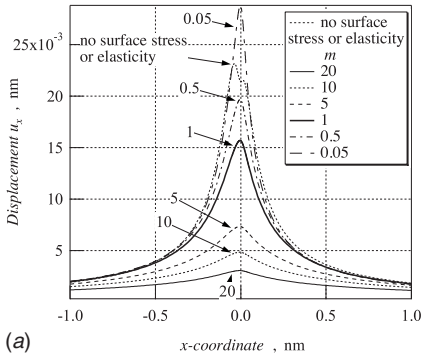

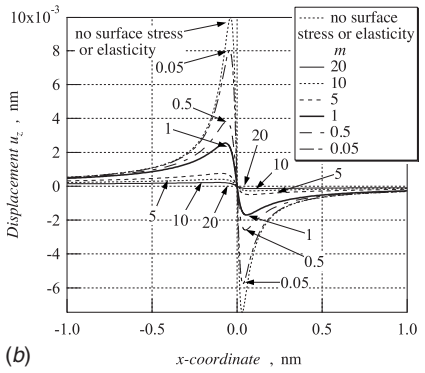

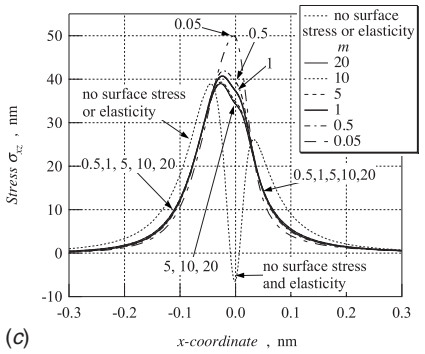

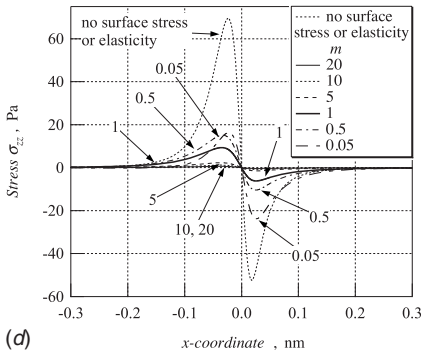

Fig. 7 Distribution of displacements and stresses for various *m* values of surface elasticity along the *x*-axis at $y=0$ and $z=-0.05$ nm for $f_x=1.0$ nN. (*a*) Displacement u_x; (*b*) displacement u_z; (*c*) stress σ_{xz}; (*d*) stress σ_{zz}.

considering and ignoring the surface stress and surface elasticity. The maximum values of u_z are 1.97×10^{-3} nm and 4.98 $\times10^{-3}$ nm, respectively, when considering and ignoring the surface stress and surface elasticity. Figures 5(*c*) and 5(*d*) show the distributions of stresses σ_{xz} and σ_{zz}, respectively. The distributions of stress, σ_{xz}, when considering and ignoring the surface stress

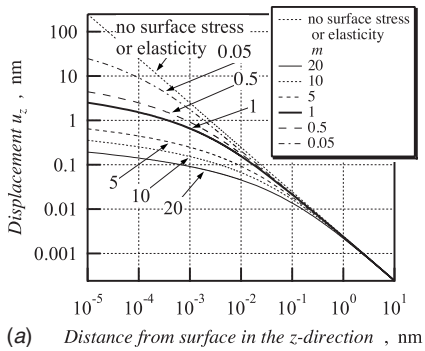

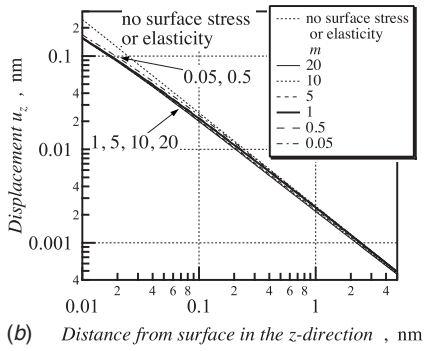

Fig. 8 Distribution of displacement, u_x, for $f_z=1$ nN against the distance from the surface. (*a*) Displacement, u_z, for various *m* values of surface stress; (*b*) Displacement, u_z, for various *m* values of surface elasticity.

and surface elasticity are slightly different, except around the origin, but those of σ_{zz} are approximately the same. The maximum values of σ_{zz} are 6.4 Pa and 40.0 Pa, respectively, when considering and ignoring the surface stress and surface elasticity. The maximum value when considering the surface stress and surface elasticity is lower than that when ignoring the surface stress and surface elasticity.

The stress distributions of σ_{zz} for f_z and σ_{xz} for f_x are influenced noticeably by the surface stress and surface elasticity. Note that these stress components are closely related to the direction of the external forces from Eqs. (4) and (5).

Next, the elastic fields are calculated using the surface elastic moduli shown in Table 1 for various values of surface stress, i.e., $m\tau_{\alpha\beta}$. Figures 6(*a*)–6(*d*) show the distributions of displacement and stress along the *x*-axis at $y=0$ and $z=-0.05$ nm. Even if *m* of

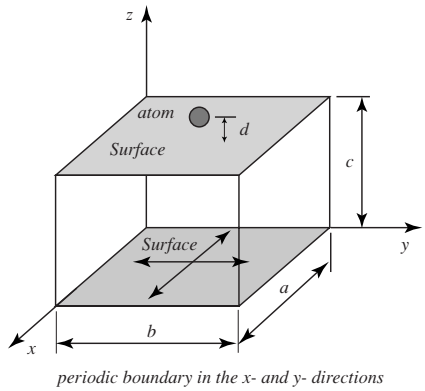

Fig. 9 Model for MD analysis with an atom on the surface. The dimensions of this model are $a=14.74$ nm, $b=14.994$ nm, $c=10.4995$ nm, and $d=0.27$ nm. The total number of atoms is 186,481.

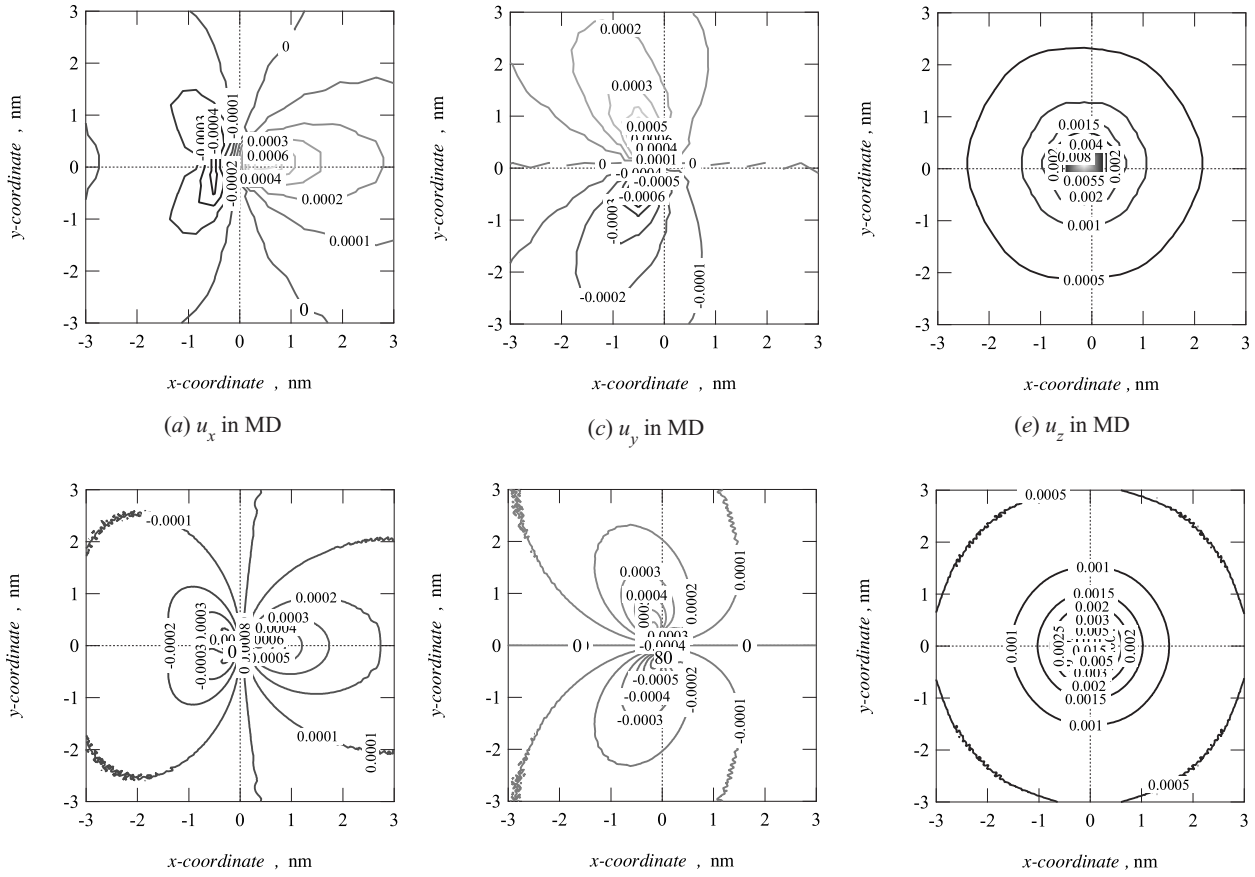

Fig. 10 Comparison of displacements for f_z=1.21 nN in the z=−0.05 nm plane

surface stress is varied, u_x and u_z vary only slightly. It is assumed that the displacements are only slightly affected by the variation of surface stress due to the tangential force. As mentioned before, surface stress affects the bulk normal stress through the surface curvature, and the tangential force is not directly related to the normal stress. Hence, u_x varies only slightly with the variation of m. As shown in Fig. 6(c), even if m is varied significantly, σ_{xz} varies only slightly. However, the distribution near the loading point when considering the surface stress and surface elasticity is significantly different than that when ignoring the surface stress and surface elasticity. The distribution of σ_{zz} shown in Fig. 6(d) reverses gradually with respect to the origin with varying the m value. This change is attributed to surface stress, because the product of the surface stress, $m\tau_{\alpha\beta}$, and the curvature becomes large due to a small variation of curvature with the increase of m. Furthermore, these results indicate that surface elasticity significantly influences the distributions of displacement and stress.

Figures 7(a)–7(d) show the displacements and stresses calculated holding the value of surface stress for various values of surface elasticity, i.e., md_{ijkl}. These results are obtained at y=0 and z=−0.05 nm. Both u_x and u_z are reduced with increasing m. As m decreases, the displacement when considering the surface stress and surface elasticity approaches that when ignoring the surface stress and surface elasticity. Figure 7(c) shows the distribution of stress, σ_{xz}, along the x-axis. Stress, σ_{xz}, does not vary much with the variation of m. Figure 7(a) shows that when m becomes large, strain ε_{xx} near the surface decreases. Hence, stress σ_{xz} does not vary significantly with m, because the product of ε_{xx} and the surface elastic modulus does not vary. Stress, σ_{zz}, shown in Fig. 7(d) decreases as m increases. This is due to the decrease in surface curvature with the increase of m, because σ_{zz} is directly related to the curvature and surface stress. Here, the surface stress does not vary.

6.4 Distribution of u_z for f_z Against the Distance From the Surface. Figure 8 shows a log-log plot of displacement u_z for f_z =1 nN at x=y=0 with respect to the distance from the surface. Figure 8(a) shows the result calculated using the value of surface elasticity for various values of surface stress. Displacement u_z was found to be influenced significantly by surface stress. Displacement u_z when considering surface stress and surface elasticity increases as the surface is approached. However, u_z when considering the surface stress and surface elasticity becomes smaller than that when ignoring the surface stress and surface elasticity. Figure 8(b) shows the result calculated using the value of surface stress for various values of surface elasticity. Figure 8(b) shows that even if the surface elasticity is varied, u_z varies only slightly. Figure 8(a) shows that the influence of surface stress on u_z is significant within 1 nm from the surface. This result is in agreement with the distance from the surface obtained while varying the surface stress, as shown in Fig. 1.

6.5 Comparison of Displacement Fields in MD and the Surface Green Function. Figure 9 shows a model in which an atom is fixed at a position of z=d from the surface. The atom is placed near an atom in the surface. Here, d is 0.27 nm, and the location is slightly farther than the distance between layers of 0.2482 nm. Figure 10 shows the displacement fields calculated using MD and the surface Green function. The results for MD may be affected slightly by the periodic boundary condition in the

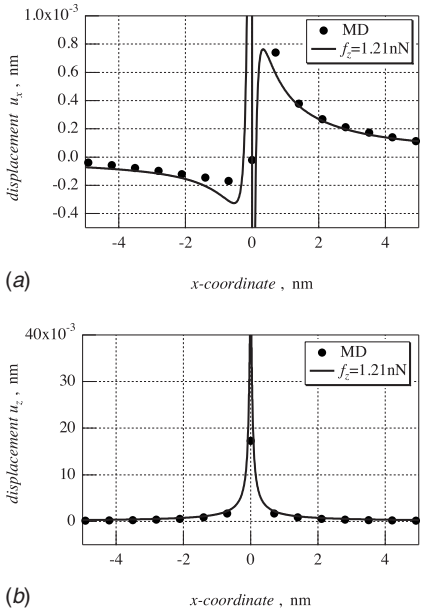

Fig. 11 Comparison of the displacement in MD and the surface Green function considering surface stresses and surface elasticity. (The solid line is the displacement at $z=-0.05$ nm.) (*a*) Displacement u_x; (*b*) displacement u_z.

x- and y-directions. The displacement for the Green function is at $z=-0.05$ nm for $f_z=1.21$ nN. Figures 10(*a*) and 10(*b*) show the displacement field of u_x. The deformation of approximately $x=-3$ nm shown in Fig. 10(*a*) may be due to the periodic boundary condition. Neglecting the influence of the boundary condition, the entire distributions of u_x in MD and the Green function are in approximate agreement. Figures 10(*c*) and 10(*d*) demonstrate the displacement fields of u_y, and these results are affected slightly by the periodic boundary condition. The entire distribution of u_y for MD may shift to the left side of the domain. Figures 10(*e*) and 10(*f*) show the displacement fields of u_z. The displacement field in MD forms a hexagonal shape reflecting the position of surface atoms. On the other hand, the displacement field in the Green function is almost circular. The plane distributions of u_x, u_y, and u_z in both methods are in fairly good agreement. Figures 11(*a*) and 11(*b*) show the x-z cross section at $y=0$ of the distributions in the MD and the surface Green function. The solid circle and the thick line indicate the results for the MD and the Green function, respectively. The obtained results are also in agreement with each other.

The derived Green functions can include the effect of the surface on the mechanical behavior of anisotropic materials, and it is hoped that these Green functions will be applied for analyzing the nanocontact between an indenter and an anisotropic substrate and developing an adhesion theory such as the Johnson-Kendall-Roberts (JKR) theory [38] in a nanoscale.

7 Conclusion

In the present paper, three-dimensional surface Green functions in anisotropic half-domains for a concentrated force and a line force were derived considering surface stresses and surface elasticity based on Stroh's formalism. The boundary condition considering the anisotropy of surface stress and surface elasticity was deduced. The surface Green function for a line force was derived in a closed form. The influence of surface stress and surface elasticity on displacements and stresses were investigated precisely for the normal and tangential forces to the surface, and the displacements and stresses frequently vary inversely with the variation in the values of surface stress and surface elasticity. The displacement fields obtained from the Green function for a concentrated force and MD were compared, and the derived Green function was shown to express the characteristics of displacement fields in MD calculation.

Acknowledgment

The author would like to thank Mr. Sakurai and Mr. Miura for their assistance in conducting this study. This research was supported by Grant-in-Aid for Scientific Research (No. 90173693).

References

[1] Ibach, H., 1997, "The Role of Surface Stress in Reconstruction, Epitaxial Growth and Stabilization of Mesoscopic Structures," Surf. Sci. Rep., **29**, pp. 195–263.
[2] Muller, P., and Saul, A., 2004, "Elastic Effects on Surface Physics," Surf. Sci. Rep., **54**, pp. 157–258.
[3] Gao, Y. F., and Suo, Z., 2003, "The Orientation of the Self-Assembled Monolayer Stripes on a Crystalline Substrate," J. Mech. Phys. Solids, **51**, pp. 147–167.
[4] Marchenko, V. I., and Parshin, A. Ya., 1980, "Elastic Properties of Crystal Surfaces," Sov. Phys. JETP, **52**, pp. 129–131.
[5] Alerhand, O. L., Vanderbilt, D., Meade, R. D., and Joannopoulos, J. D., 1988, "Spontaneous Formation of Stress Domains on Crystal Surfaces," Phys. Rev. Lett., **61**(17), pp. 1973–1976.
[6] Shilkot, L. E., and Srolovitz, D. J., 1996, "Elastic Field of a Surface Step: Atomistic Simulations and Anisotropic Elastic Theory," Phys. Rev. B, **53**(16), pp. 11120–11127.
[7] Kukta, R. V., Peralta, A., and Kouris, D., 2002, "Elastic Interaction of Surface Steps: Effect of Atomic-Scale Roughness," Phys. Rev. Lett., **88**(18), 186102.
[8] Kukta, R., Peralta, A., and Kouris, D., 2002, "Surface Step: From Atomistics to Continuum," ASME J. Appl. Mech., **69**, pp. 443–450.
[9] Kukta, R. V., and Bhattacharya, K., 2002, "A Micromechanical Model of Surface Steps," J. Mech. Phys. Solids, **50**, pp. 615–649.
[10] Shenoy, V. B., and Ciobanu, C. V., 2004, "Orientation Dependence of the Stiffness of Surfaces Steps: An Analysis Based on Anisotropic Elasticity," Surf. Sci., **554**, pp. 222–232.
[11] Gurtin, M. E., and Murdoch, A. I., 1975, "A Continuum Theory of Elastic Material Surfaces," Arch. Ration. Mech. Anal., **57**, pp. 291–323.
[12] Gurtin, M. E., and Murdoch, A. I., 1978, "Surface Stress in Solids," Int. J. Solids Struct., **14**, pp. 431–440.
[13] Gurtin, M. E., Weissmüller, J., and Larché, F., 1998, "A General Theory of Curved Deformable Interfaces in Solids at Equilibrium," Philos. Mag. A, **78**(5), pp. 1093–1109.
[14] Thomson, R., Chuang, T.-J., and Lin, I.-H., 1986, "The Role of Surface Stress in Fracture," Acta Metall., **34**(6), pp. 1133–1143.
[15] Koguchi, H., 1992, "Stress Analysis for Nano-Scaled Elastic Materials (1st Report, Formulation of Boundary Condition for Interface With Surface Stress)," Trans. Jpn. Soc. Mech. Eng., Ser. A, **58**(555), pp. 2132–2137.
[16] Koguchi, H., 1996, "Stress Analysis for Nano-Scaled Elastic Materials (Elastic Contact Problems Considering Surface Stresses)," JSME Int. J., Ser. A, **39**(3), pp. 3337–3345.
[17] Koguchi, H., 2003, "Surface Deformation Indecued by A Variation in Surface Stresses in Anisotropic Half-Regions," Philos. Mag., **83**(10), pp. 1205–1226.
[18] Koguchi, H., 1997, "Fundamental Solution for a Prismatic Dislocation Loop in a Two-Phase Transversely Isotropic Elastic Material Considering Interfacial Energy," Trans. Jpn. Soc. Mech. Eng., Ser. A, **63**(615), pp. 2417–2423.
[19] Koguchi, H., 2000, "Characteristics of Surface Wave Propagation at Nanometer Range of Wave Length," Trans. Jpn. Soc. Mech. Eng., Ser. A, **66**(645), pp. 1030–1038.
[20] Koguchi, H., 2004, "Contact and Adhesion Analysis Considering a Variation of Surface Stresses (1st Report, A Comparison of Fundamental Theory and Hertz Theory)," Trans. Jpn. Soc. Mech. Eng., Ser. A, **70**(690), pp. 289–297.
[21] Koguchi, H., 2004, "Contact and Adhesion Analysis Considering a Variation of Surface Stresses (2nd Report, A Comparison of The Present Theory and JKR Theory)," Trans. Jpn. Soc. Mech. Eng., Ser. A, **70**(697), pp. 1332–1340.
[22] Duan, H. L., Wang, J., Huang, Z. P., and Karihaloo, B. L., 2005, "Size-Dependent Effective Elastic Constants of Solids Containing Nano-Inhomogeneities With Interface Stress," J. Mech. Phys. Solids, **53**, pp. 1574–1596.
[23] Duan, H. L., Wang, J., Huang, Z. P., and Karihaloo, B. L., 2005, "Eshelby Formalism for Nano-inhomogeneities," Proc. R. Soc. London, Ser. A, **461**, pp. 3335–3353.
[24] He, L. H., and Lim, C. W., 2006, "Surface Green Function for a Soft Elastic Half-Space: Influence of Surface Stress," Int. J. Solids Struct., **43**, pp. 132–143.
[25] He, L. H., and Li, Z. R., 2006, "Impact of Surface Stress on Stress Concentration," Int. J. Solids Struct., **43**, pp. 6208–6219.
[26] Mi, C., and Kouris, D. A., 2006, "Nanoparticles Under the Influence of Surface/Interface Elasticity," J. Mech. Mater. Struct., **1**(4), pp. 763–792.
[27] Mi, C., and Kouris, D. A., 2007, "The Role of Interface Stress for Nanoparticles Embedded in Films," Journal of Solid Mechanics and Materials Engineering, **1**(10), pp. 1219–1230.
[28] Wu, K.-C., 1998, "Generalization of the Stroh Formalism to 3-Dimensional

Anisotropic," J. Elast., **51**, pp. 213–225.
[29] Ting, T. C. T., 1992, "Image Singularities of Green's Functions for Anisotropic Elastic Half-Spaces and Bimaterials," Q. J. Mech. Appl. Math., **45**, pp. 119–139.
[30] Ting, T. C. T., and Lee, V.-G., 1997, "The Three-Dimensional Elatostatic Green's Function for General Anisotropic Linear Elastic Solids," Q. J. Mech. Appl. Math., **50**(3), pp. 407–426.
[31] Ting, T. C. T., 1996, *Anisotropic Elasticity: Theory and Application*. Oxford University Press, New York.
[32] Yang, B., and Pan, E., 2001, "Three-Dimensional Green's Functions in Anisotropic Trimaterials," Int. J. Solids Struct., **39**, pp. 2235–2255.
[33] Dingreville, R., Qu, J., and Cherkaoui, M., 2005, "Surface Free Energy and Its Effect on the Elastic Behavior of Nano-Sized Particles, Wires and Films," J. Mech. Phys. Solids, **53**, pp. 1827–1854.
[34] Willis, J. R., 1965, "The Elastic Interaction Energy of Dislocation Loops in Anisotropic Media," Q. J. Mech. Appl. Math., **18**, pp. 419–433.
[35] Finnis, M. W., and Sinclair, J. E., 1984, "A Simple Empirical n-Body Potential for Transition Metals," Philos. Mag. A, **50**(1), pp. 45–55, 1986, Philos. Mag. A, **53**(1), p. 161(E).
[36] Ackland, G. J., and Finnis, M. W., 1986, "Semi-Empirical Calculation of Solid Surface Tensions in b.c.c. Transition Metals," Philos. Mag. A, **54**, pp. 301–315.
[37] Izumi, S., Hara, S., Kumagai, T., and Sakai, S., 2004, "A Method for Calculating Surface Stress and Surface Elastic Constants by Molecular Dynamics: Application to the Surface of Crystal and Amorphous Silicon," Thin Solid Films, **467**, pp. 253–260.
[38] Johnson, K. L., Kendall, K., and Roberts, A. D., 1971, "Surface Energy and Contact of Elastic Solids," Proc. R. Soc. London, Ser. A, **324**, pp. 301–342.

Youn-Sha Chan
Department of Computer and Mathematical Sciences,
University of Houston-Downtown,
One Main Street,
Houston, TX 77002

Glaucio H. Paulino
Department of Civil and Environmental Engineering,
University of Illinois,
2209 Newmark Laboratory,
205 North Mathews Avenue,
Urbana, IL 61801

Albert C. Fannjiang
Department of Mathematics,
University of California,
Davis, CA 95616

Gradient Elasticity Theory for Mode III Fracture in Functionally Graded Materials—Part II: Crack Parallel to the Material Gradation

A Mode-III crack problem in a functionally graded material modeled by anisotropic strain-gradient elasticity theory is solved by the integral equation method. The gradient elasticity theory has two material characteristic lengths ℓ and ℓ', which are responsible for volumetric and surface strain-gradient terms, respectively. The governing differential equation of the problem is derived assuming that the shear modulus G is a function of x, i.e., $G=G(x)=G_0e^{\beta x}$, where G_0 and β are material constants. A hypersingular integro-differential equation is derived and discretized by means of the collocation method and a Chebyshev polynomial expansion. Numerical results are given in terms of the crack opening displacements, strains, and stresses with various combinations of the parameters ℓ, ℓ', and β. Formulas for the stress intensity factors, K_{III}, are derived and numerical results are provided. [DOI: 10.1115/1.2912933]

1 Introduction

This work is a continuation of the paper on "Gradient Elasticity Theory for Mode III Fracture in Functionally Graded Materials—Part I: Crack Perpendicular to the Material Gradation" by Paulino et al. [1] (hereinafter referred to as Part I). In Part I, the authors considered a plane elasticity problem in which the medium contains a finite crack on the $y=0$ plane and the material gradation is perpendicular to the crack. In "Part II," the material gradation is parallel to the crack (see Fig. 1). In Part I, the shear modulus G (that rules the material gradation) is a function of y only, $G \equiv G(y)=G_0e^{\gamma y}$; while in Part II, it is a function of x, i.e., $G \equiv G(x)=G_0e^{\beta x}$. An immediate consequence of the difference in geometry, which is indicated in Fig. 1, is that the location of the crack in Part I is rather irrelevant to the problem and thus can be shifted so that the center is at the origin point (0, 0). On the other hand, if the material gradation is parallel to the crack, then the location of the crack is pertinent to the solution of the problem.

The method of solution is essentially the same in both Parts I and II, i.e., the integral equation method. However, because of differences in the geometrical configurations, some changes are expected. For instance, in Part I, the crack opening displacement profile is symmetric with respect to the y-axis, while in Part II, the symmetry of the crack profiles no longer exists. Thus, some interesting questions arise.

- How are the crack opening displacement profiles affected by the gradient elasticity and the gradation of the material?
- How are the stresses influenced under the gradient elasticity?
- How are the stress intensity factors (SIFs) calculated?
- How do the results compare to the classical linear elastic fracture mechanics (LEFM)?

We will address all the above questions. The remainder of the paper is organized as follows. First, the constitutive equations of anisotropic gradient elasticity for nonhomogeneous materials subjected to antiplane shear deformation are given. Then, the governing partial differential equations (PDEs) are derived, and the Fourier transform method is introduced and applied to convert the governing PDE into an ordinary differential equation (ODE). Afterward, the crack boundary value problem is described, and a specific complete set of boundary conditions is given. The governing hypersingular integrodifferential equation is derived and discretized using the collocation method. Next, various relevant aspects of the numerical discretization are described in detail. Subsequently, numerical results are given, conclusions are inferred, and potential extensions of this work are discussed. One appendix, providing the hierarchy of the PDEs and the corresponding integral equations, supplements the paper.

2 Constitutive Equations of Gradient Elasticity

A schematic demonstration of continuously graded microstructure in functionally graded materials (FGMs) is illustrated by Fig. 2. The linkage between gradient elasticity and graded materials within the framework of fracture mechanics and its related work has been addressed in Part I. For the sake of completeness, the notation and constitutive equations of gradient elasticity for an antiplane shear crack in a FGM are briefly given in this section and particularized to the case of an exponentially graded material along the x-direction.

For an antiplane shear problem, the relevant displacement components are as follows:

$$u = v = 0, \quad w = w(x,y) \tag{1}$$

and the nontrivial strains are as follows:

$$\epsilon_{xz} = \frac{1}{2}\frac{\partial w}{\partial x}, \quad \epsilon_{yz} = \frac{1}{2}\frac{\partial w}{\partial y} \tag{2}$$

The constitutive equations of gradient elasticity for FGMs are [1,2] as follows:

$$\sigma_{ij} = \lambda(x)\epsilon_{kk}\delta_{ij} + 2G(x)(\epsilon_{ij} - \ell^2\nabla^2\epsilon_{ij}) - \ell^2[\partial_k\lambda(x)](\partial_k\epsilon_{ll})\delta_{ij} - 2\ell^2[\partial_k G(x)](\partial_k\epsilon_{ij}) \tag{3}$$

$$\tau_{ij} = \lambda(x)\epsilon_{kk}\delta_{ij} + 2G(x)\epsilon_{ij} + 2\ell'\nu_k[\epsilon_{ij}\partial_k G(x) + G(x)\partial_k\epsilon_{ij}] \tag{4}$$

Contributed by the Applied Mechanics Division of ASME for publication in the JOURNAL OF APPLIED MECHANICS. Manuscript received February 23, 2007; final manuscript received February 27, 2007; published online August 21, 2008. Review conducted by Robert M. McMeeking.

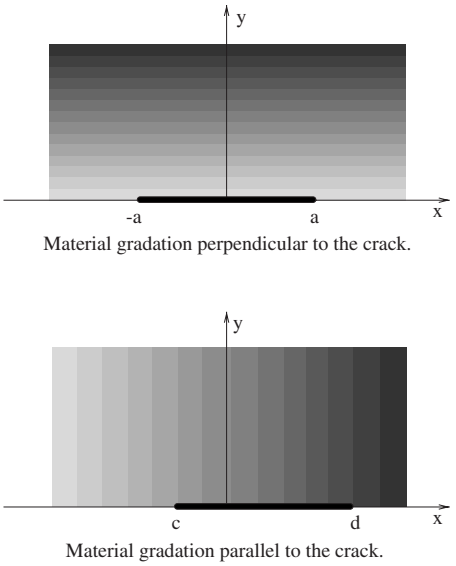

Fig. 1 A geometric comparison of the material gradation with respect to the crack location

$$\boldsymbol{\mu}_{kij} = 2\ell' \nu_k G(x)\boldsymbol{\epsilon}_{ij} + 2\ell^2 G(x)\partial_k \boldsymbol{\epsilon}_{ij} \tag{5}$$

where ℓ is the characteristic length of the material responsible for volumetric strain-gradient terms, ℓ' is responsible for surface strain-gradient terms, $\boldsymbol{\sigma}_{ij}$ is the stress tensor, and $\boldsymbol{\mu}_{ijk}$ is the couple-stress tensor. The Lamé moduli $\lambda \equiv \lambda(x)$ and $G \equiv G(x)$ are assumed to be functions of x. Moreover, $\partial_k = \partial/\partial x_k$. The parameter ℓ' is associated with surfaces and ν_k, $\partial_k \nu_k = 0$, is a director field equal to the unit outer normal n_k on the boundaries.

For a Mode-III problem, the constitutive equations above become

$$\sigma_{xx} = \sigma_{yy} = \sigma_{zz} = 0, \quad \sigma_{xy} = 0$$

$$\sigma_{xz} = 2G(x)(\boldsymbol{\epsilon}_{xz} - \ell^2\nabla^2\boldsymbol{\epsilon}_{xz}) - 2\ell^2[\partial_x G(x)](\partial_x \boldsymbol{\epsilon}_{xz}) \neq 0$$

$$\sigma_{yz} = 2G(x)(\boldsymbol{\epsilon}_{yz} - \ell^2\nabla^2\boldsymbol{\epsilon}_{yz}) - 2\ell^2[\partial_x G(x)](\partial_x \boldsymbol{\epsilon}_{yz}) \neq 0$$

$$\mu_{xxz} = 2G(x)\ell^2 \partial \boldsymbol{\epsilon}_{xz}/\partial x$$

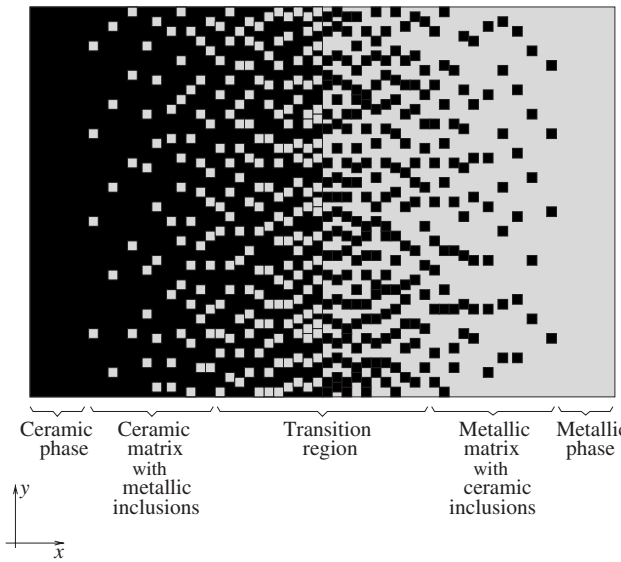

Fig. 2 A schematic illustration of a continuously graded microstructure in FGMs

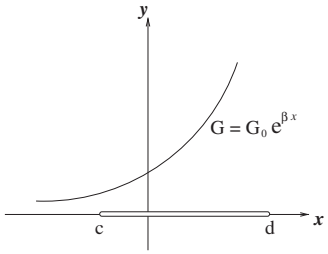

Fig. 3 Geometry of the crack problem and material gradation

$$\mu_{xyz} = 2G(x)\ell^2 \partial \boldsymbol{\epsilon}_{yz}/\partial x$$

$$\mu_{yxz} = 2G(x)(\ell^2 \partial \boldsymbol{\epsilon}_{xz}/\partial y - \ell' \boldsymbol{\epsilon}_{xz})$$

$$\mu_{yyz} = 2G(x)(\ell^2 \partial \boldsymbol{\epsilon}_{yz}/\partial y - \ell' \boldsymbol{\epsilon}_{yz}) \tag{6}$$

If G is constant, i.e., the material is homogeneous, then the constitutive equations [3,4] are[1] as follows:

$$\sigma_{xx} = \sigma_{yy} = \sigma_{zz} = 0, \quad \sigma_{xy} = 0$$

$$\sigma_{xz} = 2G(\boldsymbol{\epsilon}_{xz} - \ell^2\nabla^2\boldsymbol{\epsilon}_{xz}) \neq 0$$

$$\sigma_{yz} = 2G(\boldsymbol{\epsilon}_{yz} - \ell^2\nabla^2\boldsymbol{\epsilon}_{yz}) \neq 0$$

$$\mu_{xxz} = 2G\ell^2 \partial \boldsymbol{\epsilon}_{xz}/\partial x$$

$$\mu_{xyz} = 2G\ell^2 \partial \boldsymbol{\epsilon}_{yz}/\partial x$$

$$\mu_{yxz} = 2G(\ell^2 \partial \boldsymbol{\epsilon}_{xz}/\partial y - \ell' \boldsymbol{\epsilon}_{xz})$$

$$\mu_{yyz} = 2G(\ell^2 \partial \boldsymbol{\epsilon}_{yz}/\partial y - \ell' \boldsymbol{\epsilon}_{yz}) \tag{7}$$

It is worth to point out that each of the total stresses σ_{xz} and σ_{yz} in Eq. (6) has an extra term than the ones in (7) due to the material gradation interplay with the strain-gradient effect [2].

3 Governing Partial Differential Equation and Boundary Conditions

By imposing the only nontrivial equilibrium equation

$$\frac{\partial \sigma_{xz}}{\partial x} + \frac{\partial \sigma_{yz}}{\partial y} = 0 \tag{8}$$

the following PDE is obtained:

$$\frac{\partial}{\partial x}\left[G(x)\left(\frac{\partial w}{\partial x} - \ell^2\nabla^2\frac{\partial w}{\partial x}\right)\right] + \frac{\partial}{\partial y}\left[G(x)\left(\frac{\partial w}{\partial y} - \ell^2\nabla^2\frac{\partial w}{\partial y}\right)\right] - \ell^2\left[\frac{\partial^2 G(x)}{\partial x^2}\frac{\partial^2 w}{\partial x^2} + \frac{\partial G(x)}{\partial x}\frac{\partial^3 w}{\partial x^3} + \frac{\partial G(x)}{\partial x}\frac{\partial^3 w}{\partial x \partial y^2}\right] = 0 \tag{9}$$

If the shear modulus G is assumed as an exponential function of x (see Fig. 3),

$$G = G(x) = G_0 e^{\beta x} \tag{10}$$

then PDE (9) can be simplified as

$$-\ell^2\nabla^4 w - 2\beta\ell^2\nabla^2\frac{\partial w}{\partial x} + \nabla^2 w - \beta^2\ell^2\frac{\partial^2 w}{\partial x^2} + \beta\frac{\partial w}{\partial x} = 0 \tag{11}$$

or

[1] According to the geometry of the problem (see Fig. 3), it is the upper half-plane that is considered in the formulation. The crack is sitting on the x-axis, which is on the boundary of the upper half-plane. Thus, the outward unit normal should be $(0,-1,0)$, and not $(0, 1, 0)$. Based on Eq. (5), or the last equation in Eq. (5) of Ref. [4], the sign in front of ℓ' in the expression for both μ_{yxz} and μ_{yyz} should be "$-$" instead of "$+$."

Table 1 Governing PDEs in antiplane shear problems

Cases	Governing PDE	References
$\ell=0,\beta=0$	Laplace equation: $\nabla^2 w=0$	Standard textbooks
$\ell=0,\beta\neq 0$	Perturbed Laplace equation: $(\nabla^2+\beta\partial/\partial x)w=0$	Erdogan [7]
$\ell\neq 0,\beta=0$	Helmholtz–Laplace equation: $(1-\ell^2\nabla^2)\nabla^2 w=0$	Vardoulakis et al. [4] Fannjiang et al. [5] Zhang et al. [8]
$\ell\neq 0,\beta\neq 0$	Equation (11): $\left(1-\beta\ell^2\frac{\partial}{\partial x}-\ell^2\nabla^2\right)\left(\nabla^2+\beta\frac{\partial}{\partial x}\right)w=0$	Studied in this paper

$$\left(1-\beta\ell^2\frac{\partial}{\partial x}-\ell^2\nabla^2\right)\left(\nabla^2+\beta\frac{\partial}{\partial x}\right)w=0 \tag{12}$$

which is the governing PDE solved in the present paper.

It may be seen, from a viewpoint of perturbation, that PDE (12) can be expressed in an operator form, i.e.,

$$\mathsf{H}_\beta\mathsf{L}_\beta w=0,\quad \mathsf{H}_\beta=1-\beta\ell^2\frac{\partial}{\partial x}-\ell^2\nabla^2,\quad \mathsf{L}_\beta=\nabla^2+\beta\frac{\partial}{\partial x} \tag{13}$$

where H_β is the perturbed Helmholtz operator, L_β is the perturbed Laplacian operator, and the two operators commute ($\mathsf{H}_\beta\mathsf{L}_\beta=\mathsf{L}_\beta\mathsf{H}_\beta$). By sending $\beta\to 0$, we get the PDE [4,5]

$$(1-\ell^2\nabla^2)\nabla^2 w=0\quad \text{or } \mathsf{H}\mathsf{L}w=0 \tag{14}$$

where the Helmholtz operator $\mathsf{H}=1-\ell^2\nabla^2$ and the Laplacian operator $\mathsf{L}=\nabla^2$ are invariant under any change of variables by rotations and translations. FGM creates the perturbation and ruins the invariance. However, the perturbing term "$-\beta\ell^2(\partial/\partial x)$" in L_β, which is not purely caused by the gradation of the material, involves both the gradation parameter β and the characteristic length ℓ (the product of β and ℓ^2). It can be interpreted as a consequence of the interaction of the material gradation and the strain-gradient effect [2].

If we let $\ell\to 0$ alone, then the perturbed Helmholtz differential operator H_β will become the identity operator, and one reduces PDE (12) to

$$\left(\nabla^2+\beta\frac{\partial}{\partial x}\right)w=0 \tag{15}$$

the perturbed Laplace equation, which is the PDE that governs the Mode-III crack problem for nonhomogeneous materials with shear modulus $G(x)=G_0e^{\beta x}$ [6,7]. The limit of sending $\ell\to 0$ will lower the fourth order PDE (11) to a second order one (Eq. (15)), and a singular perturbation is expected. By taking both limits $\beta\to 0$ and $\ell\to 0$, one obtains the harmonic equation for classical elasticity. Various combinations of parameters ℓ and β with the corresponding governing PDE are listed in Table 1.

One may notice that in the governing PDE (12), there is no surface term parameter ℓ' involved. However, ℓ' does influence the solution through the boundary conditions. By the principle of virtual work, the following boundary conditions can be derived and are adopted in this paper:

$$\sigma_{yz}(x,0)=p(x),\quad x\in(c,d)$$

$$w(x,0)=0,\quad x\notin(c,d)$$

$$\mu_{yyz}(x,0)=0,\quad -\infty<x<+\infty \tag{16}$$

The first two boundary conditions in Eq. (16) are from classical LEFM, and the last one, involving the couple-stress μ_{yyz}, is needed for the higher order theory. This set of boundary conditions is the same as those adopted by Vardoulakis et al. [4] An alternative treatment of boundary conditions can be found in Ref. [9].

4 Fourier Transform

Let the Fourier transform be defined by

$$\mathcal{F}(w)(\xi)=W(\xi)=\frac{1}{\sqrt{2\pi}}\int_{-\infty}^{\infty}w(x)e^{ix\xi}dx \tag{17}$$

Then, by the *Fourier integral formula* [10],

$$\mathcal{F}^{-1}(W)(x)=w(x)=\frac{1}{\sqrt{2\pi}}\int_{-\infty}^{\infty}W(\xi)e^{-ix\xi}d\xi \tag{18}$$

where $\mathcal{F}^{-1}$ denotes the inverse Fourier transform. Now, let us assume that

$$w(x,y)=\frac{1}{\sqrt{2\pi}}\int_{-\infty}^{\infty}W(\xi,y)e^{-ix\xi}d\xi \tag{19}$$

where $w(x,y)$ is the inverse Fourier transform of the function $W(\xi,y)$. By considering each term in Eq. (11) and using Eq. (19), one obtains

$$-\ell^2\nabla^4 w=\frac{-\ell^2}{\sqrt{2\pi}}\int_{-\infty}^{\infty}\left(\xi^4W(\xi,y)-2\xi^2\frac{\partial^2W}{\partial y^2}+\frac{\partial^4W}{\partial y^4}\right)e^{-ix\xi}d\xi \tag{20}$$

$$-\beta\ell^2\nabla^2\frac{\partial w}{\partial x}=\frac{-\beta\ell^2}{\sqrt{2\pi}}\int_{-\infty}^{\infty}\left(i\xi^3W(\xi,y)-i\xi\frac{\partial^2W}{\partial y^2}\right)e^{-ix\xi}d\xi \tag{21}$$

$$\nabla^2 w=\frac{1}{\sqrt{2\pi}}\int_{-\infty}^{\infty}\left(-\xi^2W(\xi,y)+\frac{\partial^2W}{\partial y^2}\right)e^{-ix\xi}d\xi \tag{22}$$

$$-\beta^2\ell^2\frac{\partial^2 w(x,y)}{\partial x^2}=\frac{\beta^2\ell^2}{\sqrt{2\pi}}\int_{-\infty}^{\infty}\xi^2W(\xi,y)e^{-ix\xi}d\xi \tag{23}$$

$$\beta\frac{\partial w(x,y)}{\partial x}=\frac{\beta}{\sqrt{2\pi}}\int_{-\infty}^{\infty}(-i\xi)W(\xi,y)e^{-ix\xi}d\xi \tag{24}$$

Equations (20)–(24) are added according to Eq. (11), and after simplification, the governing ODE is obtained:

$$\left[\ell^2\frac{d^4}{dy^4}-(2\ell^2\xi^2+2i\beta\ell^2\xi+1)\frac{d^2}{dy^2}+(\ell^2\xi^4+2i\beta\ell^2\xi^3-\beta^2\ell^2\xi^2+\xi^2+i\beta\xi)\right]W=0 \tag{25}$$

5 Solutions of the ODE

The corresponding characteristic equation to the ODE (25) is

$$\ell^2\lambda^4-(2\ell^2\xi^2+2i\beta\ell^2\xi+1)\lambda^2+(\ell^2\xi^4+2i\beta\ell^2\xi^3-\beta^2\ell^2\xi^2+\xi^2+i\beta\xi)=0 \tag{26}$$

which can be further factorized as

$$[\ell^2\lambda^2-(1+i\beta\ell^2\xi+\ell^2\xi^2)](\lambda^2-\xi^2-i\beta\xi)=0 \tag{27}$$

Clearly, the four roots λ_i $(i=1,2,3,4)$ of the polynomial (27) above can be written as

$$\lambda_1=\frac{-1}{\sqrt{2}}\sqrt{\sqrt{\xi^4+\beta^2\xi^2}+\xi^2}-\frac{i}{\sqrt{2}}\frac{\beta\xi}{\sqrt{\sqrt{\xi^4+\beta^2\xi^2}+\xi^2}} \tag{28}$$

Table 2 Roots λ_i together with the corresponding mechanics theory and type of material

Cases	Number of roots	Roots	Mechanics theory and type of material	References
$\ell=0,\beta=0$	2	$\pm\lvert\xi\rvert$	Classical LEFM, homogeneous materials	Standard textbooks
$\ell=0,\beta\neq 0$	2	λ_1 and λ_2 in Eqs. (28) and (29), respectively	Classical LEFM, nonhomogeneous materials	Erdogan [7]
$\ell\neq 0,\beta=0$	4	$\pm\lvert\xi\rvert, \pm\sqrt{\xi^2+1/\ell^2}$	Gradient theories, homogeneous materials	Vardoulakis et al. [4] Fannjiang et al. [5]
$\ell\neq 0,\beta\neq 0$	4	The four roots λ_1–λ_4 in Eqs. (28)–(31)	Gradient theories, nonhomogeneous materials	Studied in this paper

$$\lambda_2=\frac{1}{\sqrt{2}}\sqrt{\sqrt{\xi^4+\beta^2\xi^2}+\xi^2}+\frac{i}{\sqrt{2}}\frac{\beta\xi}{\sqrt{\sqrt{\xi^4+\beta^2\xi^2}+\xi^2}} \tag{29}$$

$$\lambda_3=\frac{-1}{\sqrt{2}}\sqrt{\sqrt{(\xi^2+1/\ell^2)^2+\beta^2\xi^2}+\xi^2+1/\ell^2}-\frac{i}{\sqrt{2}}\frac{\beta\xi}{\sqrt{\sqrt{(\xi^2+1/\ell^2)^2+\beta^2\xi^2}+\xi^2+1/\ell^2}} \tag{30}$$

$$\lambda_4=\frac{1}{\sqrt{2}}\sqrt{\sqrt{(\xi^2+1/\ell^2)^2+\beta^2\xi^2}+\xi^2+1/\ell^2}+\frac{i}{\sqrt{2}}\frac{\beta\xi}{\sqrt{\sqrt{(\xi^2+1/\ell^2)^2+\beta^2\xi^2}+\xi^2+1/\ell^2}} \tag{31}$$

If $\beta\to 0$, then the imaginary part of each root λ_i $(i=1,\ldots,4)$ disappears. Thus, we have exactly the same roots found by Vardoulakis et al. [4] and Fannjiang et al. [5]. The root λ_1 corresponds to the solution of the perturbed harmonic equation $\nabla^2 w+\beta\partial w/\partial x=0$, and the root λ_3 agrees with the solution of the perturbed Helmholtz equation $(1-\beta\ell^2\partial/\partial x-\ell^2\nabla^2)w=0$. Various choices of parameters ℓ and β with their corresponding mechanics theories and materials are listed in Table 2. In contrast to the four real roots found in Part I, the four roots here are all complex and admit a more complicated expression.

By the symmetry of the geometry, one can only consider the upper half-plane $(y>0)$. By taking account of the far-field boundary condition

$$w(x,y)\to 0 \quad \text{as } \sqrt{x^2+y^2}\to+\infty \tag{32}$$

one can express the solution for $W(\xi,y)$ as

$$W(\xi,y)=A(\xi)e^{\lambda_1 y}+B(\xi)e^{\lambda_3 y} \tag{33}$$

where the nonpositive real part of λ_1 and λ_3 has been chosen to satisfy the far-field condition in the upper half-plane. Accordingly, the displacement $w(x,y)$ takes the form

$$w(x,y)=\frac{1}{\sqrt{2\pi}}\int_{-\infty}^{\infty}[A(\xi)e^{\lambda_1 y}+B(\xi)e^{\lambda_3 y}]e^{-ix\xi}d\xi \tag{34}$$

Both $A(\xi)$ and $B(\xi)$ are determined by the boundary conditions.

6 Hypersingular Integrodifferential Equation Approach

By substituting Eq. (34) into Eq. (6), we have

$$\sigma_{yz}(x,y)=2G(x)(\epsilon_{yz}-\ell^2\nabla^2\epsilon_{yz})-2\ell^2[\partial_x G(x)]\partial_x\epsilon_{yz}=\frac{G(x)}{\sqrt{2\pi}}\int_{-\infty}^{\infty}[\lambda_1 A(\xi)e^{\lambda_1 y}]e^{-ix\xi}d\xi,\quad y\geq 0 \tag{35}$$

and

$$\mu_{yyz}(x,y)=2G(x)\left(\ell^2\frac{\partial\epsilon_{yz}}{\partial y}-\ell'\epsilon_{yz}\right)=\frac{G(x)}{\sqrt{2\pi}}\int_{-\infty}^{\infty}\{(\ell^2\lambda_1^2-\ell'\lambda_1)A(\xi)e^{\lambda_1 y}+(\ell^2\lambda_3^2-\ell'\lambda_3)B(\xi)e^{\lambda_3 y}\}e^{-ix\xi}d\xi,\quad y\geq 0 \tag{36}$$

From the boundary condition in Eq. (16) imposed on the couple-stress μ_{yyz} (i.e., $\mu_{yyz}(x,0)=0$ for $-\infty<x<\infty$), one obtains the following relationship between $A(\xi)$ and $B(\xi)$:

$$B(\xi)=\frac{\ell'\lambda_1-\ell^2\lambda_1^2}{\ell^2\lambda_3^2-\ell'\lambda_3}A(\xi)=\rho(\beta,\xi)A(\xi) \tag{37}$$

with

$$\rho(\beta,\xi)=\frac{\ell'\lambda_1-\ell^2\lambda_1^2}{\ell^2\lambda_3^2-\ell'\lambda_3}=-\frac{\ell^2\xi^2+i\beta\ell^2\xi+\ell'\sqrt{\xi^2+i\beta\xi}}{\ell'\sqrt{\xi^2+i\beta\xi+1/\ell^2}+(\ell^2\xi^2+i\beta\ell^2\xi+1)} \tag{38}$$

Denote

$$\phi(x)=\frac{\partial}{\partial x}w(x,0^+)=\frac{1}{\sqrt{2\pi}}\int_{-\infty}^{\infty}(-i\xi)[A(\xi)+B(\xi)]e^{-ix\xi}d\xi=\mathcal{F}^{-1}\{(-i\xi)[A(\xi)+B(\xi)]\} \tag{39}$$

The second boundary condition in Eqs. (16) and (39) implies that

$$\phi(x)=0,\quad x\notin[c,d] \tag{40}$$

and

$$\int_c^d\phi(x)dx=0 \tag{41}$$

which is the single-valuedness condition. By Eqs. (39) and (40), we obtain

$$(-i\xi)[A(\xi)+B(\xi)]=\frac{1}{\sqrt{2\pi}}\int_{-\infty}^{\infty}\phi(x)e^{ix\xi}dx=\frac{1}{\sqrt{2\pi}}\int_c^d\phi(t)e^{i\xi t}dt \tag{42}$$

By substituting Eq. (37) into Eq. (42) above, one gets

$$A(\xi)=\frac{1}{\sqrt{2\pi}}\left[\frac{1}{(-i\xi)[1+\rho(\beta,\xi)]}\right]\int_c^d\phi(t)e^{i\xi t}dt \tag{43}$$

where

$$\frac{1}{1+\rho(\beta,\xi)}=\frac{(\ell^2\xi^2+i\beta\ell^2\xi+1)+\ell'\sqrt{\xi^2+i\beta\xi+1/\ell^2}}{1+\ell'\sqrt{\xi^2+i\beta\xi+1/\ell^2}-\ell'\sqrt{\xi^2+i\beta\xi}} \tag{44}$$

By replacing the $A(\xi)$ in Eq. (35) by Eq. (43), one obtains the following integral equation in the limit $y\to 0^+$:

$$\lim_{y\to 0^+}\sigma_{yz}(x,y)=\lim_{y\to 0^+}\frac{G(x)}{2\pi}\int_{-\infty}^{\infty}\lambda_1(\beta,\xi)\times\left[\frac{1}{(-i\xi)[1+\rho(\beta,\xi)]}\int_c^d\phi(t)e^{i\xi t}dt\right]e^{\lambda_1 y}e^{-ix\xi}d\xi$$

$$=\lim_{y\to 0^+}\frac{G(x)}{2\pi}\int_c^d\phi(t)\int_{-\infty}^{\infty}\left[\frac{\lambda_1(\beta,\xi)}{(-i\xi)[1+\rho(\beta,\xi)]}e^{\lambda_1 y}\right]\times e^{i(t-x)\xi}d\xi dt \tag{45}$$

$$=\lim_{y\to 0^+}\frac{G}{2\pi}\int_c^d\phi(t)\int_{-\infty}^{\infty}K(\xi,y)e^{i\xi(t-x)}d\xi dt,\quad -\infty<x<\infty \tag{46}$$

with

$$K(\xi,y)=\frac{\lambda_1(\beta,\xi)}{(-i\xi)[1+\rho(\beta,\xi)]}e^{\lambda_1 y} \tag{47}$$

Equation (46) is an expression for the stress $\sigma_{yz}(x,y)$ in the limit form of $y\to 0^+$, which is valid for $x\in(-\infty,\infty)$. Note that for the (first) boundary condition in Eq. (16), $\sigma_{yz}(x,0)=p(x)$, x is restricted to the crack surface (c,d). It is this boundary condition that leads to the governing hypersingular integrodifferential equation (see Eq. (55*a*) below). However, when SIFs are calculated, x takes values outside of (c,d), and the integral (46) is not singular (see Eq. (55*b*) below).

We split $K(\xi,y)$ into the singular part $K_\infty(\xi,y)$ and the nonsingular part $N(\xi,y)$:

$$K(\xi,y)=K_\infty(\xi,y)+N(\xi,y) \tag{48}$$

where $K_\infty(\xi,y)$ is the nonvanishing part of the asymptotic expansion of $K(\xi,y)$ in the powers of ξ, as $|\xi|\to\infty$. When y is set to be 0, we have

$$K_\infty(\xi,0)=-i\ell^2|\xi|\xi-\frac{\ell'}{2}i\xi+\frac{3\beta\ell^2}{2}|\xi|+\frac{\ell'\beta}{2}+\left[\left(\frac{\ell'}{2\ell}\right)^2+\frac{3\ell^2\beta^2}{8}-1\right]\frac{i\xi}{|\xi|} \tag{49}$$

Note that the real and the imaginary parts of $K_\infty(\xi,0)$ given in Eq. (49) are even and odd functions of ξ, respectively.

In view of the following distributional convergence,

$$\int_{-\infty}^{\infty}[i\xi|\xi|e^{-|\xi|y}]e^{i(t-x)\xi}d\xi\xrightarrow{y\to 0^+}\frac{4}{(t-x)^3} \tag{50}$$

$$\int_{-\infty}^{\infty}[|\xi|e^{-|\xi|y}]e^{i(t-x)\xi}d\xi\xrightarrow{y\to 0^+}\frac{-2}{(t-x)^2} \tag{51}$$

$$\int_{-\infty}^{\infty}[i\xi e^{-|\xi|y}]e^{i(t-x)\xi}d\xi\xrightarrow{y\to 0^+}2\pi\delta'(t-x) \tag{52}$$

$$\int_{-\infty}^{\infty}\left[i\frac{|\xi|}{\xi}e^{-|\xi|y}\right]e^{i(t-x)\xi}d\xi\xrightarrow{y\to 0^+}\frac{-2}{t-x} \tag{53}$$

$$\int_{-\infty}^{\infty}[1e^{-|\xi|y}]e^{i(t-x)\xi}d\xi\xrightarrow{y\to 0^+}2\pi\delta(t-x) \tag{54}$$

with $\delta(x)$ being the Dirac delta function, we obtain the limit

$$\lim_{y\to 0^+}\int_c^d\int_{-\infty}^{\infty}K_\infty(\xi,y)e^{i\xi(t-x)}d\xi\phi(t)dt$$

$$=\frac{G}{\pi}\oint_c^d\left\{\frac{-2\ell^2}{(t-x)^3}-\frac{3\beta\ell^2}{2(t-x)^2}+\frac{1-3\beta^2\ell^2/8-[\ell'/(2\ell)]^2}{t-x}+k(x,t)\right\}\phi(t)dt+\frac{\ell'}{2}\phi'(x)+\frac{\beta\ell'}{2}\phi(x)=p(x),\quad c<x<d \tag{55a}$$

$$=\frac{1}{\pi}\int_c^d\left\{\frac{-2\ell^2}{(t-x)^3}-\frac{3\beta\ell^2}{2(t-x)^2}+\frac{1-3\ell^2\beta^2/8-[\ell'/(2\ell)]^2}{t-x}+k(x,t)\right\}\phi(t)dt,\quad x<c\quad\text{or}\quad x>d \tag{55b}$$

where $\oint$ denotes the finite-part integral [11], and the regular kernel $k(x,t)$ is given by

$$k(x,t)=\int_0^{\infty}N(\xi,0)e^{i(t-x)\xi}d\xi \tag{56}$$

Equation (55*a*) is a Fredholm integral equation of the second kind with the cubic and Cauchy singular kernels.

7 Numerical Solution

To numerically solve the unknown slope function $\phi(t)$ in Eq. (55*a*), we follow the general procedure outlined in the Part I paper. For the sake of clarity and completeness, each step is presented below and particularized to the problem at hand (see Figs. 1 and 2).

7.1 Normalization. By the change of variables

$$t=(d-c)s/2+(c+d)/2\ \text{and}\ x=(d-c)r/2+(c+d)/2 \tag{57}$$

the crack surface (c,d) can be converted into $(-1,1)$, and the main integral equation (55*a*) can be rewritten in normalized form

$$\frac{1}{\pi}\oint_{-1}^{1}\left\{\frac{-2(\ell/a)^2}{(s-r)^3}-\frac{3(\ell/a)^2(a\beta)}{2(s-r)^2}+\frac{1-3(\ell/a)^2(a\beta)^2/8-[(\ell'/a)/(2\ell/a)]^2}{s-r}+\mathcal{K}(r,s)\right\}\Phi(s)ds+\frac{\ell'/a}{2}\Phi'(r)+\frac{(a\beta)(\ell'/a)}{2}\Phi(r)=\frac{P(r)}{G_0}e^{-\beta[ar+(c+d)/2]},\quad |r|<1 \tag{58}$$

where

$$a=(d-c)/2=\text{half of the crack length} \tag{59}$$

$$\Phi(r)=\phi(ar+(c+d)/2),\quad P(r)=p(ar+(c+d)/2) \tag{60}$$

$$\mathcal{K}(r,s)=ak(ar+(c+d)/2,\ as+(c+d)/2) \tag{61}$$

and $k(x,t)$ is described by Eq. (56).

Note that in Eq. (58), $G(x)$ has been written as

$$G(x)=G_0e^{\beta x}=G_0e^{\beta[((d-c)/2)r+[(c+d)/2]]}=G_0e^{(a\beta)r}(e^{a\beta})^{((d+c)/(d-c))}$$

where $a\beta=(d-c)\beta/2$ and $(d+c)/(d-c)$ are two dimensionless quantities. Together with the terms ℓ/a and ℓ'/a that appear in Eq. (58), the following dimensionless parameters are defined:

$$\tilde{\ell}=\ell/a,\quad \tilde{\ell}'=\ell'/a\ \text{and}\ \tilde{\beta}=a\beta \tag{62}$$

They will be used in the numerical implementation and results.

7.2 Representation of the Density Function. To proceed with the numerical approximation, a representation of $\Phi(s)$ is cho-

sen so that one can evaluate the hypersingular and the Cauchy singular integrals by finite part and Cauchy principal value, respectively (see Refs. [11,12]). For the cubic hypersingular integral equation (58), the solution $\Phi(s)$ can be represented as

$$\Phi(s) = g(s)\sqrt{1-s^2} \tag{63}$$

where $g(\pm 1)$ is finite and $g(\pm 1) \neq 0$ [5]. By finding numerical solution for $g(s)$, one can find the approximate solution for $\Phi(s)$. The representation (63) of $\Phi(s)$ is suggested by the following asymptotic behavior of the solution around the crack tips:

$$\text{Displacements} \sim r^{3/2}, \quad \text{strains} \sim \sqrt{r}, \quad \text{stresses} \sim r^{-3/2} \tag{64}$$

reported in Refs. [1,5].

7.3 Chebyshev Polynomial Expansion. In view of Eq. (63) and the fact that $\{U_n(s)\}$ are orthogonal on $(-1,1)$ with respect to the weight function $\sqrt{1-s^2}$, $g(s)$ can be most naturally expressed in terms of the Chebyshev polynomials of the second kind $U_n(s)$. However, the orthogonality is not required in the implementation of the numerical procedures, and either Chebyshev polynomials of the first kind $T_n(s)$ or of the second kind $U_n(s)$ may be employed in the approximation, i.e.,

$$g(s) = \sum_{n=0}^{\infty} a_n T_n(s) \quad \text{or } g(s) = \sum_{n=0}^{\infty} A_n U_n(s) \tag{65}$$

The coefficients a_n's or A_n's are numerically determined by the collocation method. As shown by Chan et al. [6], the two expansions should lead to consistent numerical results. In this paper, the expansion in terms of $U_n(s)$ is adopted, i.e.,

$$\Phi(s) = \sqrt{1-s^2}\sum_{n=0}^{\infty} A_n U_n(s) \tag{66}$$

where $U_n(s)$ is defined, as usual, by

$$U_n(s) = \frac{\sin[(n+1)\cos^{-1}(s)]}{\sin[\cos^{-1}(s)]}, \quad n = 0,1,2,\ldots \tag{67}$$

Note that the single-valuedness condition (41) or, equivalently, $\int_{-1}^{1}\Phi(s)ds = 0$ implies

$$A_0 = 0 \tag{68}$$

Thus, the running index n in Eq. (66) can start from 1 instead of 0.

7.4 Evaluation of the Derivative of the Density Function. The term $\Phi'(r)$ in Eq. (58) is evaluated using the expansion (66) and the fact that

$$\frac{d}{dr}[U_n(r)\sqrt{1-r^2}] = -\frac{n+1}{\sqrt{1-r^2}}T_{n+1}(r), \quad n \geqslant 0 \tag{69}$$

Thus

$$\Phi'(r) = \frac{d}{dr}\left[\sqrt{1-r^2}\sum_{n=0}^{\infty} A_n U_n(r)\right] = \frac{-1}{\sqrt{1-r^2}}\sum_{n=0}^{\infty}(n+1)A_n T_n(r) \tag{70}$$

7.5 Formation of the Linear System of Equations. The A_n coefficients are determined by transforming the integral equation (55*a*) into a system of linear algebraic equations in terms of the A_n's. By replacing $\Phi(s)$ in Eq. (58) by the representation (66), and using Eq. (70), one obtains the governing integral equation in discretized form

$$\begin{aligned}
&-2\tilde{\ell}^2\sum_{n=1}^{\infty}\frac{A_n}{\pi}\Xint=_{-1}^{1}\frac{U_n(s)\sqrt{1-s^2}}{(s-r)^3}ds - \frac{3\tilde{\ell}^2\tilde{\beta}}{2}\sum_{n=1}^{\infty}\frac{A_n}{\pi}\Xint-_{-1}^{1}\frac{U_n(s)\sqrt{1-s^2}}{(s-r)^2}ds \\
&+\left[1-\frac{3\tilde{\ell}^2\tilde{\beta}^2}{8}-\left(\frac{\tilde{\ell}'}{2\tilde{\ell}}\right)^2\right]\sum_{n=1}^{\infty}\frac{A_n}{\pi}\int_{-1}^{1}\frac{U_n(s)\sqrt{1-s^2}}{s-r}ds \\
&+\sum_{n=1}^{\infty}\frac{A_n}{\pi}\int_{-1}^{1}\sqrt{1-s^2}U_n(s)\mathcal{K}(r,s)ds \\
&-\frac{\tilde{\ell}'}{2\sqrt{1-r^2}}\sum_{n=1}^{\infty}(n+1)A_n T_{n+1}(r) + \frac{\tilde{\ell}'\tilde{\beta}}{2}\sqrt{1-r^2}\sum_{n=1}^{\infty}A_n U_n(r) \\
&= \frac{\mathcal{P}(r)}{G(r)}, \quad |r| < 1
\end{aligned} \tag{71}$$

We have used the running index n that starts from 1 (see Eq. (68)).

7.6 Evaluation of Singular and Hypersingular Integrals. Formulas for evaluating singular integral terms in Eq. (71) are listed below:

$$\frac{1}{\pi}\Xint-_{-1}^{1}\frac{U_n(s)\sqrt{1-s^2}}{s-r}ds = -T_{n+1}(r), \quad |r| < 1, \quad n \in \mathrm{Z}^+ \tag{72}$$

$$\frac{1}{\pi}\Xint=_{-1}^{1}\frac{U_n(s)\sqrt{1-s^2}}{(s-r)^2}ds = -(n+1)U_n(r), \quad |r| < 1, \quad n \in \mathrm{Z}^+ \tag{73}$$

$$\frac{1}{\pi}\Xint=_{-1}^{1}\frac{U_n(s)\sqrt{1-s^2}}{(s-r)^3}ds = \begin{cases} -1, & n = 0 \\ \dfrac{(n^2+n)U_{n+1}(r) - (n^2+3n+2)U_{n-1}(r)}{4(1-r^2)}, & n \geqslant 1 \end{cases} \quad |r| < 1 \tag{74}$$

The details of the calculation can be found in Ref. [13].

7.7 Evaluation of Nonsingular Integral. By combining all the results obtained so far in the numerical approximation, one may rewrite Eq. (71) in the following form:

$$\begin{aligned}
&\frac{-\tilde{\ell}^2}{2(1-r^2)}\sum_{n=1}^{\infty}A_n[(n^2+n)U_{n+1}(r) - (n^2+3n+2)U_{n-1}(r)] \\
&+\frac{3\tilde{\beta}\tilde{\ell}^2}{2}\sum_{n=1}^{\infty}(n+1)A_n U_n(r) - \left[1-\frac{3\tilde{\ell}^2\tilde{\beta}^2}{8}-\left(\frac{\tilde{\ell}'}{2\tilde{\ell}}\right)^2\right] \\
&\times\sum_{n=1}^{\infty}A_n T_{n+1}(r) + \sum_{n=1}^{\infty}\frac{A_n}{\pi}\int_{-1}^{1}\sqrt{1-s^2}U_n(s)\mathcal{K}(r,s)ds \\
&-\frac{\tilde{\ell}'}{2\sqrt{1-r^2}}\sum_{n=1}^{\infty}(n+1)A_n T_{n+1}(r) + \frac{\tilde{\ell}'\tilde{\beta}}{2}\sqrt{1-r^2}\sum_{n=1}^{\infty}A_n U_n(r) \\
&= \frac{\mathcal{P}(r)}{G(r)}, \quad |r| < 1
\end{aligned} \tag{75}$$

The regular kernel in Eq. (75) is actually a double integral, i.e.,

$$\int_{-1}^{1}\sqrt{1-s^2}U_n(s)\mathcal{K}(r,s)ds=\int_{-1}^{1}\sqrt{1-s^2}U_n(s)ak(ar,as)ds$$
$$=\int_{-1}^{1}\sqrt{1-s^2}U_n(s)\times\int_0^{\infty}aN(\xi,0)\sin[a\xi(s-r)]d\xi ds \tag{76}$$

The Fourier sine transform in Eq. (76) can be efficiently evaluated by applying fast Fourier transform (FFT) [14]. The integral along $[-1,1]$ can be readily obtained by the Gaussian quadrature method [15].

8 Stress Intensity Factors

In classical LEFM, the SIFs are defined by

$$K_{\mathrm{III}}^{C}(d)=\lim_{x\to d^+}\sqrt{2\pi(x-d)}\sigma_{yz}(x,0)\quad(x>d) \tag{77}$$

and

$$K_{\mathrm{III}}^{C}(c)=\lim_{x\to c^-}\sqrt{2\pi(c-x)}\sigma_{yz}(x,0)\quad(x<c) \tag{78}$$

After normalization, the crack surfaces are located in the interval $(-1,1)$. The density function $\Phi(t)$ is expanded in terms of Chebyshev polynomials of the second kind U_n, which, when substituted into Eq. (55*b*), give rise to the following formulas for $|r|>1$ (see Ref. [13]):

$$\frac{1}{\pi}\int_{-1}^{1}\frac{U_n(s)\sqrt{1-s^2}}{s-r}ds=-\left(r-\frac{|r|}{r}\sqrt{r^2-1}\right)^{n+1},\quad n\geq 0 \tag{79}$$

$$\frac{1}{\pi}\int_{-1}^{1}\frac{U_n(s)\sqrt{1-s^2}}{(s-r)^2}ds=-(n+1)\left(1-\frac{|r|}{\sqrt{r^2-1}}\right)\times\left(r-\frac{|r|}{r}\sqrt{r^2-1}\right)^{n},\quad n\geq 0 \tag{80}$$

$$\frac{1}{\pi}\int_{-1}^{1}\frac{U_n(s)\sqrt{1-s^2}}{(s-r)^3}ds=\frac{-1}{2}(n+1)\left(r-\frac{|r|}{r}\sqrt{r^2-1}\right)^{n-1}\times\left[n\left(1-\frac{|r|}{\sqrt{r^2-1}}\right)^2+\frac{r-\frac{|r|}{r}\sqrt{r^2-1}}{(\sqrt{r^2-1})^3}\right],\quad n\geq 0 \tag{81}$$

The highest singularity in Eqs. (79)–(81) appears in the last term in Eq. (81) and it behaves like $(r^2-1)^{-3/2}$ as $r\to 1^+$ or $r\to -1^-$. Motivated by such asymptotic behavior, we define the SIFs for strain-gradient elasticity as

$$\ell K_{\mathrm{III}}(d)=\lim_{x\to d^+}2\sqrt{2\pi(x-d)}(x-d)\sigma_{yz}(x,0)\quad(x>d) \tag{82}$$

$$\ell K_{\mathrm{III}}(c)=\lim_{x\to c^-}2\sqrt{2\pi(c-x)}(c-x)\sigma_{yz}(x,0)\quad(x<c) \tag{83}$$

Thus,

$$\ell K_{\mathrm{III}}(d)=\lim_{x\to d^+}2\sqrt{2\pi(x-d)}(x-d)\sigma_{yz}(x,0)\quad(x>d)$$
$$=\lim_{r\to 1^+}2\sqrt{2\pi\left[\left(\frac{d-c}{2}\right)r+\frac{c+d}{2}-d\right](ar-a)}\times\sigma_{yz}\left(\frac{d-c}{2}r+\frac{c+d}{2},0\right)\quad(r>1)$$
$$=2a\sqrt{2\pi a}\lim_{r\to 1^+}\sqrt{(r-1)}(r-1)\sigma_{yz}((d-c)r/2+(c+d)/2,0)\quad(r>1)$$
$$=2a\sqrt{2\pi a}\lim_{r\to 1^+}\sqrt{(r-1)}(r-1)G_0e^{a\beta r}e^{\beta(d+c)/2}\times\left(\frac{-2\ell^2}{\pi a^2}\right)\int_{-1}^{1}\frac{\Phi(s)}{(s-r)^3}ds\quad(r>1) \tag{84}$$

By using Eq. (66) in conjunction with Eq. (81), we obtain from Eq. (84)

$$K_{\mathrm{III}}(d)=2\sqrt{2\pi a}\left(\frac{-2\ell}{a}\right)G_0e^{\beta d}\lim_{r\to 1^+}(r-1)^{3/2}\times\sum_{n=0}^{N}\frac{-(n+1)}{2}\left(r-\frac{|r|}{r}\sqrt{r^2-1}\right)^{n-1}\times\left[n\left(1-\frac{|r|}{\sqrt{r^2-1}}\right)^2+\frac{r-\frac{|r|}{r}\sqrt{r^2-1}}{\sqrt{r^2-1}^3}\right]A_n$$
$$=\sqrt{\pi a}G_0e^{\beta d}(\ell/a)\sum_{n=0}^{\infty}(n+1)A_n \tag{85}$$

Similarly,

$$K_{\mathrm{III}}(c)=\sqrt{\pi a}G_0e^{\beta c}(\ell/a)\sum_{n=0}^{\infty}(-1)^n(n+1)A_n \tag{86}$$

9 Results and Discussion

The numerical results include crack surface displacements, strains, stresses, and SIFs.

9.1 Crack Surface Displacements. The (normalized) crack surface displacements shown in Figs. 4–8 are obtained by integrating the slope function (see Eq. (87) below). Figure 4 shows a full normalized crack sliding displacement profile for a homogeneous medium ($\tilde{\beta}=0$) with the strain-gradient effect. The crack profile in Fig. 4 is symmetric because the material is homogeneous. Figures 5 and 6 are for classical LEFM. Figures 7 and 8 are for the strain-gradient theory. As $\beta<0$, the material has larger shear modulus at the left side of the crack than at the right side, and thus the material is stiffer on the left and more compliant on the right, as shown in Figs. 5 and 7. Similarly, Figs. 6 and 8 illustrate the case of $\beta>0$ and confirm that the material is stiffer on the right and more compliant on the left. The variation of the shear modulus destroys the symmetry of the displacement profiles. The most prominent feature is the cusping phenomena around the crack tips, as shown in Figs. 4, 7, and 8. The difference between Figs. 5 and 6 and Figs. 7 and 8 is the cusp at the crack tips. In Figs. 5 and 6, one may observe that the profiles have a tangent line with infinite slope at the crack tips, which is a common crack behavior exhibited in the classical LEFM. However, such is not the case in gradient theory as evidenced by the numerical results shown.

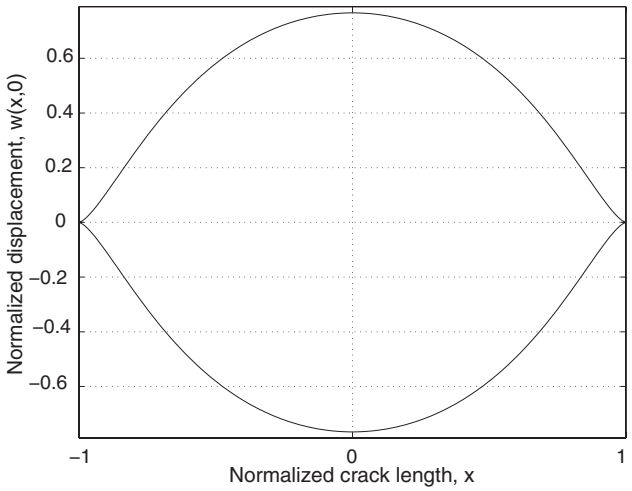

Fig. 4 Full crack displacement profile for homogeneous material ($\tilde{\beta}=0$) under uniform crack surface shear loading $\sigma_{yz}(x,0)=-p_0$ with choice of (normalized) $\tilde{\ell}=0.2$ and $\tilde{\ell}'=0$

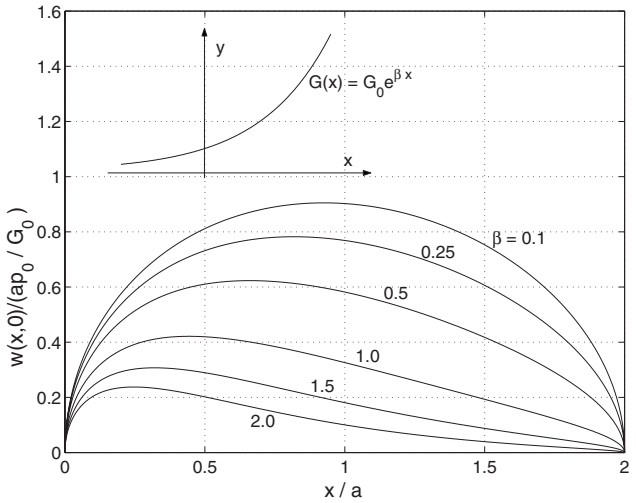

Fig. 6 Classical LEFM, i.e., $\tilde{\ell}=\tilde{\ell}'\to 0$. Crack surface displacement in an infinite nonhomogeneous plane under uniform crack surface shear loading $\sigma_{yz}(x,0)=-p_0$ and shear modulus $G(x)=G_0e^{\beta x}$. Here, $a=(d-c)/2$ denotes the half crack length.

9.2 Strains. We have used the strain-like field, $\phi(x)$ (the slope function), as the unknown density function in our integral equation formulation. The normalized version, $\Phi(x)$, with various $\tilde{\ell}$ is plotted in Fig. 9. Note that $\Phi(\pm 1)=0$ while in classical LEFM, $\Phi(\pm 1)=\pm\infty$. The vanishing slope is equivalent to the cusping at the crack tips. The (normalized) crack displacement profile $w(r,0)$ can be obtained by

$$w(r,0)=\int_{-1}^{r}\Phi(s)ds=\int_{-1}^{r}\sqrt{1-s^2}\sum_{n=0}^{N}A_nU_n(s)ds \qquad (87)$$

As ℓ decreases, $\Phi(x)$ seems to converge to the slope function of the classical LEFM case in the region away from the crack tips, where $\Phi(x)$ is very different from its classical counterpart near the crack tips.

9.3 Stresses. Similar to classical LEFM, the stress $\sigma_{yz}(x,0)$ diverges as x approaches the crack tips along the ligament (Fig. 10). Moreover, the sign of the stress changes, and as ℓ decreases, the interior part (i.e., the region apart from the two crack tips) of $\sigma_{yz}(x,0)$ seems to converge to the solution of classical LEFM. The finding of the negative near-tip stress is consistent with the results by Zhang et al. [8] who also investigated a Mode-III crack in elastic materials with strain-gradient effects; this negative stress may be considered as a necessity for the crack surface to reattach near the tips. The point worth noting here is that not all strain-gradient theories possess the negative-stress feature near the crack tips. For instance, the strain-gradient elasticity theory for cellular materials [16] and elastic-plastic materials with strain-gradient effects [17], which fall within the classical couple-stress theory framework, shows a positive-stress singularity near the crack tip. On the other hand, the strain-gradient theory proposed by Fleck and Hutchinson [18], which does not fall into the above framework, predicts a compressive stress near the tip of a tensile Mode-I crack [19,20].

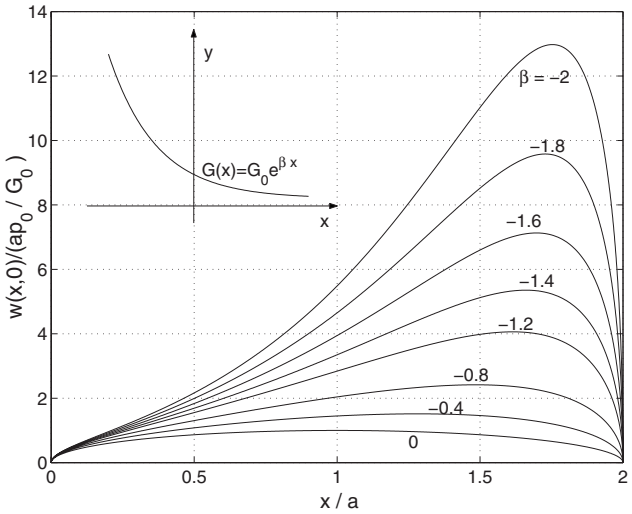

Fig. 5 Classical LEFM, i.e., $\tilde{\ell}=\tilde{\ell}'\to 0$. Crack surface displacement in an infinite nonhomogeneous plane under uniform crack surface shear loading $\sigma_{yz}(x,0)=-p_0$ and shear modulus $G(x)=G_0e^{\beta x}$. Here, $a=(d-c)/2$ denotes the half crack length.

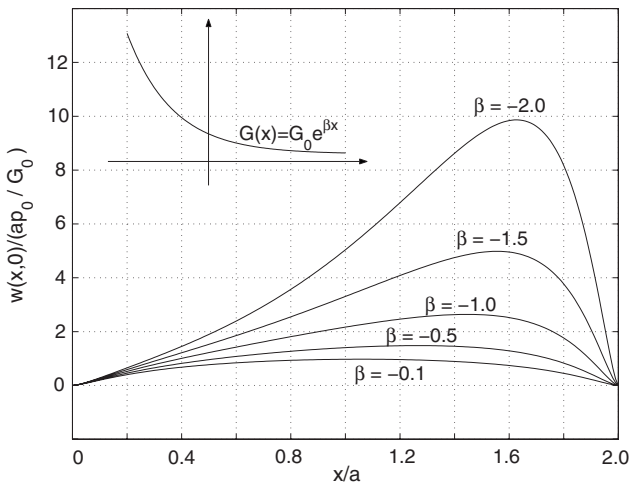

Fig. 7 Crack surface displacement in an infinite nonhomogeneous plane under uniform crack surface shear loading $\sigma_{yz}(x,0)=-p_0$ and shear modulus $G(x)=G_0e^{\beta x}$ with choice of (normalized) $\tilde{\ell}=0.10$ and $\tilde{\ell}'=0.01$. Here, $a=(d-c)/2$ denotes the half crack length.

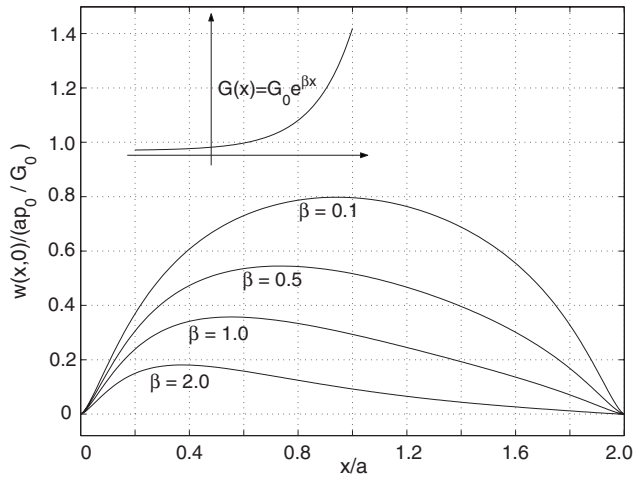

Fig. 8 Crack surface displacement in an infinite nonhomogeneous plane under uniform crack surface shear loading $\sigma_{yz}(x,0)=-p_0$ and shear modulus $G(x)=G_0e^{\beta x}$ with choice of (normalized) $\tilde{\ell}=0.10$ and $\tilde{\ell}'=0.01$. Here, $a=(d-c)/2$ denotes the half crack length.

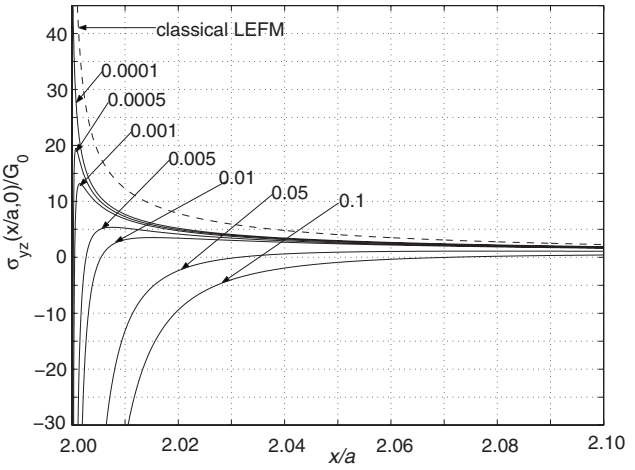

Fig. 10 Stress $\sigma_{yz}(x/a,0)/G_0$ along the ligament for $\tilde{\beta}=0.5$, $\tilde{\ell}'=0$, and various $\tilde{\ell}$. Crack surface $(c,d)=(0,2)$ located in an infinite nonhomogeneous plane is assumed to be under uniform crack surface shear loading $\sigma_{yz}(x,0)=-p_0$ and shear modulus $G(x)=G_0e^{\beta x}$. Here, $a=(d-c)/2$ denotes the half crack length.

9.4 Stress Intensity Factors. Besides using $\phi(x)$ as the unknown density function, one may also use displacement $w(x)$ to be the unknown in the formulation of the integral equation (see Appendix). By rewriting K_{III}^{C} in terms of the coefficients in the expansion for w, one obtains (see Ref. [6]) the following.

- With T_n expansion,

$$\frac{K_{\mathrm{III}}^{C}(c)}{G_0\sqrt{\pi(d-c)/2}}=e^{\beta c}\sum_{0}^{N}(-1)^n a_n \tag{88}$$

$$\frac{K_{\mathrm{III}}^{C}(d)}{G_0\sqrt{\pi(d-c)/2}}=e^{\beta d}\sum_{0}^{N}a_n$$

- With U_n expansion,

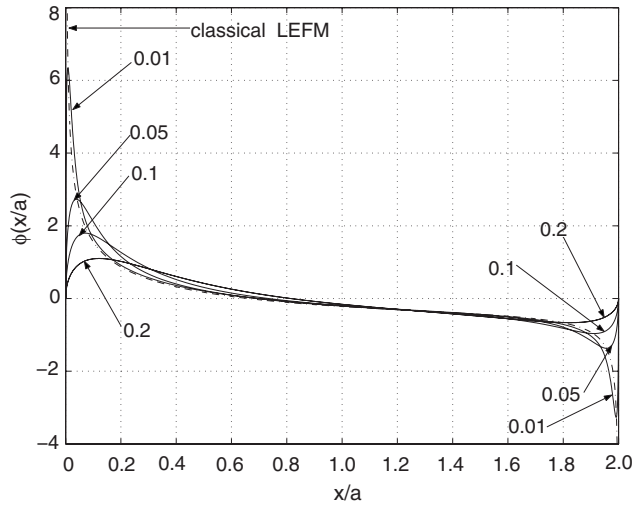

Fig. 9 Strain $\phi(x/a)$ along the crack surface $(c,d)=(0,2)$ for $\tilde{\beta}=0.5$, $\tilde{\ell}'=0$, and various $\tilde{\ell}$ in an infinite nonhomogeneous plane under uniform crack surface shear loading $\sigma_{yz}(x,0)=-p_0$ and shear modulus $G(x)=G_0e^{\beta x}$. Here, $a=(d-c)/2$ denotes the half crack length.

$$\frac{K_{\mathrm{III}}(c)}{G_0\sqrt{\pi(d-c)/2}}=e^{\beta c}\sum_{0}^{N}(-1)^n(n+1)A_n \tag{89}$$

$$\frac{K_{\mathrm{III}}(d)}{G_0\sqrt{\pi(d-c)/2}}=e^{\beta d}\sum_{0}^{N}(n+1)A_n$$

Table 3 contains the (normalized) SIFs for the case of classical LEFM by using both T_n and U_n expansions [see Eqs. (63) and (65)]. The SIFs in Table 3 have been obtained by using Eqs. (88) and (89), and they are close to the results reported by Erdogan [7].

Table 4 contains the SIFs for strain-gradient elasticity at $\tilde{\ell}=0.1$ and $\tilde{\ell}'=0.01$. One observes that the dependence of $K_{\mathrm{III}}(c)$ and $K_{\mathrm{III}}(d)$ is similar to the classical case reported in Table 3.

10 Concluding Remarks

This paper has shown that the integral equation method is an effective means of formulating crack problems for a FGM considering strain-gradient effects. The theoretical framework and numerical analysis has been utilized to solve antiplane shear crack problems in FGMs by using Casal's continuum. The behavior of

Table 3 Normalized SIFs for Mode-III crack problem in a FGM $(\ell=\ell'\to 0)$

	U_n representation		T_n representation	
$\beta\left(\frac{d-c}{2}\right)$	$\frac{K_{\mathrm{III}}(c)}{p_0\sqrt{\pi(d-c)/2}}$	$\frac{K_{\mathrm{III}}(d)}{p_0\sqrt{\pi(d-c)/2}}$	$\frac{K_{\mathrm{III}}(c)}{p_0\sqrt{\pi(d-c)/2}}$	$\frac{K_{\mathrm{III}}(d)}{p_0\sqrt{\pi(d-c)/2}}$
−2.00	1.21779	0.55672	1.21779	0.55672
−1.50	1.17801	0.63007	1.17801	0.63007
−1.00	1.14307	0.72845	1.14307	0.72845
−0.50	1.09036	0.85676	1.09036	0.85676
−0.10	1.02289	0.97312	1.02289	0.97312
0.00	1.00000	1.00000	1.00000	1.00000
0.10	0.97312	1.02289	0.97312	1.02289
0.50	0.85676	1.09036	0.85676	1.09036
1.00	0.72845	1.14307	0.72845	1.14307
1.50	0.63007	1.17801	0.63007	1.17801
2.00	0.55672	1.21779	0.55672	1.21779

Table 4 Normalized generalized SIFs for a Mode-III crack at $\tilde{\ell}=0.1$, $\tilde{\ell}=0.01$, and various values of $\tilde{\beta}$

$\tilde{\beta}$	$\frac{K_{III}(c)}{p_0\sqrt{\pi(d-c)/2}}$	$\frac{K_{III}(d)}{p_0\sqrt{\pi(d-c)/2}}$
−2.00	1.23969	0.49938
−1.00	1.12585	0.67600
−0.50	1.04849	0.80248
−0.10	0.96814	0.91658
0.00	0.94385	0.94385
0.10	0.91677	0.96828
0.50	0.80277	1.04854
1.00	0.67637	1.12584
2.00	0.49938	1.23969

the solution around the crack tips is affected by the strain-gradient theory, and not by the gradation of the materials. Also, the integral equation formulation has been found to be an adequate tool for implementing the numerical procedures and to assess physical quantities such as crack surface displacements, strains, stresses, and SIFs. Further experiments are needed for justifying the physical aspects of the method. Future work includes extension of the theory to Mode-I crack problems.

Acknowledgment

G.H.P. would like to thank the support from the National Science Foundation under Grant No. CMS 0115954 (Mechanics and Materials Program) and from the NASA-Ames "Engineering for Complex Systems Program," and the NASA-Ames Chief Engineer (Dr. Tina Panontin) through Grant No. NAG 2-1424.

A.C.F. acknowledges the support from the USA National Science Foundation (NSF) through Grant No. DMS-9971322 and UC Davis Chancellor's Fellowship.

Y.-S.C. thanks the support from the Applied Mathematical Sciences Research Program of the Office of Mathematical, Information, and Computational Sciences, U.S. Department of Energy, under Contract No. DE-AC05-00OR22725 with UT-Battelle, LLC; he also thanks the grant (No. W911NF-05-1-0029) from the U.S. Department of Defense, Army Research Office. Organized Research Award (2007) from University of Houston-Downtown is also acknowledged by Y.-S.C.

Appendix: Hierarchy of Governing Integral Equations

In this appendix, we list the type of the physical problem under antiplane shear loading, its governing PDE, and integral equation associated with the choice of the density function. The corresponding references in the literature are also provided.

1. Classical LEFM, Homogeneous Materials ($G \equiv G_0$)
   - PDE: Laplace equation $\nabla^2 w(x,y)=0$.
   - Integral equation with the density function $\phi(x) = \partial w(x,0)/\partial x$:

$$\frac{G_0}{\pi}\int_c^d \frac{\phi(t)}{t-x}dt = p(x), \quad c<x<d \tag{A1}$$

   - Integral equation with the density function $\phi(x) = w(x,0)$:

$$\frac{G_0}{\pi}\oint_c^d \frac{\phi(t)}{(t-x)^2}dt = p(x), \quad c<x<d \tag{A2}$$

Many standard textbooks have covered the Laplace equation (see, for example, Ref. [21]).

2. Classical LEFM, Nonhomogeneous Materials ($G \equiv G(y) = G_0 e^{\gamma y}$)
   - PDE: Perturbed Laplace equation $(\nabla^2 + \gamma(\partial/\partial y))w(x,y)=0$.
   - Integral equation with the density function $\phi(x) = \partial w(x,0)/\partial x$:

$$\frac{G_0}{\pi}\int_{-a}^{a}\left[\frac{1}{t-x}+\tilde{K}_\gamma(x,t)\right]\phi(t)dt = p(x), \quad -a<x<a \tag{A3}$$

Erdogan and Ozturk [22] have investigated this problem as bonded nonhomogeneous materials with an interface cut.

3. Classical LEFM, Nonhomogeneous Materials ($G \equiv G(x) = G_0 e^{\beta x}$)
   - PDE: Perturbed Laplace equation $(\nabla^2 + \beta(\partial/\partial x))w(x,y)=0$.
   - Integral equation with the density function $\phi(x) = \partial w(x,0)/\partial x$:

$$\frac{G(x)}{\pi}\int_c^d\left[\frac{1}{t-x}+\frac{\beta}{2}\log|t-x|+\tilde{N}(x,t)\right]\phi(t)dt = p(x), \quad c<x<d \tag{A4}$$

   - Integral equation with the density function $\phi(x) = w(x,0)$:

$$\frac{G(x)}{\pi}\oint_c^d\left[\frac{1}{(t-x)^2}+\frac{\beta}{2(t-x)}+N(x,t)\right]\phi(t)dt = p(x), \quad c<x<d \tag{A5}$$

The regular kernels $\tilde{N}(x,t)$ in Eq. (A4) and $N(x,t)$ in Eq. (A5) can be found in Ref. [6]. Erdogan [7] has studied this problem for bonded nonhomogeneous materials.

4. Gradient Elasticity, Homogeneous Materials ($G \equiv G_0$)
   - PDE: Helmholtz–Laplace equation $(1-\ell^2\nabla^2)\nabla^2 w(x,y)=0$.
   - Integral equation with the density function $\phi(x) = \partial w(x,0)/\partial x$:

$$\frac{1}{\pi}\oint_c^d\left\{\frac{-2\ell^2}{(t-x)^3}+\frac{1-(\ell'/\ell)^2/4}{t-x}+K_0(t-x)\right\}\phi(t)dt + \frac{\ell'}{2}\phi'(x) = \frac{p(x)}{G_0} \tag{A6}$$

Fannjiang et al. [5] have studied Eq. (A6) in detail.

5. Gradient Elasticity, Nonhomogeneous Materials ($G \equiv G(y) = G_0 e^{\gamma y}$)
   - PDE: $(1-\gamma\ell^2(\partial/\partial y)-\ell^2\nabla^2)(\nabla^2+\gamma(\partial/\partial y))w(x,y)=0$.
   - Integral equation with the density function $\phi(x) = \partial w(x,0)/\partial x$:

$$\frac{G_0}{\pi}\oint_{-a}^{a}\left\{\frac{-2\ell^2}{(t-x)^3}+\frac{5\ell^2\gamma^2/8+\ell'\gamma/4+1-(\ell'/\ell)^2/4}{t-x}+k_\gamma(x,t)\right\}\phi(t)dt+G(\ell'/2+\ell^2\gamma)\phi'(x)=p(x),\quad |x|<a \tag{A7}$$

This is the Part I paper by Paulino et al. [1].

6. Gradient Elasticity, Nonhomogeneous Materials ($G\equiv G(x)=G_0e^{\beta x}$)

- PDE: $(1-\beta\ell^2(\partial/\partial x)-\ell^2\nabla^2)(\nabla^2+\beta(\partial/\partial x))w(x,y)=0$.
- Integral equation with the density function $\phi(x)=\partial w(x,0)/\partial x$:

$$\frac{1}{\pi}\oint_{c}^{d}\left\{\frac{-2\ell^2}{(t-x)^3}-\frac{3\beta\ell^2}{2(t-x)^2}+\frac{1-3\ell^2\beta^2/8-[\ell'/(2\ell)]^2}{t-x}+k(x,t)\right\}\phi(t)dt+\frac{\ell'}{2}\phi'(x)+\frac{\beta\ell'}{2}\phi(x)=p(x)/G,\quad c<x<d$$

This is the main governing integral equation (55*a*).

- Integral equation with the density function $\phi(x)=w(x,0)$:

$$\frac{1}{\pi}\oint_{c}^{d}\left\{\frac{-6\ell^2}{(t-x)^4}-\frac{3\ell^2\beta}{(t-x)^3}+\frac{1-\left(\frac{\ell'}{2\ell}\right)^2-\frac{3\ell^2\beta^2}{8}}{(t-x)^2}+\frac{\frac{\beta}{2}\left[1-\left(\frac{\ell'}{2\ell}\right)^2\right]+\frac{\ell^2\beta^3}{16}}{t-x}+\tilde{k}(x,t)\right\}\phi(t)dt+\frac{\ell'}{2}\phi''(x)-\frac{\ell'\beta}{2}\phi'(x)-\left[\frac{1}{\ell}\left(\frac{\ell'}{2\ell}\right)^3+\frac{\ell'}{8\ell^2}\right]\phi(x)=\frac{p(x)}{G(x)},\quad c<x<d$$

References

[1] Paulino, G. H., Chan, Y.-S., and Fannjiang, A. C., 2003, "Gradient Elasticity Theory for Mode III Fracture in Functionally Graded Materials-Part I: Crack Perpendicular to the Material Gradation," ASME J. Appl. Mech., **70**(4), pp. 531–542.

[2] Chan, Y.-S., Paulino, G. H., and Fannjiang, A. C., 2006, "Change of Constitutive Relations Due to Interaction Between Strain-Gradient Effect and Material Gradation," ASME J. Appl. Mech., **73**(5), pp. 871–875.

[3] Exadaktylos, G., Vardoulakis, I., and Aifantis, E., 1996, "Cracks in Gradient Elastic Bodies With Surface Energy," Int. J. Fract., **79**(2), pp. 107–119.

[4] Vardoulakis, I., Exadaktylos, G., and Aifantis, E., 1996, "Gradient Elasticity With Surface Energy: Mode-III Crack Problem," Int. J. Solids Struct., **33**(30), pp. 4531–4559.

[5] Fannjiang, A. C., Chan, Y.-S., and Paulino, G. H., 2002, "Strain-Gradient Elasticity for Mode III Cracks: A Hypersingular Integrodifferential Equation Approach," SIAM J. Appl. Math., **62**(3), pp. 1066–1091.

[6] Chan, Y.-S., Paulino, G. H., and Fannjiang, A. C., 2001, "The Crack Problem for Nonhomogeneous Materials Under Antiplane Shear Loading—A Displacement Based Formulation," Int. J. Solids Struct., **38**(17), pp. 2989–3005.

[7] Erdogan, F., 1985, "The Crack Problem for Bonded Nonhomogeneous Materials Under Antiplane Shear Loading," ASME J. Appl. Mech., **52**(4), pp. 823–828.

[8] Zhang, L., Huang, Y., Chen, J. Y., and Hwang, K. C., 1998, "The Mode III Full-Field Solution in Elastic Materials With Strain Gradient Effects," Int. J. Fract., **92**(4), pp. 325–348.

[9] Georgiadis, H. G., 2003, "The Mode III Crack Problem in Microstructured Solids Governed by Dipolar Gradient Elasticity: Static and Dynamic Analysis," ASME J. Appl. Mech., **70**(4), pp. 517–530.

[10] Titchmarsh, E. C., 1986, *Introduction to the Theory of Fourier Integrals*, Chelsea, New York.

[11] Kaya, A. C., and Erdogan, F., 1987, "On the Solution of Integral Equations With Strongly Singular Kernels," Q. Appl. Math., **45**(1), pp. 105–122.

[12] Monegato, G., 1994, "Numerical Evaluation of Hypersingular Integrals," J. Comput. Appl. Math., **50**, pp. 9–31.

[13] Chan, Y.-S., Fannjiang, A. C., and Paulino, G. H., 2003, "Integral Equations With Hypersingular Kernels-Theory and Application to Fracture Mechanics," Int. J. Eng. Sci., **41**, pp. 683–720.

[14] Folland, G. B., 1992, *Fourier Analysis and Its Applications*, Wadsworth and Brooks/Cole Advanced Books and Software, Pacific Grove, CA.

[15] Stroud, A. H., and Secrest, D., 1966, *Gaussian Quadrature Formulas*, Prentice-Hall, New York.

[16] Chen, J. Y., Huang, Y., Zhang, L., and Ortiz, M., 1998, "Fracture Analysis of Cellular Materials: A Strain Gradient Model," J. Mech. Phys. Solids, **46**(5), pp. 789–828.

[17] Huang, Y., Chen, J. Y., Guo, T. F., Zhang, L., and Hwang, K. C., 1999, "Analytic and Numerical Studies on Mode I and Mode II Fracture in Elastic-Plastic Materials With Strain Gradient Effects," Int. J. Fract., **100**(1), pp. 1–27.

[18] Fleck, N. A., and Hutchinson, J. W., 1997, "Strain Gradient Plasticity," *Advances in Applied Mechanics*, Vol. 33, J. W. Hutchinson and T. Y. Wu, eds., Academic, New York, pp. 295–361.

[19] Chen, J. Y., Wei, Y., Huang, Y., Hutchinson, J. W., and Hwang, K. C., 1999, "The Crack Tip Fields in Strain Gradient Plasticity: The Asymptotic and Numerical Analyses," Eng. Fract. Mech., **64**, pp. 625–648.

[20] Shi, M. X., Huang, Y., and Hwang, K. C., 2000, "Fracture in a Higher-Order Elastic Continuum," J. Mech. Phys. Solids, **48**(12), pp. 2513–2538.

[21] Sneddon, I. N., 1972, *The Use of Integral Transforms*, McGraw-Hill, New York.

[22] Erdogan, F., and Ozturk, M., 1992, "Diffusion Problems in Bonded Nonhomogeneous Materials With an Interface Cut," Int. J. Eng. Sci., **30**(10), pp. 1507–1523.

Daniil Iourtchenko
e-mail: daniil@phmf.spbstu.ru
Department of Mathematical Sciences,
Saint Petersburg State Polytechnical University,
Saint Petersburg, 195251 Russia

Eirik Mo[1]
e-mail: mo@math.ntnu.no
Department of Mathematical Sciences,
Norwegian University of Science and Technology,
NO-7491 Trondheim, Norway

Arvid Naess
e-mail: arvidn@math.ntnu.no
Department of Mathematical Sciences,
Centre for Ships and Ocean Structures,
Norwegian University of Science and Technology,
NO-7491 Trondheim, Norway

Reliability of Strongly Nonlinear Single Degree of Freedom Dynamic Systems by the Path Integration Method

This paper presents a first passage type reliability analysis of strongly nonlinear stochastic single-degree-of-freedom systems. Specifically, the systems considered are a dry friction system, a stiffness controlled system, an inertia controlled system, and a swing. These systems appear as a result of implementation of the quasioptimal bounded in magnitude control law. The path integration method is used to obtain the reliability function and the first passage time. [DOI: 10.1115/1.2967896]

Keywords: probability density function, path integration, strongly nonlinear systems, control, swings, random vibrations, outcrossing rate, reliability

1 Introduction

Reliability and safety are the major concerns in designing and developing modern mechanical systems. A system's reliability may be considered as the probability that no system failure occurs within a given time interval. Often the reliability problem is associated with finding the probability that a system's response stays within a prescribed domain, an outcrossing of which leads to immediate failure. A problem of this type is called *the first passage problem* [1–3], and it has been extensively studied by a number of authors. The first passage problem is directly related to a solution of the corresponding Pontryagin equation, written with respect to the first excursion time T. Unfortunately, an exact analytical solution to this problem, even for a linear system, is yet to be found. A few strategies have been proposed over the years to deal with this type of problems. One of them is based on an averaging procedure and further problem reformulation for the system's response amplitude or energy. The Markov property of the energy envelope has been used to evaluate the probability of the first passage time for a linear system [4], systems with nonlinear stiffness [5], or nonlinear damping [6].

A number of problems have been solved numerically and analytically since then. A numerical solution to the Pontryagin equation has been developed in Refs. [7–9], whereas a numerical solution to the backward Kolmogorov–Feller equation, for a system subjected to a Poisson driven train of impulses, has been proposed in Ref. [10].

New analytical and numerical approaches have been reported in Refs. [11–13]. The method proposed in Ref. [11] can only be used in practice for problems where the stochastic aspect can be represented by a very limited number of random variables. Hence, it would not seem to be applicable for problems with stochastic process inputs of the kind studied in this paper. In Ref. [12], a method is described for estimating the exceedance probability of time variant systems with random parameters by using an improved response surface technique. However, the accuracy of such a method for the problems considered in this paper is hard to assess. Recently, a new tail-equivalent linearization method has been developed in Ref. [14], which may be used for reliability estimates for single as well as multiple-degree-of-freedom (MDOF) systems for stationary inputs.

Special attention should be paid to the reliability of systems, which appears as a result of some design or optimization procedures. Indeed, the purpose of these procedures is to satisfy certain criteria, often not related to the system's reliability. In fact, their implementation may lead to a deterioration of the system's reliability. For instance, consider a stochastic optimal control problem, which aims to reduce the mean response energy of a single-degree-of-freedom (SDOF) undamped linear oscillator, subjected to a zero-mean external Gaussian white noise, by means of a bounded in magnitude control force. It has been demonstrated in Ref. [15] that an optimal control law for a steady-state response is represented by a dry friction law. On the other hand, it has been shown by asymptotic analysis in Ref. [16] that a stochastic system with dry friction is less reliable than that of a system with linear damping. Therefore, a reliability investigation of controlled stochastic systems may be of special importance.

This paper is devoted to a reliability investigation of four types of controlled systems by application of the numerical path integration (PI) method [17]. The PI code is validated by comparing some results to the results of the Monte Carlo simulations as well as results obtained for an equivalent linear system. The latter makes sense only for "weak" nonlinearities, i.e., for small values of the control parameter r ($r \ll 1$). First, a system with dry friction is studied; its asymptotic analysis has been made in Ref. [16] with respect to the system's energy. The other three SDOF systems under consideration are systems with parametric control of their parameters. They appear as a result of application of bounded in magnitude control forces, applied consequently to the system's stiffness, inertia, or by varying a pendulum's length (swings) [18–20]. Although the idea of controlling a system's response by changing its parameters is far from being new (see examples in Ref. [21]), the proposed strategy leads to control forces of the signum type. It makes these systems *strongly nonlinear* and their analysis highly complicated, especially for large "amplitude" of jumps at switching (values of r close to unity). Since the available asymptotic techniques provide reliable estimates for nonlinear systems only in the case of small nonlinearities, it was decided to conduct a numerical investigation, comparing some obtained results to the reliability results for an equivalent linear system. The latter is constructed using values of an equivalent viscous damping coefficient and effective frequency. The path integration

[1]Corresponding author.

Contributed by the Applied Mechanics Division of ASME for publication in the JOURNAL OF APPLIED MECHANICS. Manuscript received May 8, 2007; final manuscript received June 23, 2008; published online August 21, 2008. Review conducted by Wei-Chau Xie.

method has been used earlier for these systems to estimate the stationary response probability density function (PDF) of the state space variables [22]. Here the PI method has been adapted to obtain the reliability characteristics of the considered systems. The approach is based on previous work reported in Ref. [23].

2 Problem Statement and Numerical Approach

2.1 Path Integration Approach to Reliability. The SDOF dynamic systems to be investigated in this paper can all be written in the following form:

$$\ddot{X} + g(X,\dot{X}) = \xi(t) \tag{1}$$

where $g(\cdot,\cdot)$ denotes a function to be specified in each particular case, while $\xi(t)$ throughout denotes a zero-mean stationary Gaussian white noise process satisfying $E[\xi(t)\xi(t+\tau)]=D\delta(\tau)$ for a positive intensity parameter D. The application of the external quasioptimal control policy leads to a dry friction law, whereas the application of the quasioptimal control force results in parametrically controlled systems with a jumpwise variation of either the system's stiffness, moment of inertia, or both. The latter happens through a variation of the pendulum's length and such a system is well known as a swing.

Equation (1) will be construed as an Itô stochastic differential equation (SDE), that is,

$$dZ(t) = h(Z(t))dt + bdB(t) \tag{2}$$

where the state space vector process $Z(t)=(X(t),Y(t))^T=(X(t),\dot{X}(t))^T$ has been introduced, $h=(h_1,h_2)^T$ with $h_1(Z)=Y$ and $h_2(Z)=-g(X,Y)$, $b=(0,\sqrt{D})^T$, and $B(t)$ denotes a standard Brownian motion process. From Eq. (2) it follows immediately that $Z(t)$ is a Markov process, and it is precisely the Markov property that will be used in the formulation of the PI procedure.

The reliability is defined in terms of the displacement response process $X(t)$ in the following manner, assuming that all events are well defined:

$$R(T|x_0,0,t_0) = \text{Prob}\{x_l < X(t) < x_c; t_0 < t \le T | X(t_0)=x_0, Y(t_0)=0\} \tag{3}$$

where x_l, x_c are the lower and upper threshold levels defining the safe domain of operation. Hence, the reliability $R(T|x_0,0,t_0)$, as we have defined it here, is the probability that the system response $X(t)$ stays above the threshold x_l and below the threshold x_c throughout the time interval (t_0,T) given that it starts at time t_0 from x_0 with zero velocity ($x_l<x_0<x_c$). In general, it is impossible to calculate the reliability exactly as it has been specified here since it is defined by its state in continuous time, and for most systems the reliability has to be calculated numerically, which inevitably will introduce a discretization of the time. Assuming that the realizations of the response process $X(t)$ are piecewise differentiable with bounded slope with probability one, the following approximation is introduced:

$$R(T|x_0,0,t_0) \approx \text{Prob}\{x_l < X(t_j) < x_c, j=1,\ldots,n | X(t_0)=x_0, Y(t_0)=0\} \tag{4}$$

where $t_j=t_0+j\Delta t$, $j=1,\ldots,n$, and $\Delta t=(T-t_0)/n$. With the assumptions made, the right hand side (rhs) of this equation can be made to approximate the reliability as closely as desired by appropriately choosing Δt, or equivalently n. Within the adopted approximation, it is realized that the reliability can now be expressed in terms of the joint conditional PDF

$$f_{X(t_1)\cdots X(t_n)|X(t_0),Y(t_0)}(\cdot,\ldots,\cdot|x_0,0)$$

as follows, which is just a rephrasing of Eq. (4):

$$R(T|x_0,0,t_0) \approx \int_{x_l}^{x_c}\cdots\int_{x_l}^{x_c} f_{X(t_1)\cdots X(t_n)|X(t_0)Y(t_0)} \times (x_1,\ldots,x_n|x_0,0)dx_1\cdots dx_n \tag{5}$$

Due to the Markov property of the state space vector process $Z(t)=(X(t),Y(t))^T$, we may express the joint PDF of $Z(t_1),\ldots,Z(t_n)$ in terms of the transition probability density function

$$p(z,t|z',t') = f_{Z(t)|Z(t')}(z|z') = f_{Z(t)Z(t')}(z,z')/f_{Z(t')}(z'), \quad (f_{Z(t')}(z') \neq 0)$$

in the following way:

$$f_{Z(t_1)\ldots Z(t_n)|Z(t_0)}(z_1,\ldots,z_n|z_0) = \prod_{j=1}^{n} p(z_j,t_j|z_{j-1},t_{j-1}) \tag{6}$$

This leads to the expression $(z_0=(x_0,0)^T, dz_j=dx_jdy_j, j=1,\ldots,n)$.

$$R(T|x_0,0,t_0) \approx \int_{-\infty}^{\infty}\int_{x_l}^{x_c}\cdots\int_{-\infty}^{\infty}\int_{x_l}^{x_c}\prod_{j=1}^{n} p(z_j,t_j|z_{j-1},t_{j-1})dz_1\cdots dz_n \tag{7}$$

which is the path integration formulation of the reliability problem. The numerical calculation of the reliability is done iteratively in an entirely analogous way as in standard path integration. To show that, let us introduce a reliability density function (RDF) $q(z,t|z_0,t_0)$ as follows:

$$q(z_2,t_2|z_0,t_0) = \int_{-\infty}^{\infty}\int_{x_l}^{x_c} p(z_2,t_2|z_1,t_1)p(z_1,t_1|z_0,t_0)dz_1 \tag{8}$$

and $(n>2)$,

$$q(z_k,t_k|z_0,t_0) = \int_{-\infty}^{\infty}\int_{x_l}^{x_c} p(z_k,t_k|z_{k-1},t_{k-1})q(z_{k-1},t_{k-1}|z_0,t_0)dz_{k-1}, k=3,\ldots,n \tag{9}$$

The reliability is then finally calculated approximately as $(T=t_n)$.

$$R(T|x_0,0,t_0) \approx \int_{-\infty}^{\infty}\int_{x_l}^{x_c} q(z_n,t_n|z_0,t_0)dz_n \tag{10}$$

The complementary probability distribution of the time to failure T_e, i.e., the first passage time, is given by the reliability function. The mean time to failure $\langle T_e\rangle$ can thus be calculated by the equation

$$\langle T_e\rangle = \int_0^{\infty} R(\tau|x_0,0,t_0)d\tau \tag{11}$$

To evaluate the reliability function, it is required to know the transition probability density function $p(z,t|z',t')$, which is unknown for the considered nonlinear systems. However, from Eq. (2), it is seen that for a small $t-t'$ it can be determined approximately, which is what is needed for the numerical calculation of the reliability. A detailed discussion of this and the iterative integrations of Eqs. (8) and (9) are given in Refs. [22,24]. Concerning the integrations, there is, however, one small difference between the present formulation and that described in these references. In Eqs. (8) and (9), the integration in the x-variable only extends over the interval (x_l,x_c). The infinite upper and lower limits on the y-variable are replaced by suitable constants determined by, e.g., an initial Monte Carlo simulation (MCS).

If the system response $Z(t)$ has a stationary response PDF $f_Z(z)$ as $t\to\infty$, it follows that the conditional response PDF

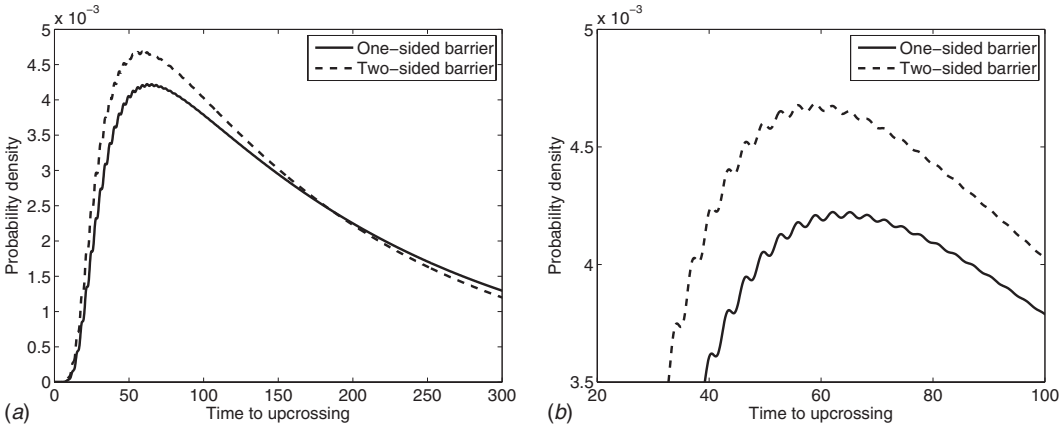

Fig. 1 Probability density of time to failure for the dry friction problem with reliability level 2.5 standard deviations and $r=0.15$ for the one- and two-sided cases

$f_{\{Z(t_n)|Z(0),x_l<X(t_j)<x_c;0\le j\le n-1\}}(z)$ will also reach a stationary density, say, $q^*(z)$, when $t_n\to\infty$, provided the system has finite memory. This means that the reliability process eventually becomes memoryless, and hence the RDF converges $q(z,t_n|z_0,t_0)\to q^*(z)Ke^{-\nu t_n}$ for some constants K and ν as $t_n\to\infty$. Also the numerical method should reach stationarity in the conditional density. This also implies that the numerically estimated reliability function must be exponential, since the same relative amount of probability mass leaves the system at every iteration. Hence in the end, the only thing one should need for a good reliability estimate is the behavior in the transient phase and the exponential decay thereafter.

2.2 General Comments About the Numerical Procedure. The numerical calculations were performed for a 256×256 mesh in the state space, with very high grid resolution around the axes for the inertia controlled system and swing system, because the PDFs have discontinuities along the axes and high spikes at the discontinuity that requires a well adapted spline representation [22]. More specifically, the grid resolution was determined by an exponentially decaying function away from each coordinate axis. Because of the discontinuities, there are no grid points on the axes themselves. However, the interpolant will be globally smooth and will assume finite values also on the axes. Hence, there is no true discontinuity in the interpolant even if the gradients of the interpolant may be very large at the axes. The time step was 0.01 for all simulations, and the noise intensity D was set to 1.0. The initial choice of time step is determined by the characteristic time constants of the dynamic system, which can be either seen from the system equations or from a short Monte Carlo simulation of the dynamic response of the system. As is typically done for verifying the convergence of numerical solutions, the accuracy of the calculated PI solution may be checked by changing repeatedly, if required, the size of the time step, for example, by a factor 2.

For all simulations, the reliability was computed using the barriers $x_c=2.5\sigma_x$, $x_c=3.0\sigma_x$, and $x_c=3.5\sigma_x$. The lower barrier is either $x_l=-\infty$, one-sided barrier case, or $x_l=-x_c$ for two-sided reliability. These bounds were far enough out in the tails that interpolation of the RDF from Eqs. (8) and (9) was no problem.

It should be mentioned that for all the systems studied in this paper, the calculated reliability function displayed a distinctive exponential behavior asymptotically, as one would expect. That is, after some transient time, the reliability function could not be distinguished from a straight line when plotted on a logarithmic scale. In addition, the PDF for the time to failure has a right tail that is exponential with the same exponent, which again is verified by plotting the PDF on a logarithmic scale. The oscillatory behavior of the PDFs of the time to failure, as seen on the close ups, largely reflects the transient dynamics of the systems due to initial conditions (see Fig. 1, for instance).

3 Monte Carlo Simulation

To check the numerical results, MCSs have been run for a few selected cases. The main problem is that the probability of crossing a high reliability level is small, so the simulation will have to run for a long time before this happens. Since a good approximation of the PDF for the first passage time needs a large number of Monte Carlo simulations, this easily becomes a very time consuming method. The verification of the numerical results by Monte Carlo simulations is therefore carried out on two levels. First, the expected first passage time is estimated directly from simulated response time histories for the lowest level ($=2.5\sigma$), where σ equals the standard deviation of stationary response. For all the models investigated in this paper, the estimated expected first passage time obtained by MCS agreed with the corresponding one calculated by PI within the accuracy of the MCS estimate, that is, within a few percent.

The second method of verification was based on the observation that the reliability function and the PDF decays exponentially after a transient time. A focus on the estimation of the rate of decay reduces the number of required simulations considerably. That is, the main statistic to estimate from the stochastic upcrossing time T is ν, given the formula

$$P(T>t|T>t_{\text{tr}})=e^{-\nu(t-t_{\text{tr}})},\quad t>t_{\text{tr}} \tag{12}$$

where t_{tr} stands for the *transient* time. Equation (12) is an approximation, since the transient never dies out completely. However, the equation is asymptotically correct as $t_{\text{tr}}\to\infty$, and numerically valid for a transient time chosen sufficiently large. An adjusted maximum likelihood estimator (MLE) for ν, which is also unbiased for a fixed transient time t_{tr}, is

$$\hat{\nu}=\frac{n-1}{\Sigma_{i=1}^{n}(T_i-t_{\text{tr}})} \tag{13}$$

for n independent upcrossing times T_i that are all larger than t_{tr}. This means that some Monte Carlo simulations with exit time shorter than the transient time will be discarded, but as the probability of exiting that early from a start at the origin is small, most results will be used.

It is important to note that estimating the full PDF, and here especially the transient behavior, is very time consuming with the Monte Carlo methods without a parametric model. Path integration, however, calculates this directly, and if only the transient behavior is needed, the PDF can be found with high accuracy with a fairly short simulation.

When comparing the results for the MC and the PI methods, remember that the strengths and weaknesses of the numerical

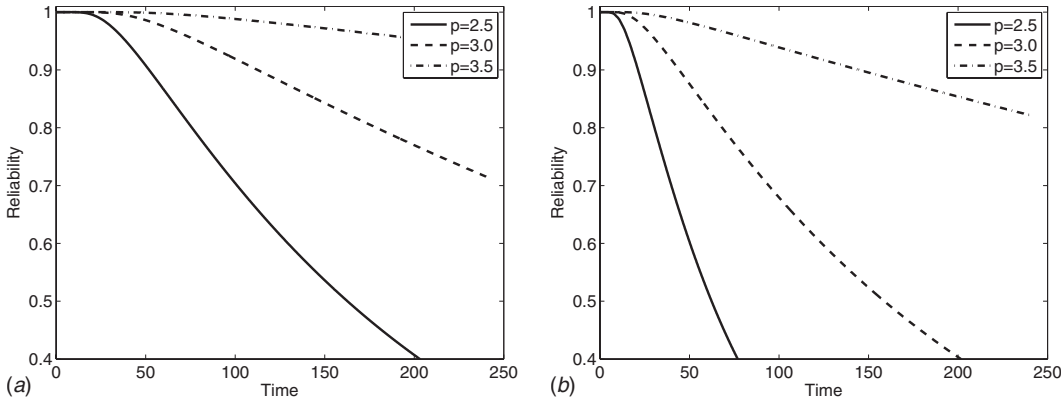

Fig. 2 One-sided reliability function of the dry friction system for different levels of *p*

methods are also very different. The main problem for the PI method is that the PDFs have sharp discontinuities or peaks that make the interpolation difficult.

The exponent can, however, be calculated between two time steps from long after the transient has died out.

The MC method relies on the parametric representation of the PDF after an estimated transient time, which is an approximation. The point estimates of parameter from MC are here calculated from 200 random samples and hence have a variance.

Since $T_i - t_{\text{tr}}$ is assumed to be exponentially distributed, $\hat{\nu}/(n-1)$ has an inverse gamma distribution, and the variance is

$$\text{Var}(\hat{\nu}) = \frac{\nu^2}{(n-2)} \tag{14}$$

Hence, instead of estimating the standard deviation of the test statistic $\hat{\nu}$ for the MC simulation, Eq. (14) gives that it is approximately $\hat{\nu}/\sqrt{198} = 0.07\hat{\nu}$.

The MC simulations were performed for all four systems, and the estimated values of ν from the PI calculations were checked against the 90% confidence intervals based on the MC results, and they were all accepted.

4 Results for a Stochastic Dry Friction System

In this section, some derivations made in Ref. [16] for a stochastic system with dry friction are recalled. It is worth mentioning that for the parametric systems the stochastic averaging procedure results in an exponential response PDF for response energy, whereas the dry friction system has an exponent in power of the square root of the response energy. Therefore, for the parametrically controlled systems, the case of small nonlinearity cannot be caught by the averaging procedure and needs to be investigated numerically. For the system with dry friction, it is possible to use an approximate analysis for a small value of the dry friction coefficient. Early results on the use of PI for an oscillator with dry friction are reported in Ref. [25].

Consider the following nonlinear system, subjected to the zero-mean, stationary Gaussian white noise $\xi(t)$ introduced above:

$$\ddot{X} + r\,\text{sign}(\dot{X}) + \Omega^2 X = \xi(t), \quad 0 \le t \le t_f \tag{15}$$

Applying the stochastic averaging procedure and following the derivations made in Ref. [16] the first passage time may be found as

$$T(c) = \frac{[\text{Ei}(2\lambda\sqrt{\bar{c}}) - \text{Ei}(2\lambda\sqrt{c})]}{2\Omega\lambda^2} - \frac{\sqrt{\bar{c}} - \sqrt{c}}{\Omega\lambda} - \frac{\ln(\bar{c}/c)}{4\Omega\lambda^2}$$
$$c = \frac{E}{D/4\Omega}, \quad \bar{c} = \frac{\bar{E}}{D/4\Omega}, \quad \lambda = \frac{2\sqrt{2}\mu}{\pi}, \quad \mu = \frac{r}{\sqrt{D\Omega}} \tag{16}$$

where $\text{Ei}(y)$ is the exponential integral function, D is the noise intensity, and $\bar{E}$ is the critical value of energy. Thus, an analytical expression (16) may be used for reliability estimates, keeping in mind that r should be small. This result may be compared with one, reported in Ref. [2], keeping in mind that the value of an equivalent viscous damping coefficient is equal to

$$\alpha_{\text{eq}}^{df} = \frac{16r^2}{3\pi^2 D}$$

It can be seen from the comparison with the result for the linear system [2] that Eq. (16) has an additional second term, which is non-negative. Moreover, the exponential integral function (16) depends on the square root of the system's energy, whereas the formula for an equivalent linear system [2] predicts dependence on the system's energy itself. Both these facts indicate that the first passage time to failure for the dry friction system should be less than that for an equivalent linear system.

Numerical simulations, conducted using the PI method, have shown that the joint response PDF has a single peak, at small values of r, which splits into two peaks, moving away from each other, when the nonlinearity parameter r increases. A peak of the probability density of time to failure moves left when the value of r increases, which indicates deterioration of the system's reliability. Figure 1 demonstrates the results of a numerical simulation for one- and two-sided probability densities of time to failure. It can be seen from Fig. 1(*a*) that both densities have similar shapes and

Table 1 Expected time to upcrossing for the dry friction system. All numbers to be $\times 10^3$.

p	2.5σ	2.5σ	3.0σ	3.0σ	3.5σ	3.5σ
r	One-sided	Two-sided	One-sided	Two-sided	One-sided	Two-sided
0.15	0.2167	0.1947	0.6009	0.5344	2.6885	2.1427
0.20	0.1344	0.1170	0.3697	0.3166	1.7757	1.2995
0.25	0.0814	0.0689	0.2169	0.1791	1.0834	0.7344

Table 2 Linear system with a damping coefficient α: expected time to upcrossing. All numbers to be $\times 10^3$.

p / α	2.5σ One-sided	2.5σ Two-sided	3.0σ One-sided	3.0σ Two-sided	3.5σ One-sided	3.5σ Two-sided
$16\cdot 0.15^2/(3\pi^2)$	0.5594	0.4884	1.7249	1.4670	4.7063	4.3196
$16\cdot 0.20^2/(3\pi^2)$	0.3808	0.3165	1.2338	0.9869	4.1552	3.5478
$0.10/\pi$	0.2859	0.2281	0.9370	0.7143	3.5829	2.8099
$16\cdot 0.25^2/(3\pi^2)$	0.2810	0.2225	0.9331	0.7046	3.6107	2.8128
$0.30/\pi$	0.1710	0.1149	0.6250	0.3927	2.9383	1.8043
$0.50/\pi$	0.1497	0.0909	0.5743	0.3265	2.8247	1.5878
$0.90/\pi$	0.1376	0.0749	0.5418	0.2831	2.6838	1.4232

are almost identical (except the peak value), which was expected, since the considered problem is symmetric. Similar behavior has been observed for other problems investigated here. Thus, figures for one- and two-sided probability densities of time to failure are not presented for parametric systems. Figure 2 presents the reliability function for $r=0.15$ (a) and $r=0.25$ (b) for different values of the crossing level $p=x_c/\sigma_x$. These results show strong dependence of the reliability function on r, i.e., an increase in r increases the slope of the reliability function, consequently decreasing the time to failure. At first glance, this may seem odd, but remember that an increase in r leads to a decrease in σ_x, and therefore in the critical level. On the other hand, an increase in the crossing level leads, as expected, to an increase in the first passage time value for a fixed value of r.

Table 1 presents the results of numerical simulations for the first passage time. The data in Table 1 may be compared with the data presented in the first, second, and fourth lines of Table 2. Direct comparison of these results, for the same level of energy dissipation in both systems, shows that the dry friction system has a significantly (at least twice) smaller value of failure time than that of the equivalent linear system, which indicates a relatively poor reliability of the dry friction system.

5 Results for Parametrically Controlled Systems

To verify the code and to qualitatively comprehend the new results, it is proposed to obtain numerical results for a linear system, subjected to external Gaussian white noise, in addition to the Monte Carlo method described in Sec, 3. The results, obtained by the PI method, very well agreed with the results of MC simulations. To compare these results with results for the considered nonlinear systems, for small values of nonlinearity parameter, one has to select a proper value of viscous damping coefficient. It should be reminded that the value of an equivalent viscous damping coefficient for stiffness and inertia controlled systems is $\alpha_{eq}=r\Omega/\pi$, and this value is tripled for a swing system [18,19]. Therefore, in order to compare the results it is decided to select $\alpha_{eq}=r/\pi$ for $r=0.1,0.3,0.5$ ($\Omega=1$). The results for the probability density function of failure time for the three largest mentioned values of α_{eq} are shown in Fig. 3. Table 2 presents the results for the mean time to failure for different values of the equivalent viscous damping coefficient, corresponding to different values of r, according to the above mentioned formulas.

5.1 System With Controlled Stiffness. Consider a stochastic system with controlled stiffness, whose motion is governed by the following equation:

$$\ddot{X}+\Omega^2 X[1+r\ \mathrm{sign}(X\dot{X})]=\xi(t),\quad 0\le t\le t_f \tag{17}$$

where $0<r<1$. The probability densities are obtained numerically by extrapolating the probability of no upcrossing by an exponential function and differentiating this numerically. The sampling points were dense $\Delta t_{samp}=0.16$ s so that the differentiation proved to be very accurate. The transient seemed noisy, but a closer look would show that there is actually a smooth oscillation. The peak-to-peak period of this oscillation seems to coincide well with the effective period of the system [22]. An interpretation is that the system's variability has to reach a certain level before the probability of exceedance is substantially high. The first substantial removal of the high-displacement part of the probability density gradually starts to affect the exceedance probability approximately one period later. This behavior is consistent with previous observations, and the same kind of oscillations is also seen in the PI results for the equivalent linear system.

Figure 4 presents the results of the failure time PDF as a function of the nonlinearity parameter r. In Fig. 5 one can observe the reliability function for different values of the upcrossing level p,

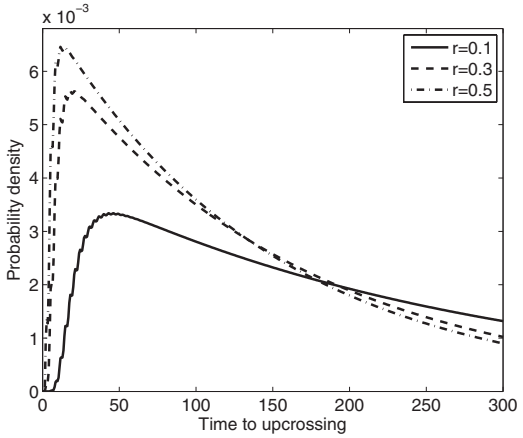

Fig. 3 Probability density of time to failure for the linear system with reliability level 2.5 standard deviations and $r=0.1$, 0.3, and 0.5

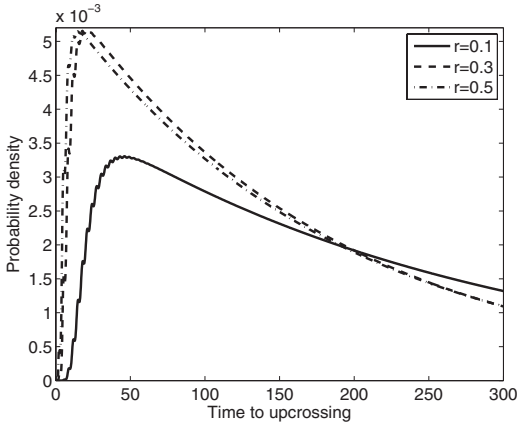

Fig. 4 Probability density of time to failure for the stiffness control problem with reliability level 2.5 standard deviations and $r=0.1,0.3,0.3$, and 0.5

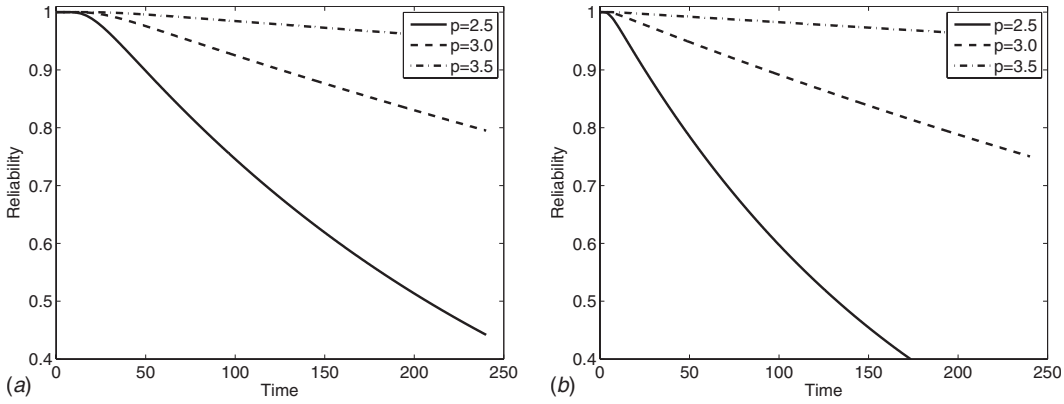

Fig. 5 Reliability function for the stiffness control problem with one-sided barrier for different levels of *p*

with $r=0.1$ (a) and $r=0.5$ (b) correspondingly. Comparing the results (a) and (b) indicates that an increase in nonlinearity influences the system's reliability much more when small values of the upcrossing level are selected. Results in Fig. 5 have been compared with results for an equivalent linear system. Direct comparison revealed that the behavior of the equivalent system, in terms of the reliability function, matches the behavior of the stiffness controlled system for small values of the nonlinearity parameter r. Meanwhile, detailed comparison for $r=0.5$ indicates that the stiffness controlled system's time to failure is bigger than that of the linear system with the same level of energy dissipation in both systems. This fact is reflected in Table 3, which shows the mean failure time for the stiffness controlled system. It should be reported that the observed behavior is different from the behavior of the two other parametric systems. Namely, it is seen, based on the numerical results, that there is no monotonic decrease in mean upcrossing time with a gradual increase in r. However, Monte Carlo simulations confirm these results for $2.5\sigma_x$.

5.2 System With Controlled Moment of Inertia. Consider a system with controlled moment of inertia:

$$\frac{d}{dt}\{[1+r\ \mathrm{sign}(\phi\dot{\phi})]\dot{\phi}\}+\Omega^2\phi=\xi(t),\quad 0\le t\le t_f \tag{18}$$

where $0<r<1$. The exponential behavior for the absorbing probability density has been observed in this case. Figure 6 presents results for the probability density function of failure time for $p=2.5$ and different values of the nonlinearity parameter. One can clearly see a trend in the peak shift to the left with the increase of r. Figure 7 illustrates results for the reliability function for $r=0.1$ (a) and $r=0.5$ (b), respectively. Comparison with the results obtained for the stiffness controlled and linear system shows that the reliability function of the inertia controlled system has a less steep angle, which indicates that this system is "more" reliable. This fact is reflected in Table 4, where for small values of r one can find that $T_{\mathrm{in}}\ge T_{\mathrm{sc}}\approx T_{\mathrm{lin}}$, whereas for large values of r one obtains $T_{\mathrm{lin}}\le T_{\mathrm{in}}\le T_{\mathrm{sc}}$.

5.3 Swings. A governing equation of motion of a mathematical pendulum with controlled length or swings may be written as

$$\frac{d}{dt}(L^2\dot{\phi})+\Omega^2 L\sin(\phi)=\xi(t),\quad 0\le t\le t_f$$
$$L=[1+r\ \mathrm{sign}(\phi\dot{\phi})],\quad \Omega^2=g/L_0 \tag{19}$$

For small values of ϕ the nonlinear term in Eq. (19) is changed to $\sin(\phi)\sim\phi$, thereby giving the linearized equation of a swing. The smooth oscillatory behavior of the PDF with a frequency close to its natural frequency has been observed. Figure 8 demonstrates the results of the numerical simulation for the PDF of failure time for different values of the nonlinearity parameter r. All peaks are shifted to the left compared with the peaks for the other systems investigated above. In Fig. 9 the numerically estimated reliability functions for $r=0.1$ (a) and $r=0.3$ (b) are presented. Since the equivalent damping coefficient for the linearized system (19) is three times bigger, the result (a) should be compared with the one obtained for the linear system with $r=0.3$. It should be reported that the reliability function of the swings has smaller decay rate, which results in a larger value of mean failure time. The latter can be observed from Table 5 for the corresponding values of the nonlinearity parameter.

6 Conclusions

In this paper, the authors have considered a first passage type reliability problem for strongly nonlinear stochastic systems, i.e., systems with signum type nonlinearity. The numerical results presented in this paper are obtained by the path integration method, which was adjusted to handle reliability problems. The results were verified by Monte Carlo simulations and the results obtained by the path integration method for an equivalent linear system. Generated results demonstrated that the reliability of all the considered systems strongly depends on the nonlinearity parameter r, especially for low values of the upcrossing level. It also has been shown that the systems with parametrically changing parameters have longer mean time to failure than those of equivalent linear systems. Thus, the parametrically controlled strongly nonlinear systems not only provide a way to dissipate the system's response energy, but also improve their first passage time reliability. On the other hand, the dry friction system or the system with an external

Table 3 Stiffness control: expected time to upcrossing. All numbers to be $\times 10^3$.

p / r	2.5σ One-sided	2.5σ Two-sided	3.0σ One-sided	3.0σ Two-sided	3.5σ One-sided	3.5σ Two-sided
0.1	0.2889	0.2304	0.9513	0.7248	3.6376	2.8612
0.3	0.1865	0.1248	0.7151	0.4453	3.4306	2.1786
0.5	0.1886	0.1130	0.8181	0.4557	4.0836	2.6258

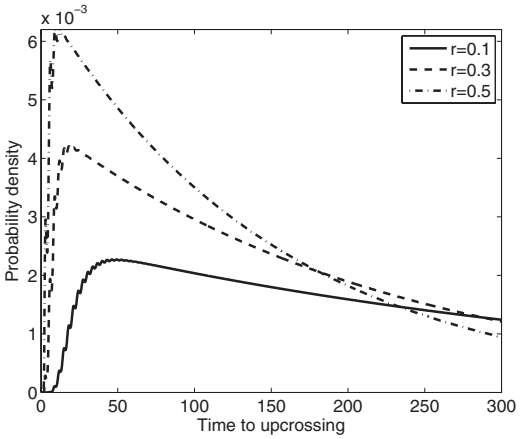

Fig. 6 Probability density of time to failure for the inertia control problem with reliability level 2.5 standard deviations and r =0.1, 0.3, and 0.5

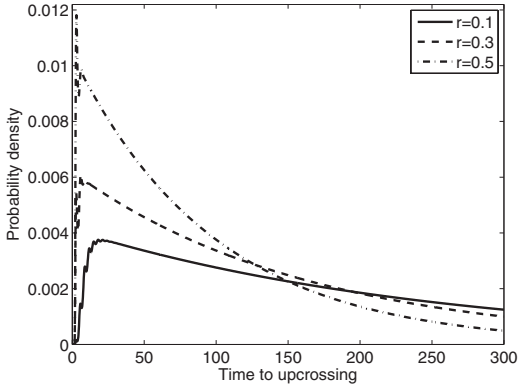

Fig. 8 Probability density of time to failure for the swing problem with reliability level 2.5 standard deviations and r=0.1, 0.3, and 0.5

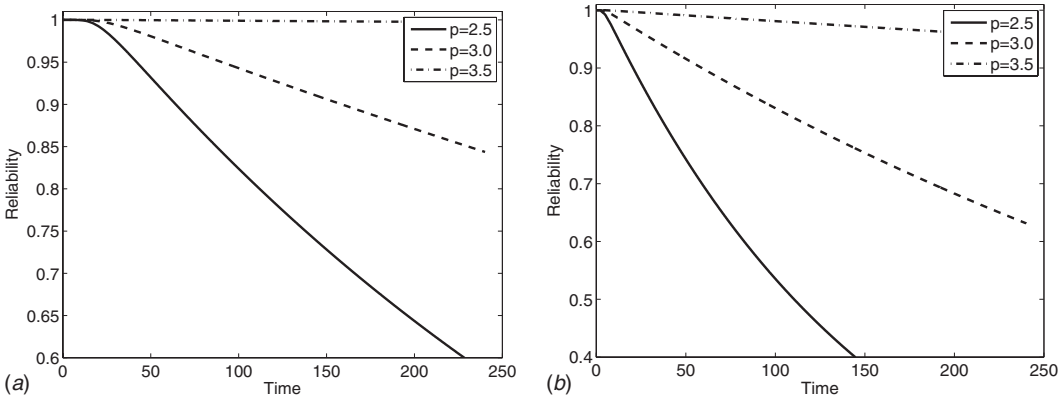

Fig. 7 Reliability function for the inertia control problem with one-sided barrier for different levels of p

Table 4 Inertia control: expected time to upcrossing. All numbers to be $\times 10^3$.

p r	2.5σ One-sided	2.5σ Two-sided	3.0σ One-sided	3.0σ Two-sided	3.5σ One-sided	3.5σ Two-sided
0.1	0.4261	0.3261	1.2842	0.8960	5.3885	5.2652
0.3	0.2323	0.1463	0.7717	0.4408	4.8281	4.2013
0.5	0.1574	0.0901	0.5158	0.2766	3.6161	2.3682

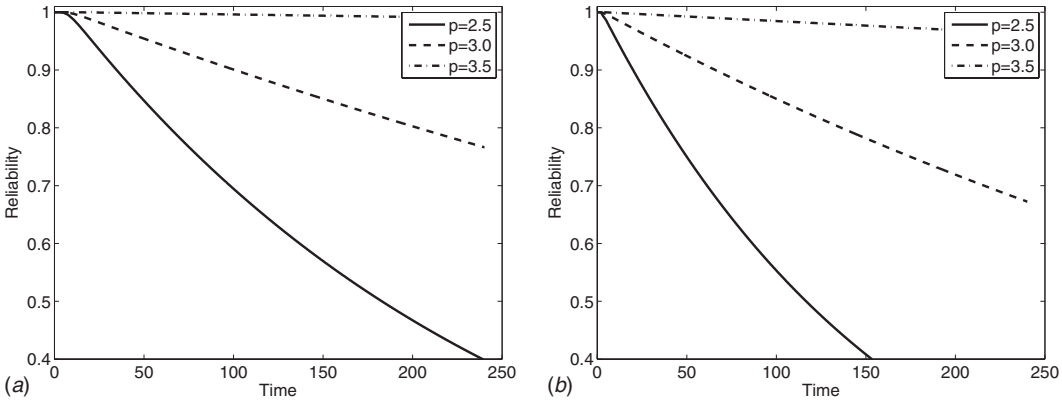

Fig. 9 Reliability function for the swing problem with one-sided barrier for different levels of p

Table 5 Linearized swing: expected time to upcrossing. All numbers to be $\times 10^3$.

p / r	2.5σ One-sided	2.5σ Two-sided	3.0σ One-sided	3.0σ Two-sided	3.5σ One-sided	3.5σ Two-sided
0.1	0.2601	0.1631	0.8759	0.4968	5.0722	4.6536
0.3	0.1671	0.0885	0.5999	0.3072	3.9651	2.7934
0.5	0.1004	0.0514	0.3256	0.1645	1.7827	0.9058

bounded in magnitude control law has poor reliability compared with its equivalent linear system, although it is capable of reducing the system's response energy.

Acknowledgment

The first author contributed to this work while staying as a Visiting Professor at the Centre for Ships and Ocean Structures (CeSOS) at NTNU, Trondheim, Norway. The financial support of this work from the Department of Mathematical Sciences at NTNU and the Research Council of Norway (NFR), partly through CeSOS, is greatly appreciated.

References

[1] Dimentberg, M. F., 1988, *Statistical Dynamics of Nonlinear and Time-Varying Systems*, Research Studies, Taunton, UK.
[2] Lin, Y. K., and Cai, G. Q., 1995, *Probabilistic Structural Dynamics*, McGraw-Hill, New York.
[3] Roberts, J. B., and Spanos, P. D., 1990, *Random Vibration and Statistical Linearization*, Wiley, New York.
[4] Roberts, J. B., 1976, "First Passage Time for the Envelope of a Randomly Excited Linear Oscillator," J. Sound Vib., **46**(1), pp. 1–14.
[5] Roberts, J. B., 1978, "First Passage Time for Oscillators With Non-Linear Restoring Forces," J. Sound Vib., **56**(1), pp. 71–86.
[6] Roberts, J. B., 1978, "First Passage Time for Oscillators With Nonlinear Damping," ASME J. Appl. Mech., **45**, pp. 175–180.
[7] Bergman, L. A., and Heinrich, J. C., 1982, "On the Reliability of the Linear Oscillator and Systems of Coupled Oscillators," Int. J. Numer. Methods Eng., **18**, pp. 1271–1295.
[8] Spencer, B. F., Jr., and Bergman, L. A., 1985, "On the Reliability of a Simple Hysteretic System," J. Eng. Mech., **111**(12), pp. 1502–1513.
[9] Bergman, L. A., and Spencer, B. F., Jr., 1987, "First Passage Time for Linear Systems With Stochastic Coefficients," Probab. Eng. Mech., **2**(1), pp. 46–53.
[10] Koyluoglu, H. U., Nielsen, S. R. K., and Iwankiewicz, R., 1994, "Reliability of Non-Linear Oscillators Subjected to Poisson Driven Impulses," J. Sound Vib., **176**(1), pp. 19–33.
[11] Chen, J. B., and Li, J., 2005, "Dynamic Response and Reliability Analysis of Non-Linear Stochastic Structures," Probab. Eng. Mech., **20**, pp. 33–44.
[12] Gupta, S., and Manohar, C. S., 2004, "Improved Response Surface Method for Time-Varying Reliability Analysis of Nonlinear Random Structures Under Non-Stationary Excitations," Nonlinear Dyn., **36**, pp. 267–280.
[13] Zhu, W. Q., Deng, M. L., and Huang, Z. L., 2002, "First-Passage Failure of Quasi-Integrable Hamiltonian Systems," ASME J. Appl. Mech., **69**, pp. 274–282.
[14] Fujimura, K., and Kiureghian, A., 2007, "Tail-Equivalent Linearization Method for Nonlinear Random Vibration," Probab. Eng. Mech., **22**, pp. 63–76.
[15] Iourtchenko, D. V., 2000, "Stochastic Optimal Bounded Control for a System With the Boltz Cost Function," J. Vib. Control, **6**, pp. 1195–1204.
[16] Dimentberg, M. F., Iourtchenko, D. V., and Bratus, A., 2000, "Optimal Bounded Control of Steady-State Random Vibrations," Probab. Eng. Mech., **15**, pp. 381–386.
[17] Risken, H., 1989, *The Fokker-Plank Equation: Methods of Solutions and Applications*, Springer-Verlag, New York.
[18] Iourtchenko D. V., and Dimentberg M. F., 2001, "Energy Balance for Random Vibrations of Piecewise-Conservative Systems," J. Sound Vib., **248**(5), pp. 913–923.
[19] Dimentberg, M. F., and Bratus, A., 2000, "Bounded Parametric Control of Random Vibrations," Proc. R. Soc. London, Ser. A, **456**, pp. 2351–2363.
[20] Iourtchenko, D. V., 2006, "Random Vibrations of Swings," J. Sound Vib., **295**, pp. 1011–1014.
[21] Panovko, Ia. G., and Gubanova, I. I., 1965, *Stability and Oscillations of Elastic Systems: Paradoxes, Fallacies, and New Concepts*, Consultants Bureau, New York.
[22] Iourtchenko, D. V., Mo, E., and Naess, A., 2006, "Response Probability Density Functions of Strongly Nonlinear Systems by the Path Integration Method," Int. J. Non-Linear Mech., **41**(5), pp. 693–705.
[23] Johnsen, J. M., 1992, "Response Statistics of Nonlinear Dynamic Systems," Ph.D. thesis, Department of Structural Engineering, Norwegian Institute of Technology, Trondheim.
[24] Naess, A., Kolnes, F. E., and Mo, E., 2007, "Stochastic Spur Gear Dynamics by Numerical Path Integration," J. Sound Vib., **302**, pp. 936–950.
[25] Naess, A., and Johnsen, J. M., 1993, "The Effect of Coulomb Damping on the Response Statistics of a SDOF Oscillator Subjected to White Noise Excitation," *Proceedings of the Second European Conference on Structural Dynamics (Eurodyn '93)*, Trondheim, Norway, Jun.

Numerical Analysis of Double Contacts of Similar Elastic Materials

N. Sundaram
e-mail: nsundara@purdue.edu

T. N. Farris
Fellow ASME
e-mail: farrist@purdue.edu

School of Aeronautics and Astronautics,
Purdue University,
315 North Grant Street,
West Lafayette, IN 47907-2023

A fast numerical method based on the Cauchy singular integral equations is presented to determine the contact pressure and extents for the contact of two-dimensional similar isotropic bodies when the contact area consists of two separate regions. The partial-slip problem is then solved to determine shear tractions using an equivalence principle. The extents of the contact are not all independent but related to a compatibility equation constraining the displacements of an elastic body in contact with an equivalent rigid body. A similar equation is found for the extents of the stick zones in partial-slip problems. The effects of load history are incorporated into the shear solution. The method is applicable to a wide range of profiles and it provides significant gains in computational efficiency over the finite element method (FEM) for both the pressure and partial-slip problems. The numerical results obtained are compared with that from the FEM for a biquadratic indenter with a single concavity and showed good agreement. Lastly, the transition behavior from double to single contacts in biquadratic profiles is investigated.
[DOI: 10.1115/1.2967897]

1 Introduction

Two-dimensional contact mechanics is a well-established area of mechanics with extensive analytical and numerical work to determine the contact area, pressure, and shear tractions under partial-slip conditions. For a review see the paper by Barber and Ciavarella [1]. Assuming that the two contacting bodies can be treated as half-spaces allows the formulation of the contact problem as a pair of Cauchy singular integral equations (SIEs) for the pressure and shear tractions. Due to the strongly singular Cauchy kernel, analytical and numerical techniques used for ordinary Fredholm integral equations are not directly applicable. As such, Muskhelishvili [2] realized this and developed the theory of SIE using complex variable methods. Using the theory of SIE, solutions have been found for a wide variety of geometries for single contacts, including flat punches, cylinders, power law punches, flat punches with rounded edges, wedges, and so on. If the indenter has a concavity, then the contact is made over two separate areas over a certain range of loads and analytical solutions are less common. Gladwell [3] determined an analytical solution for the symmetric frictionless contact of a rigid biquadratic punch and an isotropic half-space. Barber [4–6] has investigated the contact of axisymmetric concave punches and half-spaces. Shtayerman [7] obtained a solution for two interconnected flat punches of different heights.

It is often necessary to resort to numerical techniques to solve contact problems; Erdogan [8] developed a well known method to numerically invert SIEs for single contacts, in which the unknown function is represented as the product of a function bounded everywhere and a fundamental function that captures the singular behavior at the ends. The fundamental functions for SIEs with constant coefficients are the weight functions of standard orthogonal polynomial functions, whose properties are then used to find approximate solutions. In this paper, a numerical method is developed for inverting Cauchy SIEs when the domain consists of two nonintersecting segments of the real line. This method is then applied to determine the contact pressure for the indentation of an elastic half-space by a similar or rigid indenter with a concavity. The profile is allowed to be asymmetric, as well as a moment can be applied to the contact. The latter portion of this paper investigates the partial-slip problem and the slip history effects in double contacts.

With the finite element method (FEM) being as widespread and general as it is, it is necessary to explain the reasons for the development of yet another numerical tool for contacts. The reason is that the generality of the FEM comes at a price: It has significantly longer execution times and it obscures underlying physical insights that may be gained by using a semi-analytical approach. For example, all four ends of double contacts are not independent, but this is not at all obvious from the use of the FEM. In partial-slip problems, the FEM requires a fine mesh to accurately capture shear reversals, which generally takes a long time to solve. It must also be understood that a SIE based technique is *intrinsically* faster than the FEM, i.e., the ratio of the orders of time taken by the FEM to the SIE is not just a simple numerical factor because the problem is essentially reduced by one in dimension (solving on the boundary as opposed to solving over the entire domain). Furthermore, the preprocessing (meshing) burden in SIEs is almost nonexistent when compared with the FEM since a straight line segment is to be meshed. On the other hand, generating good quality efficient meshes for contact problems using the FEM is usually a laborious task. It may also be noted that the reduced computational requirements (in terms of processing power, primary memory, and secondary storage) allow SIE based codes to run on average desktops.

2 Theoretical Considerations in Frictionless Smooth Contacts

When two bodies are brought into contact, the gap function $h(x)$ between them (Fig. 1) may be written as [9]

$$h(x) = h_0(x) - u_1 + u_2 - C_0 - C_1 x \tag{1}$$

where u_1 and u_2 are the vertical *surface* displacements of the two bodies, $h_0(x)$ is the initial gap function (or the undeformed indenter profile in the case of the indentation of a flat body), C_1 is the term associated with rigid-body rotation, and C_0 with rigid-body translation. It is assumed that the rotation C_1 is small. By

Contributed by the Applied Mechanics Division of ASME for publication in the JOURNAL OF APPLIED MECHANICS. Manuscript received August 8, 2007; final manuscript received July 9, 2008; published online August 21, 2008. Review conducted by Matthew R. Begley.

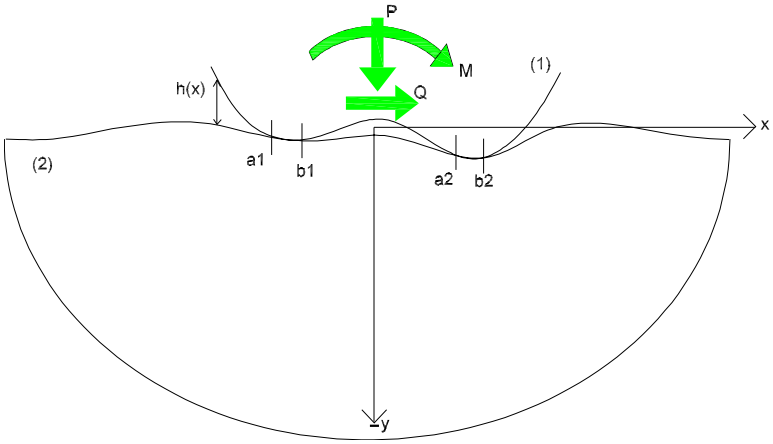

Fig. 1 Double contact configuration

definition, the gap function has to be zero inside the contact, so that

$$u_1 - u_2 = h_0(x) - C_0 - C_1 x \tag{2}$$

within the contact. The SIE governing the frictionless contact of two similar isotropic bodies is then given as

$$\frac{dh_0(x)}{dx} - C_1 = A \int_L \frac{p(s)}{x-s} ds, \quad \forall\, x \in L \tag{3}$$

where L is the set of points in contact, $p(x)$ is the pressure traction, A is a term encapsulating the elastic behavior in the plane strain, $A = 4(1-\nu^2)/\pi E$ is for similar material contact, and $2(1-\nu^2)/\pi E$ is for rigid-on-isotropic contact. The pressure traction must satisfy the equilibrium equations

$$\int_L p(x)dx = P \tag{4}$$

$$\int_L xp(x)dx = M \tag{5}$$

where P and M are, respectively, the applied normal load and the moment. Positive pressure is considered compressive in the nomenclature used above. It is important to note that the contact region L may not be contiguous, i.e., L may be the union of a number of discrete regions $L_1, L_2, \ldots, L_n$. The contact area L must be determined such that the pair of inequalities

$$p(x) > 0, \quad \forall\, x \in L \tag{6}$$

$$h(x) > 0, \quad \forall\, x \notin L \tag{7}$$

is satisfied. These conditions simply state that the contact pressure must be compressive inside the contact and there is no interpenetration outside the contact [9]. In problems with a single contact patch, these inequalities are automatically satisfied by ensuring that the contact pressure goes to zero at the ends of contact. For *multiple* contact patches, the boundedness of $p(x)$ at the ends of contact is only a necessary condition,[1] not a sufficient one, i.e., to obtain a unique solution in the most general contact problems needs explicit consideration of the inequalities. Kalker [10] obtained a unique solution by formulating a function that is minimized when the inequalities are satisfied. A theorem of Barber [9] states that the exact contact area maximizes the indentation force in the frictionless indentation by a rigid body, which he used to reframe the problem as a variational statement to obtain L. However, in the case of the 2D double contacts addressed in this paper, it is possible to obtain a solution without involving the inequalities explicitly.

Since the contact exists over two patches, consider the decomposition of the pressure traction $p(x)$ into two functions $p_1(x)$ and $p_2(x)$, such that $p_1(x)$ is nonzero only in L_1 and $p_2(x)$ is nonzero only in L_2. Thus, Eq. (3) can be rewritten as

$$\frac{dh_0(x)}{dx} - C_1 = A \int_{L_1} \frac{p_1(s)}{x-s} ds + A \int_{L_2} \frac{p_2(s)}{x-s} ds,$$
$$\forall\, x \in \{L = L_1 \cup L_2\} \tag{8}$$

3 Numerical Method

To solve the doubly connected contact problem, it is essential to have a method to numerically invert the Cauchy SIE defined in two nonintersecting segments of the real axis (while the discussion in this section is in terms of the normal indentation contact problem, this method is more generally applicable). From the theory of singular integral equations [2], it is known that for solutions to a Cauchy SIE that are bounded at all ends to exist, certain side (or consistency) conditions have to be satisfied. For arbitrarily chosen contact regions, these consistency conditions may not be met, and hence, in single contacts, it is necessary to admit one singularity in the function $p(x)$ (see Refs. [11,12]). For the double contact problem, it is clearly necessary to admit two singularities, one in each of the functions $p_1(x)$ and $p_2(x)$. The necessary singularities are to be introduced in the following square-root form:[2]

$$p_1(x) = p_0^{\mathrm{I}}(x) + \phi_1 \sqrt{\frac{b_1 - x}{x - a_1}}, \quad \forall\, x \in L_1 \tag{9}$$

$$p_2(x) = p_0^{\mathrm{II}}(x) + \phi_2 \sqrt{\frac{x - a_2}{b_2 - x}}, \quad \forall\, x \in L_2 \tag{10}$$

where $p_0^{\mathrm{I}}(x)$ and $p_0^{\mathrm{II}}(x)$ are functions that are bounded everywhere and the (unknown) constants ϕ_1 and ϕ_2 are coefficients of the singular terms. The left contact L_1 extends from a_1 to b_1 and the right contact L_2 extends from a_2 to b_2. Writing the pressure in this

[1] This discussion only applies to smooth (incomplete) contacts, where the contact size is a function of the applied load; an example of a complete contact is the indentation of a half-plane by a flat rigid punch where the pressure is unbounded at the ends.

[2] For x only $\in L_1$ or x only $\in L_2$, it may be readily recognized that this is a Cauchy SIE in which the integral kernel has a nondominant part. This nondominant part does not alter the singularity behavior at the ends.

"sum" form allows easy analytical integration of the singular part of the tractions. Notice that the form of the singularities admitted is symmetric (i.e., at the left-end of the left contact and at the right-end of the right contact). This simplifies the solution of symmetric problems.

Substituting these expressions for the pressure in Eq. (8) leads to

$$\frac{1}{A}\left(\frac{dh_0(x)}{dx}-C_1\right)=\sum_{m=1}^{2}\int_{a_m}^{b_m}\frac{p_0^m(s)}{x-s}ds+\phi_1\int_{a_1}^{b_1}\sqrt{\frac{b_1-s}{s-a_1}}\frac{ds}{x-s}+\phi_2\int_{a_2}^{b_2}\sqrt{\frac{s-a_2}{b_2-s}}\frac{ds}{x-s} \tag{11}$$

To solve the equation numerically, the domains L_1 and L_2 are discretized by division into $N^{\mathrm{I}}+1$ and $N^{\mathrm{II}}+1$ node points (or integration points), respectively. Equation (11) is enforced at $N^{\mathrm{I}}+N^{\mathrm{II}}$ and collocation points x_k^{I} and x_k^{II} in the regions L_1 and L_2, respectively. The node points and collocation points have to be as far away from each other as possible for the accurate evaluation of the integrals, and for this purpose each collocation point is set equidistant from its neighboring node points. Now Eq. (11) can be rewritten as the pair of equations

$$\frac{1}{A}\left(\frac{dh_0(x)}{dx_k^{\mathrm{I,II}}}-C_1\right)=\sum_{m=1}^{2}\int_{a_m}^{b_m}\frac{p_0^m(s)ds}{x_k^{\mathrm{I,II}}-s}+\phi_1\int_{a_1}^{b_1}\sqrt{\frac{b_1-s}{s-a_1}}\frac{ds}{x_k^{\mathrm{I,II}}-s}+\phi_2\int_{a_2}^{b_2}\sqrt{\frac{s-a_2}{b_2-s}}\frac{ds}{x_k^{\mathrm{I,II}}-s} \tag{12}$$

The integrals containing singularities can be evaluated analytically using the following:

$$\int_a^b\frac{1}{x-s}\left(\frac{s-a}{b-s}\right)^{\pm 1/2}=\begin{cases}\mp\pi\left(1-\left(\dfrac{a-x}{b-x}\right)^{\pm 1/2}\right) & \text{if } x<a\\ \mp\pi & \text{if } a<x<b\\ \mp\pi\left(1-\left(\dfrac{x-a}{x-b}\right)^{\pm 1/2}\right) & \text{if } x>b\end{cases}$$

Using these results, the two equations become

$$\frac{1}{A}\left(\frac{dh_0(x)}{dx_k^{\mathrm{I}}}-C_1\right)=\int_{a_1}^{b_1}\frac{p_0^{\mathrm{I}}(s)ds}{x_k^{\mathrm{I}}-s}+\pi\phi_1+\int_{a_2}^{b_2}\frac{p_0^{\mathrm{II}}(s)ds}{x_k^{\mathrm{I}}-s}-\pi\phi_2\left(1-\left(\frac{a_2-x_k^{\mathrm{I}}}{b_2-x_k^{\mathrm{I}}}\right)^{1/2}\right) \tag{13}$$

$$\frac{1}{A}\left(\frac{dh_0(x)}{dx_k^{\mathrm{II}}}-C_1\right)=\int_{a_1}^{b_1}\frac{p_0^{\mathrm{I}}(s)ds}{x_k^{\mathrm{II}}-s}+\pi\phi_1\left(1-\left(\frac{x_k^{\mathrm{II}}-a_1}{x_k^{\mathrm{II}}-b_1}\right)^{1/2}\right)+\int_{a_2}^{b_2}\frac{p_0^{\mathrm{II}}(s)ds}{x_k^{\mathrm{II}}-s}-\pi\phi_2 \tag{14}$$

Next, the domains of the integrals are discretized as discussed above. The integration points in the two regions are given by

$$s_i=a_1+(i-1)\Delta s^{\mathrm{I}}=a_1+(i-1)\frac{b_1-a_1}{N^{\mathrm{I}}} \tag{15}$$

$$s_j=a_2+(j-1)\Delta s^{\mathrm{II}}=a_2+(j-1)\frac{b_2-a_2}{N^{\mathrm{II}}} \tag{16}$$

The integrals can then be replaced with summations, for example, the first integral in Eq. (13) becomes

$$I_1=\int_{a_1}^{b_1}\frac{p_0^{\mathrm{I}}(s)}{x-s}ds\approx\sum_{i=1}^{N^{\mathrm{I}}}\int_{s_i}^{s_i+1}\frac{p_0^{\mathrm{I}}(s)}{x-s}ds \tag{17}$$

In between node points, the functions $p_0^{\mathrm{I}}(x)$ and $p_0^{\mathrm{II}}(x)$ are assumed to be piecewise linear as follows:

$$p_0^{\mathrm{I}}(s)\approx p_0^{\mathrm{I}}(s_i)+(s-s_i)\frac{p_0^{\mathrm{I}}(s_{i+1})-p_0^{\mathrm{I}}(s_i)}{\Delta s^{\mathrm{I}}} \tag{18}$$

$$p_0^{\mathrm{II}}(s)\approx p_0^{\mathrm{II}}(s_j)+(s-s_j)\frac{p_0^{\mathrm{II}}(s_{j+1})-p_0^{\mathrm{II}}(s_j)}{\Delta s^{\mathrm{II}}} \tag{19}$$

Thus the integral in Eq. (17) becomes

$$I_1=\sum_{\substack{i=1\\ i\neq k}}^{N^{\mathrm{I}}}\left\{p_0^{\mathrm{I}}(s_i)\left[\ln\left(\frac{|x_k^{\mathrm{I}}-s_i|}{|x_k^{\mathrm{I}}-s_{i+1}|}\right)\right]\left[1+\frac{s_i}{\Delta s^{\mathrm{I}}}-\frac{x_k^{\mathrm{I}}}{\Delta s^{\mathrm{I}}}\right]+1\right]+p_0^{\mathrm{I}}(s_{i+1})\times\left[\ln\left(\frac{|x_k^{\mathrm{I}}-s_i|}{|x_k^{\mathrm{I}}-s_{i+1}|}\right)\right]\left[-\frac{s_i}{\Delta s^{\mathrm{I}}}+\frac{x_k^{\mathrm{I}}}{\Delta s^{\mathrm{I}}}\right]-1\right]\Bigg\}+p_0^{\mathrm{I}}(s_k)-p_0^{\mathrm{I}}(s_{k+1}) \tag{20}$$

The other three integrals can be evaluated in a similar way; if the collocation point lies inside the domain of integration for any term in the sum, it is evaluated as a Cauchy principal value. After carrying out these operations, the result is $N^{\mathrm{I}}+N^{\mathrm{II}}$ equations in $N^{\mathrm{I}}+N^{\mathrm{II}}+4$ unknown variables $p_0^{\mathrm{I}}(s_i)$ ($N^{\mathrm{I}}+1$ unknowns), $p_0^{\mathrm{II}}(s_j)$ ($N^{\mathrm{II}}+1$ unknowns), and the two singularity coefficients ϕ_1 and ϕ_2. Adding the condition that the pressure must be bounded and zero at all contact ends yields four additional equations: $p_0^{\mathrm{I}}(a_1)=0$, $p_0^{\mathrm{I}}(b_1)=0$, $p_0^{\mathrm{II}}(a_2)=0$, and $p_0^{\mathrm{II}}(b_2)=0$. It is now possible to invert the system for the unknown nodal pressures for a set of guesses a_1, b_1, a_2, b_2, and C_1.

The nodal pressures thus obtained satisfy the global equilibrium equations if their nonsingular part satisfies

$$\int_{a_1}^{b_1}p_0^{\mathrm{I}}(x)dx+\int_{a_2}^{b_2}p_0^{\mathrm{II}}(x)dx=P \tag{21}$$

$$\int_{a_1}^{b_1}xp_0^{\mathrm{I}}(x)dx+\int_{a_2}^{b_2}xp_0^{\mathrm{II}}(x)dx=M \tag{22}$$

4 The Symmetric Indentation Problem

Consider a problem in which the applied moment $M=0$ and the profile is symmetric, in which case, $C_1=0$, $b_2=-a_1$, $b_1=-a_2$, and $\phi_1=\phi_2=\phi$. Thus, there are only two unknowns. There are two conditions to be satisfied, namely, P and $\phi=0$. A 2D Newton–Raphson scheme may be set up, which converges rapidly starting from an initial guess for the contact size as follows:

$$\begin{Bmatrix}a_1\\ b_1\end{Bmatrix}_{i+1}=\begin{Bmatrix}a_1\\ b_1\end{Bmatrix}_i+\begin{bmatrix}\dfrac{\partial P}{\partial a_1} & \dfrac{\partial P}{\partial b_1}\\ \dfrac{\partial \phi}{\partial a_1} & \dfrac{\partial \phi}{\partial b_1}\end{bmatrix}^{-1}\begin{Bmatrix}P-P_i\\ 0-\phi_i\end{Bmatrix} \tag{23}$$

where P_i is the integral of the nonsingular part of the pressure tractions over L in the ith iteration calculated using Eq. (21). The gradients in the matrix are evaluated numerically by calculating function values at neighboring points as follows (Δa_1 is a small change in a_1):

$$\frac{\partial P}{\partial a_1}\approx\frac{P(a_1+\Delta a_1,b_1)-P(a_1,b_1)}{\Delta a_1} \tag{24}$$

The iteration procedure is continued until the values P_i and ϕ_i converge to within some prespecified tolerance.

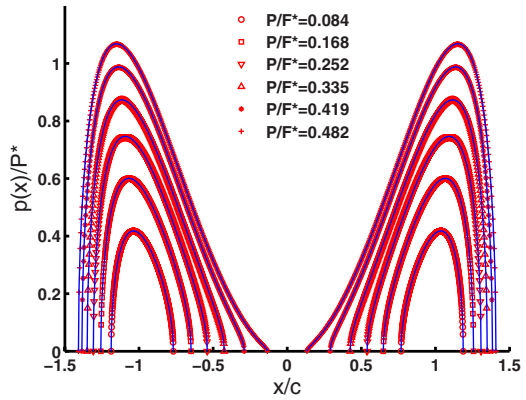

Fig. 2 Analytical (solid lines) and SIE (markers) normalized pressure tractions $p(x)/P^*$ versus x/c for different loads

For the symmetric problem, the results of the frictionless indentation of an elastic half-space by a rigid biquadratic punch[3] with the explicit equation

$$h_0(x) = \frac{x^4}{8Rc^2} - \frac{x^2}{4R} + \frac{c^2}{8R} \tag{25}$$

are shown in Fig. 2. The results compare well with Gladwell's analytical solution [3] (presented here in a slightly different form) as

$$p(x) = E\frac{|x|\sqrt{b^2-x^2}\sqrt{x^2-a^2}}{4(1-\nu^2)Rc^2}, \quad a<|x|<b \tag{26}$$

$$2c^2 = a^2 + b^2 \tag{27}$$

Both axes are normalized. The traction normalization constant is $P^* = Ec/4(1-\nu^2)R$ and the applied normal load normalization constant is $F^* = c^2/AR$. The parameter c is half the distance between the local minima of the punch. For this work, the value of $c/R = 0.08$ and the composite parameter $P^* = 3.796 \times 10^5$ are used throughout. Clearly, there is excellent agreement between the SIE method and the analytical results. As expected, the contact size increases with increased normal load and the two contacts grow toward each other. Beyond a certain critical value $P > P_{\text{crit}}$, the two contacts will merge into one and a single contact solver has to be used. The transition behavior from two contact patches to one contact patch is discussed in more detail later.

5 The Asymmetric Indentation Problem

When a moment M is present, or the profile is not symmetric, the problem is more complicated. In this case, there are five unknowns (a_1, b_1, a_2, b_2, and C_1) and nothing is known about them a priori, unlike the symmetric problem. The conditions to be satisfied are the resultant loads P, M, and the two conditions for the singularity coefficients $\phi_1 = 0$ and $\phi_2 = 0$ (which imply that a solution bounded at all ends is sought). Thus, one more condition is needed to solve the problem as follows. Any frictionless problem can be reduced to the equivalent indentation of a half-space by a rigid indenter. If the Poisson ratios are set equal, then E^* (for rigid on isotropic) $= E_s$(similar)/2. Now consider the contact over the two regions $L_1 = [a_1, b_1]$ and $L_2 = [a_2, b_2]$. Since the end points b_1 and a_2 come into contact with the rigid indenter, they must satisfy the condition

$$h_0(a_2) - h_0(b_1) - C_1 a_2 + C_1 b_1 = \int_{b_1}^{a_2} u'(x)dx \tag{28}$$

where $h_0(a_2)$ and $h_0(b_1)$ are the initial gap functions at the points a_2 and b_1, and $u'(x)$ is the slope of the vertical displacement at the surface of the half-space given by

$$u'(x) = A\left[\int_{a_1}^{b_1} \frac{p_0^{\text{I}}(s)}{x-s}ds + \int_{a_2}^{b_2} \frac{p_0^{\text{II}}(s)}{x-s}ds\right], \quad \forall\, x \tag{29}$$

and A is given by

$$A = \frac{2(1-\nu_*^2)}{\pi E_*} = \frac{4(1-\nu_s^2)}{\pi E_s} \tag{30}$$

The physical basis of Eq. (28) is that a rigid indenter can only experience rigid-body motions. It is very important to note that an arbitrarily chosen set of a_1, b_1, a_2, b_2, and C_1 will not satisfy Eq. (28) above. Thus, let a new function V (a rigid-body displacement compatibility violation function) be defined as

$$V(a_1,b_1,a_2,b_2,C_1) = h_0(a_2) - h_0(b_1) - C_1 a_2 + C_1 b_1 - \int_{b_1}^{a_2} u'(x)dx \tag{31}$$

It is clear that $V=0$ for the correct solution.[4] Equation (31) is easy to compute after the pressures are known for a set of a_1, b_1, a_2, b_2, and C_1 guess values by using Eq. (29). Thus, with $V=0$ as the fifth condition, the problem is rendered tractable. A five-dimensional Newton iteration scheme is used to converge from an initial guess of a_1, b_1, a_2, b_2, and C_1 so as to satisfy P, M, $\phi_1 = 0$, and $\phi_2 = 0$ and $V=0$ as follows:

$$\begin{Bmatrix} a_1 \\ b_1 \\ a_2 \\ b_2 \\ C_1 \end{Bmatrix}_{i+1} = \begin{Bmatrix} a_1 \\ b_1 \\ a_2 \\ b_2 \\ C_1 \end{Bmatrix}_{i} + \begin{bmatrix} \frac{\partial P}{\partial a_1} & \frac{\partial P}{\partial b_1} & \frac{\partial P}{\partial a_2} & \frac{\partial P}{\partial b_2} & \frac{\partial P}{\partial C_1} \\ \frac{\partial M}{\partial a_1} & \frac{\partial M}{\partial b_1} & \frac{\partial M}{\partial a_2} & \frac{\partial M}{\partial b_2} & \frac{\partial M}{\partial C_1} \\ \frac{\partial \phi_1}{\partial a_1} & \frac{\partial \phi_1}{\partial b_1} & \frac{\partial \phi_1}{\partial a_2} & \frac{\partial \phi_1}{\partial b_2} & \frac{\partial \phi_1}{\partial C_1} \\ \frac{\partial \phi_2}{\partial a_1} & \frac{\partial \phi_2}{\partial b_1} & \frac{\partial \phi_2}{\partial a_2} & \frac{\partial \phi_2}{\partial b_2} & \frac{\partial \phi_2}{\partial C_1} \\ \frac{\partial V}{\partial a_1} & \frac{\partial V}{\partial b_1} & \frac{\partial V}{\partial a_2} & \frac{\partial V}{\partial b_2} & \frac{\partial V}{\partial C_1} \end{bmatrix}^{-1} \begin{Bmatrix} P - P_i \\ M - M_i \\ 0 - \phi_{1i} \\ 0 - \phi_{2i} \\ 0 - V_i \end{Bmatrix} \tag{32}$$

where the subscript i indicates values obtained after i iterations, and P_i and M_i are obtained by integrating the nonsingular part of the pressure tractions over L. The gradients in the matrix are evaluated numerically as before. The asymmetric indentation problem for contacting bodies with *similar* material properties and a biquadratic profile indenter is considered. Different moments were applied at one fixed value of the normal load. The SIE re-

[3] Gladwell [3] used the term "interconnected parabolic punches;" "biquadratic" is used here to emphasize that the profile is not strictly parabolic.

[4] In other words, of all admissible solutions that are bounded everywhere, the physically correct solution is the one that satisfies $V=0$.

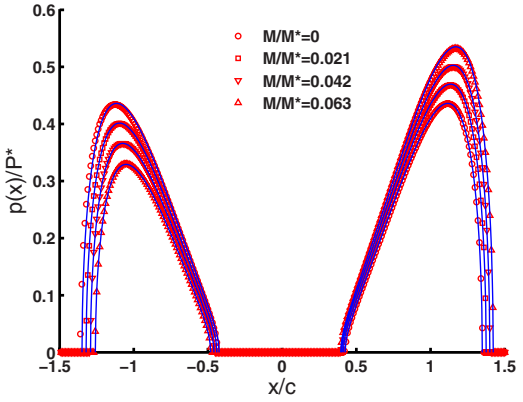

Fig. 3 SIE (solid lines) and FEM (markers) normalized pressure tractions $p(x)/P^*$ versus x/c for $P/F^*=0.1677$ and different moments M/M^*

sults (Fig. 3) were compared with the ABAQUS/STANDARD FEM software using four-noded bilinear plane strain elements. The contact element size was $c/100$ and the applied moment normalization constant was $M^*=c^3/AR$. There is excellent agreement between the FEM and the SIE predictions. The convergence time for the SIE method on a standard desktop PC was less than half a minute. With increasing moment, the difference between the right and left peak pressures increases, and the left contact shrinks in size. Eventually, at some moment M_{crit}, the left contact will "lift off," and once again, a single contact solver should be used. (Of course, a counterclockwise moment $-M_{\text{crit}}$ would have had the effect of making the right contact lift off.)

6 The Partial-Slip Problem for Elastically Similar Bodies

If friction is present, the contact can transmit shear tractions in addition to normal tractions. The simple Amontons–Coulomb frictional model is used here to develop a numerical method to determine the shear traction. It is assumed that the normal load P and the moment M are applied first, and then, while they are held constant, a shear load Q is applied to the contact (the Cattaneo–Mindlin problem). The extents of the contact pressure traction $p(x)$ and the rotation C_1 can be found as discussed above and are assumed as known in Secs. 6.1 and 7. The approach is to use the equivalence between the pressure and shear problems for double contacts. In particular, it is concluded that the equivalent problem has the same "rigid-body violation" relationship as a doubly connected normal indentation problem. (The pressure-shear equivalence is quite general and applies to a wider variety of problems than discussed here; see Refs. [13–15].)

6.1 Stick-Slip Configuration in Partial Slip. Consider the application of a shear load Q less than μP in magnitude where μ is the coefficient of friction. It is quite easy to determine that there should be four slip zones in the general case, as follows. By analogy with single contacts, assume that no slip is allowed whatsoever. Thus, the shear solution for the double contact will resemble the pressure solution for the indentation of a half-space by a double-flat punch, leading to four singularities at the four contact ends. Consequently, in the absence of an infinite coefficient of friction, four slip zones are expected in all, with one slip zone at the end of each contact. There is a stick zone between each pair of slip zones.

6.2 Equivalent Pressure Problem. Consider the application of a shear load Q after applying a normal load P. It will be assumed that the load Q is applied in such a way as to produce no moment at the contact. The SIE for the shear traction $q(x)$ is given in the stick zones as

$$\left.\frac{dg(x)}{dx}\right|_{\text{prev}} = A\int_L \frac{q(s)}{x-s}ds, \quad \forall\, x \in S \tag{33}$$

where S is the set of all points in the stick zone. Also, in the stick zones, the maximum value of shear traction is limited as per the Amontons–Coulomb friction model

$$|q(x)| < \mu p(x) \tag{34}$$

In the slip zones,

$$q(x) = \text{sgn}\left(\frac{dg(x,t)}{dt}\right)\mu p(x) \tag{35}$$

where $g(x,t)$ is the slip function. In the absence of slip history (i.e., the left hand side of Eq. (33) is zero), consider the decomposition of $q(x)$ into two shear functions in the two contacts as follows, where it is understood that $q_1(x)$ is zero in L_2 and $q_2(x)$ is zero in L_1:

$$0 = A\int_{L_1}\frac{q_1(s)}{x-s}ds + A\int_{L_2}\frac{q_2(s)}{x-s}ds: \quad x \in \{S = S_1 \cup S_2\} \tag{36}$$

For positive applied shear Q, each of the shear functions can be rewritten in terms of pressure in the contact and corrective shear tractions q_1^* and q_2^* as follows:

$$q_1(x) = \mu p_1(x) - q_1^*(x) \tag{37}$$

$$q_2(x) = \mu p_2(x) - q_2^*(x) \tag{38}$$

where each corrective shear function is nonzero only in the stick zone of that particular contact.

$$0 = A\int_{L_1}\frac{\mu p_1(s)}{x-s}ds - A\int_{L_1}\frac{q_1^*(s)}{x-s}ds + A\int_{L_2}\frac{\mu p_2(s)}{x-s}ds - A\int_{L_2}\frac{q_2^*(s)}{x-s}ds: \quad x \in \{S = S_1 \cup S_2\} \tag{39}$$

Using the pressure equation (8) and rearranging

$$\frac{1}{A}\left(\mu\frac{dh_0(x)}{dx} - \mu C_1\right) = \int_{S_1}\frac{q_1^*(s)}{x-s}ds + \int_{S_2}\frac{q_2^*(s)}{x-s}ds, \quad \forall\, x \in S \tag{40}$$

This equation is identical to the pressure equation (8), with values of the gradient dh_0/dx and rotation C_1 scaled by the coefficient of friction μ and defined over a domain S as opposed to L. It is to be noted that the corrective tractions approach zero at the ends of the stick zones just as the pressures approach zero at the ends of the contacts. The resultant load condition to be used is obtained by integrating and adding Eqs. (37) and (38) as

$$\int_{S_1} q_1^*(x)dx + \int_{S_2} q_2^*(x)dx = \mu P - Q \tag{41}$$

Once it is recognized that the problem for partial stick can be converted into an equivalent double contact pressure problem, it is easy to see that the ends of the stick zone must satisfy a rigid-body condition similar to Eq. (28), i.e., for the equivalent problem

$$\mu(h_0(a_{q2}) - h_0(b_{q1})) - C_2 a_{q2} + C_2 b_{q1} = \int_{b_{q1}}^{a_{q2}} u_*'(x)dx \tag{42}$$

where $S_1=[a_{q1}, b_{q1}]$ and $S_2=[a_{q2}, b_{q2}]$. We can now proceed exactly as in the pressure solution, with the exception that the rotation term $C_2=\mu C_1$ is known a priori. A new parameter V_q can be

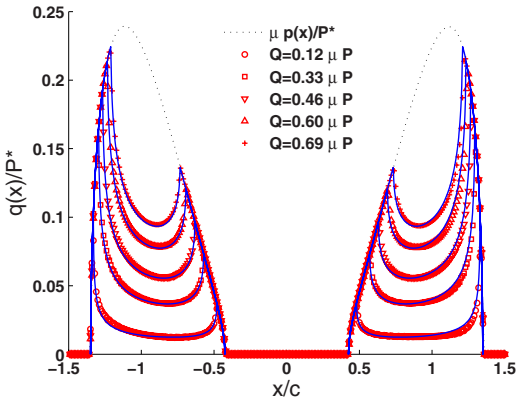

Fig. 4 SIE (solid lines) and FEM (markers) normalized shear tractions $q(x)/P^*$ versus x/c for $P/F^*=0.1677$, $M=0$, and different values of Q

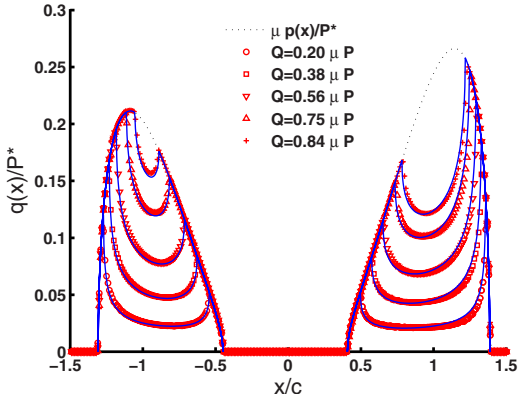

Fig. 5 SIE (solid lines) and FEM (markers) normalized shear tractions $q(x)/P^*$ versus x/c for $P/F^*=0.1677$, $M/M^*=0.0314$, and different values of Q

defined just as in Eq. (31), which quantifies the violation in Eq. (42). A four-dimensional Newton iteration scheme is used to converge from an initial guess of a_{q1}, b_{q1}, a_{q2}, and b_{q2} so as to satisfy Q, $\phi_1=0$, $\phi_2=0$, and $V_q=0$ as follows:

$$\begin{Bmatrix} a_{q1} \\ b_{q1} \\ a_{q2} \\ b_{q2} \end{Bmatrix}_{i+1} = \begin{Bmatrix} a_{q1} \\ b_{q1} \\ a_{q2} \\ b_{q2} \end{Bmatrix}_{i} + \begin{bmatrix} \frac{\partial Q}{\partial a_{q1}} & \frac{\partial Q}{\partial b_{q1}} & \frac{\partial Q}{\partial a_{q1}} & \frac{\partial Q}{\partial b_{q2}} \\ \frac{\partial \phi_1}{\partial a_{q1}} & \frac{\partial \phi_1}{\partial b_{q1}} & \frac{\partial \phi_1}{\partial a_{q1}} & \frac{\partial \phi_1}{\partial b_{q2}} \\ \frac{\partial \phi_2}{\partial a_{q1}} & \frac{\partial \phi_2}{\partial b_{q1}} & \frac{\partial \phi_2}{\partial a_{q1}} & \frac{\partial \phi_2}{\partial b_{q2}} \\ \frac{\partial V_q}{\partial a_{q1}} & \frac{\partial V_q}{\partial b_{q1}} & \frac{\partial V_q}{\partial a_{q1}} & \frac{\partial V_q}{\partial b_{q2}} \end{bmatrix}^{-1} \begin{Bmatrix} Q - Q_i \\ 0 - \phi_{1,i} \\ 0 - \phi_{2,i} \\ 0 - V_{q,i} \end{Bmatrix} \tag{43}$$

The subscripts i are used for values obtained after i iterations. We can proceed similarly in case a negative load Q is applied; the sign of shear is negative in the slip zones and Eqs. (37) and (38) are replaced with

$$-q_1(x) = \mu p_1(x) + q_1^*(x) \tag{44}$$

$$-q_2(x) = \mu p_2(x) + q_2^*(x) \tag{45}$$

and the resultant to be used is given by

$$\int_{S_1} q_1^*(x)dx + \int_{S_2} q_2^*(x)dx = -\mu P - Q \tag{46}$$

The load sequence for partial-slip problems is as follows: P and M are applied in the first step to make the contact and while they are held constant, shear load Q is applied in the second step. The shear traction results for $P/F^*=0.1677$, $M/M^*=0$, and different values of Q from 0 μP to 0.69 μP (the value of $\mu=0.55$ in this and subsequent sections) are shown in Fig. 4. The points where the shear traction begins to deviate from the $\mu p(x)$ line are the ends of the stick zone. In the absence of a moment, the left and right stick zones are symmetric, and the two stick zones diminish in size as the shear load Q is increased. Gross sliding will eventually occur when the applied load $Q=\mu P$. In Fig. 5, $P/F^*=0.1677$, $M/M^*=0.0314$, and Q varies from 0 μP to 0.84 μP. Again, there is good agreement between the SIE and the FEM. In this case, the left stick zone shrinks faster than the right stick zone. In fact, if the shear load Q is increased further, the stick zone in the left contact disappears completely while the right stick zone is still present, as shown in Fig. 6. This is to be expected at high shear loads in asymmetric double contacts and corresponds to the lift-off due to rotation in the equivalent pressure problem.

7 The Partial-Slip Problem With Slip History

In Sec. 6, the history-free shear problem was considered. Next, consider a simple loading sequence as follows, with only the normal load P and the moment M applied in the first step to make the contact, and a maximum shear load $+Q$ applied in the second step. What happens when the shear load is decreased from this maximum in a third step while keeping the normal load constant? For an infinitesimal $dQ<0$, it is expected that both contacts will go into complete stick everywhere. Further decrease in Q causes slip zones with shear tractions of opposite signs to develop at the ends of the contacts. In this case the dg/dx term on the left hand side of Eq. (33) is nonzero and thus Eq. (40) becomes

$$\frac{1}{A}\left(\mu\frac{dh_0(x)}{dx} - \left.\frac{dg}{dx}\right|_{\text{prev}} - \mu C_1\right) = \int_{S_1} \frac{q_1^*(s)}{x-s}ds + \int_{S_2} \frac{q_2^*(s)}{x-s}ds, \quad \forall\, x \in S \tag{47}$$

Again, this equation can be treated as an indentation problem, with the only difference that the additional term $dg/dx|_{\text{prev}}$ has to be incorporated into the profile gradient. Additionally, the profile used in the equivalent rigid-body violation condition has to be

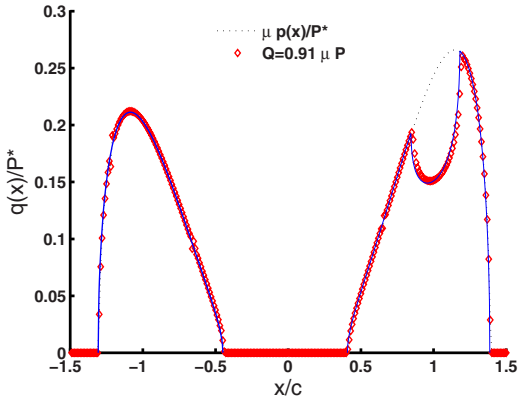

Fig. 6 SIE (solid lines) and FEM (markers) normalized shear tractions $q(x)/P^*$ versus x/c for $P/F^*=0.1677$, $M/M^*=0.0314$, and a value of Q at which there is only one stick zone

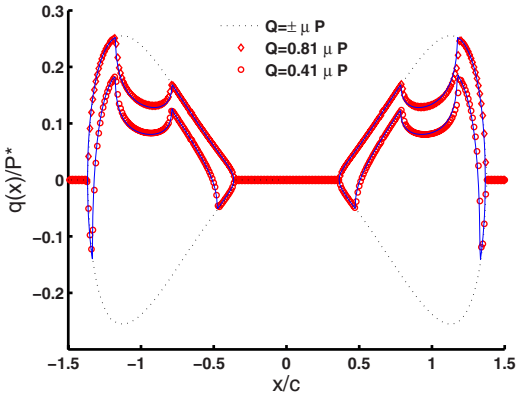

Fig. 7 SIE (solid lines) and FEM (markers) normalized shear tractions $q(x)/P^*$ versus x/c for normal loads $P/F^*=0.1887$ and $M=0$. The shear traction reverses sign in the slip zones when Q is reduced from 0.81 μP to 0.41 μP.

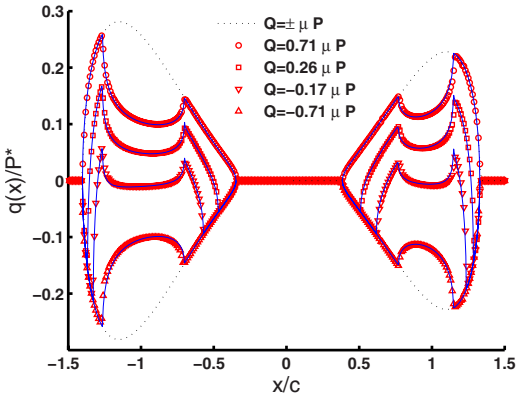

Fig. 8 SIE (solid lines) and FEM (markers) normalized shear tractions $q(x)/P^*$ versus x/c for $P/F^*=0.1887$ and $M/M^*=-0.0314$. Intermediate shear tractions when Q is reduced from 0.71 μP to −0.71 μP are shown.

modified by the *slip function* $g(x)$ calculated at the end of the *previous* step

$$\mu(h_0(a_{q2}) - h_0(b_{q1})) - g(a_{q2}) + g(b_{q1}) - C_2 a_{q2} + C_2 b_{q1} = \int_{b_{q1}}^{a_{q2}} u'_*(x)dx \tag{48}$$

An analogous procedure can be developed for the case when the shear load decreases to a minimum value $-Q$ in the second step and then starts increasing in the third step. The load sequence used to study history effects was as follows: P and M are applied in the first step to make the contact and are held constant in subsequent steps. A shear Q is applied in the second step. Q is decreased successively in the later steps. Figure 7 compares the SIE and the FEM results for $P/F^*=0.1887$, $M=0$, and Q decreased from 0.81 μP in the second step to 0.41 μP in the third step. Notice the reversal of the sign of the shear tractions in the slip zones, and the effect of the "locking-in" of slip in the stick zones. Finally, Fig. 8 shows the shear tractions at intermediate Q values for a load sequence involving the complete reversal of the shear from $Q=0.71$ μP to -0.71 μP for $P/F^*=0.1887$ and $M/M^*=-0.0314$.

8 Other Profiles

While the biquadratic punch has been used as the test profile so far, the SIE method works for any profile that is C^1 continuous within regions that come into contact. Figure 9 shows examples of the application of the SIE technique to two other kinds of profiles (material properties and μ are as before). The plot on the left shows the normalized pressure tractions obtained using the SIE when a half-space is indented by a similar double-flat punch with rounded edges. The profile (not to scale) is also plotted. The parameters of this punch were as follows: All radii are $R=3.05$ mm, both flat lengths are $0.375R$, and the inner flat-end to flat-end separation is $f=0.18R$. The applied normal load $P=1050$ N/mm and the moment $M=178$ N/mm. It must be noted that traction gradients near the contact ends for flat with rounded type profiles become steeper as the ratio of the radius to the flat-length decreases and getting a converged FEM solution becomes computationally very expensive in such cases.

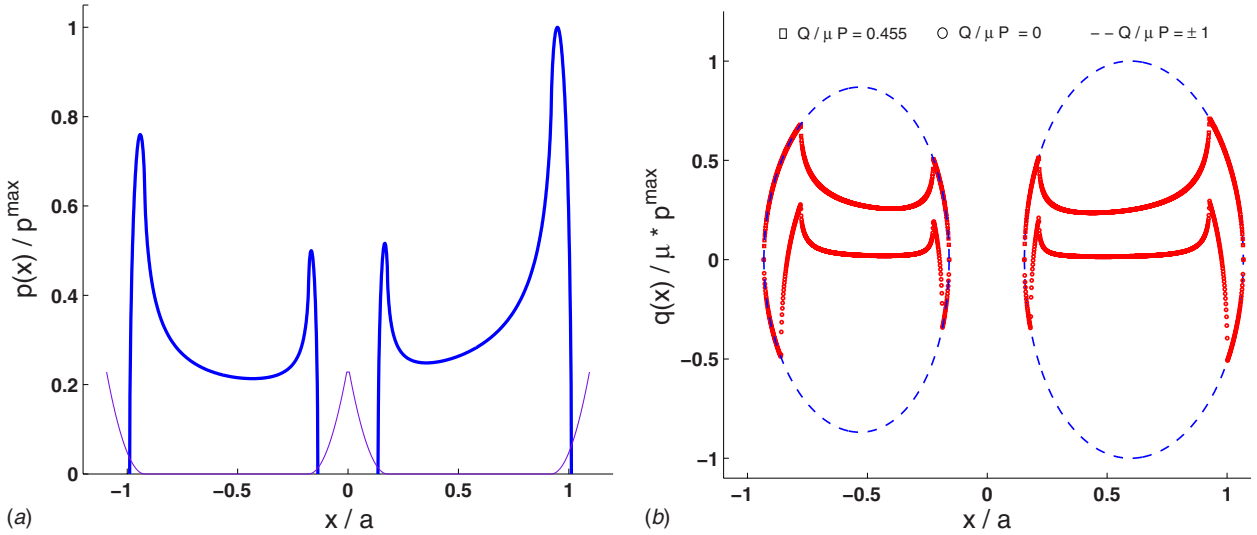

Fig. 9 (Left) SIE normalized pressure tractions $p(x)/\mu p^{max}$ for the indentation of a half-space by a double-flat punch with rounded edges. The profile (not to scale) is also superposed. (Right) SIE normalized shear tractions $q(x)/\mu p^{max}$ for a connected pair of cylinders with $Q=0.455$ μP applied in Step 2 (square markers) and partially reversed to $Q=0$ in load Step 3 (circular markers).

Table 1 Comparison of the FEM and the SIE

Problem	SIE time (s)	FEM time (s)	Real contact size (mm)	SIE mesh (mm)	FEM mesh (mm	Convergence criterion	SIE convergence (%)	FEM convergence (%)
I	15	2800	2.79	0.0023	0.0070	$p^{\max}$	<0.01	<0.5
II	29	3730	2.32	0.0019	0.0064	$q^{\max}$	<0.05	<0.6
III	42	4620	2.33	0.0019	0.0064	$q^{\min}$	<0.25	<2.0

The plot on the right in Fig. 9 shows normalized shear tractions obtained using SIEs for a pair of connected cylindrical indenters in partial slip. Both cylinders have a radius of $R=12.7$ mm and the separation between their minima is $c=0.08R$. A normal load of $P=1751$ N/mm and $M=222$ N/mm are applied in the first step and kept constant throughout. A shear load $Q=0.455\ \mu P$ is applied in the second step and partially reversed to $Q=0$ in the third step. 1200 collocation points were used to obtain both solutions. The x-axes of both plots are normalized by the respective apparent contact half-lengths.

9 Comparison of SIE and FEM Run Times

It is helpful to consider some representative problems to compare the run times of the SIE solver and the FEM. Three different problems are chosen. Problem I is a single step normal indentation problem with applied P,M for a double flat with a rounded punch. Problem II is a two-step partial-slip problem for the biquadratic indenter and Problem III is a three-step partial-slip problem with shear reversal for a biquadratic indenter. For simplicity, only analysis times are considered since the preprocessing time in FEM (while significantly greater than SIE, where it is nonexistent) varies considerably. Table 1 shows the run times and other key analysis parameters using both the FEM and the SIE to get converged tractions for these three problems. The SIE solver was run on a single CPU desktop PC. The ABAQUS/STANDARD FEM analyses were run on a 4-CPU compute server. Even so, it is clear that the SIE is much faster than the FEM for these problems, with the greatest advantage in partial-slip problems with shear reversal. Table 1 also gives a clear picture of the kind of fine meshes needed to achieve converged tractions in both the FEM and the SIE. While these results compare single analyses, the SIE solver's computational advantage over the FEM is even greater in parametric studies in which the geometry is a parameter (e.g., varying the c/R ratio for the biquadratic indenter).

10 Transition to a Single Contact Problem

It has been mentioned previously that a double contact problem can transition to a single contact one depending on the applied loads. There are two ways for this to happen. The first way (called Type A for convenience) is by applying an increasing normal load $P>P_{\text{crit}}$, which causes the two contact patches to merge into one. The exact value of this critical normal load depends on the material properties and geometry but is also moment dependent. The second way (Type B) is by applying a large moment M so that one of the contacts lifts off.

In the absence of an applied moment, it is possible to obtain an analytical expression for P_{crit} for a biquadratic punch for the Type A transition as follows. Consider a biquadratic indenter with an applied load $P>P_{\text{crit}}$. Clearly, it is in the simply connected regime. Now

$$(P-P_{\text{crit}})\to 0 \Rightarrow p(x)|_{x=x_c=0}\to 0 \tag{49}$$

This result follows directly from symmetry considerations. Furthermore, consider two points 0^- and 0^+ to the left and right of 0, respectively, when $P=P_{\text{crit}}$. Since the contact is still unbroken at these points, $p(0^-)>0$ and $p(0^+)>0$, which implies that there is a local minimum at the point $x=0$ if $p(x)$ is a smooth function. The important thing to note is that the analysis can be carried out entirely in the *single* contact regime, where by using a sine-series solution (more details on the sine-series technique are available in Ref. [9]), the pressure function is given by

$$p(\theta)=\frac{\dfrac{P}{\pi a}+\dfrac{1}{\pi A a}+\left(\dfrac{a^2}{4R}-\dfrac{a^4}{8Rc^2}\right)\cos(2\theta)-\dfrac{1}{\pi A a}\dfrac{a^4}{16Rc^2}\cos(4\theta)}{\sin(\theta)} \tag{50}$$

where a is the contact half-length and $x=a\cos(\theta)$. Using the conditions above and considering that the pressure has to vanish at the contact end points $\theta=0$, $\theta=\pi$ directly lead to

$$P_{\text{crit,sym}}=\frac{c^2}{4AR} \tag{51}$$

In case a moment M_{crit} is applied, the form of the pressure solution is no longer simple; the location of the minimum point x_c shifts from $x=0$ and is unknown. The zero traction and local minimum conditions, however, continue to hold at this point and, together with the contact end conditions, can be written as

$$0=p_0+p_2+p_4 \tag{52}$$

$$0=p_1+p_3 \tag{53}$$

$$0=p_0+p_1\cos(\theta_c)+p_2\cos(2\theta_c)+p_3\cos(3\theta_c)+p_4\cos(4\theta_c) \tag{54}$$

$$0=p_1\sin(\theta_c)+2p_2\sin(2\theta_c)+3p_3\sin(3\theta_c)+4p_4\sin(4\theta_c) \tag{55}$$

where θ_c corresponds to x_c in transformed coordinates and p_i are coefficients in the pressure cosine series, which are related to the applied loads, contact half-length a, eccentricity e, and the coefficients of the sine series h_n of the biquadratic profile. The equations given above can be converted to a set of four equations in the unknowns P_{crit}, a, e, and θ_c, which can be solved numerically for a given moment $M=M_{\text{crit}}$, thus allowing us to trace the Type A boundary, as shown in Fig. 10. It can be seen that for $P_{\text{crit}}>P_{\text{crit,sym}}$, the presence of a moment increases the value of P_{crit} to cause the transition. Furthermore, it is clear that Type A transition cannot occur for $P_{\text{crit}}<P_{\text{crit,sym}}$; the transition of Type B can, however, occur below this value. In this case the conditions at the transition are not known, so it becomes necessary to solve a series of contact problems to estimate the transition loads. It must be emphasized that the above discussion only applies to the transition behavior in biquadratic punches because of the strong influence of the profile geometry on determining it.

11 Conclusions

A fast SIE based numerical method was developed to solve 2D double contact problems for similar isotropic bodies. The method makes it possible to obtain the contact extents, the pressure traction, the stick-zone extents, and the shear tractions and allows for slip history effects, such as shear load reversal. In the pressure, as well as in the partial-slip problem, it was possible to obtain the physically correct contact/stick-zone extents using additional compatibility equations. The results of all analyses were compared with the FEM using a biquadratic indenter and showed good

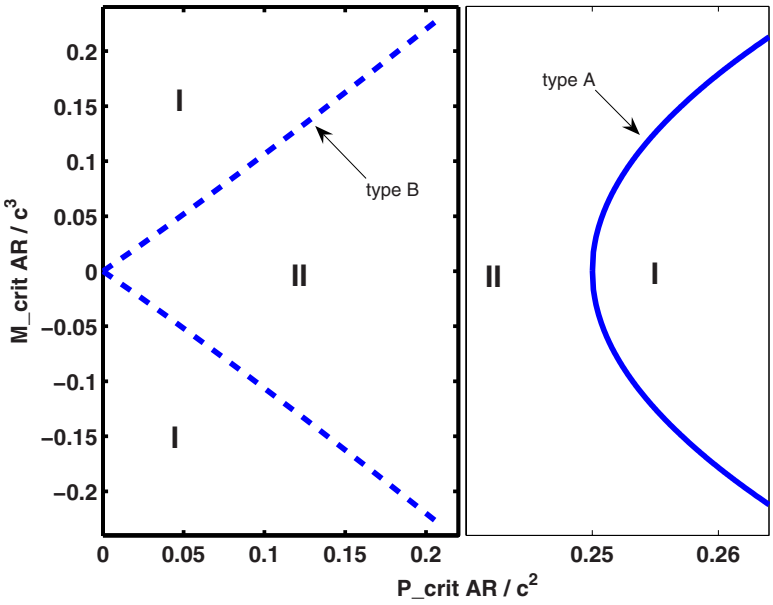

Fig. 10 Transition behavior for a biquadratic punch; the solid lines represent a Type A transition boundary and the dashed line represents the Type B transition boundary. I and II represent the areas of single and double contacts, respectively.

agreement. The SIE based method provides significant savings in computational cost over the FEM. Lastly, the transition behavior from two contacts to one was studied for the biquadratic indenter, and a technique was developed to predict the normal loads and moments at which the two contacts merge.

Acknowledgment

This work is supported partially by DARPA on a subcontract to GE Aircraft Engines. The authors also wish to thank the anonymous reviewers for their suggestions.

References

[1] Barber, J. R., and Ciavarella, M., 2000, "Contact Mechanics," Int. J. Solids Struct., **37**, pp. 29–43.
[2] Muskhelishvili, N. I., 1992, *Singular Integral Equations*, Dover, New York.
[3] Gladwell, G. M., 1980, *Contact Problems in the Classical Theory of Elasticity*, Monographs and Textbooks on Mechanics of Solids and Fluids, Sijthoff and Noordhoff, The Netherlands.
[4] Barber, J. R., 1976, "Indentation of the Semi-Infinite Elastic Solid by a Concave Rigid Punch," J. Elast., **6**(2), pp. 149–159.
[5] Barber, J. R., 1983, "The Solution of Elasticity Problems for the Half-Space by the Method of Green and Collins," Appl. Sci. Res., **40**, pp. 135–157.
[6] Barber, J. R., 1983, "A Four-Part Boundary Value Problem in Elasticity—Indentation by a Discontinuously Concave Punch," Appl. Sci. Res., **40**, pp. 159–167.
[7] Shtayerman, I. Y., 1949, *Contact Problem of the Theory of Elasticity*, Gostekhizdat, Moscow, Leningrad.
[8] Erdogan, F., 1969, "Approximate Solution of Systems of Singular Integral Equations," SIAM J. Appl. Math., **17**(6), pp. 1041–1059.
[9] Barber, J. R., 2002, *Elasticity*, Solid Mechanics and Its Applications, 2nd ed., Kluwer, The Netherlands.
[10] Kalker, J. J., 1977, "Variational Principles of Contact Elastostatics," J. Inst. Math. Appl., **20**, pp. 199–219.
[11] Erdogan, F., and Gupta, G. D., 1972, "On the Numerical Solution of Singular Integral Equations," Q. J. Math., **29**, pp. 525–534.
[12] Rajeev, P. T., and Farris, T. N., 2002, "Numerical Analysis of Fretting Contacts of Dissimilar Isotropic and Anisotropic Materials," J. Strain Anal. Eng. Des., **37**(6), pp. 503–517.
[13] Ciavarella, M., 1998, "The Generalized Cattaneo Partial Slip Plane Contact Problem: I—Theory," Int. J. Solids Struct., **35**(18), pp. 2349–2362.
[14] Ciavarella, M., 1998, "The Generalized Cattaneo Partial Slip Plane Contact Problem: II—Examples," Int. J. Solids Struct., **35**(18), pp. 2363–2378.
[15] Jäger, J., 1997, "Half-Planes Without Coupling Under Contact Loading," Arch. Appl. Mech., **67**, pp. 247–259.

Dynamic Stability of Cracked Viscoelastic Rectangular Plate Subjected to Tangential Follower Force

Zhong-min Wang

Yan Wang

Yin-feng Zhou

School of Sciences,
Xi'an University of Technology,
Xi'an 710054, P.R.C.

Based on the thin plate theory and the two-dimensional viscoelastic differential type constitutive relation, the differential equation of motion of a viscoelastic plate containing an all-over part-through crack and subjected to uniformly distributed tangential follower force is established in Laplace domain. Then, by performing the Laplace inverse transformation, the differential equation of motion of the plate in the time domain is obtained. The expression of the additional rotation induced by the crack is given. The complex eigenvalue equations of the cracked viscoelastic plate subjected to uniformly distributed tangential follower force are obtained by the differential quadrature method, and the δ method is adopted at the crack continuity conditions. The general eigenvalue equations of the cracked viscoelastic plate subjected to uniformly distributed tangential follower force under the different boundary conditions are calculated. The transverse vibration characteristics, type of instability, and corresponding critical loads of the cracked viscoelastic plate subjected to uniformly distributed tangential follower force are analyzed.
[DOI: 10.1115/1.2936927]

Keywords: dynamic stability, follower force, viscoelastic plate, crack, differential quadrature method

1 Introduction

The dynamic stability of elastic systems subjected to follower force is widely applied in practical engineering, such as beam, plate, shell, pipe conveying fluid, bridge, and aerofoil. A vast amount of research work has been performed on the dynamic stability of the nonconservation elastic rectangular plate. Adali [1] considered the stability of a rectangular plate under nonconservative and conservative forces. Leipholz and Pfendt [2] analyzed the critical force of a rectangular plate with free edges and subjected it to uniformly distributed follower forces using the extended Galerkin theory. Wang and Ji [3] investigated the dynamic stability of six typical rectangular plates with two opposite edges simply supported and under the action of uniformly distributed tangential follower force. Zuo and Shreyer [4], Kim and Park [5], Kim and Kim [6], and Jayaraman and Struthers [7] have introduced solutions involving the problems of divergence and flutter instabilities of nonconservative plates.

Thin plates are the basic structures in practical engineering. Some of these with crack damage are not avoidable and are quite adverse for the normal work of the structures, and the crack can result in a change of dynamic characteristics and stability. Therefore, an analysis of the effect of crack damage on transverse vibration and stability of thin plate has important theoretical significance. Much research work had been done on the vibration of plate with crack [8,9]. Lee and Lim [10] determined the natural frequencies of a rectangular plate with a centrally located crack by using the Rayleigh method. Solecki [11] studied bending vibration of a rectangular plate with arbitrarily located rectilinear crack. Khadem ane Rezaee [12] took an analytical approach and investigated the vibration of the plate with an all-over part-through crack. Han and Ren [13] analyzed the effect of cracks on the dynamic characteristics of plates by means of a model of zero dimension element with crack. With the development of material science, viscoelastic rectangular plates have been widely applied in many engineering fields. In the research on dynamical problem of viscoelastic plate with crack, Hu and Fu [14] introduced linear free vibration of a viscoelastic plate with a crack and four edges simply supported by the Galerkin method. To the authors' knowledge, few papers have been presented on stability problems for cracked viscoelastic plates subjected to follower force.

The aim of this paper is to construct the differential equation of motion of the cracked viscoelastic plate subjected to uniformly distributed tangential follower force by introducing a viscoelastic differential operator. The equation is suitable for various linear viscoelastic differential models. The δ method is applied at the crack continuity conditions. The complex eigenvalue equations of the cracked viscoelastic plate subjected to follower force constituted by elastic behavior in dilatation and the Kelvin–Voigt model for distortion are obtained by the differential quadrature method. The computational program is prepared to solve the eigenvalue equations and to obtain the eigenvalue curves. The transverse vibration characteristics and dynamic stability of the viscoelastic plate containing an all-over part-through crack subjected to uniformly distributed tangential follower forces are analyzed.

2 Differential Equation of Motion

Figure 1 shows a viscoelastic rectangular thin plate subjected to uniformly distributed tangential follower forces q_0 and with an all-over part-through crack of depth h_1 in the z direction. The edge is parallel to the y direction, and the location is at $x=a_1$. The plate has the length a, width b, and thickness h in the x, y, and z directions, respectively. The thin plate is divided by a crack into two domains.

The three-dimensional linear viscoelastic differential constitutive equations is are

$$P's_{Iij} = Q'e_{Iij}$$

Contributed by the Applied Mechanics Division of ASME for publication in the JOURNAL OF APPLIED MECHANICS. Manuscript received April 16, 2007; final manuscript received March 27, 2008; published online August 21, 2008. Review conducted by Zhigang Suo.

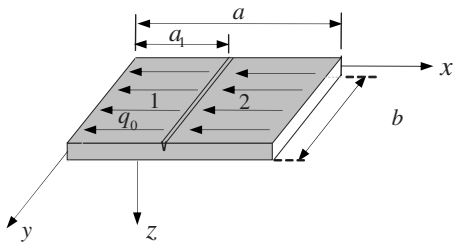

Fig. 1 The cracked viscoelastic rectangular plate subjected to uniformly distributed tangential follower forces

$$P''\sigma_{Iii} = Q''\varepsilon_{Iii} \tag{1}$$

where the differential operator $P' = \Sigma_{k=0}^{l} p_k'(d^k/dt^k)$, $Q' = \Sigma_{k=0}^{r} q_k'(d^k/dt^k)$, $P'' = \Sigma_{k=0}^{l_1} p_k''(d^k/dt^k)$, $Q'' = \Sigma_{k=0}^{r_1} q_k''(d^k/dt^k)$; p_k', q_k', and p_k'', q_k'' depend on the properties of the material; e_{ij} and s_{ij} are the deviatoric tensor of stress and strain, respectively; σ_{ii} and ε_{ii} are the spherical tensor of stress and strain, respectively.

According to the Kirchhoff hypothesis, the thin plate is an in plane stress ($\sigma_z = 0$). The stress component of each point in the plate is σ_{Ix}, σ_{Iy}, τ_{Ixy}, ε_{Ix}, ε_{Iy}, ε_{Ixy} ($I = 1,2$). The constitutive equations of the linear viscoelastic material in the Laplace domain [15] are

$$\bar{P}'(\bar{P}'\bar{Q}'' + 2\bar{Q}'\bar{P}'')\bar{\sigma}_{Ix} = \bar{Q}'(2\bar{P}'\bar{Q}'' + \bar{Q}'\bar{P}'')\bar{\varepsilon}_{Ix} + \bar{Q}'(\bar{P}'\bar{Q}'' - \bar{Q}'\bar{P}'')\bar{\varepsilon}_{Iy}$$

$$\bar{P}'(\bar{P}'\bar{Q}'' + 2\bar{Q}'\bar{P}'')\bar{\sigma}_{Iy} = \bar{Q}'(\bar{P}'\bar{Q}'' - \bar{Q}'\bar{P}'')\bar{\varepsilon}_{Ix} + \bar{Q}'(2\bar{P}'\bar{Q}'' + \bar{Q}'\bar{P}'')\bar{\varepsilon}_{Iy}$$

$$\bar{Q}'\bar{\varepsilon}_{Ixy} = \bar{P}'\bar{\tau}_{Ixy} \tag{2}$$

where $\bar{P}'$, $\bar{Q}'$, $\bar{P}''$, and $\bar{Q}''$ are the Laplace transform of the differential operator P', Q', P'', and Q''.

The geometry equations of the viscoelastic plate are the same as those of the elastic plate. According to D'Alembert's principle, an equilibrium equation of the viscoelastic plate subjected to uniformly distributed tangential follower force is given by

$$\frac{\partial^2 M_{Ix}}{\partial x^2} + 2\frac{\partial^2 M_{Ixy}}{\partial x \partial y} + \frac{\partial^2 M_{Iy}}{\partial y^2} - q_0(a-x)\frac{\partial^2 w_I^*}{\partial x^2} - \rho h \frac{\partial^2 w_I^*}{\partial t^2} = 0 \tag{3}$$

where ρ is the density of material, q_0 is a force per unit area, w_I^* ($I = 1,2$) is the transverse displacement of the plate or deflection, and M_x, M_y, and M_{xy} are defined as the bending moment and twisting moment on the per unit width of the plate, respectively.

For convenience, let $\bar{P}_0 = \bar{P}'\bar{Q}'' + 2\bar{Q}'\bar{P}''$ in Eq. (2), i.e., $\bar{P}_0 = \Sigma_{k=1}^{m}(p_0)_k s_1^k$, where $(p_0)_k$ is the coefficient depending on the material property and the polynomial $\bar{P}_0$ about the Laplace variable s_1 is independent of spatial coordinates. Multiplying the result of the Laplace transformation of Eq. (3) by $\bar{P}_0\bar{P}'$, if the partial derivative is continuous, Eq. (3) can be rewritten as

$$\bar{P}'\left(\frac{\partial^2[\bar{P}_0(\bar{M}_{Ix})]}{\partial x^2}\right) + 2\bar{P}_0\left(\frac{\partial^2[\bar{P}'(\bar{M}_{Ixy})]}{\partial x \partial y}\right) + \bar{P}'\left(\frac{\partial^2[\bar{P}_0(\bar{M}_{Iy})]}{\partial y^2}\right) - \bar{P}_0\bar{P}' q_0(a-x)\frac{\partial^2 \bar{w}_I}{\partial x^2} - \rho h \bar{P}_0 \bar{P}' s_1^2 \bar{w}_I = 0 \tag{4}$$

where $\bar{w}_I$ is the Laplace transform of the deflection w_I^*.

Substituting the relations of the Laplace transformation of the bending moment M_x, M_y and the twisting moment M_{xy} into Eq. (4), the differential equation of motion of the viscoelastic plate subjected to uniformly distributed tangential follower force in the Laplace domain is derived as

$$\frac{h^3}{12}\bar{Q}'(2\bar{P}'\bar{Q}'' + \bar{Q}'\bar{P}'')\nabla^4 \bar{w}_I + \bar{P}'(\bar{P}'\bar{Q}'' + 2\bar{Q}'\bar{P}'')\rho h s_1^2 \bar{w}_I + \bar{P}'(\bar{P}'\bar{Q}'' + 2\bar{Q}'\bar{P}'') + q_0(a-x)\frac{\partial^2 \bar{w}_I}{\partial x^2} = 0 \tag{5}$$

Equation (5) is suitable for various linear viscoelastic differential constitutive relations, and the corresponding differential equations of motion are derived by introducing the Laplace transform $\bar{P}'$, $\bar{Q}'$, $\bar{P}''$, and $\bar{Q}''$ of the differential operator.

We assume that the material of the plate obeys the elastic behavior in dilatation and the Kelvin–Voigt model in distortion. The constitutive equations are as follows [16]:

$$s_{ij} = 2Ge_{ij} + 2\eta \dot{e}_{ij}$$

$$\sigma_{ii} = 3K\varepsilon_{ii} \tag{6}$$

where G, η, and K are the shear elastic modulus, viscous coefficient, and bulk elastic modulus, respectively. Performing the Laplace transformation of Eq. (6), one can obtain the polynomial $\bar{P}' = 1$, $\bar{Q}' = 2G + 2\eta s_1$, $\bar{P}'' = 1$, and $\bar{Q}'' = 3K$. Substituting the above polynomial to Eq. (5) and carrying out the Laplace inverse transformation, the differential equation of motion of the cracked viscoelastic plate subjected to uniformly distributed tangential follower force is

$$\frac{h^3}{12}\left(A_3 + A_4\frac{\partial}{\partial t} + A_5\frac{\partial^2}{\partial t^2}\right)\nabla^4 w_I^* + \rho h\left(A_1 + A_2\frac{\partial}{\partial t}\right)\frac{\partial^2 w_I^*}{\partial t^2} + q_0(a-x) \times \left(A_1 + A_2\frac{\partial q}{\partial t}\right)\frac{\partial^2 w_I^*}{\partial x^2} = 0 \tag{7}$$

where $A_1 = 3K + 4G$, $A_2 = 4\eta$, $A_3 = 2G(6K + 2G)$, $A_4 = 8G\eta + 12K\eta$, $A_5 = 4\eta^2$, $K = E/3(1-2\nu)$, $G = E/2(1+\nu)$, and ν is Poisson's ratio.

At the crack location $x = x_c = a_1$, one can write the continuity conditions as follows:

$$w_1^*(x_c^-, y, t) = w_2^*(x_c^+, y, t)$$

$$w_{1,x}^*(x_c^-, y, t) + \Theta - w_{2,x}^*(x_c^+, y, t) = 0$$

$$M_{1x}(x_c^-, y, t) = M_{2x}(x_c^+, y, t)$$

$$V_{1x}(x_c^-, y, t) = V_{2x}(x_c^+, y, t) \tag{8}$$

where $V_{Ix} = Q_{Ix} + M_{Ixy,y}$ and Θ is the additional rotation induced by the crack. The α_{bb} denotes the nondimensional compliance coefficient, and g_b is a dimensionless function of the relative crack depth $s = h_1/h$. These are given by [9,12,14]

$$\alpha_{bb} = \int_0^s g_b{}^2 d\zeta$$

$$g_b = \zeta^{1/2}(1.99 - 2.47\zeta + 12.97\zeta^2 - 23.17\zeta^3 + 24.80\zeta^4) \tag{9}$$

Performing the Laplace transform of Eq. (8) and multiplying by the polynomial $\bar{P}_0$ and $\bar{P}_0\bar{P}'$, one yields

$$\bar{w}_1(x_c^-, y) = \bar{w}_2(x_c^+, y)$$

$$\bar{w}_{1,x}(x_c^-, y) + \bar{\Theta} - \bar{w}_{2,x}(x_c^+, y) = 0$$

$$\bar{P}_0(\bar{M}_{1x}(x_c^-, y)) = \bar{P}_0(\bar{M}_{2x}(x_c^+, y))$$

$$\bar{P}_0\bar{P}'(\bar{Q}_{1x}(x_c^-,y)) + \bar{P}_0\bar{P}'(\bar{M}_{1xy,y}(x_c^-,y)) = \bar{P}_0\bar{P}'(\bar{Q}_{2x}(x_c^+,y)) + \bar{P}_0\bar{P}'(\bar{M}_{2xy,y}(x_c^+,y)) \tag{10}$$

where

$$\bar{P}_0\bar{P}'(\bar{Q}_{Ix}) + \bar{P}_0\bar{P}'(\bar{M}_{Ixy,y}) = -\int_{-h/2}^{h/2} z^2\bar{P}'\left[\bar{Q}_0\frac{\partial^3\bar{w}_I}{\partial x^3} + \bar{Q}_1\frac{\partial^3\bar{w}_I}{\partial x\partial y^2}\right]dz - 2\int_{-h/2}^{h/2} z^2\bar{P}_0\bar{Q}'\left(\frac{\partial^3\bar{w}_I}{\partial x\partial y^2}\right)dz$$

$$\bar{P}_0(\bar{M}_{Ix}) = -\int_{-h/2}^{h/2} z^2\left[\bar{Q}_0\frac{\partial^2\bar{w}_I}{\partial x^2} + \bar{Q}_1\frac{\partial^2\bar{w}_I}{\partial y^2}\right]dz,$$

$$\bar{P}_0 = \bar{P}'(\bar{P}'\bar{Q}'' + 2\bar{Q}'\bar{P}'')$$

$$\bar{Q}_1 = \bar{Q}'(\bar{P}'\bar{Q}'' - \bar{Q}'\bar{P}''), \quad \bar{Q}_0 = \bar{Q}'(2\bar{P}'\bar{Q}'' + \bar{Q}'\bar{P}'')$$

$$\bar{\Theta} = \frac{12}{3\bar{Q}'\bar{Q}''}\left(2\bar{P}'\bar{Q}'' + \bar{P}''\bar{Q}' - \frac{(\bar{P}'\bar{Q}'' - \bar{P}''\bar{Q}')^2}{2\bar{P}'\bar{Q}'' + \bar{P}''\bar{Q}'}\right)\alpha_{bb}\bar{\sigma}_b$$

$$\bar{\sigma}_b = -\frac{3\bar{Q}'\bar{Q}''(2\bar{P}'\bar{Q}'' + \bar{P}''\bar{Q}')h}{2\{(2\bar{P}'\bar{Q}'' + \bar{P}''\bar{Q}')^2 - (\bar{P}'\bar{Q}'' - \bar{P}''\bar{Q}')^2\}}\left(\frac{\partial^2\bar{w}_1}{\partial x^2} + \frac{\bar{P}'\bar{Q}'' - \bar{P}''\bar{Q}'}{2\bar{P}'\bar{Q}'' + \bar{P}''\bar{Q}'}\frac{\partial^2\bar{w}_1}{\partial y^2}\right) \tag{11}$$

Substituting the polynomial $\bar{P}'$, $\bar{Q}'$, $\bar{P}''$, and $\bar{Q}''$ into Eq. (11) and performing the Laplace inverse transformation of $\bar{\Theta}$, one yields the additional rotation expression

$$\left(A_6 + A_7\frac{\partial}{\partial t}\right)\Theta = -6h\alpha_{bb}\left[\left(A_6 + A_7\frac{\partial}{\partial t}\right)\frac{\partial^2 w_1^*}{\partial x^2} + \left(A_8 - A_7\frac{\partial}{\partial t}\right)\frac{\partial^2 w_1^*}{\partial y^2}\right] \tag{12}$$

where $A_6=6K+2G$, $A_7=2\eta$, and $A_8=3K-2G$.

Introducing dimensionless parameters and variables,

$$\xi = \frac{x}{a}, \quad \varsigma = \frac{y}{b}, \quad w_I = \frac{w_I^*}{a}, \quad c = \frac{a}{b}, \quad r = \frac{h}{a}, \quad q = \frac{12q_0a^3(1-\nu^2)}{Eh^3}$$

$$\tau = \frac{th}{a^2}\sqrt{\frac{E}{12\rho(1-\nu^2)}}, \quad H = \frac{h}{a^2}\sqrt{\frac{E}{12\rho(1-\nu^2)}}\frac{\eta}{E} \tag{13}$$

Substituting Eq. (13) into Eq. (7), one obtains

$$\left[1 + \frac{4(2-\nu)(1+\nu)}{3}H\frac{\partial}{\partial\tau} + \frac{4(1-2\nu)(1+\nu)^2}{3}H^2\frac{\partial^2}{\partial\tau^2}\right]\nabla^4 w_I + q(1-\xi)\left[1 + \frac{4(1-2\nu)(1+\nu)}{3(1-\nu)}H\frac{\partial}{\partial\tau}\right]\frac{\partial^2 w_I}{\partial\xi^2} + \left[1 + \frac{4(1-2\nu)(1+\nu)}{3(1-\nu)}H\frac{\partial}{\partial\tau}\right]\frac{\partial^2 w_I}{\partial\tau^2} = 0 \tag{14}$$

where τ is the dimensionless time, H is the dimensionless delay time of material, and $\nabla^4 w_I = \partial^4 w_I/\partial\xi^4 + 2c^2(\partial^4 w_I/\partial\xi^2\partial\varsigma^2) + c^4(\partial^4 w_I/\partial\varsigma^4)$.

The dimensionless continuity conditions at the crack location ($\xi=\xi_c$) is

$$w_1(\xi_c^-,\varsigma,\tau) = w_2(\xi_c^+,\varsigma,\tau)$$

$$\frac{\partial w_1(\xi_c^-,\varsigma,\tau)}{\partial\xi} - \frac{\partial w_2(\xi_c^+,\varsigma,\tau)}{\partial\xi} = \theta$$

$$B_1\frac{\partial^2 w_1(\xi_c^-,\varsigma,\tau)}{\partial\xi^2} + B_2c^2\frac{\partial^2 w_1(\xi_c^-,\varsigma,\tau)}{\partial\varsigma^2} = B_1\frac{\partial^2 w_2(\xi_c^+,\varsigma,\tau)}{\partial\xi^2} + B_2c^2\frac{\partial^2 w_2(\xi_c^+,\varsigma,\tau)}{\partial\varsigma^2}$$

$$B_1\frac{\partial^3 w_1(\xi_c^-,\varsigma,\tau)}{\partial\xi^3} + B_3c^2\frac{\partial^3 w_1(\xi_c^-,\varsigma,\tau)}{\partial\xi\partial\varsigma^2} = B_1\frac{\partial^3 w_2(\xi_c^+,\varsigma,\tau)}{\partial\xi^3} + B_3c^2\frac{\partial^3 w_2(\xi_c^+,\varsigma,\tau)}{\partial\xi\partial\varsigma^2} \tag{15}$$

where $B_1=(1+(2/3)(1-2\nu)(1+\nu)H(\partial/\partial\tau))$, $B_2=(\nu-(2/3)(1-2\nu)(1+\nu)H(\partial/\partial\tau))$, $B_3=[(2-\nu)+2(1-2\nu)(1+\nu)H(\partial/\partial\tau)]$,

$$B_1\theta = -6r\alpha_{bb}\left[B_1\frac{\partial^2 w(\xi_c^-,\varsigma,\tau)}{\partial\xi^2} + B_2c^2\frac{\partial^2 w(\xi_c^-,\varsigma,\tau)}{\partial\varsigma^2}\right] \tag{16}$$

Suppose that the solution to Eq. (14) takes the form $w_I(\xi,\varsigma,\tau)=W_I(\xi,\varsigma)e^{j\omega\tau}$, $j=\sqrt{-1}$. A dimensionless differential equation of motion of the viscoelastic plate is given by

$$D_1\nabla^4 W_I + q(1-\xi)D_2\frac{\partial^2 W_I}{\partial\xi^2} - D_2\omega^2 W_I = 0 \tag{17}$$

where

$$D_1 = 1 - \frac{4(1-2\nu)(1+\nu)^2}{3}H^2\omega^2 + \frac{4(2-\nu)(1+\nu)}{3}H\omega j$$

$$D_2 = 1 + \frac{4(1-2\nu)(1+\nu)}{3(1-\nu)}H\omega j$$

where ω is the dimensionless complex frequency.

Substituting $w_I(\xi,\varsigma,\tau)=W_I(\xi,\varsigma)e^{j\omega\tau}$ into Eq. (15), the crack continuity conditions are as follows:

$$W_1(\xi_c^-,\varsigma) = W_2(\xi_c^+,\varsigma)$$

$$D_3\left(\frac{\partial W_1(\xi_c^-,\varsigma)}{\partial\xi} - \frac{\partial W_2(\xi_c^+,\varsigma)}{\partial\xi}\right) = -6r\alpha_{bb}\left(D_3\frac{\partial^2 W_1(\xi_c^-,\varsigma)}{\partial\xi^2} + D_4c^2\frac{\partial^2 W_1(\xi_c^-,\varsigma)}{\partial\varsigma^2}\right)$$

$$D_3\frac{\partial^2 W_1(\xi_c^-,\varsigma)}{\partial\xi^2} + D_4c^2\frac{\partial^2 W_1(\xi_c^-,\varsigma)}{\partial\varphi^2} = D_3\frac{\partial^2 W_2(\xi_c^+,\varsigma)}{\partial\xi^2} + D_4c^2\frac{\partial^2 W_2(\xi_c^+,\varsigma)}{\partial\varsigma^2}$$

$$D_3\frac{\partial^3 W_1(\xi_c^-,\varsigma)}{\partial\xi^3} + D_5c^2\frac{\partial^3 W_1(\xi_c^-,\varsigma)}{\partial\xi\partial\varsigma^2} = D_3\frac{\partial^3 W_2(\xi_c^+,\varsigma)}{\partial\xi^3} + D_5c^2\frac{\partial^3 W_2(\xi_c^+,\varsigma)}{\partial\xi\partial\varsigma^2} \tag{18}$$

where $D_3=1+(2/3)(1-2\nu)(1+\nu)Hj\omega$, $D_4=\nu-(2/3)(1-2\nu)(1+\nu)Hj\omega$, and $D_5=2(1-2\nu)(1+\nu)Hj\omega+(2-\nu)$.

3 Complex Eigenvalue Equation

The complex eigenvalue equations of the cracked viscoelastic plate constituted by the elastic behavior in dilatation and the Kelvin–Voigt model for distortion are derived by the differential quadrature method. The differential quadrature method [17] is used to approximate the partial derivatives of a function with respect to a spatial variable at any discrete point as the weighted linear sum of the function values at all the discrete points chosen in the solution domain of the spatial variable. Postulate a smooth function $f(x,y)$ in the region $0\leq x\leq a$, $0\leq y\leq b$; the partial de-

rivative of the rth order with respect to x of function $f(x,y)$ at point (x_i,y_j), the partial derivative of the sth order with respect to y, and the mixed partial derivative of the sth order with respect to y and the rth order with respect to x are, respectively, approximated as [18]

$$\frac{\partial^r f(x_i,y_j)}{\partial x^r} = \sum_{k=1}^{N} A_{ik}^{(r)} f(x_k,y_j) \quad (i=1,2,\ldots,N;\ r=1,2,\ldots,N-1) \tag{19}$$

$$\frac{\partial^s f(x_i,y_j)}{\partial y^s} = \sum_{m=1}^{M} A_{jm}^{(s)} f(x_i,y_m) \quad (j=1,2,\ldots,M;\ s=1,2,\ldots,N-1) \tag{20}$$

$$\frac{\partial^{r+s} f(x_i,y_j)}{\partial x^r \partial y^s} = \sum_{k=1}^{N} A_{ik}^{(r)} \sum_{m=1}^{M} A_{jm}^{(s)} f(x_i,y_m) \tag{21}$$

where N and M are the numbers of nodes in x and y directions, respectively; $A_{ik}^{(r)}$ and $A_{jm}^{(s)}$ are weight coefficients, and they are determined as [19]

$$A_{ik}^{(1)} = \begin{cases} \displaystyle\prod_{\substack{\mu=1 \\ \mu\neq i,k}}^{N} (x_i - x_\mu) \Big/ \prod_{\substack{\mu=1 \\ \mu\neq k}}^{N} (x_k - x_\mu) & (i,k=1,2,\ldots,N;\ k\neq i) \\ \displaystyle\sum_{\substack{\mu=1 \\ \mu\neq i}}^{N} \frac{1}{x_i - x_\mu} & (i,k=1,2,\ldots,N;\ k=i) \end{cases} \tag{22}$$

$$A_{jm}^{(1)} = \begin{cases} \displaystyle\prod_{\substack{\mu=1 \\ \mu\neq j,m}}^{M} (y_j - y_\mu) \Big/ \prod_{\substack{\mu=1 \\ \mu\neq m}}^{M} (y_m - y_\mu) & (j,m=1,2,\ldots,M;\ m\neq j) \\ \displaystyle\sum_{\substack{\mu=1 \\ \mu\neq j}}^{M} \frac{1}{y_j - y_\mu} & (j,m=1,2,\ldots,M;\ m=j) \end{cases} \tag{23}$$

In the case of $r=2,3,\ldots,N-1$; $s=2,3,\ldots,M-1$, they are as follows:

$$A_{ik}^{(r)} = \begin{cases} r\left(A_{ii}^{(r-1)} A_{ik}^{(1)} - A_{ik}^{(r-1)}/(x_i - x_k)\right) & (i,k=1,2,\ldots,N;\ k\neq i) \\ \displaystyle -\sum_{\substack{\mu=1 \\ \mu\neq i}}^{N} A_{i\mu}^{(r)} & (i=1,2,\ldots,N;\ 1\leqslant r\leqslant (N-1)) \end{cases} \tag{24}$$

$$A_{jm}^{(s)} = \begin{cases} s\left(A_{jj}^{(s-1)} A_{jm}^{(1)} - A_{jm}^{(s-1)}/(y_j - y_m)\right) & (j,m=1,2,\ldots,M;\ m\neq j) \\ \displaystyle -\sum_{\substack{\mu=1 \\ \mu\neq j}}^{M} A_{j\mu}^{(s)} & (j=1,2,\ldots,M;\ 1\leqslant s\leqslant (M-1)) \end{cases} \tag{25}$$

According to the procedures of the differential quadrature method, Eq. (17) can be given in the form

$$\begin{aligned} &\sum_{k=1}^{N} A_{ik}{}^{(4)} W_{kj} + 2c^2 \sum_{m=1}^{N} A_{jm}{}^{(2)} \sum_{k=1}^{N} A_{ik}{}^{(2)} W_{km} + c^4 \sum_{k=1}^{N} A_{jk}{}^{(4)} W_{ik} + q(1-\xi) \sum_{k=1}^{N} A_{ik}{}^{(2)} W_{kj} \\ &+ \left[\frac{4(2-\mu)(1+\mu)}{3} Hj \left(\sum_{k=1}^{N} A_{ik}{}^{(4)} W_{kj} + 2c^2 \sum_{m=1}^{N} A_{jm}{}^{(2)} \sum_{k=1}^{N} A_{ik}{}^{(2)} W_{km} + c^4 \sum_{k=1}^{N} A_{jk}{}^{(4)} W_{ik} + \frac{4(1-2\mu)(1+\mu)}{3(1-\mu)} Hjq(1-\xi) \sum_{k=1}^{N} A_{ik}{}^{(2)} W_{kj} \right) \right] \omega \\ &+ \left[\frac{-4(1-2\mu)(1+\mu)^2}{3} H^2 \left(\sum_{k=1}^{N} A_{ik}{}^{(4)} W_{kj} + 2c^2 \sum_{m=1}^{N} A_{jm}{}^{(2)} \sum_{k=1}^{N} A_{ik}{}^{(2)} W_{km} + c^4 \sum_{k=1}^{N} A_{jk}{}^{(4)} W_{ik} \right) - W_{ij} \right] \omega^2 - \frac{4(1-2\mu)(1+\mu)}{3(1-\mu)} HjW\omega^3 = 0 \end{aligned} \tag{26}$$

The differential quadrature forms of the continuity conditions Eq. (18) at the crack are

$$W_{cj} - W_{cj} = 0 \quad (j=1,2,\ldots,N)$$

$$D_3 \sum_{k=1}^{N} A_{c+1,k}{}^{(1)} W_{kj} + D_3 \sum_{k=1}^{N} A_{c+1,k}{}^{(1)} W_{kj} + 6r\alpha_{bb} \left(D_3 \sum_{k=1}^{N} A_{c+1,k}{}^{(2)} W_{kj} + D_4 c^2 \sum_{k=1}^{N} A_{c+1,k}{}^{(2)} W_{kj} \right) = 0$$

Table 1 The critical loads of the elastic plate subjected to follower force with different boundary conditions

Aspect ratio	Boundary conditions	Present solution		Existing solution [3]	
$c=1$	SSSS	$q_{d1}=67.5$	$q_{d2}=132.10$	$q_{d1}=67.4$	$q_{d2}=131.60$
	CSCS	$q_{d1}=143.5$	$q_f=168$		
$c=1.5$	SSSS	$q_{d1}=136.75$	$q_{d2}=224.72$	$q_{d1}=136.56$	$q_{d2}=221.28$
	CSCS	$q_f=202.75$			
$c=2.0$	SSSS	$q_{d1}=224.8$	$q_{d2}=340.5$	$q_{d1}=223.55$	$q_{d2}=340.34$
	CSCS	$q_f=251.5$			

$$D_3\sum_{k=1}^{N} A_{c+2,k}^{(2)} W_{kj} + D_4 c^2 \sum_{m=1}^{N} A_{c+2,m}^{(2)} W_{km} = D_3\sum_{k=1}^{N} A_{c+2,k}^{(2)} W_{kj} + D_4 c^2 \sum_{m=1}^{N} A_{c+2,m}^{(2)} W_{km}$$

$$D_3\sum_{k=1}^{N} A_{c+3,k}^{(3)} W_{kj} + D_5 c^2 \sum_{k=1}^{N} A_{c+3,k}^{(1)} \sum_{m=1}^{N} A_{c+3,m}^{(2)} W_{km} = D_3\sum_{k=1}^{N} A_{c+3,k}^{(3)} W_{kj} + D_5 c^2 \sum_{k=1}^{N} A_{c+3,k}^{(1)} \sum_{m=1}^{N} A_{c+3,m}^{(2)} W_{km} \tag{27}$$

In this paper, choosing $N=M$, one may note that the boundary conditions are applied and the continuity conditions at the crack line are needed. One adopts the weight coefficient method to treat the boundary problem of the plate with four edges simply supported, does the δ method combined with the weight coefficient method to treat the boundary conditions of the plate with two opposite edges simply supported and other edges clamped, and applies the δ method to deal with the crack continuous conditions. The differential quadrature form of boundary conditions of four edges simply supported and two opposite edges simply supported and other edges clamped are given, respectively, by

$$W_{1j} = W_{Nj} = W_{i1} = W_{iN} = 0 \quad (i,j = 1,2,\ldots,N)$$

$$\sum_{k=1}^{N} A_{ik}^{(2)} W_{kj} = 0 \quad (i = 1,N\ j = 1,2,\ldots,N)$$

$$\sum_{k=1}^{N} A_{jk}^{(2)} W_{ik} = 0 \quad (j = 1,N\ i = 1,2,\ldots,N) \tag{28}$$

$$W_{1j} = W_{Nj} = W_{i1} = W_{iN} = 0 \quad (i,j = 1,2,\ldots,N)$$

$$\sum_{k=1}^{N} A_{ik}^{(1)} W_{kj} = 0 \quad (i = 2,N-1\ j = 2,3,\ldots,N-2)$$

$$\sum_{k=1}^{N} A_{jk}^{(2)} W_{ik} = 0 \quad (j = 1,N\ i = 1,2,\ldots,N) \tag{29}$$

Equations (26)–(28) or Eq. (29) can be written into the matrix form

$$(\omega^3[\boldsymbol{Q}] + \omega^2[\boldsymbol{R}] + \omega[\boldsymbol{G}] + [\boldsymbol{K}])\{W_{kj}\} = \{0\} \tag{30}$$

where the matrix $[\boldsymbol{Q}]$, $[\boldsymbol{R}]$, $[\boldsymbol{G}]$, and $[\boldsymbol{K}]$ involve such parameters as dimensionless delay time H, aspect ratio of the plate, dimensionless complex frequency, and crack parameter. Equation (30) is a generalized eigenvalue problem. Then, the complex eigenvalue equation of the cracked viscoelastic plate subjected to uniformly distributed tangential follower force is that coefficient determinant equal to zero, that is,

$$\left|\omega^3[\boldsymbol{Q}] + \omega^2[\boldsymbol{R}] + \omega[\boldsymbol{G}] + [\boldsymbol{K}]\right| = 0 \tag{31}$$

By solving the eigenvalue equations, one can obtain the complex frequency and eigenvalue curves of the viscoelastic plate with crack. The dynamic characteristic, type of instability, and corresponding critical load of the viscoelastic plate subjected to follower force are obtained.

4 Numerical Result and Analyses

Let $H\to 0$ and $s\to 0$. One may obtain the problem of dynamic stability of the intact elastic plate subjected to follower force. In the present work, the critical loads of the nonconservative elastic plate with four edges simply supported (referred to by the letters SSSS), two opposite edges simply supported, and two other edges clamped (CSCS) are first calculated, which can be seen in Table 1, where q_{d1}, q_{d2}, and q_f denote the first order and second order mode divergence loads and flutter load, respectively. For the case of $c=1$, the variations of the first two dimensionless complex frequencies of the transverse free vibration of elastic plate with crack are given in Figs. 2 and 3. The natural frequencies of the plate decrease due to the presence of a crack with the increase in the crack depth. It should be noted that the existence of the crack can reduce the stiffness of the elastic plate, and with increase in the crack depth, the stiffness of the plate structure constantly decreases.

4.1 Cracked Plate With Four Edges Simply Supported. In the present work, the dynamic stability of the viscoelastic rectangular plate containing an all-over part-through crack subjected to uniformly distributed tangential follower force is analyzed.

Figure 4 shows that the variation of the ratio of the real part of the first two order dimensionless complex frequencies ω of the cracked viscoelastic plate to the real part of the dimensionless complex frequencies ω_0 of the intact elastic plate varied with the crack depth for $H=10^{-3}$. The crack location changes from $\xi=0$ to the center of the plate $\xi=0.5$. This means that the comparison is made with the results known in the elastic plate. It should be noted that the frequencies of the viscoelastic plate decrease with the increase in dimensionless delay time, and due to a crack, the frequency decreases are more changeable. For a certain value of the depth, with the crack getting closer to the center of the plate, the real part of the dimensionless complex frequency ω decreases. For a certain value of the crack location, with an increase in the

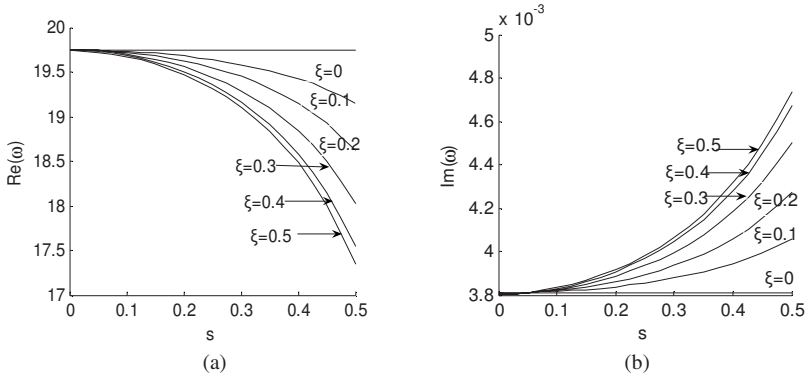

Fig. 2 The first dimensionless complex frequency varied with the crack depth at different crack locations (c=1.0, $H\rightarrow 0$)

crack depth, the real part of the dimensionless complex frequency ω decreases, and the corresponding value of the variation ratio also increases. The second vibration mode takes the same situation.

Figures 5 and 6 show the variation curve of the cracked plate for $H=10^{-3}$ and $\xi=0.5$. The plate was subjected to uniformly distributed tangential follower force $q=50$. It can be seen that in the case of a viscoelastic rectangular plate containing an all-over part-through crack subjected to uniformly distributed tangential follower force, and comparing the results with those of $q=0$, the real part of the dimensionless frequency decreases.

Figures 7–9 show the stability characteristics of the viscoelastic plate containing an all-over part-through crack and subjected to uniformly distributed tangential follower force in the case of $H=10^{-3}$, $\xi=0.5$, $s=0.5$, and aspect ratios $c=1.0, 1.5, 2.0$. As shown in the figure, the reduction in frequencies and the critical load decrement of the divergence type are conspicuous due to the crack. The influence of aspect ratio on the critical loads of the viscoelastic plate is obvious; with the aspect ratio increase, the critical loads increase, while the types of instability remain. It can be compared to the elastic system, where the mode frequencies and the critical load of the viscoelastic plate decrease. With the increase in dimensionless delay time, the real part of the dimensionless complex frequency ω decreases, while its imaginary part changes from zero to positive values, and the imaginary values increase with an increase in H and mode order. This means that the frequencies decrease, while the damping increases; i.e., the systems do not behave as undamped harmonic motion but as

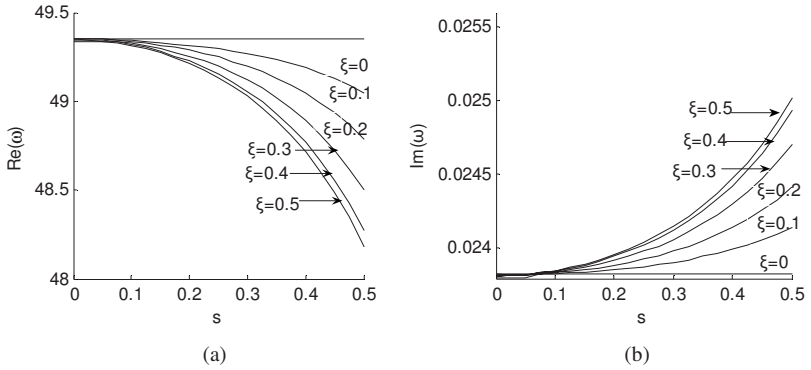

Fig. 3 The second dimensionless complex frequency varied with the crack depth at different crack locations (c=1.0, $H\rightarrow 0$)

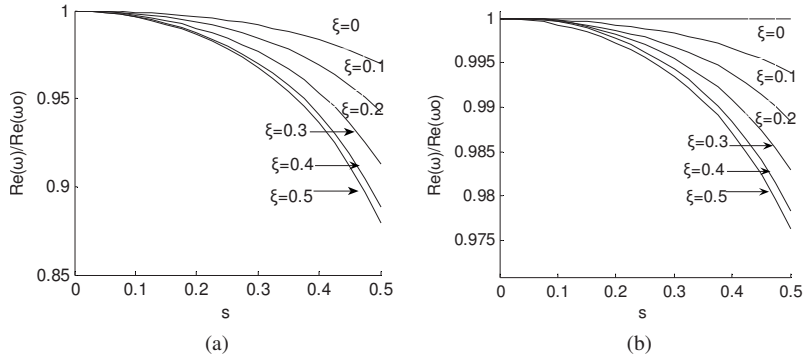

Fig. 4 The real part of the first two order dimensionless frequency ratio: (*a*) first and (*b*) second versus the crack depth for various crack locations (c=1.0, $H=10^{-3}$)

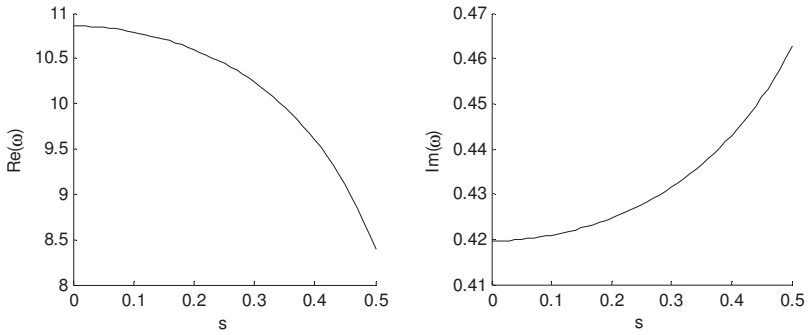

Fig. 5 The first dimensionless complex frequency varied with the crack depth (c=1.0, H=10^{-3}, q=50)

damped vibration. With the increase of q, the real part of ω decreases, while its imaginary part remains a positive value and increases with the increase of the mode order. When the follower force increases to the first order critical load,$\mathrm{Re}(\omega)=0$, and $\mathrm{Im}(\omega)>0$ and $\mathrm{Im}(\omega)<0$ occur, which shows that the plate experiences divergence instability. When the follower force further increases to the second order critical load, the real part of the second order complex frequency becomes zero. Then, the second order mode shows divergence instability. When the follower force keeps increasing, the change is the same as the third order mode.

4.2 Cracked Plate With Two Opposite Edges Simply Supported and Two Other Edges Clamped. Figure 10 shows the variation of ratio of the real part of the first two order dimensionless complex frequencies for $H=10^{-3}$ and $c=1.0$. It can be seen that when $\xi=0$, the real part of the dimensionless complex frequency ω is the biggest, and by getting closer to the center of the plate, the real part of the dimensionless complex frequency ω decreases; there is a symmetrical curve for the structure.

Figure 11 shows the variation of the first order dimensionless complex frequencies ω of the cracked plate for $H=10^{-3}$ and $\xi=0.5$. The plate was subjected to uniformly distributed tangential follower force of $q=0,130,140$. With increasing uniformly distributed tangential follower force, the real part of the dimensionless mode frequency decreases. When $q=140$, the imaginary part of the first order dimensionless complex frequency has two branches with positive and negative values; obviously, this shows that the plate undergoes divergence instability.

Figure 12 shows the stability of the viscoelastic plate contain-

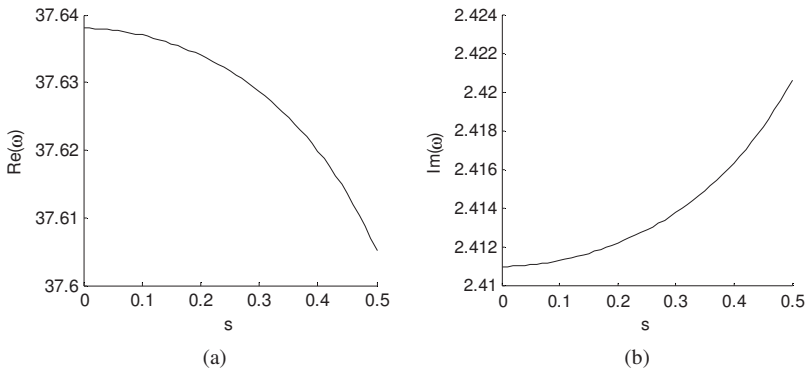

Fig. 6 The second dimensionless complex frequency varied with the crack depth (c=1.0, H=10^{-3}, q=50)

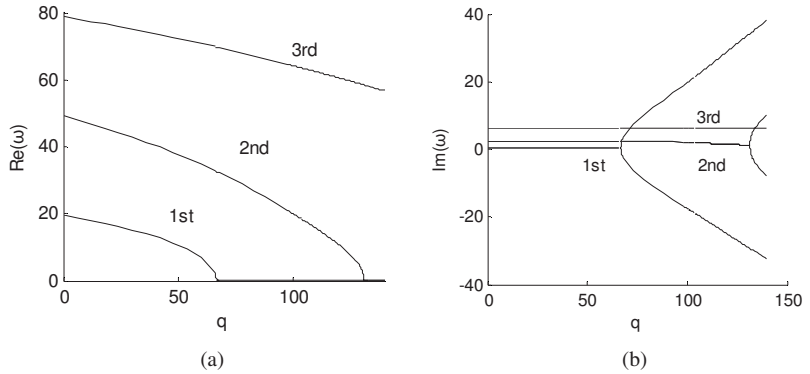

Fig. 7 The first three order dimensionless complex frequencies versus dimensionless follower force q (c=1.0, H=10^{-3})

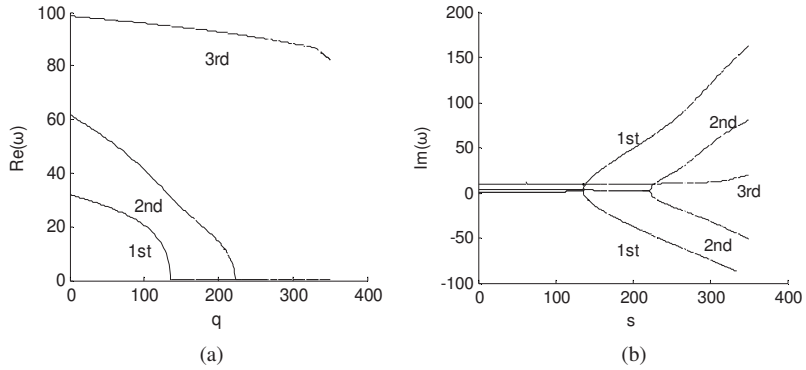

Fig. 8 The first three order dimensionless complex frequencies versus dimensionless follower force q ($c=1.5$, $H=10^{-3}$)

ing an all-over part-through crack and subjected to uniformly distributed tangential follower force in the case of $H=10^{-5}$, $\xi=0.5$, $s=0.5$, and aspect ratio $c=1.0$. As shown in the figure, it can be compared to the intact nonconservative plate, the reduction in mode frequencies and the critical load decrement are conspicuous due to the crack. With the increase of q, the real part of ω decreases, while its imaginary part remains zero. When the follower force increases to the first order critical load, the real part of ω is zero. This shows that the plate undergoes divergence instability in the first order mode; the corresponding critical load is a divergent load. Subsequently, when $\mathrm{Re}(\omega)=0$, and $\mathrm{Im}(\omega)>0$, and $\mathrm{Im}(\omega)<0$ occur, the plate undergoes divergence instability. When the follower force further increases to $q\approx 164$, the plate regains stability in the first order mode, By maintaining the increase of the follower force, the plate undergoes a coupled-mode flutter of the first and third modes.

Figure 13 shows the stability of the viscoelastic plate containing an all-over part-through crack and subjected to uniformly distributed tangential follower force in the case of $H=10^{-3}$, $\xi=0.5$, $s=0.5$, and aspect ratio $c=1.0$. For greater dimensionless delay time, the imaginary parts of dimensionless complex frequencies no longer remain zero; the first and third modes do not couple. This shows that the plate does not exhibit a coupled-mode flutter. With the increase of the follower force, the plate first shows divergence instability in the first mode, then does a single-mode flutter.

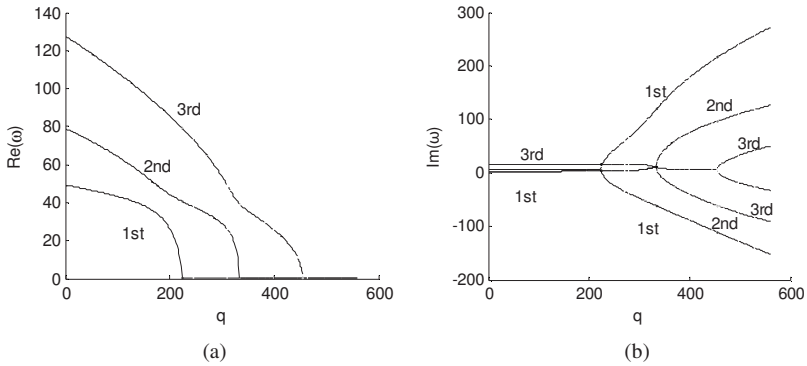

Fig. 9 The first three order dimensionless complex frequencies versus dimensionless follower force q ($c=2.0$, $H=10^{-3}$)

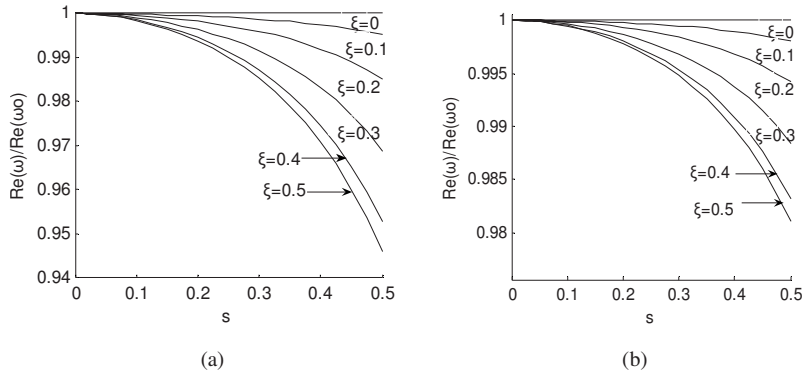

Fig. 10 The real part of the first two order dimensionless frequency ratio: (*a*) first and (*b*) second versus the crack depth for various crack locations ($c=1.0$, $H=10^{-3}$)

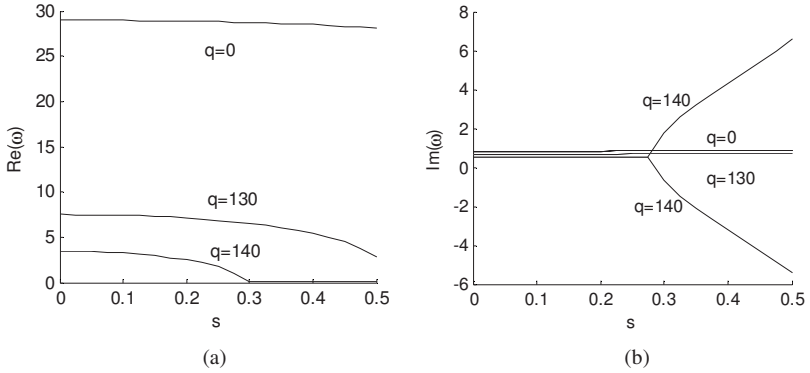

Fig. 11 The first dimensionless complex frequency varied with the crack depth ($H=10^{-3}$)

Figures 14–17 show the stability of the viscoelastic plate containing an all-over part-through crack and subjected to uniformly distributed tangential follower force in the case of $H=10^{-5}$ and $H=10^{-3}$, $\xi=0.5$, $s=0.5$, and aspect ratio $c=1.5,2.0$, respectively. As shown in the figures, the influence of the aspect ratio on the critical loads and types of instability of the viscoelastic plate is obvious. When $c>1$ and $H=10^{-5}$, the first and second modes couple. In this case, the instability type are the coupled-mode flutter, and the corresponding critical load is the flutter load. With the increase of dimensionless delay time, the first and second modes undergo a single-mode flutter.

Figures 18 and 19 give the variation of the first three order dimensionless complex frequencies of the intact plate and cracked plate with dimensionless follower force for the $H=5\times10^{-3}$. As shown in the figure, with the increase of follower force, the first order mode of the cracked plate shows divergence instability; the corresponding critical load is a divergent load; after then, the intact plate undergoes divergence instability. For greater follower force, the intact plate undergoes a single-mode flutter, and then the cracked plate occurs.

5 Conclusion

The numerical method is obtained to investigate the type of instability of the cracked viscoelastic plate subjected to follower force with different boundary conditions. The differential quadrature method is developed. The natural vibration characteristics and dynamic stability of the viscoelastic plate containing an all-over part-through crack and subjected to uniformly distributed tangential follower force are investigated. One can obtain a quantitative

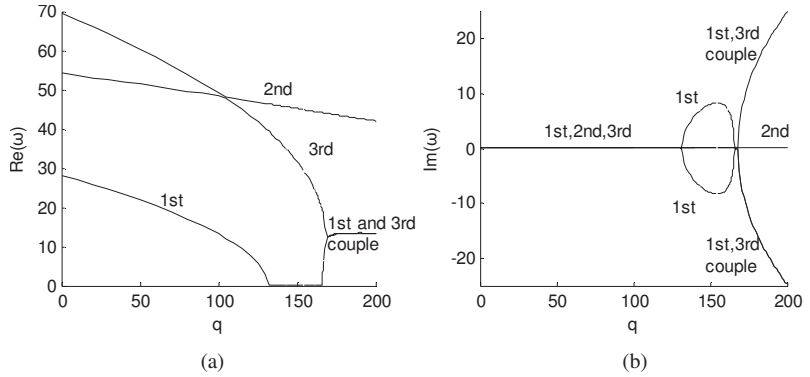

Fig. 12 The first three order dimensionless complex frequencies versus dimensionless follower force q ($H=10^{-5}$, $c=1.0$)

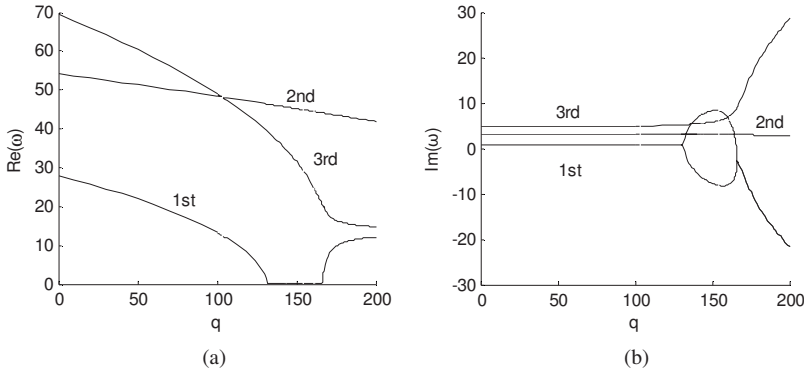

Fig. 13 The first three order dimensionless complex frequencies versus dimensionless follower force q ($H=10^{-3}$, $c=1.0$)

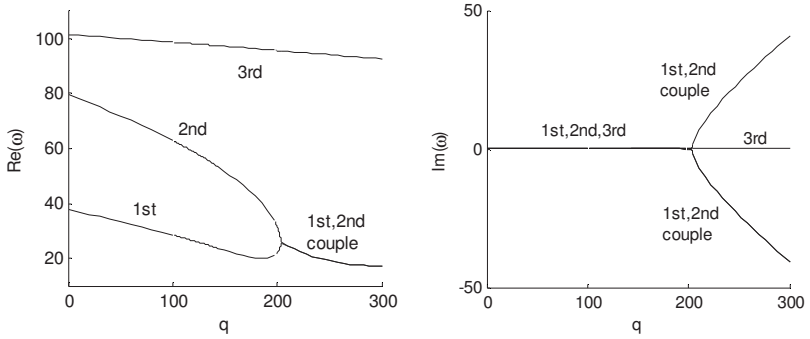

Fig. 14 The first three order dimensionless complex frequencies versus dimensionless follower force q ($H=10^{-5}$, $c=1.5$)

analysis evidence of the influence of the crack damage on the mode parameter, type of instability, and critical loads.

It can be seen from the results of the numerical calculation that the presence of crack would affect the vibration characteristics of the viscoelastic rectangular plate and would lead to local flexibility increase. As a result, the corresponding stiffness of the plate diminishes. The existence of the crack can reduce the stability of the system. The increase of aspect ratios would not affect the type of instability of the viscoelastic plate subjected to follower force with four edges simply supported but would increase the critical loads of each order mode. For smaller dimensionless delay time, the influence of the aspect ratios for the type of instability of the viscoelastic plate subjected to follower force with two opposite edges simply supported and with two other edges clamped is conspicuous. In the case of $c=1$, by increasing the follower force, at first the plate undergoes divergence instability in the first order mode, then the plate undergoes a coupled-mode flutter of the first and third modes. In the case of $c>1$, with the increase of the aspect ratios, the corresponding critical load increases obviously. For greater dimensionless relaxation delay time, in the case of $c=1$, at first the plate undergoes divergence instability in the first mode, and then does a single-mode flutter. In the case of $c>1$, the first order and second order modes change the coupled-mode flutter into a single-mode flutter.

The present approach can be extended to a situation showing the vibration characteristics and the dynamic stability of various linear viscoelastic differential type model plates containing an all-

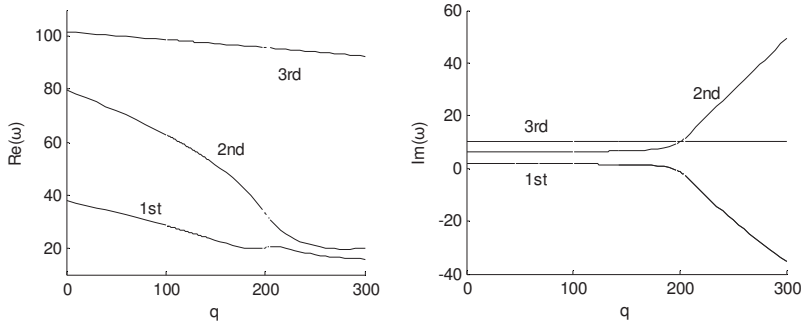

Fig. 15 The first three order dimensionless complex frequencies versus dimensionless follower force q ($H=10^{-3}$, $c=1.5$)

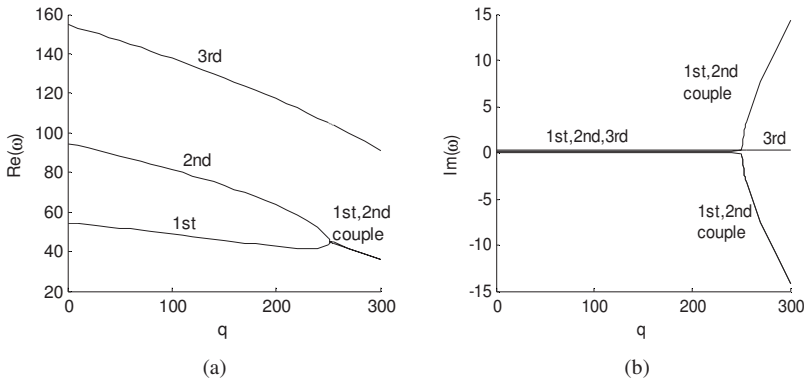

Fig. 16 The first three order dimensionless complex frequencies versus dimensionless follower force q ($H=10^{-5}$, $c=2.0$)

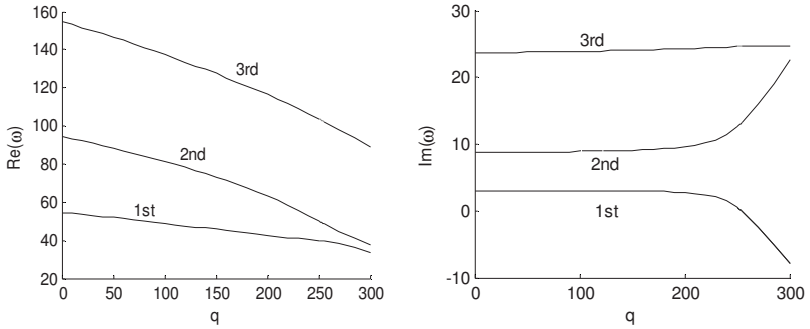

(a) (b)

Fig. 17 The first three order dimensionless complex frequencies versus dimensionless follower force q ($H=10^{-3}$, $c=2.0$)

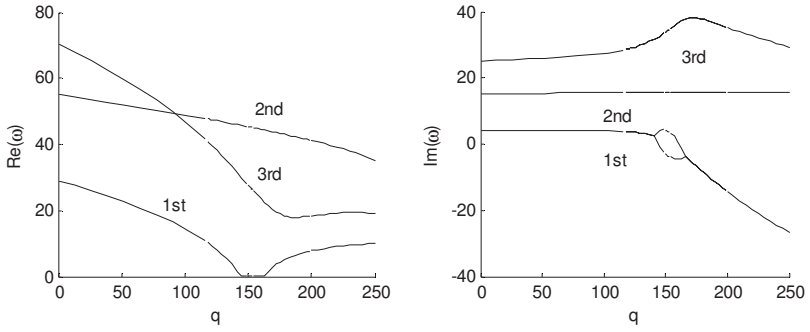

(a) (b)

Fig. 18 The first three order dimensionless complex frequencies versus dimensionless follower force q ($H=5\times10^{-3}$, $c=1.0$, $s=0$)

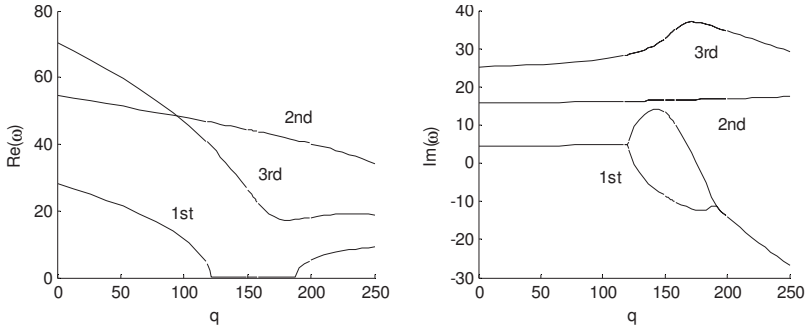

(a) (b)

Fig. 19 The first three order dimensionless complex frequencies versus dimensionless follower force q ($H=5\times10^{-3}$, $c=1.0$, $s=0.5$, $\xi=0.288$)

over part-through crack, with different boundary conditions and subjected to nonconservative and conservative forces.

Acknowledgment

The author gratefully acknowledges the support of the Natural Science Foundation of Shaanxi Province of China (No. 2005A18) and the Foundation of Excellent Doctoral Dissertations of Xi'an University of Technology.

References

[1] Adali, S., 1982, "Stability of a Rectangular Plate Under Non-Conservative and Conservative Forces," Int. J. Solids Struct., **18**, pp. 1043–1052.

[2] Leipholz, H. H., and Pfendt, F., 1983, "Application of Extend Equations of Galerkin to Stability Problems of Rectangular Plates With Free Edges and Subjected to Uniformly Distributed Follower Forces," Comput. Methods Appl. Mech. Eng., **37**, pp. 341–365.

[3] Wang, Z. M., and Ji, Y. Z., 1992, "The Dynamic Stability of Rectangular Plates Under the Action of Tangential Follower Force," Journal of Vibration Engineering, **5**(1), pp. 78–83 (in Chinese).

[4] Zuo, Q. H., and Shreyer, H. L., 1996, "Flutter and Divergence Instability of Non-Conservative Beams and Plates," Int. J. Solids Struct., **33**(9), pp. 1355–1367.

[5] Kim, J. H., and Park, J. H., 1998, "On the Dynamic Stability of Rectangular Plates Subjected to Intermediate Follower Forces," J. Sound Vib., **209**(5), pp. 882–888.

[6] Kim, J. H., and Kim, H. S., 2000, "A Study on the Dynamic Stability of Plate Under Follower Force," Comput. Struct., **74**, pp. 351–363.

[7] Jayaraman, G., and Struthers, A., 2005, "Divergence and Flutter Instability of Elastic Specially Orthotropic Plates Subject to Follower Forces," J. Sound Vib., **281**, pp. 357–373.

[8] Lynn, P. P., and Kumbasar, N., 1967, "Free Vibration of Thin Rectangular Plates Having Narrow Cracks With Simply Supported Edges," *Developments in Mechanics, Proceedings of the Tenth Mechanics Conference*, Fort Collins,

Colorado State University, pp. 153–167.
[9] James, R. R., and Levy, N., 1972, "The Part-Through Surface Crack in an Elastic Plate," ASME J. Appl. Mech., **39**, pp. 185–194.
[10] Lee, H. P., and Lim, S. P., 1993, "Vibration of Cracked Rectangular Plates Including Transverse Shear Deformation and Rotary Inertia," Comput. Struct., **49**(4), pp. 715–718.
[11] Solecki, R., 1985, "Bending Vibration of Rectangular Plate With Arbitrarily Located Rectilinear Crack," Eng. Fract. Mech., **22**(4), pp. 687–695.
[12] Khadem, S. E., and Rezaee, M., 2000, "An Analytical Approach for Obtaining the Location and Depth of an All-Over Part-Through Crack on Externally In-Plane Loaded Rectangular Plate Using Vibration Analysis," J. Sound Vib., **230**(2), pp. 291–308.
[13] Han, Z. N., and Ren, W. M., 1997, "Transverse Vibration of Rectangular Plates With Cracks," Journal of Vibration and Shock, **16**(3), pp. 45–49 (in Chinese).
[14] Hu, H., and Fu, Y. M., 2006, "Linear Free Vibration of a Viscoelastic Plate With an All-Over Part-Through Crack," Journal of Changsha University of Science and Technology (Natural Science), **3**(1), pp. 19–26 (in Chinese).
[15] Flügge, W., 1975, *Viscoelasticity*, Springer-Verlag, New York.
[16] Yang, T. Q., 2004, *Viscoelasticity Theory and Applications*, Science, Beijing.
[17] Teo, T. M., and Liew, K. M., 1999, "A Differential Quadrature Procedure for Three-Dimensional Buckling Analysis of Rectangular Plates," Int. J. Solids Struct., **36**, pp. 1149–1168.
[18] Civalek, Ö., 2004, "Application of Differential Quadrature (DQ) and Harmonic Differential Quadrature (HDQ) for Buckling Analysis of Thin Isotropic Plates and Elastic Columns," Eng. Struct., **26**, pp. 171–186.
[19] Al-Saifl, A. S. J., and Zhengyou, Zh., 2004, "Upwind Local Differential Quadrature Method for Solving Coupled Viscous Flow and Heat Transfer Equations," Appl. Math. Mech., **25**(10), pp. 1034–1041.

Mechanics of Microtubule Buckling Supported by Cytoplasm

Hanqing Jiang
e-mail: hanqing.jiang@asu.edu

Jiaping Zhang

Department of Mechanical and Aerospace Engineering, Arizona State University, Tempe, AZ 85287

The cytoskeleton provides the mechanical scaffold and maintains the integrity of cells. It is usually believed that one type of cytoskeleton biopolymer, microtubules, bears compressive force. In vitro experiments found that isolated microtubules may form an Euler buckling pattern with a long-wavelength for very small compressive force. This, however, does not agree with in vivo experiments where microtubules buckle with a short-wavelength. In order to understand the structural role of microtubules in vivo, we developed mechanics models that study microtubule buckling supported by cytoplasm. The microtubule is modeled as a linearly elastic cylindrical tube while the cytoplasm is characterized by different types of materials, namely, viscous, elastic, or viscoelastic. The dynamic evolution equations, the fastest growth rate, the critical wavelength, and compressive force, as well as equilibrium buckling configurations are obtained. The ability for a cell to sustain compressive force does not solely rely on microtubules but is also supported by the elasticity of cytoplasm. With the support of the cytoplasm, an individual microtubule can sustain a compressive force on the order of 100 pN. The relatively stiff microtubules and compliant cytoplasm are combined to provide a scaffold for compressive force. [DOI: 10.1115/1.2966216]

1 Introduction

It is believed that the mechanical behavior of an eukaryotic cell is primarily governed by a network of filament systems called the cytoskeleton [1]. The cytoskeleton supports a large volume of cytoplasm as well as provides the mechanical scaffold and maintains the integrity of cells [1–3]. Many cellular functions such as gene expression, cell division, motility, signal transduction, wound healing, and apoptosis are mediated by the physical properties of cytoskeleton. There are three major filamentous biopolymers comprising the cytoskeleton: microtubules, actin filaments, and intermediate filaments. Each cytoskeleton filament has different atomic structures and therefore has distinct mechanical functions and properties. For example, a microtubule (Fig. 1(*a*)) is a long (up to 50 μm), hollow cylindrical tube with inner and outer diameters of 15.4 nm and 25 nm, respectively [1,4]. The tube wall is formed from a dimerization of globular proteins (α-β tubulins) with one guanosine triphosphate (GTP) or guanosine diphosphate (GDP) nucleotide. Under the right conditions, tubulin heterodimers will polymerize to form long chained protofilaments (Fig. 1(*b*)), which bind to GDP in a circular arrangement to form a microtubule [1].

Microtubules are the stiffest biopolymers in cytoskeleton, and their bending rigidity is about 100 times larger than that of actin filaments, and therefore it is believed that microtubules typically carry most of the compressive forces [5–9]. Such large aspect ratio (25 nm in diameter/50 μm in length), however, suggests that isolated microtubules will exhibit classic Euler buckling with a single long-wavelength buckling pattern, as shown in Fig. 2(*a*). Using the reported bending rigidity $E_{\mathrm{MT}}I=2\times10^{-23}$ N m^2 [10], the critical load for Euler buckling of a microtubule is $P^c=4\pi^2E_{\mathrm{MT}}I/L^2=0.3$ pN, where E_{MT} is Young's modulus of microtubules, I is the moment of inertia, and $L(=50\ \mu\mathrm{m})$ is the length of a microtubule. This critical load for buckling is even one order of magnitude smaller than the microtubule polymerization force ($\sim$4 pN) measured in vitro [11], which suggests that the microtubules *cannot* sustain compressive force because they would buckle at a very small critical force. Another contradiction is that the single long-wavelength buckling pattern (Fig. 2(*a*)) does not agree with the highly curved microtubules observed in living cells [11,12], as illustrated in Fig. 2(*b*).

In order to understand the structural role of microtubules in living cells, Brangwynne et al. [13] conducted experimental studies on microtubule buckling in vivo. They found that individual microtubules can bear compressive forces that are about 100 times greater in vivo than they can in vitro. In vivo, microtubules also buckle at short-wavelengths ($\lambda=3\ \mu$m). The mechanism for short-wavelength buckling was qualitatively explained by the lateral mechanical reinforcement supported by the surrounding elastic cytoskeleton. This study shed light on the mechanical role of microtubules in living cells although precise mechanics analysis is still needed.

This paper presents a structured analysis of the quantitative mechanics of microtubule buckling. In order to investigate the effects of surrounding cytoplasm on the buckling of microtubules, the cytoplasm is modeled using three different types of materials: viscous, elastic, and viscoelastic. Each cytoplasm model displays unique yet important results. This paper is organized as follows. Section 2 describes the microtubule model that is applied for various cytoplasm models. The analyses of microtubule buckling on viscous, elastic, and viscoelastic cytoplasms are given in Secs. 3–5, respectively, along with the corresponding discussions. Section 6 summarizes the results and discusses the importance of this study to biological understanding of the structural role of microtubules

2 Microtubule Modeling

The microtubule is modeled as an elastic cylindrical tube with outer diameter $D_o(=25$ nm) and inner diameter $D_i(=15.4$ nm). The microtubule is embedded in a three-dimensional cytoplasm and subject to an axial compressive force $P(>0)$ that leads to microtubule buckling with a short-wavelength (Fig. 2(*b*)). The von Karman theory [14] is used to account for the finite rotation effect in the buckling analysis. The axial strain in the microtubule is

Contributed by the Applied Mechanics Division of ASME for publication in the JOURNAL OF APPLIED MECHANICS. Manuscript received December 20, 2007; final manuscript received May 22, 2008; published online August 21, 2008. Review conducted by Krishna Garikipati.

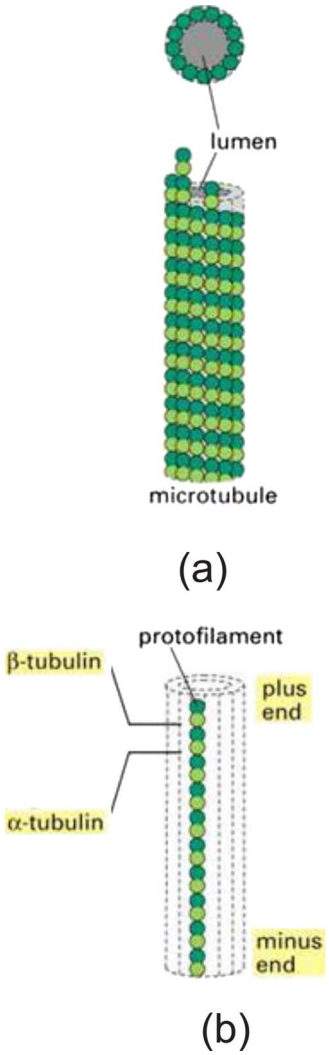

Fig. 1 The structure of a microtubule [1]. (*a*) The microtubule is a hollow cylindrical tube formed from 13 protofilaments aligned in parallel. (*b*) One protofilament consists of a string α-β heterodimers.

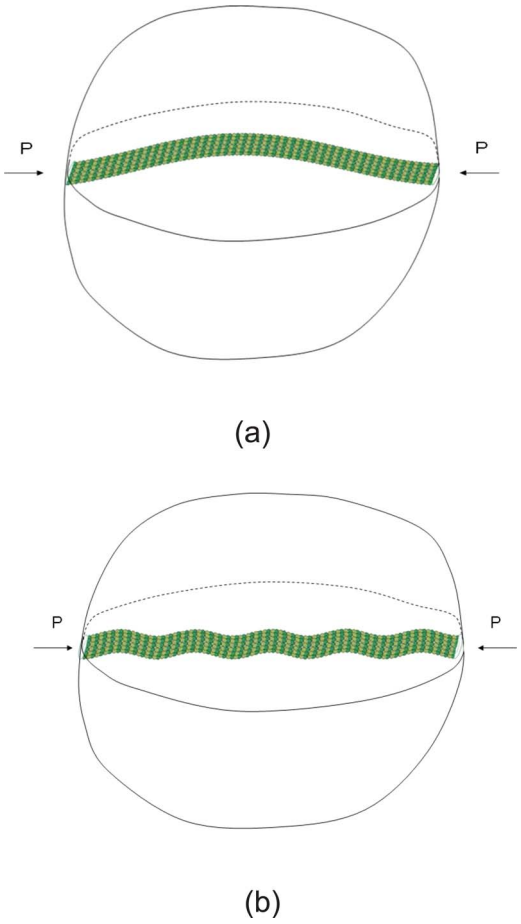

Fig. 2 (*a*) Microtubule buckles to a single long-wavelength pattern and (*b*) microtubule buckles to short-wavelength pattern

$$\varepsilon_{11} = \frac{\partial u_1}{\partial x_1} + \frac{1}{2}\left(\frac{\partial u_3}{\partial x_1}\right)^2 \tag{1}$$

where u_1 is the axial displacement and u_3 is the vertical displacement. The coordinate system is shown in Fig. 3, where x_1 is in the axial direction, x_2 is in the diameter direction, and x_3 is in the vertical direction. The linearly elastic constitutive model gives the axial force $N_{11}=E_{\mathrm{MT}}S\varepsilon_{11}$, where $S=\pi/4(D_o^2-D_i^2)$ is the cross-sectional area of the microtubule. The shear traction T_1 and normal traction T_3 at the microtubule/cytoplasm interface can be obtained from the equilibrium of forces [14]

$$T_1 = \frac{\partial N_{11}}{\partial x_1} \tag{2}$$

and

$$T_3 = E_{\mathrm{MT}} I \frac{\partial^4 u_3}{\partial x_1^4} - N_{11}\frac{\partial^2 u_3}{\partial x_1^2} - \frac{\partial N_{11}}{\partial x_1}\frac{\partial u_3}{\partial x_1} \tag{3}$$

where $I=\pi/64(D_o^4-D_i^4)$ is the moment of inertia of microtubules. The relatively stiff microtubule/compliant cytoplasm system has negligible shear stress at the interface, i.e., $T_1 \approx 0$ [15]. Equation (2) then gives constant axial force N_{11} and constant axial strain ε_{11}.

The buckling profile of the microtubule can be expressed as

$$u_3 = A\cos(kx_1) \tag{4}$$

where the multiple short-wavelength buckling pattern is assumed, the amplitude A and wave number k are to be determined, and $\lambda=2\pi/k$ is the buckling wavelength. The constant axial strain ε_{11} gives the axial displacement $u_1=kA^2\sin(2kx_1)/8$, where the condition $\int_0^{2\pi/k}(\partial u_1/\partial x_1)dx_1=0$ has been imposed to be consistent

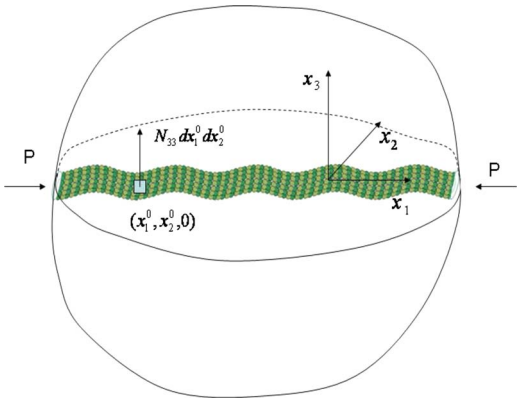

Fig. 3 The coordinate system used in the analysis

with the overall cytoplasm deformation [16]. Due to axial compressive force P, the axial strain then becomes

$$\varepsilon_{11} = \frac{1}{4}A^2k^2 - \frac{P}{E_{\mathrm{MT}}S} \tag{5}$$

and the vertical traction T_3 at the microtubule/cytoplasm interface is

$$T_3 = -\beta\cos(kx_1) \tag{6}$$

where

$$\beta = -E_{\mathrm{MT}}IAk^4 - E_{\mathrm{MT}}S\left(\frac{1}{4}A^2k^2 - \frac{P}{E_{\mathrm{MT}}S}\right)Ak^2 \tag{7}$$

For the buckling profile in Eq. (4), the bending energy per unit wavelength of the microtubule becomes

$$U_b = \frac{k}{2\pi}\int_0^{2\pi/k}\frac{1}{2}E_{\mathrm{MT}}I\left(\frac{\partial^2 u_3}{\partial x_1^2}\right)^2 dx_1 = \frac{1}{4}E_{\mathrm{MT}}Ik^4A^2 \tag{8}$$

The energy per unit wavelength due to axial strain is given by

$$U_a = \frac{1}{2}N_{11}\varepsilon_{11} = \frac{1}{2}E_{\mathrm{MT}}S\left(\frac{1}{4}A^2k^2 - \frac{P}{E_{\mathrm{MT}}S}\right)^2 \tag{9}$$

3 Microtubule Buckling on Viscous Cytoplasm

We first model the surrounding cytoplasm as a three-dimensional viscous flow since the major element of cytoplasm, cytosol, typically consists of fluid. Cytoplasmic streaming is such a three-dimensional viscous flow in the cells and surrounds the cytoskeleton [17]. The viscous cytoplasm is assumed to be incompressible, i.e.,

$$\nabla\cdot\dot{\mathbf{u}} = 0 \tag{10}$$

where $\dot{\mathbf{u}}$ is the velocity, i.e., $\dot{\mathbf{u}} = d\mathbf{u}/dt$; t is the time. Some biological experiments have shown that upon forces (e.g., centrifugal forces), the cytoplasmic streaming becomes steady on the time scale of minutes (e.g., Refs. [18,19]). Moreover, the biological study used measured values to estimate the Reynolds number and found that the Reynolds number Re is very low for cytoplasmic streaming, for instance, $Re < 10^{-3}$, as reported by Pickard [20]. With the conditions of steady state and low Reynolds number of cytoplasmic streaming that surrounds the cytoskeleton, we model the viscous cytoplasm as Stokes flow that is characterized by Stokes equation

$$-\nabla P + \eta\nabla^2\dot{\mathbf{u}} = 0 \tag{11}$$

where P is the pressure and h is the dynamic viscosity of cytoplasm. A vertical traction $-T_3 = \beta\cos(kx_1)$ (where T_3 is given in Eq. (6)) is applied over the area $[|x_2| \le R, x_3 = 0]$ where the microtubule contacts with the viscous cytoplasm. The traction $-T_3$ is assumed to be uniform over the diameter of the microtubule (but periodic in the x_1 direction), which gives the following stress traction in the x_3 direction within the three-dimensional viscous cytoplasm:

$$N_{33} = -\frac{T_3}{2R} = \frac{\beta}{2R}\cos(kx_1) \tag{12}$$

over the diameter $(2R = (D_i + D_o)/2)$ of the microtubules (Fig. 3).

Instead of solving this three-dimensional Stokes equation with stress traction N_{33} as a boundary condition for the area $[|x_2| \le R, x_3 = 0]$ and traction free for the other areas, we use the solution of flow due to a point force. We now consider the flow due to a unit point force at a point of $\mathbf{x}^0 = (x_1^0, x_2^0, 0)$ within the three-dimensional viscous cytoplasm. The Stokes equation with a singular point force term is then given by

$$-\nabla P + \eta\nabla^2\dot{\mathbf{u}} + \mathbf{e}_3\delta(\mathbf{x} - \mathbf{x}^0) = 0 \tag{13}$$

where $\mathbf{e}_3$ is the unit vector in the x_3 direction and δ is the Dirac delta function. Using the Stokes stream function method, the flow due to a point force can be resolved and the details were given by Pozrikidis [21]. The vertical velocity $\dot{u}_3$ at a point $\mathbf{x} = (x_1, x_2, 0)$ is given by $1/8\pi\eta\sqrt{(x_1 - x_1^0)^2 + (x_2 - x_2^0)^2}$. Then for the distributed stress traction N_{33} given by Eq. (12), the vertical velocity $\dot{u}_3$ at a point $\mathbf{x} = (x_1, x_2, 0)$ is the integration over the area covered by microtubule,

$$\begin{aligned}\dot{u}_3(x_1, x_2, 0) &= \int_{-R}^{R}\int_{-\infty}^{\infty}\frac{\beta\cos(kx_1^0)}{2R}\frac{1}{8\pi\eta} \\ &\quad\times\frac{1}{\sqrt{(x_1 - x_1^0)^2 + (x_2 - x_2^0)^2}}dx_1^0dx_2^0 \\ &= \int_{-R}^{R}\frac{\beta\cos(kx_1)}{8\pi R\eta}Y_0(k|x_2^0 - x_2|)dx_2^0\end{aligned} \tag{14}$$

where Y_0 is the modified Bessel function of the second kind [22]. Since the diameter of microtubules $R(=12.5\ \mathrm{nm})$ is much smaller than the observed buckling wavelength $\lambda(=3\ \mu\mathrm{m})$, then $k|x_2^0 - x_2| \le 2kR = 4\pi R/\lambda \ll 1$. The velocity in Eq. (14) then can be approximately expressed as

$$\begin{aligned}\dot{u}_3(x_1, x_2, 0) &= \int_{-R}^{R}\frac{\beta\cos(kx_1)}{8\pi R\eta}\left(\ln\frac{k|x_2^0 - x_2|}{2} + \gamma\right)dx_2^0 \\ &= \frac{\beta\cos(kx_1)}{8\pi R\eta}\{2R(1-\gamma) + 2R\ln 2 - (R + x_2)\ln[k(R \\ &\quad + x_2)] - (R - x_2)\ln[k(R - x_2)]\}\end{aligned} \tag{15}$$

where

$$\gamma = \lim_{n\to\infty}\left[\sum_{i=1}^{n}\frac{1}{i} - \ln(n)\right] = 0.577$$

is Euler's constant.

The viscous cytoplasm and the buckled microtubule are coupled through the continuity condition across the microtubule/cytoplasm interface. Specifically, the vertical velocity $\dot{u}_3$ of the viscous cytoplasm in Eq. (15) is continuous with the vertical velocity of the microtubule resulted from the displacement in Eq. (4) at the interface. We realize that the vertical velocity in Eq. (15) also depends on the x_2 direction so that this continuity is on the average sense, i.e., the average vertical velocity of the viscous cytoplasm over the diameter of the microtubule

$$\dot{u}_3^{\mathrm{avg}}(x_1) = \frac{1}{2R}\int_{-R}^{R}\dot{u}_3(x_1, x_2, 0)dx_2 = \frac{\beta\cos(kx_1)}{8\pi\eta}[3 - 2\gamma - 2\ln(kR)] \tag{16}$$

is the same as the vertical velocity of the microtubule from the displacement in Eq. (4). Thus the continuity condition is

$$\frac{dA}{dt} = \frac{\beta}{8\pi\eta}[3 - 2\gamma - 2\ln(kR)] \tag{17}$$

We consider that the microtubule buckling originated from the accumulation of small fluctuations, which consists of many small perturbation components with each component expressed as a sinusoidal form as in Eq. (4). For small perturbation with vertical displacement A, β in Eq. (7) is linearized by keeping the first-order terms of A,

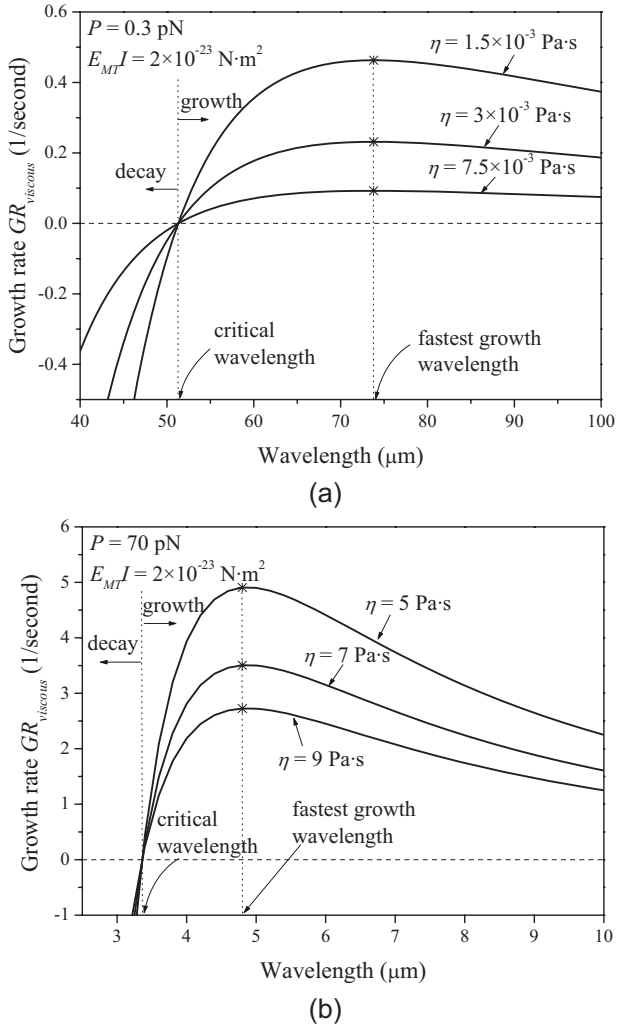

Fig. 4 The relationship of growth rate and wavelength for viscous cytoplasm. (*a*) Growth rate versus wavelength for small axial compressive force and (*b*) growth rate versus wavelength for large axial compressive force.

$$\beta = E_{\mathrm{MT}} I \left(\frac{P}{E_{\mathrm{MT}} I} - k^2 \right) k^2 A \tag{18}$$

The linear ordinary differential equation for small perturbation A then becomes

$$\frac{dA}{dt} = \frac{E_{\mathrm{MT}} I}{8\pi\eta} \left(\frac{P}{E_{\mathrm{MT}} I} - k^2 \right) [3 - 2\gamma - 2\ln(kR)] k^2 A \tag{19}$$

Let $A_0 = A(t=0)$ be the initial amplitude, the evolution of the vertical displacement is

$$A(t) = A_0 \exp\left\{ \frac{E_{\mathrm{MT}} I}{8\pi\eta} \left(\frac{P}{E_{\mathrm{MT}} I} - k^2 \right) [3 - 2\gamma - 2\ln(kR)] k^2 t \right\} = A_0 e^{\mathrm{GR}_{\mathrm{viscous}} t} \tag{20}$$

where

$$\mathrm{GR}_{\mathrm{viscous}} = \frac{E_{\mathrm{MT}} I}{8\pi\eta} \left(\frac{P}{E_{\mathrm{MT}} I} - k^2 \right) [3 - 2\gamma - 2\ln(kR)] k^2 \tag{21}$$

denotes the growth rate of the initial perturbation.

Figure 4 shows $\mathrm{GR}_{\mathrm{viscous}}$ versus wavelength for fixed bending rigidity $E_{\mathrm{MT}} I = 2 \times 10^{-23}$ N m^2 [10] and various axial compressive force P and viscosity η. Figure 4(*a*) gives the growth rate $\mathrm{GR}_{\mathrm{viscous}}$ and wavelength relationship for small compressive force ($P = 0.3$ pN) and low viscosity $\eta = 1.5 \times 10^{-3} - 7.5 \times 10^{-3}$ Pa s to model the fluid-phase cytosol that is only several times as viscous as water (e.g., Refs. [23–25]). When $\mathrm{GR}_{\mathrm{viscous}} > 0$ for certain wavelengths, the initial fluctuations characterized by these wavelengths grow in an exponential law (Eq. (20)), while when $\mathrm{GR}_{\mathrm{viscous}} < 0$ for some wavelengths, the initial fluctuations associated with these wavelengths decay and the microtubules remain straight. The critical condition $\mathrm{GR}_{\mathrm{viscous}} = 0$ gives the critical wavelength

$$\lambda^c_{\mathrm{viscous}} = 2\pi \sqrt{\frac{E_{\mathrm{MT}} I}{P}} \tag{22}$$

The critical wavelength $\lambda^c_{\mathrm{viscous}}$ does not depend on viscosity η and is 51.3 μm, shown in Fig. 4(*a*). The initial fluctuations with wavelengths greater than $\lambda^c_{\mathrm{viscous}}$ will grow; however, the fluctuations with wavelengths smaller than $\lambda^c_{\mathrm{viscous}}$ will decay. Equation (22) also indicates that no matter how small the force is, there exists a critical wavelength $\lambda^c_{\mathrm{viscous}}$ to ensure growth from initial fluctuations. In other words, dynamic growth is guaranteed to occur in viscous cytoplasm.

It is also noticed that the critical wavelength $\lambda^c_{\mathrm{viscous}}$ is identical to the critical length for Euler buckling, which suggests that a very small axial compressive force (on the order of 1 pN depending on the microtubule length) may lead to microtubule buckling with a large wavelength. However, the buckling of microtubules on viscous cytoplasm due to a small compressive force does not indicate that the microtubules cannot bear a compressive force. The growth or decay in this section is just the initial stage, while the compressive force that microtubule can sustain is determined by final equilibrium stage as to be discussed in Sec. 4.

Each curve in Fig. 4(*a*) has a maximum (marked by $*$ in Fig. 4(*a*)), which denotes the fastest growth rate. The corresponding fastest growth wavelength is determined by $\partial \mathrm{GR}_{\mathrm{viscous}} / \partial k = 0$,

$$\lambda = 2\pi \sqrt{\frac{E_{\mathrm{MT}} I}{2P} \frac{5 - 4\gamma - 4\ln(2\pi R/\lambda)}{1 - \gamma - \ln(2\pi R/\lambda)}} \tag{23}$$

Numerical results show that $5 - 4\gamma - 4\ln(2\pi R/\lambda) / 1 - \gamma - \ln(2\pi R/\lambda) \approx 4$ for all wavelengths, such that

$$\lambda^{\text{fastest growth}}_{\mathrm{viscous}} \approx 2\pi \sqrt{\frac{2E_{\mathrm{MT}} I}{P}} \tag{24}$$

Equation (24) clearly shows that the fastest growth wavelength is independent of viscous cytoplasm, while the corresponding fastest growth rate is inversely proportional to the viscosity. More importantly, the fastest growth rate is about 1/s, which suggests that the growth of initial fluctuation is on the order of seconds. This time scale agrees well with in vivo experiments of Brangwynne et al. [13].

Corresponding to the force generated by optical and magnetic tweezers, the growth rate $\mathrm{GR}_{\mathrm{viscous}}$ and wavelength relationship for cells due to a large compressive force ($P = 70$ pN) and moderate viscosity ($\eta = 5 - 9$ Pa s [25]) are shown in Fig. 4(*b*). Similar curves are shown and the critical and fastest growth wavelengths are 3.3 μm and 4.8 μm, respectively.

The study for viscous cytoplasm shows the following.

(1) Any small fluctuations that have wavelength greater than critical wavelength (Eq. (22)) will grow no matter how small the compressive force P is.
(2) Cytoplasm viscosity only affects the growth rate; the smaller the viscosity, the larger the growth rate; cytoplasm viscosity cannot determine the occurrence of the growth.
(3) Critical wavelength and fastest growth wavelength do not depend on viscosity.
(4) The compressive force that a microtubule can sustain before buckling is very small if the surrounding is a viscous cytoplasm.

It should be pointed out that the steadiness of cytoplasmic streaming and small perturbation (Eq. (20)) are two distinct concepts. The former indicates that the cytoplasmic streaming is steady upon external force/stress. While the latter, the small perturbation, evolves to respond to the steady cytoplasmic streaming, which is not steady, as shown in Eq. (20).

4 Microtubule Buckling on Elastic Cytoplasm

The elasticity of the cytoplasm originated from the cytoskeleton [26]. The elastic cytoplasm stores the deformation energy to stabilize the microtubules/cytoplasm system such that the equilibrium configuration (e.g., equilibrium wavelength) is determined by the energetics of the system. In this section, we study the final equilibrium stage by modeling the cytoplasm as a three-dimensional linearly elastic solid in this section. The shear modulus μ_e is used to characterize the incompressible elastic cytoplasm. The energetically favorable buckling pattern is determined using the energy method.

The three-dimensional elastic cytoplasm is subject to vertical traction $-T_3$ (where T_3 is given in Eq. (6)) within the area $[|x_2| \le R, x_3=0]$. The normal traction $-T_3$ is assumed to be uniform over the microtubule diameter $2R$, which gives the nonvanishing stress traction in the x_3 direction $N_{33}=-T_3/2R=\beta\cos(kx_1)/2R$ the same as Eq. (12) in viscous analysis.

Based on Gaussian's divergence theorem, the strain energy per unit wavelength in the elastic cytoplasm is

$$U_s = \frac{k}{2\pi}\cdot\frac{1}{2}\int_V \boldsymbol{\sigma}:\boldsymbol{\varepsilon}dV = \frac{k}{4\pi}\int_{S_\sigma} N_{33}u_3^{\text{cytoplasm}}dS = \frac{k}{4\pi}\int_{-R}^{R}\int_0^{2\pi/k} N_{33}u_3^{\text{cytoplasm}}dx_1dx_2 \tag{25}$$

where S_σ is the area $[|x_2|\le R, x_3=0]$ where the microtubule contacts with the cytoplasm and $u_3^{\text{cytoplasm}}$ is the displacement on the area S_σ, which is obtained analytically from Kelvin's solution [27].

For a unit normal point force at $\mathbf{x}^0=(x_1^0,x_2^0,0)$ within a three-dimensional infinite elastic solid, Kelvin's solution gives the vertical displacement at the point $\mathbf{x}=(x_1,x_2,0)$ as $(1/8\pi\mu_e)1/\sqrt{(x_1-x_1^0)^2+(x_2-x_2^0)^2}$. For the distributed load N_{33}, the displacement at point $\mathbf{x}=(x_1,x_2,0)$ for elastic cytoplasm is the integration over the entire microtubule diameter $2R$,

$$\begin{aligned} u_3^{\text{cytoplasm}}(x_1,x_2,0) &= \int_{-R}^{R}\int_{-\infty}^{\infty}\frac{\beta\cos(kx_1^0)}{16\pi R\mu_e}\times\frac{1}{\sqrt{(x_1-x_1^0)^2+(x_2-x_2^0)^2}}dx_1^0dx_2^0 \\ &= \frac{\beta\cos(kx_1)}{8\pi R\mu_e}\{2R(1-\gamma)+2R\ln 2 - (R+x_2)\ln[k(R+x_2)] - (R-x_2)\ln[k(R-x_2)]\} \end{aligned} \tag{26}$$

where the condition $R/\lambda \ll 1$ has been used. Because the microtubule/elastic cytoplasm interface is replaced by the normal traction in Eq. (6), the above displacement for the elastic cytoplasm is continuous with the displacement in Eq. (4) for the buckled microtubule only on the average sense.

The strain energy in the elastic cytoplasm is then obtained from Eqs. (25) and (26) as

$$\begin{aligned} U_s &= \frac{k}{4\pi}\int_{x_2=-R}^{R}\int_{x_1=0}^{2\pi/k}\frac{\beta}{2R}\cos(kx_1)\frac{\beta\cos(kx_1)}{8\pi R\mu_e}\{2R(1-\gamma)+2R\ln 2 \\ &\quad -(R+x_2)\ln[k(R+x_2)]-(R-x_2)\ln[k(R-x_2)]\}dx_1dx_2 \\ &= \frac{\beta^2}{32\pi\mu_e}[3-2\gamma-2\ln(kR)] \end{aligned} \tag{27}$$

The total potential energy Π_{tot} of the system is the sum of bending energy (Eq. (8)) and axial strain energy (Eq. (9)) in the microtubule and the strain energy in the elastic cytoplasm (Eq. (27)). However, for the microtubule vertical displacement in Eq. (4) and the cytoplasm vertical displacement in Eq. (26), which are not continuous, the potential energy becomes

$$\Pi_{\text{tot}} = U_b + U_m + U_s - \int_{S_\sigma}\Lambda(u_3-u_3^{\text{cytoplasm}})dS \tag{28}$$

where Λ is the Lagrange multiplier. The variation of the above potential energy with respect to Λ requires $u_3=u_3^{\text{cytoplasm}}$ and the variation with respect to the displacement u_3 or $u_3^{\text{cytoplasm}}$ gives Λ to be the traction T_3 (Eq. (6)) at the interface. In the following the Lagrange multiplier Λ is replaced by the traction T_3 in Eq. (6). The potential energy is then obtained as

$$\Pi_{\text{tot}} = \frac{1}{2}E_{\text{MT}}S\left(\frac{1}{4}A^2k^2-\frac{P}{E_{\text{MT}}S}\right)^2+\frac{1}{4}E_{\text{MT}}Ik^4A^2+\frac{1}{2}\beta A-\frac{\beta^2}{32\pi\mu_e}[3-2\gamma-2\ln(kR)] \tag{29}$$

which depends on buckling amplitude A and wavelength $\lambda=2\pi/k$.

The minimization of potential energy Π_{tot} in Eq. (29) with respect to the buckling amplitude A, $\partial\Pi_{\text{tot}}/\partial A=0$, gives

$$A=\begin{cases}\dfrac{2}{k}\sqrt{\dfrac{P-P^c_{\text{elastic}}}{E_{\text{MT}}S}}, & P\ge P^c_{\text{elastic}} \\ 0, & P<P^c_{\text{elastic}}\end{cases} \tag{30}$$

where

$$P^c_{\text{elastic}} = \frac{8\pi\mu_e}{k^2}\frac{1}{3-2\gamma-2\ln(kR)}+E_{\text{MT}}Ik^2 \tag{31}$$

is the critical compressive force for buckling. Equation (30) suggests that the buckling occurs only when the compressive force P reaches a critical force P^c_{elastic} given by Eq. (31), in which the wave number k is to be determined.

The minimization of potential energy with respect to the wave number, $\partial\Pi_{\text{tot}}/\partial k=0$, gives the following nonlinear equation for k:

$$k\left(\frac{E_{\text{MT}}I}{\mu_e}\right)^{1/4}=\left\{\frac{16\pi[1-\gamma-\ln(kR)]}{[3-2\gamma-2\ln(kR)]^2}\right\}^{1/4} \tag{32}$$

For reported microtubule bending rigidity $E_{\text{MT}}I=2\times10^{-23}$ N m^2 [10] and the wide range of shear modulus of the surrounding $\mu_e=1-1000$ Pa [28], the numerical results show that

$$k^c_{\text{elastic}}\approx\frac{5}{4}\left(\frac{\mu_e}{E_{\text{MT}}I}\right)^{1/4} \tag{33}$$

or equivalently,

$$\lambda^c_{\text{elastic}}=\frac{8\pi}{5}\left(\frac{E_{\text{MT}}I}{\mu_e}\right)^{1/4} \tag{34}$$

At this critical wavelength, the amplitude A is

$$A=\frac{8}{5}\left(\frac{E_{\text{MT}}I}{\mu_e}\right)^{1/4}\sqrt{\frac{P-P^c_{\text{elastic}}}{E_{\text{MT}}S}} \tag{35}$$

and the critical force P^c_{elastic} is

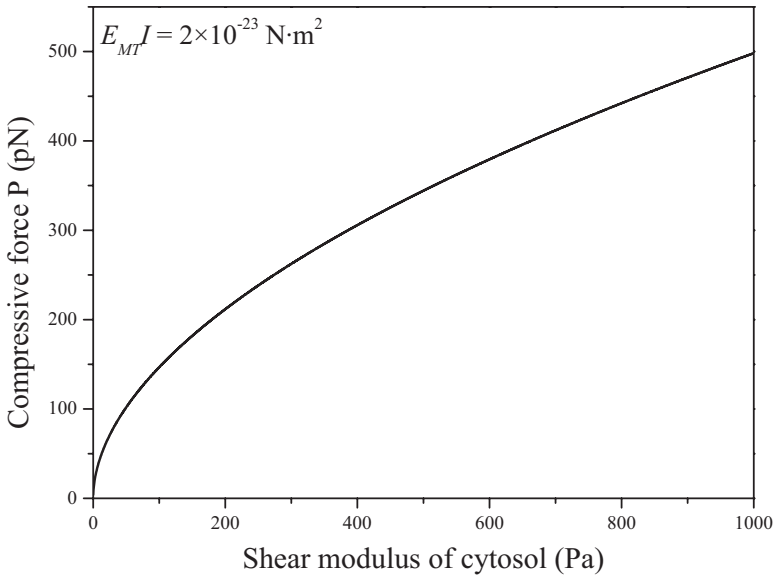

Fig. 5 The relationship between the compressive force *P* that an individual microtubule bears before buckling and the shear modulus of the elastic cytoplasm

$$P^c_{\text{elastic}} = \frac{25}{16}\sqrt{E_{\text{MT}}I\mu_e}\left\{1 + \frac{2048\pi}{625[3 - 2\gamma - 2\ln(2\pi R/\lambda^c_{\text{elastic}})]}\right\} \tag{36}$$

The buckling wavelength given by Eq. (34) is independent of axial compressive force P and solely determined by the ratio of shear modulus of the elastic cytoplasm and the bending rigidity of microtubules. Therefore, the buckling wavelength is an intrinsic property of microtubules/elastic cytoplasm systems and completely determined by their mechanical properties. Since the reported shear modulus μ_e of cytoplasm has extremely large scattering, ranging from 0.1 Pa to 1000 Pa [28], the buckling wavelength also exhibits large scattering. The smallest wavelength is about 1.9 μm while the largest wavelength is 19 μm. If a median value of μ_e=200 Pa is used, the present analysis gives 2.8 μm wavelength, which agrees very well with experiments of Brangwynne et al. [13].

The critical axial compressive force P^c_{elastic} to buckle microtubules (Eq. (36)) depends on both the bending rigidity of microtubules and the shear modulus of the cytoplasm. Therefore, the compressive force that an individual microtubule can bear depends on both the bending rigidity of microtubules and the shear modulus of cytoplasm as well. Figure 5 shows the relationship between the compressive force P that an individual microtubule sustains before buckling and the shear modulus of cytoplasm for a given bending rigidity of microtubules as $E_{\text{MT}}I=2\times10^{-23}$ N m^2 [10]. The results show that the compressive force is on the order of 100 pN, except when the shear modulus is less than 20 Pa. This study clearly indicates that the ability of a cell to bear compressive force depends on both microtubules and cytoplasm: The relatively stiff microtubules are combined with the compliant cytoplasm to sustain the compressive force.

The main findings for microtubule buckling on elastic cytoplasm are the following.

(1) The buckling wavelength does not depend on the axial force P but on the ratio of shear modulus of the elastic cytoplasm and bending rigidity of the microtubules.
(2) The compressive force is on the order of 100 pN for most cytoplasm with a shear modulus larger than 20 Pa.
(3) The ability to sustain compressive force is governed by both stiff microtubules and compliant cytoplasm.

5 Microtubule Buckling on Viscoelastic Cytoplasm

In this section, we study microtubule buckling supported by the viscoelastic cytoplasm. Cytoplasm exhibits both viscosity from fluid and elasticity from solid cytoskeleton networks, which has been shown in various experiments [29].

The surrounding cytoplasm that consists of fluid and cytoskeleton is modeled as an isotropic linearly viscoelastic material. The stress-strain relation is described in an integral form [30]

$$\boldsymbol{\sigma}(t) = 2\int_{-\infty}^{t}\mu(t-\tau)\frac{\partial\boldsymbol{\varepsilon}(\tau)}{\partial\tau}d\tau + \boldsymbol{\delta}\int_{-\infty}^{t}\lambda(t-\tau)\frac{\partial(\boldsymbol{\varepsilon}:\boldsymbol{\delta})}{\partial\tau}d\tau \tag{37}$$

where t is the time, $\mu(t)$ and $\lambda(t)$ are time-dependent relaxation moduli, and $\boldsymbol{\delta}$ is the second-order identity tensor. The equilibrium equation without body force and inertia term is $\nabla\cdot\boldsymbol{\sigma}=0$. The strain-displacement relation is linear, i.e., $\boldsymbol{\varepsilon}=(\nabla\mathbf{u}+\mathbf{u}\nabla)/2$. Within the three-dimensional viscoelastic cytoplasm, only the area $[|x_2| \leq R, x_3=0]$ that contacts with the buckled microtubule has prescribed traction $-T_3=\beta\cos(kx_1)$, where T_3 is given in Eq. (6). We also assume that the traction $-T_3$ is uniformly distributed over the diameter of microtubules, i.e., $N_{33}=-T_3/2R=\beta\cos(kx_1)/2R$ (Fig. 3). A boundary value problem for viscoelastic cytoplasm is then established.

This viscoelastic problem can be solved by the elastic-viscoelastic correspondence principle [30]. The stress-strain relationship is given by Laplace transform of Eq. (37),

$$\bar{\boldsymbol{\sigma}}(s) = 2s\bar{\mu}(s)\bar{\boldsymbol{\varepsilon}}(s) + s\bar{\lambda}(s)[\bar{\boldsymbol{\varepsilon}}(s):\boldsymbol{\delta}]\boldsymbol{\delta} \tag{38}$$

where a bar over a variable denotes its Laplace transformed form and s is the transform variable. The nonvanishing stress traction in Laplace transformed form is

$$\bar{N}_{33} = \frac{\bar{\beta}\cos(kx_1)}{2R}, \quad |x_2| \leq R, x_3 = 0 \tag{39}$$

Equations (38) and (39) are identical to that of linear elasticity if the transform of viscoelastic variables (e.g., $\bar{\boldsymbol{\sigma}}(s)$ and $\bar{\boldsymbol{\varepsilon}}(s)$) are associated with the corresponding elastic variables (e.g., $\boldsymbol{\sigma}$ and $\boldsymbol{\varepsilon}$) and the transformed moduli (e.g., $s\bar{\mu}(s)$ and $s\bar{\lambda}(s)$) are associated with elastic moduli μ_e and λ_e. Thus the solution of the Laplace transformed viscoelastic problem can be directly obtained from

the solution of the corresponding elastic problem by replacing μ_e and λ_e with $s\bar{\mu}(s)$ and $s\bar{\lambda}(s)$. The corresponding elastic problem for Eqs. (38) and (39) has been resolved in Sec. 4 using Kelvin's solution [27]. Then the displacement at point $\mathbf{x}=(x_1,x_2,0)$ due to a distributed load (Eq. (39)) in viscoelastic cytoplasm is obtained from the corresponding elastic solution given by Eq. (26),

$$\bar{u}_3(x_1,x_2,0,s) = \int_{-R}^{R}\int_{-\infty}^{\infty} \frac{\bar{\beta}\cos(kx_1^0)}{16\pi R s\bar{\mu}(s)} \frac{1}{\sqrt{(x_1-x_1^0)^2+(x_2-x_2^0)^2}} dx_1^0 dx_2^0$$

$$= \frac{\bar{\beta}\cos(kx_1)}{8\pi R s\bar{\mu}(s)}\{2R(1-\gamma)+2R\ln 2-(R+x_2)\ln[k(R+x_2)]-(R-x_2)\ln[k(R-x_2)]\} \quad (40)$$

The viscoelasticity of cytoplasm is specifically modeled as a Kelvin model [30], i.e., the viscoelastic system is modeled as a spring and a dashpot in parallel, and the shear relaxation modulus is

$$\mu(t) = \mu_e + \eta\delta(t) \quad (41)$$

where μ_e is the stiffness of the spring and η is the viscosity of the dashpot. The spring is used to model the elastic cytoskeleton such that μ_e is the shear modulus in Sec. 4. The dashpot models the viscous fluid and therefore η is the viscosity in Sec. 3. Here the viscoelasticity analysis involves both elasticity through shear modulus μ_e and viscosity η, and therefore exhibits profound effects on the microtubule buckling, as shown in the following.The Laplace transform of the shear relaxation modulus is

$$\bar{\mu}(s) = \frac{\mu_e}{s} + \eta \quad (42)$$

Substitute Eq. (42) into Eq. (40) and the inverse Laplace transform gives

$$\dot{u}_3(x_1,x_2,0) = -\frac{\mu_e}{\eta}u_3 + \frac{\beta\cos(kx_1)}{8\pi R\eta}\{2R(1-\gamma)+2R\ln 2-(R+x_2)\ln[k(R+x_2)]-(R-x_2)\ln[k(R-x_2)]\} \quad (43)$$

Similar to viscous analysis in Sec. 3, the viscoelastic cytoplasm is coupled with the buckled microtubule via the stress and velocity continuity condition across the interface. To be specific, the vertical velocity of the viscoelastic cytoplasm at the microtubule/cytoplasm interface (Eq. (43)) is continuous with the microtubule velocity derived from Eq. (4) on the average sense, i.e., the average velocity of the viscoelastic cytoplasm over the microtubule diameter $2R$,

$$\dot{u}_3^{\text{avg}}(x_1) = \frac{1}{2R}\int_{-R}^{R}\dot{u}_3(x_1,x_2,0)dx_2 = -\frac{\mu_e}{\eta}u_3 + \frac{\beta\cos(kx_1)}{8\pi\eta}[3-2\gamma-2\ln(kR)] \quad (44)$$

is the same as the microtubule velocity given by Eq. (4). Thus the continuity condition is

$$\frac{dA}{dt} = -\frac{\mu_e}{\eta}A + \frac{\beta}{8\pi\eta}[3-2\gamma-2\ln(kR)] \quad (45)$$

Here we only consider the initial growth of buckling from the small perturbation of A in Eq. (4) such that β is linearized (the same as Eq. (18)), and the linear ordinary differential equation for small perturbation A becomes

$$\frac{dA}{dt} = \left\{-\frac{\mu_e}{\eta} + \frac{E_{\text{MT}}I}{8\pi\eta}\left(\frac{P}{E_{\text{MT}}I}-k^2\right)[3-2\gamma-2\ln(kR)]k^2\right\}A \quad (46)$$

Compared with the differential equation of A in viscous analysis (Eq. (19)), μ_e/η comes into play in viscoelastic analysis. $\mu_e/\eta=0$ corresponds to viscous cytosol presented in Sec. 3, while

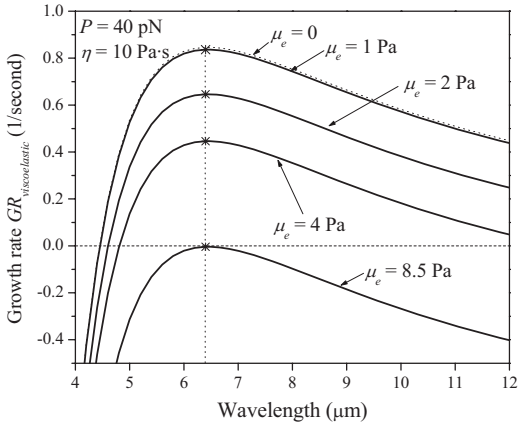

Fig. 6 The relationship of growth rate and wavelength for viscoelastic cytoplasm with different shear moduli

$\mu_e/\eta\to\infty$ denotes that the elasticity prevails in the viscoelastic cytoplasm. Let the initial amplitude be A_0, the evolution of the amplitude is

$$A = A_0\exp\left\langle\left\{-\frac{\mu_e}{\eta}+\frac{E_{\text{MT}}I}{8\pi\eta}\left(\frac{P}{E_{\text{MT}}I}-k^2\right)[3-2\gamma-2\ln(kR)]k^2\right\}t\right\rangle = A_0 e^{\text{GR}_{\text{viscoelastic}}t} \quad (47)$$

where

$$\text{GR}_{\text{viscoelastic}} = -\frac{\mu_e}{\eta}+\frac{E_{\text{MT}}I}{8\pi\eta}\left(\frac{P}{E_{\text{MT}}I}-k^2\right)[3-2\gamma-2\ln(kR)]k^2 \quad (48)$$

is the growth rate for viscoelastic cytoplasm.

The stability of the perturbed microtubules depends on the sign of the growth rate $\text{GR}_{\text{viscoelastic}}$. When $\text{GR}_{\text{viscoelastic}}>0$ for some wavelengths, the initial fluctuations associated with these wavelengths grow in an exponential law with growth rate $\text{GR}_{\text{viscoelastic}}$. While when $\text{GR}_{\text{viscoelastic}}<0$ for some wavelengths, the initial fluctuations characterized by these wavelengths decay and the microtubules are stable. The critical condition is $\text{GR}_{\text{viscoelastic}}=0$. The three stages of evolution of perturbed microtubules are shown in Fig. 6. The parameters used in Fig. 6 are bending rigidity $E_{\text{MT}}I=2\times10^{-23}$ N m^2 [10], $P=40$ pN, viscosity $\eta=10$ Pa s, and shear modulus $\mu_e=0-8.5$ Pa. Compared with Fig. 4 for viscous cytoplasm, the introduction of shear modulus has important effects.

With the increase in shear modulus μ_e from 0 (corresponding to viscous case) to finite value, the viscoelastic cytoplasm becomes more "elastic" and all of the curves shift downward but do not change shape, which leads to an increase in the critical wavelength. For example, the critical wavelength for $\mu_e=2$ Pa is 4.6 μm, while it is 4.9 μm for $\mu_e=4$ Pa. The fastest growth wavelength is determined by $\partial\text{GR}_{\text{viscoelastic}}/\partial k=0$,

$$\lambda = 2\pi\left[\frac{E_{\text{MT}}I}{P}\frac{5-4\gamma-4\ln(2\pi R/\lambda)}{3-2\gamma-2\ln(2\pi R/\lambda)}\right]^{1/2} \quad (49)$$

with an approximated expression as

$$\lambda_{\text{viscoelastic}}^{\text{fastest growth}} \approx 2\pi\sqrt{\frac{2E_{\text{MT}}I}{P}} \quad (50)$$

which is independent of shear modulus μ_e and the same as that for viscous analysis given by Eq. (24). Equation (50) suggests that once the dynamic growth occurs, the fastest growth wavelength is completely determined by the axial compressive force P and the bending rigidity $E_{\text{MT}}I$ of microtubules but does not depend on the properties of the cytoplasm (elasticity μ_e and viscosity η).

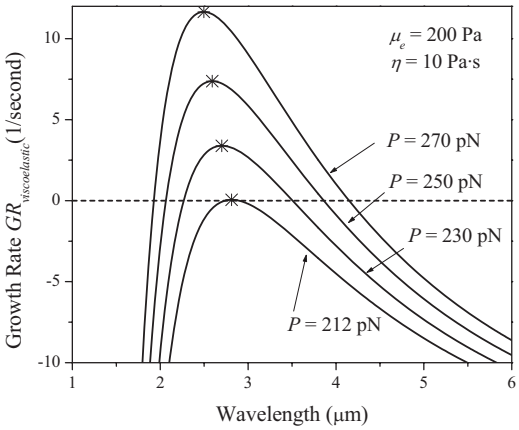

Fig. 7 The relationship of growth rate and wavelength for viscoelastic cytoplasm with different axial compressive forces

If shear modulus further increases, e.g., $\mu_e=8.5$ Pa in Fig. 6, the growth rate $GR_{viscoelastic}<0$ for all wavelengths. This suggests that the buckling is suppressed by the viscoelastic cytoplasm. The critical shear modulus μ_e^c is determined by setting $GR_{viscoelastic}=0$ and $\partial\mu_e^c/\partial k=0$, which gives

$$\mu_e^c = \frac{P^2}{32\pi E_{MT} I}\left[3-2\gamma-2\ln\left(\sqrt{\frac{P}{2EI}}R\right)\right] \tag{51}$$

For a given axial force P, cytoplasm with shear modulus larger than μ_e^c prevents the growth for all wavelengths. The elasticity of the cytoplasm allows the system the ability to block microtubule buckling, while the viscosity of the cytoplasm does not block microtubule buckling and only affects the growth rate. In Fig. 6, the growth rate $GR_{viscoelastic}$ is about 1/s, which suggests that if buckling process occurs, it occurs on the order of seconds.

Figure 7 shows the growth rate curve for different axial force P with shear modulus $\mu_e=200$ Pa and viscosity $\eta=10$ Pa s. The critical wavelength and fastest growth wavelength increase with the decrease in the axial force P. When $P=212$ pN, the growth rate is zero, which gives a critical axial compressive force $P^c_{viscoelastic}$. If the axial compressive force is less than $P^c_{viscoelastic}$, the initial perturbation will decay and the microtubule buckling does not occur. The critical force $P^c_{viscoelastic}$ is obtained by solving $GR_{viscoelastic}=0$ and $\partial P^c_{viscoelastic}/\partial k=0$,

$$P^c_{viscoelastic} = \frac{25}{16}\sqrt{E_{MT} I \mu_e}\left\{1+\frac{2048\pi}{625[3-2\gamma-2\ln(kR)]}\right\} \tag{52}$$

and the corresponding critical wavelength is

$$\lambda^c_{viscoelastic} = \frac{8\pi}{5}\left(\frac{E_{MT} I}{\mu_e}\right)^{1/4} \tag{53}$$

The critical force and wavelength are identical to that for the elastic cytoplasm, which indicates that the threshold for microtubule buckling is completely governed by cytoplasm elasticity. Therefore, the discussion of the compressive force that an individual microtubule can bear in the elastic analysis also holds here.

6 Discussion and Concluding Remarks

In this study, mechanics models for the analysis of microtubule buckling supported by cytoplasm have been reported. The microtubule is modeled as a linearly elastic cylindrical tube while the cytoplasm is characterized by viscous, elastic, or viscoelastic material. The microtubule is coupled with the cytoplasm through interface continuity conditions. The dynamic evolution equations, fastest growth rate, critical wavelength, and critical compressive force, as well as equilibrium buckling configurations are obtained.

To understand the process completely, one must not only consider the energy of deformed configuration but also the dynamics. The dynamic effect is due to the cytoplasm viscosity that affects the growth rate, while the energetic process is governed by the cytoplasm elasticity that determines the occurrence of buckling. Once the buckling occurs, the final equilibrium configuration is completely determined by the elasticity. These processes, namely, dynamic growth and elastic equilibrium, are similar for the bilayer structures that have been studied previously [31–37]. The ability of a cell to sustain compressive force is not solely determined by microtubules but also the elasticity of cytoplasm. With the support of the cytoplasm, an individual microtubule can sustain a compressive force on the order of 100 pN. The relatively stiff microtubules and compliant cytoplasm are combined to provide a scaffold for compressive force.

In addition to the mechanics explanation of microtubule buckling supported by cytoplasm, the findings in this study can be influential due to the concise analytical description of the critical force and wavelength. For example, since the bending rigidity of microtubules is well accepted on the range of 0.4×10^{-23}–4×10^{-23} N m^2, the expression for critical wavelength provides a means to measure the shear modulus of cytoplasm that is closely related to many diseases, such as cancer [38].

There exists some related works. For example, Liu et al. [39] studied the buckling of a microtubule bundle in tubulin solution. They observed a short-wavelength buckling pattern and obtained a power law for buckling wavelength $\lambda\propto R(E_{MT}/\mu_e)^{1/4}$, which is the same as the current analysis. Im and Huang [36] showed the similar relation between buckling wavelength and ratio of thin film and substrate for thin film buckling on an elastic-viscoelastic bilayer. A recent work by Das et al. [40] studied the mechanism of microtubule buckling in cells. Similar relations between buckling profiles and substrate modulus were obtained. The main difference is that the current analysis has a more quantitative mechanics analysis.

Acknowledgment

H.J. acknowledges the financial support from the Fulton School of Engineering at ASU. H.J. also acknowledges the partial support from NSF CMMI-0700440. The discussion with Professor Rui Huang in the University of Texas in Austin is also acknowledged.

References

[1] Alberts, B., Johnson, A., Lewis, J., Raff, M., Roberts, K., and Walter, P., 2003, *Molecular Biology of the Cell*, Garland Science, New York.
[2] Howard, J., and Hyman, A. A., 2003, "Dynamics and Mechanics of the Microtubule Plus End," Nature (London), **422**, pp. 753–758.
[3] Bao, G., and Suresh, S., 2003, "Cell and Molecular Mechanics of Biological Materials," Nat. Mater., **2**, pp. 715–725.
[4] Karsenti, E., Nedelec, F., and Surrey, T., 2006, "Modelling Microtubule Patterns," Nat. Cell Biol., **8**, pp. 1204–1211.
[5] Kolodney, M. S., and Wysolmerski, R. B., 1992, "Isometric Contraction by Fibroblasts and Endothelial-Cells in Tissue-Culture-A Quantitative Study," J. Cell Biol., **117**, pp. 73–82.
[6] WatermanStorer, C. M., and Salmon, E. D., 1997, "Actomyosin-Based Retrograde Flow of Microtubules in Migrating Epithelial Cells Influences Dynamic Instability and is Associated With Microtubule Breakage and Treadmilling," Mol. Biol. Cell, **8**, p. 17.
[7] Putnam, A. J., Cunningham, J. J., Dennis, R. G., Linderman, J. J., and Mooney, D. J., 1998, "Microtubule Assembly is Regulated by Externally Applied Strain in Cultured Smooth Muscle Cells," J. Cell. Sci., **111**, pp. 3379–3387.
[8] Wang, N., Naruse, K., Stamenovic, D., Fredberg, J. J., Mijailovich, S. M., Toric-Norrelykke, I. M., Polte, T., Mannix, R., and Ingber, D. E., 2001, "Mechanical Behavior in Living Cells Consistent With the Tensegrity Model," Proc. Natl. Acad. Sci. U.S.A., **98**, pp. 7765–7770.
[9] Stamenovic, D., Mijailovich, S. M., Tolic-Norrelykke, I. M., Chen, J. X., and Wang, N., 2002, "Cell Prestress. II. Contribution of Microtubules," Am. J. Physiol.: Cell Physiol., **282**, pp. C617–C624.
[10] Gittes, F., Mickey, B., Nettleton, J., and Howard, J., 1993, "Flexural Rigidity of Microtubules and Actin-Filaments Measured From Thermal Fluctuations in Shape," J. Cell Biol., **120**, pp. 923–934.
[11] Dogterom, M., and Yurke, B., 1997, "Measurement of the Force-Velocity Re-

lation for Growing Microtubules," Science, **278**, pp. 856–860.
[12] Gittes, F., Meyhofer, E., Baek, S., and Howard, J., 1996, "Directional Loading of the Kinesin Motor Molecule as it Buckles a Microtubule," Biophys. J., **70**, pp. 418–429.
[13] Brangwynne, C. P., MacKintosh, F. C., Kumar, S., Geisse, N. A., Talbot, J., Mahadevan, L., Parker, K. K., Ingber, D. E., and Weitz, D. A., 2006, "Microtubules can Bear Enhanced Compressive Loads in Living Cells Because of Lateral Reinforcement," J. Cell Biol., **173**, pp. 733–741.
[14] Timoshenko, S., and Gere, J., 1961, *Theory of Elastic Stability*, McGraw-Hill, New York.
[15] Huang, Z. Y., Hong, W., and Suo, Z., 2005, "Nonlinear Analyses of Wrinkles in a Film Bonded to a Compliant Substrate," J. Mech. Phys. Solids, **53**, pp. 2101–2118.
[16] Chen, X., and Hutchinson, J. W., 2004, "Herringbone Buckling Patterns of Compressed Thin Films on Compliant Substrates," ASME J. Appl. Mech., **71**, pp. 597–603.
[17] Berk, A., Zipursky, S. L., Matsudaira, P., David, B., and Darnell, J., 2001, *Molecular Cell Biology*, Scientific American Library, New York.
[18] Sugi, H., and Chaen, S., 2003, "Force-Velocity Relationships in Actin-Myosin Interactions Causing Cytoplasmic Streaming in Algal Cells," J. Exp. Biol., **206**, pp. 1971–1976.
[19] Chaen, S., Inoue, J., and Sugi, H., 1995, "The Force-Velocity Relationship of the Atp-Dependent Actin-Myosin Sliding Causing Cytoplasmic Streaming in Algal Cells, Studied Using a Centrifuge Microscope," J. Exp. Biol., **198**, pp. 1021–1027.
[20] Pickard, W. F., 2003, "The Role of Cytoplasmic Streaming in Symplastic Transport," Plant, Cell Environ., **26**, pp. 1–15.
[21] Pozrikidis, C., 1997, *Introduction to Theoretical and Computational Fluid Dynamics*, Oxford University Press, New York.
[22] Abramowitz, M., and Stegun, I. A., 1972, *Handbook of Mathematical Functions With Formulas, Graphs, and Mathematical Tables*, Dover, New York.
[23] Fushimi, K., and Verkman, A. S., 1991, "Low Viscosity in the Aqueous Domain of Cell Cytoplasm Measured by Picosecond Polarization Microfluorimetry," J. Cell Biol., **112**, pp. 719–725.
[24] Swaminathan, R., Hoang, C. P., and Verkman, A. S., 1997, "Photobleaching Recovery and Anisotropy Decay of Green Fluorescent Protein GFP-S65T in Solution and Cells: Cytoplasmic Viscosity Probed by Green Fluorescent Protein Translational and Rotational Diffusion," Biophys. J., **72**, pp. 1900–1907.
[25] Bicknese, S., Periasamy, N., Shohet, S. B., and Verkman, A. S., 1993, "Cytoplasmic Viscosity Near the Cell Plasma-Membrane-Measurement by Evanescent Field Frequency-Domain Microfluorimetry," Biophys. J., **65**, pp. 1272–1282.
[26] Mofrad, M. R. K., and Kamm, R. D., 2006, *Cytoskeletal Mechanics: Models and Measurements*, Cambridge University Press, Cambridge.
[27] Kachanov, M., Shafiro, B., and Tsukrov, I., 2003, *Handbook of Elasticity Solutions*, Kluwer Academic, Boston.
[28] Canetta, E., Duperray, A., Leyrat, A., and Verdier, C., 2005, "Measuring Cell Viscoelastic Properties Using a Force-spectrometer: Influence of Protein-Cytoplasm Interactions," Biorheology, **42**, pp. 321–333.
[29] Kasza, K. E., Rowat, A. C., Liu, J. Y., Angelini, T. E., Brangwynne, C. P., Koenderink, G. H., and Weitz, D. A., 2007, "The Cell as a Material," Curr. Opin. Cell Biol., **19**, pp. 101–107.
[30] Christensen, R. M., 1971, *Theory of Viscoelasticity: An Introduction*, Academic, New York.
[31] Huang, R., 2005, "Kinetic Wrinkling of an Elastic Film on a Viscoelastic Substrate," J. Mech. Phys. Solids, **53**, pp. 63–89.
[32] Huang, R., and Im, S. H., 2006, "Dynamics of Wrinkle Growth and Coarsening in Stressed Thin Films," Phys. Rev. E, **74**, p. 026214.
[33] Huang, R., and Suo, Z., 2002, "Wrinkling of a Compressed Elastic Film on a Viscous Layer," J. Appl. Phys., **91**, pp. 1135–1142.
[34] Huang, R., and Suo, Z., 2002, "Instability of a Compressed Elastic Film on a Viscous Layer," Int. J. Solids Struct., **39**, pp. 1791–1802.
[35] Huang, Z. Y., Hong, W., and Suo, Z., 2004, "Evolution of Wrinkles in Hard Films on Soft Substrates," Phys. Rev. E, **70**, p. 030601.
[36] Im, S. H., and Huang, R., 2005, "Evolution of Wrinkles in Elastic-viscoelastic Bilayer Thin Films," ASME J. Appl. Mech., **72**, pp. 955–961.
[37] Jiang, H., Khang, D.-Y., Song, J., Sun, Y., Huang, Y., and Rogesr, J. A., 2007, "Finite Deformation Mechanics in Buckled Thin Films on Compliant Supports," Proc. Natl. Acad. Sci. U.S.A., **104**, pp. 15607–15612.
[38] Suresh, S., 2007, "Biomechanics and Biophysics of Cancer Cells," Acta Mater., **55**, pp. 3989–4014.
[39] Liu, Y. F., Guo, Y. X., Valles, J. M., and Tang, J. X., 2006, "Microtubule Bundling and Nested Buckling Drive Stripe Formation in Polymerizing Tubulin Solutions," Proc. Natl. Acad. Sci. U.S.A., **103**, pp. 10654–10659.
[40] Das, M., Levine, A. J., and MacKinstosh, F. C., 2008, "Buckling and Force Propagation Along Intracellular Microtubules," e-print arXiv:0709.2344.

Influence of Road Camber on Motorcycle Stability

Simos Evangelou
Department of Electrical and Electronic Engineering,
and Department of Mechanical Engineering,
Imperial College London,
London SW7 2AZ, UK
e-mail: s.evangelou@imperial.ac.uk

David J. N. Limebeer[1]
e-mail: d.limebeer@imperial.ac.uk

Maria Tomas Rodriguez
e-mail: maria.tomas@imperial.ac.uk

Department of Electrical and Electronic Engineering,
Imperial College London,
London SW7 2AZ, U.K

This paper studies the influence of road camber on the stability of single-track road vehicles. Road camber changes the magnitude and direction of the tire force and moment vectors relative to the wheels, as well as the combined-force limit one might obtain from the road tires. Camber-induced changes in the tire force and moment systems have knock-on consequences for the vehicle's stability. The study makes use of computer simulations that exploit a high-fidelity motorcycle model whose parameter set is based on a Suzuki GSX-R1000 sports machine. In order to study camber-induced stability trends for a range of machine speeds and roll angles, we study the machine dynamics as the vehicle travels over the surface of a right circular cone. Conical road surfaces allow the machine to operate at a constant steady-state speed, a constant roll angle, and a constant road camber angle. The local road-tire contact behavior is analyzed by approximating the cone surface by moving tangent planes located under the road wheels. There is novelty in the way in which adaptive controllers are used to center the vehicle's trajectory on a cone, which has its apex at the origin of the inertial reference frame. The results show that at low speed both the weave- and wobble-mode stabilities are at a maximum when the machine is perpendicular to the road surface. This trend is reversed at high speed, since the weave- and wobble-mode dampings are minimized by running conditions in which the wheels are orthogonal to the road. As a result, positive camber, which is often introduced by road builders to aid drainage and enhance the friction limit of four-wheeled vehicle tires, might be detrimental to the stability of two-wheeled machines.
[DOI: 10.1115/1.2937140]

1 Introduction

The role of road camber on the stability of motorcycles is an issue that arises in the context of loss-of-control accident investigations when high-speed cornering is involved. Superelevated roads are commonplace, and their banking is designed primarily to assist drainage and to improve the tire adhesion limit of four-wheeled vehicles. In the context of training, advanced police motorcycle riders are taught about the influence of road camber on tire adhesion using simple static-equilibrium-based ideas [1]. They are taught that superevaluated cross fall has a favorable influence on the vehicle's behavior, because it makes the road wheels more nearly vertical relative to the road. The teaching in Ref. [1] does not extend to the role of camber on machine stability, because this is a considerably more complex issue.

Our aim is to investigate the influence of road camber on the primary oscillatory modes of motorcycles. Insight is obtained from a high-fidelity computer model that has been developed for this purpose. In "flat-road" models the tires' normal load is parallel with the earth's gravitational field, while the tires' lateral and longitudinal forces are orthogonal to it. Similarly, the tires' aligning moment is in the direction of gravity, while the overturning and rolling resistance moments lie in a horizontal ground plane. In the case of cambered roads, the tires' normal load is no longer parallel to gravity, and the roadway is no longer horizontal or flat. The model presented here studies the consequences of these changes in detail.

The earliest dynamic models for two-wheeled vehicles go back over a century and were developed in the context of the bicycle. In the same way, early research on motorcycle dynamics was confined to small perturbations from straight running and relatively simple vehicle models. References [2,3] provide a comprehensive review of much of this early literature. Simple models with rigid-body type frame representations, and constraint-based tire representations predict a single oscillatory mode known as "weave." Following the introduction of frame flexibility, and/or force generating tire models, a second oscillatory mode is predicted, which is known as "wobble." In the case that one or more of these modes is stable, but lightly damped, the potential exists for undesirable vehicle behavior. In later work, these models were extended to include small perturbations from a steady-state cornering condition [4–9]. It is clear from these studies that under certain operating conditions some of the machine's modes can be lightly damped, or even unstable. This theoretical work has been supplemented by extensive measurement programs [10–24].

The weave mode combines rolling, yawing, and steering in a fish-tailing motion and is well damped at moderate speeds, but becomes less so as the machine's forward speed increases. The natural frequency of this mode rises from zero at very low speed to somewhere in the range of 2–4 Hz, depending on the mass and size of the machine; the lower frequencies correspond to heavier motorcycles. The wobble mode involves primarily a caster shimmy type steering oscillation, and has an oscillatory frequency that is essentially independent of speed and is normally in the 6–9 Hz range, the precise frequency being governed primarily by the mechanical trail, the front tire cornering stiffness, and the front frame steer inertia [25]. Computer simulation studies indicate that the torsional stiffness of the motorcycle frame at the steering head determines whether a machine will be prone to wobbling at medium speeds (a compliant frame) or at high speeds (a stiff frame) [26,27]. In cornering, the lateral (out-of-plane) modes and the in-plane modes associated with tire deflections and suspension motions become coupled, as was first shown in any detail by Koenen [4]. The motorcycle becomes prone to resonant forcing, which is induced by regular road undulations, when the displacement forcing they produce is tuned to the lightly damped modes of the machine. Moderate roll angles and high speeds are likely to represent the worst case conditions [28].

This paper is organized as follows. Section 2 describes the

[1]Corresponding author.

Contributed by the Applied Mechanics Division of ASME for publication in the JOURNAL OF APPLIED MECHANICS. Manuscript received July 18, 2007; final manuscript received January 7, 2008; published online August 21, 2008. Review conducted by N. Sri Namachchivaya.

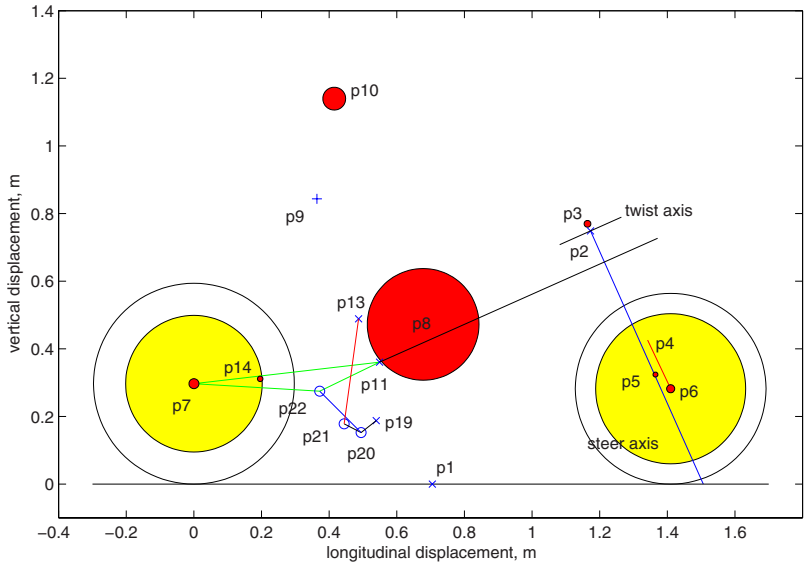

Fig. 1 Scaled diagrammatic side-view of the motorcycle model in its nominal configuration. The seven constituent bodies are shown as (dark) circles, with their radii proportional to their mass. All the points critical to building the model are individually marked. For example, the largest mass is the rear frame with its mass center located at p8.

background to the motorcycle model that will be used in this study. Some of the important characteristics of the standard prior-art motorcycle-rider system are described in Sec. 2.1. The modeling of cambered roads is described in Sec. 2.2, where the computation of road normals and tangent planes is described. The standard motorcycle model control systems are extended in Sec. 2.3, where a new adaptive roll-angle control system is introduced. A single-wheel model that is used to study roll-angle equilibria and tire adhesion limits is introduced in Sec. 2.4 and analyzed in Sec. 2.5. This model is based on a "thick tire" and is used to study force and moment balances as well as certain aspects of the road-tire contact geometry. The machine's static stability limits are studied in Sec. 2.6. The influence of road camber on a high-fidelity motorcycle model is analyzed in Sec. 3 with the conclusions drawn in Sec. 4.

2 Motorcycle Model

2.1 Prior Model. The motorcycle model used in this study is representative of modern road-going sports machines, and has a parameter set that is based on the Suzuki GSX-R1000. The machine geometry is shown in Fig. 1, in which the motorcycle's seven constituent masses are represented by (dark) circles that have a diameter that is proportional to the mass of the associated body. All the critical points (mass centers, linkage pivot points, and so on) are individually marked. The main frame is allowed unrestricted translational and rotational motions. The swinging arm, the monoshock linkage system, the rider, and front frame are all pinned to it. The (rear) monoshock suspension is restrained by a parallel spring and damper, while the front suspension is based on a standard telescopic fork that allows linear in-line displacements. The main frame is modeled as a single rigid body save for a torsional frame flexibility degree of freedom at the steering head—this freedom accommodates small angular displacements that are perpendicular to the steering axis. Aerodynamic influences are modeled using drag and lift forces, which are proportional to the square of the speed. The road tires are treated as "wide," flexible in compression, and care is taken to track dynamically the migration of both ground-contact points as the machine rolls, pitches, and steers. Both contact points, which are taken as the points closest to the road surface, will move laterally and circumferentially over the tires' surface; these points represent the center of the road-tire contact patch. The tire forces and moments are generated from the normal load, the tires' camber angle relative to the road, and the combined slip using "magic formalas" [29–32]. The lateral compliance of the tires' carcass is modeled using standard linear time-varying relaxation length type tire models [31]. Relaxation effects have a lagging influence on the generation of the lateral forces and aligning moments.

The machine's trim state is controlled using feedback loops, which control the steering torque and the drive to the rear wheel. The drive moment is controlled using a proportional-integral controller that acts on a speed error; this allows the vehicle to follow an arbitrary speed reference. The steering controller is proportional integral derivative in its general structure, and acts on a roll-angle error. The steering controller allows the vehicle to maintain a fixed roll angle, or follow a low-bandwidth roll-angle reference signal. A motorcycle model incorporating all of the above features has its origins in Ref. [5], and is extended in Refs. [8,9]. The model is written in LISP and makes use of the multibody modeling code AUTOSIM [33] and can be obtained from the website.[2] The Autosim model can be configured to solve the nonlinear equations of motion, or it can be used to generate a symbolic state-space representation that describes small perturbation around a prescribed trim condition. For the purposes of this study, both the tire and controller modeling had to be extended. These extensions are described next.

2.2 Cambered Road Modeling. Suppose that the road over which the vehicle will travel is described in Cartesian coordinates by the differentiable road-surface function

$$S(x,y,z) = 0 \tag{1}$$

A general point P on the road surface S is denoted $S(P)$, and is described by the vector

[2]http://www.imperial.ac.uk/controlandpower/motorcycles/

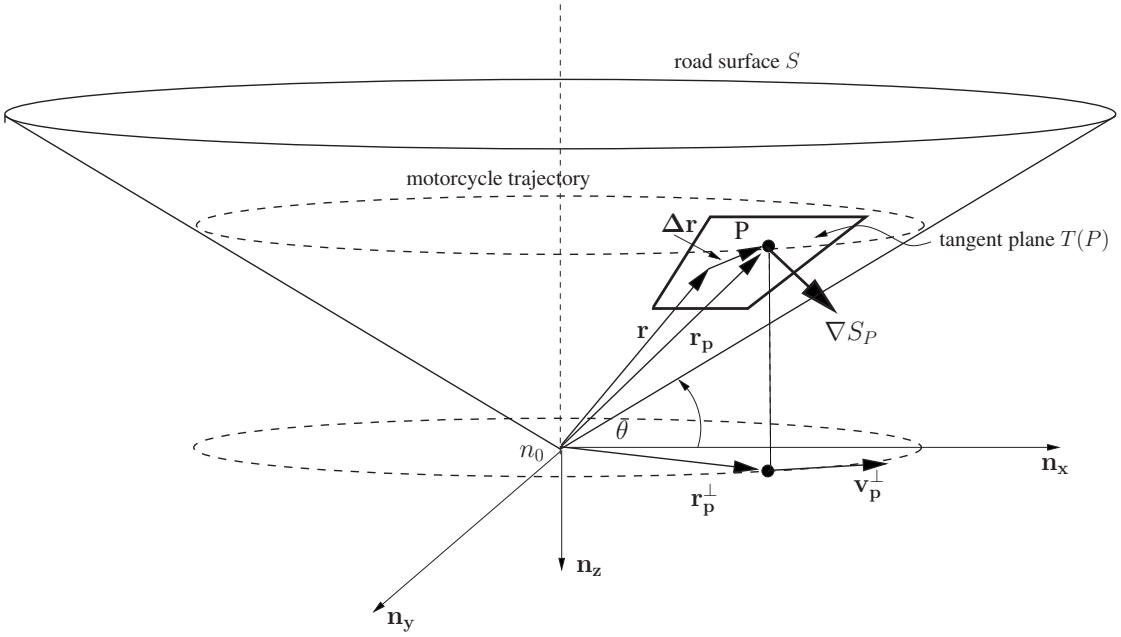

Fig. 2 The road surface used for cambered road stability studies is a right circular cone (as illustrated, the cone is inverted for positive camber angles in the range 90 deg$>\theta\geqslant$0). The central axis of the cone is aligned with the inertial axis $\mathbf{n}_z$, with its vertex at the origin n_0 of the inertial reference system. For camber angles in the range 90 deg$>\theta\geqslant$0, the motorcycle is assumed to ride on the interior surface of the cone along a circular trajectory. Only positive yaw rate operating conditions are considered (clockwise when seen from above), which means that for positive roll angles the machine leans toward the central axis of the cone. The nominal rear-wheel ground-contact point is *P*. The actual rear-wheel ground-contact point is assumed to move over the tangent plane *T*(*P*); the normal to the plane *T*(*P*) is the vector ∇S_P. A second tangent plane is used to describe locally the road surface under the front wheel. The vector $\mathbf{r}_p^\perp$ is the projection of $\mathbf{r}_p$ onto the ground plane, while $\mathbf{v}_p^\perp$ is the velocity of *P* projected onto the ground plane.

$$\mathbf{r}_P = x_P\mathbf{n}_x + y_P\mathbf{n}_y + z_p\mathbf{n}_z \tag{2}$$

in which $\mathbf{n}_x$, $\mathbf{n}_y$, and $\mathbf{n}_z$ are the standard basis vectors in a SAE coordinate system. A normal to the surface at $S(P)$ is given by ([34], p. 285)

$$\nabla S_P = \left.\frac{\partial S}{\partial x}\right|_P \mathbf{n}_x + \left.\frac{\partial S}{\partial y}\right|_P \mathbf{n}_y + \left.\frac{\partial S}{\partial z}\right|_P \mathbf{n}_z \tag{3}$$

A tangent plane $T(P)$, which contains the point $S(P)$, is described by

$$\langle(\mathbf{r}-\mathbf{r}_P), \nabla S_P\rangle = 0 \tag{4}$$

for any vector $\mathbf{r}-\mathbf{r}_P$ in $T(P)$. This follows from the fact that $\mathbf{r}-\mathbf{r}_P$ must be perpendicular to any normal to the plane.

In the context of the present study, we are particularly interested in conical road surfaces, because they allow motorcycles to operate at trim conditions that are characterized by a prescribed constant speed, a constant roll angle, and a constant road camber angle. Figure 2 illustrates such a conical road surface and is described by

$$S(x,y,z) = \sqrt{x^2+y^2}\tan\theta + z = 0 \tag{5}$$

A unit-length normal at $S(P)$ is given by

$$\nabla S_P = \left.\frac{x\sin\theta}{\sqrt{x^2+y^2}}\right|_P \mathbf{n}_x + \left.\frac{y\sin\theta}{\sqrt{x^2+y^2}}\right|_P \mathbf{n}_y + \cos\theta\mathbf{n}_z \tag{6}$$

If $\mathbf{r}$ defines a general point in $T(P)$, the vector $\Delta\mathbf{r}=\mathbf{r}-\mathbf{r}_P$ is orthogonal to ∇S_P if it lies in $T(P)$. Thus, the tangent plane $T(P)$ in Fig. 2 is defined by

$$(x-x_P)\frac{x_P\sin\theta}{\sqrt{x_P^2+y_P^2}} + (y-y_P)\frac{y_P\sin\theta}{\sqrt{x_P^2+y_P^2}} + (z-z_P)\cos\theta = 0 \tag{7}$$

for a general point $(x,y,z)\in T(P)$.

With these ideas in mind, the motorcycle model described in Sec. 2.1 was modified to accommodate conical road surfaces. The essential idea is to represent the road surface locally using tangent planes that move under each of the road wheels. These planes are characterized by normals computed at the *nominal* (associated with the nominal configuration) ground-contact points. These points are treated as fixed in the main frame's body-fixed coordinate system. Contact point excursions are then represented as motions over the two tangent planes, which are fully characterized by normal vectors of the type given in Eq. (6). In the case of flat-road models, these normal vectors are given by the static vector $\mathbf{n}_z$. For the purposes of tire force and moment calculations, it is necessary to compute normal loads and aligning moments in the direction of Eq. (6). The tire camber angles are calculated relative to the planes (7), rather than the horizontal ground plane. The lateral and longitudinal tire forces, as well as the overturning moment act in the plane described by Eq. (7) rather than the ground plane. These changes are straightforward to implement by reworking the tire kinematics calculations described previously in Ref. [9], for example.

These ideas are further illustrated in Fig. 3, which show part of a motorcycle road tire moving over an inclined road surface with camber angle θ. As before, the motorcycle's roll angle (ϕ) is defined relative to the inertial $\mathbf{n}_z$-axis. Under these conditions, the tire camber angle is approximately $\phi-\theta$, and it is this angle that informs the magic formulas of the tires' camber angle status, and it is this angle that generates the tires' camber force. The normal load is perpendicular to the road, and the lateral force lies in the road surface.

2.3 Adaptive Steering Controller. Another challenge facing

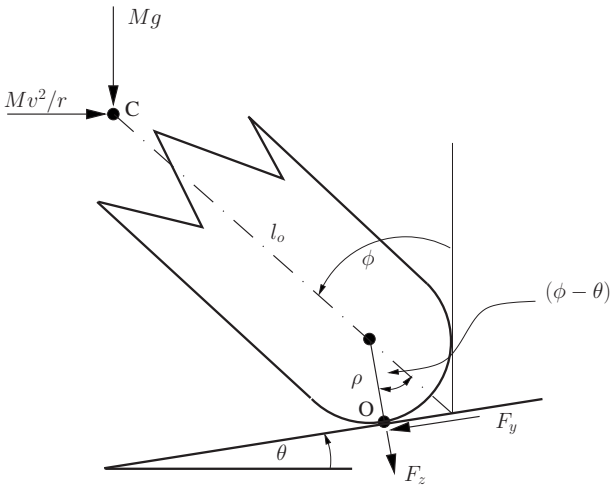

Fig. 3 Contact between an inclined road surface and a motorcycle tire in a single-wheel model. The total mass of the machine and rider is *M*, the total weight is therefore *Mg*, and the centripetal force is Mv^2/r. The tire crown radius is ρ, and the distance between the motorcycle's mass center *C* and the center of the tire crown is l_o. The road camber angle is θ, while the motorcycle roll angle is ϕ; the motorcycle comes out of the page for positive yaw rates ($\dot{\psi}>0$). The tire's normal load and side force are given by F_z and F_y, respectively, and are applied at the contact point *O*. The force F_z is normal to the road surface, while F_y is tangent to it.

the motorcycle modeler, in the context of cambered road studies, is the correct positioning of the machine relative to the cone. When seeking to achieve a fixed-speed, fixed-roll-angle, and fixed-camber-angle trim condition, the first objective is to achieve the desired speed and roll-angle conditions. This can be done using known methods, but the center of the circular trajectory will be at an arbitrary location in the ground plane. The new aspect to the vehicle control problem is to move the fixed-speed fixed-roll-angle trajectory toward the $\mathbf{n}_z$ axis so that it eventually rotates around it. This problem was solved using the adaptive-reference roll-angle feedback controller illustrated in Fig. 4. This scheme is informed by the fact that for a steady-state circular trajectory, the radial position vector and the corresponding velocity vector are orthogonal to each other. Intuitively, if an origin-centered trim trajectory is to be achieved, one should steer toward the origin if the angle between the position vector and the velocity vector is greater than 90 deg, and away from it if the angle is less than

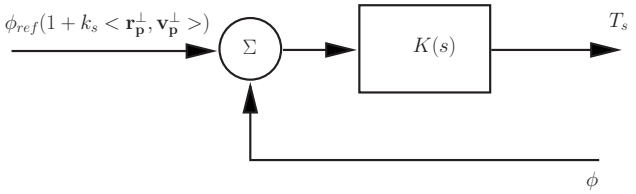

Fig. 4 Roll-angle feedback loop used in the simulation model. The steering torque T_s is generated from the difference between the roll angle ϕ and the adaptive roll angle reference $\phi_{ref}(1+k_s\langle \mathbf{r}_p^{\perp},\mathbf{v}_p^{\perp}\rangle)$; $\mathbf{r}_p^{\perp}$ and $\mathbf{v}_p^{\perp}$ are defined in Fig. 2. If the motorcycle is moving toward the inertial axis $\mathbf{n}_z$, the adaptive gain term $k_s\langle \mathbf{r}_p^{\perp},\mathbf{v}_p^{\perp}\rangle$ adjusts the roll-angle reference so as to steer the machine away from it. Conversely, if the motorcycle is moving away from $\mathbf{n}_z$, the adaptive gain term $k_s\langle \mathbf{r}_p^{\perp},\mathbf{v}_p^{\perp}\rangle$ steers the machine toward it. The adaptive roll-angle term thus has the effect of centering the machine trajectory on $\mathbf{n}_z$ and becomes noncontributory once the machine's trajectory has been centered; in this event, $\langle \mathbf{r}_p^{\perp},\mathbf{v}_p^{\perp}\rangle=0$.

90 deg. If these vectors remain orthogonal, no position-related steering is required. These ideas are implemented in the adaptive control system illustrated in Fig. 4, which "adapts" the roll-angle reference to the correction term $k_s\langle \mathbf{r}_p^{\perp},\mathbf{v}_p^{\perp}\rangle$. The gain k_s is constant, and $\langle\cdot,\cdot\rangle$ represents the inner product between the machine's position and velocity vectors projected onto the ground plane. Clearly, as the angle between $\mathbf{r}_p^{\perp}$ and $\mathbf{v}_p^{\perp}$ passes through 90 deg, the sign of the inner product term changes. The stability of the system is obviously crucial, but a formal stability analysis appears prohibitively difficult to carry out. It turned out that this loop is easy to tune by trial and very effective in terms of its operation. Figure 5(*a*) shows the machine being moved by the adaptive reference scheme from an arbitrary ground-plane position to an origin-centered orbital trajectory. Figure 5(*b*) shows the machine operating under full feedback control as it slowly accelerates up the conical road surface. The roll angle is maintained at a constant reference value of $\phi=0$ deg, while its speed is increased at a constant acceleration of 0.005 $\mathrm{m/s^2}$.

2.4 Single-Wheel Model. Cambered road surfaces in combination with profiled tires make the prediction of viable operating conditions a nontrivial exercise. In order to establish if a particular operating condition represents a potentially stable equilibrium, we will study the conditions required for a roll-angle equilibrium as well as the possible violation of the road-tire adhesion limits. To do this, we will make use of the simple single-wheel model illustrated in Fig. 3, in which both road camber and tire profiling are taken into account. This single-wheel model is reminiscent of the inverted-pendulum type model described in Ref. [35], but with the steering locked in the straight-running position. In the context of this model, the important parameters are the tire profile and friction limit, the location of the machine's mass center, the road camber angle, and the machine's roll angle and speed. The distance $l_o+\rho$ is the height of the machine's mass center above a level road surface when it is in its nominal configuration. The parameter ρ is the single-wheel tire crown radius and must be chosen to represent both wheels. It should be emphasized that this simple model can only be used for a restricted range of purposes, and when such things as the wheel's gyroscopic moments are justifiably neglected. Care has been taken to cross check the utility of this model with the high-fidelity model described in Sec. 2.1. In order to compare the single-wheel abstraction with the high-fidelity model, representative values for l_o and ρ are required. For present purposes, we have set ρ equal to the average value of the front and rear tire crown radii: $\rho=(0.095+0.06)/2=0.0775$ m. One can then find a value for l_o from the height of the machine's mass center. In its nominal configuration, the height of the mass center of the whole machine above the ground is $l=0.5091$ m, which gives $l_o=l-\rho=0.4316$ m. Necessary conditions for a stable steady-state roll equilibrium are studied next.

2.5 Equilibrium Modeling. Valuable insight into the influence of road camber on the steady-state tire force and moment system can be obtained from simple static-equilibrium based calculations. These calculations also provide insight into the machine's stable domain of operation, which is limited by its static roll stability and the tire friction limit. The machine has a stable trim state for only a limited range of negative roll-angle conditions; we will show that the precise conditions depend on the tire's crown radius and the tire friction limit. We begin by referring again to the single-wheel model illustrated in Fig. 3 and then resolve forces in the F_y and F_z directions, respectively. This gives

$$F_y = M\frac{v^2}{r}\cos\theta - Mg\sin\theta \tag{8}$$

and

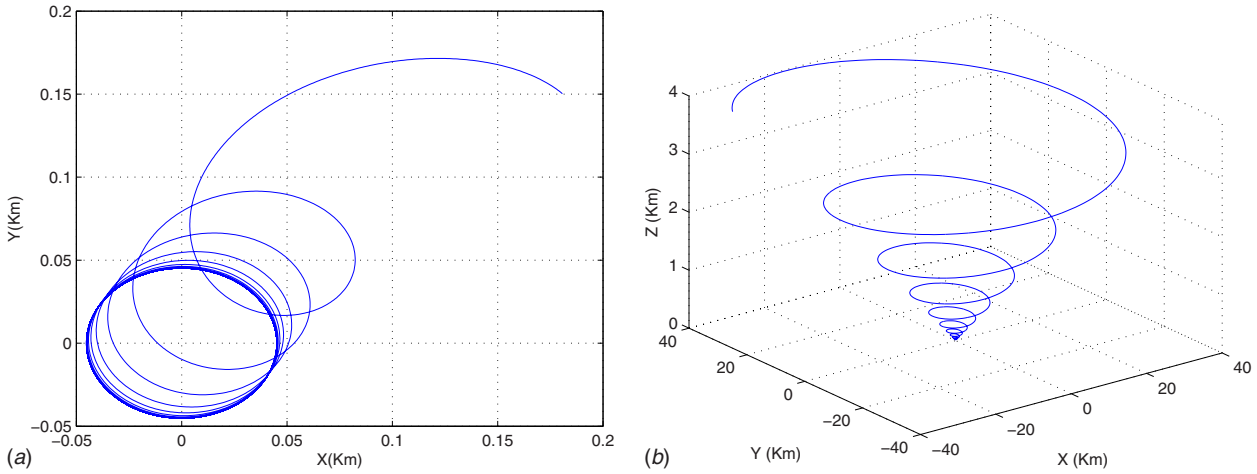

Fig. 5 Adaptive roll-reference controller centering the motorcycle trajectory on n_z. (*a*) The machine trajectory begins at the initial point (180, 150) in the ground plane, which is outside the origin-centered equilibrium circle for the motorcycle cornering at 10 m/s with a roll angle of 15 deg; under these conditions, the equilibrium radius of curvature is 45 m. In this simulation, the adaptive roll-angle reference gain is $k_s=5.0\times10^{-4}$ (see Fig. 4). (*b*) Motorcycle running on the surface of a cone with camber angle $\theta=5$ deg. In this simulation, the machine accelerates from 5 m/s to 75 m/s at 0.005 m/s^2, with the motorcycle roll angle maintained at $\phi=0$ deg; this trajectory begins at (0,0) in the ground plane.

$$F_z = -M\frac{v^2}{r}\sin\theta - Mg\cos\theta \tag{9}$$

Taking moments around the ground-contact point O gives

$$\frac{Mv^2}{r}(l_o\cos\phi + \rho\cos\theta) = Mg(l_o\sin\phi + \rho\sin\theta) \tag{10}$$

from which it follows that machine trajectory has radius of curvature

$$r = \frac{v^2(l_o\cos\phi + \rho\cos\theta)}{g(l_o\sin\phi + \rho\sin\theta)} \tag{11}$$

under trim conditions. Eliminating Mv^2/r from Eqs. (8) and (9) using Eq. (11) gives

$$F_y = \frac{Mgl_o\sin(\phi-\theta)}{l_o\cos\phi + \rho\cos\theta} \tag{12}$$

which simplifies to

$$F_y^{\text{thin}} = \frac{Mg\sin(\phi-\theta)}{\cos\phi}$$

in the case of a "thin" tire ($\rho=0$). In the same way,

$$F_z = -\frac{Mg(l_o\cos(\phi-\theta)+\rho)}{l_o\cos\phi + \rho\cos\theta} \tag{13}$$

or

$$F_z^{\text{thin}} = -\frac{Mg\cos(\phi-\theta)}{\cos\phi}$$

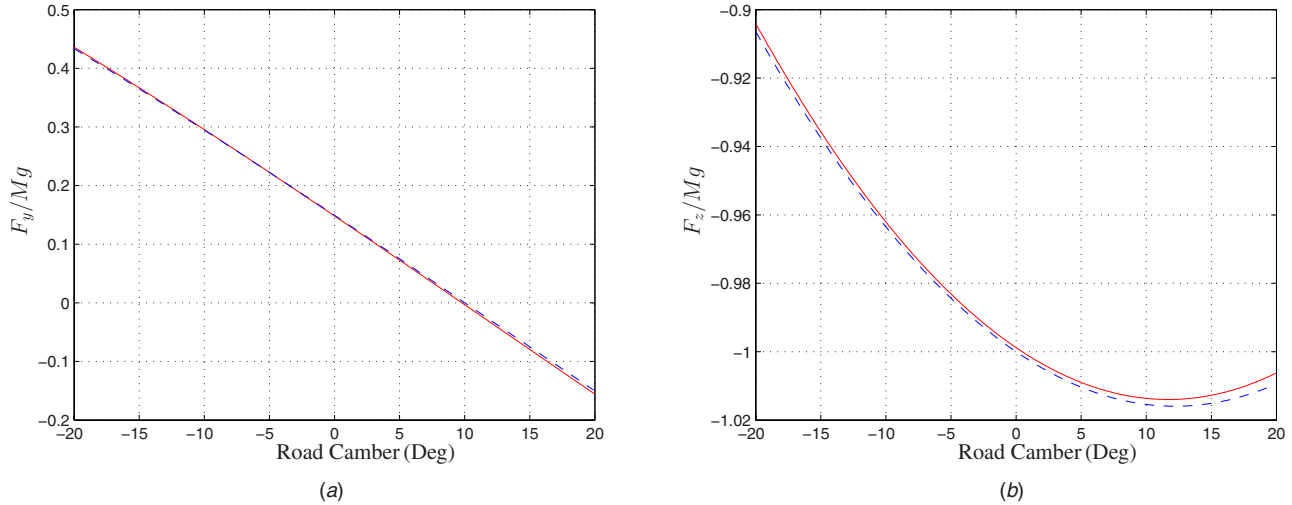

Fig. 6 Approximate and exact side force and normal loads as functions of camber angle; the machine roll angle is $\phi=10$ deg. (*a*) Normalized side force; the dashed curve comes from Eq. (12), while the solid curve is computed using the high-fidelity model at a forward speed of 10 m/s. (*b*) Normalized normal load; the dashed curve comes from Eq. (13), while the solid curve is computed using the high-fidelity model.

in the case of a thin tire.

Figure 6(*a*) shows the approximate normalized tire side-force calculated using Eq. (12) in comparison to the total normalized tire side force computed using the high-fidelity model described in Sec. 2.1. The agreement is very good, and as would be expected, F_y vanishes when the motorcycle tire is perpendicular to the road. A similar comparison appears in Fig. 6(*b*), where the approximate and exact normal loads are compared as a function of camber angle. Again, as is expected, the normal load on the tires is at a maximum when the camber angle is approximately $\theta=10$ deg, with the exact figure coming from the solution to Eq. (13). Given the accuracy of Eqs. (12) and (13) relative to the high-fidelity model, one would expect a similar level of veracity from Eq. (11). This is indeed the case as has been confirmed by computation; confirmatory plots have not been included in order to save space.

2.6 Tire Adhesion Limits. For a stable static equilibrium, one requires

$$\mu_{\text{limit}} > |F_y/F_z| = |l_o \sin(\phi-\theta)/(l_o \cos(\phi-\theta)+\rho)|$$

or what is equivalent

$$|\phi-\theta| < \arctan(\mu_{\text{limit}}) + \arcsin\left(\frac{\mu_{\text{limit}}\rho}{l_o\sqrt{1+\mu_{\text{limit}}^2}}\right) \tag{14}$$

which simplifies to

$$|\phi-\theta| < \arctan(\mu_{\text{limit}})$$

in the case of the thin tire. In condition (14), μ_{limit} is the friction limit, which faces its most demanding challenge when $\phi-\theta$ is at a maximum. In the case that $\mu_{\text{limit}}=1.6$, $l_o=0.4316$ m, and $\rho=0.0775$ m, the friction limit requires $|\phi-\theta|<58$ deg $+8.8$ deg $=66.8$ deg; the tire profiling increases the admissible tire-road camber angle by 8.8 deg over that achievable with an equivalent thin tire.

If a stable equilibrium is to exist (in roll), the following condition

$$l_o \sin\phi + \rho \sin\theta \geq 0 \tag{15}$$

must hold, which places another restriction on the admissible values of the machine roll and road camber angles. Condition (15) also shows that stable cornering can be achieved, even if the machine is running with zero roll angle, providing the tire generates an overturning moment. As is clear from Fig. 3, a thick tire will generate an overturning moment by virtue of its geometry. There are two roll-related stability limits illustrated in Fig. 7 that will now be analyzed. These limits correspond to the cases in which the denominator and numerator of Eq. (11) vanish. The required positivity of the moment arms in Eq. (10) and the path radius of curvature enforce Eq. (15) as a necessary condition for a stable static roll equilibrium. In the case that the left hand side of Eq. (15) vanishes, the machine will operate in the condition illustrated in Fig. 7(*a*), which corresponds to straight running on a static roll stability boundary. In the case of a thin tire, which produces no overturning moment, stable equilibria can only be supported by non-negative roll angles. Since the moment arms in Eq. (11) represent non-negative distances, the following must hold;

$$l_o \cos\phi + \rho \cos\theta > 0 \tag{16}$$

In the limiting case that $v^2/r\to\infty$, the quantity on the left hand side of Eq. (16) tends to zero; see Eq. (11). This leads to a second roll-related stability limit that can only be approached asymptotically; a physical interpretation of this operating condition is illustrated in Fig. 7(*b*). The friction limits and the two roll-related stability limits are combined in Fig. 8 to define the machine's stable operating region.

The extreme "wall of death" situation is considered briefly. When $\theta=90$ deg, Eq. (8) yields $F_y=Mg$ so that

$$F_z\mu_{\text{limit}} > Mg \tag{17}$$

is required in order to keep the machine stable. Under these conditions $F_z=Mv^2/r$, so that

$$v > \sqrt{\frac{rg}{\mu_{\text{limit}}}} \tag{18}$$

is required for stable equilibrium operation. In the case that $r=10$ m and $\mu_{\text{limit}}=1.6$, the machine speed must be $v>7.83$ m/s. It should be pointed out that there is nothing "special" about a camber angle of $\theta=90$ deg, and other high camber angle condition can be analyzed in a straightforward way. Figure 9 illustrates the equilibrium machine roll angle as a function of $v^2/(rg)$. The curves in Fig. 9(*a*) come from solving Eq. (10), with the corre-

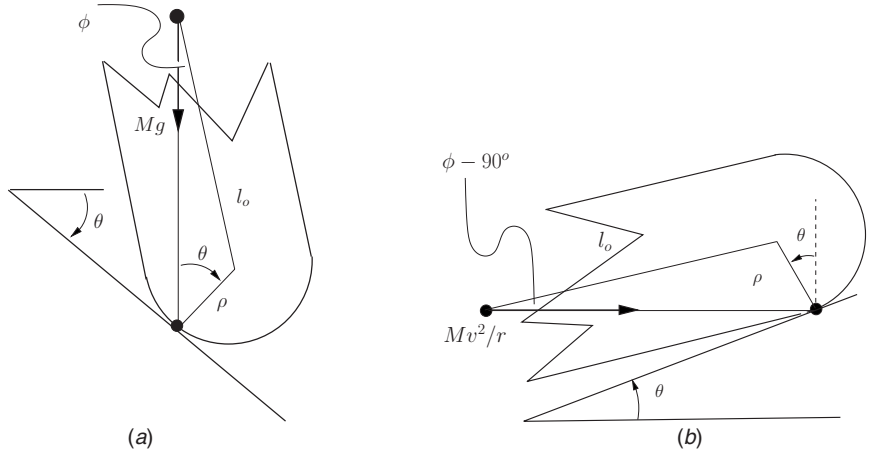

Fig. 7 Roll-angle stability limits. (*a*) Condition (15) shows that one static roll stability limit is reached when the machine mass center lies directly above the ground contact. It follows from Eq. (11) that under these conditions the machine's path curvature approaches zero ($r\to\infty$) for all operating points along this stability boundary. (*b*) The condition $l_o\cos\phi+\rho\cos\theta>0$ shows that a static roll stability limit is approached when the centripetal force passes through the ground-contact point. This operating condition can only be approached asymptotically as $v^2/r\to\infty$; note that the gravitational force is ignored due to its negligible influence in this case.

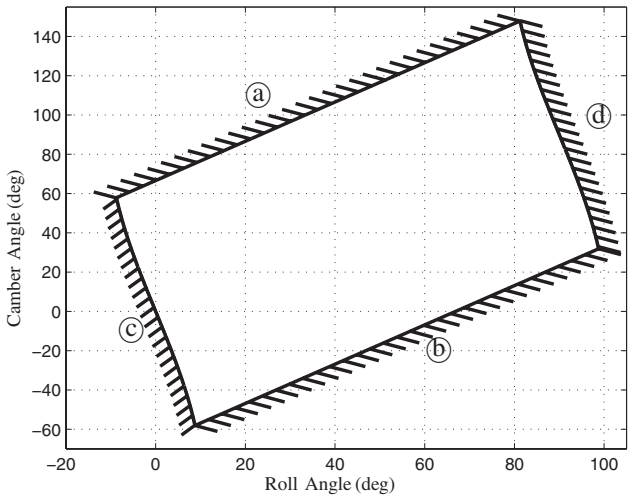

Fig. 8 Static stability limits. In order for a stable trim-state to exist, the motorcycle must operate within the cross-hatched region illustrated. This region is defined by the following: ⓐ is the friction limit given by $\phi-\theta>-\arcsin(\mu_{\text{limit}}\rho/(l_o(1+\mu_{\text{limit}}^2)^{1/2}))-\arctan(\mu_{\text{limit}})$, in which $l_o=0.4316$ m, $\rho=0.0775$ m and $\mu_{\text{limit}}=1.6$ are used for illustration; ⓑ is the friction limit given by $\phi-\theta<\arcsin(\mu_{\text{limit}}\rho/(l_o(1+\mu_{\text{limit}}^2)^{1/2}))+\arctan(\mu_{\text{limit}})$. The limits ⓐ and ⓑ taken together come from Eq. (14). The boundary ⓒ is the vertical roll stability limit given by inequality $l_o\sin\phi+\rho\sin\theta\geq 0$, (see Fig. 7(*a*)); ⓓ horizontal roll stability limit given by inequality $l_o\cos\phi+\rho\cos\theta>0$ (see Fig. 7(*b*)). Under wall of death conditions, the road camber angle is given by $\theta=90$ deg, and stable roll angles exist between $\phi=23.5$ deg and roll angles approaching 90 deg.

sponding machine operation condition illustrated in Fig. 9(*b*), where the resultant of the gravitational and centripetal forces pass through the tire-road contact point. Observe how higher values of road camber angles require higher minimum values of $v^2/(rg)$ and lower machine roll angles that approach the boundary ⓓ in Fig. 8 asymptotically.

3 Results

The main results of this paper are now presented and comprise root-locus diagrams, or plots derived from eigenvalue calculations, which were generated from a symbolic linearization of the high-fidelity model described in Sec. 2. All the results are for the open-loop machine, and so the drive and roll controllers are removed from the linearized model used to generate the results presented here. The computation of the machine's eigenvalues is a two-step process in which the trim states are found prior to the evaluation of the linearized model and the eigenvalue calculations. In the first stage of the process, the controllers described in Secs. 2.1 and 2.3 are used to drive the nonlinear model into a desired trim condition. Once the desired trim condition has been established, the trim states are used evaluate the state-space **A** matrices of the linearized models.

The first result, shown in Fig. 10, is a set of root-locus diagrams for the machine operating at zero roll angle. The speed is increased from 5 m/s to 75 m/s, with four road camber angles considered. Since the vehicle roll angle is $\phi=0$ deg, it follows from inequality (15) that only positive road camber angles can be considered. The zero road camber (flat road) curve is a familiar plot that has been referred to in previous papers [8,9,36]. It can be seen from Fig. 10 that the wobble-mode frequency varies between approximately 47 rad/s and 57 rad/s, while the weave mode resonant frequency varies between 9 rad/s and 28 rad/s. Apart from relatively low speeds (below 15 m/s), the damping of the wobble and weave modes decreases with increased speed. The key observation from Fig. 10 is the fact that the damping of both the wobble and weave modes decreases with increased road camber for speeds below 30 m/s, while at high speeds, this trend reverses and both the wobble- and weave-mode dampings increase with increased road camber. In order to clarify the quantitative nature of these trends, the real parts of the wobble- and weave-mode eigenvalues, as a function of speed, are plotted in Fig. 11. Figure

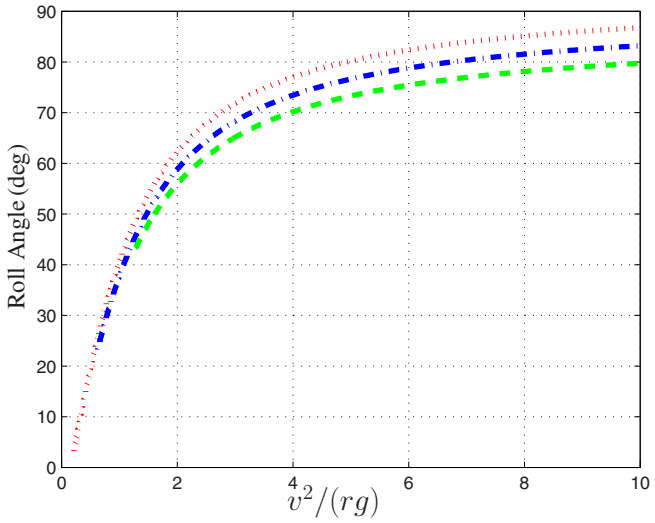

(*a*)

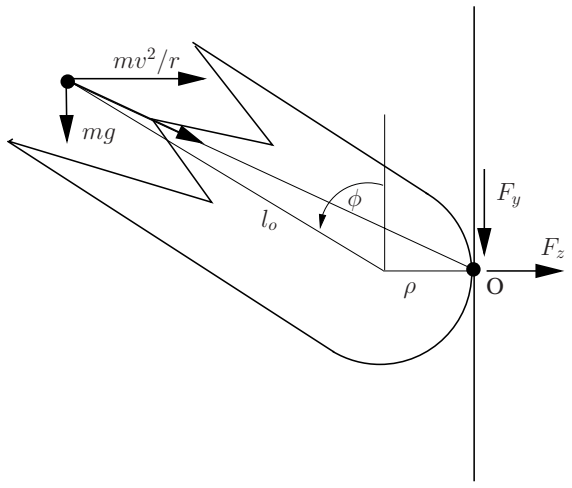

(*b*)

Fig. 9 Stable operation under wall of death type conditions. (*a*) shows the equilibrium roll angle as a function of $v^2/(rg)$, and was generated using Eq. (10) for three different road camber angles, and with $l_o=0.4316$ m and $\rho=0.0775$ m. The dotted curve corresponds to a camber angle of $\theta=70$ deg, the dot-dash curve to $\theta=90$ deg, and the dashed curve to $\theta=110$ deg. For $\theta>90$ deg, the vehicle traverses the interior of a *noninverted* cone; the lowest viable value of $v^2/(rg)$ comes from the friction limit condition $\phi-\theta>-\arcsin(\mu_{\text{limit}}\rho/(l_o(1+\mu_{\text{limit}}^2)^{1/2}))-\arctan(\mu_{\text{limit}})$ (boundary ⓐ in Fig. 8), while the limiting value associated with $v^2/(rg)\to\infty$ and the corresponding highest roll angles come from the horizontal roll stability limit (boundary ⓓ). (*b*) shows the motorcycle in roll equilibrium against the wall of death; the resultant of the gravitational and centripetal forces act through the tire contact point *O*.

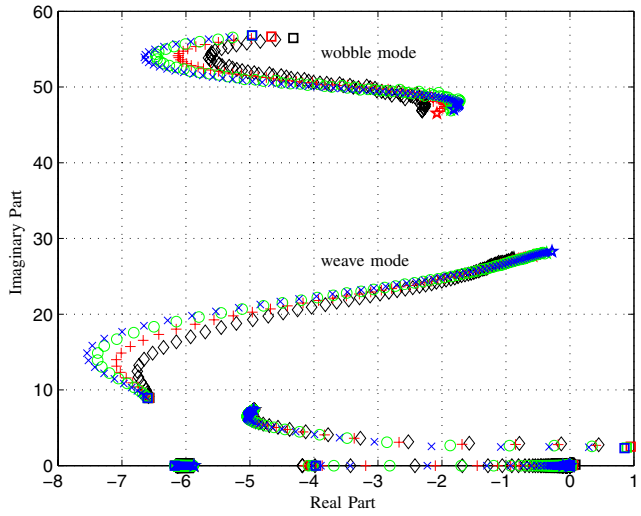

Fig. 10 Root loci for four road camber angles showing the wobble- and weave-mode eigenvalues as a function of speed. The motorcycle roll angle is ϕ=0 deg, and the speed is varied from 5 m/s to 75 m/s. The highest speed is marked with a ⋆ and the lowest speed with a □. The road cambers are annotated as 0 deg, ×; 5 deg, ○; 10 deg, +; 15 deg, ◇.

11(*a*) shows that at low speed a road camber angle of 15 deg increases the real part of the wobble-mode eigenvalue from approximately −5.0 to −4.3; at 15 m/s, it increases from −6.7 to −5.7; at 30 m/s, there is virtually no change, while at 75 m/s, the trend reverses and the real part of the wobble mode decreases from −1.8 to −2.3 as road camber is introduced. The high-speed trend is the most important, because at high speed the wobble-mode damping is at its lowest, and the introduction of 15 deg of road camber causes the wobble-mode half-amplitude decay time to increase by almost 25% from 0.3 s to 0.38 s. Figure 11(*b*) shows that at low speed a road camber increase of 15 deg has little or no effect on the weave-mode damping; at 15 m/s, the real part of the weave-mode eigenvalue increases from −7.6 to −6.5; there is no change in the weave-mode damping at 30 m/s, while at 75 m/s, the real part of the weave-mode eigenvalue decreases from −0.3 to −0.9. Again, the high-speed trend is the most important one from a safety perspective, because under these conditions the weave mode is lightly damped and the introduction of road camber causes the half-amplitude decay time to decrease from 2.3 s to 0.77 s. The overall conclusion is that the damping of the high-speed wobble and weave modes both decrease as the vehicle becomes more nearly perpendicular to the road surface.

Figure 12 shows a set of root-locus diagrams for the machine operating at 5 deg and 15 deg of roll angle. Direct calculation using Eq. (15) shows that at 5 deg of roll angle, the road camber can be decreased to −29 deg without a loss of static roll stability. Therefore, in comparison to Fig. 10, the range of road camber angles investigated can be expanded to include adverse (negative) road camber conditions. The key observation from Fig. 12(*a*) is the fact that the high-speed damping of both the wobble and weave modes is lowest at 5 deg of road camber, which is the condition under which the tires are almost perpendicular to the road. The damping of both modes then gets progressively higher as the angle between the tires and the road increases. It will be shown in a subsequent figure that this trend is insensitive to the sign of the tire-to-road roll-angle increase. As before, at low speed, both the wobble- and weave-mode dampings are greatest when the road camber angle is 5 deg. Figure 12(*b*) serves only to reinforce the observation that the high-speed weave- and wobble-mode dampings are lowest when the road tires are perpendicular to the road and that this trend then reverses at low speed. In order to clarify the quantitative nature of these trends, the real parts of the wobble and weave modes, as a function of road camber angle, are plotted in Figs. 13 and 14, respectively. In each case, the (*a*) plot corresponds to 10 m/s, which is representative of the low-speed behavior, while the (*b*) plots correspond to the 75 m/s, which is representative of high speeds. At low speeds, it can be seen that the wobble-mode damping is greatest when the road camber angle and the machine roll angle are equal, or in other words when the tire is perpendicular to the road. This is true of each of the four machine-roll-angle test conditions. It is also interesting to note that the damping of both modes is insensitive to the sign of the tire-road camber angle. For the 5 deg roll-angle case, the modal damping of both modes are very similar for road camber angles of zero and 10 deg, $|\phi-\theta|$=5 deg and is the same in each case. Indeed, these plots indicate a direct relationship between the modal damping and the tires' normal load, which is a function of $|\phi-\theta|$ rather than $\phi-\theta$; note that F_z is an even function of $\phi-\theta$; see Eq. (13). At high speed, the opposite is true in that an orthogonal relationship between the tire and the road is detrimental to the stability of the high-speed wobble mode. In the

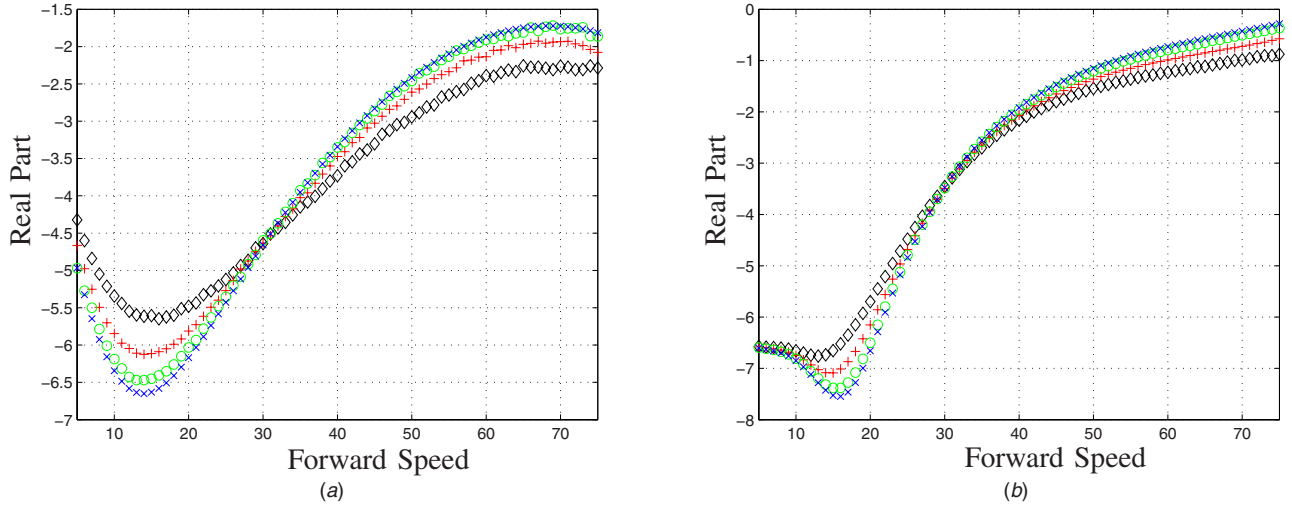

Fig. 11 Real parts of the wobble- and weave-mode eigenvalues as a function of speed for four different road camber angles, and a motorcycle roll angle of ϕ=0 deg. The real part of the wobble-mode eigenvalue is shown in (*a*), while the real part of the weave-mode eigenvalue is shown in (*b*). The road camber curves are annotated as 0 deg, ×; 5 deg, ○; 10 deg, +; 15 deg, ◇.

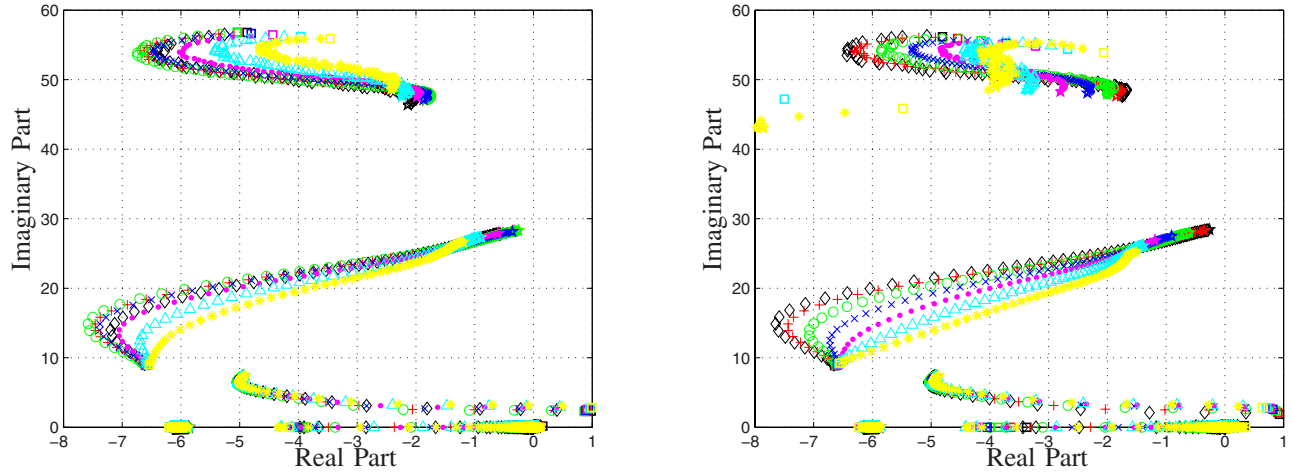

Fig. 12 Root loci for seven road camber angles, with a motorcycle roll angle of ϕ=5 deg (*a*), and ϕ=15 deg (*b*). The speed is varied from 5 m/s to 75 m/s; the highest speed is marked with a ⋆ and the lowest speed with a □. The road cambers are annotated as −15 deg, ∗; −10 deg, △; −5 deg, ●; 0 deg, ×; 5 deg, ○; 10 deg, +; 15 deg, ◇.

extreme high-speed case corresponding to a machine roll angle of 15 deg, the wobble-mode half-amplitude decay time increases from 0.1507 s (θ=−20 deg) to 0.41 s (θ=20 deg).

The road camber-related behavior of the weave mode is examined in detail in Fig. 14. As with the wobble mode, at low speeds, it can be seen that the weave-mode damping is greatest when the road camber angle and the machine roll angle are equal, or when the tire is perpendicular to the road. In the extreme case, at low speed, which corresponds to a machine roll angle of 15 deg, the real part of the weave-mode eigenvalue increases from −6.8 at a positive road camber angle of θ=20 deg to −5.7 at an adverse camber of θ=−20 deg. The important case corresponds to the 75 m/s high-speed situation when positive camber has a destabilizing influence on the weave mode. As with the wobble mode, at high speed, an orthogonal relationship between the tire and the road is destabilizing. In the extreme high-speed case corresponding to a machine roll angle of 15 deg, the weave-mode half-amplitude decay time increases from 0.46 s (θ=−15 deg) to 2.48 s (θ=15 deg).

The concluding set of results is for a moderately high roll angle of ϕ=30 deg. The central aim is to establish that the trends alluded to above hold good at higher vehicle roll angles. Figure 15 shows a set of root loci corresponding to a machine roll angle of 30 deg; the speed is increased from 5 m/s to 75 m/s, with seven road camber angles considered. It is clear that the high-speed weave-mode behavior retains its prior behavior with its damping increasing as the tire-to-road camber angle increases. It is also clear that the low-speed weave-mode damping is relatively insensitive to road camber. It is not clear from this plot if there is a low-speed trend reversal of the type observed earlier. The computation of the wobble-mode behavior at high roll angles proved problematic, because despite extensive controller tuning, it is difficult to maintain a constant trim state under these operating conditions. The overall trends are still clear. At high speeds, the wobble-mode damping decreases as the tire becomes more nearly orthogonal to the road, with this trend reversing at lower speeds. Quantitative clarity is established in Fig. 16 where the real parts of

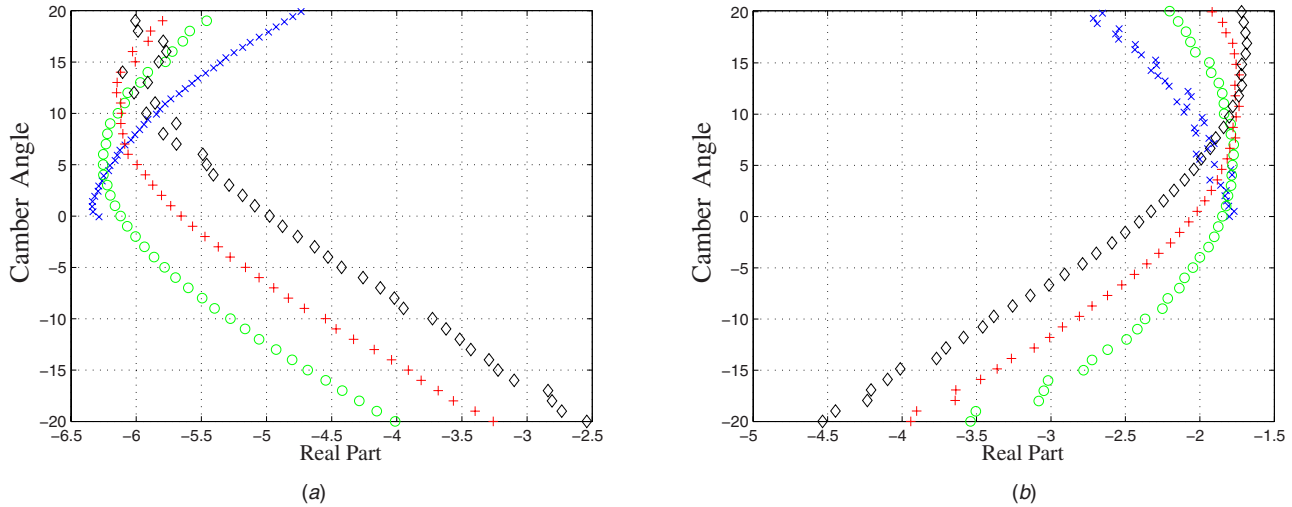

Fig. 13 Real part of the wobble-mode eigenvalue as a function of the road camber angle for four different machine roll angles. The motorcycle's forward speed is constant at (*a*) 10 m/s and (*b*) 75 m/s. The motorcycle roll-angle curves are annotated as 0 deg, ×; 5 deg, ○; 10 deg, +; 15 deg, ◇.

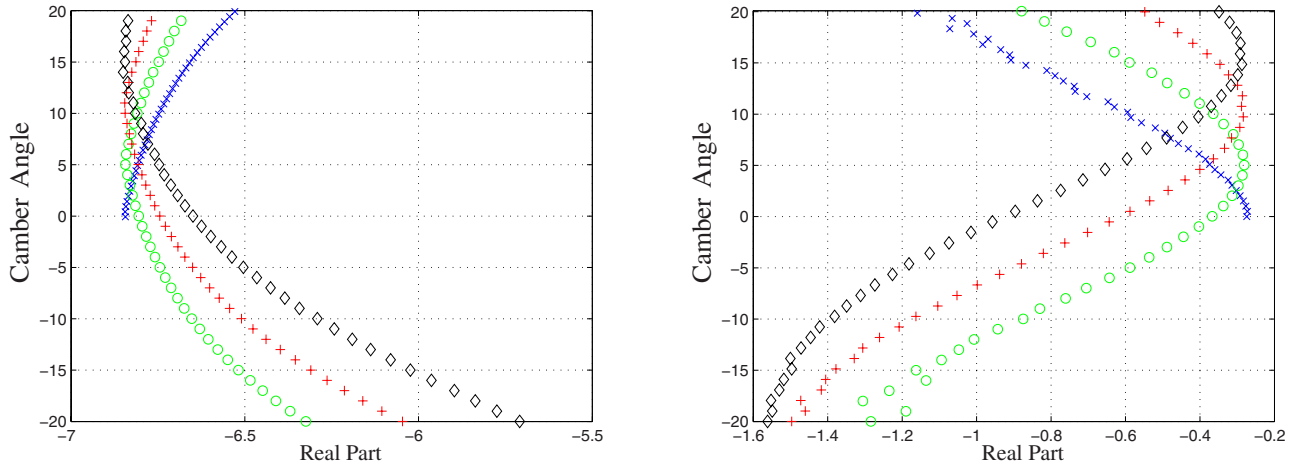

Fig. 14 Real part of the weave-mode eigenvalue as a function of the road camber angle for four different machine roll angles. The motorcycle's forward speed is constant at (*a*) 10 m/s and (*b*) 75 m/s. The motorcycle roll-angle curves are annotated as 0 deg, ×; 5 deg, ○; 10 deg, +; 15 deg, ◇.

the wobble- and weave-mode eigenvalues are plotted as a function of speed for seven different road camber angles, and a motorcycle roll angle of ϕ=30 deg. The (*a*) plot shows that the low-speed wobble mode is most damped for high positive camber and least damped for high negative camber, with the 30 deg change in camber angle decreasing the real part of the wobble mode from approximately −1.0 to −3.4. The wobble-mode damping then becomes relatively insensitive to camber at 40 m/s, with the wobble-mode damping trend again reversing at high speed. The (*b*) plot shows that the low-speed weave-mode damping is insensitive to camber, with the real part of the weave mode increasing from −6.7 to −6.3 as the road camber is swept from 15 deg to −15 deg. This trend, such as it is, reverses at a speed of approximately 50 m/s. At 75 m/s, the weave-mode damping is lowest for high positive camber and highest for maximum adverse camber, with the change in the real part of the weave-mode eigenvalue similar to that observed in the zero roll-angle case.

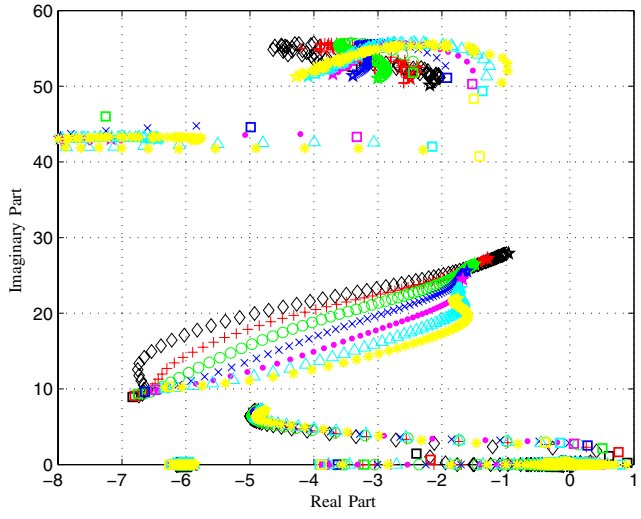

Fig. 15 Root-loci for seven road camber angles, with a motorcycle roll angle of ϕ=30 deg; the speed is varied from 5 m/s to 75 m/ s. The highest speed is marked with a ⋆ and the lowest speed with a □. The road cambers are annotated as −15 deg, ∗; −10 deg, △; −5 deg, ●; 0 deg, ×; 5 deg, ○; 10 deg, +; 15 deg, ◇.

4 Conclusions

The influence of road camber on motorcycle stability is an issue that sometimes arises in loss-of-control motorcycle accident investigations. A typical scenario involves high-speed cornering on a superelevated motorway. The overarching contribution of this paper is to clarify the influence of road camber on the stability of the two important oscillatory modes of behavior associated with single-track vehicles known as wobble and weave. It must be emphasized that the conclusions drawn pertain to a particular class of high-powered sports motorcycles, and are not claimed to be "true for all motorcycles."

Contributions include a method of "forcing" a complex nonlinear simulation model to operate stably at a prescribed fixed speed, fixed roll-angle, and fixed road-camber-angle operating condition. This involved a number of enhancements to an existing model including the introduction of local tangent plane approximations for a conical road surface. Separate tangent planes are required for each of the road tires, since extensive force, moment, and power balance testing established that one such tangent plane was inadequate at low speeds. It was also found necessary to introduce adaptive references into both the roll-angle steering control loop and the rear-wheel drive loop. The first of these adaptive references was used to center the machine's cornering trajectory on an arbitrary prescribed point in the ground plane (usually the origin n_0 of the inertial reference frame). Adaptation in the speed reference of the rear-wheel drive controller was used to remove persistent low-frequency height oscillations that can occur as the vehicle revolves around its cornering trajectory. This phenomenon is at its most troublesome at large radii of cornering curvature.

Important insights are obtained from the simple static force and moment balance calculations presented in Secs. 2.5 and 2.6. It is believed that the single-wide-tire model presented represents a good balance between fidelity and simplicity for the purposes to which it is put here. These include the analysis of the way in which the steady-state tire normal-load and side forces vary with road camber, the calculation of the machine's cornering radius of curvature as a function of speed, roll angle and road camber angle, and the quantitative characterization of the static roll stability boundary. The veracity of this simple analysis was established by comparison to the complex dynamic model presented.

The conventional wisdom as it is taught to advanced police riders [1], which is based on simple equilibrium considerations, focuses on achieving riding conditions that minimize steady-state tire side forces and maximize the tire normal loading. While this

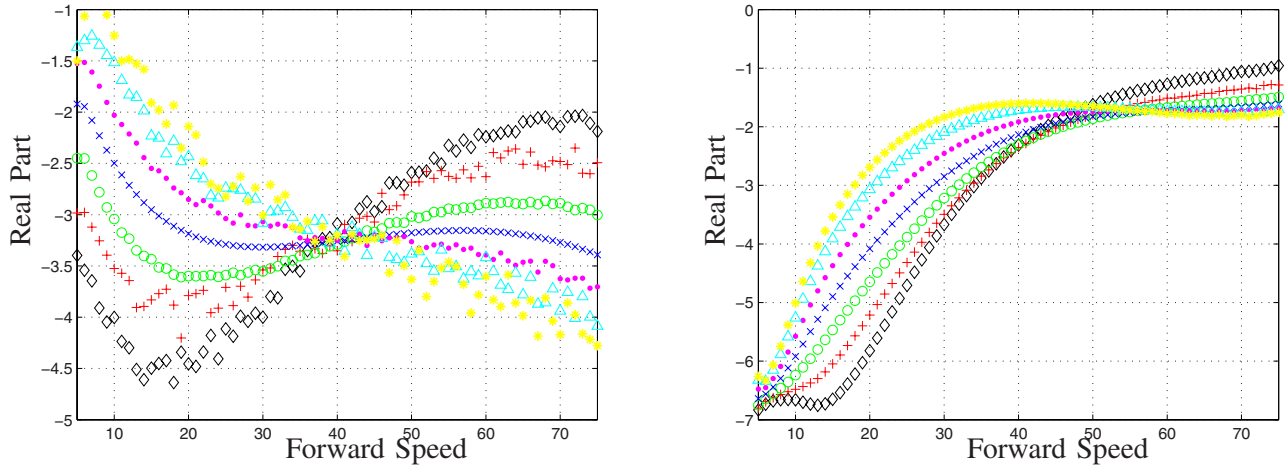

Fig. 16 Real parts of the wobble- and weave-mode eigenvalues as a function of speed for seven different road camber angles and a motorcycle roll angle of ϕ=30 deg. The real part of the wobble-mode eigenvalue is shown in the (*a*) figure, while the weave-mode behavior is shown in the (*b*) plot. The road camber curves are annotated as −15 deg, ∗; −10 deg, △; −5 deg, ●; 0 deg, ×; 5 deg, ○; 10 deg, +; 15 deg, ◇.

is probably the best thing to do in the context of four-wheeled vehicles, it is not necessarily the right advice to give to motorcyclists. It has been demonstrated by high-fidelity dynamic modeling that the damping of the high-speed wobble and the high-speed weave modes are at their minimum when the road tires are vertical to the road. As the tire-road inclination angle increases, the high-speed wobble and weave-mode damping increases also. This increased damping does not appear sensitive to the sign of the tire-to-road inclination angle $(\theta-\phi)$ and appears instead sensitive to $|\theta-\phi|$; see Figs. 13 and 14. It is therefore concluded that increased tire loading has a destabilizing effect on the high-speed wobble- and high-speed weave-mode stabilities, because it too increases with $|\theta-\phi|$; see Eq. (13) and the simplification that appears immediately after it. At low speeds, these trends reverse and the wobble and weave-mode dampings increase as the tires become more nearly vertical with the road. Under these more benign conditions, the conventional police training advice appears to hold good.

Acknowledgment

This work was supported by a Portfolio Partnership held with the British Engineering and Physical Sciences Research Council.

References

[1] Coyne, P., 1996, *Motorcycle Roadcraft: The Police Rider's Handbook*, Stationary Office Books, London.
[2] Limebeer, D. J. N., and Sharp, R. S., 2006, "Bicycles, Motorcycles and Models," IEEE Control Syst. Mag., **26**(50), pp. 34–61.
[3] Meijaard, J. P., Papadopoulos, J. M., Ruina, A., and Schwab, A. L., 2007, "Linearized Dynamics Equations for the Balance and Steer of a Bicycle: A Benchmark and Review," Proc. R. Soc. London, Ser. A, **463**, pp. 1955–1982.
[4] Koenen, C., 1983, "The Dynamic Behaviour of Motorcycles When Running Straight Ahead and When Cornering," Ph.D. thesis, Delft University of Technology, Delft, Netherlands.
[5] Sharp, R. S., and Limebeer, D. J. N., 2001, "A Motorcycle Model for Stability and Control Analysis," Multibody Syst. Dyn., **6**(2), pp. 123–142.
[6] Cossalter, V., and Lot, R., 2002, "A Motorcycle Multi-Body Model for Real Time Simulations Based on the Natural Coordinates Approach," Veh. Syst. Dyn., **37**(6), pp. 423–447.
[7] Sharp, R. S., 2001, "Stability, Control, and Steering Responses of Motorcycles," Veh. Syst. Dyn., **35**(4,5), pp. 291–318.
[8] Sharp, R. S., Evangelou, S., and Limebeer, D. J. N., 2003, "Improved Modelling of Motorcycle Dynamics," *ECCOMAS Thematic Conference on Advances in Computational Multibody Dynamics*, J. Ambósio, ed., Lisbon, Jul. 1–4.
[9] Sharp, R. S., Evangelou, S., and Limebeer, D. J. N., 2004, "Advances in the Modelling of Motorcycle Dynamics," Multibody Syst. Dyn., **12**(3), pp. 251–281.
[10] Döhring, E., 1956, "Steering Wobble in Single-Track Vehicles," ATZ, **58**(10), pp. 282–286.
[11] Eaton, D. J., 1973, "Man-Machine Dynamics in the Stabilization of Single-Track Vehicles," Ph.D., thesis, University of Michigan.
[12] Watanabe, Y., and Yoshida, K., 1973, "Motorcycle Handling Performance for Obstacle Avoidance," Second International Congress on Automotive Safety, San Francisco.
[13] Jennings, G., 1974, "A Study of Motorcycle Suspension Damping Characteristics," SAE Paper No. 740628.
[14] Roe, G. E., and Thorpe, T. E., 1976, "A Solution of the Low-Speed Wheel Flutter Instability in Motorcycles," J. Mech. Eng. Sci., **18**(2), pp. 57–65.
[15] Verma, M. K., 1978, "Theoretical and Experimental Investigation of Motorcycle Dynamics," Ph.D. thesis, University of Michigan.
[16] McKibben, J. S., 1978, "Motorcycle Dynamics—Fact, Fiction and Folklore," SAE Paper No. 780309.
[17] Aoki, A., 1979, "Experimental Study on Motorcycle Steering Performance," SAE Paper No. 790265.
[18] Weir, D. H., and Zellner, J. W., 1979, "Experimental Investigation of the Transient Behaviour of Motorcycles," SAE Paper No. 790266.
[19] Thomson, B., and Rathgeber, H., 1984, "Automated Systems Used for Rapid and Flexible Generation of System Models Exemplified by a Verified Passenger Car and a Motorcycle Model," *Dynamics of Vehicles on Roads and on Railway Tracks*, J. K. Hedrick, ed., Swets and Zeitlinger, Lisse, pp. 645–654.
[20] Bayer, B., 1988, "Flattern und pendeln bei krafträdern," Automobil Industrie, **2**, pp. 193–197.
[21] Takahashi, T., Yamada, T., and Nakamura, T., 1984, "Experimental and Theoretical Study of the Influence of Tires on Straight-Running Motorcycle Weave Response," SAE Paper No. 840248.
[22] Otto, W. M., 1980, "Effect of Motorcycle Accessories on Stability," *Proceedings of International Motorcycle Safety Conference*, Linthicum, MD, Motorcycle Safety Foundation, Washington, pp. 1560–1581.
[23] Sugizaki, M., and Hasegawa, A., 1988, "Experimental Analysis of Transient Response of Motorcycle Rider Systems," SAE Paper No. 881783.
[24] Biral, F., Bortoluzzi, D., Cossalter, V., and Da Lio, M., 2003, "Experimental Study of Motorcycle Transfer Functions for Evaluating Handling," Veh. Syst. Dyn., **39**(1), pp. 1–26.
[25] Evangelou, S., and Limebeer, D., 2000, "LISP Programming of the "Sharp 1971" Motorcycle Model," http://www.imperial.ac.uk/controlandpower/motorcycles/
[26] Sharp, R. S., and Alstead, C. J., 1980, "The Influence of Structural Flexibilities on the Straight Running Stability of Motorcycles," Veh. Syst. Dyn., **9**(6), pp. 327–357.
[27] Spierings, P. T. J., 1981, "The Effects of Lateral Front Fork Flexibility on the Vibrational Modes of Straight-Running Single-Track Vehicles," Veh. Syst. Dyn., **10**(1), pp. 21–35.
[28] Limebeer, D. J. N., Sharp, R. S., and Evangelou, S., 2002, "Motorcycle Steering Oscillations Due to Road Profiling," ASME J. Appl. Mech., **69**(6), pp. 724–739.
[29] de Vries, E. J. H., and Pacejka, H. B., 1998, "The Effect of Tyre Modeling on the Stability Analysis of a Motorcycle," *Proceedings of AVEC'98*, Nagoya, Japan, pp. 355–360.
[30] de Vries, E., and Pacejka, H., 1998, "Motorcycle Tyre Measurements and Models," *Proceedings of 15th IAVSD Symposium on the Dynamics of Vehicles on Roads and on Tracks*, L. Palkovics, ed., Budapest, Hungary, Aug. 25–29, 1997, Veh. Syst. Dyn. **28**, pp. 280–298.

[31] Pacejka, H. B., 2002, *Tyre and Vehicle Dynamics*, Butterworth-Heinemann, Oxford.
[32] Tezuka, Y., Ishii, H., and Kiyota, S., 2001, "Application of the Magic Formula Tire Model To Motorcycle Maneuverability Analysis," JSAE Rev., **22**, pp. 305–310.
[33] Mechanical Simulation Corporation, 1998, AUTOSIM 2.5+ Reference Manual, Ann Arbor, MI, http://www.carsim.com
[34] Kreyszig, E., 1967, *Advanced Engineering Mathematics*, Wiley, New York.
[35] Timoshenko, S., and Young, D. H., 1948, *Advanced Dynamics*, McGraw-Hill, New York.
[36] Evangelou, S., Limebeer, D. J. N., Sharp, R. S., and Smith, M. C., 1967, "Mechanical Steering Compensators for High-Performance Motorcycles," ASME J. Appl. Mech., **74**, pp. 332–346.

Scratching of Elastic/Plastic Materials With Hard Spherical Indenters

Shane E. Flores
Michael G. Pontin
Frank W. Zok

Materials Department,
University of California,
Santa Barbara, CA 93106

A mechanistic framework has been developed for interpreting scratch tests performed with spherical indenters on elastic/plastic materials. The pertinent scaling relations have been identified through a plastic analysis and the model has been subsequently calibrated by finite element calculations. The results show that the ratio of scratch force to normal force (or apparent friction coefficient) can be partitioned into two additive components: one due to interfacial friction and another associated with plastic deformation. The plastic component scales parabolically with the normal force and depends only weakly on the true (elastic) friction coefficient. A simple formula for the scratch force, based on the plastic analysis and the numerical results, has been derived. Finally, experimental measurements on two material standards commonly used for nanoindenter calibration have been used to verify the theoretical results. [DOI: 10.1115/1.2966268]

1 Introduction

The advent of instrumented nanoindenters some two decades ago has enabled an unprecedented capability for probing the mechanical properties of materials over a wide range of length scales (from nm to mm) and forces (from μN to N). In addition to their now-routine use in measuring material stiffness and hardness, nanoindenters allow studies of creep, dynamic loading, thin film behavior, fracture, and adhesion. Good summaries of the test methods and the underlying mechanics are presented in textbooks by Bhushan [1] and Fischer-Cripps [2] as well as a recent review article by Gouldstone et al. [3]. A comparatively recent advancement in the field has been the development of instrumented indenter probes that can be displaced in a precise manner both normal and tangential to the sample surface. These probes allow measurement of tribological properties—those involving friction, abrasion, and wear—at length scales and force ranges typical of normal indentation [4–15]. Despite the technological advancements, analysis protocols for extracting fundamental material properties from such tests have not reached maturity levels comparable to those used to ascertain modulus and hardness from indentation tests.

The principal goal of the present article is to outline a mechanistic framework for interpreting measurements from scratch tests on elastic/plastic materials with spherical indenters. The latter shape selection is motivated by the fact that, at low force levels, stresses beneath a spherical indenter are below the elastic limits and hence the tribological properties can be ascertained in the absence of plasticity; yet, at higher force levels, responses in the transitional elastic/plastic and the fully plastic regimes can also be probed. In contrast, with sharp-tipped indenters such as the cube-corner, Berkovich, and cone, the accessible behavioral domains are far more restricted. That is, because of the self-similar deformation fields associated with sharp tips, the strain level is fixed (independent of normal force) and dictated by indenter shape [16–18]. Probing material properties over a range of strains requires use of indenters of varying shapes. Even then, if the tips are very sharp, measurements cannot be made in the elastic domain. Selection of the spherical indenter is further motivated by the recognition that the asperities that make contact during sliding of surfaces are more closely represented by protuberances with a constant (finite) curvature rather than ones with infinitely sharp points.

As a prelude to forthcoming results and to provide perspective, the test conditions of interest and the dominant behavioral domains are illustrated in Fig. 1. Here a rigid sphere is pressed into contact with a flat slab of plastically deformable material with normal force F_N and subsequently slid across the slab surface with lateral force F_L. At sufficiently low levels of F_N, wherein the contact is elastic, sliding occurs subject to Coulomb's law, with friction coefficient $\mu \equiv F_L/F_N$. In contrast, at high force levels, both initial normal contact and subsequent sliding involve plastic deformation. In this domain, the normalized scratch force (or *apparent* friction coefficient), F_L/F_N, increases approximately parabolically with F_N and exceeds the *true* (elastic) friction coefficient. An intermediate force range exists within which deformation involves comparable amounts of elastic and plastic strains and the curves in Fig. 1 transition accordingly. The high load domain is the main focus of the present article.

The remainder of this article consists of three parts. In the first, an approximate analytical model of scratching of a rigid, perfectly plastic material based on a virtual work analysis is presented. The model is used to identify the scaling relation between the scratch force and the geometric and material properties (resulting in the nondimensional parameters of the coordinate axes in Fig. 1). Next, finite element calculations are used to investigate the effects of normal force and friction coefficient on scratch force, with the goal of ascertaining the key nondimensional parameters. Finally, experimental measurements on two material standards are presented and compared with the model predictions.

2 Analytical Model

A lower-bound estimate of the scratch force is obtained using established theorems of classical plasticity. The geometry to be analyzed is depicted by the schematic in the top right corner of Fig. 1. Scratching proceeds in two steps. First, a rigid spherical indenter of radius R is pushed into a flat semi-infinite slab of rigid, perfectly plastic material with normal force, F_N. The radius, a, of the resulting indentation is given by [19]

$$a = \sqrt{C_1 R u_0} = \sqrt{\frac{F_N}{C_2 \pi \sigma_y}} \tag{1}$$

where u_0 is the maximum penetration depth, σ_y is the material yield strength, $C_1 = 2.7$, and $C_2 = 3.0$. The indenter is then moved

Contributed by the Applied Mechanics Division of ASME for publication in the JOURNAL OF APPLIED MECHANICS. Manuscript received January 22, 2008; final manuscript received June 30, 2008; published online August 22, 2008. Review conducted by Zhigang Suo.

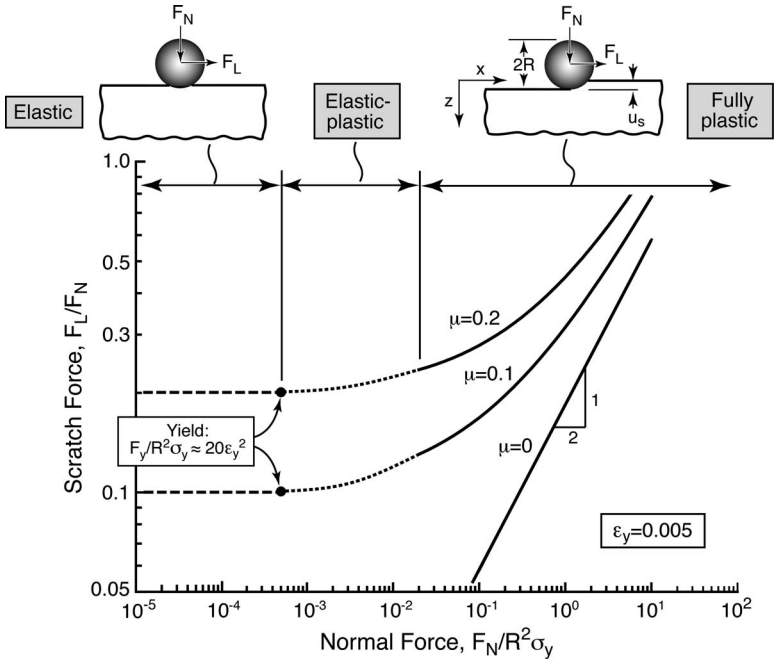

Fig. 1 Overview of the scratch configuration, the dominant behavioral domains, and the trends in scratch force with normal force and friction coefficient

laterally (in the x-direction) while maintaining constant normal force. Three additional assumptions are invoked. (i) Sliding at the interface between the two bodies obeys Coulomb's law. (ii) The scratch depth u_s is equal to the initial indentation depth u_0 (verified by subsequent finite element calculations). (iii) The forces at the indenter/material interface remain below those needed to produce sticking friction.

In the steady-state domain, the rate of work done by scratching, $dW/dx=F_L$, can be partitioned into two components: one, dW_p/dx, due to plastic deformation beneath the indenter tip, and another, dW_f/dx, from frictional sliding. The rate of dissipation is obtained from an analysis of the following virtual sequence of operations (illustrated in Fig. 2). (i) A thin slab of thickness dx perpendicular to the scratch direction and upstream from the scratch tip is removed from the sample. (ii) The slab is indented by a *cylindrical* roller of radius R under plane strain conditions to produce a *cylindrical* divot of width $2a$ and depth u_s (identical to those in the scratch wake). (iii) The indenter is slid across the surface of the slab a distance dx. (iv) The deformed slab is "pasted" onto the opposite face, downstream from the scratch tip, thereby advancing the indenter tip by a distance dx. The work done during this sequence (in Steps (ii) and (iii) in particular) is

$$\frac{dW}{dx} = F_L = \int_0^{u_0} f_N(u)du + \mu F_N \tag{2}$$

where $f_N(u)$ is the force per unit length of cylinder, given by

$$f_N(u) = 2a\sigma_y C_3 \tag{3}$$

where $C_3 \approx 2.5-3$ [20]. Combining Eqs. (1)–(3) and integrating yields

$$\frac{F_L}{F_N} = \mu + k_0\sqrt{\frac{F_N}{R^2\sigma_y}} \tag{4}$$

where

$$k_0 \equiv \frac{4C_3}{3C_1(\pi C_2)^{3/2}} \approx 0.05 \tag{5}$$

This relation identifies the two pertinent nondimensional parameters: the normalized scratch force, F_L/F_N, and the normalized normal force, $F_N/R^2\sigma_y$. These represent the parameters on the coordinate axes in Fig. 1 and are utilized in the presentation of subsequent numerical and experimental results.

3 Numerical Analysis

3.1 Finite Element Model. Calculations of scratch response were performed using the commercial finite element code

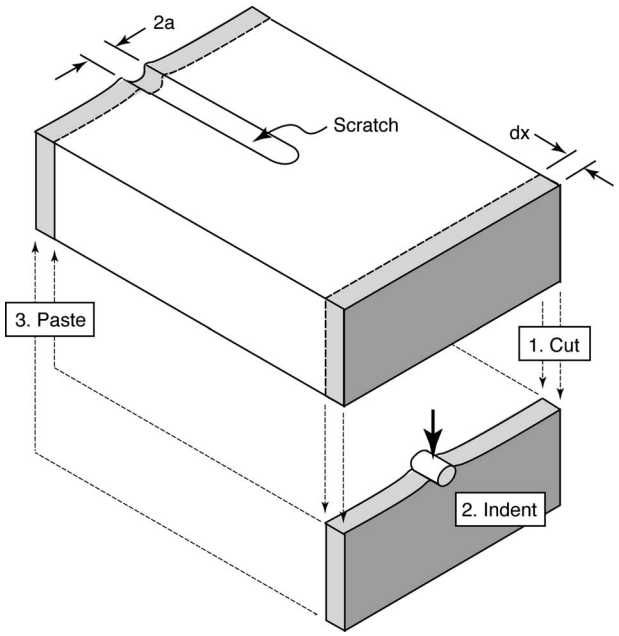

Fig. 2 Schematic of virtual cutting, indenting, and pasting operations used to model steady-state scratching

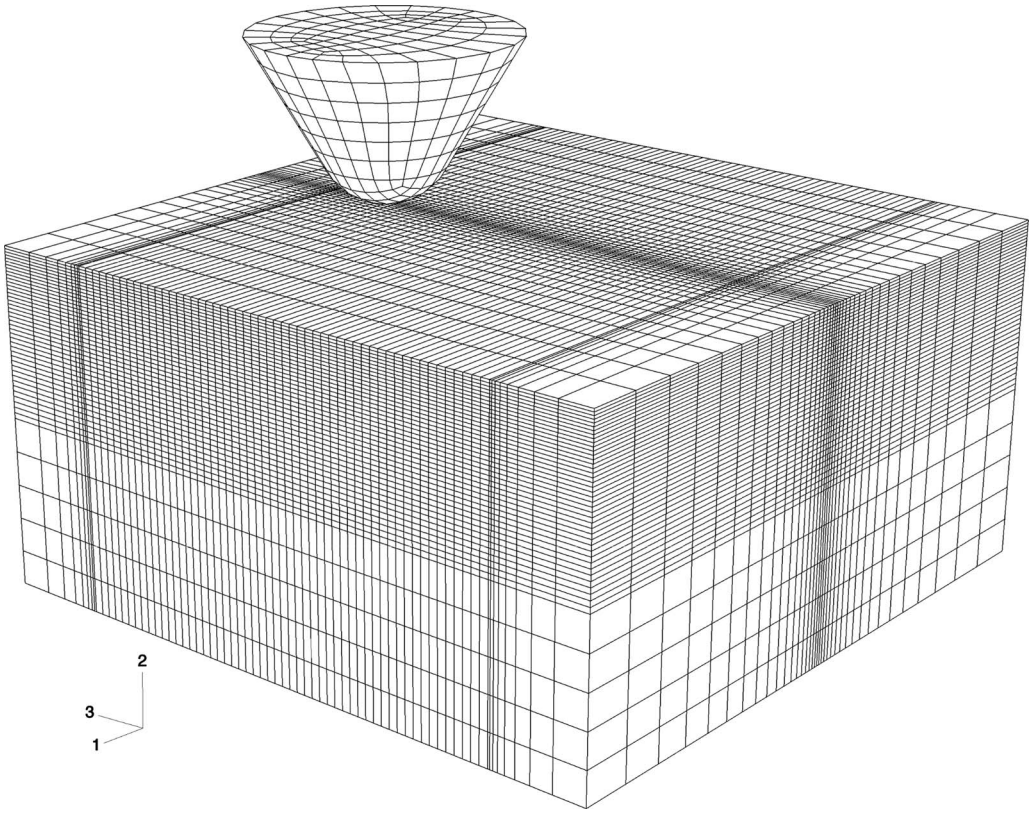

Fig. 3 Finite element mesh used for scratch and indentation simulations

ABAQUS/EXPLICITV6.4. For consistency with the experiments described in the next section, the indenter is modeled as a rigid axisymmetric cone with a full apical angle $2\theta=60$ deg and a spherical tip of radius R. All other length scales are subsequently normalized by R so the absolute value of R is arbitrary. The indenter is meshed with four-noded 3D rigid elements. The material being indented is represented by a biased mesh (refined near the indentation surface and coarser toward its base) using eight-noded 3D brick elements with reduced integration (Fig. 3). Although all results are presented in a nondimensional form, the absolute material properties for most calculations were selected to be close to those of typical engineering polymers ($\sigma_y=60$ MPa, $E=3$ GPa, and $\nu=0.3$). To assess the effects of yield strain, several simulations were performed with the same values of σ_y and ν but with a higher modulus: $E=300$ GPa. To ensure numerical stability, the hardening rate subsequent to yielding was taken to be 3 MPa (finite but small). Surface sliding was allowed to occur in accordance with Coulomb's law, with friction coefficients $\mu=0$, 0.125, or 0.25. The bottom surface of the specimen was fixed while symmetry boundary conditions were applied to its sides.

The calculations were performed in two steps, consistent with those described in Sec. 2. That is, a normal load was applied to the indenter, up to peak values in the range $F_N/R^2\sigma_y \leqslant 1$ and peak normal displacements $u_0/R \leqslant 0.2$, and the indenter then displaced laterally up to a displacement of $w/R \approx 3$.

3.2 Indentation. An initial assessment of the numerical results was made by comparing the indentation response with existing analytical and experimental results. To facilitate the comparisons, the forces and displacements have been normalized by their corresponding values at the onset of yield, F_y and u_y, given by [1,20]

$$F_y = 21.2\frac{R^2\sigma_y^3}{\bar{E}^2} \tag{6}$$

and

$$u_y = 6.3\frac{R\sigma_y^2}{\bar{E}^2} \tag{7}$$

where $\bar{E}$ is the plane strain modulus.

Two limiting behavioral domains exist. When F/F_y is not much greater than unity, the spatial extent of plasticity and the magnitude of the plastic strains are small and hence the indentation response is given to a good approximation by the elastic (Hertzian) solution [1,20]

$$\frac{F}{F_y} = \left(\frac{u}{u_y}\right)^{3/2} \tag{8}$$

At the other limit, where $F/F_y \gg 1$, the force-displacement response asymptotically approaches that for a rigid, perfectly plastic material, given by [1,20]

$$\frac{F}{F_y} = 5.5\left(\frac{u}{u_y}\right) \tag{9}$$

Comparisons of the numerical results and the analytical solutions are presented in Fig. 4. Also shown are experimental results for steel (from a previous study) as well as those for polymethylmethacrylate (PMMA) (from the present study, described below). Good agreement is obtained over the entire loading range. Additionally, friction has a minimal effect over the range of μ values examined here, consistent with previous numerical investigations [19,21].

Parenthetically, the indentation response over the entire loading range can be adequately described by a simple formula that combines the results in Eqs. (8) and (9). Here the total displacement at a prescribed force is taken as the sum of those for purely elastic and purely plastic indentations, namely,

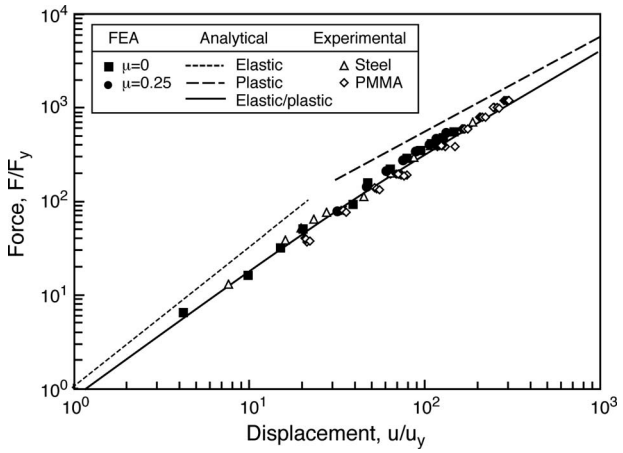

Fig. 4 Indentation of elastic-plastic materials with a rigid spherical indenter. Analytical solutions: Eq. (8) for elastic contact, Eq. (9) for plastic contact, and Eq. (10) for elastic/plastic contact. Data for steel adapted from Johnson [20]. Finite element results and experimental measurements on PMMA are from the present study.

$$\frac{u}{u_y} = \left(\frac{F}{F_y}\right)^{2/3} + 0.18\left(\frac{F}{F_y}\right) \tag{10}$$

This relation reduces to that in Eq. (8) as $F/F_y \to 0$ and that in Eq. (9) when $F/F_y \gg 1$. Upon comparison with the numerical results (Fig. 4), it appears to be reasonably accurate over the intermediate force range as well.

3.3 Scratching. Representative results from the scratch simulations are presented in Fig. 5. For normal forces above that needed to initiate yield, both the normal displacement u/R and the scratch force F_L/F_N initially increase slightly with w/R (a consequence of the loss of contact between the indenter and the material in the scratch wake), reach a peak, and then decrease and saturate at constant values, independent of scratch displacement. One manifestation of the steady state is the development of a uniform plastic strain field that translates with the indenter tip during sliding, as illustrated in Fig. 6. An additional notable result is that, for the case where $\mu=0$, the scratch depth at steady state is essentially identical to the initial indentation depth (following application of the normal force), consistent with the underlying assumption of the model in Sec. 2. For nonzero values of μ, the steady-state scratch depth falls somewhat below the indentation depth (Fig. 5(*d*)).

Based on dimensional analysis, the critical scratch displacement, w_c/R, needed to achieve steady state is expected to scale with the indent size, a/R. Recognizing that, for small indents, $a/R \propto \sqrt{u/R}$, it follows that the corresponding normal displacement $u_c/R \propto (w_c/R)^2$. An inspection of the numerical results reveals that the onset of steady state can be adequately described by $u_c/R \approx 0.1(w_c/R)^2$ (Fig. 5(*b*)).

The effects of the normal force and the friction coefficient on the scratch force are summarized in Fig. 7. When plotted as F_L/F_N versus $\sqrt{F_N/R^2\sigma_y}$, the results are linear for a fixed value of μ, consistent with Eq. (4). Moreover, upon extrapolation to $F_N/R^2\sigma_y=0$ (where the material response is purely elastic), $F_L/F_N \to \mu$, as required. However, in apparent contradiction to Eq. (4), the slopes of the lines in Fig. 7 are not constant but rather exhibit a weak (nearly linear) dependence on μ, characterized by

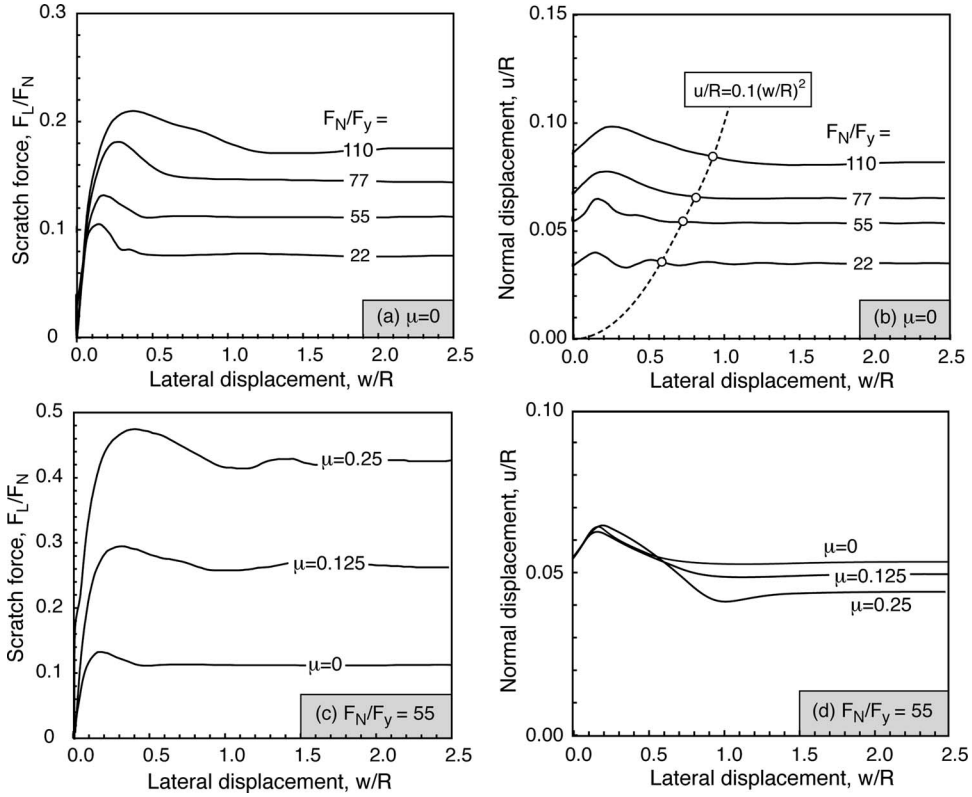

Fig. 5 Results of finite element calculations, showing the effects of normal force and friction coefficient on scratch force and scratch depth. The open circles in (*b*) denote the approximate points at which steady state is attained.

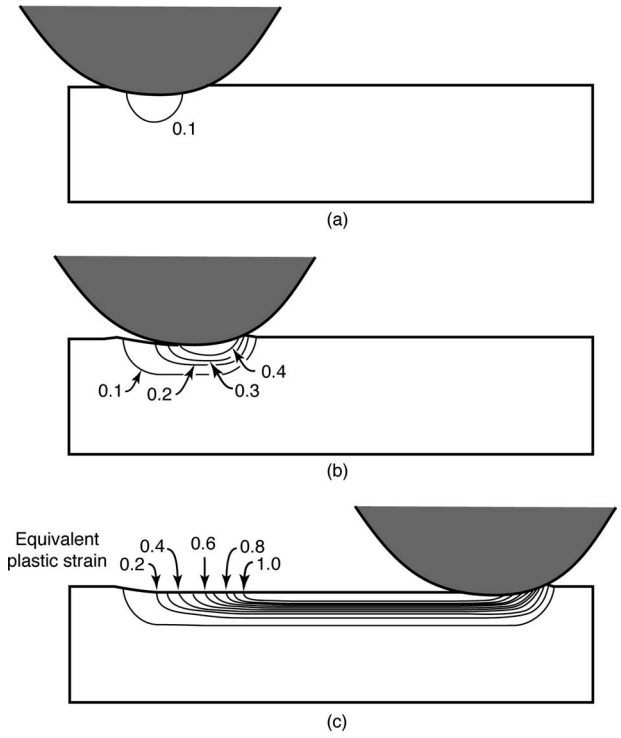

Fig. 6 Development of plastic strain beneath the indenter during a typical scratch simulation for scratch displacements, w/R, of (*a*) 0, (*b*) 0.25, and (*c*) 2.5 for $((F_N/R^2\sigma_y)^{1/2}=0.76$, $\mu=0.125$)

$$k_0 = k_1(1 + k_2\mu) \tag{11}$$

where $k_1=0.184$ and $k_2=1.75$. This result is depicted by the solid lines in Figs. 1 and 7. For friction coefficients $0 \leqslant \mu \leqslant 0.25$, k_0 falls in the rather narrow range 0.18–0.26. Furthermore, these values are considerably higher than the analytical prediction ($k_0 \approx 0.05$), consistent with the lower-bound nature of the model.

The effects of the elastic modulus appear to be small. For the case where $\mu=0$, the scratch forces increase by only about 10% as E is increased by two orders of magnitude (from 3 GPa to 300 GPa).

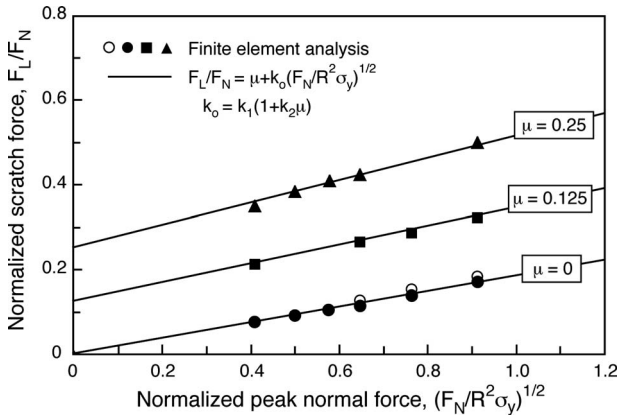

Fig. 7 Effects of normal force and friction coefficient on scratch force. The solid lines calculated using the formula shown with $k_1=0.184$ and $k_2=1.75$. Filled symbols: $E=3$ GPa. Open symbols: $E=300$ GPa.

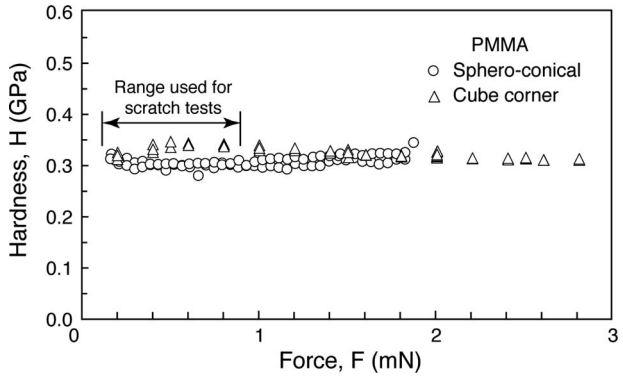

Fig. 8 Indentation hardness of PMMA, measured over a wide force range using both spheroconical and cube-corner indenters

4 Experimental Measurements

4.1 Materials and Test Methods. Scratch tests were performed on two material standards commonly used for indenter calibration: PMMA and a 99.999% pure (100) Al crystal. Scratching was performed using a 60 deg conical diamond indenter with a 1 μm tip radius. The test protocol consisted of (i) applying a normal load in the range 0.07–1.0 mN (for reasons described below) over a period of 5 s, (ii) holding at the peak load for 5 s, (iii) displacing the indenter tip laterally over a distance of 10 μm at a rate of 0.33 μm/s, and (iv) holding for an additional 5 s before unloading. Material response was characterized by the normalized scratch force, F_L/F_N, and the scratch depth, u/R. Remnant scratches were imaged by scanning probe microscopy (SPM).

The normal forces used for the preceding scratch tests were selected on the basis of two criteria: (i) that deformation be well into the plastic domain, i.e., $F/F_y \gg 1$, and (ii) that the scratch depth remain below R, to prevent contact of the conical surface of the indenter with the test sample. To this end, preliminary indentation tests were performed using a cube-corner tip to ascertain hardness and modulus. Combining these property values with Eq. (6) and taking the lower limit on the allowable force to be $\sim 10F_y$, the first criterion can be expressed as

$$\sqrt{F_N/R^2\sigma_y} \geq 15\varepsilon_y \tag{12}$$

where $\varepsilon_y=\sigma_y/E$. Yield strains obtained from the cube-corner indentations are $\varepsilon_y=0.02$ and 0.002 for PMMA and Al, respectively, and the corresponding critical forces $\sqrt{F_N/R^2\sigma_y} \approx 0.3$ and 0.03. A further assessment was made by a series of tests with the spheroconical indenter over a wide force range, to confirm that the deformation was indeed well into the plastic domain, as manifested in a constant value of hardness (independent of peak force). Indentation results of this type are plotted on Fig. 8. The maximum allowable normal force to satisfy the second criterion was estimated from the measured hardness and modulus coupled with the result in Eq. (12) and the condition $u/R<1$. The key property values are summarized in Table 1.

The true (elastic) friction coefficient was measured by scratch tests performed using an indenter with a 50 μm radius tip. Strictly, the forces for such tests should remain below that for yield, i.e., $\sqrt{F_N/R^2\sigma_y} \leqslant 5\varepsilon_y \approx 0.1$ for PMMA and 0.01 for Al. However, as demonstrated below, this criterion is overly stringent, since F_L/F_N remains essentially unchanged to significantly higher force levels.

4.2 Scratch Measurements. Typical scratch measurements are presented in Fig. 9. For PMMA, the results closely resemble those obtained from the finite element analysis. Notably, both F_L/F_N and u/R initially increase with w/R, reach a peak, and then fall back to steady-state values. The predicted onset of steady

Table 1 Summary of indentation properties

	PMMA	Al
Hardness, H (MPa)	320 ± 10	390 ± 20
Modulus, $\bar{E}$ (GPa)	5.0 ± 0.1	73 ± 7
Yield stress, σ_y (MPa)[a]	105 ± 4	131 ± 6
Yield force, F_y (μN)[b]	1.0 ± 0.1	0.009 ± 0.003
Yield displacement, u_y (nm)[b]	2.8 ± 0.3	0.020 ± 0.006

[a]Taken to be $H/3$.
[b]Corresponds to $R=1$ μm.

state, given by $u_c/R \approx 0.1(w_c/R)^2$, agrees well with the measurements. Once at steady state, F_L/F_N and u/R exhibit minimal fluctuations. Although similar features are obtained with the Al sample, the reductions in F_L/F_N and u/R from their peaks to their steady-state values are considerably greater. Furthermore, both F_L/F_N and u/R exhibit periodic fluctuations with w/R, with wavelengths that increase with F_N.

The differences in steady-state response of the two materials appear to correlate with the scratch shapes, ascertained from SPM images (Fig. 10). In PMMA, the scratches are remarkably uniform along their length, consistent with the constancy of F_L/F_N and u/R. In contrast, in Al, the scratches exhibit scalloped edges, with characteristic wavelengths that mimic the oscillations in F_L/F_N and u/R. It is surmised that this behavior is due to a stick-slip phenomenon.

Scratch force measurements from about 100 tests with the 1 μm radius indenter are summarized in Fig. 11(*a*). When plotted as F_L/F_N versus $\sqrt{F_N/R^2\sigma_y}$ (assuming $\sigma_y=H/3$), the results are linear for both materials and exhibit similar slopes: $k_0=0.17$ and 0.26 for PMMA and Al, respectively. These values are in reasonable agreement with those obtained from the finite element calculations: $0.18 \leqslant k_0 \leqslant 0.26$ for $0 \leqslant \mu \leqslant 0.25$. The results of scratch tests performed with the 50 μm radius tip are plotted on Fig. 11(*b*). The apparent friction coefficients obtained from the latter tests initially decrease with increasing normal force (likely due to fine-scale surface roughness [1]) but then reach plateau levels and remain constant with further increases in force. For PMMA, yielding initiates at $\sqrt{F_N/R^2\sigma_y} \approx 0.09$—somewhat above the values in

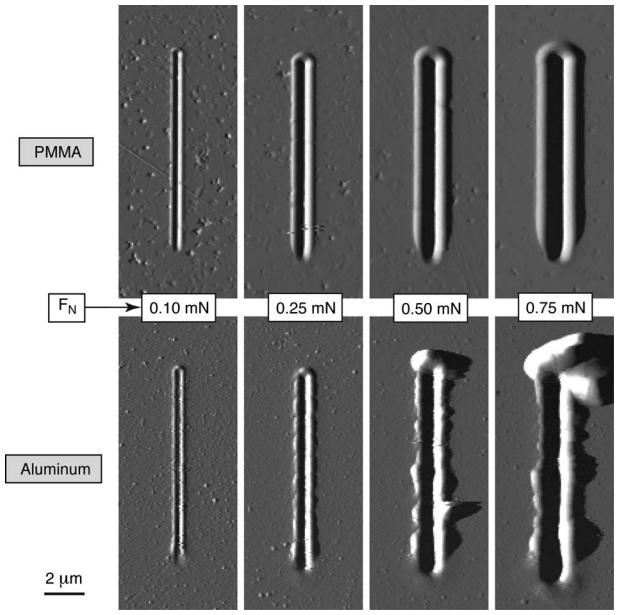

Fig. 10 SPM images of scratches in PMMA (top) and Al (bottom) at various levels of normal force

Fig. 11(*b*)—and thus the plateau value, $F_L/F_N=0.27 \pm 0.02$, is deemed to be the intrinsic friction coefficient. For Al, yielding is predicted to occur at a lower force, $\sqrt{F_N/R^2\sigma_y} \approx 0.01$, near the transition. Although the plateau is seemingly in the postyielding domain, the effect of plasticity (via Eq. (4), plotted as a dashed line in Fig. 11(*b*)) is negligible over the force range of interest. As a result, the average plateau value, $F_L/F_N=0.20 \pm 0.01$, is taken as the friction coefficient for this system. Both friction coefficients obtained in this manner are virtually identical to those inferred from extrapolations of the data in Fig. 11(*a*) to $\sqrt{F_N/R^2\sigma_y}=0$.

5 Concluding Remarks

A mechanistic framework for interpreting scratch tests on plastically deformable materials has been presented. Three behavioral

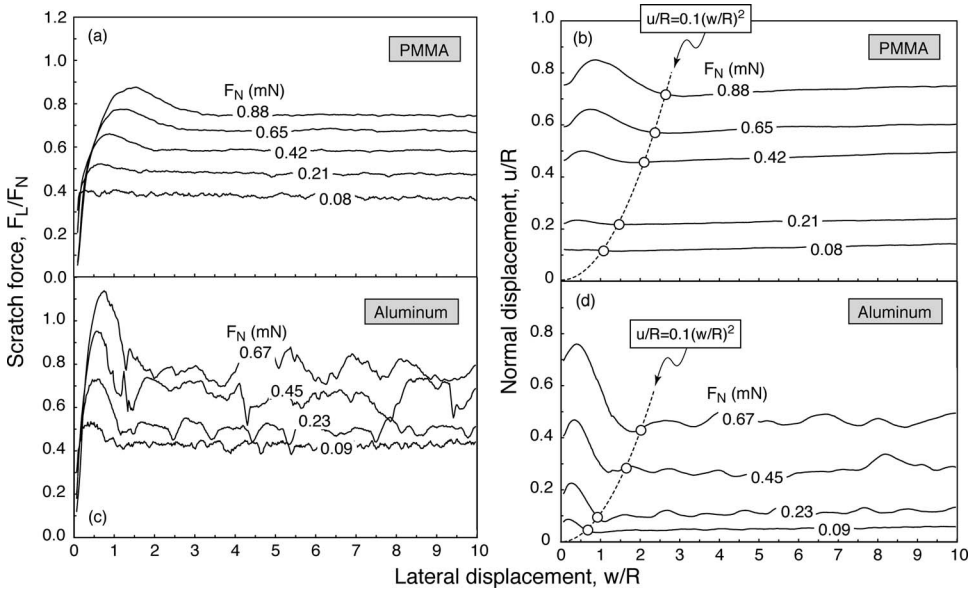

Fig. 9 Experimental measurements of scratch force and normal displacement for (*a*) and (*b*) PMMA and (*c*) and (*d*) Al. The open circles in (*b*) and (*d*) denote approximate points at which steady state is attained.

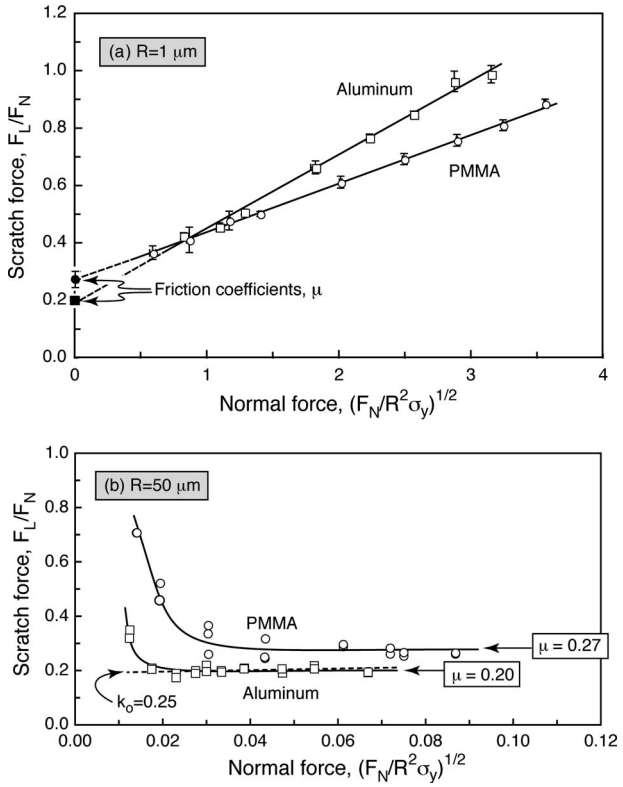

Fig. 11 Summary of scratch force measurements. Tests performed with (*a*) 1 μm and (*b*) 50 μm tip radius indenters. The error bars represent standard deviations. The values of F_L/F_N at $F_N/R^2\sigma_y=0$ in (*a*) were obtained from the plateau values in (*b*). The dashed line in (*b*) represents the predicted dependence on $\sqrt{F_N/R^2\sigma_y}$ through Eqs. (4) and (11) for $\mu=0.2$.

domains have been identified. For smooth surfaces, the scratch force F_L/F_N is constant when the normal force is below that needed to initiate yield ($\sqrt{F_N/R^2\sigma_y} \leq 5\varepsilon_y$) and exhibits a linear dependence on $\sqrt{F_N/R^2\sigma_y}$ in the high force domain ($\sqrt{F_N/R^2\sigma_y} \geq 15\varepsilon_y$). Within the transition ($5\varepsilon_y \leq \sqrt{F_N/R^2\sigma_y} \leq 15\varepsilon_y$), the effects of plasticity are small and, thus, to a good approximation, $F_L/F_N \approx \mu$.

Although not explicitly addressed in this study, a fourth domain may arise at low force levels. For most real surfaces (ones that are not atomically smooth), contact initially occurs at discrete asperities [1]. If the number density of asperities (per unit nominal contact area) remains constant and the asperities deform elastically, the true contact area would scale as $A_t \propto a^2 \propto F_N^{2/3}$. Assuming, at the simplest level, that the lateral force needed for sliding is proportional to A_t, it follows that the friction coefficient should scale as $\mu \equiv F_L/F_N \propto F_N^{-1/3}$. This prediction is qualitatively consistent with the reduction in friction coefficient with increasing F_N for both PMMA and Al at the lowest force levels.

Strictly, the present numerical results are applicable to materials that exhibit time-independent, essentially perfectly plastic behavior subsequent to yielding. The effects of viscoplasticity (pertinent to polymers such as PMMA) and strain hardening (intrinsic to pure Al) have yet to be probed. Such effects may account for the slight differences in values of k_0 obtained for the two materials as well as discrepancies between the experimental values and those from the finite element calculations.

Acknowledgment

The authors gratefully acknowledge financial support from the National Institute of Health (NIHR01DE014672).

References

[1] Bhushan, B., 1999, *Principles and Applications of Tribology*, Wiley, New York.
[2] Fisher-Cripps, A. C., 2004, *Nanoindentation*, Springer, New York.
[3] Gouldstone, A., Chollacoop, N., Dao, M., Li, J., Minor, A. M., and Shen, Y. L., 2007, "Indentation Across Size Scales and Disciplines: Recent Developments in Experimentation and Modeling," Acta Mater., **55**, pp. 4015–4039.
[4] Pontin, M. G., Moses, D. N., Waite, J. H., and Zok, F. W., 2007, "A Nonmineralized Approach to Abrasion Resistant Biomaterials," Proc. Natl. Acad. Sci. U.S.A., **104**(34), pp. 13559–13564.
[5] Lafaye, S., and Troyon, M., 2006, "On the Friction Behavior in Nanoscratch Testing," Wear, **261**(7–8), pp. 905–913.
[6] Krupička, A., Johansson, M., and Hult, A., 2003, "Use and Interpretation of Scratch Tests on Ductile Polymer Coatings," Prog. Org. Coat., **46**(1), pp. 32–48.
[7] Bucaille, J. L., Felder, E., and Hochstetter, G., 2004, "Experimental and Three-Dimensional Finite Element Study of Scratch Test of Polymers at Large Deformations," ASME J. Tribol., **126**(2), pp. 372–379.
[8] Wong, J. S. S., Sue, H. J., Zeng, K. Y., Li, R. K. Y., and Mai, Y. W., 2004, "Scratch Damage of Polymers in Nanoscale," Acta Mater., **52**(2), pp. 431–443.
[9] Liu, Z., Sun, J., and Shen, W., 2002, "Study of Plowing and Friction at the Surfaces of Plastic Deformed Metals," Tribol. Int., **35**(8), pp. 511–522.
[10] Charitidis, C. A., and Logothetidis, S., 2005, "Effects of Normal Load on Nanotribological Properties of Sputtered Carbon Nitride Films," Diamond Relat. Mater., **14**(1), pp. 98–108.
[11] Ma, X. G., Komvopoulos, K., Wan, D., Bogy, D. B., and Kim, Y. S., 2003, "Effects of Film Thickness and Contact Load on Nanotribological Properties of Sputtered Amorphous Carbon Thin Films," Wear, **254**(10), pp. 1010–1018.
[12] Adams, M. J., Allan, A., Briscoe, B. J., Doyle, P. J., Gorman, D. M., and Johnson, S. A., 2001, "An Experimental Study of the Nano-Scratch Behaviour of Poly(Methyl Methacrylate)," Wear, **251**(1–12), pp. 1579–1583.
[13] Habelitz, S., Marshall, S. J., Marshall, G. W., Jr., and Balooch, M., 2001, "The Functional Width of the Dentino-Enamel Junction Determined by AFM-Based Nanoscratching," J. Struct. Biol., **135**(3), pp. 294–301.
[14] Subhash, G., and Zhang, W., 2002, "Investigation of the Overall Friction Coefficient in Single-Pass Scratch Test," Wear, **252**(1–2), pp. 123–134.
[15] Felder, E., and Bucaille, J. L., 2006, "Mechanical Analysis of the Scratching of Metals and Polymers With Conical Indenters at Moderate and Large Strains," Tribol. Int., **39**(2), pp. 70–87.
[16] Wredenberg, F., and Larsson, P. L., 2007, "On the Numerics and Correlation of Scratch Testing," J. Mech. Mater. Struct., **2**, pp. 573–594.
[17] Bellamare, S., Dao, M., and Suresh, S., 2007, "The Frictional Sliding Response of Elasto-Plastic Materials in Contact With a Conical Indenter," Int. J. Solids Struct., **44**, pp. 1970–1989.
[18] Bellamare, S. C., Dao, M., and Suresh, S., 2008, "Effects of Mechanical Properties and Surface Friction on Elasto-Plastic Sliding Contact," Mech. Mater., **40**, pp. 206–219.
[19] Mesarovic, S. D., and Fleck, N. A., 1999, "Spherical Indentation of Elastic-Plastic Solids," Proc. R. Soc. London, Ser. A, **455**, pp. 2707–2728.
[20] Johnson, K. L., 2001, *Contact Mechanics*, Cambridge University Press, Cambridge, UK.
[21] Park, Y. J., and Pharr, G. M., 2004, "Nanoindentation With Spherical Indenters: Finite Element Studies of Deformation in the Elastic-Plastic Transition Regime," Thin Solid Films, **447–448**, pp. 246–250.

A Materials Selection Protocol for Lightweight Actively Cooled Panels

Lorenzo Valdevit
Mechanical and Aerospace Engineering Department,
University of California,
Irvine, CA 92697-3975

Natasha Vermaak

Frank W. Zok

Anthony G. Evans

Materials Department,
University of California,
Santa Barbara, CA 93106-5050

This article provides a materials selection methodology applicable to lightweight actively cooled panels, particularly suitable for the most demanding aerospace applications. The key ingredient is the development of a code that can be used to establish the capabilities and deficiencies of existing panel designs and direct the development of advanced materials. The code is illustrated for a fuel-cooled combustor liner of a hypersonic vehicle, optimized for minimum weight subject to four primary design constraints (on stress, temperatures, and pressure drop). Failure maps are presented for a number of candidate high-temperature metallic alloys and ceramic composites, allowing direct comparison of their thermostructural performance. Results for a Mach 7 vehicle under steady-state flight conditions and stoichiometric fuel combustion reveal that, while C–SiC satisfies the design requirements at minimum weight, the Nb alloy Cb752 and the Ni alloy Inconel X-750 are also viable candidates, albeit at about twice the weight. Under the most severe heat loads (arising from heat spikes in the combustor), only Cb752 remains viable. This result, combined with robustness benefits and fabrication facility, emphasizes the potential of this alloy for scramjets. [DOI: 10.1115/1.2966270]

Keywords: active cooling, lightweight structures, sandwich panels, hypersonics, multifunctional optimization, thermal stresses, materials selection

1 Introduction

Components that experience extreme heat flux, while simultaneously supporting pressure loads, are frequently encountered in aerospace and power systems. In some cases, the challenge can be addressed by using an efficient means for spreading the heat and then convecting or radiating to the environment from a large area. Heat pipes are especially effective for this purpose [1]. This strategy is not always viable, whereupon active cooling by a fluid pumped through the structure is required. In such cases, before embarking on materials development and fabrication, it would be most beneficial to have a procedure that simultaneously selects the preferred material and design, while also highlighting the inadequacies of existing materials. The task is complicated by the intertwining of material properties and geometric parameters. Namely, the optimal geometries depend on materials properties in a highly coupled way. The purpose of this article is to describe the principles governing the development of a code that couples material choices with design parameters and to present an illustration.

The procedure is illustrated for a fuel-cooled combustor liner of a hydrocarbon-powered hypersonic vehicle (Fig. 1) [2,3]. This choice is timely because, while the potential to achieve positive thrust from a scramjet has been recently demonstrated [2–4], selecting materials and generating designs that resist the thermomechanical loads for the duration of a typical mission have proved to be daunting. Some aspects of the design and performance of actively cooled combustion systems have been explored [5–8], including geometry optimization [9–12]. However, a comprehensive treatment that accounts for the complete set of thermomechanical constraints is lacking.

The structure of this article is as follows. A synopsis of the analysis and optimization protocol is outlined in Sec. 2. Analytical models for temperature distributions and thermomechanical stresses are presented in Secs. 3 and 4. Also included are the results from computational fluid dynamics (CFD) and finite element (FE) calculations, designed to critically assess the accuracy of the model predictions and the key underlying assumptions. Formulation of the optimization scheme and its application to a combustor liner of a notional Mach 7 scramjet vehicle are contained in Sec. 5: inclusive of an assessment of the suitability of a wide range of candidate structural materials. The implications for materials selection follow. For facility of presentation, the analytic details are presented in Appendixes.

2 Principles and Procedures

A prototypical combustor wall for an aerospace system (Fig. 1) comprises a sandwich plate subject to three loading mechanisms: external pressure from the combustion gases, internal pressure from the coolant, and thermal loads due to the temperature differences between the combustion side and the vehicle exterior. In addition to the obvious thermostructural requirements (no melting and no yielding/fracture), the design may be limited by fuel-specific constraints (e.g., avoiding coking while promoting cracking) and the need to limit pressure losses in the cooling system.

A variety of shapes can be envisioned for the cooling ducts. Rectangular, triangular, or rhombic cross section can be manufactured to ensure thin walls and are easiest to model analytically. The present study focuses on rectangular ducts. Extension to other periodic shapes is elementary and is not expected to modify the main conclusions.

The protocol employed for thermostructural analysis and design optimization consists of the following steps (Fig. 2). (i) A range is defined for the expected heating loads (represented by the heat transfer coefficient h_G of the hot gases) and the cooling efficiency (represented by the coolant flow rate per unit width of panel, $\dot{V}^{\text{eff}}$). (ii) A candidate material is selected and its physical and mechanical properties either measured or obtained from handbooks. (iii) At each point in $(h_G, \dot{V}^{\text{eff}})$ space, the design parameters are systematically varied over a prescribed range and the temperatures

Contributed by the Applied Mechanics Division of ASME for publication in the JOURNAL OF APPLIED MECHANICS. Manuscript received February 24, 2008; final manuscript received June 6, 2008; published online August 22, 2008. Review conducted by Martin Ostoja-Starzewski.

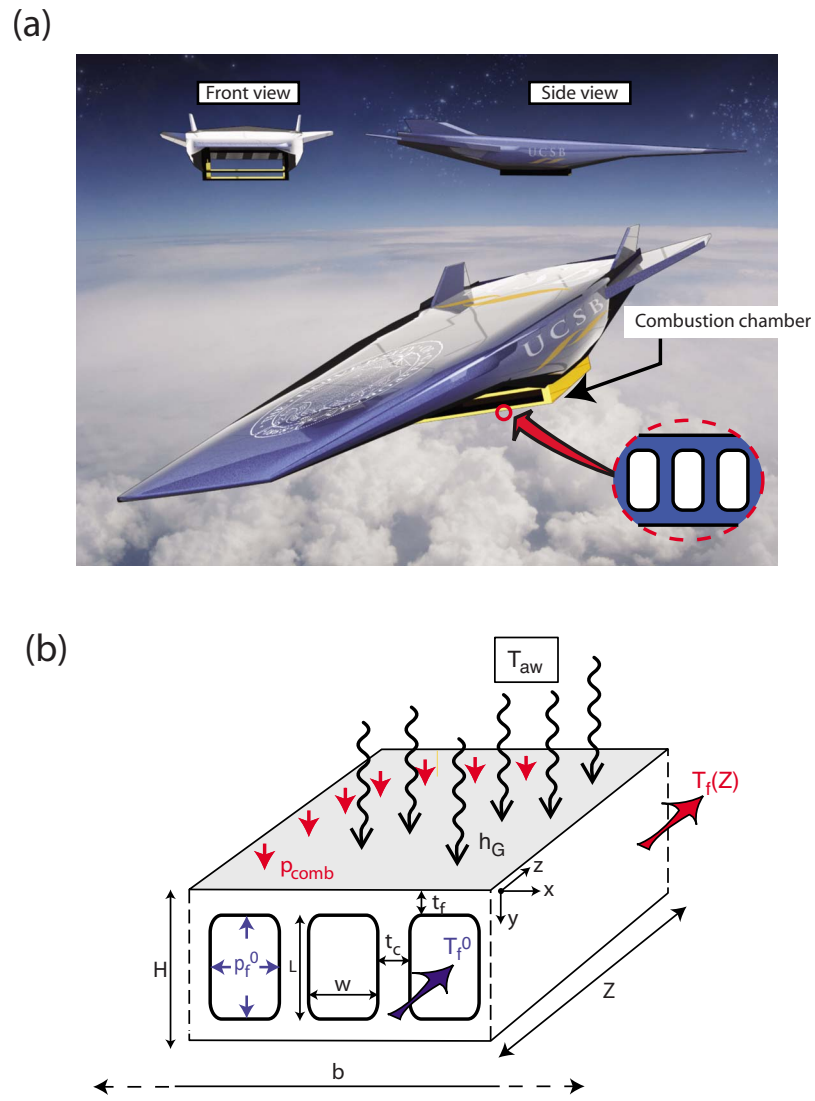

Fig. 1 (***a***) **Artist rendition of a prototypical hypersonic air-breathing vehicle.** (***b***) **Schematic of actively cooled panel with thermostructural loads.**

and stresses calculated for each combination. Upon comparison with material and coolant properties, the viability of the design is ascertained. (iv) provided that solutions exist, the design is optimized for minimum mass, subject to a number of design constraints. Otherwise, if a solution is not found, the point $(h_G, \dot{V}^{\text{eff}})$ is deemed external to the design space. (v) Once the entire design space has been scanned for each candidate material, comparisons are made of materials on the basis of structural robustness (namely, the extent of feasible solution area in $(h_G, \dot{V}^{\text{eff}})$ space) and weight efficiency.

Temperatures in the panel have been derived using a two-dimensional resistance network model and the solutions verified by the CFD and FE calculations. The utility of the temperature predictions is twofold. First, they are used to ensure that the conditions remain within allowable limits for the material and the coolant. Second, they become input for calculation of thermal stresses. To permit formulation of the structural constraints, these stresses are superimposed on those induced by the pressure loads, both external to the liner (inside the combustion chamber) and within the cooling channels. The thermomechanical stresses are required to remain below the local temperature-dependent material strength. A constraint on pressure drop is also imposed.

The assessment facilitates three goals. (i) It determines the relative merits of representative categories of high-temperature materials (Tables 1 and 2), inclusive of refractory alloys and ceramic matrix composites (CMCs). (ii) It provides a focus for the development of advanced materials that outperform existing options. (iii) It assesses the possible benefits of superposing a thermal barrier coating (TBC), such as yttria-stabilized zirconia (YSZ), motivated by the extensive use of such coatings in aeroturbines [13].

3 Temperature Distribution

To obtain analytic estimates of the temperatures, three simplifications are invoked. (i) The top face of the panel is exposed to hot gases at a uniform adiabatic wall temperature T_{aw} and constant heat transfer coefficient h_G, whereas the bottom face and the sides are thermally insulated. Consequently, all of the heat passed through the top face is carried away by the cooling fluid. (ii) No heat is conducted along the length of the panel in either the structure or the coolant. This assumption results in slightly conservative temperature estimates. (iii) The coolant temperature is uniform at each cross section, increasing monotonically with distance z along the panel length from an initial value T_f^o at the channel inlet to its maximum $T_f^{\max}$ at the outlet.

The thermal resistance network is illustrated in Fig. 3 and the solutions for the key temperatures are detailed in Appendix A. The

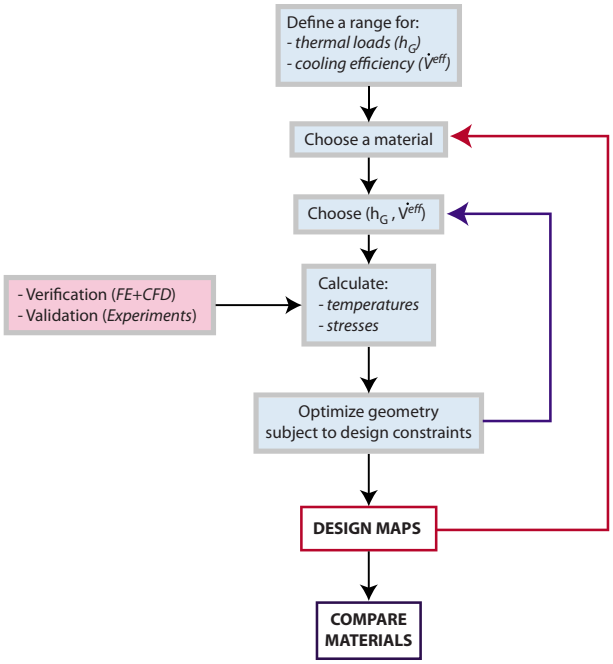

Fig. 2 Schematic of the materials selection procedure

main goals are to ascertain the maximum temperatures in the material $T_m^{\max}$ and in the fuel $T_f^{\max}$. Additionally, for the ensuing determination of thermal stresses, four temperature differences are defined. The first two are those across the top face (in the y-direction): one directly above the core web, ΔT_{tf}^{c}, and the second at the midpoint between a pair of webs, ΔT_{tf}^{w}. The second two, $\Delta T_{\text{panel}}^{c}$ and $\Delta T_{\text{panel}}^{w}$, are those across the entire panel (also in the y-direction), measured from the middle of the top face to the bottom face, directly above and between the core webs. The analysis indicates that all the preceding temperature differences are greatest at the inlet ($z=0$).

CFD calculations, performed using the commercial code, FLUENT©, were used to assess the uniformity of the heat transfer coefficient around the internal surface of the channel and the effect of longitudinal conduction. The panel used for these calculations has a near-optimal geometry (detailed in Sec. 5) and made from Inconel X-750 (a Ni-based superalloy). Approximate chemical compositions and pertinent material properties are summarized in Tables 1 and 2. The coolant is taken to be JP-7 jet fuel (Table 3). Both the fuel and the solid are meshed using three-dimensional elements. The fuel flow rate and hot gas temperature are selected to be representative of a notional Mach 7 cruise vehicle (Sec. 5). The results (Fig. 4(*a*)) affirm that h_C is essentially uniform over the interior surface of the top face, where the vast majority of the heat is transferred to the fuel. The variations around the corners and along the core and bottom face are deemed unimportant, because the heat transfer averaged over the channel perimeter conforms to the value obtained from established correlations [14], with an accuracy of about 10%. Additionally, the axial distribution of the section-averaged h_C confirms that full thermal and kinematical developments are attained after the fuel has traveled a distance of a few hydraulic diameters (Fig. 4(*b*)). Effects of longitudinal conduction within the solid were ascertained by comparing CFD calculations with and without axial conduction. For the parameter values selected, the two sets of results are indistinguishable.

A further assessment of the predicted temperatures was made through FE calculations of the same panel, performed using the ABAQUS© code. The mesh consists of quadratic generalized plane strain elements with reduced integration (CPEG8RHT). Convective boundary conditions are applied both to the top face ($h_G=445$ W/m^2 K, $T_{\text{aw}}=3050$ K) and the internal channel surfaces ($h_C=2266$ W/m^2 K, $T_f=653$ K). The fuel temperature corresponds to the predicted exit temperature for the relevant geometry and boundary conditions, assuming an entry fuel temperature $T_f^o=400$ K. The remainder of the cell perimeter is thermally insulated.

The steady-state temperature distribution at the channel outlet and the corresponding analytic predictions at eight critical locations are shown in Fig. 5. The comparisons reveal that the maximum temperature in the structure is captured to within 1% accuracy. Moreover, the temperature differences that drive the thermal stresses ($\Delta T_{\text{panel}}=(\Delta T_{\text{panel}}^{c}+\Delta T_{\text{panel}}^{w})/2$ and $\Delta T_{tf}=\Delta T_{tf}^{c}$, see Appendix B for details) are also predicted adequately (within about 8%). FE calculations for other panel designs and material properties yielded similar consistency between the numerical results and analytic predictions.

Table 1 Approximate chemical compositions of the candidate metallic alloys

Material	Approximate chemical composition (wt %)
Inconel 625	Ni–20% Cr–10% Mo–5% Fe–3% Nb
Inconel X-750	Ni–15% Cr–7% Fe–2.5% Ti
Ti 6Al 4V	Ti–6% Al–4% V
Ti β 21S	Ti–15% Mo–2.7% Nb–3% Al–0.2% Si
NARloy-Z	Cu–3% Ag–0.5% Zr
GRCop-84	Cu–6.5% Cr–5.8% Nb
Nb-Cb752	Nb–10% W–2.5% Zr

4 Stress Distributions

Stress estimates were obtained using standard concepts of plate bending and stretching and assuming the materials to be linear elastic. Derivations and solutions are in Appendix B. In practice, some nonlinearity may occur in the most highly stressed locations, enabling stress redistribution and shakedown [15,16]. Conse-

Table 2 Thermal and mechanical properties of the candidate materials

Material	T^* (K)	σ_Y (T_f^0) (MPa)	$d\sigma_Y/dT$ (MPa/K)	E (GPa)	CTE (10^{-6}/K)	k_s (W/m K)	ρ_s (kg/m^3)
Inconel 625	1100	427	−0.31	164	14.0	20.0	8440
Inconel X-750	1100	795	−0.39	128	16.0	23.0	8276
Ti–6Al–4V	675	909	−0.83	90	10.0	11.0	4430
Ti-β-21S	815	1222	−1.46	100	10.3	21.0	4940
NARloy-Z	811	99	−0.009	125	17.0	350.0	9130
GRCop-84	973	205	−0.18	90	19.0	285.0	8756
Nb–Cb752	1470	382	−0.17	110	7.4	50.0	9030
SiC–SiC	1640	200	—	240	4.1	25(∥), 20 (⊥)	2900
C–SiC	1810	200	—	100	2.0	15(∥), 5 (⊥)	2000
TBC (ZrO_2)						1.0	3000

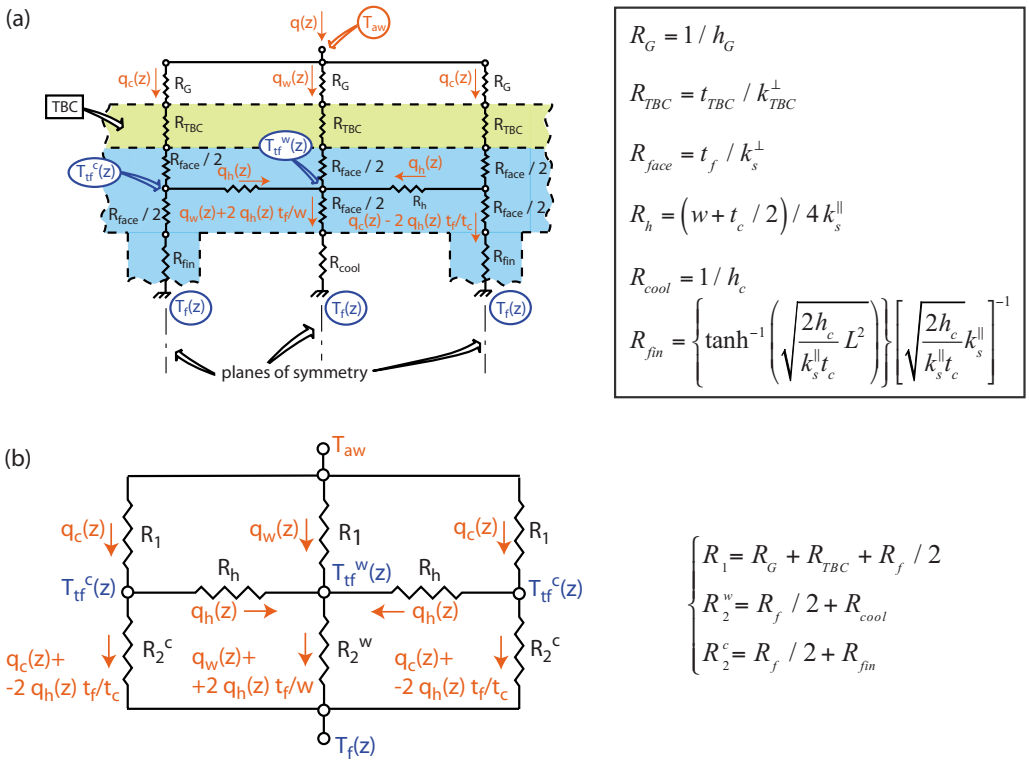

Fig. 3 (*a*) **Thermal resistance network used to determine temperature distributions, along with expressions for all relevant thermal resistances.** (*b*) **Effective network.**

quently, in the absence of high cycle fatigue, the ensuing results are conservative. A subsequent article will incorporate yielding and shakedown and provide an assessment of the extent of the conservatism. Although the present analysis is for a flat panel, its extension to cylindrical configurations is straightforward.

4.1 Boundary Conditions. Two idealized sets of boundary conditions are considered.

I. Linear frictionless supports along the edges in the z-direction (Fig.6(a)). This constraint prevents bending in the *z*-direction, while allowing it in the *x*-direction (albeit with no rotation at the ends). Uniform thermal expansion is allowed along all directions. The analog for a cylinder would be the absence of constraint on

Table 3 Physical properties of JP-7 jet fuel

Fuel	k_f (W/m K)	μ_f (Pa s)	c_p (J/kg K)	Pr_f	ρ_f (kg/m^3)	T_{coke} (K)
JP-7	0.11	1.984×10^{-4}	2575	4.64	800	975

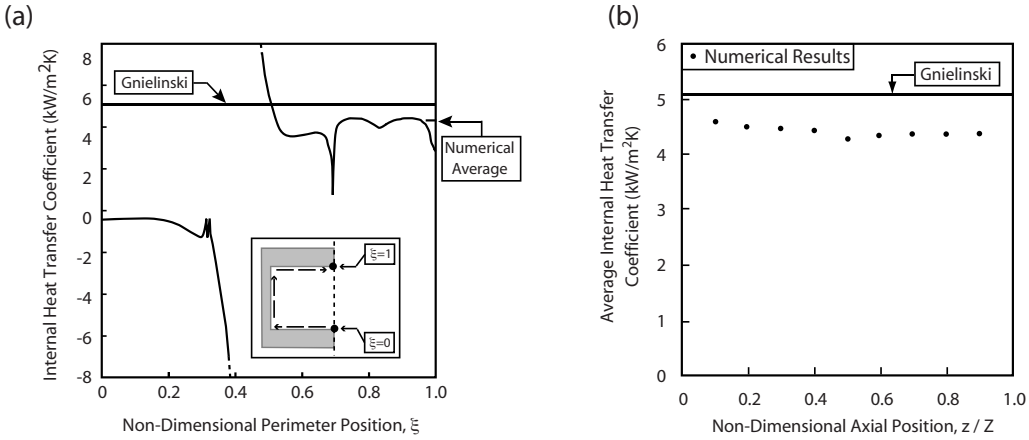

Fig. 4 Distribution of the heat transfer coefficient in the cooling channel extracted from the CFD simulation of a near-optimal Inconel X-750 panel. (*a*) **Variation of pointwise h_c around channel perimeter at $z/Z=0.9$.** (*b*) **Variation of cross-section averaged h_c along the axial direction. The value extracted from the Gnielinski correlation (Eq. (A1)) and used in the analytical model is depicted for comparison.**

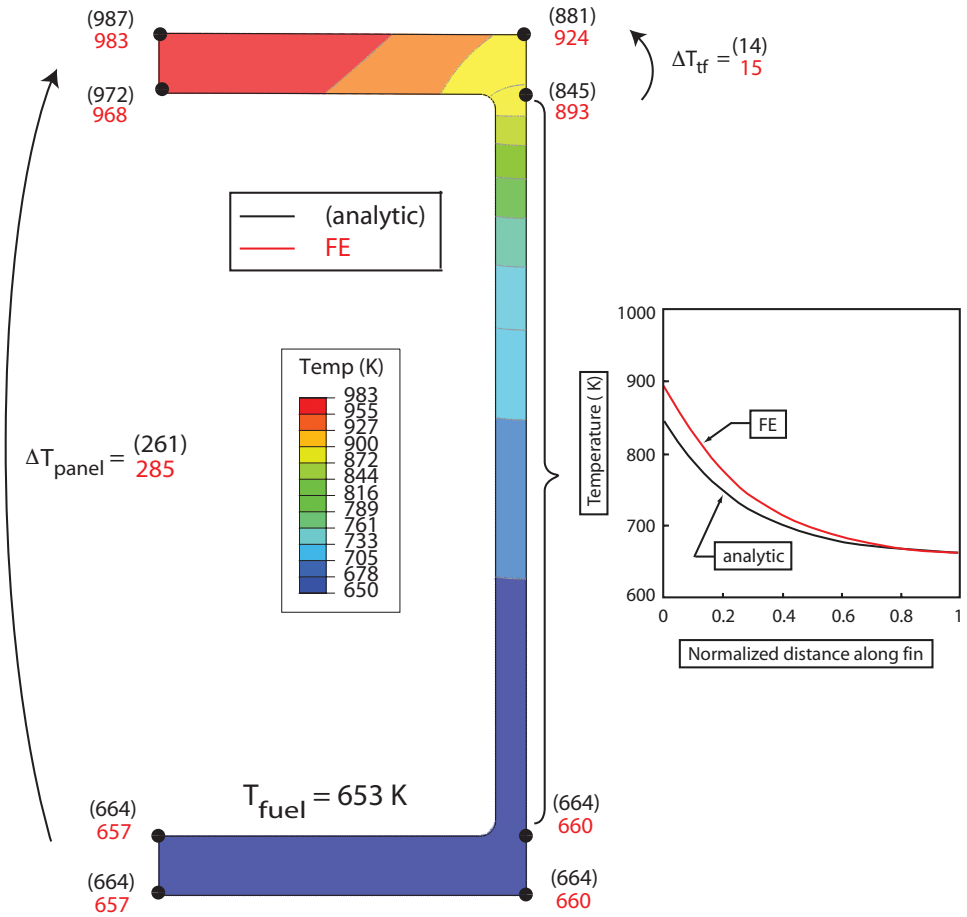

Fig. 5 Comparison of analytical and numerical (FE) temperature distributions for an optimal Inconel X-750 panel. All temperatures are in Kelvin. Values in parentheses are analytical predictions. Both the maximum temperature in the structure and the temperature differences that drive the thermal stresses are captured accurately.

changes in both the diameter and axial length. This boundary condition can also represent *multiple* linear frictionless supports (Fig. 6(*b*)) by simply re-interpreting the panel width b as the support spacing.

II. Two-dimensional continuous bed of rollers (Fig. 6(c)). Uniform thermal expansion is permitted in all directions. The external pressure does not cause panel-level bending but the internal pressure can bend individual face segments.

The use of rollers instead of frictional supports allows uniform thermal expansion of the panel (with no bending). While the practical implementation may be challenging, attaining these conditions is essential to viable solutions. Otherwise, if the plate is clamped on all sides, the maximum temperature increase that can be sustained without yielding is only $\Delta T_{\max}=(1-\nu)\sigma_Y/E\alpha$ (with E being Young's modulus, α the thermal expansion coefficient, σ_Y the material yield strength, and ν Poisson's ratio) [17], well below the upper use temperature of all of the materials (Fig. 6(*d*)).

Both the pressure drop and the temperature variation along the panel length have been neglected. This assumption, combined with the imposed boundary conditions, ensures that generalized plane strain conditions are attained along the z-direction.

4.2 Failure Locations. Although the temperature differences, and hence the thermal stresses, are greatest at the channel inlet, the material strength is also greatest at this location. Typical strength reductions with increasing temperature suggest the possibility of preferential failure at the outlet, where the temperature is at its maximum. To ensure accurate prediction of failure initiation, thermal stresses should be ascertained at *each cross section* and compared with material strength at the pertinent (local) temperature. Additionally, the stresses due to pressure loads vary with location within the same cross section and can be of opposite sign relative to those caused by thermal loads. Thus, establishing a priori the failure location is not straightforward.

To address this problem, a set of 18 "critical points" has been identified for close scrutiny, clustered around two failure-susceptible channels: one at the periphery closest to the supports and the other at the center (Fig. 7). Failure of the structure is averted provided that, for metallic alloys, the Mises stress at each point remains below the elastic limit. The analog for CMCs is based on a maximum or minimum principal stress criterion. The internal pressure in the core channels (which induces large tensile stresses in all members) combined with the relatively stubby shape of the optimized members make it unnecessary to design against buckling [18–26].

The accuracy of the stress predictions was verified by FE calculations. Illustrative results are presented for the optimized Inconel X-750 panel subject to the thermal loads described in the preceding section. The calculations use type II boundary conditions and an internal fuel pressure of 4 MPa (The pressure in the combustion chamber can be neglected since it has minimal effect on the stresses for the selected boundary condition.) The bottom is constrained against translation in the y-direction and periodic boundary conditions are imposed on the vertical sides (one side is constrained against translation in the x-direction, whereas all nodes on the other are required to displace equally in the x-direction). The top is traction free.

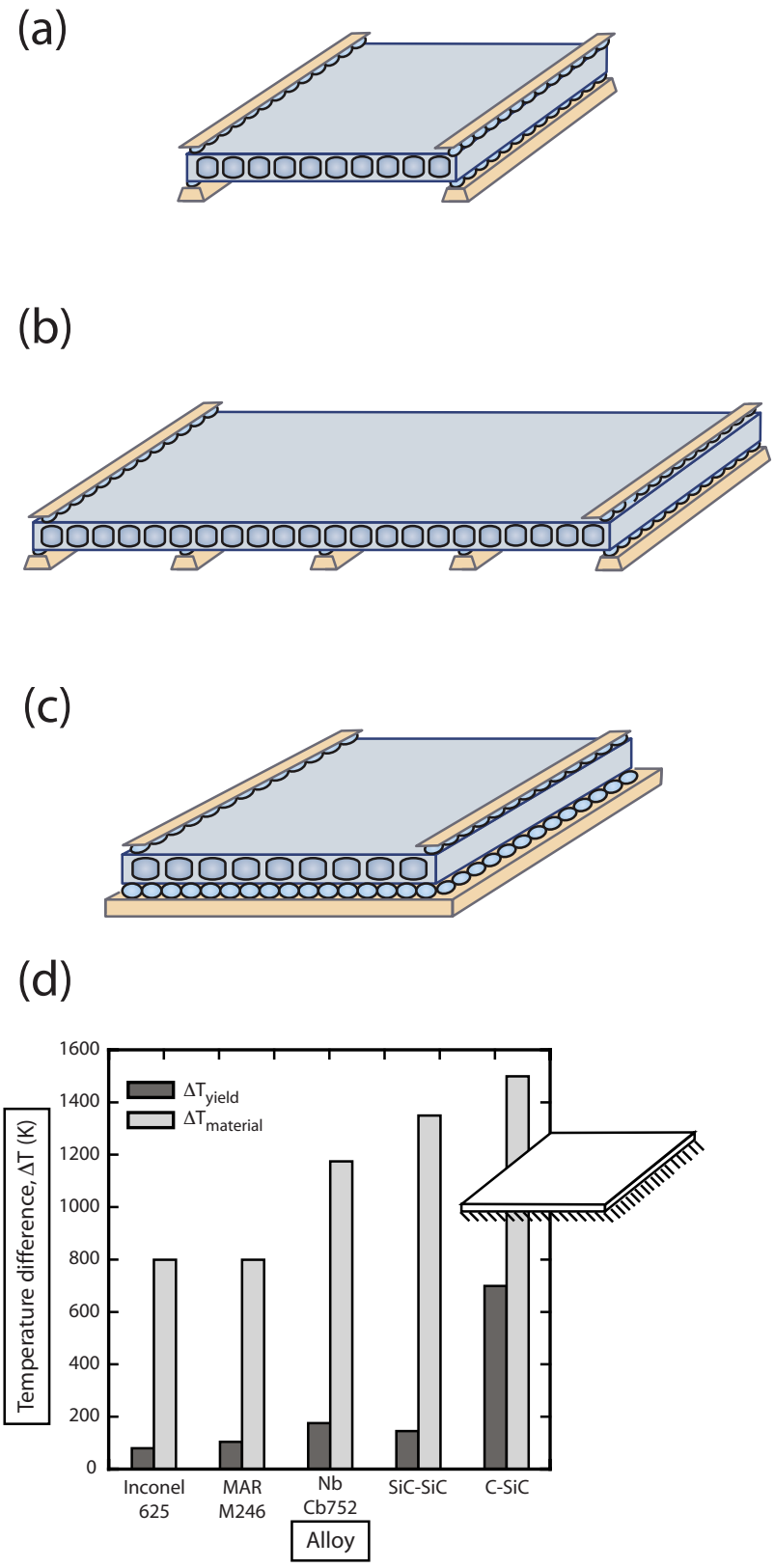

Fig. 6 Mechanical boundary conditions. [(*a*) and (*b*)] Linear rollers on two sides (Type I). (*b*) Multiple linear rollers with regular spacing. (*c*) Uniform two-dimensional bed of rollers, with impeded rotation at the ends (Type II). (*d*) Benchmark boundary condition: plate sitting on rigid foundation (inset). The chart compares the temperature increase from room temperature to the material upper use limit needed to cause yielding. Under this boundary condition, the full high-temperature potential of the materials is not exploited.

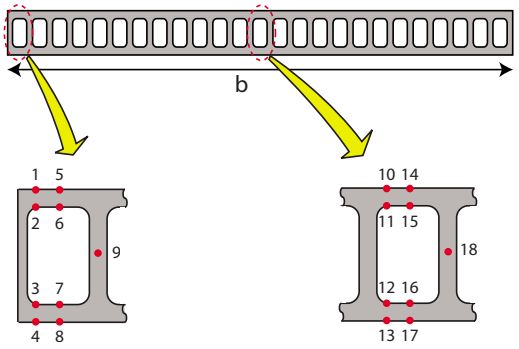

Fig. 7 Unit cells susceptible to local yielding and the 18 critical points

The resulting distribution in the Mises stress is plotted on Fig. 8. Also shown are comparisons between the numerical results and the analytic predictions along the four critical trajectories, corresponding to the external and internal surfaces of both face sheets, for thermal, mechanical, and combined thermomechanical loadings. The analytic prediction is accurate to within 1% at the most highly stressed location (Point 1) and within ~10% at other locations on the top face. The corners (Point 2), where stress intensification is evident, are exceptions. This discrepancy has not been pursued for several reasons. (i) For this particular simulation, because of the relatively low temperature at the corners (Fig. 5), the yield strength is high (Table 2) and, given the stress distribution (Fig. 8), both corners remain elastic. We speculate that this concept generalizes to metallic systems, but a formal proof requires further analysis. (ii) Even if localized plasticity at the corners could not be avoided, the metallics can be readily designed to assure shakedown, wherein local plasticity occurs only during the first few thermomechanical cycles. Such a solution may not be possible for CMCs. (iii) The stress intensification can be reduced by increasing the fillet radius without imposing a significant weight penalty.

The agreement on the bottom face is somewhat worse (~20% at Point 3). This result is implicit in the model, which underestimates the thermal stress in the bottom face to ensure conservative stress estimates on the top face. This choice was made because the critical condition (yielding or fracture) typically occurs in the top face. Comparisons performed for other materials and geometries showed similar correlations.

The numerical calculations confirm that the combined thermomechanical stresses are not necessarily the most dangerous. At Point 5, for instance, the thermal stresses alone are greater than those under thermomechanical loading.

5 Materials Selection for Scramjet Combustor Liners

The materials selection procedure exposed in Sec. 2 is applied to the combustor liner of a Mach 7 scramjet cruise vehicle operating with JP-7 jet fuel. The choice is motivated by the realization

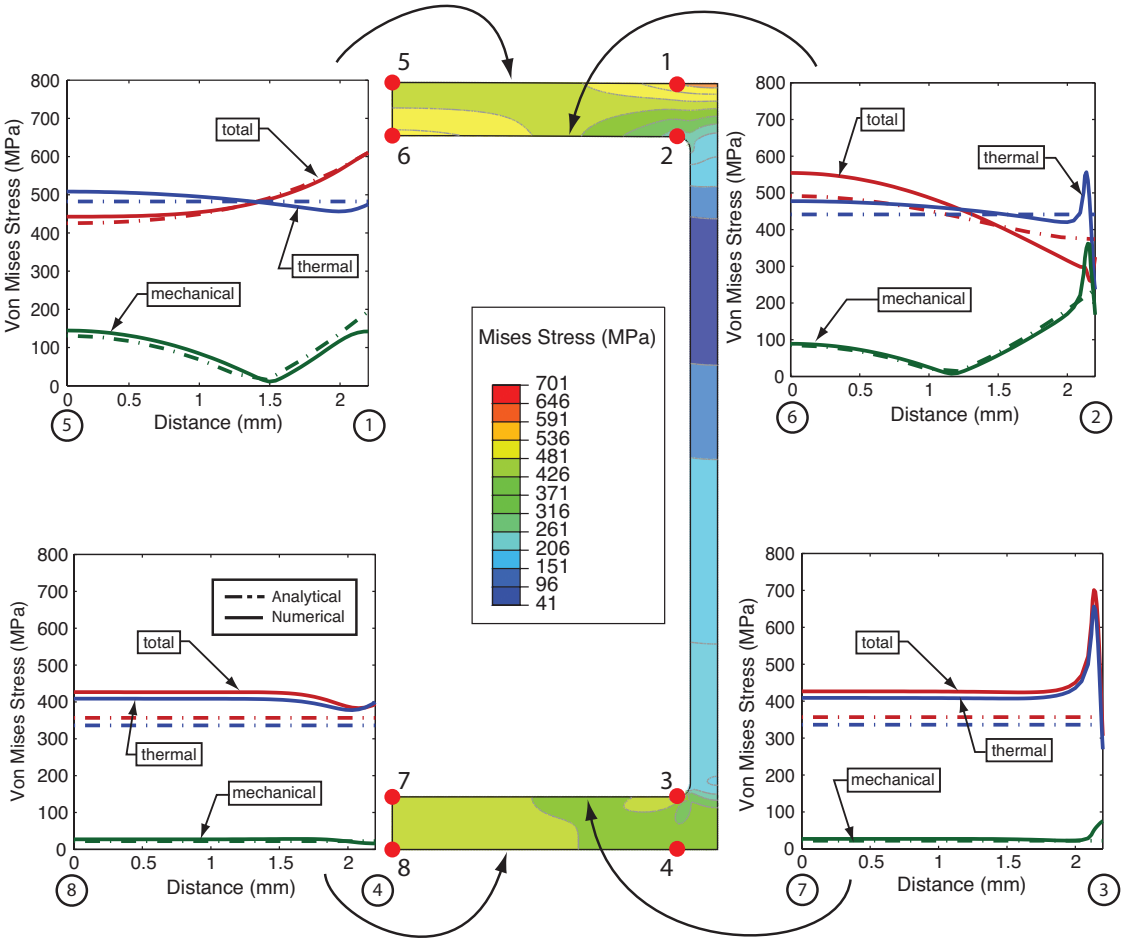

Fig. 8 Comparison of analytical and numerical (FE) von Mises stress distributions for an optimal Inconel X-750 panel. The plots show the results for thermal, mechanical, and combined thermomechanical stresses along the four paths. With the exception of Points 2 and 3, clearly affected by stress intensification, the agreement is satisfactory, particularly on the top face, where the highest stresses generally occur.

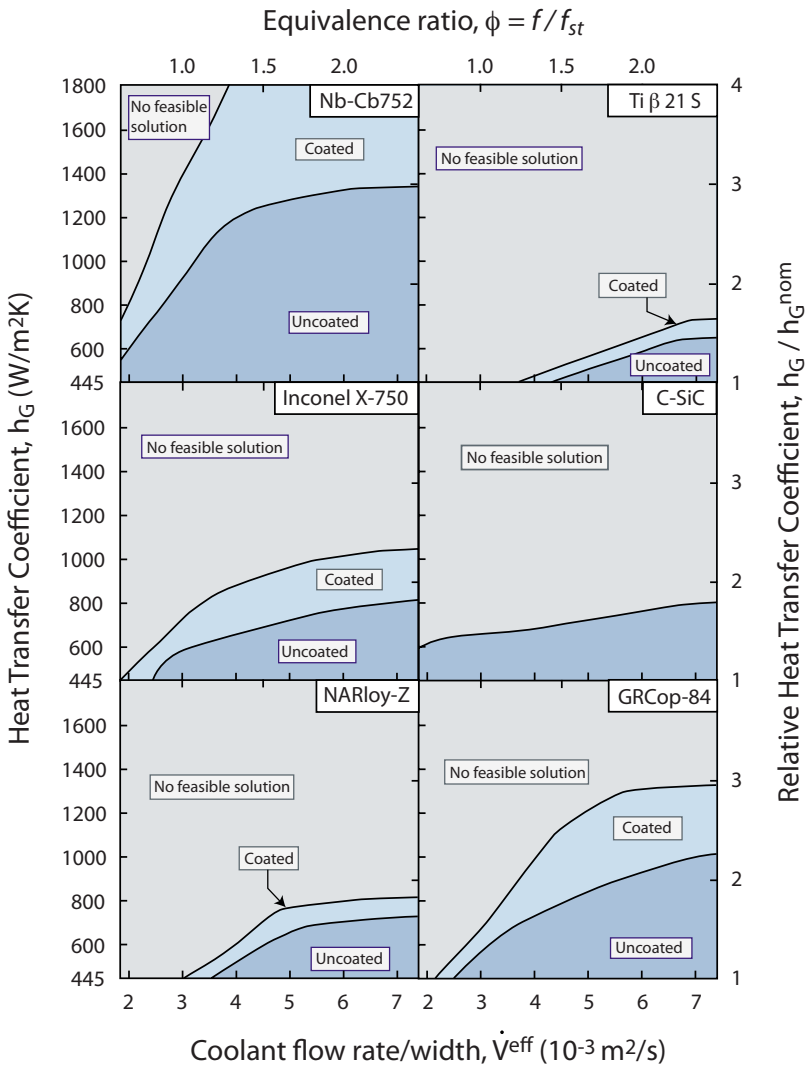

Fig. 9 Design maps for several materials considered in this study, with and without a TBC. The normalizing parameters for the equivalence ratio ($\phi = f/f_{st}$) and the heat transfer coefficient (h_G/h_G^{nom}) are those expected for steady-state Mach 7 flight conditions.

that the design of vehicles in this velocity range is most mature and in urgent need of technological advancements in high-temperature materials and structures.

5.1 Thermomechanical Loads. The thermomechanical loads on the combustor liners depend on nearly every aspect of the vehicle design, including the size and shape of the compression ramp, the size of the combustion chamber, details of the injection system, and combustion efficiency. For the present illustration, the vehicle is assumed to be 10 m long and 2.5 m tall, with a bilinear compression ramp that generates three oblique shocks. The pertinent aerothermodynamic conditions for the prescribed vehicle velocity and optimal flight altitude are detailed in Ref. [3]. Fuel enters the cooling channels with pressure $p_f^o = 4$MPa and initial temperature $T_f^o = 400$ K. On the combustion side, the pressure $p_{comb} = 0.16$ MPa, the adiabatic wall temperature $T_{aw} = 3050$ K and the heat transfer coefficient $h_G = 445$ W/m² K. To assess the effects of potential heat spikes in the combustion chamber, heat transfer coefficients up to 1800 W/m² K are considered. For the stress analysis, Type I boundary conditions are used with an unsupported span, $b = 0.5$ m.

For stoichiometric combustion, the fuel flow rate (per unit width of combustor) is $\dot{V}_{st} = 0.008$ m²/s. Since the total perimeter of the combustor liner is $2(b + H_{comb})$, with H_{comb} the height of the chamber, the effective flow rate per unit width of liner is $\dot{V}_{st}^{eff} = \dot{V}_{st} b / 2(b + H_{comb})$. Upon specifying the dimensions ($b = 0.5$ m and $H_{comb} = 15$ cm), then $\dot{V}_{st}^{eff} = 0.003$ m²/s. To address offstoichiometric combustion, an equivalence ratio ϕ is introduced, defined by $\phi = f/f_{st}$, where f is the actual fuel-to-air mass ratio and f_{st} is the corresponding stoichiometric value. The actual flow rate then becomes $\dot{V}^{eff} = \phi \dot{V}_{st}^{eff}$. The range $0.6 < \phi < 2.5$ is used for subsequent calculations.

5.2 Design Constraints. A candidate design is deemed acceptable provided it satisfies four principal constraints: (i) the stresses induced by the pressure and the thermal loads remain below representative levels of material strength, σ_Y; (ii) the maximum material temperature T_m^{max} does not exceed the upper use limit, T^*; (iii) the fuel temperature remains below that for coking ($T_{coke} = 975$ K [27]); and (iv) the pressure drop through the channels is acceptably low ($\Delta p \leq 0.1$ MPa). Additionally, to ensure that designs can be manufactured, secondary constraints are imposed on some dimensions, notably: channel width $w \geq 2$ mm, channel height $L \geq 5$ mm, face and core wall thicknesses t_c and $t_f \geq 0.4$ mm, and TBC thickness ≤ 0.3 mm.

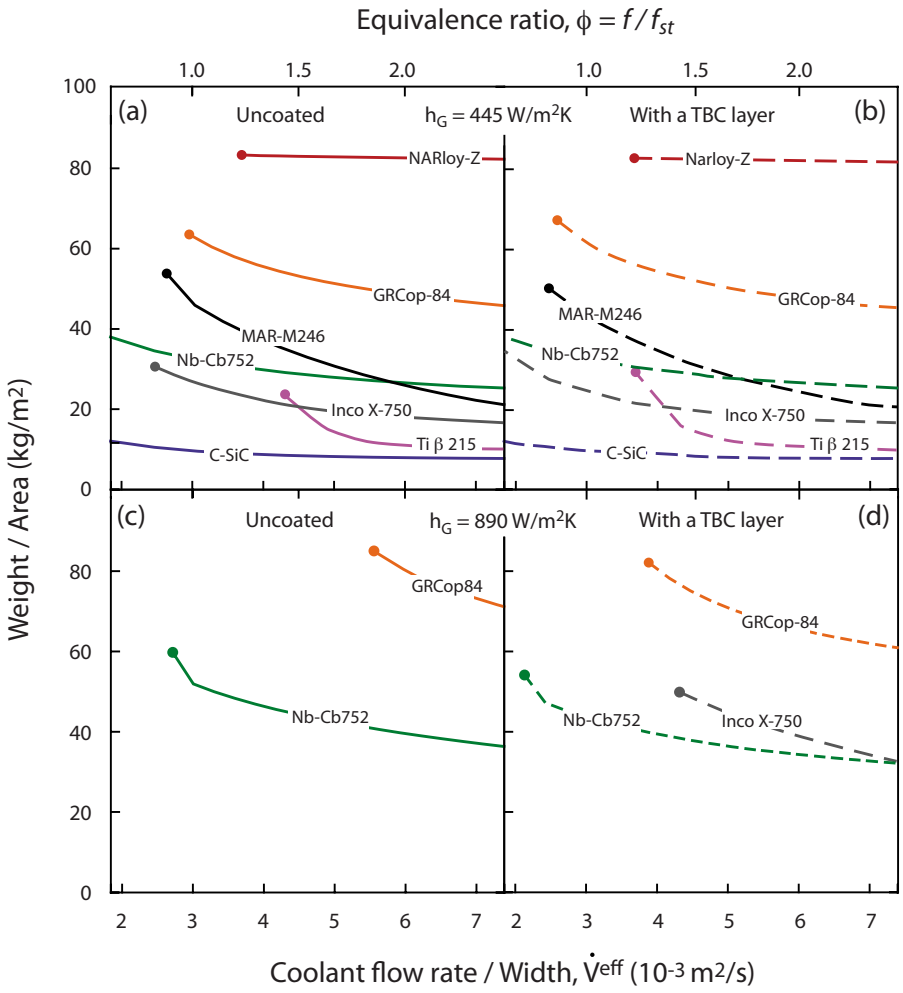

Fig. 10 Minimum weight comparison at two levels of heat transfer: (*a*) and (*b*) h_G=445 and (*c*) and (*d*) 890 W/m² K. [(*a*) and (*c*)] the solid lines represent the results for uncoated materials whereas [(*b*) and (*d*)] the dashed lines are those for TBC coated materials.

For metallic alloys, the yield strength is assumed to decrease linearly with temperature for $T \leq T^*$. For the CMCs, the tensile and compressive strengths are assumed equal and independent of temperature. Caveats on this choice are discussed later.

5.3 Optimization Scheme. Whenever a solution exists, the design was optimized for minimum weight. The mass of the TBC is included to ensure that a finite layer emerges only if it reduces the overall weight. Numerical optimizations were performed using the quadratic optimizer MINCON in MATLAB™. Several randomly generated initial guesses were used to escape from local minima. In some cases, a manual optimization scheme was employed to verify the accuracy of the numerical results.

5.4 Principal Results and Interpretation. The procedure was implemented for a suite of high-temperature materials. Approximate chemical compositions of the candidate metallic alloys are listed in Table 1; relevant mechanical properties (for metallic and ceramic systems) are summarized in Table 2. Design maps are presented in two formats. (i) In the first (Fig. 9), the ordinate is h_G, motivated by the appreciation that shocks passing through the combustor can cause local elevations. The abscissa is the fuel flow rate, $\dot{V}^{\text{eff}}$. The normalizing parameters for the equivalence ratio ($\phi = f/f_{\text{st}}$) and the heat transfer coefficient (h_G/h_G^{nom}) are those expected for steady-state Mach 7 flight conditions. The map specifies domains within which the material can function, with and without a TBC, as well as a domain of inadmissibility. In this scheme, the weight is a function of the location on the map. (ii) In the second (Fig. 10), h_G is fixed (at either 445 W/m² K or 890 W/m² K), the ordinate is the weight of the optimized panel and the abscissa is again the fuel flow rate.

The overarching implications from Fig. 9 are as follows. (i) In all cases where solutions are obtained, increasing the flow rate is beneficial, indicating that the cooling efficiency limits the design (as opposed to the fuel pressure drop). (ii) Among the selected materials, most provide a solution for the nominal Mach 7 conditions (h_G=445 W/m² K). The exceptions are Inconel 625, Ti–6Al–4V, and SiC–SiC, which are *not viable* anywhere within the design space. (iii) The outcome changes radically if the heat load is doubled. Namely, for h_G=890 W/m² K, only the Nb alloy Cb752 and the Cu alloy GRCop-84 are viable without a TBC (albeit an environmental barrier coating will be needed to avert oxidation [28]). Furthermore, Cb752 is the only material that can survive without a TBC at near-stoichiometric fuel flow rates (ϕ =1). (iv) The operational design space of essentially all metallics can be increased by using a TBC, although the benefit differs among materials: Cb752, Inconel X-750, and GRCop-84 showing the largest advantage.

Figure 10 compares the optimal panel weights for cases with and without a TBC. For h_G=445 W/m² K, C–SiC offers the lightest structure (by a factor greater than 2 relative to most metallic

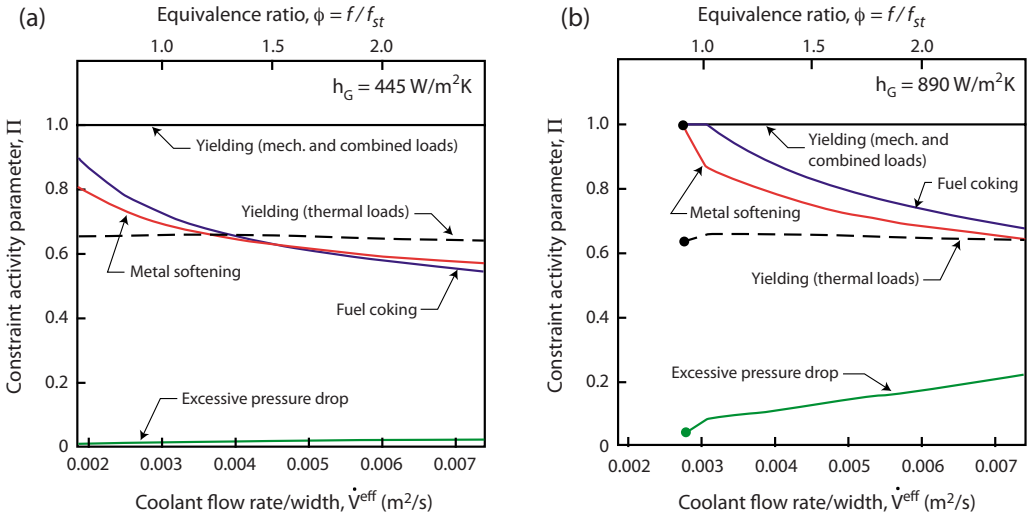

Fig. 11 Constraint activity map for Cb752 for h_G values of (a) 445 W/m^2 K and (*b*) 890 W/m^2 K. Constraint is active when its activity parameter reaches unity. At the lower thermal load, only the therm-omechanical constraints are active (yielding under mechanical and combined loads). When the thermal load is doubled, at low flow rates, both the solid and fuel temperatures approach their maximum allowable value.

alloys), followed by Inconel X-750 and Cb752. Ti-β21S provides a lightweight alternative but only when high fuel flow rates are permitted. For h_G=890 W/m^2 K, the only viable uncoated materials are Cb752 and GRCop-84. However, these two materials exhibit vastly different weight efficiencies: Cb752 is half the weight of GRCop-84. When a TBC is used, the selection is expanded to include Inconel X-750. (Perhaps surprisingly, C–SiC is not viable at this heat flux, with or without a TBC, because both the thermal and the pressure-induced stresses on the hot face exceed its compressive strength). A caveat to this outcome is discussed below. Although a TBC on the Cb752 would enable a slightly lighter structure, its use would be predicated on the tradeoff between weight savings and added cost. Finally, while increasing the fuel flow rate generally results in lighter structures, the weight savings is unlikely to be significant enough to overcome the weight penalty associated with the extra fuel.

The design maps of Fig. 9 and the weight analysis of Fig. 10 do not divulge the significant amount of valuable information contained in the code about optimal geometries, temperatures, stresses, and the relative importance of the various design constraints. Complete description of these results is beyond the scope of this paper but will be presented in subsequent more detailed assessments. One notable observation is that, for essentially all of the materials and design space, the thermomechanical constraint is always active. That is, the design is limited by the occurrence of yielding or fracture. This feature is illustrated for Cb752 in Fig. 11, expressed in terms of constraint activity parameters, Π (defined in such a way that unity signals activation of the constraint). Occasionally, other constraints are also active. For example, at low fuel flow rates and high heat flux, the maximum temperatures in both the structure and the fluid reach their allowable limits.

6 Conclusions

A materials selection strategy has been presented for actively cooled panels, with implications for aerospace structures. The procedure encompasses a geometry optimization tool coupled with analytical models for temperatures and thermomechanical stresses. A thermal network approach has been used to derive the temperature distribution, accounting for the possible presence of a TBC. A sandwich panel analysis has been adopted for the thermomechanical stress calculations. The accuracy of the model predictions and the underlying assumptions has been verified numerically, employing a combination of FE and CFD calculations.

The methodology has been applied to the combustor liner of a Mach 7 hydrocarbon-powered vehicle. Realistic operating conditions have been estimated based on established aerothermodynamics considerations [3]. Many of the candidate materials present feasible designs for at least a limited range of operating loads, representative of steady-state flight conditions and stoichiometric fuel combustion. However, the suite of material options is sensitive to the operating loads and the permitted fuel flow rate. In the present illustration, only Cb752 is viable at the highest heat load and under stoichiometric fuel combustion. This result, combined with robustness benefits and fabrication facility, emphasizes its potential for superior performance, subject to the proviso that oxidation is averted through the use of environmental barrier coatings. For higher fuel flow rates and/or the addition of a TBC, GRCop-84 and Inconel X-750 become viable, although Cb752 remains the most weight efficient.

Finally, since the thermomechanical constraint is almost always active in the optimized designs, elevations in the high-temperature strength of the candidate alloys would yield direct benefits in weight efficiency. Furthermore, based on observations that C–SiC can sustain larger temperature gradients than the present model assumes [29], it should re-emerge as a viable candidate for the more severe thermal environments once a revised local-basis failure criterion has been established.

Acknowledgment

This work was supported by the ONR through a MURI program on Revolutionary Materials for Hypersonic Flight (Contract No. N00014-05-1-0439). The authors are thankful to David Marshall of Teledyne, and Thomas A. Jackson and William M. Roquemore of AFRL for insightful discussions.

Nomenclature

A_f = cross-sectional area of the face in a unit cell (m^2)
A_c = cross-sectional area of the core web in a unit cell (m^2)
b = combustor width (m)
$c_{p,f}$ = specific heat of the coolant (J/kg K)

D_h = hydraulic diameter of the cooling ducts (m)
E = Young's modulus (Pa)
f = friction factor
ϕ = fuel/air mass ratio
f_{st} = stoichiometric fuel/air mass ratio
H = panel thickness (m)
H_{comb} = combustion chamber height (m)
h_G = heat transfer coefficient on the combustor side ($W/m^2\,K$)
h_G^{nom} = heat transfer coefficient on the combustor side for a notional Mach 7 vehicle ($W/m^2\,K$)
h_C = heat transfer coefficient on the cooling channel walls ($W/m^2\,K$)
$k_s^{\perp}$ = through-thickness thermal conductivity of the material (W/m K)
$k_s^{\parallel}$ = in-plane thermal conductivity of the material (W/m K)
k_f = thermal conductivity of the coolant (W/m K)
k_{TBC} = through-thickness thermal conductivity of the TBC (W/m K)
L = height of cooling channel (m)
p_f = pressure in the coolant (Pa)
p_f^0 = entry pressure in the coolant (Pa)
p_{comb} = pressure in the combustion chamber (Pa)
Pr = Prandtl number
q_w = heat flux into the web (W/m^2)
q_c = heat flux convected from the top face into the coolant (W/m^2)
q_h = horizontal heat flux in the top face (W/m^2)
R_G = external convective thermal resistance ($W/m^2\,K)^{-1}$
R_{cool} = internal convective thermal resistance ($W/m^2\,K)^{-1}$
R_{TBC} = conductive thermal resistance across the TBC ($W/m^2\,K)^{-1}$
R_{face} = conductive thermal resistance across the top face ($W/m^2\,K)^{-1}$
R_h = conductive thermal resistance along the top face ($W/m^2\,K)^{-1}$
R_1, R_2^w, R_2^c = combination of thermal resistances ($W/m^2\,K)^{-1}$
R_w^*, R_c^*, R_h^* = non-dimensional combination of thermal resistances
Re = Reynolds number
T_{aw} = adiabatic wall temperature in the combustor (K)
T_f = coolant temperature (K)
T_f^0 = entry coolant temperature (K)
T_f^{max} = maximum coolant temperature (K)
T_m^{max} = maximum temperature in the material (K)
T_{tf}^w = temperature on the top side of the top face, over a web (K)
T_{tf}^c = temperature on the top side of the top face away from a web (K)
$T^{(i)}$ = temperature at a location i in the material (K)
T^* = maximum allowable temperature in the material (K)
T_{coke} = coking temperature of the coolant (K)
t_f = face sheet thickness (m)
t_c = core web thickness (m)
u = coolant velocity (m/s)
$\dot{V}^{eff}$ = volumetric fuel flow rate per unit width of the panel (m^2/s)
$\dot{V}_{st}$ = stoichiometric volumetric fuel flow rate per unit width of the combustor (m^2/s)
$\dot{V}_{st}^{eff}$ = stoichiometric volumetric fuel flow rate per unit width of the panel (m^2/s)
w = width of cooling channel (m)
Z = panel length (m)
α = coefficient of thermal expansion of the material (K^{-1})
Δp = viscous pressure drop across the panel (Pa)
ΔT_{panel}^c = temperature difference across the panel away from the core web (K)
ΔT_{panel}^w = temperature difference across the panel above a core web (K)
ΔT_{panel} = relevant temperature difference across the panel (K)
ΔT_{tf}^c = temperature difference across the top face away from the core web (K)
ΔT_{tf}^w = temperature difference across the top face above a core web (K)
ΔT_{tf} = relevant temperature difference across the top face (K)
x, y, z = geometric coordinates
ϕ = equivalence ratio
ν_f = kinematic viscosity of the coolant (m^2/s)
υ = Poisson's ratio of the material
σ_Y = yield strength of a metallic material (Pa)
σ_{ult} = ultimate stress for a CMC (Pa)
$\sigma_{core,y}^{p_f}$ = stress in the core web along the y-direction due to the pressure p_f (Pa)
$\sigma_{core,z}^{p_f}$ = stress in the core web along the z-direction due to the pressure p_f (Pa)
$\sigma_{face,x}^{p_f}$ = stress in the face sheet along the x-direction due to the pressure p_f (Pa)
$\sigma_{face,z}^{p_f}$ = stress in the face sheet along the z-direction due to the pressure p_f (Pa)
$\sigma_{face,x}^{p_{comb}}$ = stress in the face sheet along the x-direction due to the pressure p_{comb} (Pa)
$\sigma_{face,z}^{p_{comb}}$ = stress in the face sheet along the z-direction due to the pressure p_{comb} (Pa)
$\sigma_{face,x}^{\Delta T_{panel}}$ = stress in the face sheet along the x-direction due to the temperature difference ΔT_{panel} (Pa)
$\sigma_{face,z}^{\Delta T_{panel}}$ = stress in the face sheet along the z-direction due to the temperature difference ΔT_{panel} (Pa)
$\sigma_{face,x}^{\Delta T_{tf}}$ = stress in the face sheet along the x-direction due to the temperature difference ΔT_{tf} (Pa)
$\sigma_{face,z}^{\Delta T_{tf}}$ = stress in the face sheet along the z-direction due to the temperature difference ΔT_{tf} (Pa)
$\sigma_{m,x}^{(i)}$ = mechanical stress at location i along the x-direction (Pa)
$\sigma_{m,z}^{(i)}$ = mechanical stress at location i along the z-direction (Pa)
$\sigma_{T,z}^{(i)}$ = thermal stress at location i along the x-direction (Pa)
$\sigma_{T,x}^{(i)}$ = thermal stress at location i along the z-direction (Pa)
ρ_f = mass density of the coolant (kg/m^3)
θ = nondimensional fin temperature: $(T(y)-T_{fuel})/(T(0)-T_{fuel})$

Appendix A: Thermal Resistance Model

The Model

Among the nine thermal resistances in the model network (Fig. 3(*a*)), six are independent:

- top face/hot gas boundary: $R_G = 1/h_G$
- across TBC (when present): $R_{\text{TBC}} = t_{\text{TBC}}/k_{\text{TBC}}^{\perp}$
- across hot face (y-direction): $R_{\text{face}} = t_f/k_s^{\perp}$
- along hot face (x-direction)[1]: $R_h = (w + t_c/2)/4k_s^{\parallel}$
- top face/coolant boundary: $R_{\text{cool}} = 1/h_c$
- core web (modeled as a 1D thermal fin [30,31]): $R_{\text{fin}} = \{\tanh^{-1}(\sqrt{2h_C/k_s^{\parallel}t_c}L^2)\}[\sqrt{2h_C/k_s^{\parallel}t_c}k_s^{\parallel}]^{-1}$.

Here, h_G and h_C are the heat transfer coefficients on the hot gas side and coolant sides, respectively; $k_s^{\perp}$ and $k_s^{\parallel}$ are the through-thickness and in-plane thermal conductivities of the material (the distinction being important for CMCs, wherein $k_s^{\perp} \ll k_s^{\parallel}$); and k_{TBC} is the through-thickness conductivity of the TBC (its in-plane value is taken as zero, due to the columnar structure of coatings produced by physical vapor deposition).

Assuming flow in the cooling channels is turbulent and fully developed, h_C is given by the Gnielinski correlation [14,32]:

$$h_C = \frac{k_f}{D_h}\text{Nu} = \frac{k_f}{D_h}\frac{(f/2)(\text{Re}-1000)\text{Pr}}{1+12.7\sqrt{f/2}(\text{Pr}^{2/3}-1)} \tag{A1}$$

where k_f is the thermal conductivity of the coolant, Pr is the Prandtl number, $D_h = 2wL/(w+L)$ is the hydraulic diameter, and Re is the Reynolds number:

$$\text{Re} \equiv \frac{uD_h}{\nu_f} = \frac{\dot{V}^{\text{eff}}D_h H(w+t_c)}{LwH\nu_f} \tag{A2}$$

with ν_f being the kinematic viscosity, $\dot{V}^{\text{eff}}$ the volumetric flow rate per unit width of panel (see Sec. 5.2), and f is the friction factor, given by $f = 0.046\text{Re}^{-1/5}$ in the domain $2\times10^4 < \text{Re} < 10^6$ [32,33].

The model can be simplified into the effective network of Fig. 3(*b*), characterized by four resistances, R_1, R_2^w, R_2^c, R_h, where

$$R_1 = R_G + R_{\text{TBC}} + R_f/2$$

$$R_2^w = R_f/2 + R_{\text{cool}}$$

$$R_2^c = R_f/2 + R_{\text{fin}} \tag{A3}$$

(with R_h previously defined). The temperatures of interest are those on the top face, directly over (T_{tf}^c) and midway between (T_{tf}^w) the core members, at both the inlet ($z=0$) and the outlet ($z=Z$). Since the three fluxes q_w, q_c, q_h are also unknown, five equations are needed to close the system:

$$T_{\text{aw}} - T_{\text{fuel}} = q_w R_1 + (q_w + 2q_h t_f/w)R_2^w$$

$$T_{\text{aw}} - T_{\text{fuel}} = q_c R_1 + (q_c - 2q_h t_f/t_c)R_2^c$$

$$T_{\text{aw}} - T_{tf}^w = q_w R_1$$

$$T_{\text{aw}} - T_{tf}^c = q_c R_1$$

$$T_{tf}^c - T_{tf}^w = q_h R_h \tag{A4}$$

The solution gives the heat fluxes:

$$q_c = \frac{T_{\text{aw}} - T_f}{R_1}R_c^*$$

$$q_w = \frac{T_{\text{aw}} - T_f}{R_1}R_w^*$$

$$q_h = \frac{T_{\text{aw}} - T_f}{R_1}R_h^* \tag{A5}$$

where

$$R_w^* = \frac{R_1[R_2^c R_h + R_1(R_h + 2R_2^c t_f/t_c + 2R_2^w t_f/w)]}{R_2^c R_2^w R_h + R_1^2(R_h + 2R_2^c t_f/t_c + 2R_2^w t_f/w) + R_1\{R_2^w R_h + R_2^c[R_h + 2R_2^w(t_f/t_c + t_f/w)]\}}$$

$$R_c^* = \frac{R_1[R_2^w R_h + R_1(R_h + 2R_2^c t_f/t_c + 2R_2^w t_f/w)]}{R_2^c R_2^w R_h + R_1^2(R_h + 2R_2^c t_f/t_c + 2R_2^w t_f/w) + R_1\{R_2^w R_h + R_2^c[R_h + 2R_2^w(t_f/t_c + t_f/w)]\}}$$

$$R_h^* = \frac{R_1^2(R_2^c - R_2^w)}{R_2^c R_2^w R_h + R_1^2(R_h + 2R_2^c t_f/t_c + 2R_2^w t_f/w) + R_1\{R_2^w R_h + R_2^c[R_h + 2R_2^w(t_f/t_c + t_f/w)]\}} \tag{A6}$$

Additionally, at the channel inlet,

$$\frac{T_{\text{aw}} - T_{tf}^w}{T_{\text{aw}} - T_f} = R_w^*$$

$$\frac{T_{\text{aw}} - T_{tf}^c}{T_{\text{aw}} - T_f} = R_c^* \tag{A7}$$

The coolant temperature is obtained via an energy balance

$$\rho_f c_{p,f}\dot{V}^{\text{eff}}\frac{dT_f}{dz} = \frac{wq_w(z) + t_c q_c(z)}{w + t_c} \tag{A8}$$

where $\rho_f c_{p,f}$ is its volumetric specific heat. Combining with Eq. (A5) gives

$$\frac{d(T_{\text{aw}} - T_f)}{dz} + \frac{1}{R_1\rho_f c_{p,f}\dot{V}^{\text{eff}}}\left(\frac{w}{w+t_c}R_w^* + \frac{t_c}{w+t_c}R_c^*\right)(T_{\text{aw}} - T_f) = 0 \tag{A9}$$

The solution to this differential equation yields the longitudinal distribution of the coolant temperature:

$$\frac{T_{\text{aw}} - T_f}{T_{\text{aw}} - T_f^0} = \exp(-\beta z) \tag{A10}$$

where

[1]The horizontal resistance is not properly conductive, as convection occurs along one of the sides. FE calculations reveal that using an effective length equal to half the actual length yields accurate results (hence the factor of 4).

$$\beta = \frac{1}{R_1 \rho_f c_{p,f} \dot{V}^{\text{eff}}} \left(\frac{w}{w + t_c} R_w^* + \frac{t_c}{w + t_c} R_c^* \right) \tag{A11}$$

The temperature distribution on the hot face can be expressed in similar form, via Eqs. (A7) and (A10):

$$\frac{T_{\text{aw}} - T_{tf}^w}{T_{\text{aw}} - T_f^0} = R_w^* \exp(-\beta z)$$

$$\frac{T_{\text{aw}} - T_{tf}^c}{T_{\text{aw}} - T_f^0} = R_c^* \exp(-\beta z) \tag{A12}$$

All temperatures achieve their maximum at the outlet ($z = Z$).

From the preceding analysis, the temperatures at the 18 points in Fig. 5 are as follows:

$$T^{(i)} = T_{\text{aw}} - (T_{\text{aw}} - T_f^0) \cdot \begin{cases} \left(1 - \frac{1}{2}\frac{R_f}{R_1}\right) R_c^* \exp(-\beta z) & \text{at Points 1 and 10} \\ \left[R_c^* + \left(\frac{1}{2} R_c^* - R_h^* \frac{t_f}{t_c} \right) \frac{R_f}{R_1} \right] \exp(-\beta z) & \text{at Points 2 and 11} \\ \left[1 - \frac{\theta(L)}{\theta_0} \frac{R_{\text{fin}}}{R_1} \left(R_c^* - 2 R_h^* \frac{t_f}{t_c} \right) \right] \exp(-\beta z) & \text{at Points 3, 4, 7, 8, 12, 13, 16, and 17} \\ \left(1 - \frac{1}{2}\frac{R_f}{R_1}\right) R_w^* \exp(-\beta z) & \text{at Points 5 and 14} \\ \left[R_w^* + \left(\frac{1}{2} R_w^* + R_h^* \frac{t_f}{w} \right) \frac{R_f}{R_1} \right] \exp(-\beta z) & \text{at Points 6 and 15} \\ \left[1 - \frac{\theta(L/2)}{\theta_0} \frac{R_{\text{fin}}}{R_1} \left(R_c^* - 2 R_h^* \frac{t_f}{t_c} \right) \right] \exp(-\beta z) & \text{at Points 9 and 18} \end{cases} \tag{A13}$$

where $\theta(y)/\theta_0$ is the nondimensional fin temperature:

$$\frac{\theta(y)}{\theta_0} = \frac{T(y) - T_f}{T(0) - T_f} = \frac{\cosh\left[\sqrt{\frac{2h_C}{k_s^{\parallel} t_c}} (L - y) \right]}{\cosh\left[\sqrt{\frac{2h_C}{k_s^{\parallel} t_c}} L \right]} \tag{A14}$$

with y the coordinate oriented along the fin.

Once all the temperatures in the system are known, simple algebraic manipulation provides the temperature difference across the top face (directly above and midway between the core members):

$$\frac{\Delta T_{tf}^c(z)}{T_{\text{aw}} - T_f^0} = \left(R_c^* - R_h^* \frac{t_f}{t_c} \right) \frac{R_f}{R_1} \exp(-\beta z)$$

$$\frac{\Delta T_{tf}^w(z)}{T_{\text{aw}} - T_f^0} = \left(R_w^* + R_h^* \frac{t_f}{w} \right) \frac{R_f}{R_1} \exp(-\beta z) \tag{A15}$$

and across the entire panel (above and between the core members):

$$\frac{\Delta T_{\text{panel}}^c}{T_{\text{aw}} - T_f^0} = \left[\frac{R_2{}^c}{R_1} - \frac{R_{\text{fin}}}{R_1} \frac{\theta(L)}{\theta_0} \right] \left(R_c^* - 2 R_h^* \frac{t_f}{t_c} \right) \exp(-\beta z)$$

$$\frac{\Delta T_{\text{panel}}^w}{T_{\text{aw}} - T_f^0} = \left[\left(R_w^* + 2 R_h^* \frac{t_f}{w} \right) \frac{R_2{}^w}{R_1} - \left(R_c^* - 2 R_h^* \frac{t_f}{t_c} \right) \frac{R_{\text{fin}}}{R_1} \frac{\theta(L)}{\theta_0} \right] \exp(-\beta z) \tag{A16}$$

Appendix B: Stress Analysis

Coolant Pressure

The coolant pressure p_f (assumed uniform along z and equal to p_f^0, given that $\Delta p \ll p_f^0$) induces uniform tensile stresses in the core members (at Points 9 and 18), given by

$$\frac{\sigma_{\text{core},y}^{p_f}}{p_f} = \frac{w}{t_c}, \quad \frac{\sigma_{\text{core},z}^{p_f}}{p_f} = \nu \frac{\sigma_{\text{core},y}^{p_f}}{p_f} \tag{B1}$$

with ν the Poisson ratio of the material. It also induces combined tension/bending in the face segments. For Boundary Condition I, these are

$$\frac{\sigma_{\text{face},x}^{p_f}}{p_f} = \begin{cases} L/2t_f + (w/t_f)^2/2 & \text{at Points 2, 3, 11, and 12} \\ L/2t_f - (w/t_f)^2/2 & \text{at Points 1, 4, 10, and 13} \\ L/2t_f + (w/t_f)^2/4 & \text{at Points 5, 8, 14, and 17} \\ L/2t_f - (w/t_f)^2/4 & \text{at Points 6, 7, 15, and 16} \end{cases}$$

$$\frac{\sigma_{\text{face},z}^{p_f}}{p_f} = \nu \frac{\sigma_{\text{face},x}^{p_f}}{p_f} \tag{B2}$$

The same solutions apply to boundary condition Type II with the exception of those for the bottom face segments, which lack the bending component. Along this face (at Points 3, 4, 7, 8, 12, 13, 16, and 17), the stresses are simply

$$\frac{\sigma_{\text{face},x}^{p_f}}{p_f} = \frac{L}{2t_f}, \quad \frac{\sigma_{\text{face},z}^{p_f}}{p_f} = \nu \frac{\sigma_{\text{face},x}^{p_f}}{p_f} \tag{B3}$$

Combustor Gas Pressure

For Boundary Condition I, the panel behaves globally as a clamped-clamped plate under uniform pressure, p_{comb}. With the usual assumption that the shear force is supported by the core and the moment by the face sheets [19], the stresses in the faces are

$$\frac{\sigma_{x,\text{face}}^{p_{\text{comb}}}}{p_{\text{comb}}} = \begin{cases} \dfrac{1}{12}\dfrac{b^2}{(H-t_f)t_f} & \text{at Points 1, 2, 5, and 6} \\ -\dfrac{1}{12}\dfrac{b^2}{(H-t_f)t_f} & \text{at Points 3, 4, 7, and 8} \\ \dfrac{1}{24}\dfrac{b^2}{(H-t_f)t_f} & \text{at Points 12, 13, 16, and 17} \\ -\dfrac{1}{24}\dfrac{b^2}{(H-t_f)t_f} & \text{at Points 10, 11, 14, and 15} \end{cases}$$

$$\frac{\sigma_{z,\text{face}}^{p_{\text{comb}}}}{p_{\text{comb}}} = \nu\frac{\sigma_{x,\text{face}}^{p_{\text{comb}}}}{p_{\text{comb}}} \tag{B4}$$

In contrast, for boundary condition Type II, bending is prohibited and, since $p_{\text{comb}} \ll p_f$, the additional stress on the top face can be neglected. For similar reasons, the stresses exerted on the core members can also be neglected for both boundary conditions.

Thermal Load

The temperature difference across the top face causes compression along its top surface and tension along its bottom surface (at the boundary with the coolant). These stresses are

$$\sigma_{\text{face},x}^{\Delta T_{tf}} = \sigma_{\text{face},z}^{\Delta T_{tf}} = \begin{cases} -\dfrac{E\alpha\Delta T_{tf}}{2(1-\nu)} & \text{at Points 1, 5, 10, and 14} \\ \dfrac{E\alpha\Delta T_{tf}}{2(1-\nu)} & \text{at Points 2, 6, 11, and 15} \end{cases} \tag{B5}$$

with E and α the Young modulus and the coefficient of thermal expansion of the material, respectively. Additionally, the average temperature difference between the top and bottom faces, $\Delta T_{\text{panel}} = (\Delta T_{\text{panel}}^{w} + \Delta T_{\text{panel}}^{c})/2$, causes the panel to deform uniformly in each of the x- and z-directions, inducing compression in the top face and tension in the bottom face [17]. Accounting for the stretching stiffness of the core members along the z-direction and assuming that the temperatures of the core and the bottom face are the same at steady state, the resulting additional stresses are

$$\sigma_{\text{face},x}^{\Delta T_{\text{panel}}} = \begin{cases} -\dfrac{E\alpha\Delta T_{\text{panel}}}{2(1-\nu)} & \text{at Points 1, 2, 5, 6, 10, 11, 14, and 15} \\ \dfrac{E\alpha\Delta T_{\text{panel}}}{2(1-\nu)} & \text{at Points 3, 4, 7, 8, 12, 13, 16, and 17} \end{cases}$$

$$\sigma_{\text{face},z}^{\Delta T_{\text{panel}}} = \begin{cases} -\dfrac{E\alpha\Delta T_{\text{panel}}(A_f + A_c)}{(1-\nu)(2A_f + A_c)} & \text{at Points 1, 2, 5, 6, 10, 11, 14, and 15} \\ \dfrac{E\alpha\Delta T_{\text{panel}}A_f}{(1-\nu)(2A_f + A_c)} & \text{at Points 3, 4, 7, 8, 12, 13, 16, and 17} \end{cases} \tag{B6}$$

where $A_f = t_f(w+t_c)$ and $A_c = (H-2t_f)t_c$ are the cross-sectional areas of the face and the core in a unit cell, respectively. These results apply to both boundary conditions.

Failure Conditions

For metals, failure is defined as the onset of yielding. The von Mises criterion is used, namely,

$$\max_{i=1-18}\left\{\left(\frac{\sigma_{m,x}^{(i)}}{\sigma_Y(T^{(i)})} + \frac{\sigma_{T,x}^{(i)}}{\sigma_Y(T^{(i)})} - \frac{\sigma_{m,z}^{(i)}}{\sigma_Y(T^{(i)})} - \frac{\sigma_{T,z}^{(i)}}{\sigma_Y(T^{(i)})}\right)^2 + \left(\frac{\sigma_{m,x}^{(i)}}{\sigma_Y(T^{(i)})} + \frac{\sigma_{T,x}^{(i)}}{\sigma_Y(T^{(i)})}\right)^2 + \left(\frac{\sigma_{m,z}^{(i)}}{\sigma_Y(T^{(i)})} + \frac{\sigma_{T,z}^{(i)}}{\sigma_Y(T^{(i)})}\right)^2\right\} = 2 \tag{B7}$$

with the stress components and the temperature at each location i given by Eqs. (B2)–(B6) and (A13), respectively. The yield strength of the material σ_Y is assumed to linearly decrease with temperature (Table 2).

Well-designed CMCs typically fail when the *normal stress* along the primary fiber orientation attains either the ultimate tensile strength or the compressive strength. Assuming for simplicity that the strengths in tension and compression are identical and temperature independent (reasonable for SiC/SiC and C/SiC [34,35]), the ensuing condition is

$$\max_{i=1-18}\left\{\max\left\{\frac{|\sigma_{m,x}^{(i)} + \sigma_{T,x}^{(i)}|}{\sigma_{\text{ult}}}, \frac{|\sigma_{m,z}^{(i)} + \sigma_{T,z}^{(i)}|}{\sigma_{\text{ult}}}\right\}\right\} = 1 \tag{B8}$$

Pressure Drop

The pressure drop in the coolant due to viscous dissipation over the length of the panel is [32]

$$\Delta p = \frac{2\rho_f f Z(\dot{V}^{\text{eff}})^2}{H^2(1-\bar{\rho})^2 D_h} \tag{B9}$$

with $\bar{\rho} = 1 - Lw/[H(w+t_c)]$ the relative density of the panel.

References

[1] Steeves, C. A., He, M. Y., Valdevit, L., Kasen, S. D., Wadley, H. N. G., and Evans, A. G., 2008, "Feasibility of Metallic Structural Heat Pipes as Sharp Leading Edges for Hypersonic Vehicles," ASME J. Appl. Mech., in press.

[2] Curran, E. T., and Murthy, S. N. B., 2000, *Scramjet Propulsion*, American Institute of Aeronautics and Astronautics, Reston, VA.

[3] Heiser, W. H., and Pratt, D. T., 1994, *Hypersonic Airbreathing Propulsion*, AIAA, Washington, DC.

[4] Bertin, J. J., 1994, *Hypersonic Aerothermodynamics*, American Institute of Aeronautics and Astronautics, Washington, DC.

[5] Buchmann, O. A., 1979, "Thermal-Structural Design Study of an Airframe-Integrated Scramjet," Technical Report No. NASA 3141.

[6] Rakow, J. F., and Waas, A. M., 2005, "Thermal Buckling of Metal Foam Sandwich Panels for Convective Thermal Protection Systems," J. Spacecr. Rockets, **42**(5), pp. 832–844.

[7] Rakow, J. F., and Waas, A. M., 2005, "Thermomechanical Response of Actively Cooled Metal Foam Sandwich Panels for Thermal Protection Systems," 46th AIAA/ASME/ASCE/AHS/ASC Structures, Structural Dynamics & Materials Conference, AIAA, Austin, TX.

[8] Song, K. D., Choi, S. H., and Scotti, S. J., 2006, "Transpiration Cooling Experiment for Scramjet Engine Combustion Chamber by High Heat Fluxes," J. Propul. Power, **22**(1), pp. 96–102.

[9] Scotti, S. J., Martin, C. J., and Lucas, S. H., 1988, "Active Cooling Design for

Scramjet Engines Using Optimization Methods," Technical Report No. NASA 100581.
[10] Youn, B., and Mills, A. F., 1995, "Cooling Panel Optimization for the Active Cooling System of a Hypersonic Aircraft," J. Thermophys. Heat Transfer, **9**(1), pp. 136–143.
[11] Flieder, W. C., Richard, C. E., Buchmann, O. A., and Walters, F. M., 1971, "An Analytical Study of Hydrogen Cooled Panels for Application to Hypersonic Aircraft," Technical Report No. NASA CR-1650.
[12] Walters, F. M., and Buchmann, O. A., 1971, "Heat Transfer and Fluid Flow Analysis of Hydrogen-Cooled Panels and Manifold Systems," Technical Report No. NASA CR-66925.
[13] Evans, A. G., Mumm, D. R., Hutchinson, J. W., Meier, G. H., and Pettit, F. S., 2001, "Mechanisms Controlling the Durability of Thermal Barrier Coatings," Prog. Mater. Sci., **46**(5), pp. 505–553.
[14] Gnielinski, V., 1976, "New Equations for Heat and Mass-Transfer in Turbulent Pipe and Channel Flow," Int. Chem. Eng., **16**(2), pp. 359–368.
[15] Bree, J., 1969, "Incremental Growth Due to Creep and Plastic Yielding of Thin Tubes Subjected to Internal Pressure and Cyclic Thermal Stresses," J. Strain Anal., **3**(2), pp. 122–127.
[16] Bree, J., 1989, "Plastic-Deformation of a Closed Tube Due to Interaction of Pressure Stresses and Cyclic Thermal-Stresses," Int. J. Mech. Sci., **31**(11–12), pp. 865–892.
[17] Boley, B. A., and Weiner, J. H., 1960, *Theory of Thermal Stresses*, Wiley, New York.
[18] Rathbun, H. J., Zok, F. W., and Evans, A. G., 2005, "Strength Optimization of Metallic Sandwich Panels Subject to Bending," Int. J. Solids Struct., **42**(26), pp. 6643–6661.
[19] Valdevit, L., Hutchinson, J. W., and Evans, A. G., 2004, "Structurally Optimized Sandwich Panels With Prismatic Cores," Int. J. Solids Struct., **41**(18–19), pp. 5105–5124.
[20] Valdevit, L., Wei, Z., Mercer, C., Zok, F. W., and Evans, A. G., 2006, "Structural Performance of Near-Optimal Sandwich Panels With Corrugated Cores," Int. J. Solids Struct., **43**(16), pp. 4888–4905.
[21] Wei, Z., Zok, F. W., and Evans, A. G., 2006, "Design of Sandwich Panels With Prismatic Cores," ASME J. Eng. Mater. Technol., **128**(2), pp. 186–192.
[22] Wicks, N., and Hutchinson, J. W., 2001, "Optimal Truss Plates," Int. J. Solids Struct., **38**(30–31), pp. 5165–5183.
[23] Wicks, N., and Hutchinson, J. W., 2004, "Performance of Sandwich Plates With Truss Cores," Mech. Mater., **36**(8), pp. 739–751.
[24] Zok, F. W., Rathbun, H., He, M., Ferri, E., Mercer, C., McMeeking, R. M., and Evans, A. G., 2005, "Structural Performance of Metallic Sandwich Panels With Square Honeycomb Cores," Philos. Mag., **85**(26–27), pp. 3207–3234.
[25] Zok, F. W., Rathbun, H. J., Wei, Z., and Evans, A. G., 2003, "Design of Metallic Textile Core Sandwich Panels," Int. J. Solids Struct., **40**(21), pp. 5707–5722.
[26] Zok, F. W., Waltner, S. A., Wei, Z., Rathbun, H. J., McMeeking, R. M., and Evans, A. G., 2004, "A Protocol for Characterizing the Structural Performance of Metallic Sandwich Panels: Application to Pyramidal Truss Cores," Int. J. Solids Struct., **41**(22–23), pp. 6249–6271.
[27] National Research Council (US) Committee on the National Aerospace Initiative, 2004, *Evaluation of the National Aerospace Initiative*, National Academy, Washington, DC.
[28] Novak, M. D., and Levi, C. G., 2007, "Oxidation and Volatilization of Silicide Coatings for Refractory Niobium Alloys," ASME IMECE, Seattle, WA.
[29] Marshall, D. B., personal communication.
[30] Lu, T. J., Valdevit, L., and Evans, A. G., 2005, "Active Cooling by Metallic Sandwich Structures With Periodic Cores," Prog. Mater. Sci., **50**(7), pp. 789–815.
[31] Valdevit, L., Pantano, A., Stone, H. A., and Evans, A. G., 2006, "Optimal Active Cooling Performance of Metallic Sandwich Panels With Prismatic Cores," Int. J. Heat Mass Transfer, **49**(21–22), pp. 3819–3830.
[32] Bejan, A., 2004, *Convection Heat Transfer*, Wiley, Hoboken, NJ.
[33] Moody, L. F., 1944, "Friction Factors for Pipe Flow," Trans. ASME, **66**, pp. 671–684.
[34] Wang, M., and Laird, C., 1996, "Characterization of Microstructure and Tensile Behavior of a Cross-Woven C–SiC Composite," Acta Mater., **44**(4), pp. 1371–1387.
[35] Wang, M. D., and Laird, C., 1996, "Damage and Fracture of a Cross Woven C/SiC Composite Subject to Compression Loading," J. Mater. Sci., **31**(8), pp. 2065–2069.

Nonlinear Response of a Shallow Sandwich Shell With Compressible Core to Blast Loading

Renfu Li
Postdoctoral Fellow

George A. Kardomateas
Professor of Aerospace Engineering
Fellow ASME

George J. Simitses
Professor Emeritus of Aerospace Engineering
Fellow ASME

Georgia Institute of Technology,
Atlanta, GA 30332-0150

This paper investigates the nonlinear dynamic response of a shallow sandwich shell subject to blast loading with consideration of core compressibility. The shallow shell consists of two laminated composite or metallic face sheets and an orthotropic compressible core. Experimental results and finite element simulations in literature have shown that the core exhibits considerable compressibility when a sandwich panel is subjected to impulse loading. To address this issue properly in the analysis, a new nonlinear compressible core model is proposed in the current work. The system of governing equations is derived by means of Hamilton's principle in combination with the Reissner–Hellinger's variational principle. The analytical solution for the simply supported shallow shell is formulated using an extended Galerkin procedure combined with the Laplace transform. Numerical results are presented. These results demonstrate that this advanced sandwich model can capture the transient responses such as the stress shock wave effect and the differences in the transient behaviors of the face sheets and the core when a sandwich shadow shell is subjected to a blast loading. However, in the steady state dynamic stage, all the displacements of the face sheets and the core tend to be identical. This model can be further used to study the energy absorption ability of the core and the effects of different material and geometrical parameters on the behaviors of sandwich structures subject to blast loading. [DOI: 10.1115/1.2937154]

Keywords: shallow sandwich shell, blast, impact, laminated face sheets, compressible core, dynamic response, sudden loading

1 Introduction

The response of suddenly loaded structural configurations is essential in ensuring their integrity. Sudden loading can occur, for example, due to blast from an explosive device and this entails both distributed particle impact from the explosion fragments and the overpressure from the shock wave. This study deals with the dynamic response of sandwich shallow shells to a blast pressure pulse. There have been indeed recently many efforts to investigate the blast response of structures and suggest ways of mitigating their detrimental effects through an optimal sandwich construction design. Several papers have addressed various aspects of the problem [1–7]. A typical sandwich structure consists of two stiff metallic/composite face sheets and a soft honeycomb/foam core. This layout gives the sandwich material system the integrity of high stiffness and strength with little resultant weight penalty and high-energy absorption capability and has led to many successful applications of sandwich structures in the construction of marine vessels, aerospace vehicles, and civil infrastructure.

In the study of the response of a sandwich structure to a static loading or a dynamic loading of long duration, it has been customary to neglect the deformation of the core in the transverse direction [8,9]. The core would then be considered infinitely rigid in the thickness direction and assumed to only carry the shear stresses. Though there are two transversely compressive core models proposed in literature [10–12], the transversely rigid core model has been found to be working well in most of the studies involving static or dynamic-long-duration loading. However, experimental and numerical results [3–7] have shown that the core undergoes significant deformation when the sandwich structure experiences a sudden, impulsive loading and the core plays an important role in the absorption of the impact energy. Therefore, a model including the core transverse flexibility would offer a better prediction over the classic transversely rigid core model in the study of the transient response of sandwich structures. A detailed look into the two currently available transversely compressive core models would reveal that the transverse strains in the models in Refs. [12,10,11] are constant and linear functions with regard to the variable in the transverse direction, respectively. However, the observations in Refs. [6,7] clearly demonstrate that the core transverse deformation/strain is highly nonlinear with regard to the variable in the thickness direction. Therefore, a more refined core model is needed in order to obtain a better understanding of the dynamic behavior of a sandwich construction under sudden, blast loading. Furthermore, up to date, most of the studies for the response of sandwich construction to blast loading have focused on flat panels or plates. Very few works on this topic are available for the sandwich shallow shell configuration, which is very often used in engineering construction, for example, in ship hulls. Therefore, the investigation of the behavior of the sandwich shallow shell to blast loading has both practical and theoretical importance.

In this paper, we shall properly address these issues by first proposing an advanced sandwich shallow shell model that accounts for the highly nonlinear compressibility of the core. The transient behavior of the face sheets and the core will be analyzed in some detail. We organize this paper as follows: A nonlinear transversely compressible core theory is proposed in Sec. 2. In the model, the strain of the core in the transverse direction is no longer constant or linear but a third order function with regard to the transverse variable. The derivation of the governing equations

Contributed by the Applied Mechanics Division of ASME for publication in the JOURNAL OF APPLIED MECHANICS. Manuscript received September 21, 2007; final manuscript received March 9, 2008; published online August 22, 2008. Review conducted by Horacio D. Espinosa.

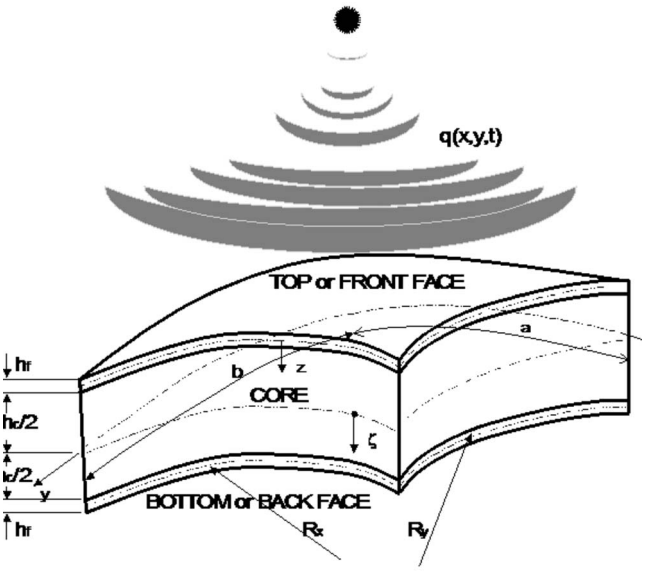

Fig. 1 A sandwich shallow shell subject to a sudden, blast impact

and boundary and initial conditions is presented in Sec. 3. These unknowns in the equations are highly coupled in terms of both spatial and time variables. The solution procedure for solving the nonlinear partial governing equations is presented in Sec. 4. Applications and discussions of numerical results are given in Sec. 5. In sec. 6, we present some conclusions and related work in the future.

2 Formulation

2.1 Basic Assumptions. The sandwich shell treated here is composed of two thin faces of high stiffness and a thick soft core (Fig. 1), whose compressibility will also be taken into account. Because of the core compressibility, the widely used [4] assumption that the transverse displacements of the two face sheets and the core displacements are equal will not be adopted in this study. We shall employ the following assumptions:

1 The face sheets satisfy the Kirchhoff–Love assumptions and the thicknesses are small compared with the overall thickness of the sandwich section. In the current study, the two face sheets are further assumed to have identical thickness.
2 The curvatures of each shell in the two directions may not be equal and the total thickness of the shell section is small compared to its radii of curvatures.
3 The core is compressible in the transverse direction, that is, its thickness may change.
4 The bonding between the face sheets and the core is assumed to be perfect.
5 Uniformly distributed shock wave pressure on the front face of the shell, will be considered. The intensities of the loading would range from causing indentation to core crushing or initiating face damage.

2.2 Kinematics for the Thin Face Sheets and the Compressible Core of a Sandwich Shallow Shell. Thin Face Sheets. Let a Cartesian coordinates system (x,y,z) be on the middle plane of the core, as shown in Fig. 1. The middle surfaces of the two face sheets and the core can then be defined in terms of a set of curvilinear coordinates (α,β,ζ) as $x=x(\alpha,\beta)$, $y=y(\alpha,\beta)$, and $z=(\alpha,\beta)$. Considering the shallow shell assumptions that the terms $z_{,\alpha}^2$ and $z_{,\beta}^2$ can be neglected in comparison to unity [13], the curvilinear coordinate system can be approximated by the Cartesian coordinates in the middle surface and the transverse displacements through the thickness can be approximated by the middle surface displacement for a thin shallow shell. We also define by ζ a global transverse coordinate from the midsurface of the core, as opposed to the local transverse coordinate from the midsurface of each phase (face sheet or core), which is denoted by z.

For thin face sheets, the transverse displacements can be viewed as undergoing no change through the thickness. Therefore, the displacements in the face sheets can be expressed as

$$u^t(x,y,\zeta,t) = u_o^t(x,y,t) - \left(\zeta + \frac{h_c+h_f}{2}\right) w_{,x}^t(x,y,t) \tag{1a}$$

$$v^t(x,y,\zeta,t) = v_o^t(x,y,t) - \left(\zeta + \frac{h_c+h_f}{2}\right) w_{,y}^t(x,y,t) \tag{1b}$$

$$w^t(x,y,\zeta,t) = w^t(x,y,t), \quad -h_f - \frac{h_c}{2} \leqslant \zeta \leqslant -\frac{h_c}{2} \tag{1c}$$

for the top face sheet, and

$$u^b(x,y,\zeta,t) = u_o^b(x,y,t) - \left(\zeta - \frac{h_c+h_f}{2}\right) w_{,x}^b(x,y,t) \tag{2a}$$

$$v^b(x,y,\zeta,t) = v_o^b(x,y,t) - \left(\zeta - \frac{h_c+h_f}{2}\right) w_{,y}^b(x,y,t) \tag{2b}$$

$$w^b(x,y,\zeta,t) = w^b(x,y,t), \quad \frac{h_c}{2} \leqslant \zeta \leqslant \frac{h_c}{2} + h_f \tag{2c}$$

for the bottom face sheet. Omitting the superscripts t and b, the nonlinear strain-displacement relations for the face sheets can take the following form:

$$[\epsilon] = \begin{bmatrix} \epsilon_x \\ \epsilon_y \\ \gamma_{xy} \end{bmatrix} = [\epsilon_o] + z[k] = \begin{bmatrix} \epsilon_{ox} + zk_x \\ \epsilon_{oy} + zk_y \\ \gamma_{oxy} + zk_{xy} \end{bmatrix}, \quad z = \zeta \pm \frac{h_c+h_f}{2} \tag{3}$$

in which the "$\pm$;" sign in the variable z corresponds to the top and bottom face sheets, respectively, and $[\epsilon_o]$ is the middle surface strain given by

$$[\epsilon_o] = \begin{bmatrix} \epsilon_{ox} \\ \epsilon_{oy} \\ \gamma_{oxy} \end{bmatrix} = \begin{bmatrix} u_{o,x} + \frac{1}{2}w_{,x}^2 + w/R_x \\ v_{o,y} + \frac{1}{2}w_{,y}^2 + w/R_y \\ u_{o,y} + v_{o,x} + w_{,x}w_{,y} + 2w/R_{xy} \end{bmatrix} \tag{4}$$

Moreover, $[k]$ is the curvature

$$[k] = \begin{bmatrix} k_x \\ k_y \\ k_{xy} \end{bmatrix} = \begin{bmatrix} -w_{,xx} \\ -w_{,yy} \\ -2w_{,xy} \end{bmatrix} \tag{5}$$

where R_x, R_y, and R_{xy} are the radii of the curvature for the middle surfaces.

Higher Order Theory for Compressible Cores. The compressibility in the thickness direction of the core can be important for the absorption ability of a sandwich shallow shell subject to a suddenly applied loading. This compressibility implies that the displacement in the thickness direction should be a function of the variable in the transverse direction and satisfy equilibrium equations and continuity conditions along the face sheets/core interface. In literature, this function is often approximated in a linear or quadratic form [4,10]. In this paper, a fourth order nonlinear core theory is formulated. Details of the formulation are given in Appendix A. Based on this model, the transverse displacement can be expressed as follows:

$$w^c(x,y,\zeta,t) = \left(1 - \frac{2\zeta^2}{h_c^2} - \frac{8\zeta^4}{h_c^4}\right) w_o^c(x,y,t) + \left(\frac{2\zeta^2}{h_c^2} + \frac{8\zeta^4}{h_c^4}\right) \bar{w}(x,y,t) - \left(\frac{\zeta}{h_c} + \frac{4\zeta^3}{h_c^3}\right) \hat{w}(x,y,t), \quad -\frac{h_c}{2} \leqslant \zeta \leqslant \frac{h_c}{2} \tag{6}$$

and the in-plane displacements in the core are

$$u^c(x,y,\zeta,t) = \bar{u}(x,y,t) - \frac{\zeta}{h_c/2}\hat{u}(x,y,t) + \zeta\frac{h_f}{h_c} w_{,x}^c(x,y,\zeta,t) \tag{7a}$$

$$v^c(x,y,\zeta,t) = \bar{v}(x,y,t) - \frac{\zeta}{h_c/2}\hat{v}(x,y,t) + \zeta\frac{h_f}{h_c} w_{,y}^c(x,y,\zeta,t) \tag{7b}$$

where $w_0^c(x,y,t)$ is the transverse displacement of the middle surface of the core, $\bar{w}(x,y,t)$ and $\hat{w}(x,y,t)$, $\bar{u}(x,y,t)$ and $\hat{u}(x,y,t)$, and $\bar{v}(x,y,t)$, and $\hat{v}(x,y,t)$ are defined in Appendix A.

This leads to the following strain-displacement relations for the core:

$$\epsilon_z^c = \left(-\frac{1}{2h_c} + \frac{2\zeta}{h_c^2} - \frac{6\zeta^2}{h_c^3} + \frac{16\zeta^3}{h_c^4}\right) w^t(x,y,t) - \left(\frac{4\zeta}{h_c^2} + \frac{32\zeta^3}{h_c^4}\right) w_o^c(x,y,t) + \left(\frac{1}{2h_c} + \frac{2\zeta}{h_c^2} + \frac{6\zeta^2}{h_c^3} + \frac{16\zeta^3}{h_c^4}\right) w^b(x,y,t) \tag{8a}$$

$$\gamma_{xz}^c = -\frac{2}{h_c}\hat{u}(x,y,t) + \eta_1(\zeta) w_{,x}^t(x,y,t) + \eta_2(\zeta) w_{o,x}^c(x,y,t) + \eta_3(\zeta) w_{,x}^b(x,y,t) \tag{8b}$$

$$\gamma_{yz}^c = -\frac{2}{h_c}\hat{v}(x,y,t) + \eta_1(\zeta) w_{,y}^t(x,y,t) + \eta_2(\zeta) w_{o,y}^c(x,y,t) + \eta_3(\zeta) w_{,y}^b(x,y,t) \tag{8c}$$

in which

$$\eta_1(\zeta) = -\frac{1}{2}\left(1 + 2\frac{h_f}{h_c}\right)\frac{\zeta}{h_c} + \left(1 + 3\frac{h_f}{h_c}\right)\frac{\zeta^2}{h_c^2} - 2\left(1 + 4\frac{h_f}{h_c}\right)\frac{\zeta^3}{h_c^3} + 4\left(1 + 5\frac{h_f}{h_c}\right)\frac{\zeta^4}{h_c^4} \tag{9a}$$

$$\eta_2(\zeta) = \left(1 + \frac{h_f}{h_c}\right) - 2\left(1 + \frac{3h_f}{h_c}\right)\frac{\zeta^2}{h_c^2} - 8\left(1 + \frac{5h_f}{h_c}\right)\frac{\zeta^4}{h_c^4} \tag{9b}$$

$$\eta_3(\zeta) = \frac{1}{2}\left(1 + 2\frac{h_f}{h_c}\right)\frac{\zeta}{h_c} + \left(1 + 3\frac{h_f}{h_c}\right)\frac{\zeta^2}{h_c^2} + 2\left(1 + 4\frac{h_f}{h_c}\right)\frac{\zeta^3}{h_c^3} + 4\left(1 + 5\frac{h_f}{h_c}\right)\frac{\zeta^4}{h_c^4} \tag{9c}$$

The core is considered undergoing large rotation with a small displacement; therefore, the in-plane strains can be neglected.

2.3 Constitutive Relations. The equations developed so far can be applied to general materials. In the following sections, we shall assume the face sheets to be orthotropic laminated composites and the core to be orthotropic as well. The stress-strain relationship for any layer of the face sheets is

$$\begin{bmatrix}\sigma_x\\ \sigma_y\\ \tau_{xy}\end{bmatrix} = \begin{bmatrix}Q_{11} & Q_{12} & Q_{16}\\ Q_{12} & Q_{22} & Q_{26}\\ Q_{16} & Q_{26} & Q_{66}\end{bmatrix}\begin{bmatrix}\epsilon_x\\ \epsilon_y\\ \gamma_{xy}\end{bmatrix} \quad \text{or } [\sigma] = [Q][\epsilon] \tag{10}$$

where Q_{ij} for $i,j=1,2,6$ are the plane-stress reduced stiffness coefficients. With Eqs. (3)–(5), (8*a*)–(8*c*), and (10), one can compute the resultants for the top/front face sheet of the sandwich shallow shell:

$$[N^t] = \begin{bmatrix}N_x^t\\ N_y^t\\ N_{xy}^t\end{bmatrix} = \int_{-h_c/2-h_f}^{-h_c/2}[\sigma^t]d\zeta = \int_{-h_c/2)-h_f}^{-h_c/2}[Q^t][\epsilon^t]d\zeta = [A^t][\epsilon_0^t] + [B^t][k^t] \tag{11a}$$

$$[M^t] = \begin{bmatrix}M_x^t\\ M_y^t\\ M_{xy}^t\end{bmatrix} = \int_{-h_c/2-h_f}^{-h_c/2}[\sigma^t]\left(\zeta + \frac{h_c + h_f}{2}\right)d\zeta = [B^t][\epsilon_o^t] + [D^t][k^t] \tag{11b}$$

in which the stiffness coefficients are

$$[A_{ij}^t, B_{ij}^t, D_{ij}^t] = \int_{-h_c/2-h_f}^{-h_c/2} Q_{ij} \times \left[1, \zeta + \frac{h_c + h_f}{2}, \left(\zeta + \frac{h_c + h_f}{2}\right)^2\right]d\zeta, \quad i,j = 1,2,6 \tag{12}$$

Applying a similar procedure, one can obtain the following resultant expressions for the bottom/back face sheet:

$$[N^b] = [A^b][\epsilon_0^b] + [B^b][k^b] \tag{13a}$$

$$[M^b] = [B^b][\epsilon_o^b] + [D^b][k^b] \tag{13b}$$

with the stiffness coefficients reading as

$$[A_{ij}^b, B_{ij}^b, D_{ij}^b] = \int_{h_c/2}^{h_c/2+h_f} Q_{ij} \times \left[1, \zeta - \frac{h_c + h_f}{2}, \left(\zeta - \frac{h_c + h_f}{2}\right)^2\right]d\zeta, \quad i,j = 1,2,6 \tag{14}$$

The stress-strain relations for an orthotropic core can be written as

$$\sigma_z^c = E^c\epsilon_z^c, \quad \tau_{xz}^c = G_{xz}^c\gamma_{xz}^c, \quad \tau_{yz}^c = G_{yz}^c\gamma_{yz}^c \tag{15}$$

3 Governing Equations

The equations of motion and appropriate boundary conditions can be derived using Hamilton's principle. The sandwich shell is subjected to a sudden loading $q(x,y,t)$ on the front face sheet. Let the strain energy be denoted by U, the external potential by W, and the kinetic energy by T, then the variational principle is stated as

$$\delta\int_{t_o}^{t_1}[T - (U - W)]dt = 0 \tag{16}$$

in which

$$\delta T = \int_{t_o}^{t_1}\int_{-b/2}^{b/2}\int_{-a/2}^{a/2}\left[\int_{-h_c/2-h_f}^{-h_c/2}\rho^t(\dot{u}^t\delta\dot{u}^t + \dot{v}^t\delta\dot{v}^t + \dot{w}^t\delta\dot{w}^t)d\zeta + \int_{-h_c/2}^{h_c/2}\rho^c(\dot{u}^c\delta\dot{u}^c + \dot{v}^c\delta\dot{v}^c + \dot{w}^c\delta\dot{w}^c)d\zeta + \int_{h_c/2}^{h_c/2+h_f}\rho^b(\dot{u}^b\delta\dot{u}^b + \dot{v}^b\delta\dot{v}^b + \dot{w}^b\delta\dot{w}^b)d\zeta\right]dxdydt \tag{17}$$

$$\delta U = \int_{t_o}^{t_1}\int_{-b/2}^{b/2}\int_{-a/2}^{a/2}\left[\int_{-h_c/2-h_f}^{-h_c/2}(\sigma_x^t\delta\epsilon_x^t + \sigma_y^t\delta\epsilon_y^t + \tau_{xy}^t\delta\gamma_{xy}^t)d\zeta + \int_{-h_c/2}^{h_c/2}(\sigma_z^c\delta\epsilon_z^c + \sigma_{xz}^c\delta\gamma_{xz}^c + \tau_{yz}^c\delta\gamma_{yz}^c)d\zeta + \int_{h_c/2}^{h_c/2+h_f}(\sigma_x^b\delta\epsilon_x^b + \sigma_y^b\delta\epsilon_y^b + \tau_{xy}^b\delta\gamma_{xy}^b)d\zeta\right]dxdydt \tag{18}$$

$$\delta W = \int_{t_o}^{t_1} \int_{-b/2}^{b/2} \int_{-a/2}^{a/2} q(x,y,t)\,\delta w^t dx dy dt \tag{19}$$

where ρ is the mass density. The superscript t in Eqs. (18), (17), and (19) denotes the corresponding values for the top face sheet whereas t when appearing in the variable list of the functions refers to time. The equation of motion and the boundary conditions can be obtained by substituting the stress-strain relations (10) and (15) and displacements (6) and (7*a*)–7(c) into Eqs. (18), (17), and (19), then into Eq. (16) and employing integration by parts. This results in seven equations, three for each face sheet and one for the core. There are seven unknowns: u_o^t, v_o^t, w^t, w_o^c, u_o^b, v_o^b, and w^b.

The resulting equations for the top face sheet are

$$N_{x,x}^t + N_{xy,y}^t - \left(\rho^t h_f + \rho^c \frac{h_c}{3}\right)\ddot{u}_o^t - \rho^c \frac{h_c}{6}\ddot{u}_o^b + \rho^c \frac{h_c h_f}{420}(23\ddot{w}_{,x}^t + 17\ddot{w}_{o,x}^c - 5\ddot{w}_{,x}^b) - G_{xz}^c\left[\frac{1}{h_c}(u_o^t - u_o^b) - \frac{11}{15}w_{o,x}^c - \alpha_4(w_{,x}^t + w_{,x}^b)\right] = 0 \tag{20}$$

$$N_{xy,x}^t + N_{y,y}^t - \left(\rho^t h_f + \rho^c \frac{h_c}{3}\right)\ddot{v}_o^t - \rho^c \frac{h_c}{6}\ddot{v}_o^b + \rho^c \frac{h_c h_f}{420}(23\ddot{w}_{,y}^t + 17\ddot{w}_{o,y}^c - 5\ddot{w}_{,y}^b) - G_{yz}^c\left[\frac{1}{h_c}(v_o^t - v_o^b) - \frac{11}{15}w_{o,y}^c - \alpha_4(w_{,y}^t + w_{,y}^b)\right] = 0 \tag{21}$$

and

$$M_{x,xx}^t + 2M_{xy,xy}^t + M_{y,yy}^t + (N_x^t w_{,x}^t)_{,x} + (N_{xy}^t w_{,x}^t)_{,y} + (N_{yx}^t w_{,y}^t)_{,x} + (N_y^t w_{,y}^t)_{,y} - \left(\rho^t h_f + \frac{29}{315}\rho^c h_c\right)\ddot{w}^t - \rho^c \frac{37 h_c}{630}\left(\ddot{w}_o^c - \frac{11}{37}\ddot{w}^b\right) + \left(\frac{\partial^2}{\partial x^2} + \frac{\partial^2}{\partial y^2}\right) \times \left[\left(\rho^t \frac{h_f^3}{12} + \rho^c \frac{19 h_c h_f^2}{1155}\right)\ddot{w}^t + \frac{\rho^c h_c h_f^2}{27720}(199\ddot{w}_o^c - 61\ddot{w}^b)\right] - \rho^c \frac{h_c h_f}{420}[23(\ddot{u}_{o,x}^t + \ddot{v}_{o,y}^t) + 5(\ddot{u}_{o,x}^b + \ddot{v}_{o,y}^b)] + \alpha_1 h_c(G_{xz}^c w_{,xx}^t + G_{yz}^c w_{,yy}^t) + \alpha_2 h_c(G_{xz}^c w_{o,xx}^c + G_{yz}^c w_{o,yy}^c) - \alpha_3 h_c(G_{xz}^c w_{,xx}^b + G_{yz}^c w_{,yy}^b) - \alpha_4[G_{xz}^c(u_{o,x}^t - u_{o,x}^b) + G_{yz}^c(v_{o,y}^t - v_{o,y}^b)] - (N_x^t/R_x^t + 2N_{xy}^t/R_{xy}^t + N_y^t/R_y^t) - \frac{61}{21}\frac{E^c}{h_c}\left(w^t - \frac{358}{305}w_o^c + \frac{53}{305}w^b\right) + q(x,y,t) = 0 \tag{22}$$

in which $\alpha_i (i = 1, \ldots, 4)$ are constants in terms of the ratio of face thickness and core thickness as follows:

$$\alpha_1 = \frac{29}{315} + \frac{373}{630}\frac{h_f}{h_c} + \frac{247}{252}\left(\frac{h_f}{h_c}\right)^2, \quad \alpha_2 = \frac{37}{630} + \frac{37}{630}\frac{h_f}{h_c} - \frac{383}{630}\left(\frac{h_f}{h_c}\right)^2 \tag{23a}$$

$$\alpha_3 = \frac{11}{630} + \frac{11}{630}\frac{h_f}{h_c} - \frac{23}{180}\left(\frac{h_f}{h_c}\right)^2, \quad \alpha_4 = \frac{2}{15} + \frac{h_f}{2h_c} \tag{23b}$$

A similar set of equations for the motion of the bottom face sheet can be derived, and this is listed in Appendix B.

The equations of motion for the compressible core are

$$\alpha_5 h_c(G_{xz}^c w_{o,xx}^c + G_{yz}^c w_{o,yy}^c) + \alpha_2 h_c[G_{xz}^c(w_{,xx}^t + w_{,xx}^b) + G_{yz}^c(w_{,yy}^t + w_{,yy}^b)] - \frac{194}{315}\hat{\rho} w_o^c - \frac{37 h_c}{630}\rho^c(\ddot{w}^t + \ddot{w}^b) - \frac{17 h_f h_c}{210}\rho^c(\hat{u}_{,x} + \hat{v}_{,y}) + \frac{181 h_f^2 h_c}{6930}\rho^c\left(\frac{\partial^2}{\partial x^2} + \frac{\partial^2}{\partial y^2}\right)\left[\ddot{w}_o^c + \frac{199}{724}(\ddot{w}^t + \ddot{w}^b)\right] - \frac{358}{105}\frac{E^c}{h_c}(2w_o^c - w^t - w^b) - \frac{11}{15}G_{xz}^c(u_{o,x}^t - u_{o,x}^b) - \frac{11}{15}G_{yz}^c(v_{o,y}^t - v_{o,y}^b) = -0 \tag{24}$$

where

$$\alpha_5 = \frac{194}{315} + \frac{194}{315}\frac{h_f}{h_c} + \frac{383}{315}\left(\frac{h_f}{h_c}\right)^2 \tag{25}$$

Assuming that the sandwich shells are made of orthotropic materials and substituting Eq. (4) into Eqs. (13*a*) and (13*b*) and then Eqs. (20)–(22), one can rewrite the nonlinear governing equations for the top face sheet as

$$A_{11}^t u_{o,xx}^t + A_{66}^t u_{o,yy}^t + (A_{12}^t + A_{66}^t)v_{o,xy}^t - \frac{G_{xz}^c}{h_c}(u_o^t - u_o^b) - \left(\rho^t h_f + \rho^c \frac{h_c}{3}\right)\ddot{u}_o^t - \rho^c \frac{h_c}{6}\ddot{u}_o^b = \hat{f}_1^t \tag{26a}$$

$$(A_{21}^t + A_{66}^t)u_{o,xy}^t + A_{66}^t v_{o,xx}^t + A_{22}^t v_{o,yy}^t - \frac{G_{yz}^c}{h_c}(v_o^t - v_o^b) - \left(\rho^t h_f + \rho^c \frac{h_c}{3}\right)\ddot{v}_o^t - \rho^c \frac{h_c}{6}\ddot{v}_o^b = \hat{f}_2^t \tag{26b}$$

$$D_{11}^t w_{,xxxx}^t + 2(D_{12}^t + 2D_{66}^t)w_{,xxyy}^t + D_{22}^t w_{,yyyy}^t + \frac{61}{21}\frac{E^c}{h_c}\left(w^t - \frac{358}{305}w_o^c + \frac{53}{305}w^b\right) + \left(\rho^t h_f + \rho^c \frac{29 h_c}{315}\right)\ddot{w}^t + \rho^c \frac{37 h_c}{630}\left(\ddot{w}_o^c - \frac{11}{37}\ddot{w}^b\right) - \left(\frac{\partial^2}{\partial x^2} + \frac{\partial^2}{\partial y^2}\right)\left[\left(\rho^t \frac{h_f^3}{12} + \rho^c \frac{19 h_f^2 h_c}{1155}\right)\ddot{w}^t + \frac{\rho^c h_f^2 h_c}{27720} \times (199\ddot{w}_o^c - 61\ddot{w}^b)\right] - \alpha_1 h_c(G_{xz}^c w_{,xx}^t + G_{yz}^c w_{,yy}^t) - \alpha_2 h_c(G_{xz}^c w_{o,xx}^c + G_{yz}^c w_{o,yy}^c) + \alpha_3 h_c(G_{xz}^c w_{,xx}^b + G_{yz}^c w_{,yy}^b) = q(x,y,t) + \hat{f}_3^t \tag{26c}$$

in which

$$\hat{f}_1^t = -G_{xz}^c\left[\frac{11}{15}w_{o,x}^c + \alpha_4(w_{,x}^t + w_{,x}^b)\right] - A_{11}w_{,x}^t w_{,xx}^t - (A_{12} + A_{66})w_{,y}^t w_{,xy}^t - A_{66}w_{,x}^t w_{,yy}^t - A_{11}\frac{w_{,x}^t}{R_x} - A_{12}\frac{w_{,x}^t}{R_y} - \rho^c \frac{h_f h_c}{420}(23\ddot{w}_{,x}^t + 17\ddot{w}_{o,x}^c - 5\ddot{w}_{,x}^b) \tag{27a}$$

$$\hat{f}_2^t = -G_{yz}^c\left[\frac{11}{15}w_{o,y}^c + \alpha_4(w_{,y}^t + w_{,y}^b)\right] - (A_{21}+A_{66})w_{,x}^t w_{,xy}^t - A_{66}w_{,xx}^t w_{,y}^t - A_{22}w_{,y}^t w_{,yy}^t - A_{21}\frac{w_{,y}^t}{R_x} - A_{22}\frac{w_{,y}^t}{R_y} - \rho^c\frac{h_f h_c}{420}(23\ddot{w}_{,y}^t + 17\ddot{w}_{o,y}^c - 5\ddot{w}_{,y}^b) \quad (27b)$$

$$\hat{f}_3^t = -\alpha_4[G_{xz}^c(u_{o,x}^t - u_{o,x}^b) + G_{yz}^c(v_{o,y}^t - v_{o,y}^b)] + (N_x^t w_{,x}^t)_{,x} + (N_{xy}^t w_{,x}^t)_{,y} + (N_{yx}^t w_{,y}^t)_{,x} + (N_y^t w_{,y}^t)_{,y} - \left(\frac{N_x^t}{R_x^t} + \frac{N_y^t}{R_y^t}\right) - \rho^c\frac{h_f h_c}{420}[23(\ddot{u}_{o,x}^t + \ddot{v}_{o,y}^t) + 5(\ddot{u}_{o,x}^b + \ddot{v}_{o,y}^b)] \quad (27c)$$

The first terms in the expressions for $\hat{f}_1^t$ and $\hat{f}_2^t$ reflect the effects of the higher order core theory, the second to fourth terms represent the effects from the von Karman nonlinear theory, the fifth to seventh terms represent the effects from the initial curvatures of the shallow shell, and the last terms can be viewed as the excitation produced by the transverse motion for the in-plane motion. Moreover, $\hat{f}_3^t$ includes the membrane-bending coupling effect. One can also see that the $\hat{f}_3^t$ includes the effects from the curvatures of the shell and the in-plane motion on the transverse motion. In $\hat{f}_1^t$, $\hat{f}_2^t$, and $\hat{f}_3^t$, we can further group the nonlinear terms and define

$$\hat{F}_1^t = A_{11}w_{,x}^t w_{,xx}^t + (A_{12}+A_{66})w_{,y}^t w_{,xy}^t + A_{66}w_{,x}^t w_{,yy}^t \quad (28a)$$

$$\hat{F}_2^t = (A_{21}+A_{66})w_{,x}^t w_{,xy}^t + A_{66}w_{,xx}^t w_{,y}^t \quad (28b)$$

$$\hat{F}_3^t = \frac{N_x^t}{R_x^t} + \frac{N_y^t}{R_y^t} - [(N_x^t w_{,x}^t)_{,x} + (N_{xy}^t w_{,x}^t)_{,y} + (N_{yx}^t w_{,y}^t)_{,x} + (N_y^t w_{,y}^t)_{,y}] \quad (28c)$$

Similarly, one can also recast the equations for core as follows:

$$\alpha_5 h_c(G_{xz}^c w_{o,xx}^c + G_{yz}^c w_{o,yy}^c) + \alpha_2 h_c[G_{xz}^c(w_{,xx}^t + w_{,xx}^b) + G_{yz}^c(w_{,yy}^t + w_{,yy}^b)] - \frac{194}{315}\rho^c h_c w_o^c - \frac{358}{105}\frac{E^c}{h_c}(2w_o^c - w^t - w^b) - \frac{37h_c}{630}\rho^c(\ddot{w}^t + \ddot{w}^b) + \frac{181h_f^2 h_c}{6930}\rho^c\left(\frac{\partial^2}{\partial x^2} + \frac{\partial^2}{\partial y^2}\right)\times\left[\ddot{w}_o^c + \frac{199}{724}(\ddot{w}^t + \ddot{w}^b)\right] = \hat{f}^c \quad (29)$$

where

$$\hat{f}^c = \frac{17h_f h_c}{210}\rho^c(\hat{u}_{,x} + \hat{v}_{,y}) + \frac{11}{15}G_{xz}^c(u_{o,x}^t - u_{o,x}^b) + \frac{11}{15}G_{yz}^c(v_{o,y}^t - v_{o,y}^b) \quad (30)$$

Finally, for the bottom face sheet, the equations of motion become

$$A_{11}^b u_{o,xx}^b + A_{66}^b u_{o,yy}^b + (A_{12}^b + A_{66}^b)v_{o,xy}^b + \frac{G_{xz}^c}{h_c}(u_o^t - u_o^b) - \left(\rho^b h_f + \frac{h_c}{3}\rho^c\right)\ddot{u}_o^b - \rho^c\frac{h_c}{6}\ddot{u}_o^t = \hat{f}_1^b \quad (31a)$$

$$(A_{21}^b + A_{66}^b)u_{o,xy}^b + A_{66}^b v_{o,xx}^b + A_{22}^b v_{o,yy}^b + \frac{G_{yz}^c}{h_c}(v_o^t - v_o^b) - \left(\rho^b h_f + \frac{h_c}{3}\rho^c\right)\ddot{v}_o^b - \rho^c\frac{h_c}{6}\ddot{v}_o^t = \hat{f}_2^b \quad (31b)$$

$$D_{11}^b w_{,xxxx}^b + 2(D_{12}^b + 2D_{66}^b)w_{,xxyy}^b + D_{22}^b w_{,yyyy}^b + \frac{61}{21}\frac{E^c}{h_c}\left(\frac{53}{305}w^t - \frac{358}{305}w_o^c + w^b\right) + \left(\rho^b h_f + \rho^c\frac{29h_c}{315}\right)\ddot{w}^b + \rho^c\frac{37h_c}{630}\left(\ddot{w}_o^c - \frac{11}{37}\ddot{w}^t\right) - \left(\frac{\partial^2}{\partial x^2} + \frac{\partial^2}{\partial y^2}\right)\left[\left(\rho^b\frac{h_f^3}{12} + \rho^c\frac{19h_f^2 h_c}{1155}\right)\ddot{w}^b + \rho^c\frac{h_f^2 h_c}{27720}(199\ddot{w}_o^c - 61\ddot{w}^t)\right] + \alpha_3 h_c(G_{xz}^c w_{,xx}^t + G_{yz}^c w_{,yy}^t) - \alpha_2 h_c(G_{xz}^c w_{o,xx}^b + G_{yz}^c w_{o,yy}^b) - \alpha_1 h_c(G_{xz}^c w_{,xx}^c + G_{yz}^c w_{,yy}^c) = \hat{f}_3^b \quad (31c)$$

in which

$$\hat{f}_1^b = G_{xz}^c\left[\frac{11}{15}w_{o,x}^c + \alpha_4(w_{,x}^t + w_{,x}^b)\right] - A_{11}^b w_{,x}^b w_{,xx}^b - (A_{12}^b + A_{66}^b)w_{,y}^b w_{,xy}^b - A_{66}^b w_{,x}^b w_{,yy}^b - A_{11}^b\frac{w_{,x}^b}{R_x} - A_{12}^b\frac{w_{,x}^b}{R_y} + \rho^c\frac{h_f h_c}{420}(23\ddot{w}_{,x}^b + 17\ddot{w}_{o,x}^c - 5\ddot{w}_{,x}^t) \quad (32a)$$

$$\hat{f}_2^b = G_{yz}^c\left[\frac{11}{15}w_{o,y}^c + \alpha_4(w_{,y}^t + w_{,y}^b)\right] - (A_{21}^b + A_{66}^b)w_{,x}^b w_{,xy}^b - A_{66}^b w_{,xx}^b w_{,y}^b - A_{22}^b w_{,y}^b w_{,yy}^b - A_{21}^b\frac{w_{,y}^b}{R_x} - A_{22}^b\frac{w_{,y}^b}{R_y} - \rho^c\frac{h_f h_c}{420}(5\ddot{w}_{,y}^t - 17\ddot{w}_{o,y}^c - 23\ddot{w}_{,y}^b) \quad (32b)$$

$$\hat{f}_3^b = -\alpha_4[G_{xz}^c(u_{,x}^t - u_{,x}^b) + G_{yz}^c(v_{,y}^t - v_{,y}^b)] + (N_x^b w_{,x}^b)_{,x} + (N_{xy}^b w_{,x}^b)_{,y} + (N_{yx}^b w_{,y}^b)_{,x} + (N_y^b w_{,y}^b)_{,y} - \left(\frac{N_x^b}{R_x^b} + \frac{N_y^b}{R_y^b}\right) + \rho^c\frac{h_f h_c}{420}[5(\ddot{u}_{o,x}^t + \ddot{v}_{o,y}^t) + 23(\ddot{u}_{o,x}^b + \ddot{v}_{o,y}^b)] \quad (32c)$$

As before, we can group the nonlinear terms and define

$$\hat{F}_1^b = A_{11}^b w_{,x}^b w_{,xx}^b + (A_{12}^b + A_{66}^b)w_{,y}^b w_{,xy}^b + A_{66}^b w_{,x}^b w_{,yy}^b \quad (33a)$$

$$\hat{F}_2^b = (A_{21}^b + A_{66}^b)w_{,x}^b w_{,xy}^b + A_{66}^b w_{,xx}^b w_{,y}^b + A_{22}^b w_{,y}^b w_{,yy}^b \quad (33b)$$

$$\hat{F}_3^b = \frac{N_x^b}{R_x^b} + \frac{N_y^b}{R_y^b} - [(N_x^b w_{,x}^b)_{,x} + (N_{xy}^b w_{,x}^b)_{,y} + (N_{yx}^b w_{,y}^b)_{,x} + (N_y^b w_{,y}^b)_{,y}] \quad (33c)$$

4 Solution Procedure

In this section, the solution procedure for the dynamic response of sandwich shallow shells will be demonstrated through the study of the simply supported case. The boundary conditions along the $x=0$, a and $y=0$, b sides (Fig. 1) read as

$$u_0^t = 0, \quad u_0^b = 0, \quad v_0^t = 0, \quad v_0^b = 0, \quad w^t = 0, \quad w^c = 0, \quad w^b = 0 \quad (34)$$

and

$$M_{xx}^t = 0, \quad M_{xx}^b = 0 \quad \text{for } x = 0, a \quad (35a)$$

$$M_{yy}^t = 0, \quad M_{yy}^b = 0 \quad \text{for } y = 0, b \quad (35b)$$

The displacements can be assumed as

$$u_o^t = \sum_{m,n} U_{mn}^t(t)\cos\frac{m\pi x}{a}\sin\frac{n\pi y}{b}$$

$$v_0^t = \sum_{m,n} V_{mn}^t(t)\sin\frac{m\pi x}{a}\cos\frac{n\pi y}{b} \tag{36a}$$

$$u_o^b = \sum_{m,n} U_{mn}^b(t)\cos\frac{m\pi x}{a}\sin\frac{n\pi y}{b}$$

$$v_0^b = \sum_{m,n} V_{mn}^b(t)\sin\frac{m\pi x}{a}\cos\frac{n\pi y}{b} \tag{36b}$$

$$w^t = \sum_{m,n} W_{mn}^t(t)\sin\frac{m\pi x}{a}\sin\frac{n\pi y}{b}$$

$$w^b = \sum_{m,n} W_{mn}^b(t)\sin\frac{m\pi x}{a}\sin\frac{n\pi y}{b} \tag{36c}$$

$$w_o^c = \sum_{m,n} W_{mn}^c(t)\sin\frac{m\pi x}{a}\sin\frac{n\pi y}{b}$$

where $U_{mn}^t(t)$, $V_{mn}^t(t)$, $U_{mn}^b(t)$, $V_{mn}^b(t)$, $W_{mn}^t(t)$, $W_{mn}^b(t)$, and $W_{mn}^c(t)$ are unknown functions of time t. These displacements satisfy the boundary conditions. Substituting Eqs. (36*a*)–(36*d*) into Eqs. (26*a*)–(26*c*), (29), and (31*a*)–(31*c*) with $\hat{F}_i^t$, $\hat{F}_i^b (i=1,2,3)$, and $q(x,y,t)$ being expressed into the following form:

$$\hat{F}_1^t = \sum_{mn} \hat{F}_{1mn}^t(t)\cos\frac{m\pi x}{a}\sin\frac{n\pi y}{b}$$

$$\hat{F}_2^t = \sum_{mn} \hat{F}_{2mn}^t(t)\sin\frac{m\pi x}{a}\cos\frac{n\pi y}{b} \tag{37a}$$

$$\hat{F}_3^t = \sum_{mn} \hat{F}_{3mn}^t(t)\sin\frac{m\pi x}{a}\sin\frac{n\pi y}{b}$$

$$\hat{F}_1^b = \sum_{mn} \hat{F}_{1mn}^b(t)\cos\frac{m\pi x}{a}\sin\frac{n\pi y}{b}$$

$$\hat{F}_2^b = \sum_{mn} \hat{F}_{2mn}^b(t)\sin\frac{m\pi x}{a}\cos\frac{n\pi y}{b} \tag{37b}$$

$$\hat{F}_3^b = \sum_{mn} \hat{F}_{3mn}^b \sin\frac{m\pi x}{a}\sin\frac{n\pi y}{b}$$

$$q(x,y,t) = \sum_{mn} \hat{Q}_{mn}(t)\sin\frac{m\pi x}{a}\sin\frac{n\pi y}{b} \tag{37d}$$

we can obtain sets of second order ordinary differential equations with regard to the variable time in matrix form:

$$[\mathbf{M}_{mn}]\ddot{U}_{mn}(t) + [\mathbf{s}_{mn}]\dot{U}_{mn}(t) + [\boldsymbol{\kappa}_{mn}]\mathbf{U}_{mn}(t) = \mathbf{F}_{mn}(t) \tag{37e}$$

where $[\mathbf{M}_{mn}]$ is the equivalent mass matrix, $[\mathbf{s}_{mn}]$ is the damping coefficient matrix, and $[\boldsymbol{\kappa}_{mn}]$ is the equivalent spring constant matrix. These are 7×7 matrices for a given pair (m,n).

The displacement vector $\mathbf{U}_{mn}$ is defined as $\mathbf{U}_{mn} = [U_{mn}^t(t), V_{mn}^t(t), W_{mn}^t(t), W_{mn}^c(t), U_{mn}^b(t), V_{mn}^b(t), W_{mn}^b(t)]^T$ and the loading vector $\mathbf{F}_{mn} = [\hat{F}_{1mn}^t(t) + \hat{Q}_{mn}(t), \hat{F}_{2mn}^t(t), \hat{F}_{3mn}^t(t), 0, \hat{F}_{1mn}^b(t), \hat{F}_{2mn}^b(t), \hat{F}_{3mn}^b(t)]^T$. The $\hat{F}_{jmn}^t(t)$, $\hat{F}_{jmn}^b(t)$, $\hat{Q}_{mn}(t)$ are obtained from Eqs. (37*a*)–(37*d*) as

$$\hat{Q}_{mn}(t) = \frac{4}{ab}\int_0^a\int_0^b q(x,y,t)\sin\frac{m\pi x}{a}\sin\frac{n\pi y}{b} \tag{37f}$$

$$\hat{F}_{1mn}^t(t) = \frac{4}{ab}\int_0^a\int_0^b \hat{F}_1^t\cos\frac{m\pi x}{a}\sin\frac{n\pi y}{b} \tag{37g}$$

$$\hat{F}_{1mn}^b(t) = \frac{4}{ab}\int_0^a\int_0^b \hat{F}_1^b\cos\frac{m\pi x}{a}\sin\frac{n\pi y}{b} \tag{38}$$

with similar expressions for the rest of the $\hat{F}_{jmn}^t(t)$ and $\hat{F}_{jmn}^b(t)$.

Next, applying the Laplace transform

$$\tilde{U}(s) = L[U(t)](s) = \int_0^\infty U(t)e^{-st}dt \tag{39}$$

to Eq. (38), one can further obtain

$$(s^2[\mathbf{M}_{mn}] + s[\mathbf{s}_{mn}] + [\boldsymbol{\kappa}_{mn}])\tilde{U}_{mn}(s) = \tilde{\mathbf{F}}_{mn}(s) \tag{40}$$

In the Laplace space, the solution in terms of the displacements to Eq. (40) can be obtained without much difficulty if the loading vector $\tilde{\mathbf{F}}_{mn} = [\tilde{F}_{1mn}^t + \tilde{Q}_{mn}(s), \tilde{F}_{2mn}^t, \tilde{F}_{3mn}^t, 0, \tilde{F}_{1mn}^b, \tilde{F}_{2mn}^b, \tilde{F}_{3mn}^b]^T$ is constant, then Eq. (40) is a set of linear algebraic equations, which can be solved directly for $\tilde{U}_{mn} = [\tilde{U}_{mn}^t, \tilde{V}_{mn}^t, \tilde{W}_{mn}^t, \tilde{W}_{mn}^c, \tilde{U}_{mn}^b, \tilde{V}_{mn}^b, \tilde{W}_{mn}^b]^T$ and then the displacements in time domain $U_{mn} = [U_{mn}^t(t), V_{mn}^t(t), W_{mn}^t(t), W_{mn}^c(t), U_{mn}^b(t), V_{mn}^b(t), W_{mn}^b(t)]^T$ can be recovered using the inverse Laplace transform without much difficulty. Subsequently, the solution for the displacements can be found by using Eqs. (36*a*)–(36*d*). However, the loading coefficients $\tilde{F}_{jmn}^t$ and $\tilde{F}_{jmn}^b$ were derived from expressions (28*a*)–(28*c*) and (33*a*)–(33*c*), which are nonlinear functions of the displacements. However, the right-hand side of Eq. (40), $\tilde{\mathbf{F}}_{mn}$, are nonlinear functions of $\tilde{U}_{mn}$. Therefore, an iterative procedure is developed as follows: (1) First, $\tilde{Q}_{mn}$ is a known function once the applied load is given. If the right-hand side of Eq. (40) is approximated by $\tilde{\mathbf{F}}_{mn} = [\tilde{Q}_{mn}, 0, 0, 0, 0, 0, 0]^T$, then a first approximation to the solution is easily obtained as $\{\tilde{U}_{mn}(s) = s^2[\mathbf{M}_{mn}] + s[\mathbf{s}_{mn}] + [\boldsymbol{\kappa}_{mn}]\}^{-1}\tilde{\mathbf{F}}_{mn}$ (the superscript -1 denotes matrix inversion). (2) Application of the inverse Laplace transform to $\tilde{U}_{mn}(s)$ can lead to the corresponding solution $U_{mn}(t)$. Then, making use of Eqs. (36*a*)–(36*d*), (33*a*)–(33*c*), and (28*a*)–(28*c*), one can determine the functions $\hat{F}_1^t$, $\hat{F}_2^t$, $\hat{F}_3^t$ and $\hat{F}_1^b$, $\hat{F}_2^b$, $\hat{F}_3^b$ and then the corresponding to these Laplace transforms $\tilde{F}_1^t$, $\tilde{F}_2^t$, $\tilde{F}_3^t$ and $\tilde{F}_1^b$, $\tilde{F}_2^b$, $\tilde{F}_3^b$. (3) The next approximation for the displacements is found by solving Eq. (40) with the updated vector $\tilde{\mathbf{F}}_{mn} = [\tilde{F}_{1mn}^t + \tilde{Q}_{mn}(s), \tilde{F}_{2mn}^t, \tilde{F}_{3mn}^t, 0, \tilde{F}_{1mn}^b, \tilde{F}_{2mn}^b, \tilde{F}_{3mn}^b]^T$. This procedure continues until the in-plane and transverse displacements are determined by the nth iteration with a convergence tolerance ϵ applied on the displacements normalized by the total height of the sandwich section, such that $\epsilon \leq 10^{-5}$ between two consecutive steps.

5 Applications and Discussions

The formulas and solution procedure in the foregoing sections can be applied to investigate the nonlinear transient response of a shallow shell subjected to a sudden blast loading [14]. Detailed analysis of a few example problems are presented in this section.

Uniformly Distributed and Exponentially Decaying Blast Loading on an Orthotropic Sandwich Shallow Shell. In this example, both the top and bottom face sheets of the sandwich shallow shell are made of E-glass/polyester composite material with stiffnesses (in GPa): $E_1=50.8$, $E_2=35.7$, $G_{12}=7.1$; Poisson's ratios: $\nu_{12}=0.35$, $\nu_{21}=0.246$; and mass density $\rho^{t,b}=1632\ \mathrm{kg/m^3}$. The ortho-

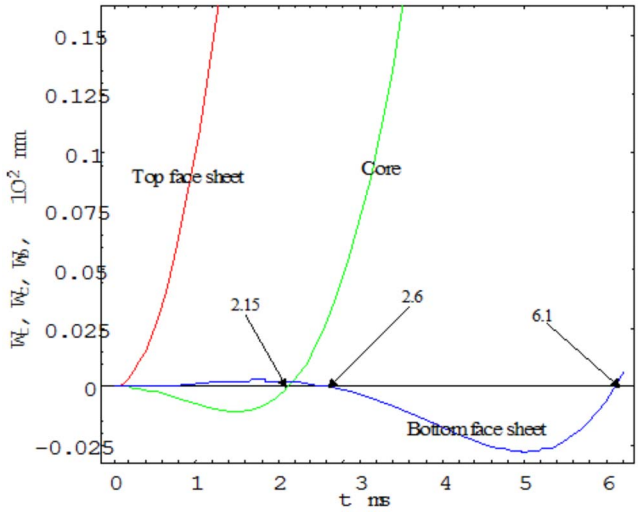

Fig. 2 Transient response of a sandwich shallow shell at the very early stage of blast loading

tropic core material has the following properties: $E^c=1.005$ GPa, $G^c_{xz}=120.6$ MPa, $G^c_{yz}=75.8$ MPa, $\nu_c=0.3$, and $\rho^c=64$ kg/m^3. The top and bottom face sheets have an identical thickness $h_f=1.0$ mm and the thickness of the core is $h_c=20.0$ mm. The geometric dimensions of the shell (Fig. 1) read as (in mm): $a=800$, $b=500$, $R_x=1000$, and $R_y=600$. The top face sheet is subjected to blast loading, which is uniformly distributed over the entire sheet surface, but its intensity varies with time exponentially:

$$p_i(t)=q_m e^{-t/\alpha}, \quad t\geq 0 \tag{41}$$

We use in this example the values from Ref. [4]: $q_m=60.86$ MPa and $\alpha=3.33435$.

The results in Fig. 2 are the transverse displacements for the center points in the top face sheet, core middle plane, and bottom face sheet, respectively, within a few micrometers after the blast loading impact on the front surface of the top face sheet. An interesting phenomenon can be observed in the early blast loading stage: the top face sheet, core, and bottom face sheet behaviors are very different: (1) The displacement for the top face sheet increases with time positively (relative to the loading direction) due to the continuously applied loading; (2) the displacement for the middle plane in the core is negative when time $t\leqslant 2.15$ μs, then it becomes positive; and (3) the displacement of the bottom face sheet changes from positive to negative around time $t=2.6$ μs, then it becomes positive again after time $t=6.1$ μs. This phenomenon reflects the impact shock stress wave propagation in the sandwich shell. The blast loading impacts on the surface of the top face sheet at the instant of time $t=0^+$ μs and induces a shock wave propagating through the thickness of the shell. During this time period, a negative pressure zone, which is similar to the cavitation zone in water, behind the shock wave front, is created in the core. This is why we see the displacement of the middle plane of the core negative up to $t_a=2.15$ μs. This negative pressure zone reaches the bottom face sheet around $t_b=2.6$ μs. The displacement of the bottom face sheet then becomes negative until $t_c=6.1\mu$s, when this zone is dissipated. One may also interestedly note that the propagation velocity of the cavity zone is nonlinear since $t_c\geqslant 2t_b$. This observation clearly demonstrates that the nonlinear higher core theory in this paper can give us deep insight on what happens at the different phases of the sandwich construction when it is subjected to a blast loading.

Two points need to be further explained in Fig. 2. First, it can be observed that the midpoint back face displacement is double that of the midpoint core and this is because these two displacements are at different time instants and the back face and the core are different materials. There is actually no direct relation between them due to the core compressibility, which can mask the otherwise intuitively derived behavior, i.e., the core can expand in the process and therefore show larger back face displacement than at an earlier instant. Furthermore, as the wave propagates in the sandwich, energy is still added in the material system in this early time period, which can make up for the energy dissipation as the wave propagates in the sandwich. Therefore, the larger back face deflection in Fig. 2 is quite plausible. Second, it can be seen that during the early part of loading, the face sheets deform in one direction and the core in the opposite and this is due to the core compressibility and the shock wave propagation and reflection. It should be noted that the curve of the core deflection is the deflection of the initial midpoint of the core, not the current core midpoint location. In other words, in this early phase, a negative pressure zone is induced within the core and, since the core is compressible, it expands in the process of shock wave propagation. This negative pressure results in part of the sandwich structure deforming in the opposite direction. Therefore, the observed deflections are compatible.

The results plotted in Fig. 3 show that the popular assumption that the displacements of the middle planes in the top face sheet, the core, and the bottom face sheet are identical may be true only at some time instants. Most of the time, the transient responses of these three displacements are different, as will be further shown in the following discussion.

Presented in Fig. 4 is the transient response in terms of the displacements $[W_t(t), W_c(t), W_b(t)]$ for the center points in the middle plane of the sandwich shallow shell in a short time period ($0\leqslant t\leqslant 6$ ms) after the blast loading is applied on the surface of the top face sheet. The maximum values of these displacements happen around time $t=0.2$ ms and then decrease to near-half of the maximum values quickly. One can see that the solution converges as the time increases. The detailed drawings in Sections A and B show that the curves representing the displacements are tangled in the sense that the core midplane displacement exceeds that of the midplane bottom face sheet due to the compressibility of the core. This observation would further indicate that the nonlinear core theory may be a good model to study the behavior of sandwich structures subjected impact loading.

The behavior of the sandwich shell in the stage from the transient response to the steady dynamic response is demonstrated in Fig. 5. It can be seen that after time $t\geqslant 12$ ms, the sandwich structure enters into a steady state dynamic response region. One interesting result in the figure observed from the steady state dynamics response is that the curve for the displacement of the core is not in the middle between the curves of the top and bottom face sheets. This is due to the nonlinearity in the core transverse displacement.

Finally, Fig. 6 shows the stress profile σ_{zz} through the thickness and as a function of time. It can be seen that at the top face sheet, the stresses are always compressive and the highest in magnitude. The bottom face sheet shows lower stresses and they can even be at brief times tensile. This would indicate that damage would most likely initiate at the front (top) face sheet or even more likely at the front (top) face sheet/core interface. Such has been preliminary experimental evidence [15].

6 Conclusions

In this work, a higher order nonlinear core theory is proposed and is incorporated into the constitutive equations. A set of nonlinear governing equations is formulated and the solution procedure is obtained using the extended Galerkin method and the Laplace transform. Numerical results are presented to demonstrate the application of this higher order core model for the transient response of a composite sandwich shallow shell subject to blast loading. The observations obtained in the forgoing study suggest the following conclusions: (1) This nonlinear higher order core model can be used to capture the complex behavior such as cavi-

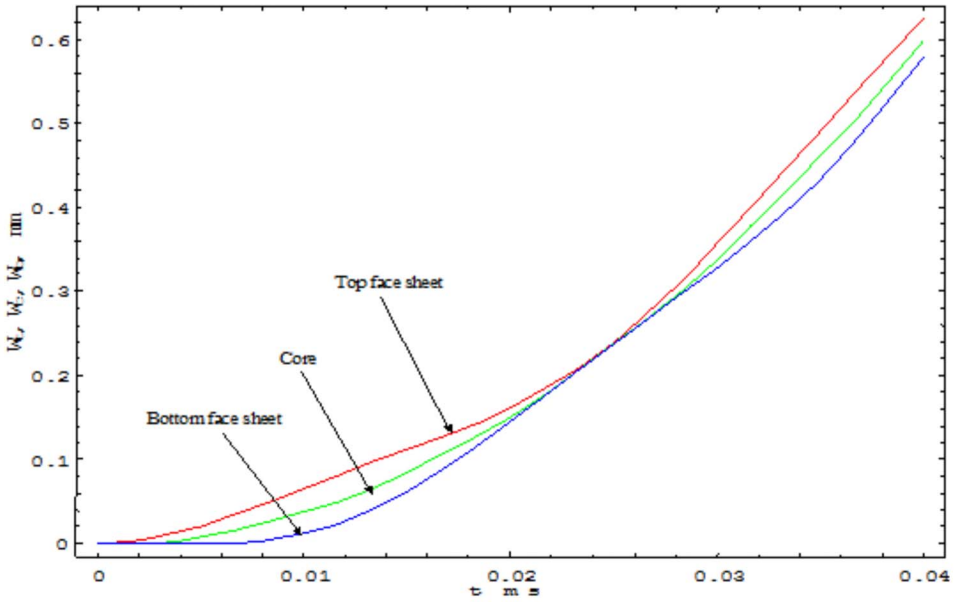

Fig. 3 Transient response of a sandwich shallow shell at a larger time scale of blast loading

tation in the core caused by the shock wave in the sandwich shell during the very early stage following the blast loading and the high levels of core thickness reduction; (2) the conventional assumption that the middle plane of the top face sheet, the core, and the bottom face sheet is identical may be not adequate in studying blast loading problems; (3) the highest in magnitude stresses are observed at the front (top) face sheet, which indicates that damage would most likely initiate at the front (top) face sheet/core interface.

Acknowledgment

The financial support of the Office of Naval Research, Grant No. N00014-07-10373, and the interest and encouragement of the Grant Monitor, Dr. Y. D. S. Rajapakse, are both gratefully acknowledged.

Appendix A: Derivation of the Fourth Order Nonlinear Compressible Core Theory

Let the displacements in the core be approximated by a fourth order polynomial in terms of the displacements in the top face sheet, middle plane of the core, and bottom face sheet. Then, the transverse displacement in the core can be expressed as

$$w^c(x,y,\zeta,t) = \left(\beta_0 - \beta_2\frac{\zeta^2}{h_c^2} - \beta_4\frac{\zeta^4}{h_c^4}\right)w_o^c(x,y,t) + \left(\beta_2\frac{\zeta^2}{h_c^2} + \beta_4\frac{\zeta^4}{h_c^4}\right)\bar{w}(x,y,t) - \left(\beta_1\frac{\zeta}{h_c} + \beta_3\frac{\zeta^3}{h_c^3}\right)\hat{w}(x,y,t), \quad -\frac{h_c}{2} \le \zeta \le \frac{h_c}{2} \tag{A1}$$

in which $w_0^c(x,y)$ is the transverse displacement of the middle surface of the core, and $\bar{w}(x,y)$ and $\hat{w}(x,y)$ are, respectively, the average and difference of the middle surface transverse displacements for the two face sheets,

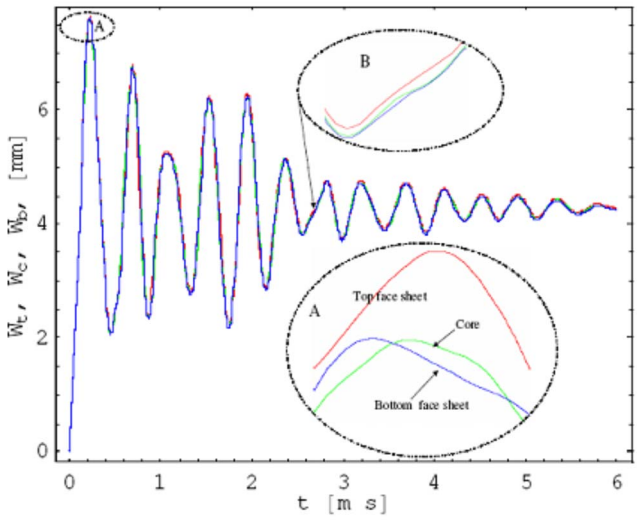

Fig. 4 Transient response of a sandwich shallow shell at an even larger time scale following blast loading

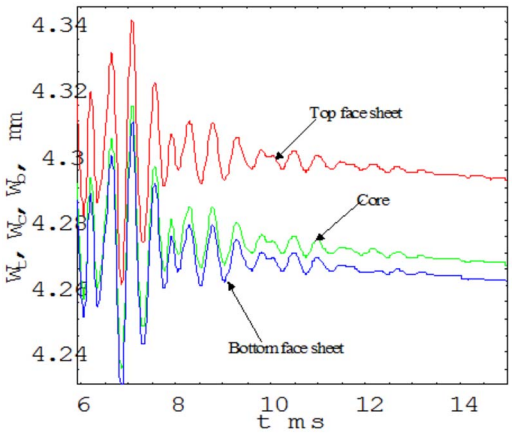

Fig. 5 The stage from transient to steady dynamic response for a sandwich shallow shell subject to blast loading

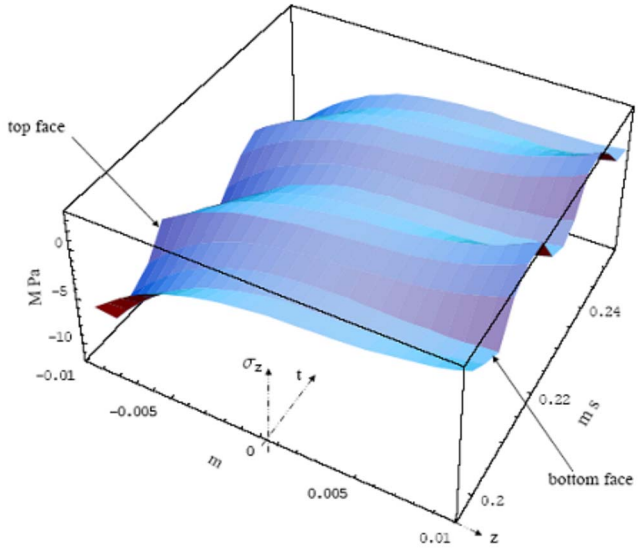

Fig. 6 Stress profiles following blast loading

$$\bar{w}(x,y,t) = \frac{1}{2}[w^t(x,y,t) + w^b(x,y,t)]$$

$$\hat{w}(x,y,t) = \frac{1}{2}[w^t(x,y,t) - w^b(x,y,t)] \tag{A2}$$

The in-plane displacements in the core can also be approximated as follows (fifth power of ζ):

$$u^c(x,y,\zeta,t) = \bar{u}(x,y,t) + \beta_5\frac{\zeta}{h_c}\hat{u}(x,y,t) + \zeta\frac{h_f}{h_c}w^c_{,x}(x,y,\zeta,t) \tag{A3a}$$

$$v^c(x,y,\zeta,t) = \bar{v}(x,y,t) + \beta_6\frac{\zeta}{h_c}\hat{v}(x,y,t) + \zeta\frac{h_f}{h_c}w^c_{,y}(x,y,\zeta,t) \tag{A3b}$$

where $\bar{u}(x,y,t)$, $\hat{u}(x,y,t)$ and $\bar{v}(x,y,t)$, $\hat{v}(x,y,t)$ are, again, respectively, the average and difference of the middle surface in-plane displacements for the two face sheets:

$$\bar{u}(x,y,t) = \frac{1}{2}[u^t_o(x,y,t) + u^b_o(x,y,t)]$$

$$\hat{u}(x,y,t) = \frac{1}{2}[u^t_o(x,y,t) - u^b_o(x,y,t)] \tag{A4a}$$

$$\bar{v}(x,y,t) = \frac{1}{2}[v^t_o(x,y,t) + v^b_o(x,y,t)]$$

$$\hat{v}(x,y,t) = \frac{1}{2}[v^t_o(x,y,t) - v^b_o(x,y,t)] \tag{A4b}$$

Therefore, there are seven constants β_i, $i=0,6$, to be determined from displacement continuity as follows.

Top face sheet/core interface, $\zeta=-h_c/2$:

$$u^c(x,y,\zeta,t)|_{\zeta=-h_c/2} = u^t_o(x,y,t) - \frac{h_f}{2}w^t_{,x}(x,y,t) \tag{A5a}$$

$$v^c(x,y,\zeta,t)|_{\zeta=-h_c/2} = v^t_o(x,y,t) - \frac{h_f}{2}w^t_{,y}(x,y,t) \tag{A5b}$$

$$w^c(x,y,\zeta,t)|_{\zeta=-h_c/2} = w^t(x,y,t) \tag{A5c}$$

Bottom face sheet/core interface, $\zeta=h_c/2$:

$$u^c(x,y,\zeta,t)|_{\zeta=h_c/2} = u^b_o(x,y,t) + \frac{h_f}{2}w^b_{,x}(x,y,t) \tag{A5d}$$

$$v^c(x,y,\zeta,t)|_{\zeta=h_c/2} = v^b_o(x,y,t) + \frac{h_f}{2}w^b_{,y}(x,y,t) \tag{A5e}$$

$$w^c(x,y,\zeta,t)|_{\zeta=h_c/2} = w^b(x,y,t) \tag{A5f}$$

Also, at the midsurface of the core, $\zeta=0$:

$$w^c(x,y,\zeta,t)|_{\zeta=0} = w^c_0(x,y,t) \tag{A5g}$$

Substitution of Eqs. (A1), (A3*a*), and (A3*b*) into the seven continuity conditions (A5*a*)–(A5*g*) leads to

$$\beta_0 = \beta_1 = 1, \quad \beta_2 = -2, \quad \beta_3 = -4, \quad \beta_4 = -8, \quad \beta_5 = \beta_6 = -1/2 \tag{A6}$$

Appendix B: The Governing Equations for the Bottom Face Sheet

One can see that the governing equations are nonlinear. Substituting equations Eq. (4) into Eqs. (13*a*) and (13*b*) and then Eqs. (20)–(22), the governing equations for the bottom face sheet can be written as

$$N^b_{x,x} + N^b_{xy,y} - \left(\rho^b h_f + \rho^c\frac{h_c}{3}\right)\ddot{u}^b_o - \rho^c\frac{h_c}{6}\ddot{u}^t_o + \rho^c\frac{h_f h_c}{420}(5\ddot{w}^t_{,x} - 17\ddot{w}^c_{o,x} - 23\ddot{w}^b_{,x}) + G^c_{xz}\left[\frac{(u^t_o - u^b_o)}{h_c} - \frac{11}{15}w^c_{o,x} - \alpha_4(w^t_{,x} + w^b_{,x})\right] = 0 \tag{B1a}$$

$$N^b_{xy,x} + N^b_{y,y} - \left(\rho^b h_f + \rho^c\frac{h_c}{3}\right)\ddot{v}^b_o - \rho^c\frac{h_c}{6}\ddot{v}^t_o + \rho^c\frac{h_f h_c}{420}(5\ddot{w}^t_{,y} - 17\ddot{w}^c_{o,y} - 23\ddot{w}^b_{,y}) + G^c_{yz}\left[\frac{(v^t_o - v^b_o)}{h_c} - \frac{11}{15}w^c_{o,y} - \alpha_4(w^t_{,y} + w^b_{,y})\right] = 0 \tag{B1b}$$

$$M^b_{x,xx} + 2M^b_{xy,xy} + M^b_{y,yy} + (N^b_x w^b_{,x})_{,x} + (N^b_{xy}w^b_{,x})_{,y} + (N^b_{yx}w^b_{,y})_{,x} + (N^b_y w^b_{,y})_{,y} - \left(\rho^b h_f + \rho^c\frac{29h_c}{315}\right)\ddot{w}^b - \rho^c\frac{37h_c}{630}\left(\ddot{w}^c_0 - \frac{11}{37}\ddot{w}^t\right) + \left(\frac{\partial^2}{\partial x^2} + \frac{\partial^2}{\partial y^2}\right)\left[\left(\rho^t\frac{h_f^3}{12} + \rho^c\frac{19h_f^2h_c}{1155}\right)\ddot{w}^b + \rho^c\frac{h_f^2h_c}{27720}(199\ddot{w}^c_o - 61\ddot{w}^t)\right] + \rho^c\frac{h_f h_c}{420}[5(\ddot{u}^t_{o,x} + \ddot{v}^t_{o,y}) + 23(\ddot{u}^b_{o,x} + \ddot{v}^b_{o,y})] - \alpha_3 h_c(G^c_{xz}w^t_{,xx} + G^c_{yz}w^t_{,yy}) + \alpha_2 h_c(G^c_{xz}w^b_{,xx} + G^c_{yz}w^b_{,yy}) + \alpha_1 h_c(G^c_{xz}w^c_{o,xx} + G^c_{yz}w^c_{o,yy}) - \alpha_4[G^c_{xz}(u^t_{o,x} - u^b_{o,x}) + G^c_{yz}(v^t_{o,y} - v^b_{o,y})] - \left(\frac{N^b_x}{R^b_x} + \frac{N^b_y}{R^b_y}\right) - \frac{61}{21}\frac{E^c}{h_c}\left(\frac{53}{305}w^t - \frac{358}{305}w^c_o + w^b\right) = 0 \tag{B1c}$$

References

[1] Taylor, G. I., 1986, "The Pressure and Impulse of Submarine Explosion Waves on Plates," *The Scientific Papers of G.I. Taylor*, Vol. III, Cambridge University Press, UK, Cambridge, pp. 287–303.

[2] Vinson, J. R., 1999, *The Behavior of Sandwich Structures of Isotropic and Composite Materials*, Technomic Lancaster, PA.

[3] Xue, Z., and Hutchinson, J. W., 2003, "Preliminary Assessment of Sandwich Plates Subject to Blast Loads," Int. J. Mech. Sci., **45**, pp. 687–705.

[4] Librescu, L., Oh, S.-Y., and Hohe, J., 2004, "Linear and Non-Linear Dynamic Response of Sandwich Panels to Blast Loading," Composites, Part B, **35**, pp. 673–683.
[5] Deshpande, V. S., and Fleck, N. A., 2005, "One-Dimensional Response of Sandwich Plates to Underwater Shock Loading," J. Mech. Phys. Solids, **53**, pp. 2347–2383.
[6] Liang, Y., Spuskanyuk, A. V., Flores, S. E., Hayhurst, D. R., Hutchinson, J. W., McMeeking, R. M., and Evans, A. G., 2007, "The Response of Metallic Sandwich Panels to Water Blast," ASME J. Appl. Mech., **74**(1), pp. 81–99.
[7] Nemat-Nasser, S., Kang, W. J., McGee, J. D., Guo, W.-G., and Issacs, J. B., 2007, "Experimental Investigation of Energy-Absorption Characteristics of Components of Sandwich Structures," Int. J. Impact Eng., **34**, pp. 1119–1146.
[8] Plantema, F. J., 1966, *Sandwich Construction*, Wiley, New York.
[9] Allen, H. G., 1969, *Analysis and Design of Structural Sandwich Panels*, Pergamon, Oxford.
[10] Frostig, Y., 1992, "Behavior of Delaminated Sandwich Beams With Transversely Flexible Core-Hight Order Theory," Compos. Struct., **20**, pp. 1–16.
[11] Li, R., Frostig, Y., and Kardomateas, G. A., 2001, "Nonlinear High-Order Response of Imperfect Sandwich Beams With Delaminated Faces," AIAA J., **39**,(9), pp. 1782–1787.
[12] Hause, T., Librescu, L., and Camarda, C. J., 1998, "Post-Buckling of Anisotropic Flat and Doubly-Curved Sandwich Panels Under Complex Loading Conditions," Int. J. Solids Struct., **35**, pp. 3007–3027.
[13] Gould, P. L., 1977, *Static Analysis of Shells*, D. C. Heath. and Company, Lexington, MA.
[14] Cole, R. H., 1965, *Underwater Explosion*, Dover, New York.
[15] Shukla, A., 2007, private communication.

Singularities Interacting With a Coated Circular Inhomogeneity Revisited

Seung Tae Choi
Mem.ASME
Micro Systems Lab,
Samsung Advanced Institute of Technology,
P.O. Box 111,
Suwon 440-600, Republic of Korea
e-mail: stchoi@kaist.ac.kr

Singularities interacting with a coated circular inhomogeneity are analyzed with the method of analytic continuation and the Schwarz–Neumann's alternating technique. It is shown that the solution for singularities in a homogeneous medium can be used as a building block of the solution for the same singularities interacting with a coated circular inclusion. The obtained solutions have series forms independent of any specific information about singularities, and thus they can be interpreted as general solutions for a variety of singularities. [DOI: 10.1115/1.2937149]

Keywords: isotropic elasticity, singularity, coated circular inclusion, analytic continuation, alternating technique

Elastic interactions between coated inhomogeneities and singularities, such as dislocations and point forces, have received a considerable amount of attention in literature of solid mechanics [1–5]. A coated circular inhomogeneity or inclusion denotes a circular inhomogeneity covered with a dissimilar material with uniform thickness. Mainly, the method of analytic continuation [6,7] and the Schwarz–Neumann's alternating technique [8] were used to solve the interaction problems. Most previous researches have been devoted to point forces and edge dislocations, while the elastic analyses of other singularities, such as point moment, dislocation dipole, and circular transformation strain spot, interacting with inhomogeneities are also of recent interest in micromechanics [6]. Unlike the analytic continuation of potential functions across straight interfaces [6,9,10], the analytic continuation across circular interfaces produces additional terms depending on the specific information of singularities [7], which hinders obtaining general solutions for a variety of singularities. In this study, a unified approach to the problem of singularities interacting with a coated circular inclusion is developed, in which the method of analytic continuation is alternatively applied to two concentric circular interfaces, so that the obtained solutions are independent of any specific information about singularities.

The components of the stresses σ_{ij} and displacements u_i for an isotropic solid under plane deformation are expressed in terms of Muskhelishvili's complex potentials $\Phi(z)$ and $\Psi(z)$ as follows [11]:

$$\frac{\sigma_{11}+\sigma_{22}}{2} = \Phi(z) + \bar{\Phi}(\bar{z}) \tag{1}$$

$$\frac{\sigma_{22}-\sigma_{11}}{2} + i\sigma_{12} = \bar{z}\Phi'(z) + \Psi(z) \tag{2}$$

$$2G(u_1 - iu_2) = \kappa\bar{\varphi}(\bar{z}) - \bar{z}\varphi'(z) - \psi(z) \tag{3}$$

where $\kappa = 3-4\nu$ for plane-strain deformation and $(3-\nu)/(1+\nu)$ for plane-stress deformation, and ν and G are Poisson's ratio and the shear modulus, respectively. Here, the overbar $(\bar{})$ represents the complex conjugate and the prime $()'$ the derivative with respect to $z=x+iy$. The functions $\varphi(z)$ and $\psi(z)$ in Eq. (3) are related to Muskhelishvili's potentials by $d\varphi(z)/dz=\Phi(z)$ and $d\psi(z)/dz=\Psi(z)$, respectively. Another potential $\Omega^R(z)$ is defined for mathematical convenience as

$$\Omega^R(z) \equiv \bar{\Phi}\left(\frac{R^2}{z}\right) - \frac{R^2}{z}\bar{\Phi}'\left(\frac{R^2}{z}\right) - \frac{R^2}{z^2}\bar{\Psi}\left(\frac{R^2}{z}\right) \tag{4}$$

It is noted that unlike the potentials $\Phi(z)$ and $\Psi(z)$, the potential $\Omega^R(z)$ is holomorphic in the inverse domain of the analytic domain of the potentials $\Phi(z)$ and $\Psi(z)$ with respect to the circle with radius R and center at the origin, and thus the potential $\Omega^R(z)$ is dependent on the length parameter R. To apply the method of analytic continuation to circular interfaces with different radii, the following transformation can be derived from Eq. (4):

$$\Omega^{\mathrm{I}}(z) = \frac{r_{\mathrm{II}}^2}{r_{\mathrm{I}}^2}\Omega^{\mathrm{II}}\left(\frac{r_{\mathrm{II}}^2}{r_{\mathrm{I}}^2}z\right) + \left(1-\frac{r_{\mathrm{II}}^2}{r_{\mathrm{I}}^2}\right)\left[\bar{\Phi}\left(\frac{r_{\mathrm{I}}^2}{z}\right) - \frac{r_{\mathrm{I}}^2}{z}\bar{\Phi}'\left(\frac{r_{\mathrm{I}}^2}{z}\right)\right] \tag{5}$$

where $\Omega^{\mathrm{I}}(z)$ and $\Omega^{\mathrm{II}}(z)$ represent $\Omega^R(z)$ with $R=r_{\mathrm{I}}$ and $R=r_{\mathrm{II}}$, respectively.

The potentials for a singularity at $z=s$ in an infinite homogeneous medium can be written in general as $\Phi_0(z)=\Sigma_{m=1}^{M}A_m/(z-s)^m$ and $\Psi_0(z)=\Sigma_{m=1}^{M}B_m/(z-s)^m$, where the coefficients A_m and B_m typically depend on s and the nature of the singularity. Several examples of the complex potentials $\Phi_0(z)$ and $\Psi_0(z)$ (or equivalently $\Phi_0(z)$ and $\Omega_0^R(z)$ with the definition of $\Omega^R(z)$ given in Eq. (4)) are given in Ref. [6].

To analyze a singularity interacting with a coated circular inclusion as shown in Fig. 1, precisely the same procedure as that of Choi and Earmme [9,10] can be used. Three cases for the position of a singularity are separately dealt with.

Case I: A Singularity Embedded in S_c. With the aid of Eq. (5), the problem given in Fig. 1 is now considered, in which materials a, b, and c occupying regions $S_a: r_{\mathrm{I}} \le r_{\mathrm{I}}$, $S_b: r_{\mathrm{I}} \le r \le r_{\mathrm{II}}$, and $S_c: r_{\mathrm{II}} \le r$, respectively, are perfectly bonded along two concentric circular interfaces $\Gamma_{\mathrm{I}}: r=r_{\mathrm{I}}$ and $\Gamma_{\mathrm{II}}: r=r_{\mathrm{II}}$. The complex potentials for the three regions are assumed to have series forms. By then applying the method of analytic continuation to the two interfaces alternatively, the unknown potentials are expressed in terms of $\Phi_0(z)$ and $\Omega_0^{\mathrm{II}}(z)$, in which the elastic constants of material c are implied. This procedure is similar to the four steps described in Appendix A of Choi and Earmme [9]. Therefore, the details are suppressed here, but the results are as follows:

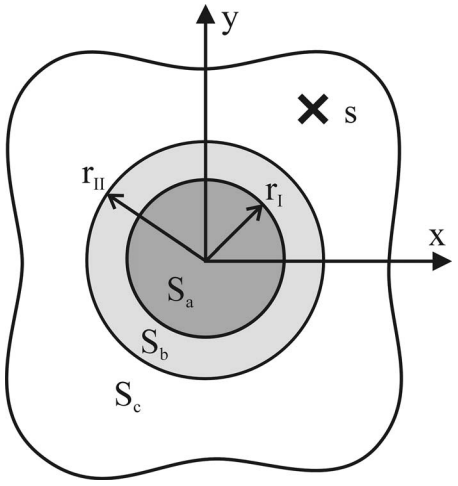

Fig. 1 A singularity interacting with a coated circular inclusion

Contributed by the Applied Mechanics Division of ASME for publication in the JOURNAL OF APPLIED MECHANICS. Manuscript received August 5, 2007; final manuscript received March 28, 2008; published online August 22, 2008. Review conducted by Zhigang Suo.

$$\Phi(z)=\begin{cases}\Phi_a(z)=\displaystyle\sum_{n=1}^{\infty}\left\{(1+\Lambda_{ab})[\Phi_n(z)+d_n]+\frac{e_n}{1-\beta_{ab}}\right\} & \text{in } S_a\\ \Phi_b(z)=\displaystyle\sum_{n=1}^{\infty}[\Phi_n(z)+\tilde{\Phi}_n(z)] & \text{in } S_b\\ \Phi_c(z)=\Phi_0(z)+\Pi_{bc}\Omega_0^{\mathrm{II}}(z)+d_0+\dfrac{e_0}{1+\beta_{bc}}+\displaystyle\sum_{n=1}^{\infty}\left\{(1+\Lambda_{cb})[\tilde{\Phi}_n(z)+f_n(z)]+\frac{g_n(z)}{1-\beta_{cb}}\right\} & \text{in } S_c\end{cases} \tag{6a}$$

$$\Omega(z)=\begin{cases}\Omega_a^{\mathrm{I}}(z)=\displaystyle\sum_{n=1}^{\infty}\left[(1+\Pi_{ab})\Omega_n^{\mathrm{I}}(z)+\frac{e_n}{1+\beta_{ab}}\right] & \text{in } S_a\\ \Omega_b^{\mathrm{I}}(z)=\displaystyle\sum_{n=1}^{\infty}[\Omega_n^{\mathrm{I}}(z)+\tilde{\Omega}_n^{\mathrm{I}}(z)] & \text{in } S_b\\ \Omega_c^{\mathrm{II}}(z)=\Omega_0^{\mathrm{II}}(z)+\Lambda_{bc}\Phi_0(z)+\Lambda_{bc}d_0+\dfrac{e_0}{1-\beta_{bc}}+\displaystyle\sum_{n=1}^{\infty}\left[(1+\Pi_{cb})\tilde{\Omega}_n^{\mathrm{II}}(z)+\frac{g_n(z)}{1+\beta_{cb}}\right] & \text{in } S_c\end{cases} \tag{6b}$$

where the recurrence formulas for $\Phi_n(z)$, $\Omega_n^{\mathrm{I}}(z)$ (or equivalently $\Omega_n^{\mathrm{II}}(z)$), $\tilde{\Phi}_n(z)$, and $\tilde{\Omega}_n^{\mathrm{I}}(z)$ (or equivalently $\tilde{\Omega}_n^{\mathrm{II}}(z)$) ($n=1,2,\ldots$) are given, respectively, as

$$\Phi_{n+1}(z)=\begin{cases}(1+\Lambda_{bc})[\Phi_0(z)+d_0]+\dfrac{e_0}{1-\beta_{bc}} & (n=0)\\ \Pi_{cb}\tilde{\Omega}_n^{\mathrm{II}}(z)+f_n(z)+\dfrac{g_n(z)}{1+\beta_{cb}} & (n=1,2,\ldots)\end{cases} \tag{7a}$$

$$\Omega_{n+1}^{\mathrm{II}}(z)=\begin{cases}(1+\Pi_{bc})\Omega_0^{\mathrm{II}}(z)+\dfrac{e_0}{1+\beta_{bc}} & (n=0)\\ \Lambda_{cb}\tilde{\Phi}_n(z)+\Lambda_{cb}f_n(z)+\dfrac{g_n(z)}{1-\beta_{cb}} & (n=1,2,\ldots)\end{cases} \tag{7b}$$

$$\tilde{\Phi}_n(z)=\Pi_{ab}\Omega_n^{\mathrm{I}}(z)+d_n+\frac{e_n}{1+\beta_{ab}}\quad(n=1,2,\ldots) \tag{7c}$$

$$\tilde{\Omega}_n^{\mathrm{I}}(z)=\Lambda_{ab}\Phi_n(z)+\Lambda_{ab}d_n+\frac{e_n}{1-\beta_{ab}}\quad(n=1,2,\ldots) \tag{7d}$$

In Eqs. (6*a*), (6*b*), and (7*a*)–(7*d*), α_{ab} and β_{ab} are two nondimensional Dundurs parameters and Λ_{ab} and Π_{ab} are another pair of nondimensional parameters, of which the definitions are given in Eqs. (4) and (5), respectively, of Choi and Earmme [10]. It is worth noting that in Eqs. (6*a*), (6*b*), and (7*a*)–(7*d*) $\Omega_n^{\mathrm{I}}(z)$ and $\tilde{\Omega}_n^{\mathrm{I}}(z)$ can be transformed into $\Omega_n^{\mathrm{II}}(z)$ and $\tilde{\Omega}_n^{\mathrm{II}}(z)$, respectively, with Eq. (5), and vice versa. The unknown coefficients d_n and e_n ($n=0,1,2,\ldots$) and the unknown functions $f_n(z)$ and $g_n(z)$ ($n=1,2,\ldots$) are given as follows:

$$d_n=\begin{cases}-\dfrac{2\beta_{bc}}{1+\alpha_{bc}-2\beta_{bc}}\mathrm{Re}[\Phi_0(0)]+i\dfrac{2\alpha_{bc}}{1-\alpha_{bc}}\mathrm{Im}[\Phi_0(0)] & (n=0)\\ -\dfrac{2\beta_{ab}}{1+\alpha_{ab}-2\beta_{ab}}\mathrm{Re}[\Phi_n(0)]+i\dfrac{2\alpha_{ab}}{1-\alpha_{ab}}\mathrm{Im}[\Phi_n(0)] & (n=1,2,\ldots)\end{cases} \tag{8a}$$

$$e_n=\begin{cases}\dfrac{(1+\alpha_{bc})(3\beta_{bc}-\alpha_{bc})}{1+\alpha_{bc}-2\beta_{bc}}\mathrm{Re}[\Phi_0(0)]-i\dfrac{(\alpha_{bc}+\beta_{bc})(1+\alpha_{bc})}{1-\alpha_{bc}}\mathrm{Im}[\Phi_0(0)] & (n=0)\\ \dfrac{(1+\alpha_{ab})(3\beta_{ab}-\alpha_{ab})}{1+\alpha_{ab}-2\beta_{ab}}\mathrm{Re}[\Phi_n(0)]-i\dfrac{(\alpha_{ab}+\beta_{ab})(1+\alpha_{ab})}{1-\alpha_{ab}}\mathrm{Im}[\Phi_n(0)] & (n=1,2,\ldots)\end{cases} \tag{8b}$$

$$f_n(z)=\frac{(\alpha_{cb}-\beta_{cb})}{1-\alpha_{cb}+2\beta_{cb}}r_{\mathrm{II}}^2\,\mathrm{Re}(\xi_n)-i\frac{\alpha_{cb}-\beta_{cb}}{1+\alpha_{cb}}r_{\mathrm{II}}^2\,\mathrm{Im}(\xi_n)+\frac{(\alpha_{cb}-\beta_{cb})\zeta_n+(\alpha_{cb}+\beta_{cb})\bar{\varsigma}_n}{1-\alpha_{cb}}\frac{r_{\mathrm{II}}^2}{z}\quad(n=1,2,\ldots) \tag{9a}$$

$$g_n(z)=-(\alpha_{cb}-\beta_{cb})\left[\frac{1+\alpha_{cb}}{1-\alpha_{cb}+2\beta_{cb}}\mathrm{Re}(\xi_n)-i\,\mathrm{Im}(\xi_n)\right]r_{\mathrm{II}}^2-\frac{\alpha_{cb}+\beta_{cb}}{1-\alpha_{cb}}[(\alpha_{cb}-\beta_{cb})\zeta_n+(1+\beta_{cb})\bar{\varsigma}_n]\frac{r_{\mathrm{II}}^2}{z}\quad(n=1,2,\ldots) \tag{9b}$$

where ς_n, ζ_n, and ξ_n $(n=1,2,\ldots)$ are determined by

$$\varsigma_n \equiv \lim_{x\to 0}\frac{d}{dz}\left[\tilde{\bar{\Phi}}_n\left(\frac{r_{\mathrm{II}}^2}{z}\right)\right], \quad \zeta_n \equiv \lim_{x\to 0}\frac{d}{dz}\left[\tilde{\bar{\Psi}}_n\left(\frac{r_{\mathrm{II}}^2}{z}\right)\right], \quad (10)$$

$$\xi_n \equiv \lim_{x\to 0}\frac{1}{2}\frac{d^2}{dz^2}\left[\tilde{\bar{\Psi}}_n\left(\frac{r_{\mathrm{II}}^2}{z}\right)\right] \quad (n=1,2,\ldots)$$

Equations (6*a*) and (6*b*) together with Eqs. (7*a*)–(7*d*), (8*a*), (8*b*), (9*a*), (9*b*), and (10) are the complete solution for a singularity in region S_c interacting with a coated circular inclusion.

Case II: A Singularity Embedded in S_b. Similar to Case I, if a singularity is located in region S_b, the solution has the same form as that given in Eqs. (6*a*) and (6*b*) except for $\Phi_c(z)$ and $\Omega_c^{\mathrm{II}}(z)$ in the region S_c given as

$$\Phi_c(z) = (1+\Lambda_{cb})[\Phi_0(z)+f_0(z)] + \frac{g_0(z)}{1-\beta_{cb}} + \sum_{n=1}^{\infty}\left\{(1+\Lambda_{cb})[\tilde{\Phi}_n(z) + f_n(z)] + \frac{g_n(z)}{1-\beta_{cb}}\right\} \quad \text{in } S_c \quad (11a)$$

$$\Omega_c^{\mathrm{II}}(z) = (1+\Pi_{cb})\Omega_0^{\mathrm{II}}(z) + \frac{g_0(z)}{1+\beta_{cb}} + \sum_{n=1}^{\infty}\left[(1+\Pi_{cb})\tilde{\Omega}_n^{\mathrm{II}}(z) + \frac{g_n(z)}{1+\beta_{cb}}\right] \quad \text{in } S_c \quad (11b)$$

The recurrence formulas for $\Phi_n(z)$, $\Omega_n^{\mathrm{I}}(z)$ (or equivalently $\Omega_n^{\mathrm{II}}(z)$), $\tilde{\Phi}_n(z)$, and $\tilde{\Omega}_n^{\mathrm{I}}(z)$ (or equivalently $\tilde{\Omega}_n^{\mathrm{II}}(z)$) $(n=1,2,\ldots)$ have the same forms as those given in Eqs. (7*a*)–(7*d*) except for $\Phi_1(z)$ and $\Omega_1^{\mathrm{II}}(z)$ given as

$$\Phi_1(z) = \Phi_0(z) + \Pi_{cb}\Omega_0^{\mathrm{II}}(z) + f_0(z) + \frac{g_0(z)}{1+\beta_{cb}} \quad (12a)$$

$$\Omega_1^{\mathrm{II}}(z) = \Omega_0^{\mathrm{II}}(z) + \Lambda_{cb}\Phi_0(z) + \Lambda_{cb}f_0(z) + \frac{g_0(z)}{1-\beta_{cb}} \quad (12b)$$

The unknown coefficients d_n and e_n $(n=1,2,\ldots)$ and the unknown functions $f_n(z)$ and $g_n(z)$ $(n=1,2,\ldots)$ have the same forms as those given in Eqs. (8*a*), (8*b*), (9*a*), and (9*b*), respectively, in which ς_0, ζ_0, and ξ_0, respectively, are given as

$$\varsigma_0 \equiv \lim_{x\to 0}\frac{d}{dz}\left[\bar{\Phi}_0\left(\frac{r_{\mathrm{II}}^2}{z}\right)\right], \quad \zeta_0 \equiv \lim_{x\to 0}\frac{d}{dz}\left[\bar{\Psi}_0\left(\frac{r_{\mathrm{II}}^2}{z}\right)\right], \quad (13)$$

$$\xi_0 \equiv \lim_{x\to 0}\frac{1}{2}\frac{d^2}{dz^2}\left[\bar{\Psi}_0\left(\frac{r_{\mathrm{II}}^2}{z}\right)\right]$$

and ς_n, ζ_n, and ξ_n $(n=1,2,\ldots)$ have the same form as Eq. (10). For this Case II, the elastic constants in $\Phi_0(z)$ and $\Omega_0^{\mathrm{II}}(z)$ are for material b.

Case III: A Singularity Embedded in S_a. By the same argument as in Case I, the case in which a singularity is located in region S_a has the following solution:

$$\Phi(z) = \begin{cases} \Phi_0(z) + \Pi_{ab}\Omega_0^{\mathrm{I}}(z) + f_0(z) + \dfrac{g_0(z)}{1+\beta_{ba}} + \displaystyle\sum_{n=1}^{\infty}\left\{(1+\Lambda_{ab})[\tilde{\Phi}_n(z)+d_n] + \frac{e_n}{1-\beta_{ab}}\right\} & \text{in } S_a \\ \displaystyle\sum_{n=1}^{\infty}[\Phi_n(z)+\tilde{\Phi}_n(z)] & \text{in } S_b \\ \displaystyle\sum_{n=1}^{\infty}\left\{(1+\Lambda_{cb})[\Phi_n(z)+f_n(z)] + \frac{g_n(z)}{1-\beta_{cb}}\right\} & \text{in } S_c \end{cases} \quad (14a)$$

$$\Omega(z) = \begin{cases} \Omega_a^{\mathrm{I}}(z) = \Omega_0^{\mathrm{I}}(z) + \Lambda_{ba}\Phi_0(z) + \Lambda_{ba}f_0(z) + \dfrac{g_0(z)}{1-\beta_{ba}} + \displaystyle\sum_{n=1}^{\infty}\left[(1+\Pi_{ab})\tilde{\Omega}_n^{\mathrm{I}}(z) + \frac{e_n}{1+\beta_{ab}}\right] & \text{in } S_a \\ \Omega_b^{\mathrm{I}}(z) = \displaystyle\sum_{n=1}^{\infty}[\Omega_n^{\mathrm{I}}(z)+\tilde{\Omega}_n^{\mathrm{I}}(z)] & \text{in } S_b \\ \Omega_c^{\mathrm{II}}(z) = \displaystyle\sum_{n=1}^{\infty}\left[(1+\Pi_{cb})\Omega_n^{\mathrm{II}}(z) + \frac{g_n(z)}{1+\beta_{cb}}\right] & \text{in } S_c \end{cases} \quad (14b)$$

where the recurrence formulas for $\Phi_n(z)$, $\Omega_n^{\mathrm{I}}(z)$ (or equivalently $\Omega_n^{\mathrm{II}}(z)$), $\tilde{\Phi}_n(z)$, and $\tilde{\Omega}_n^{\mathrm{I}}(z)$ (or equivalently $\tilde{\Omega}_n^{\mathrm{II}}(z)$), respectively, are given as

$$\Phi_{n+1}(z) = \begin{cases} (1+\Lambda_{ba})[\Phi_0(z)+f_0(z)] + \dfrac{g_0(z)}{1-\beta_{ba}} & (n=0) \\ \Pi_{ab}\tilde{\Omega}_n^{\mathrm{I}}(z) + d_n + \dfrac{e_n}{1+\beta_{ab}} & (n=1,2,\ldots) \end{cases} \quad (15a)$$

$$\Omega_{n+1}^{\mathrm{II}}(z) = \begin{cases} (1+\Pi_{ba})\Omega_0^{\mathrm{II}}(z) + \dfrac{g_0(z)}{1+\beta_{ba}} & (n=0) \\ \Lambda_{ab}\tilde{\Phi}_n(z) + \Lambda_{ab}d_n + \dfrac{e_n}{1-\beta_{ab}} & (n=1,2,\ldots) \end{cases} \quad (15b)$$

$$\tilde{\Phi}_n(z) = \Pi_{cb}\Omega_n^{\mathrm{II}}(z) + f_n(z) + \frac{g_n(z)}{1+\beta_{cb}} \quad (n=1,2,\ldots) \quad (15c)$$

$$\tilde{\Omega}_n^{\mathrm{II}}(z) = \Lambda_{cb}\Phi_n(z) + \Lambda_{cb}f_n(z) + \frac{g_n(z)}{1-\beta_{cb}} \quad (n=1,2,\ldots) \quad (15d)$$

The unknown coefficients d_n and e_n and the unknown functions $f_n(z)$ and $g_n(z)$ are as follows:

$$d_n = -\frac{2\beta_{ab}}{1+\alpha_{ab}-2\beta_{ab}}\,\mathrm{Re}[\tilde{\Phi}_n(0)] + i\frac{2\alpha_{ab}}{1-\alpha_{ab}}\,\mathrm{Im}[\tilde{\Phi}_n(0)] \quad (n=1,2,\ldots) \tag{16a}$$

$$e_n = \frac{(1+\alpha_{ab})(3\beta_{ab}-\alpha_{ab})}{1+\alpha_{ab}-2\beta_{ab}}\,\mathrm{Re}[\tilde{\Phi}_n(0)] - i\frac{(\alpha_{ab}+\beta_{ab})(1+\alpha_{ab})}{1-\alpha_{ab}}\,\mathrm{Im}[\tilde{\Phi}_n(0)] \quad (n=1,2,\ldots) \tag{16b}$$

$$f_n(z) = \begin{cases} \dfrac{(\alpha_{ba}-\beta_{ba})}{1-\alpha_{ba}+2\beta_{ba}} r_{\mathrm{I}}^2\,\mathrm{Re}(\xi_0) - i\dfrac{\alpha_{ba}-\beta_{ba}}{1+\alpha_{ba}} r_{\mathrm{I}}^2\,\mathrm{Im}(\xi_0) + \dfrac{(\alpha_{ba}-\beta_{ba})\zeta_0 + (\alpha_{ba}+\beta_{ba})\bar{\varsigma}_0}{1-\alpha_{ba}}\dfrac{r_{\mathrm{I}}^2}{z} & (n=0) \\ \dfrac{(\alpha_{cb}-\beta_{cb})}{1-\alpha_{cb}+2\beta_{cb}} r_{\mathrm{II}}^2\,\mathrm{Re}(\xi_n) - i\dfrac{\alpha_{cb}-\beta_{cb}}{1+\alpha_{cb}} r_{\mathrm{II}}^2\,\mathrm{Im}(\xi_n) + \dfrac{(\alpha_{cb}-\beta_{cb})\zeta_n + (\alpha_{cb}+\beta_{cb})\bar{\varsigma}_n}{1-\alpha_{cb}}\dfrac{r_{\mathrm{II}}^2}{z} & (n=1,2,\ldots) \end{cases} \tag{17a}$$

$$g_n(z) = \begin{cases} -(\alpha_{ba}-\beta_{ba})\left[\dfrac{1+\alpha_{ba}}{1-\alpha_{ba}+2\beta_{ba}}\,\mathrm{Re}(\xi_0) - i\,\mathrm{Im}(\xi_0)\right] r_{\mathrm{I}}^2 - \dfrac{\alpha_{ba}+\beta_{ba}}{1-\alpha_{ba}}[(\alpha_{ba}-\beta_{ba})\zeta_0 + (1+\beta_{ba})\bar{\varsigma}_0]\dfrac{r_{\mathrm{I}}^2}{z} & (n=0) \\ -(\alpha_{cb}-\beta_{cb})\left[\dfrac{1+\alpha_{cb}}{1-\alpha_{cb}+2\beta_{cb}}\,\mathrm{Re}(\xi_n) - i\,\mathrm{Im}(\xi_n)\right] r_{\mathrm{II}}^2 - \dfrac{\alpha_{cb}+\beta_{cb}}{1-\alpha_{cb}}[(\alpha_{cb}-\beta_{cb})\zeta_n + (1+\beta_{cb})\bar{\varsigma}_n]\dfrac{r_{\mathrm{II}}^2}{z} & (n=1,2,\ldots) \end{cases} \tag{17b}$$

$$\varsigma_0 \equiv \lim_{x\to 0}\frac{d}{dz}\left[\bar{\Phi}_0\left(\frac{r_{\mathrm{I}}^2}{z}\right)\right], \quad \zeta_0 \equiv \lim_{x\to 0}\frac{d}{dz}\left[\bar{\Psi}_0\left(\frac{r_{\mathrm{I}}^2}{z}\right)\right], \tag{18a}$$

$$\xi_0 \equiv \lim_{x\to 0}\frac{1}{2}\frac{d^2}{dz^2}\left[\bar{\Psi}_0\left(\frac{r_{\mathrm{I}}^2}{z}\right)\right]$$

$$\varsigma_n \equiv \lim_{x\to 0}\frac{d}{dz}\left[\bar{\Phi}_n\left(\frac{r_{\mathrm{II}}^2}{z}\right)\right], \quad \zeta_n \equiv \lim_{x\to 0}\frac{d}{dz}\left[\bar{\Psi}_n\left(\frac{r_{\mathrm{II}}^2}{z}\right)\right], \tag{18b}$$

$$\xi_n \equiv \lim_{x\to 0}\frac{1}{2}\frac{d^2}{dz^2}\left[\bar{\Psi}_n\left(\frac{r_{\mathrm{II}}^2}{z}\right)\right], \quad (n=1,2,\ldots)$$

Equations (14*a*) and (14*b*) with Eqs. (15*a*)–(15*d*), (16*a*), (16*b*), (17*a*), (17*b*), (18*a*), and (18*b*) are the complete solution for a singularity in region S_a. Here, the elastic constants in $\Phi_0(z)$ and $\Omega_0^{\mathrm{I}}(z)$ are for material *a*.

In conclusion, a unified approach to the problem of singularities interacting with a coated circular inclusion is developed, in which the method of analytic continuation is alternatively applied to two concentric circular interfaces. A homogeneous solution for singularities serves as a building block for deriving a solution for the same singularities interacting with a coated circular inclusion in a series form. The obtained solutions do not depend on any specific information about singularities, and thus they can be interpreted as general solutions for a variety of singularities.

References

[1] Luo, H. A., and Chen, Y., 1991, "An Edge Dislocation in a Three-Phase Composite Cylinder Model," ASME J. Appl. Mech., **58**, pp. 75–86.

[2] Qaissaunee, M. T., and Santare, M. H., 1995, "Edge Dislocation Interacting With an Elliptical Inclusion Surrounded by an Interfacial Zone," Q. J. Mech. Appl. Math., **48**, pp. 465–482.

[3] Xiao, Z. M., and Chen, B. J., 2000, "A Screw Dislocation Interacting With a Coated Fiber," Mech. Mater., **32**, pp. 485–494.

[4] Liu, Y. W., Jiang, C. P., and Cheung, Y. K., 2003, "A Screw Dislocation Interacting With an Interphase Layer Between a Circular Inhomogeneity and the Matrix," Int. J. Eng. Sci., **41**, pp. 1883–1898.

[5] Chao, C. K., Chen, F. M., and Shen, M. H., 2006, "Circularly Cylindrical Layered Media in Plane Elasticity," Int. J. Solids Struct., **43**, pp. 4739–4756.

[6] Suo, Z., 1989, "Singularities Interacting With Interfaces and Cracks," Int. J. Solids Struct., **25**, pp. 1133–1142.

[7] Lee, K. W., Choi, S. T., and Earmme, Y. Y., 1999, "A Circular Inhomogeneity Problem Revisited," ASME J. Appl. Mech., **66**, pp. 276–278.

[8] Sokolnikoff, I. S., 1956, *Mathematical Theory of Elasticity*, McGraw-Hill, New York, pp. 318–326.

[9] Choi, S. T., and Earmme, Y. Y., 2002, "Elastic Study on Singularities Interacting With Interfaces Using Alternating Technique: Part I. Anisotropic Trimaterial," Int. J. Solids Struct., **39**, pp. 943–957.

[10] Choi, S. T., and Earmme, Y. Y., 2002, "Elastic Study on Singularities Interacting With Interfaces Using an Alternating Technique: Part II. Isotropic Trimaterial," Int. J. Solids Struct., **39**, pp. 1199–1211.

[11] Muskhelishvili, N. I., 1953, *Some Basic Problems of the Mathematical Theory of Elasticity*, Noordhoff, Groningen, pp. 105–175.

Erratum: "Application of Miniature Ring-Core and Interferometric Strain/Slope Rosette to Determine Residual Stress Distribution With Depth—Part I: Theories" [Journal of Applied Mechanics, 2007, 74(2), pp. 298–306]

Keyu Li and Wei Ren

In "References," the titles of the journals "Adv. Comput. Math.," "Exp. Tech.," and "Opt Laser Technol." were mistakenly printed and must be corrected as follows:

Ref. [6] Adv. Composite Mater.
Ref. [9] Exp. Mech.
Ref. [10] Exp. Mech.
Ref. [13] Exp. Mech.
Ref. [14] Opt. Lasers Eng.

Erratum: "Electrostatic Forces and Stored Energy for Deformable Dielectric Materials" [Journal of Applied Mechanics, 2005, 72(4), pp. 581–590]

Robert M. McMeeking and Chad M. Landis

In this Erratum we point out and correct an omission of an important term in Eq. (8) of our original paper. This equation was a statement of the conservation of angular momentum and we inadvertently omitted the electrical body couple term that is needed in this momentum balance. In Eq. (9) the electrical body force components b_i^E are defined. A similar equation is needed to define the electrical body couple as

$$c_i^E = \epsilon_{ijk}\sigma_{jk}^M$$

Then, the correct statement of the balance of angular momentum and its analysis is given as

$$\int_V c_i^E dV + \int_V \epsilon_{ijk}x_j(b_k + b_k^E)dV + \int_S \epsilon_{ijk}x_j(T_k + T_k^E)dS = \frac{d}{dt}\int_V \rho\epsilon_{ijk}x_j v_k dV,$$

$$\int_V \epsilon_{ijk}\sigma_{jk}^M dV + \int_V \epsilon_{ijk}x_j(b_k + b_k^E)dV + \int_S \epsilon_{ijk}x_j\sigma_{lk}n_l dS = \int_V \rho\epsilon_{ijk}\frac{dx_j}{dt}v_k + \rho\epsilon_{ijk}x_j\frac{dv_k}{dt} + \underbrace{\frac{d\rho}{dt}\epsilon_{ijk}x_j v_k + \rho v_{l,l}\epsilon_{ijk}x_j v_k}_{\frac{d\rho}{dt}+\rho v_{l,l}=0} dV,$$

$$\int_V \epsilon_{ijk}\sigma_{jk}^M dV + \int_V \epsilon_{ijk}x_j(b_k + b_k^E)dV + \int_V \epsilon_{ijk}x_j\sigma_{lk,l} + \epsilon_{ijk}x_{j,l}\sigma_{lk}dV = \int_V \underbrace{\rho\epsilon_{ijk}v_j v_k}_{0} + \rho\epsilon_{ijk}x_j\frac{dv_k}{dt}dV,$$

$$\int_V \epsilon_{ijk}\sigma_{jk}^M dV + \int_V \epsilon_{ijk}x_j\underbrace{\left(\sigma_{lk,l} + b_k + b_k^E - \rho\frac{dv_k}{dt}\right)}_{0}dV + \int_V \epsilon_{ijk}\delta_{jl}\sigma_{lk}dV = 0,$$

$$\int_V \epsilon_{ijk}(\sigma_{jk} + \sigma_{jk}^M)dV = 0$$

The result of this analysis appears in Eq. (13) of the original manuscript as

$$\sigma_{ji} + \sigma_{ji}^M = \sigma_{ij} + \sigma_{ij}^M$$

Note that Eq. (13) does not follow from the original Eq. (8), but does follow from this corrected version. Hence, Eq. (13) and all of the remaining equations within the original manuscript are correct.

